

Kathrin Schulte  
Cameron Tropea  
Bernhard Weigand *Editors*

# Droplet Dynamics Under Extreme Ambient Conditions

OPEN ACCESS



Springer

# **Fluid Mechanics and Its Applications**

## **Founding Editor**

René Moreau

Volume 124

## **Series Editor**

André Thess, German Aerospace Center, Institute of Engineering  
Thermodynamics, Stuttgart, Germany

The purpose of this series is to focus on subjects in which fluid mechanics plays a fundamental role. As well as the more traditional applications of aeronautics, hydraulics, heat and mass transfer etc., books will be published dealing with topics, which are currently in a state of rapid development, such as turbulence, suspensions and multiphase fluids, super and hypersonic flows and numerical modelling techniques. It is a widely held view that it is the interdisciplinary subjects that will receive intense scientific attention, bringing them to the forefront of technological advancement. Fluids have the ability to transport matter and its properties as well as transmit force, therefore fluid mechanics is a subject that is particularly open to cross fertilisation with other sciences and disciplines of engineering. The subject of fluid mechanics will be highly relevant in such domains as chemical, metallurgical, biological and ecological engineering. This series is particularly open to such new multidisciplinary domains. The median level of presentation is the first year graduate student. Some texts are monographs defining the current state of a field; others are accessible to final year undergraduates; but essentially the emphasis is on readability and clarity.

**Springer and Professor Thess welcome book ideas from authors. Potential authors who wish to submit a book proposal should contact Dr. Mayra Castro, Senior Editor, Springer Heidelberg, e-mail: [mayra.castro@springer.com](mailto:mayra.castro@springer.com)**

Indexed by SCOPUS, EBSCO Discovery Service, OCLC, ProQuest Summon, Google Scholar and SpringerLink

Kathrin Schulte · Cameron Tropea ·  
Bernhard Weigand  
Editors

# Droplet Dynamics Under Extreme Ambient Conditions



Springer

*Editors*

Kathrin Schulte  
Institute of Aerospace Thermodynamics  
University of Stuttgart  
Stuttgart, Germany

Cameron Tropea  
Fluid Dynamics and Aerodynamics  
Technical University of Darmstadt  
Darmstadt, Germany

Bernhard Weigand  
Institute of Aerospace Thermodynamics  
University of Stuttgart  
Stuttgart, Germany



ISSN 0926-5112

ISSN 2215-0056 (electronic)

Fluid Mechanics and Its Applications

ISBN 978-3-031-09007-3

ISBN 978-3-031-09008-0 (eBook)

<https://doi.org/10.1007/978-3-031-09008-0>

© The Editor(s) (if applicable) and The Author(s) 2022. This book is an open access publication.

**Open Access** This book is licensed under the terms of the Creative Commons Attribution 4.0 International License (<http://creativecommons.org/licenses/by/4.0/>), which permits use, sharing, adaptation, distribution and reproduction in any medium or format, as long as you give appropriate credit to the original author(s) and the source, provide a link to the Creative Commons license and indicate if changes were made.

The images or other third party material in this book are included in the book's Creative Commons license, unless indicated otherwise in a credit line to the material. If material is not included in the book's Creative Commons license and your intended use is not permitted by statutory regulation or exceeds the permitted use, you will need to obtain permission directly from the copyright holder.

The use of general descriptive names, registered names, trademarks, service marks, etc. in this publication does not imply, even in the absence of a specific statement, that such names are exempt from the relevant protective laws and regulations and therefore free for general use.

The publisher, the authors, and the editors are safe to assume that the advice and information in this book are believed to be true and accurate at the date of publication. Neither the publisher nor the authors or the editors give a warranty, expressed or implied, with respect to the material contained herein or for any errors or omissions that may have been made. The publisher remains neutral with regard to jurisdictional claims in published maps and institutional affiliations.

This Springer imprint is published by the registered company Springer Nature Switzerland AG  
The registered company address is: Gewerbestrasse 11, 6330 Cham, Switzerland

# Preface

This book summarizes the main results of the Collaborative Research Center Trans-regio 75 (SFB-TRR 75), which was funded by the German Research Foundation (DFG) from January 2010 to June 2022.

The overall goal of the SFB-TRR 75 was to improve the understanding of fundamental droplet processes, especially those occurring under extreme ambient conditions. These include, for example, near-critical thermodynamic conditions, very low temperatures, strong electric fields, or extreme gradients of boundary conditions. This goal was achieved through close collaboration between scientists from the University of Stuttgart, the Technical University of Darmstadt, the Technical University of Berlin, and the German Aerospace Center (DLR) in Lampoldshausen from the fields of thermodynamics, fluid mechanics, mathematics, computer science, electrical engineering, and visualization. Accompanied by experimental studies, they developed new analytical and numerical descriptions that are prerequisites for the prediction and optimization of technical systems with droplets and sprays as well as for the prediction of droplet-related occurrences in nature.

The focus evolved throughout the project from the consideration of small systems with single droplets, to droplet interactions and to more complex fluid systems.

All members of the SFB-TRR 75 are very grateful for the financial support and guidance from the German Research Foundation during the project period (project number 84292822).

Stuttgart, Germany  
Darmstadt, Germany  
Stuttgart, Germany  
November 2021

Kathrin Schulte  
Cameron Tropea  
Bernhard Weigand

# Contents

<b>Collaborative Research on Droplet Dynamics Under Extreme Ambient Conditions .....</b>	1
Bernhard Weigand, Kathrin Schulte, Andreas Dreizler, Claus-Dieter Munz, and Cameron Tropea	
<b>Interactive Visualization of Droplet Dynamic Processes .....</b>	29
Moritz Heinemann, Filip Sadlo, and Thomas Ertl	
<b>Development of Numerical Methods for the Simulation of Compressible Droplet Dynamics Under Extreme Ambient Conditions .....</b>	47
Steven Jöns, Stefan Fechter, Timon Hitz, and Claus-Dieter Munz	
<b>Analysis and Numerics of Sharp and Diffuse Interface Models for Droplet Dynamics .....</b>	67
Jim Magiera and Christian Rohde	
<b>Stopping Droplet Rebound with Polymer Additives: A Molecular Viewpoint .....</b>	87
Eunsang Lee, Hari Krishna Chilukoti, and Florian Müller-Plathe	
<b>Modelling of Droplet Dynamics in Strong Electric Fields .....</b>	107
Erion Gjonaj, Yun Ouedraogo, and Sebastian Schöps	
<b>Modelling and Numerical Simulation of Binary Droplet Collisions Under Extreme Conditions .....</b>	127
Johanna Potyka, Johannes Kromer, Muyuan Liu, Kathrin Schulte, and Dieter Bothe	
<b>Investigation of the Behaviour of Supercooled Droplets Concerning Evaporation, Sublimation and Freezing Under Different Boundary Conditions .....</b>	149
Jonathan Reutzsch, Verena Kunberger, Martin Reitzle, Stefano Ruberto, and Bernhard Weigand	

<b>Experimental Investigations of Near-critical Fluid Phenomena by the Application of Laser Diagnostic Methods .....</b>	169
Grazia Lamanna, Christoph Steinhause, Andreas Preusche, and Andreas Dreizler	
<b>Modeling and Simulation of a Turbulent Multi-component Two-phase Flow Involving Phase Change Processes Under Supercritical Conditions .....</b>	189
Dennis Kuetemeier and Amsini Sadiki	
<b>Experimental Investigation of Transient Injection Phenomena in Rocket Combusters at Vacuum with Cryogenic Flash Boiling .....</b>	211
Andreas Rees and Michael Oschwald	
<b>Modelling and Simulation of Flash Evaporation of Cryogenic Liquids .....</b>	233
Jan Wilhelm Gärtnner, Daniel D. Loureiro, and Andreas Kronenburg	
<b>Mass Transport Across Droplet Interfaces by Atomistic Simulations ...</b>	251
Matthias Heinen, Simon Homes, Gabriela Guevara-Carrion, and Jadran Vrabec	
<b>Numerical Simulation of Heat Transfer and Evaporation During Impingement of Drops onto a Heated Wall .....</b>	269
Henrik Sontheimer, Christiane Schlawitschek, Stefan Batzdorf, Peter Stephan, and Tatiana Gambaryan-Roisman	
<b>High Resolution Measurements of Heat Transfer During Drop Impingement onto a Heated Wall .....</b>	291
Alireza Gholijani, Sebastian Fischer, Tatiana Gambaryan-Roisman, and Peter Stephan	
<b>Impact of Supercooled Drops onto Cold Surfaces .....</b>	311
Mark Gloerfeld, Markus Schremb, Antonio Criscione, Suad Jakirlic, and Cameron Tropea	
<b>Interaction of Drops and Sprays with a Heated Wall .....</b>	333
Johannes Benedikt Schmidt, Jan Breitenbach, Ilia V. Roisman, and Cameron Tropea	
<b>Mechanical and Electrical Phenomena of Droplets Under the Influence of High Electric Fields .....</b>	355
Jens-Michael Löwe, Michael Kempf, and Volker Hinrichsen	

# Collaborative Research on Droplet Dynamics Under Extreme Ambient Conditions



Bernhard Weigand, Kathrin Schulte, Andreas Dreizler, Claus-Dieter Munz, and Cameron Tropea

**Abstract** A fundamental understanding of droplet dynamics is important for the prediction and optimization of technical systems involving drops and sprays. The Collaborative Research Center (CRC) SFB-TRR 75 was established in January 2010 to focus on the dynamics of basic drop processes, and in particular on processes involving extreme ambient conditions, for example near thermodynamic critical conditions, at very low temperatures, under the influence of strong electric fields, or in situations involving extreme gradients of the boundary conditions. The goal of the CRC was to gain a profound physical understanding of the essential processes, which is the basis for new analytical and numerical descriptions as well as for improved predictive capabilities. This joint initiative involved scientists at the University of Stuttgart, the TU Darmstadt, the TU Berlin, and the German Aerospace Center (DLR) in Lampoldshausen. This first chapter provides a brief overview of the overall structure of this CRC as well as a summary of some selected scientific achievements of the subprojects involved. For further details the reader is referred to the subsequent chapters of this book related to the individual subprojects.

---

B. Weigand (✉) · K. Schulte

Institute of Aerospace Thermodynamics, University of Stuttgart, Stuttgart, Germany  
e-mail: [bernhard.weigand@itlr.uni-stuttgart.de](mailto:bernhard.weigand@itlr.uni-stuttgart.de)

K. Schulte

e-mail: [kathrin.schulte@itlr.uni-stuttgart.de](mailto:kathrin.schulte@itlr.uni-stuttgart.de)

A. Dreizler

Reactive Flows and Diagnostics, Darmstadt, Technical University Darmstadt, Darmstadt, Germany  
e-mail: [dreizler@rsm.tu-darmstadt.de](mailto:dreizler@rsm.tu-darmstadt.de)

C.-D. Munz

Institute of Aerodynamics and Gas Dynamics, University of Stuttgart, Stuttgart, Germany  
e-mail: [munz@iag.uni-stuttgart.de](mailto:munz@iag.uni-stuttgart.de)

C. Tropea

Institute of Fluid Mechanics and Aerodynamics, Technical University Darmstadt, Darmstadt, Germany  
e-mail: [tropea@sla.tu-darmstadt.de](mailto:tropea@sla.tu-darmstadt.de)

## 1 Introduction

Many processes in nature and technology are influenced by droplet dynamics. These include ubiquitous phenomena and applications, such as rain clouds or fuel injection into combustion chambers, but also highly advanced devices such as rocket engines or spray based production processes in the pharmaceutical industry. Due to their omnipresence, droplets have been the focus of scientific interest for a long time: Plateau [34] and Lord Rayleigh [38] for example studied the generation of droplets from liquid jets under the influence of surface tension in the 19th century. The books of Pruppacher and Klett [37] and of Lefebvre [23] can be seen as seminal works in the field of droplets in nature or engineering, respectively. While there are many scientific results available about droplet processes in complex systems, they are often restricted to moderate ambient conditions. However, many processes take place under extreme ambient conditions. This holds for the near critical or supercritical conditions in modern combustion engines as well as for thunderstorm clouds with their high electric fields or supercooled droplets impinging on airplane wings, to name just a few examples. Much less research has been conducted in these areas, which is due to the increased effort in theoretical and numerical modelling or the necessary complexity of experimental equipment. Therefore, detailed research in this area not only demands extensive methodological development or improvement of experimental techniques and numerical models, but also very close interaction between numerical and experimental research. Thus, the consequential involvement of expertise from fields like thermodynamics, fluid mechanics, mathematics, computer sciences, electrical engineering and visualization is required. The SFB-TRR 75 combined the knowledge and expertise of scientists from all the above-mentioned disciplines. The multitude of thermodynamic processes with droplets under extreme ambient conditions can be divided into a few classes: The CRC set itself the goal of investigating the following extreme ambient conditions in droplet dynamic processes in more detail:

- Droplets near the critical point and at high pressures
- Droplets in strong force fields (e.g. electric fields)
- Droplets at extreme temperatures in thermodynamic non-equilibrium
- Droplet processes with extreme gradients (e.g. at the three-phase contact line)

According to the basic insight that complex droplet dynamic processes can be determined by the interaction of numerous elementary processes, the CRC concentrated since 2010 on illuminating the physics behind such basic processes in a generic manner. In order to give these rather abstract extreme ambient conditions a concrete reference to individual processes and systems, the investigations within this CRC have been carried out in connection with selected guiding examples. These guiding examples are:

1. Phase transition of supercooled and potentially electrically charged droplets in clouds
2. Impact of supercooled large droplets on aircraft components

3. Behaviour of water droplets on insulating surfaces in high voltage power transmission systems
4. Behaviour of droplets in rocket combustion chambers
5. Behaviour of fuel sprays in future combustion systems

In each of these guiding examples, one or more processes under extreme ambient conditions can be observed. Selected results of the work in the SFB-TRR 75 are summarized in [54, 55, 57, 58]. The CRC comprises 18 subprojects in three research areas, which are listed below together with the individual principle investigators of the subprojects:

#### Research Area A: Methods and Fundamentals

- SP-A1: Interactive visualization of droplet dynamic processes (T. Ertl)
- SP-A2: Development of numerical methods for the simulation of compressible droplet dynamic processes under extreme conditions (C.-D. Munz)
- SP-A3: Analysis and numerical simulations of front and phase field models for droplet dynamics (C. Rohde)
- SP-A4: Molecular dynamics simulation of droplet evaporation in the non-linear response regime (F. Müller-Plathe)
- SP-A5: Simulation of the mechanical deformation and movement of droplets under the influence of strong electric fields (E. Gjonaj, S. Schöps)
- SP-A7: Modelling and simulation of droplet collisions at modified ambient pressures, with high velocity and concentration gradients and for immiscible fluids (D. Bothe, K. Schulte)

#### Research Area B: Free Droplets

- SP-B1: Investigation of the behaviour of supercooled droplets concerning evaporation, condensation and freezing at different boundary conditions (B. Weigand)
- SP-B2: Experimental investigation of droplet evaporation under extreme conditions using temporally highly resolved laser diagnostic methods (G. Lamanna, A. Dreizler)
- SP-B3: Modelling and simulation of droplet evaporation in different gas environments under supercritical conditions (A. Sadiki)
- SP-B4: Experimental investigation of transient injection phenomena in rocket combustors at vacuum conditions with flash evaporation (M. Oschwald)
- SP-B5: Modelling and simulation of the flash evaporation of cryogenic liquids (A. Kronenburg)
- SP-B6: Droplets subjected to temperature and velocity gradients using atomistic simulations (J. Vrabec)

#### Research Area C: Droplets with Wall-Interactions

- SP-C1: Numerical simulation of the transport processes during drop impingement onto heated walls with special consideration of the evaporating three-phase contact line (T. Gambaryan-Roisman, P. Stephan)

- SP-C2: Highly resolved measurements of heat transfer during drop impingement onto a heated wall with particular consideration of evaporation at the three phase contact line (P. Stephan, T. Gambaryan-Roisman)
- SP-C3: Impact of supercooled droplets onto cold surfaces (S. Jakirlic, C. Tropea)
- SP-C4: Interaction of a single drop with a heated wall at high ambient pressures (I.V. Roisman, C. Tropea)
- SP-C5: Mechanical and electrical phenomena of droplets under the influence of high electric fields (V. Hinrichsen)
- SP-Z: Administration of the SFB-TRR 75 (B. Weigand)

The declared goal of the SFB-TRR 75 was to gain a deeper physical understanding of processes with droplets under extreme ambient conditions. Based on this, methods to describe them experimentally, analytically and/or numerically have been identified and implemented. The better understanding of the basic underlying processes enables more precise predictions of their behaviour and dynamics and, thus, also an improvement of the prediction of processes in larger and more complex systems in nature or in engineering applications.

## 2 Research Area A: Methods and Fundamentals

Many challenges exist in multiphase flows under extreme ambient conditions. There are not only open questions in engineering applications, but also in the fundamental physical, mathematical and numerical modelling. Projects to address these challenges with respect to methods and fundamental tools were combined together in Research Area A. Numerical and analytical methods were developed, which were prerequisites for conducting the work in the other research areas. The topics in Research Area A have been linked to the three main areas:

- Numerical methods for the direct numerical simulation of droplet dynamics
- Thermodynamic modelling of surface phenomena
- Visualization

### 2.1 *Numerical Methods for the Direct Numerical Simulation of Droplet Dynamics*

The improvement and extension of the mathematical and numerical modelling of multiphase interfaces were the focus of subprojects in Research Area A. The development of simulation tools for the direct numerical simulation of droplets in the fully compressible regime was the objective in SP-A2 and SP-A3.

To emphasize the consistency of the thermodynamic and hydrodynamic modelling, a sharp interface approximation of the phase transition front was applied in SP-A2 (see Jöns et al. [in this volume](#)). The phase interface is considered as a discontinuity in the macroscopic continuum equations. Direct numerical simulations of flows with droplets require several components for the simulation tool: A solver for compressible multicomponent flows with an equation of state for real fluids, methods for coupling the different fluids and algorithms for tracking the material or phase boundaries. In SP-A2 the sharp interface coupling is based on the ghost fluid method and on the solution of the multiphase Riemann problem [8]. The tracking of the material boundary is performed by a level-set approach. Level-set and the flow equations are all calculated with a discontinuous Galerkin method, in which locally the resolution can be improved by h-p adaptation. The thermodynamical modelling for the two-phase flow scenarios in a high pressure and temperature environment was considered in [9]. Phase transition effects are included by the solution of the two-phase Riemann problem at the interface, supplemented by a phase transition model based on classical irreversible thermodynamics. An exact as well as an approximate Riemann solver were constructed. Numerical results compared to molecular dynamics data for evaporation in a shock tube and steady state evaporation exhibited a good agreement with the reference data from molecular dynamics, see [15, 16]. Figure 1 shows the distribution of the velocity magnitude for a 2D shock-/drop interaction, where the interface is depicted by a white line.

The modelling of liquid–vapour flow with phase transition requires accurate physical and mathematical models and the implementation into efficient numerical methods and programs. In SP-A3 (see Magiera and Rohde [in this volume](#)), compressible models for the dynamics of single droplets and droplet ensembles were developed and studied analytically and numerically. Both, a sharp interface approach and a diffuse interface approach were considered. There was a close cooperation between SP-A2 and SP-A3, with the focus on the numerical modelling and application and into the mathematical foundations, respectively (see [8, 17]). Analytical Riemann solvers for basic isothermal two-phase flow scenarios were developed in SP-A3. For complex thermodynamical settings, an interface solver was constructed based

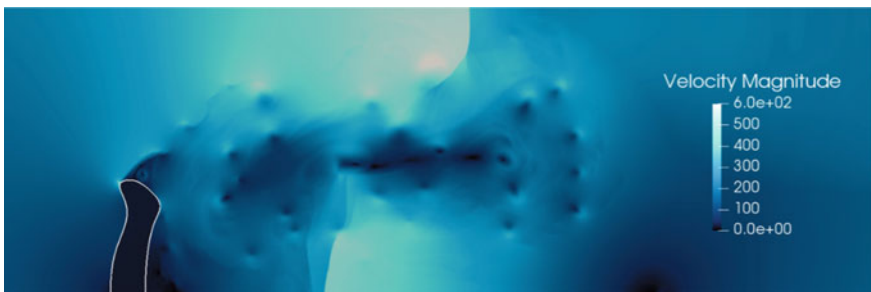


**Fig. 1** Velocity magnitude distribution of a 2D shock-/drop interaction. The phase interface is depicted in white

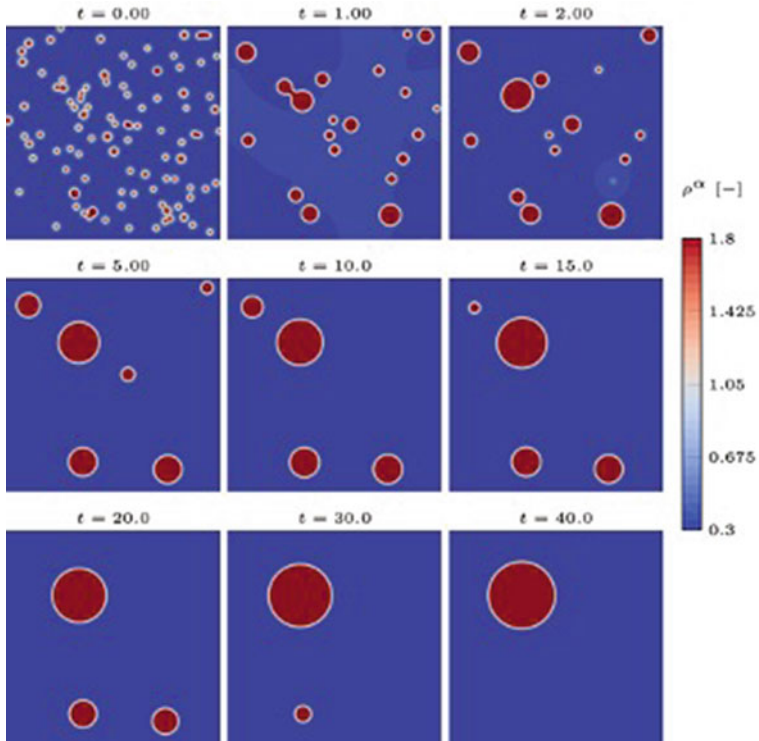


**Fig. 2** Evolution of a droplet ensemble and trend to (spherical) equilibrium. (*Source* [17], reprinted with permission from Elsevier under No. 5039260334246.)

on molecular dynamics simulations [17]. It was shown to be even applicable for two-phase flows with multiple components. To understand merging and splitting phenomena for droplet ensembles, diffuse interface models were considered [30]. For the Navier–Stokes–Korteweg systems variants, numerical schemes were developed by reformulating the capillarity operator by a relaxation procedure such that the hyperbolicity of the full set of equations are recovered. Figure 2 shows the evolution of a group of droplets towards a single large droplet by coalescence [28].

In the subproject SP-A5 (see Gjonaj et al. [in this volume](#)) droplet dynamics in strong electric fields has been investigated numerically by means of an electrohydrodynamic (EHD) simulation model [33]. The fluid flow is in the incompressible regime and has been simulated via OpenFOAM, coupled to an electro-quasi-static field computation based on the charge conservation equation. This coupling allows the charge convection and relaxation phenomena to be included in the simulations, which are typical for droplet and spray processes. Furthermore, the model contains a detailed description of contact angle dynamics for capillary flows in the presence of electric fields and charges. One class of applications was the simulation of oscillating droplets on the surface of high voltage insulators. For this investigation, there was

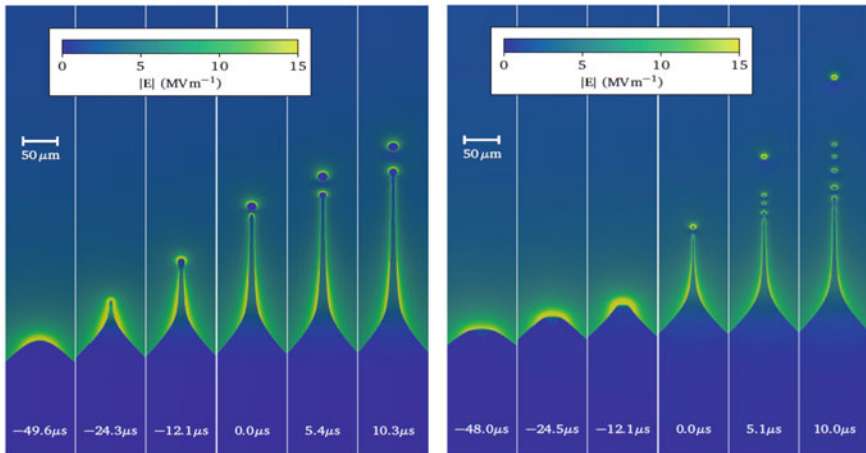


**Fig. 3** Onset of electrospray from a sessile droplet shown at different time instants. The colour map depicts electric field strength. Left: methanol. Right: a heptane mixture. The electrical conductivity of the heptane mixture is chosen to be nearly one order of magnitude smaller than that of methanol. Adapted figure with permission from [32], Copyright 2020 by the IEEE

close cooperation between SP-A5 and SP-C5 focusing on the experimental validation of simulation results obtained with the EHD model. The contact angle characteristics resulting from this analysis provide the basic measure for the estimation of the inception field thresholds for electrical discharges occurring on the insulation layer of high voltage devices [31]. The second class of applications was the numerical characterization of electrosprays. Extensive electrospray simulations for various liquids with different electrical and mechanical properties provided quantitative insights into the electrospray dynamics. In particular, scaling laws for the charge-radius droplet characteristics were determined for different applied voltages and capillary flow rates in the transient as well as in the steady state electrospray regime [32]. The simulation results in Fig. 3 illustrate exemplarily the effect of electrical conductivity on the droplet size and density distributions at the onset of electrospray for two selected liquids.

## 2.2 Thermodynamic Modelling and Surface Phenomena

An important topic in multiphase flows is the accurate thermodynamic modelling of the surface phenomena. Such research topics were considered by the projects SP-A4 and SP-A7. This work was important for the further development of simulation tools, but also for the analysis and interpretation of experimental results. Molecular dynamic simulations with many particles performed in SP-A4 contributed to the study of evaporation of nanometer droplets at hot surfaces. Here, non-equilibrium

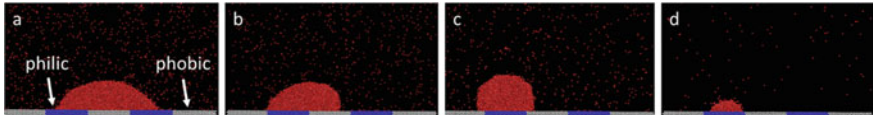


**Fig. 4** Evaporation of a nanodrop from a surface with contact-line pinning and unpinning. **a** Both contact lines reside on the solvophilic surface regions (blue, contact angle  $67^\circ$ ). **b** When the drop becomes too small to span the distance between the solvophobic regions, one contact line unpins and quickly traverses the solvophobic region (white, contact angle  $115^\circ$ ). Such jumps are characteristic for chemically nanopatterned surfaces. **c** The drop is too big for one solvophobic region and therefore squeezed into an unfavourable shape with a large contact angle. **d** The drop has shrunk enough to fit onto one solvophilic region, the contact angle is back to its equilibrium value [61]

molecular dynamics were developed, by which steady evaporation processes were observed in detail at different complex surfaces.

The understanding of basic mechanisms in heat transfer, adhesion, and phase transition requires insight into the local phenomena of liquid–gas and liquid–solid contact. Since the characteristic length at these interfaces measures only a few molecular diameters, one needs microscopic simulations to gauge thermodynamic and continuum models. Molecular dynamics simulations investigate these phenomena on a molecular scale. Simulations in SP-A4 with many fluid particles contributed to the study of evaporation of nanometer-size droplets from hot surfaces. For this purpose, new non-equilibrium techniques were developed, by which evaporation processes can be observed in detail at different complex surfaces in a steady state for better statistics [62]. The evaporating droplet is replenished by rapidly duplicating molecules at its center, while removing molecules in the gas phase far away from its surface. Incidentally, this splitting method can also be used to calculate mutual diffusion coefficients by reverse non-equilibrium molecular dynamics [4].

The models and algorithms were applied to investigate phenomena as different as the jump pinning/unpinning motion of the contact line during droplet evaporation from a nanopatterned surface (see Fig. 4) and the strong influence of the contact line curvature on the contact angles and the contact area of a drop, both in equilibrium and during evaporation [60]. SP-A4 investigated the rebound of impinging drops from solvophobic surface and its suppression by small amounts of polymer additives. Two molecular modes of action have been shown to work side by side [22] (see also Lee et al. [in this volume](#)).

Collision processes play a major role in different science and engineering problems ranging from cloud dynamic processes to technical spray applications. A realistic description of the droplet dynamics needs the understanding of the elementary process of binary droplet collisions. The focus of SP-A7 (see Potyka et al. [in this volume](#)) was the proper modelling of the collision process according to the collision outcome bouncing, coalescence or drop disintegration, as well as the collision of different liquids. The program Free Surface 3D (FS3D) has been further developed with respect to the predictive description of these phenomena and to capture the complete physics of the droplet collision numerically. In particular, an integrated subgrid-scale

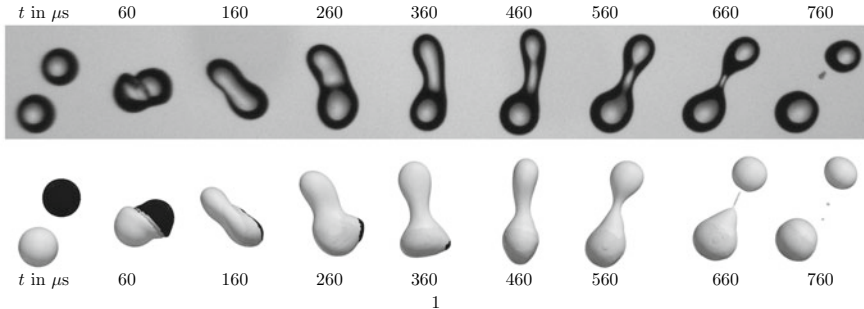


**Fig. 5** Morphological comparison of simulation results (bottom) for an off-center collision of a silicon oil M5 (light) and a 50% glycerol-water solution (dark) with experimental results (top) (see [35] for further details). Pictures of experiments provided by courtesy of C. Planchette. A tool developed in SP-A1 (see Heinemann et al. [in this volume](#)) has been used for the visual analysis

modeling based on an enhanced lubrication approximation allows to account for the rarefied flow dynamics inside the thin gas layer between colliding droplets [25]. High-resolution simulations predicted droplet collisions in the spattering regime and provided detailed insights into the evolution of the rim instability [24]. For the case of collision of immiscible liquids, the complexity of the process strongly increases due to the occurrence of a triple line. An enhanced continuous surface stress model was introduced for an accurate surface force computation, which is also applicable to thin films [35]. Moreover, a new face-based interface reconstruction has been developed and extended to the case with appearance of triple lines [19]. For collisions of fully wetting liquids, excellent agreement with experimental data was achieved in different collision regimes; an example is shown in Fig. 5.

### 2.3 Visualization

The third topic in Research Area A was visualization, which contributed to nearly all other projects. The main goal of SP-A1 (see Heinemann et al. [in this volume](#)) was the development of new and improved algorithms especially for interactive visualization of droplet dynamic processes from large, time-dependent simulations and experimental data. These research activities included the development of new methods for the analysis of single droplets and droplet groups, but at the end also for the investigation of sprays. Here, the challenge was the analysis of the enormous amount of data. Novel visualization techniques were required to handle the increasing complexity of simulation and experimental data and the complex physical phenomena under investigation. The visualization of phase transitions constituted an essential research field. Techniques were developed to analyse multiphase processes such as evaporation, icing and drop impingement. Coalescence and break-up events needed to be visually presented in an interactive exploratory way. As an example a visual-

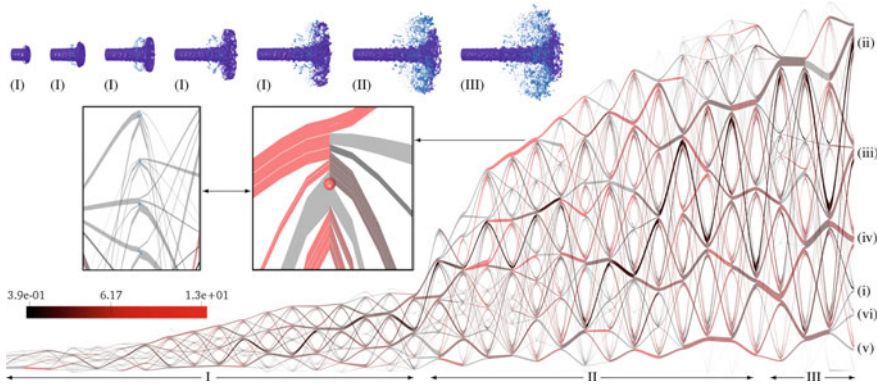


**Fig. 6** Jet dataset with selected time steps shown. (Top) Jet (purple) is injected from left, and due to its high velocity at the nozzle, it splatters into various-sized droplets (blue). (Bottom) Parametric graph shows the space-time evolution of the jet stream. Edge clusters represent droplets with similar area to volume ratio. The box in the middle shows an enlarged node with volume distribution indicated on the clustered edges. A node cluster can be unfolded (left box) and folded back to reveal the actual edge connectivity and drop geometry. Here, highly deformed ligaments with large area to volume ratio are visible. ©2017 IEEE. Reprinted, with permission, from [18]

ization of a jet breakup is shown in Fig. 6. Tools for the visual analysis of energy transport were designed to obtain information about phase transitions, also in the context of the three-phase contact line. New visual tools were necessary for the analysis of large droplet groups and sprays, as well as for various physical phenomena investigated in SFB-TRR 75. SP-A1 spanned visualization techniques for observing physical phenomena, such as energy transport or collisions for single droplets, to the analysis of large-scale simulations with sprays and jets. In addition, the task of finding relevant structures, features of interest or a general dataset overview was addressed in this subproject.

### 3 Research Area B: Free Droplets

In Research Area B, different phenomena of free drops under different extreme thermodynamic and fluid dynamics conditions were investigated. The overall scientific objective was to understand the physical mechanisms underlying these droplet dynamic processes. Based on this physical understanding, models were developed and validated. The necessary validation data were provided in this research area, partly using new laser diagnostic approaches. The mathematical models formed the necessary basis for numerical simulations of systems defined via the CRC guiding examples. The investigations in Research Area B focused on

- Phase transitions of supercooled droplets (evaporation, melting and freezing processes) that are in thermodynamic non-equilibrium

- Transcritical evaporation and mixing processes
- Flash evaporation of cryogenic liquids under near vacuum conditions

### 3.1 Phase Transition of Supercooled Droplets

The formation of ice crystals of arbitrary structures, e.g. also by collisions within clouds, is still very poorly understood. However, this is of importance for a correct description of cloud dynamics. SP-B1 focused on this topic for free droplets, whereas SP-C3 in Research Area C focused on the wall interaction of supercooled droplets. The dynamics of supercooled droplets is characterized by their metastable state and the resulting phase change. An improved understanding and a more accurate prediction of the phase changes of and in supercooled droplets is of fundamental interest, e.g. for the understanding of cloud dynamics at high altitudes and for the development of improved climate models. The focus in SP-B1 (see Reutzsch et al. [in this volume](#)) was therefore on studying evaporation, sublimation and freezing of supercooled water droplets. On the one hand, physically consistent numerical models, capable of calculating all three phase transitions, were developed [43, 45]. On the other hand, the numerical work within the program FS3D was validated and compared with different experimental results [44, 47]. In an optical levitator, the dynamics of supercooled water droplets was investigated by light scattering and shadowgraphy methods for ambient conditions corresponding to temperatures appearing in clouds at high altitudes. From this, sublimation and evaporation rates of frozen and supercooled droplets were determined and compared with direct numerical simulation (DNS) results. Figure 7 shows on the left the temporal development of an ice crystal from

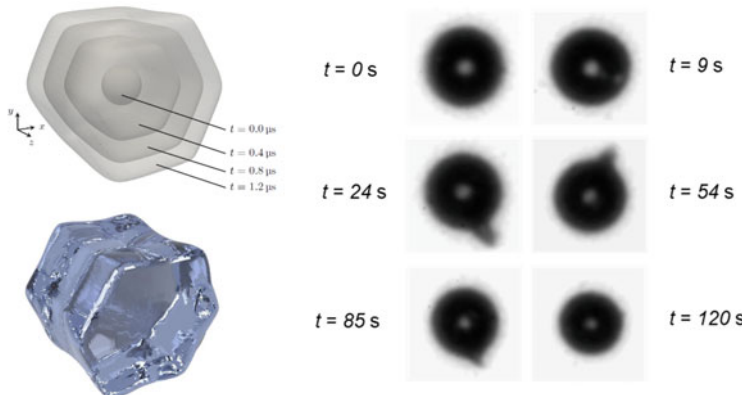


**Fig. 7** Temporal evolution and rendered simulation of freezing ice particle (left); Experimental results for the time evolution of a levitated drop from liquid to frozen state (right)

a spherical seed and a rendered picture of the simulation result. On the right in Fig. 7, the time evolution of a levitated drop is shown from the liquid to the frozen state.

### 3.2 Transcritical Evaporation and Mixing Processes

The transcritical and supercritical region of fluids involve extremely high pressures and temperatures. These conditions, which are important e.g. for energy conversion systems, are still poorly understood with respect to evaporation and mixing. This topic has been investigated in SP-B2, SP-B3 and SP-B6.

The focus of SP-B2 [20, 21] is on dynamics of single droplets at near critical conditions, see also Lamanna et al. [in this volume](#). Figure 8 exemplarily shows the mixture fraction of n-hexane in the wake of an evaporating droplet and gas temperatures assuming adiabatic mixing [2]. Contrary to sprays, droplets provide a simplified configuration, for which analytical solutions can be obtained to describe the simultaneous exchange of mass and energy at high pressure conditions. For an experimental investigation, a high-pressure, temperature controlled test rig, equipped with an electrical droplet generator, was built to perform experiments under well-controlled conditions. Several laser diagnostic methods have been developed and improved. Spontaneous Raman scattering [2] and combined laser induced fluorescence and phosphorescence [36] enabled the measurement of gas composition in the wake of an evaporating droplet, gas temperatures and, for the case of acetone, mean droplet temperatures. Laser-induced thermal acoustics has been extended to enable the measurement of the acoustic damping rates in the supercritical region of pure fluids [56]. Based on these measurements, the importance of bulk viscosity in the liquid-like supercritical region was assessed and closure models for describing momentum transport and dissipation effects in supercritical fluids were evaluated. For the example of the onset of single-phase mixing, the analysis revealed that in the presence of large temperature and concentration gradients evaporation processes are highly important.

In SP-B3 (see Kuetemeier and Sadiki [in this volume](#)), the dynamics of sprays under transcritical conditions was investigated using large-eddy simulation (LES). Multi-component real fluid systems were considered. Based on models for the simulation of evaporating single droplets, the goal was to further develop innovative models for sprays. For this purpose, a regime spanning evaporation model and a subgrid scale model taking anisotropy into account were integrated into an Euler-Euler as well as an Euler-Lagrange simulation. As a new approach, the entropy inequality (second law of thermodynamics) was considered in the large-eddy simulation. Thus, on the one hand, the physical consistency of the subgrid scale modeling was ensured and on the other hand, the potential of entropy production as an analytical tool for the assessment of fluid dynamic processes was explored. Obtained by means of the developed Eulerian-Eulerian method, Fig. 9 shows exemplarily the field of mass density evolution during the disintegration of an elliptic jet of supercritical fluoroketone injected into a supercritical helium environment. The numerical model includes a description

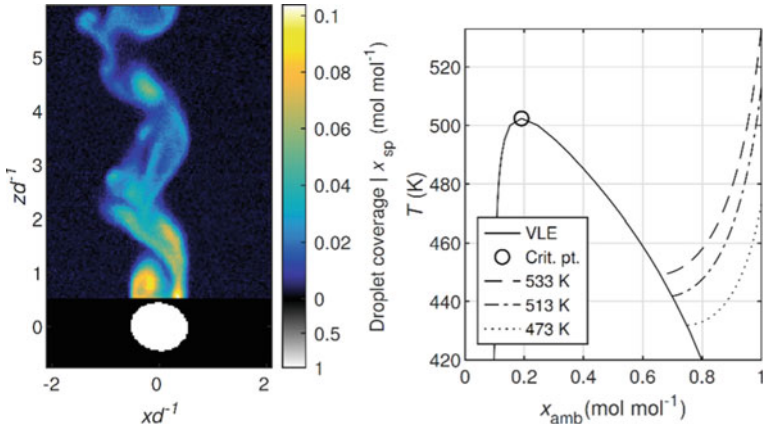


**Fig. 8** n-hexane droplets in nitrogen atmosphere. Single droplet mixture fraction result for nitrogen atmosphere temperature of 533 K, injector temperature of 473 K and pressure of MPa (left). Number density data estimated adiabatic mixing temperature curves dependent on mixture fraction. Varying ambient nitrogen temperature as shown, injector temperature fixed at 473 K and a pressure of MPa (right)

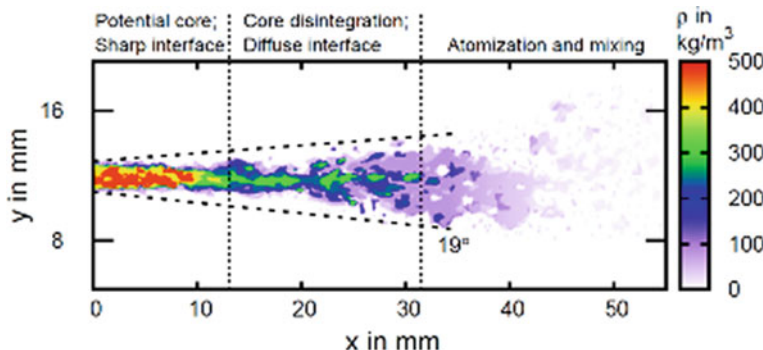


**Fig. 9** Instantaneous field of mass density at mid-plane section of the fluoroketone jet: Eulerian-Eulerian-based LES results of a grid resolution with ca. 3 million control volumes. Jet spreading angle: 19° (Experiment: 20°) and effect chain of processes evolving

of the two-phase flow fluid with phase change as multi-component mixtures in which the real fluid properties are accounted for by a composite Peng-Robinson equation of state. It reproduces correctly the jet disintegration regimes as observed experimentally (see [29]) in terms of penetration length along with mass density and jet spreading angle. The effect chain of the evolving processes is especially consistently reproduced.

The behaviour of droplets under strong non-equilibrium conditions is poorly understood. In the associated heat and mass transfer phenomena, the phase boundary between droplets and their environment plays a crucial role. Due to its typically very

small spatial extent, the phase boundary in non-equilibrium can be directly simulated using atomistic molecular dynamics, providing detailed insight on a sound physical basis. In SP-B6 (Heinen et al. [in this volume](#)), liquids and gases interacting with each other across a phase boundary, such as liquid nitrogen and gaseous hydrogen, were studied under non-equilibrium conditions using atomistic simulations. One focus was on the question under which conditions the atomization process transitions from a two-phase behaviour to dense-fluid mixing. The influence of strong temperature and composition gradients was considered with respect to heat and mass transfer

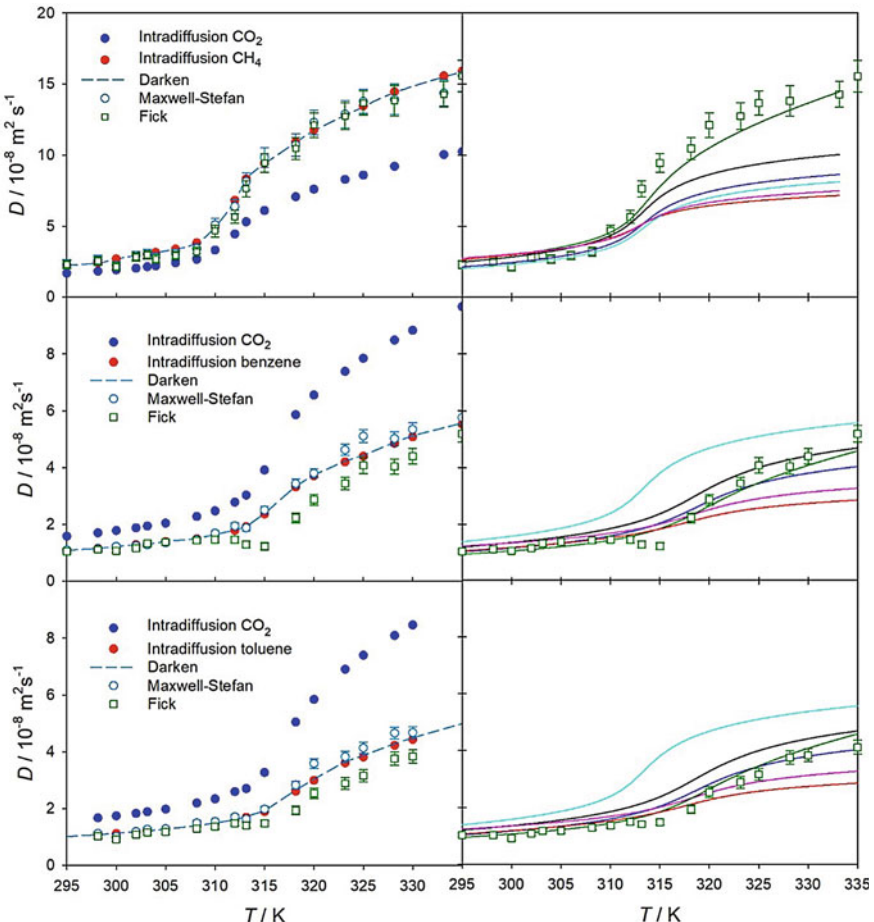


**Fig. 10** Left: Temperature dependence of the intra-, Maxwell-Stefan and Fick diffusion coefficients for the mixtures (top), (center) and (bottom) at 9 MPa and  $= 0.99 \text{ mol mol}^{-1}$ . Right: Simulation results for the Fick diffusion coefficient (green squares) are compared with predictive equations (lines) by Sassi et al. (black) [48], Wilke and Chang (blue) [59], Catchpole and King (green) [3], He and Yu (red) [14] and Scheibel (cyan) [49]

as well as the physical quantities of the phase boundary. In addition, for trans- and supercritical fluid conditions, diffusion coefficients for binary solute systems were predicted by equilibrium molecular dynamics simulation and the Green-Kubo formalism. Several predictive equations for the Fick diffusion coefficient [3, 14, 48, 49, 59] were compared with present simulation results. As shown in Fig. 10, although some equations were able to reasonably predict the temperature dependence of the Fick diffusion coefficient at the studied conditions, none of the studied equations could be established as reliable.

### 3.3 *Flash Evaporation of Cryogenic Liquids Under Near-Vacuum Conditions*

Although important phenomena of spray dynamics and flash boiling have been described in the literature, valid and physically consistent modelling is lacking. Furthermore, similar to the studies of supercritical droplets, only very few validation data under well-controlled boundary conditions were available. Therefore, a combined experimental and numerical approach has been followed by SP-B4 and SP-B5.

At high altitude, liquid fuels are injected under cryogenic conditions into rocket combustion chambers where very low pressures prevail. The associated pressure drop leads to superheating and subsequently to eruptive vaporization (flash boiling) with rapid expansion. To investigate this complex phenomenon, a test rig was set up in SP-B4 (see Rees and Oschwald [in this volume](#)) with a special cryogenic injection system for the injection of molecular nitrogen under flash boiling conditions [41]. High-speed shadowgraphy and phase Doppler measurements were used to study the spray jet topology, droplet size and droplet velocity for a wide range of parameters. With increasing superheat, the transition from narrow and turbulent sprays to wide opened, fine and well atomized sprays was observed. Based on the experimental results, a new break-up regime called wide flashing regime for highly superheated jets was found [42]. The transition to this regime is visualized in Fig. 11 using shadowgraphy images. The phase Doppler measurements in wide flashing liquid nitrogen sprays revealed fast and large droplets close to the injector, while the sprays become more monodisperse with slow and small droplets for an increasing distance to the injector [39, 40]. This extensive database is available for the validation of numerical simulations.

Numerical simulation of flash boiling is of great importance e.g. for the design of rocket combustors. For this a detailed phenomenological understanding of bubble growth and bubble-bubble interactions and their effect on spray breakup, droplet dynamics and subsequent mixing processes is needed. Complementary to the experimental studies in SP-B4, DNS [5, 6, 26] and RANS [10] simulations were conducted in SP-B5 (see Gärtnert et al. [in this volume](#)). RANS simulations were also performed for the overall process to investigate fluid dynamic effects and shock wave formation downstream of the injector [10]. Figure 12 shows an example of the temporal devel-

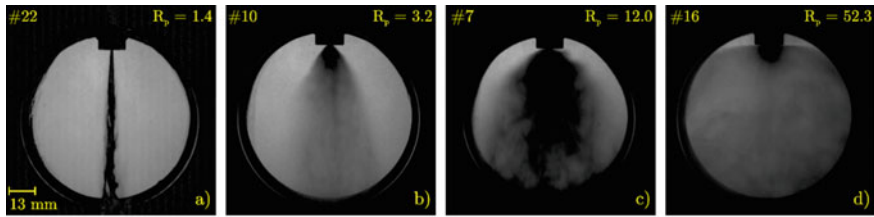


**Fig. 11** LN2 sprays with different degrees of superheat for the atomization regimes **a** aerodynamic break-up, **b** transition regime and **c** fully flashing regime and the new **d** wide flashing regime

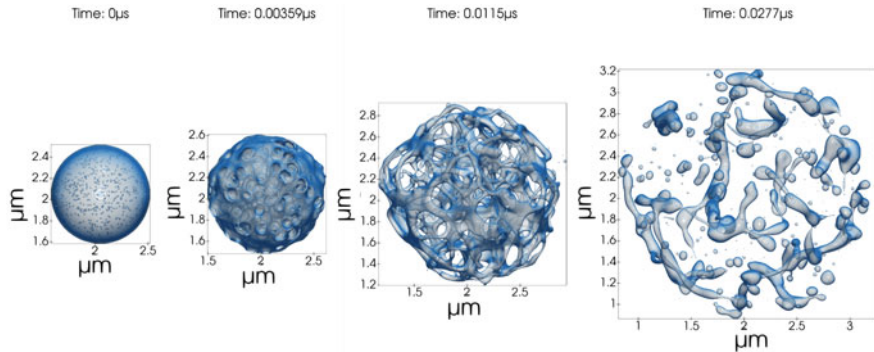


**Fig. 12** Time sequence of the spray breakup process and droplet generation. Break-up in the ligament stretching regime with conditions 120 K, 5, We 3.62, Oh 0.104

opment of the spray break-up process and droplet generation for selected boundary conditions [26]. As an important result for this aspect, it was found that only bubbles close to the jet surface grow significantly. Bubbles at distances greater than ten bubble diameters from the jet interface can be neglected in the dynamics of jet expansion and break-up [5].

#### 4 Research Area C: Droplets with Wall-Interactions

In Research Area C drops with wall interactions have been studied. The extreme ambient conditions were related to elevated pressure, hot and/or cold walls, and applied electric fields. The overall goal in all of these studies was to better understand the physical phenomena involved in the respective interactions with the aim to improve predictive capabilities through physics based models. All of the subprojects included in the research program involved experiments, theoretical analyses and numerical simulations, yielding well verified and advanced models. The investigations in Research Area C focused on

- Droplet and spray interactions with hot walls

- Droplet/-wall interactions with cold walls
- Droplet/-wall interactions under the presence of strong electric fields

#### 4.1 *Droplet and Spray Interactions with Hot Walls*

The applications in mind when conceiving this research area were diverse, but timely and challenging. Three subprojects (SP-C1, SP-C2 and SP-C4) involved drops impinging onto hot walls, a phenomenon encountered in numerous situations, but especially when the drops are used for cooling, either with or without phase change. At higher wall temperatures of course, the drops evaporate, greatly increasing the heat flux from the wall, since the latent heat of vaporization is exploited. However, this phase change also introduces a strong influence of the thermodynamic conditions on the hydrodynamics of drop impact. This is a particular challenge, extending beyond the well-established knowledge base of isothermal drop impact onto walls. Furthermore, at high heat flux levels, the heat removed from the substrate must also be taken into account, becoming a conjugate heat transfer problem. In combusting systems this occurs often at elevated pressures; hence, this extreme condition was also investigated. At extremely high wall temperatures, typical of transient cooling and/or quenching, the challenge is further to predict the Leidenfrost point, i.e. the transition from film boiling to nucleate boiling.

SP-C1 (see Sontheimer et al. [in this volume](#)) and SP-C2 (see Gholijani et al. [in this volume](#)) address the same physical phenomenon, the former in terms of numerical simulations and the latter in terms of laboratory experiments. In both cases the drop impingement is onto a substrate at a temperature above the saturation temperature but below the Leidenfrost temperature of the impinging liquid, i.e. the liquid is wetting the substrate surface and evaporating at the same time. This generic situation applies e.g. for spray cooling at moderate heat flux levels. The heat transfer mechanism is a combination of single phase convective heat transfer and phase-change heat transfer. The hydrodynamics of isothermal drop impact are already well known; however, in the non-isothermal case with a superheated wall, there is a strong interaction of heat transfer and hydrodynamics, and this is specifically addressed in SP-C1 and SP-C2. The associated heat transfer represents a particular challenge due to numerous factors. For one, drop impacts are characterized by an inertia dominated spreading phase followed by a surface tension dominated retracting phase. The internal flow in the drop, which is totally different in these two phases, strongly affects the thermal boundary layers in both, the drop and the substrate. Hence, the exact internal flow behaviour and the velocity of the three-phase contact line during the spreading and retracting phases become important for the convective and the evaporative heat transfer and vice versa. A particular emphasis in SP-C1 and SP-C2 is placed on correctly measuring and modelling this “micro region” flow and heat transfer. The numerical treatment of this problem requires modelling at both, the macro and the micro scale, and an appropriate connection between the two. A very revealing physical insight afforded by SP-C1 is illustrated in Fig. 13, in which the heat transfer paths from

substrate to drop to gas is graphically shown for the spreading and receding phase of a drop impact. These exemplary results, obtained through numerical simulation, underline the importance of the contact line micro region.

The heat transfer from single drop impacts was characterized in dependence of impact parameters and material parameters, expressed in dimensionless form [12]. This work was then extended to the case of multiple drop impacts, either vertically coalescing or side-by-side. Furthermore, the influence of elevated pressure on the heat transfer was quantified. These results then represent a first step to extend basic knowledge about single drop impacts to spray impingement by supplying appropriate scaling parameters of the net heat transfer.

SP-C2, the experimental pendant to SP-C1, addresses the challenge of measuring the heat transfer in the micro region around the three-phase contact line. For this, two dedicated and novel experimental facilities were designed and constructed. In one facility the concept of a moving wall and stationary contact line in laboratory coordinates was introduced. This simplifies the observation of phenomena at the contact line. The substrate was heated using Joule heating of a chromium layer: A chromium nitride layer with high emissivity was used together with an infrared camera with high spatial and temporal resolution to monitor the evolution of the temperature profile near the contact line. In this manner the transient heat flux at the three-phase contact line could be computed.

The experimental results confirm the associated numerical simulations in SP-C1. The heat flux at the forward moving contact line reached levels twice as high as at a receding contact line. This is due to the stronger micro-convection at the contact line and the thinner boundary layer inside the drop. Additional experiments were performed at elevated pressures, confirming a decrease in overall heat flux due to the reduction in latent heat of vaporization, which specifically reduces the evaporation in the receding phase.

The peak heat flux observed at the steady state three-phase contact line was also observed for the transient phases during drop impact. Besides varying the impact parameters of drop size and impact velocity, also the influence of structured and porous substrates was investigated. Finally, experimental data for vertical and horizontal coalescing drops were collected for comparison with the accompanying numerical simulations [1, 11]. An example measurement result of the time resolved impact of two drops captured with a side view camera and the associated computed heat flux distributed across the wetted area is shown in Fig. 14.

When a drop impacts onto a heated wall, the associated heat transfer depends on numerous quantities, above all the temperature of the substrate. In general the heat transfer is categorized according to the so-called boiling curve regimes: convective heat transfer, nucleate boiling, transition boiling and film boiling, whereby the latter two are separated by the Leidenfrost point. In the framework of SP-C4 (see Schmidt et al. [in this volume](#)) the transition regime was further elucidated, revealing the phenomenon of thermal atomization, in which the drop makes contact with the substrate resulting in a large number of small secondary droplets, followed by a levitation of the remaining drop liquid and a break-up of the liquid fragments into larger drops through the Rayleigh-Plateau instability. For all of the above-mentioned regimes,

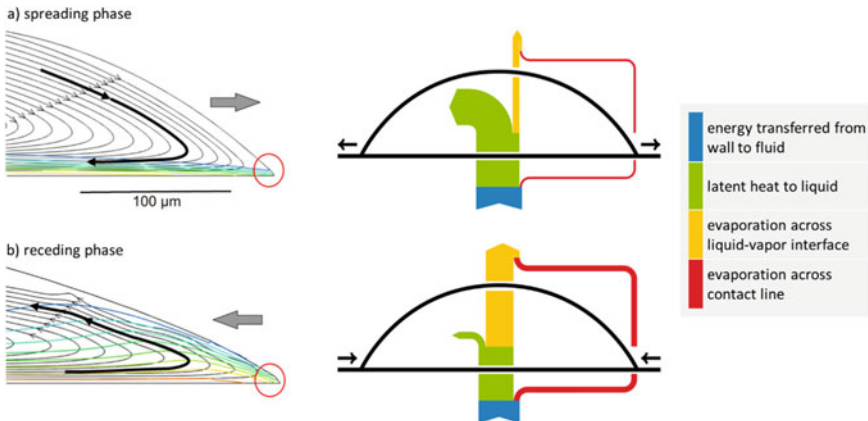


**Fig. 13** Heat transfer paths during the **a** spreading phase and **b** receding phase of the drop impact. The isotherms with a spacing of 2 K and streamlines are shown in a moving reference frame close to the contact line

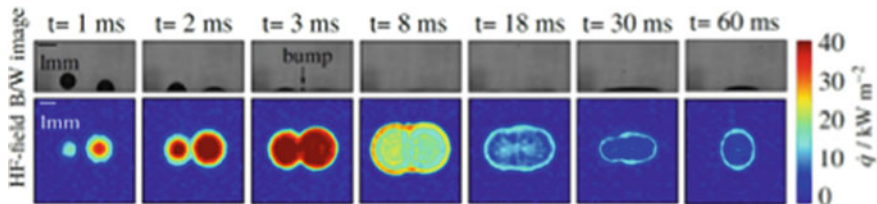


**Fig. 14** Side view images of an impact and merger of two drops (upper line) and bottom view computed images of heat flux of a horizontal coalescence of two drops (lower line). (, , , )

theoretical models were developed and validated to predict the heat transferred upon drop impact and the drop lifetime until complete evaporation. A further insight was gained about the threshold temperature, from which on drops rebound and the prediction of this point for a given drop impact and substrate material. The threshold point separates film boiling, in which the heat transfer is very low, from nucleate boiling, which exhibits very high heat transfer; thus, at the Leidenfrost point the heat transfer takes a minimum value. In Fig. 15a–c different outcomes of drop impact, deposition, partial and complete rebound, are shown after impact of the substrate at various initial temperatures. The dependence of the drop residence time on the wall temperature is shown in Fig. 15d. The novel insight gained is related to the importance of the substrate material, in particular the thermal effusivity of the substrate. The heat transfer at these high temperatures is strongly a conjugate heat transfer problem; hence, the rate at which the thermal boundary in the substrate develops becomes an important factor in defining this point [50].

While the initial research program was concerned with the impact of single drops onto heated surfaces, later work investigated the impact of sprays, as would be found

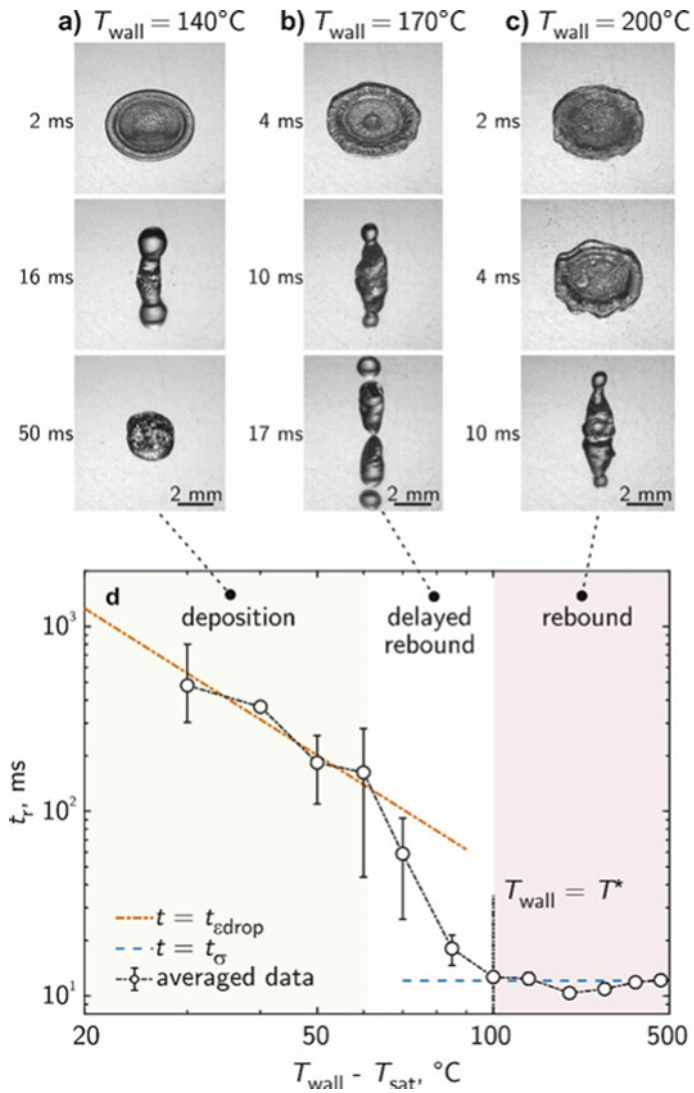


**Fig. 15** Typical outcome phenomena of a drop impact in the regimes drop deposition, drop dancing and drop rebound are shown in **a**, **b** and **c**. In **d** the residence time of the drops at the surface is shown as a function of the surface temperature in comparison with the theoretical models. The temperature indicates the onset of drop rebounds

in spray cooling scenarios. This transient spray cooling deviates in some manner from the steady state boiling curve view mentioned above, since the thermal history of the substrate becomes influential. In particular, this work revealed the relative duration in which the various heat transfer regimes were applicable.

## 4.2 *Droplet-Wall Interactions with Cold Walls*

With reference to icing phenomena in the aviation industry, SP-C3 (see Gloerfeld et al. [in this volume](#)) examined the impact of supercooled drops onto cold surfaces and their subsequent solidification and accretion. Although the prediction of ice accretion is a standard step in the aircraft certification process, most presently used computational models are highly empirical and are not completely recognized as a confirmation of airworthiness. This is especially true for more recent regulatory stipulations, in which also icing from supercooled large droplets (SLD) must be considered.

Although the degree of supercooling can be quite substantial ( $10^{\circ}\text{C}$ ), in practice SLD can remain in a meta-stable liquid state, even after impacting onto a solid surface. The freezing is initiated by heterogeneous nucleation, which is influenced by numerous factors, including the surface topology, temperature, possible contamination, all which may lead to a nucleation embryo. This is an extreme challenge to predict, since the microscopic boundary conditions at work are not all known. Thus, in SP-C3 a statistical approach was taken to formulate nucleation models expressing the freezing delay between impact and first nucleation. Once nucleation occurs, the freezing continues with dendrite propagation through the bulk, by which a small volume of the liquid solidifies and the remainder warms to the melting temperature. Models for this dendritic phase have also been developed [51]. At this stage, the drop then solidifies according to the Stephan problem.

The complexity is increased with impacting drops because the wetted area on the surface changes with time as the drop spreads and possible retreats, depending on the wettability. Within the drop both a hydrodynamic and thermal boundary layer develop and this then also influences the material parameters, especially the viscosity. These influences on the hydrodynamics can alter the impact outcome, but also the final iced area on the surface [53]. Also for this interaction between thermodynamics and hydrodynamics, appropriate models have been proposed and validated with experimental data [52].

A quantity of great interest and importance upon drop impact is the residual volume, i.e. what portion of the impacting liquid remains on the substrate? This directly influences the rate of ice accretion, which is an elusive quantity to measure and in SP-C3 a novel method of measuring residual volume, also for drops which have solidified on the substrate, has been developed and applied to deliver first data on residual mass as a function of impact parameters [13]. The associated models which have been developed are directly appropriate for integration into icing codes. Measurements have also been performed for the case of impacting dendritic drops,



**Fig. 16** Image sequence of a dendritic frozen drop impacting with a velocity of originating from a drop with an initial supercooling of

i.e. drops in which the dendrites have already formed. Such an impact is pictured in the image sequence of Fig. 16.

#### 4.3 *Droplet-/Wall Interactions Under the Presence of Strong Electric Fields*

SP-C5 (see Löwe et al. [in this volume](#)) involved sessile drops exposed to various high voltage electric fields, including alternating, transient and direct voltage. The specific aims were twofold. For one, the influence of an electric field on the probability of partial discharge was investigated, since partial discharges greatly affect the durability of insulators employed in high voltage power lines [46]. The challenge here is that the influence is indirect: the electric field induces drop oscillations and deformations and these then influence the field concentration around the drop, especially at the three-phase contact line through drop deformation. The second aim was directed at the influence of electric fields on the heterogeneous nucleation rate of supercooled liquid sessile drops. This phenomenon is also of relevance to power transmission, where icing influences the performance of the insulators [7]. Ice accretion alters the shape of the insulators by bridging the space between the weather sheds and may lead to increased creeping currents or to a flash-over. The initial interest in SP-C5 lay in the effect of strong electric fields on sessile drops, whereby not only the strength and nature of the electric field was interesting—alternating, transient or direct voltage, but also the orientation, either tangential or normal. Rather early it became clear, that also the charge on the droplet would play a significant role and one example of this influence is pictured in the image sequences of Fig. 17.

The drop deformation due to an applied electric field is presumed also to occur on sessile drops residing on insulators of power transmission lines. Especially the deformed drop shape at the three-phase contact line leads to strong electric field concentration and, thus, to a higher probability of partial discharges. Such partial discharges can severely deteriorate the surface of the insulating material and enhance the aging process. In SP-C5 the partial discharge inception field strength could be quantitatively determined and influencing factors identified such as electric field frequency, surface inclination, presence of further droplets, constant or alternating electric field, contact angle, or electric charge on the droplet. A second focus in SP-C5 was the influence of an applied electric field on the nucleation of supercooled

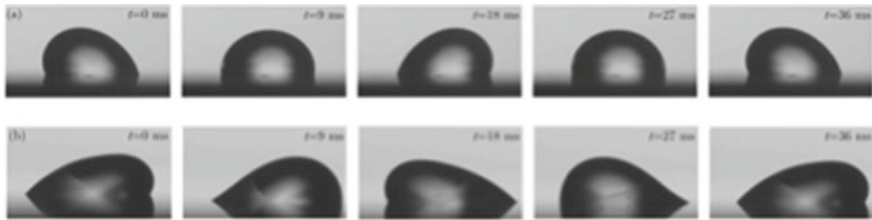


**Fig. 17** Comparison of one cycle of an uncharged and a charged drop in resonance mode 1. **a** Uncharged drop with a volume of 20 l and a voltage frequency of 27 Hz at an electric field strength of 3.81 kV/cm and **b** charge drop (0.646 nC) with a volume of 20 l and a voltage frequency of 217 Hz at an electric field strength of 4.42 kV/cm. Reprinted (adapted) figure with permission from [27], Copyright 2020 by the American Physical Society

sessile drops. Again, solidification of sessile drops on powerline insulators, represent an increased hazard of creeping currents or flash-overs. This was a particular challenging task, since nucleation is a process only captured by statistical models and the question arises whether the influence of an electric field is significant enough to be distinguished above the inherent statistical various of the nucleation? This demanded the development of a dedicated facility to lower the variability introduced in normal experimental procedure. Based on this, experiments with a large ensemble of samples could then be performed, increasing the statistical significance of the results. The conditions under which an electric field can have an influence on heterogeneous nucleation was then quantified in dependence of various boundary conditions.

## 5 Conclusions

This introductory chapter has outlined the structure of the Collaborative Research Center SFB-TRR 75 and illustrated some selected scientific achievements of this project. This joint initiative involved scientists at the University of Stuttgart, the TU Darmstadt, the TU Berlin, and the German Aerospace Center (DLR) in Lampoldshausen. The project started in January 2010 and ended in June 2022. Within the CRC a strong interaction of the individual projects and involved scientists took place. Great progress can be reported in the area of droplet dynamics related to extreme ambient conditions in this project over the past 12 years. This progress is related to the development of analytical models, for example for phase change problems, sophisticated numerical methods, e.g. for droplet motion in compressible flows, for phase change problems involving droplets or droplet motion in strong electric fields. All analytical and numerical model developments have been supported and validated by highly sophisticated experiments in all investigated areas. After the development of new or improved experimental, theoretical and numerical methods, these methods were increasingly used to study interaction mechanisms and complex fluid systems.

The new findings were made publicly available in numerous publications and by selected data sets via the homepage of the CRC: [www.sfbtrr75.de](http://www.sfbtrr75.de).

**Acknowledgements** The authors gratefully acknowledge the German Research Foundation (DFG) for the financial support of the project SFB-TRR 75 under the project number 84292822.

## References

1. Batzdorf S, Breitenbach J, Schlawitschek C, Roisman I, Tropea C, Stephan P, Gambaryan-Roisman T (2017) Heat transfer during simultaneous impact of two drops onto a hot solid substrate. *Int J Heat Mass Transf* 113:898–907
2. Bork B, Preusche A, Weckenmann F, Lamanna G, Dreizler A (2017) Measurement of species concentration and estimation of temperature in the wake of evaporating n-heptane droplets at trans-critical conditions. *Proc Combust Inst* 36(2):2433–2440
3. Catchpole OJ, King MB (1994) Measurement and correlation of binary diffusion coefficients in near critical fluids. *Ind Eng Chem Res* 33:1828–1837
4. Chilukoti HK, Müller-Plathe F, Yang H (2018) Application of reverse nonequilibrium molecular dynamics to the calculation of the mutual diffusion coefficient of alkane mixtures. *J Phys Chem B* 122(39):9210–9217
5. Dietzel D, Hitz T, Munz CD, Kronenburg A (2019) Numerical simulation of the growth and interaction of vapour bubbles in superheated liquid jets. *Int J Multiph Flow* 103:112
6. Dietzel D, Hitz T, Munz CD, Kronenburg A (2019) Single vapour bubble growth under flash boiling conditions using a modified HLLC Riemann solver. *Int J Multiph Flow* 116:250–269
7. Farzaneh M, Chisholm WA (2009) Insulators for Icing and Polluted Environments. IEEE Press series on power engineering, Wiley-Blackwell, Oxford
8. Fechter S, Munz CD, Rohde C, Zeiler C (2017) A sharp interface method for compressible liquid-vapor flow with phase transition and surface tension. *J Comput Phys* 336:347–374. <https://doi.org/10.1016/j.jcp.2017.02.001>
9. Fechter S, Munz CD, Rohde C, Zeiler C (2018) Approximate Riemann solver for compressible liquid vapor flow with phase transition and surface tension. *Comput Fluids* 169:169–185. <https://doi.org/10.1016/j.compfluid.2017.03.026>
10. Gärtnner JW, Kronenburg A, Rees A, Sender J, Oschwald M, Lamanna G (2020) Numerical and experimental analysis of flashing cryogenic nitrogen. *Int J Multiph Flow* 130:103360
11. Gholijani A, Gambaryan-Roisman T, Stephan P (2020) Experimental investigation of hydrodynamics and heat transport during vertical coalescence of multiple successive drops impacting a hot wall under saturated vapor atmosphere. *Exp Therm Fluid Sci* 118:110145
12. Gholijani A, Schlawitschek C, Gambaryan-Roisman T, Stephan P (2020) Heat transfer during drop impingement onto a hot wall: the influence of wall superheat, impact velocity, and drop diameter. *Int J Heat Mass Transf* 153:119661
13. Gloerfeld M, Roisman IV, Hussong J, Tropea C (2021) Measurements and modelling of the residual mass upon impact of supercooled liquid drops. *Exp Fluids* 62(10):1–11
14. He CH, Yu YS (1998) New equation for infinite-dilution diffusion coefficients in supercritical and high-temperature liquid solvents. *Ind Eng Chem Res* 37:3793–3798
15. Hitz T, Heinen M, Vrabec J, Munz CD (2020) Comparison of macro- and microscopic solutions of the Riemann problem I. Supercritical shock tube and expansion into vacuum. *J Comput Phys* 402:109077. <https://doi.org/10.1016/j.jcp.2019.109077>

16. Hitz T, Jöns S, Heinen M, Vrabec J, Munz CD (2021) Comparison of macro- and microscopic solutions of the Riemann problem II. Two-phase shock tube. *J Comput Phys* 429:110027. <https://doi.org/10.1016/j.jcp.2020.110027>
17. Hitz T, Keim J, Munz CD, Rohde C (2020) A parabolic relaxation model for the Navier-Stokes-Korteweg equations. *J Comput Phys* 109714. <https://doi.org/10.1016/j.jcp.2020.109714>
18. Karch GK, Beck F, Ertl M, Meister C, Schulte K, Weigand B, Ertl T, Sadlo F (2018) Visual analysis of inclusion dynamics in two-phase flow. *IEEE Trans Vis Comput Graph* 24(5):1841–1855
19. Kromer J, Potyka J, Schulte K, Bothe D (2021) Efficient three-material plic interface positioning on unstructured polyhedral meshes. [arXiv:2105.08972](https://arxiv.org/abs/2105.08972)
20. Lamanna G, Steinhausen C, Weckenmann F, Weigand B, Bork B, Preusche A, Dreizler A, Stierle R, Gross J (2020) Laboratory experiments of high-pressure fluid drops: Chapter 2. In: American Institute of Aeronautics and Astronautics (ed.) High-pressure flows for propulsion applications, pp 49–109
21. Lamanna G, Steinhausen C, Weigand B, Preusche A, Bork B, Dreizler A, Stierle R, Groß J (2018) On the importance of non-equilibrium models for describing the coupling of heat and mass transfer at high pressure. *Int Commun Heat Mass Transf* 98:49–58
22. Lee E, Chilukoti HK, Müller-Plathe F (2021) Rebound suppression of a droplet impacting on a supersolvophobic surface by a small amount of polymer additives. *ACS Macro Lett* 10(2):192–196
23. Lefebvre AH (1989) Atomization and sprays, vol 1989. HDemisphere pub. Corp., New York (1989)
24. Liu M, Bothe D (2016) Numerical study of head-on droplet collisions at high Weber numbers. *J Fluid Mech* 789:785–805
25. Liu M, Bothe D (2019) Toward the predictive simulation of bouncing versus coalescence in binary droplet collisions. *Acta Mech* 230(2):623–644
26. Loureiro DD, Kronenburg A, Reutzsch J, Weigand B, Vogiatzaki K (2021) Droplet size distributions in cryogenic flash atomization. *Int J Multiph Flow* 142:103705
27. Löwe JM, Hinrichsen V, Roisman IV, Tropea C (2020) Behavior of charged and uncharged drops in high alternating tangential electric fields. *Phys Rev E* 101(2):023102
28. Magiera J, Ray D, Hesthaven JS, Rohde C (2020) Constraint-aware neural networks for Riemann problems. *J Comput Phys* 409:109345. <https://doi.org/10.1016/j.jcp.2020.109345>
29. Muthukumaran C, Vaidyanathan A (2015) Experimental study of elliptical jet from supercritical to subcritical conditions using planar laser induced fluorescence. *Phys Fluids* 27(3):034109
30. Neusser J, Rohde C, Schleper V (2015) Relaxation of the Navier-Stokes-Korteweg equations for compressible two-phase flow with phase transition. *Int J Numer Methods Fluids* 79(12):615–639. <https://doi.org/10.1002/fld.4065>
31. Ouedraogo Y (2020) Modelling of electrohydrodynamic droplet motion under the influence of strong electric fields. PhD thesis, Technische Universität, Darmstadt
32. Ouedraogo Y, Gjonaj E, De Gersem H, Schoeps S (2020) Simulation of transient electrospray dynamics in conductive fluids. *IEEE Trans Mag* 56(3)
33. Ouedraogo Y, Gjonaj E, Weiland T, De Gersem H, Steinhausen C, Lamanna G, Weigand B, Preusche A, Dreizler A, Schremb M (2017) Electrohydrodynamic simulation of electrically controlled droplet generation. *Int J Heat Fluid Flow* 64:120–128
34. Plateau JAF (1873) Statique expérimentale et théorique des liquides soumis aux seules forces moléculaires, vol 2. Gauthier-Villars
35. Potyka J, Schulte K (2021) New approaches for the interface reconstruction and surface force computation for volume of fluid simulations of droplet interaction of immiscible liquids. [arXiv:2104.11108](https://arxiv.org/abs/2104.11108)
36. Preusche A, Dreizler A, Steinhausen C, Lamanna G, Stierle R (2020) Non-invasive, spatially averaged temperature measurements of falling acetone droplets in nitrogen atmosphere at elevated pressures and temperatures. *J Supercrit Fluids* 166:105025
37. Pruppacher HR, Klett JD (1997) Microphysics of clouds and precipitation. Kluwer Academic Publishers (1997)

38. Rayleigh L (1878) On the instability of jets. *Proc. Lond. Math. Soc.* s1-10(1):4–13
39. Rees A, Araneo L, Salzmann H, Kurudzija E, Suslov D, Lamanna G, Sender J, Oschwald M (2019) Investigation of velocity and droplet size distributions of flash boiling LN2-jets with phase doppler anemometry. In: 29th ILASS-Europe conference. Paris, France
40. Rees, A., Araneo, L., Salzmann, H., Lamanna, G., Sender, J., Oschwald, M.: Droplet velocity and diameter distributions in flash boiling liquid nitrogen jets by means of phase doppler diagnostics. *Exp. Fluids* **61**(182) (2020)
41. Rees A, Oschwald M (2021) Cryogenic test bench for the experimental investigation of cryogenic injection in rocket combustors under high-altitude conditions. In: CEC/ECMC virtual conference. (accepted)
42. Rees A, Salzmann H, Sender J, Oschwald M (2020) About the morphology of flash boiling liquid nitrogen sprays. *At Sprays* 30(10):713–740
43. Reitzle M, Kieffer-Roth C, Garcke H, Weigand B (2017) A volume-of-fluid method for three-dimensional hexagonal solidification processes. *J Comput Phys* 339:356–369
44. Reitzle M, Ruberto S, Stierle R, Gross J, Janzen T, Weigand B (2019) Direct numerical simulation of sublimating ice particles. *Int J Therm Sci* 145:105953
45. Reutzsch J, Kieffer-Roth C, Weigand B (2020) A consistent method for direct numerical simulation of droplet evaporation. *J Comput Phys* 413:109455
46. Reynders JP, Jandrell IR, Reynders SM (1999) Review of aging and recovery of silicone rubber insulation for outdoor use. *IEEE Trans Dielectr Electr Insul* 6(5):620–631
47. Ruberto S, Reutzsch J, Roth N, Weigand B (2017) A systematic experimental study on the evaporation rate of supercooled water droplets at subzero temperatures and varying relative humidity. *Exp Fluids* 58(5):55
48. Sassié PR, Mourier P, Caude MH, Rosset RH (1987) Measurement of diffusion coefficients in supercritical carbon dioxide and correlation with the equation of Wilke and Chang. *Anal Chem* 59:1164–1170
49. Scheibel EG (1954) Liquid diffusivities. *Ind Eng Chem* 46:2007–2008
50. Schmidt JB, Hofmann J, Tenzer FM, Breitenbach J, Tropea C, Roisman IV (2021) Thermosuperrepellency of a hot substrate caused by vapour percolation. *Commun Phys* 4(1):181
51. Schremb M, Campbell JM, Christenson HK, Tropea C (2017) Ice layer spreading along a solid substrate during solidification of supercooled water: Experiments and modeling. *Langmuir* 33(19):4870–4877
52. Schremb M, Roisman IV, Tropea C (2018) Normal impact of supercooled water drops onto a smooth ice surface: experiments and modelling. *J Fluid Mech* 835:1087–1107
53. Schremb M, Tropea C (2016) Solidification of supercooled water in the vicinity of a solid wall. *Phys Rev E* 94(5):052804
54. Schulte K, Weigand B, Tropea C (2016) Selected results of the collaborative research center “droplet dynamics under extreme boundary conditions” SFB-TRR 75. In: ILASS-Europe 2016
55. Schulte K, Weigand B, Tropea C (2018) Selected results of the collaborative research center “droplet dynamics under extreme ambient conditions” SFB-TRR 75. In: 14th international conference on liquid atomization and spray systems ICLASS (2018)
56. Steinhäusen C, Gerber V, Preusche A, Weigand B, Dreizler A, Lamanna G (2021) On the potential and challenges of laser-induced thermal acoustics for experimental investigation of macroscopic fluid phenomena. *Exp Fluids* 62(1)
57. Tropea C, Weigand B (2015) Droplet dynamics under extreme boundary conditions: the collaborative research council SFB-TRR 75. In: 13th international conference on liquid atomization and spray systems ICLASS
58. Weigand B, Tropea C (2012) Droplet dynamics under extreme boundary conditions: The collaborative research center SFB-TRR 75. In: 12th international conference on liquid atomization and spray systems ICLASS, pp 2–6
59. Wilke CR, Chang P (1955) Correlation of diffusion coefficients in dilute solutions. *AIChE J* 1:264–270
60. Zhang J, Leroy F, Müller-Plathe F (2014) Influence of contact-line curvature on the evaporation of nanodroplets from solid substrates. *Phys Rev Lett* 113(4):046101

61. Zhang J, Müller-Plathe F, Leroy F (2015) Pinning of the contact line during evaporation on heterogeneous surfaces: slowdown or temporary immobilization? Insights from a nanoscale study. *Langmuir* 31(27):7544–7552
62. Zhang J, Müller-Plathe F, Yahia-Ouahmed M, Leroy F (2013) A steady-state non-equilibrium molecular dynamics approach for the study of evaporation processes. *J Chem Phys* 139(13):134701

**Open Access** This chapter is licensed under the terms of the Creative Commons Attribution 4.0 International License (<http://creativecommons.org/licenses/by/4.0/>), which permits use, sharing, adaptation, distribution and reproduction in any medium or format, as long as you give appropriate credit to the original author(s) and the source, provide a link to the Creative Commons license and indicate if changes were made.

The images or other third party material in this chapter are included in the chapter's Creative Commons license, unless indicated otherwise in a credit line to the material. If material is not included in the chapter's Creative Commons license and your intended use is not permitted by statutory regulation or exceeds the permitted use, you will need to obtain permission directly from the copyright holder.



# Interactive Visualization of Droplet Dynamic Processes



Moritz Heinemann , Filip Sadlo , and Thomas Ertl

**Abstract** This article presents an overview of visual analysis techniques specifically developed for high-resolution direct numerical multiphase simulations in the droplet dynamic context. Visual analysis of such data covers a large range of tasks, starting from observing physical phenomena such as energy transport or collisions for single droplets to the analysis of large-scale simulations such as sprays and jets. With an increasing number of features, coalescence and breakup events might happen, which need to be visually presented in an interactive exploratory way to gain a deeper insight into physics. But also the task of finding relevant structures, features of interest, or a general dataset overview becomes non-trivial. We present an overview of new approaches developed in our SFB-TRR 75 project A1 covering work from the last decade to the current work-in-progress. They are the basis for relevant contributions to visualization research as well as useful tools for close collaborations within the SFB.

## 1 Introduction

Understanding droplets and droplet dynamic processes is very important in many areas of nature and technical systems. Modern research expands knowledge utilizing high-resolution computer simulations and experimental measurements producing a very large amount of data. However, these data need to be analysed and visualized to allow gaining insights. Also in the context of droplets, flow visualization is the adequate approach to do so. Traditionally, flow visualization focused on single-phase flow, but of course, observing droplets involves at least two phases, adding additional complexity to the analysis and visualization task.

---

M. Heinemann · T. Ertl

Visualization Research Center (VISUS), University of Stuttgart, Stuttgart, Germany

e-mail: [moritz.heinemann@visus.uni-stuttgart.de](mailto:moritz.heinemann@visus.uni-stuttgart.de)

F. Sadlo

Interdisciplinary Center for Scientific Computing (IWR), Heidelberg University,  
Heidelberg, Germany

In this work, we mainly analyse datasets resulting from simulations carried out with the Free Surface 3D (FS3D) [2] software. FS3D is a Computational Fluid Dynamics (CFD) solver, which employs the Volume of Fluid (VOF) method [9]. The resulting data are defined on a grid, where each cell stores the volume fraction of each phase in addition to a velocity vector. The VOF method does not inherently track an interface between phases but reconstructs it in each time step based on the VOF-field using piecewise linear interface calculation (PLIC). For interpretability, PLIC is incorporated in the visualization for surface representation [13].

## 2 Surface Reconstruction from Multiphase Volume of Fluid Simulations

The interface between different phases is probably one of the most interesting and mostly considered quantities when analysing the result of multiphase fluid simulations. Unfortunately, the VOF method does not track an interface and therefore it needs to be reconstructed. This is not only required during the simulation but also for the visualization. The reconstruction of an interface from a VOF-field can be interpreted as an isosurface extraction problem. However, traditional isosurface extraction introduces a reconstruction error. This can especially be seen by observing cells that are defined as interface cells according to the VOF method, but for which the isosurface lies completely outside of these cells. Therefore, fluid engineers should prefer to view the surface reconstructed with the PLIC method, as this is the standard method used within the simulation code, even if this reconstruction has the drawback of not being continuous. An example of a PLIC surface is shown in Fig. 1.

The work of Karch et al. [13] presented a visualization approach as well as a generalization of the PLIC method as a higher-order approximation of the interface.

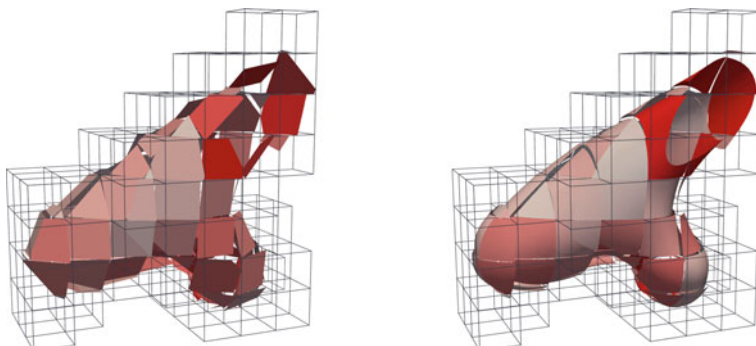
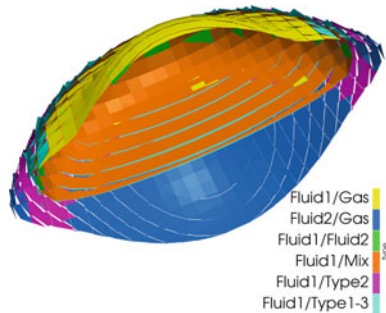


**Fig. 1** Left: Standard PLIC reconstruction of a droplet interface. Right: Generalization of the PLIC surface to a higher-order approximation. The colour-scale shows the maximum discontinuity  $\delta_{\max}$  to neighbouring cells. ©2013 IEEE. Reprinted, with permission, from [13]

**Fig. 2** PLIC surface visualization with ParaView for a three-phase simulation. Coloured are the different classes of species setups used within FS3D to determine special cases where the precomputed normals must be used



While this still maintains the piecewise characteristic, the surface becomes much smoother as can be seen in Fig. 1 (right).

A more recent challenge are simulations including three instead of just two phases or species. In such simulations, a second volume fraction field is required. Unfortunately, this makes it much harder to calculate a gradient in these fields. The gradient is required for the PLIC algorithm. According to this algorithm a PLIC patch within a cell is placed by using the negative gradient as patch normal. Further these patches are then placed iteratively to find a position such that the cell volume below the interface matches exactly the volume fraction of the cell. By using two VOF-fields, we now have the problem when looking up neighbouring cells for the calculation of partial derivatives for the gradient, these cells might be occupied with the second field and therefore no values would be available. To handle such cases, classification of the species within a  $3 \times 3 \times 3$  stencil around each cell is required to apply special calculations depending on the setup. These special cases are already handled within FS3D [15], see also Potyka et al. [in this volume](#) during simulation and the normals for the PLIC surface in these cells are stored as additional resulting data. For the visualization part, we implemented respective cell classification and take these additional normals into account. Further, the handling of three species requires an extension to the classic PLIC surface placement algorithm to work on tetrahedral cells instead of just cuboid cells, because in cells with all three phases some space is already occupied by the third species. An example of such a result is shown in Fig. 2.

### 3 Analysis of Breakup and Coalescence

Multiphase flow analysis and visualization often focus on the phase interface surface. However, in several applications droplet breakup and coalescence events occur which are very interesting because of the underlying physics. Karch et al. [11] introduce a space-time graph representation that allows exploring such events in a structured way. An example is shown in Fig. 3. There, a 3D spatial view (Fig. 3a) and a 2D parametric view (Fig. 3b) are combined. The 3D spatial view provides context to the position and surface shape of a feature. Next to this, the 2D parametric view shows

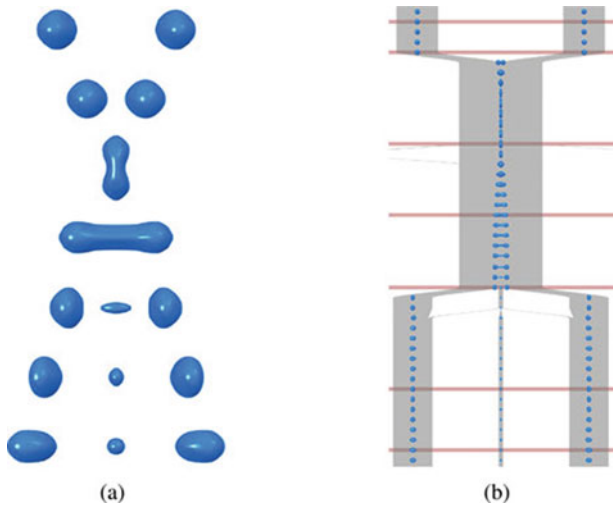


**Fig. 3** A space-time graph for a dataset with colliding droplets. Time increases in downward direction. **a** Droplet surfaces are shown for the time steps 0.021 s, 0.026 s, 0.039 s, 0.050 s, 0.060 s, 0.075 s and 0.084 s. **b** Space-time graph, where the red lines mark the time steps from **a** ©2017 IEEE. Reprinted, with permission, from [11]

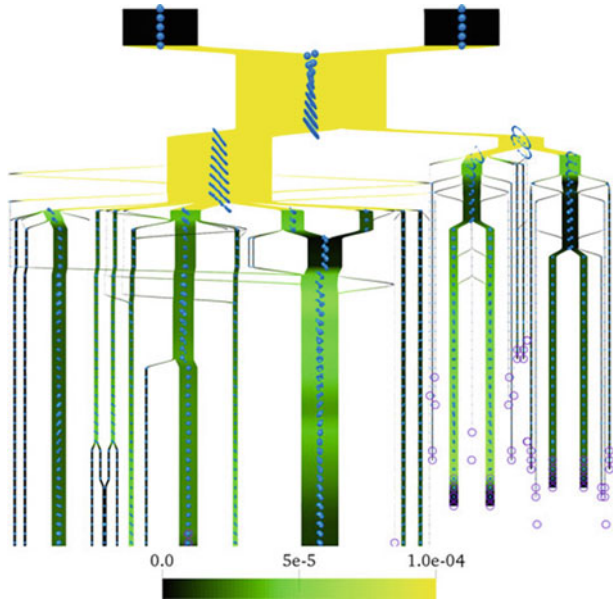


**Fig. 4** Space-time graph for a larger dataset with additional mapping of angular momentum to colour. ©2017 IEEE. Reprinted, with permission, from [11]

the graph structure providing connectivity information of feature instances between time steps. For this work, initially, the different features need to be tracked. This includes spatial and temporal tracking. Spatial connectivity is obtained by finding face-connected cells with a volume fraction  $f > 0$ . Temporal tracking is achieved by tracking particles seeded within each cell of a feature to the next time step and match the resulting positions to spatial features within this time step. To provide additional context in the visualization, the space-time graph is rendered as a Sankey diagram, where the volume of a droplet determines the width of the graph edges (Fig. 3b). Further, these edges can be extended to map additional quantities of single droplets, for example, angular momentum, to colour (Fig. 4).

## 4 Visual Analysis of Droplet Dynamics in Large-Scale Multiphase Spray Simulations

Large jet simulations generate terabytes of data containing thousands of droplets and ligaments resulting from atomization processes. This makes it a laborious task to find interesting behaviour of single outlier droplets as well as finding general behaviour patterns in the overall droplet set. These difficulties not only cover the interactive analysis task itself from a user perspective but also the fact that processing such large amounts of data is not easy when targeting a highly interactive system. We try to overcome these problems by introducing a new visual analysis system utilizing modern machine learning and clustering techniques [8].

Our method uses multiple preprocessing steps to calculate useful physical quantities and other indicator values assisting the user in the following analysis process. Starting from the raw simulation output, the first step is to extract droplets from the VOF-field. This is achieved by using face-connected component labelling on grid cells that contain the fluid phase. In the next step, for each droplet instance, a vector of physical quantities is calculated as a reduced abstract description of this droplet instance. The quantities are volume, surface area, surface area to volume ratio, angular momentum, velocity, momentum, angular velocity, total energy, kinetic energy, rotational energy, and residual energy. In addition, we store a geometric surface representation, which later will be used for rendering.

To observe single droplets over time, we need to track the individual droplet instances between the time steps of the simulation. This is done by tracing virtual particles using the velocity field, according to the method introduced by Karch et al. [11]. The result is a graph containing temporal dependencies between all droplet instances in all time steps of the simulation. From this, we can easily detect and exclude all split and merge events in order to focus on the actual behaviour of single droplets.

We utilize hierarchical clustering according to Ward's method [10] on the droplets within the abstract physical quantity space as a method to detect general behaviour patterns. Hierarchical clustering has shown the best results in practice, compared to density-based clustering algorithms such as DBSCAN [6]. The underlying problem

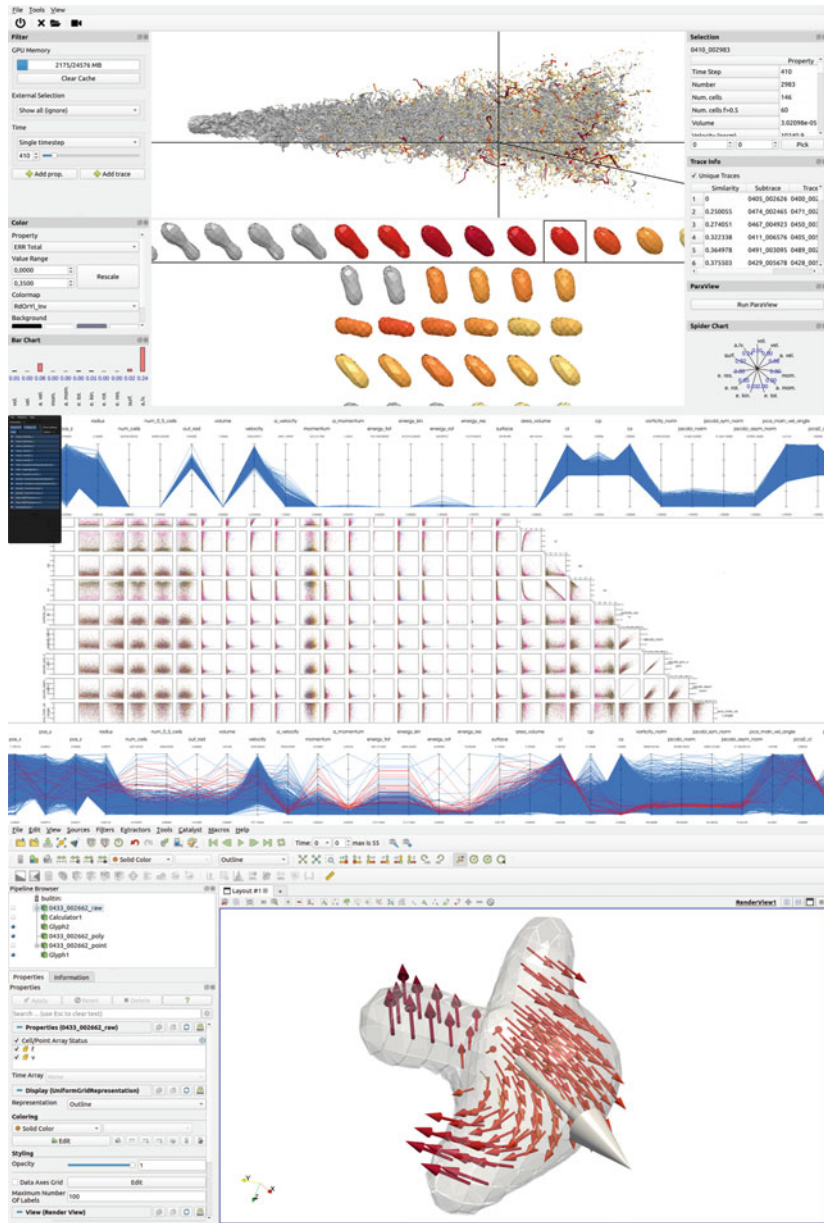


**Fig. 5** Overview of our visual analysis system (adapted from [8]). On top is the 3D surface view, where the droplets are shown in the spatial context represented by their surfaces. Additionally, quantities can be mapped to colour and a timeline of single selected droplets can be displayed. Middle shows the quantity relation view. Here techniques such as parallel coordinate plots and a scatterplot matrix allow presenting a large number of data points. Bottom is the flow view, which is a fully integrated ParaView instance allowing detailed flow analysis of a single droplet selected within the surface view

is, that the distances between data points vary depending on the type of cluster and DBSCAN will only detect a single large cluster with very similar droplets. All other droplets will be single outliers and no further clustering structure can be found among them. Unfortunately, hierarchical clustering has worse algorithmic scaling performance and limits the number of data points to be clustered at a time. Therefore, we applied the clustering to time-averaged droplet quantities instead of using each individual droplet instance.

As a complementary method to focus on individual anomalous droplets, we utilize neural network-based machine learning based on previous work by Tkachev et al. [16]. We define a measure of anomaly in how likely the temporal behaviour of a droplet is predictable with a relatively small neural network. Therefore, we use the separation and collision-free time series of individual droplets. This time series is cut into overlapping fixed-size windows of size  $k$ , where we feed the quantity vector of  $k - 1$  first subsequent time steps into a neural network, to predict the  $k$ -st time step. The norm of the difference between the predicted and actual values are used as the anomaly measurement value. One special aspect of our method is, that we train a separate neural network for each quantity because the quantities seem to vary in how likely they are predictable. This avoids that a less likely predictable quantity influences another one.

Finally, we include all our precomputed values into an interactive system, as depicted in Fig. 5. The system consists of three different views, each supporting a different task. The 3D surface view provides a spatial context to the droplets and shows their surface. Many filtering options allow for selecting quantity value ranges of interest for aggregating data. Each quantity can be mapped to the droplet surface by colour. In addition, the temporal development of selected droplets is shown next to similar time series. The quantity relation view uses information visualization techniques such as parallel coordinates and scatterplot matrices to present a large number of droplets within the abstract quantity space. This allows searching for general patterns and behaviour types between these quantities. Highly interactive framerates are achieved by using the MegaMol framework [7] as the technical basis for this view. The flow view is a fully integrated ParaView [1] instance, which is used to support a deep analysis of a single selected droplet using the original simulation output.

The system is used to analyse a jet dataset [4, 5] with the help of different tools. First, we can take a look at the quantity relation view to find high-level relations between the quantities. An example of the radius to velocity relation is shown in Fig. 6. Here, the two main clusters within the scatterplot result from a two nozzle setup within the simulation, where the outer velocity is higher than the inner velocity. The linkage between the different tools of the systems allows to easily view selected droplets from the scatterplot within the 3D surface view for spatial and geometric context.

Automated clustering can pre-filter the droplets into groups of similar quantities and droplet behaviour. The quantity relation view allows to interpret the different clusters and inspect their value ranges (Fig. 7), even if there is no direct physical

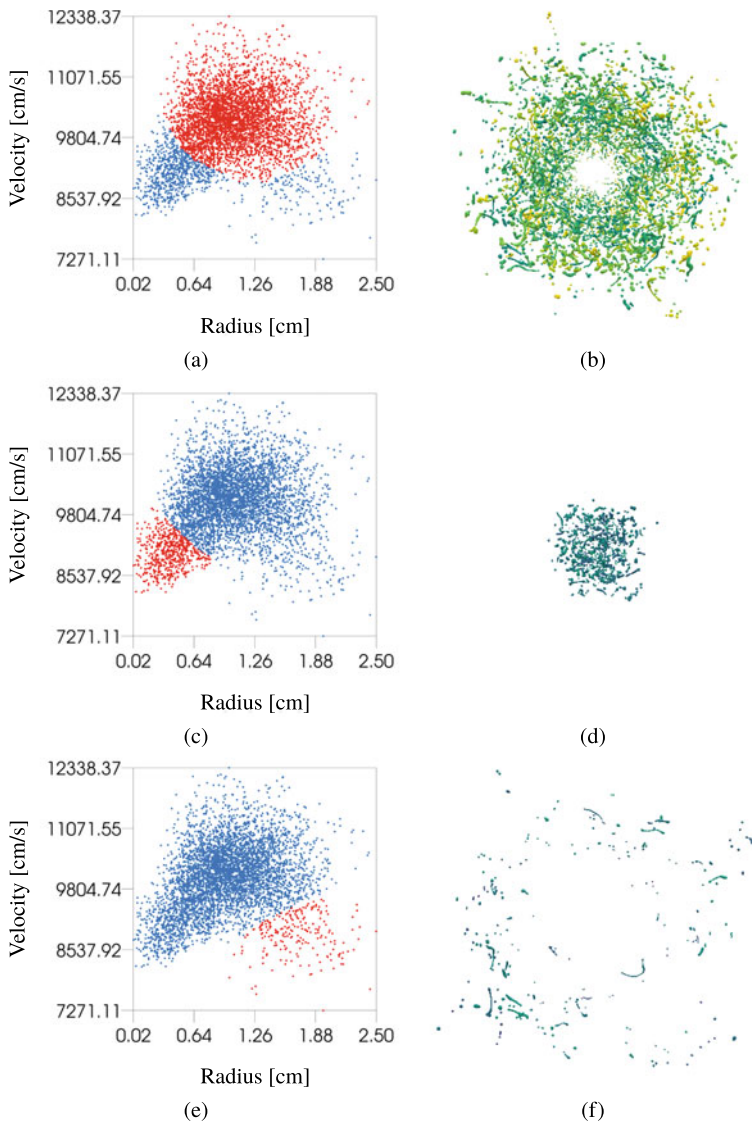


**Fig. 6** Analysis example using scatterplot matrices to investigate the relation between radius (distance to jet centre) and velocity (adapted from [8]). Selection in the scatterplot (red) (a, c, e) is linked to the 3D surface view and can be used to only display selected droplets (b, d, f). The dataset shows two clusters of different velocity (a, c) (next to a few outliers e), which are related to the radius

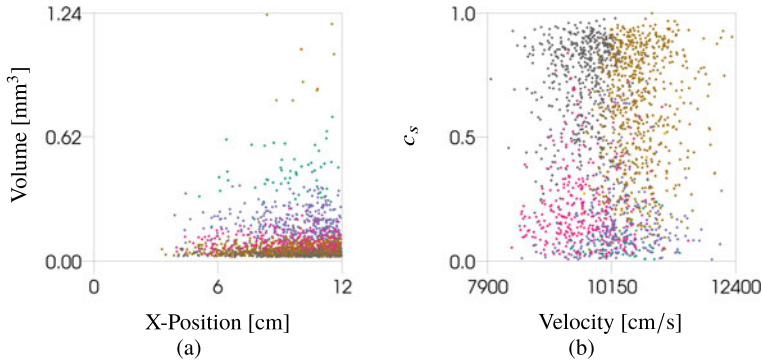


**Fig. 7** The scatterplot matrix also allows the user to interpret the clusters within the physical quantity ranges (adapted from [8]). **a** Here we can see, that volume is a very significant factor to distinguish different clusters. **b** Cluster separation can be seen along the velocity dimension as well as the spherical anisotropy dimension

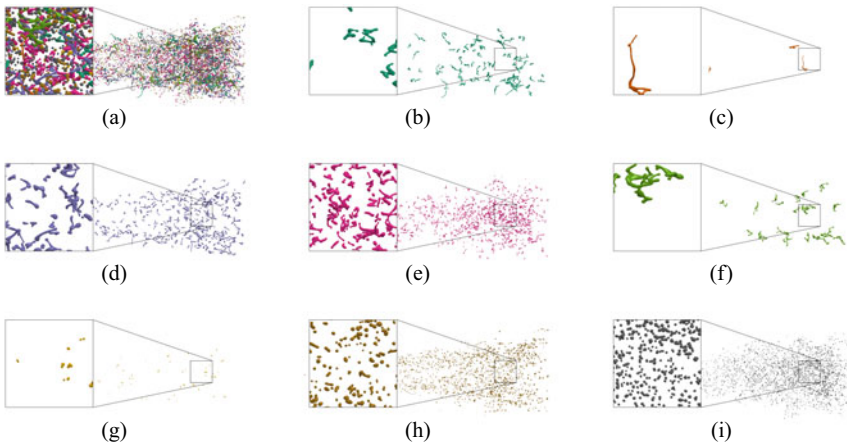


**Fig. 8** The 3D surface view shows that clusters consist of droplets with similar shapes and sizes (adapted from [8]). All droplets of a cluster are shown with the same surface colour. **a** All clusters in one view. **b-i** Each of the 8 clusters shown individually

interpretation. Within the 3D surface view, we can observe a similar size and droplet shape for all droplets of the same cluster (Fig. 8).

The prediction anomaly value is especially useful for highlighting interesting droplets and for hypothesis forming and validation during analysis. We found different droplet internal flow structures for different patterns of anomaly along with the time series of droplets. For example, droplets with a constantly high anomaly value or slowly decreasing value seem to exhibit saddle-type flow patterns. In contrast, low

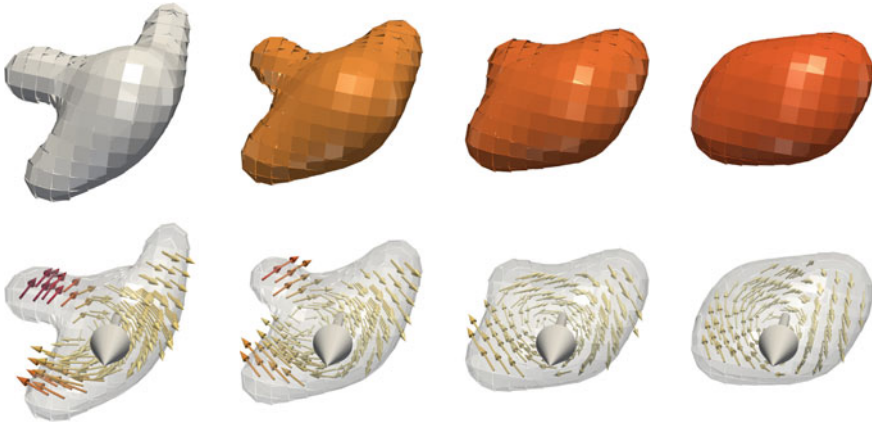


**Fig. 9** Time series of a single droplet that exhibits increasing anomaly (in top row mapped to colour). Detailed flow analysis with the integrated ParaView instance (bottom row) exhibits a vortex structure within this droplet (adapted from [8])

anomaly droplets tend to show a shear flow pattern. We found only one droplet with increasing anomaly (Fig. 9). This is the only droplet we could find where its internal flow exhibits a vortex.

## 5 Geometric Approaches to the Analysis of Jets

Spray simulations result often in complex surface structures. Many droplets and ligaments are rugged and interwoven, making visual analysis hard, especially due to the occlusion. Therefore, existing analysis approaches are based on calculating statics and other quantities such as mass or velocity distributions or by just visualizing subsets of the data by slicing and clipping. All these methods are based on reducing the observed data, which has the drawback of either losing details (as by global statistics) or context (as by slicing or clipping). In this work, we aim to overcome these problems by using geometric transformations to reduce occlusion, while trying to keep relevant structures and minimize distortion effects.

The most simple, straightforward approach is to transform the surface representation from cylindrical coordinates to Cartesian coordinates. This allows to view a jet from all sides at the same time, but of course, introduces distortion. Figure 10 shows selected time steps from an animation of this transformation. Nevertheless, in cases where the relative position of structures is more of interest than the actual shape of the objects this method can still be effective to some degree.

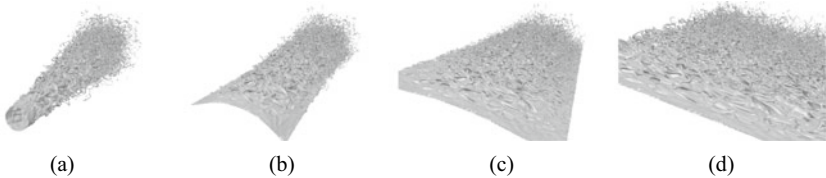


**Fig. 10** **a–d** Selected time steps of an animation of the jet data undergoing transformation from the original surface view interpreted as cylindrical coordinates to Cartesian coordinates

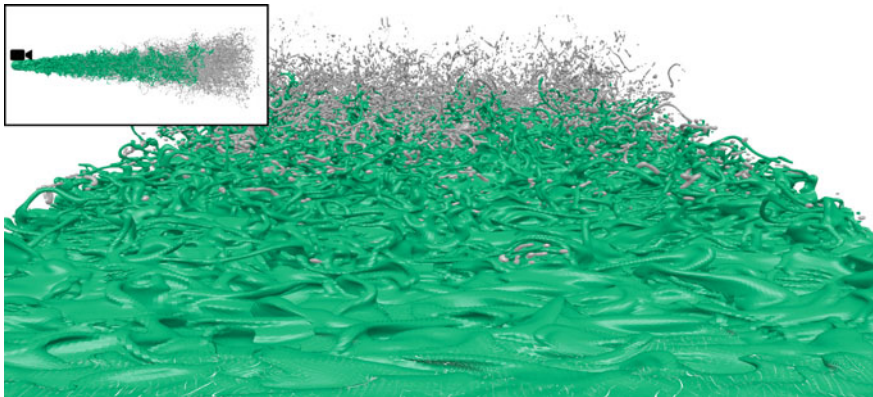


**Fig. 11** Jet simulation data transformed from cylindrical coordinates to Cartesian coordinates. The view looks from the nozzle along the flow direction. The jet base is highlighted in green which conveys that a large number of components is still connected to the base

With a second method, we try to keep the shape of single droplets persistent. Therefore, we extract droplets and calculate the PLIC surface representation within the original simulation domain in the same way as in Sect. 4. Then, we transform the centre of mass and the orientation of a droplet from cylindrical to Cartesian coordinates. This retains the shape of individual droplets, while only the distance between them is distorted.

We implemented a dedicated tool that allows us to dynamically change the transformation method at interactive speeds during rendering. Figures 11 and 12 show the data undergoing the straightforward coordinate transformation. While some distortion may affect the droplets, this view is especially useful to observe the base of the jet. All sides can be observed at the same time and surface structures and waves can easily be compared, even if they may be located on the opposite side of the jet within the original spatial domain. To focus on the droplets themselves, the droplet-based transformation as shown in Fig. 13 might be more useful. We can see the undistorted droplets next to each other providing spatial context. The disadvantage of this is, of course, that the distances between droplets are distorted.

These methods are still work-in-progress and will be extended in various ways. First, we will investigate a combination of transformations, where the inner droplets

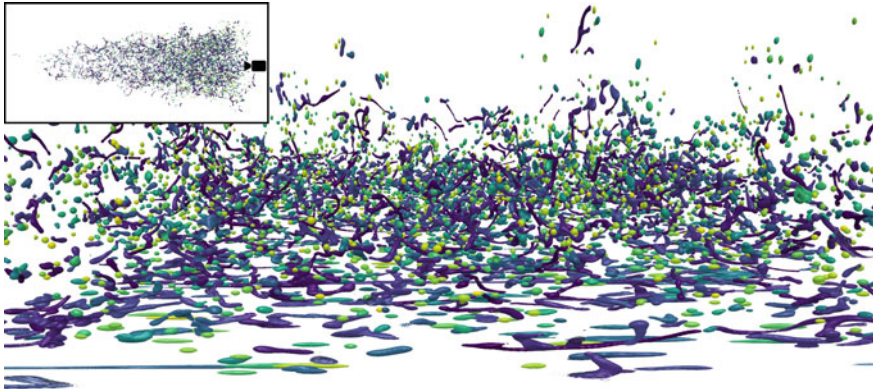


**Fig. 12** Opposite view direction compared to Fig. 11. The droplets at the bottom originate from the centre of the jet and are distorted sideways, while the droplets at the top originate from the outer areas and are squashed together. In between is an area of relatively undistorted droplets. Additionally, the droplets are coloured by the spherical anisotropy  $c_s$  using the Viridis colourmap (purple maps to low spherical shape and yellow would highlight an ideal sphere). This allows to visually separate droplets from ligaments

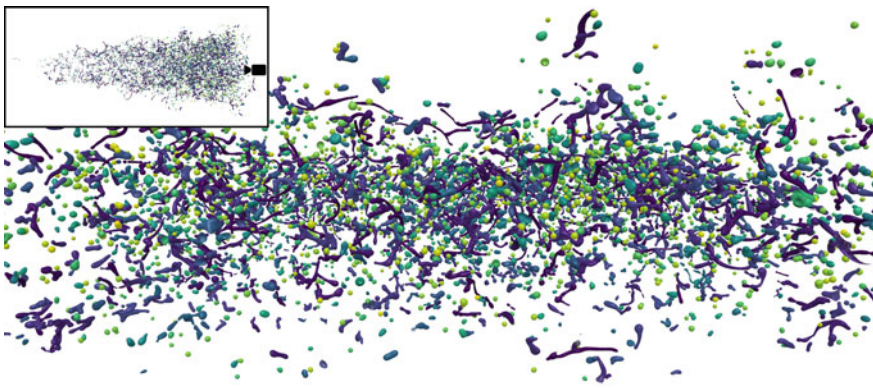


**Fig. 13** Same view as Fig. 12, but with the droplet position transformation. Now we can see the original shape of each droplet, but still, the distance between the droplets is distorted

are transformed as in Fig. 12, while the outer droplets are only moved as in Fig. 13. The challenge will be to find a smooth transition area, to prevent a prominent visual edge and avoid potentially possible droplet collisions. Next, we will introduce non-linear transformations to find a compromise between fluid and non-fluid phase distortion.

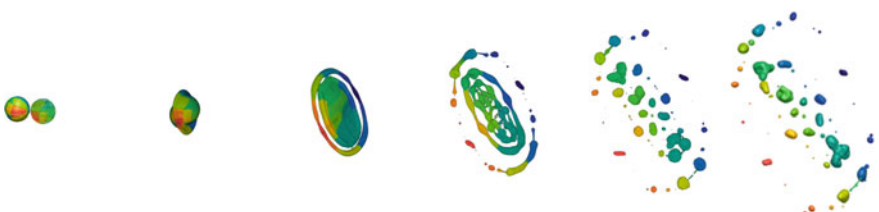
## 6 Multi-Component Visualization

Karch et al. [12] presented a method for analysing feature separation in advected scalar fields by calculating separation surfaces. The method is based on the idea to track the movement of small fluid portions by representing them as virtual particles which are tracked along the velocity field. In more detail, the method will place virtual particles at a user-defined starting time step within the fluid phase. Then, the particles are advected with the velocity field to a selected end time step. As the particles are used to represent a fluid portion around them, it is now possible to label each particle with the name of the feature in which it is located within the end time step. Now within the starting time step, the labels can be used to extract continuous regions of particles with the same label. The borders between these regions show, where the fluid will separate at a later time step and can be visualized as separation surfaces.

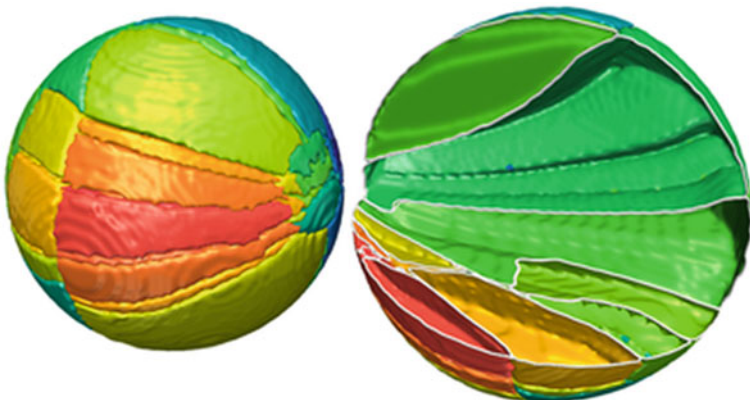
Unfortunately, during direct multiphase simulations often only every  $n$ th time step is saved to disk. Due to this relatively coarse temporal resolution, the advected particles will diverge from the actual VOF-field. Therefore, Karch et al. [12] suggested several corrector methods to keep the virtual particles within the VOF-phase.

Figure 14 shows the temporal development of the separation surfaces within a binary droplet collision. Figure 15 provides a detailed clip of the separation surfaces within the starting time step.

Currently, this approach is extended to support multiphase simulations with more than two phases or species. For this work, we are using a dataset of Potyka and Schulte [15] simulating a crossing separation (see also Potyka et al. [in this volume](#)). This is a head-on collision of a 50% water and 50% glycerol droplet with a silicon oil M5 droplet. The relative collision velocity is  $3.17 \text{ m s}^{-1}$  and the radius of both droplets is around  $200 \mu\text{m}$ . The dataset is shown in Fig. 16. The basic principle of our method works the same as for two phases, but the labelling must now handle multiple phases together and also the correctors need to be adopted. Figure 17 shows very early results using this method on the dataset. As the corrector methods are not



**Fig. 14** Separation surfaces within a binary droplet collision (adapted from [12]). The virtual particles are seeded in the starting time step (left) and labelled (here represented by colour) by the separated features in the end time step (right)



**Fig. 15** Detailed separation surface from the binary collision in Fig. 14 (adapted from [12])

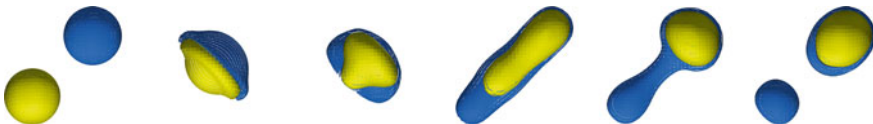


**Fig. 16** Crossing separation simulation by Potyka and Schulte (cf. [15], see also Potyka et al. in this volume for further details). Head-on collision of a water-glycerol droplet (yellow) with a silicon oil M5 droplet (blue). It can be seen that the silicon oil droplet flows around the glycerol/water droplet and then splits up

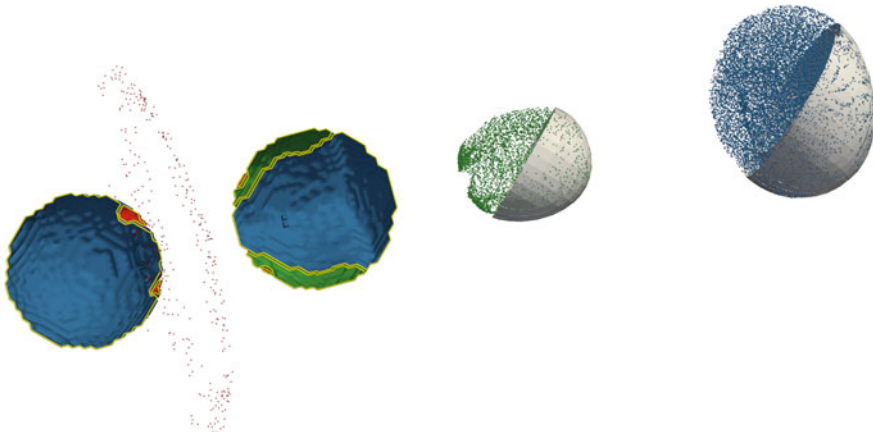


**Fig. 17** Composition of the separation surfaces within the start time step (left two droplets), the advected particles at the end time step (small dots), and separated features at the end time step (right two droplets). We can see that the blue labels are based on the final feature, which contains portions of both initial materials

fully adopted to three species, we can see that some particles are advected wrongly (marked red in Fig. 17). We expect to significantly reduce the number of such wrongly advected particles once the implementation of these correctors is finished.

## 7 Two-Phase Flow Visualization on High-Resolution Displays

The surface of jets or similar two-phase simulations is very often highly complex with many detailed small scale structures. The limited size of standard workstation screens forces the users to choose between having an overview or zooming into a smaller region of interest for details. A powerwall [14] as a large-scale high-resolution display has the potential to overcome this limitation. Users can see the full geometric expansion of a dataset and small scale structures at the same time and they can freely move in front of the powerwall to observe the details, while the global context remains. Further, the powerwall can be used by multiple users at the same time, allowing for interactive collaboration.

Using a powerwall for flow visualizations brings various technical difficulties compared to a desktop workstation. The powerwall installed at the Visualization Research Center of the University of Stuttgart is driven by ten 4K projectors and the images need to be rendered in a distributed cluster. Therefore, standard visualization software, cannot simply be used without further adjustments. We have chosen to build on the Unreal Engine [3], as it already supports distributed rendering. This includes synchronising settings and parameters across the render cluster and support for splitting a camera into multiple local tiles, which can later seamlessly be shown as a single image. While the Unreal Engine has the advantage of providing features for utilizing the powerwall and great rendering results, we still need to integrate our multiphase datasets. Both, for performance reasons and simplicity we have decided to externally pre-compute a geometric surface representation of the multiphase simulations using PLIC. This representation is stored in glTF format and can be imported as an asset into the Unreal Engine. Figure 18 shows an example, where two users collaborate and interactively analyse a jet simulation dataset.

With this development, we have demonstrated that with some technical effort the potential of the powerwall can be utilized for multiphase flow visualization. The Unreal Engine is a good technical foundation to set up the cluster environment and to render high-quality images, however, common visualization tools such as filtering, clipping and the handling of additional data values per droplet are not yet supported by the engine and must be implemented. We now aim at evaluating the analysis process and compare it to standard flow visualization techniques on desktop screens. In order to benefit from collaboration, the interaction concept would need to be extended to multiple users such that more than one person is able to control the view.



**Fig. 18** Surface of a jet simulation is rendered on the VISUS powerwall and is interactively explored by two users

## 8 Conclusions

Even after a decade of research and development, interactive visualization of multiphase flow remains a challenging problem. While also single-phase flow visualization techniques continue to make progress, not all of these advances can be easily transferred to multiphase flow. As modelling and simulation of droplet phenomena have evolved over the years within the SFB-TRR 75, so have the requirements for visual analysis. Datasets have grown in size and complexity and many research questions cannot be answered by standard postprocessing tools. In this paper, we have reported on several new visualization techniques resulting from research in the project A01. Most of them are published together with our collaboration partners, others are still work-in-progress. The contributions cover a large span of topics ranging from phase interface visualization, topology representation of breakup and coalescence as well as tracking of separation surfaces, occlusion reduction within complex structures such as jets, assisted analysis and hypothesis forming tools to reveal relevant structures in large datasets, to visualization on high-resolution powerwalls. Concerning the visual analysis of simulations of more than two phases, only first steps have been taken and many options for future research became visible. Machine learning techniques were introduced as a means for identifying droplets with interesting features and we expect more such approaches to be helpful for comparative visualization and exploration of simulation ensembles.

**Acknowledgements** We kindly acknowledge the financial support by the Deutsche Forschungsgemeinschaft (DFG, German Research Foundation) - Project SFB-TRR 75, project number 84292822.

## References

1. Ayachit U (2015) The ParaView guide: a parallel visualization application. Kitware, Inc
2. Eisenschmidt K, Ertl M, Gomaa H, Kieffer-Roth C, Meister C, Rauschenberger P, Reitzle M, Schlottke K, Weigand B (2016) Direct numerical simulations for multiphase flows: an overview of the multiphase code FS3D. *Appl Math Comput* 272:508–517. <https://doi.org/10.1016/j.amc.2015.05.095>
3. Epic Games: Unreal engine (2021). <https://www.unrealengine.com>
4. Ertl M (2019) Direct numerical investigations of non-newtonian drop oscillations and jet breakup. PhD thesis, University of Stuttgart. <https://doi.org/10.18419/opus-10764>
5. Ertl M, Weigand B (2017) Analysis methods for direct numerical simulations of primary breakup of shear-thinning liquid jets. *Atomiz Sprays* 27(4):303–317. <https://doi.org/10.1615/AtomizSpr.2017017448>
6. Ester M, Kriegel HP, Sander J, Xu X (1996) A density-based algorithm for discovering clusters in large spatial databases with noise. In: Proceedings of the second international conference on knowledge discovery and data mining, KDD'96. AAAI Press, Portland, Oregon, pp 226–231
7. Gralka P, Becher M, Braun M, Frieß F, Müller C, Rau T, Schatz K, Schulz C, Krone M, Reina G, Ertl T (2019) MegaMol - a comprehensive prototyping framework for visualizations. *Eur Phys J Spec Top* 227(14):1817–1829. <https://doi.org/10.1140/epjst/e2019-800167-5>
8. Heinemann M, Frey S, Tkachev G, Straub A, Sadlo F, Ertl T (2021) Visual analysis of droplet dynamics in large-scale multiphase spray simulations. *J Vis* 24(5):943–961. <https://doi.org/10.1007/s12650-021-00750-6>
9. Hirt CW, Nichols BD (1981) Volume of fluid (VOF) method for the dynamics of free boundaries. *J Comput Phys* 39(1):201–225. [https://doi.org/10.1016/0021-9991\(81\)90145-5](https://doi.org/10.1016/0021-9991(81)90145-5)
10. Johnson SC (1967) Hierarchical clustering schemes. *Psychometrika* 32(3):241–254. <https://doi.org/10.1007/BF02289588>
11. Karch GK, Beck F, Ertl M, Meister C, Schulte K, Weigand B, Ertl T, Sadlo F (2018) Visual analysis of inclusion dynamics in two-phase flow. *IEEE Trans Visual Comput Graph* 24(5):1841–1855. <https://doi.org/10.1109/TVCG.2017.2692781>
12. Karch GK, Sadlo F, Boblest S, Ertl M, Weigand B, Gaither K, Ertl T (2017) Visualization of feature separation in advected scalar fields. <https://arxiv.org/abs/1705.05138>
13. Karch GK, Sadlo F, Meister C, Rauschenberger P, Eisenschmidt K, Weigand B, Ertl T (2013) Visualization of piecewise linear interface calculation. In: 2013 IEEE pacific visualization symposium (PacificVis), pp 121–128. <https://doi.org/10.1109/PacificVis.2013.6596136>
14. Müller C, Reina G, Ertl T (2013) The VVand: a two-tier system design for high-resolution stereo rendering. In: CHI POWERWALL 2013 workshop
15. Potyka J, Schulte K (2021) New approaches for the interface reconstruction and surface force computation for volume of fluid simulations of droplet interaction of immiscible liquids. <https://arxiv.org/abs/2104.11108>
16. Tkachev G, Frey S, Ertl T (2019) Local prediction models for spatiotemporal volume visualization. *IEEE Trans Vis Comput Graph* 1. <https://doi.org/10.1109/TVCG.2019.2961893>

**Open Access** This chapter is licensed under the terms of the Creative Commons Attribution 4.0 International License (<http://creativecommons.org/licenses/by/4.0/>), which permits use, sharing, adaptation, distribution and reproduction in any medium or format, as long as you give appropriate credit to the original author(s) and the source, provide a link to the Creative Commons license and indicate if changes were made.

The images or other third party material in this chapter are included in the chapter's Creative Commons license, unless indicated otherwise in a credit line to the material. If material is not included in the chapter's Creative Commons license and your intended use is not permitted by statutory regulation or exceeds the permitted use, you will need to obtain permission directly from the copyright holder.



# Development of Numerical Methods for the Simulation of Compressible Droplet Dynamics Under Extreme Ambient Conditions



Steven Jöns, Stefan Fechter, Timon Hitz, and Claus-Dieter Munz

**Abstract** The computation of two-phase flow scenarios in a high pressure and temperature environment is a delicate task, for both the physical modeling and the numerical method. In this article, we present a sharp interface method based on a level-set ghost fluid approach. Phase transition effects are included by the solution of the two-phase Riemann problem at the interface, supplemented by a phase transition model based on classical irreversible thermodynamics. We construct an exact Riemann solver, as well as an approximate Riemann solver. We compare numerical results against molecular dynamics data for an evaporation shock tube and a stationary evaporation case. In both cases, our numerical method shows a good agreement with the reference data.

## 1 Introduction

To accurately predict phase transition in fluid flows with high pressure and temperature, e.g., nozzles and rocket combustion chambers, several obstacles need to be overcome. On the one hand, the lack of thermodynamic equilibrium necessitates sophisticated models for the phase transition process. Thereby, one needs to consider the microscale nature of the transition from a liquid to a vapor and the macroscopic impact on the surrounding fluid flow. On the other hand, if the pressures and temperatures are in the vicinity of the critical point, the compressibility of both fluids can not be neglected.

In the collaborative research council *SFB-TRR75*, a numerical framework for this scenario was developed in subproject *TP-A2*. The first and second funding period laid the groundwork in close cooperation with *TP-A3*: a sharp interface level-set ghost fluid method [14]. In this method, the grid size is assumed to be much larger than the width of the interfacial transition zone. Therefore, the interface is approximated as a discontinuity. The phases are treated individually from each other, while suitable

---

S. Jöns (✉) · S. Fechter · T. Hitz · C.-D. Munz

Institute of Aerodynamics and Gas Dynamics (IAG), University of Stuttgart, Stuttgart, Germany  
e-mail: [joens@iag.uni-stuttgart.de](mailto:joens@iag.uni-stuttgart.de)

jump conditions at the interface ensure the correct physical coupling. The bulk phases are treated with a discontinuous Galerkin spectral element method (DGSEM) [4, 23, 32] and real gas equations of state [17, 22]. The computationally efficient high-order DGSEM scheme can resolve fine details in the fluid flow. The use of a finite-volume sub-cell shock capturing [43] allows simulating the classical phenomena in compressible gas dynamics, e.g., shock waves. The position of the phase interface is captured by a level-set method, which is also treated via the DGSEM. The coupling of the two phases is done by applying a ghost fluid method [16, 37], in which the ghost states are defined from a Riemann solver. Two-phase Riemann solvers were proposed within the *SFB-TRR75* by Fechter et al. [12, 15]. They included considerations on evaporation, valid under isothermal conditions.

During the third funding period of the *SFB-TRR75*, the work of *TP-A2* focussed on evaporation in non-isothermal conditions. This was a challenging task, as the complicated thermodynamic mechanisms and the non-linear energy equation quickly lead to instabilities in the numerical scheme if the modelling of the evaporation process is not accurate. To gain more insight into the compressible evaporation process, a fruitful cooperation with *TP-B6* was started. By comparing molecular dynamics data from *TP-B6* with solutions of the authors sharp-interface method in [24, 25], a strategy was developed to validate different evaporation models. Thereby, the method of Hitz et al. [25] was constructed, that was able to simulate a non-isothermal shock tube scenario with evaporation. Deviations from the molecular dynamics data of *TP-B6* were limited to the temperature profile. Discussions of related scenarios exist in literature by the experiments of Simões-Moreira and Shepherd [42]. However, a description of the observed evaporation was only possible with a mixture approach. Le Métayer successfully made use of the Chapman-Jouguet theory in [34], though this approach is limited to the case of the maximum possible mass flux, which strongly simplifies the thermodynamic consideration. The method developed in *TP-A2* on the other hand, is a more general approach, applicable to any subcritical evaporation scenario when the appropriate material parameters are known.

Further work in the third funding period were related to improvements in the sharp-interface method for accurate simulations of droplet dynamics, including merging phenomena, c.f., [30, 38]. The numerical framework of *TP-A2* was used in cooperation with *TP-B5* to investigate bubble growth in a superheated liquid [9, 10]. Similar, a diffuse interface method, based on the Navier–Stokes Korteweg Equations, was developed together with *TP-A3* [26].

In this article, we focus on the building blocks for a non-isothermal evaporation model that were developed in the third funding period. We build on the results achieved in Hitz et al. [25] and propose a novel thermodynamic closure for the conditions at the interface, based on classical irreversible thermodynamics. We formulate two different Riemann solvers and compare results of the sharp interface method against molecular dynamics data for the evaporation shock tube scenario from [25] as well as a stationary evaporation case from *TP-B6* [21].

The article is structured as follows. In Sect. 2 we describe the governing equations, followed by a description of our numerical framework in Sect. 3. The evaporation model, as well as its inclusion into an exact and an approximate Riemann solver, are

discussed in Sect. 4. Afterwards, numerical results are presented in Sect. 5, followed by our conclusion.

## 2 Governing Equations

We consider a sharp interface setting of two pure phases without a mixing zone. Hence, the domain of interest  $\Omega$  is divided into a liquid region  $\Omega^L$  and a vapor region  $\Omega^V$ , separated by the interface which is described by the hypersurface  $\Gamma$ . It is infinitesimally thin and neither carries mass, nor energy.

### 2.1 Conservation Equations

The two regions  $\Omega_L$  and  $\Omega_V$  are each governed by its own set of compressible Euler equations with heat conduction:

$$\mathbf{U}_t + \nabla \cdot \mathbf{F}(\mathbf{U}) = 0, \quad \text{with} \quad \mathbf{U} = \begin{pmatrix} \rho \\ \rho\mathbf{v} \\ \rho e \end{pmatrix} \quad \text{and} \quad \mathbf{F}(\mathbf{U}) = \begin{pmatrix} \rho\mathbf{v} \\ \rho\mathbf{v} \otimes \mathbf{v} + \mathbf{I}p \\ \mathbf{v}(\rho e + p) + \mathbf{q} \end{pmatrix}, \quad (1)$$

where  $\rho$  denotes the density,  $\mathbf{v} = (u, v, w)^T$  the velocity vector,  $p$  the pressure,  $e$  the specific total energy, and  $\mathbf{q}$  the heat flux vector. We model the heat flux by Fourier's law

$$\mathbf{q} = -\lambda \nabla T, \quad (2)$$

where  $T$  is the temperature and  $\lambda$  is the thermal conductivity. The total energy of the fluid  $\rho e$  is composed of the internal energy  $\rho \epsilon$  and the kinetic energy:

$$\rho e = \rho \epsilon + \frac{1}{2} \rho \mathbf{v} \cdot \mathbf{v}. \quad (3)$$

### 2.2 Equation of State

In each fluid, pressure and specific internal energy are linked via an appropriate equation of state (EOS). Within our framework, algebraic, as well as multiparameter EOS, can be used. The tabulation technique of Föll et al. [17] ensures efficiency. In this paper, we rely on multiparameter EOS given in the form of the reduced Helmholtz energy:

$$\frac{\psi(\rho, T)}{RT} = F^0(\delta, \theta) + F^r(\delta, \theta), \quad (4)$$

with  $\mathcal{R}$  denoting the specific gas constant,  $\delta = \rho/\rho_c$  the reduced density,  $\theta = T_c/T$  the inverse reduced temperature,  $F^0$  the ideal gas contribution of the reduced Helmholtz energy, and  $F'$  the residual contribution. The main benefit of using EOS in this form is given by the fact that all other thermodynamic properties can be derived by exact differentiation of Eq. (4).

## 2.3 Interface Capturing

The position of the phase interface is implicitly given by the root of a level-set function  $\phi(\mathbf{x})$ , following [44]. From the level-set field, geometrical properties, e.g. the interface normal vector  $\mathbf{n}^{\text{LS}}$  and the interface curvature  $\kappa$  can be calculated [30]. The level-set transport equation

$$\phi_t + \mathbf{v}^{\text{LS}} \cdot \nabla \phi = 0, \quad (5)$$

describes the transport of  $\phi$  by a velocity-field  $\mathbf{v}^{\text{LS}}$ . Since  $\mathbf{v}^{\text{LS}}$  is obtained from the interface conditions, this velocity needs to be extrapolated into the remaining domain by solving the Hamilton-Jacobi equations

$$\frac{\partial v_i^{\text{LS}}}{\partial \tau} + \text{sign}(\phi) \mathbf{n}^{\text{LS}} \cdot \nabla v_i^{\text{LS}} = 0, \quad (6)$$

with the direction-wise components  $v_i^{\text{LS}}$  of the velocity field  $\mathbf{v}^{\text{LS}}$  and the pseudo time  $\tau$ , following [2].

Ideally, the level-set function fulfills the signed distance property. However, Eq. (5) does not preserve it. Hence, the level-set function needs to be reinitialized. Following [44], we use the Hamilton-Jacobi equation

$$\phi_t + \text{sign}(\phi) (|\nabla \phi| - 1) = 0, \quad (7)$$

to retain the signed distance property. The solutions of Eqs. (5)–(7) are only necessary in a narrow band encompassing the interface. Outside this narrow band, the level-set function is set to the bands fixed radius and the velocity field is set to zero.

## 3 Numerical Methods

In the following, we describe our numerical framework, which is based on the papers [13, 14, 30, 38]. The domain of interest  $\Omega$  is discretized into  $n_{\text{Elems}}$  non-overlapping hexahedral elements  $\Omega_e$ , with  $e = 1, \dots, n_{\text{Elems}}$ . The computational mesh is used as a baseline for both the conservation equations as well as level-set specific equations.

### 3.1 Conservation Equations

The conservation equations are discretized by the discontinuous Galerkin spectral element method (DGSEM) [31] with finite-volume sub-cells [39, 43]. In the high-order DGSEM, the ansatz function for the state and the flux is a polynomial of degree  $N$

$$\mathbf{U}_h(\mathbf{x}, t) = \sum_{i,j,k=0}^N \hat{\mathbf{U}}_{ijk}(t) \ell_{ijk}(\mathbf{x}) \quad \text{and} \quad \mathbf{F}_h(\mathbf{x}, t) = \sum_{i,j,k=0}^N \hat{\mathbf{F}}_{ijk}(t) \ell_{ijk}(\mathbf{x}), \quad (8)$$

with  $\ell_{ijk}$  being the polynomial basis function given by the tensor product of one-dimensional Lagrange polynomials. The weak formulation of the governing equations

$$\frac{\partial}{\partial t} \int_{\Omega_e} \mathbf{U}_h \ell_{ijk} d\mathbf{x} + \oint_{\partial\Omega_e} \hat{\mathbf{F}}^* \cdot \mathbf{n} \ell_{ijk} ds - \int_{\Omega_e} \mathbf{F}_h \cdot \nabla \ell_{ijk} d\mathbf{x} = 0, \quad (9)$$

is solved, where  $\mathbf{n}$  denotes the outward pointing normal vector of the element boundary and  $\hat{\mathbf{F}}^*$  a numerical flux function that couples neighbouring elements with each other. The integrals in Eq. (9) are solved by Gaussian quadrature using the same set of  $N + 1$  Gauss-Legendre points as in the polynomial ansatz. Solution gradients, e.g. of the temperature, can be calculated by applying the BR1 lifting procedure [3]. Details on the implementation can be found in [4, 23, 32].

As the DGSEM is a high-order method, discontinuities, e.g., shocks and phase boundaries, will ultimately lead to the appearance of the unwanted Gibbs phenomena. To stabilize the solution in these areas, we combine the DGSEM with a finite-volume (FV) sub-cell method following [43]. Areas, in which sub-cells are needed, are identified by a modal indicator [39] for shocks and the position of the level-set root for the interface. In the respective elements, the solution representation is switched from a polynomial of degree  $N$  to  $N + 1$  equidistantly spaced FV sub-cells. This switch is conservative because of

$$\int_{\Omega_e} \mathbf{U} d\mathbf{x} \equiv \int_{\Omega_e} \mathbf{U}_{DG} d\mathbf{x} = \int_{\Omega_e} \mathbf{U}_{FV} d\mathbf{x}. \quad (10)$$

The FV scheme in the sub-cells is extended to a second-order total variation diminishing (TVD) scheme with a minmod limiter. A correct coupling of the polynomial and FV solution is ensured, by using the FV representation for the flux calculation and then projecting to the polynomial discretization for the discontinuous Galerkin (DG) elements. Once elements are no longer troubled, i.e., the FV sub-cells are no longer necessary, the solution representation is switched back to the DG polynomial. Next to the stabilization of the DG scheme, the sub-cell approach locally refines the computational grid, improving the spatial localization of the strong gradient.

### 3.2 Interface Capturing

The level-set transport equation (5) is discretized with a DGSEM method for hyperbolic equations with non-conservative products [11, 30], using the framework of path-conservative schemes of [8]. As in the flow equations, the solution ansatz for the level-set function is a polynomial of degree  $N$

$$\phi_h(\mathbf{x}, t) = \sum_{i,j,k=0}^N \hat{\phi}_{ijk}(t) \ell_{ijk}(\mathbf{x}). \quad (11)$$

The weak formulation of Eq. (5) reads as

$$\frac{\partial}{\partial t} \int_{\Omega_e} \phi_h \ell_{ijk} d\mathbf{x} + \oint_{\partial\Omega_e} \mathbf{B}(\mathbf{x}) \cdot \nabla \phi_h \ell_{ijk} ds + \int_{\Omega_e} \mathbf{B}(\mathbf{x}) \cdot \nabla \phi_h \ell_{ijk} d\mathbf{x} = 0, \quad (12)$$

with  $\mathbf{B}(\mathbf{x}) = \mathbf{v}^{LS}$ . Herein, the path-conservative jump term  $\mathbf{B}(\mathbf{x}) \cdot \nabla \phi_h$  is approximated by a path-conservative Rusanov Riemann solver from [11].

Although the level-set function is by definition a smooth signed-distance function, in practical applications discontinuities may occur, e.g., at the edge of the narrow band or in the case of merging droplets. Therefore, the FV sub-cell approach is used for the level-set transport as well. For details on the path-conservative scheme and the FV shock-capturing we refer to [11] and [30]. In addition to the level-set transport, the two sets of Hamilton-Jacobi equations, (6) and (7) are each solved with a fifth-order WENO scheme [29] in combination with a third-order low storage Runge-Kutta method with three stages.

### 3.3 The Level-Set Ghost Fluid Method

The methods described above are the building blocks of our sharp interface method. A key component of an accurate simulation of interfacial flows is a correct coupling of the two phases. We follow the methodology presented in [37], with a Riemann solver based ghost fluid method. Therein, the solution of the Riemann Problem with the states left and right of the phase interface is constructed. Given the solution, the numerical flux at the interface can be calculated for each phase. We will detail the discussion on this topic in Sect. 4.2.

In our numerical framework, the solution is advanced in time by the following steps:

1. The level-set function is reinitialized.
2. Using the information given by the level-set function, the computational domain is decomposed into  $\Omega_L$  and  $\Omega_V$ . The domain boundaries coincide with the finite volume sub-cells, creating a surrogate phase boundary.

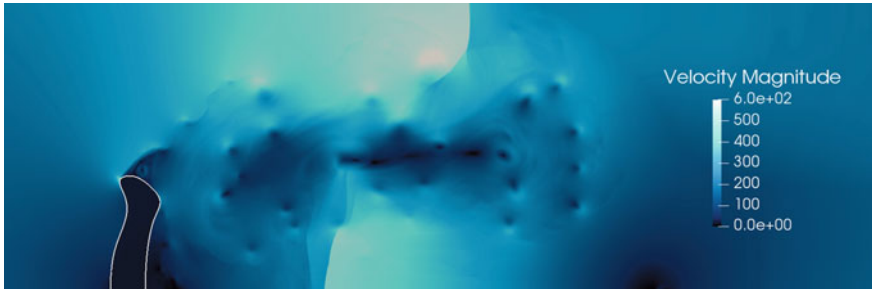


**Fig. 1** Velocity magnitude distribution of a 2D shock-drop interaction. The phase interface is depicted in white

3. Based on modal smoothness indicators and geometrical information of the level-set function, the DG-FV distribution of the fluid solution and the level-set function are updated.
4. Normal vector and curvature at the phase interface are calculated.
5. The two-phase Riemann problem is solved at the interface, providing the boundary condition for each phase and the velocity of the phase boundary at the interface.
6. The interface velocity is extrapolated into the volume to obtain a velocity field for the level-set transport.
7. An explicit fourth-order Runge-Kutta (RK) scheme from [7] is used to advance the level-set function and the fluid solution for each phase in time.

Our numerical framework is capable of predicting complex two-phase flow cases. Without phase transition and with slight modifications to the algorithm detailed in [30], the prediction of colliding droplets, merging droplets and shock-drop interactions have been shown in [30, 38, 47]. The distribution of the velocity magnitude of such a shock-drop interaction is shown in Fig. 1. Here, a shock with a Mach number of  $M = 1.47$  impinged on an initially round water column with a Weber number of  $We = 12$ . The deformation of the water column, as well as the complex velocity field can be seen. For further details on the simulation we refer to [30]. In addition to the scenarios depicted above, bubble growth in a superheated liquid was also investigated with our numerical framework in [9, 10]. In the following, we focus on considering phase transition. Fechter et al. [15] started the modeling of phase transition in this context. It was further continued by Hitz et al. in [25]. In the following, we build on their work and propose a novel closure for the two-phase Riemann problem.

## 4 Evaporation in the Sharp Interface Framework

In our numerical method, phase transition effects are included via two fundamental building blocks: A thermodynamic consistent model of evaporation at an interface and a Riemann solver to solve the two-phase Riemann problem. We will first discuss

the former and then consider the transfer of this model to the solution of the two-phase Riemann problem.

## 4.1 Complete Evaporation at an Interface

We consider complete evaporation, i.e., evaporation of a pure liquid into a pure vapor, in a reference frame normal to the interface. To ensure the conservation of mass, momentum and energy at an evaporating interface, the following jump conditions need to be upheld:

$$[\![\dot{m}]\!] = 0, \quad (13)$$

$$\dot{m} [\![\mathbf{v} \cdot \mathbf{n}^I]\!] + [\![p]\!] = \Delta p, \quad (14)$$

$$\dot{m} \left[ \epsilon + \frac{p}{\rho} + \frac{1}{2} (\mathbf{v} \cdot \mathbf{n}^I - \zeta)^2 \right] + [\![\mathbf{q} \cdot \mathbf{n}^I]\!] = 0, \quad (15)$$

where  $\dot{m}$  denotes the evaporation mass flux,  $\mathbf{n}^I$  the normal vector of the interface,  $\Delta p$  is the surface tension force and  $\zeta$  the velocity of the interface. The jump brackets for an arbitrary quantity  $\alpha$  are defined as  $[\![\alpha]\!] = \alpha_{\text{vap}} - \alpha_{\text{liq}}$ , with  $\alpha_{\text{vap}}$  and  $\alpha_{\text{liq}}$  being the value of  $\alpha$  at the interface on the side of the vapor and the liquid, respectively. It is necessary to include the heat flux in Eq. (15), in order to describe phase transition with the Euler equations, as was shown by Hantke and Thein in [18].

In addition to Eqs. (13)–(15), we consider the entropy jump condition at the phase interface

$$\dot{m} [\![s]\!] + \left[ \frac{\mathbf{q} \cdot \mathbf{n}^I}{T} \right] = \eta_\Gamma, \quad (16)$$

with the specific entropy  $s$ , the temperature  $T$ , and  $\eta_\Gamma$  the entropy production term at the interface. As was shown by Hitz et al. [25],  $\eta_\Gamma$  can be written as

$$\eta_\Gamma := -\dot{m} \left[ \frac{g}{T} + \frac{1}{2} \frac{(\mathbf{v} \cdot \mathbf{n}^I - \zeta)^2}{T} \right] + j_e \left[ \frac{1}{T} \right], \quad (17)$$

with the specific Gibbs energy  $g$  and an interfacial energy flux  $j_e = \dot{m}(h + \frac{1}{2}(\mathbf{v} \cdot \mathbf{n}^I - \zeta)^2) + \mathbf{q} \cdot \mathbf{n}^I$ . In order to fulfill the second law of thermodynamics, it must always hold

$$\eta_\Gamma \geq 0. \quad (18)$$

If the entropy production term  $\eta_\Gamma$  is non-vanishing then the system departs from thermodynamic equilibrium. Assuming that the local equilibrium hypothesis is still valid, the theory of classical irreversible thermodynamics (CIT) [35] can derive a thermodynamic consistent solution for this situation. The CIT was already used by Hitz et al. in [25], where the numerical treatment was supplemented by a subgrid

model to calculate the heat flux in the vicinity of the phase interface. We depart from this approach and define closure relations for both mass and energy fluxes, solely based on the CIT, similar to [6].

Starting from the entropy production at the interface as given by Eq.(17), one can identify two thermodynamic fluxes,  $\dot{m}$  and  $\dot{j}_e$ , and two thermodynamic forces,  $f_m = -\left[\frac{g}{T} + \frac{1}{2}\frac{(\mathbf{v} \cdot \mathbf{n}')^2}{T}\right]$  and  $f_e = \left[\frac{1}{T}\right]$ . In systems where two thermodynamic fluxes of the same tensorial order arise in the entropy production term, one generally speaks of coupled transport phenomena. Typical examples for such processes are thermoelectricity and thermodiffusion [35]. In these cases, the interdependence between the two fluxes is not negligible. Following the CIT, we assume linear flux-force relations and define phenomenological equations for the mass and energy flux as

$$\dot{m} = L_{mm} f_m + L_{me} f_e, \quad (19)$$

$$\dot{j}_e = L_{em} f_m + L_{ee} f_e, \quad (20)$$

where  $L_{mm}$ ,  $L_{me}$ ,  $L_{em}$  and  $L_{ee}$  are the so-called Onsager coefficients. These are material parameters, and they may depend on local state variables but not on their respective thermodynamic force. Since all forces in Eq. (17) are even under time reversal, the cross coefficients need to uphold the Onsager reciprocal relation, namely

$$L_{me} = L_{em}. \quad (21)$$

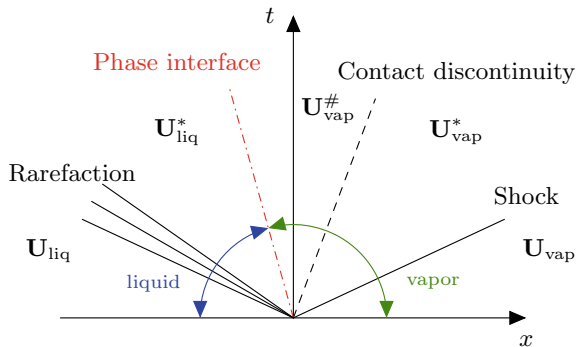
Based on kinetic theory, a few sets of models for the Onsager coefficients exist in the literature, see e.g., [5, 28]. However, they differ in their formulation of entropy production and are therefore currently not used in our framework. For the time, we restrict ourselves to the use of empirical fits.

## 4.2 Riemann Solvers for Evaporation

Given the evaporation model presented above, we can solve the two-phase Riemann problem at the interface. It is defined as an initial value problem with piecewise-constant initial states with, e.g., the left state being pure liquid and the right state pure vapor. As shown by the molecular dynamics data in [25], the solution of this type of Riemann problem adheres to the wave structure shown in Fig. 2. The outermost waves are classical non-linear waves, e.g., shock or rarefaction waves in the bulk phases. The inner waves are the classical contact discontinuity and the phase interface.

The phase interface appearing in the solution is not associated with any eigenvalue of the Euler equations and stems from the non-convexity of the EOS inside the spinodal region of the two-phase dome. For a problem with phase transition, the solution must find a path through the spinodal region, in which the hyperbolicity of the equations is lost. Menikoff and Plohr discussed the appearance of anomalous

**Fig. 2** Exemplary wave structure of the two-phase Riemann problem



wave structures when considering phase transition in [36]. They argue that the Euler equations do not include all relevant physical effects, leading to a non-uniqueness of the solution. The classical approaches to obtain a unique solution, like the Lax criterion or Liu's entropy criterion, are not sufficient in this case.

To solve the problem of the non-uniqueness, we use the concept of a kinetic relation, initially proposed by Abeyaratne and Knowles [1]. The kinetic relation is a condition that provides the correct evaporation mass flux. In addition, it directly controls the entropy production at the interface. Following the framework of Rohde and Zeiler [40, 41] and its extension of Hitz et al. [25], we write the kinetic relation in the form

$$\mathcal{K}_{m,e} = \sum_i f_i J_i - G(\dot{m}, \dot{J}_e) = 0, \quad (22)$$

with  $f_i$ , and  $J_i$  being thermodynamic forces and fluxes, respectively;  $G(\dot{m}, \dot{J}_e)$  is a microscale measure of the entropy production. Using the phenomenological equations (19)–(20), one can derive the following kinetic relation:

$$\mathcal{K}_{m,e} = \dot{m} f_m + \dot{J}_e f_e - f_m (L_{mm} f_m + L_{me} f_e) - f_e (L_{em} f_m + L_{ee} f_e) = 0. \quad (23)$$

Equation (23) is an extension to the kinetic relation proposed by Hitz et al. [25]. However, the same conclusions can be drawn: Equation (23) is quadratic in both energy and mass flux and therefore very complex. A simplification is needed to ensure a successful incorporation into an iterative algorithm to solve the two-phase Riemann problem. The approach of Hitz et al. [25] was to assume an isothermal interface on a subgrid-level together with a subgrid model for heat transfer. We depart from this approach and simplify Eq. (23) by applying the CIT.

The kinetic relation governs the entropy production at the interface. This can either be done by directly comparing the macroscopic entropy production, given as the sum of the fluxes times the forces, or, with the microscopic entropy production, given by the phenomenological equations. In an alternative approach, one can define a kinetic relation of the form

$$\mathcal{K}_m = \dot{m} - L_{mm} f_m - L_{me} f_e = 0, \quad (24)$$

which directly controls the mass flux, by again comparing the macroscopic mass flux with the one predicted by the CIT. To ensure the correct entropy production at the interface, we calculate the heat fluxes such that the interfacial energy flux equals the one predicted by the CIT with Eq. (20). Thus, if  $\mathcal{K}_m$  is fulfilled, the entropy production at the interface is given by Eq. (17) and  $\mathcal{K}_{m,e}$  is naturally fulfilled as well.

Given Eq. (24), we proceed to discuss the Riemann solvers. In our numerical framework, two different approaches are available. First, an exact Riemann solver following Hitz et al. [25] as well as an approximate Riemann solver based on the work of Fechter et al. [15].

#### 4.2.1 Exact Riemann Solver

The exact solver of Hitz et al. [25], originally based on the work of Fechter et al. [14], is able to resolve the full Riemann fan and thus find a solution of all three inner states. To ensure stability during the iteration process, an additional contact wave is included as shown in Fig. 3a. This procedure was proposed in [14, 48]. The additional contact wave is later removed once a solution has been found. The target function of the iteration scheme is defined by

$$\mathbf{G}_{TRP}(\tau_1, T_1, \tau_2, T_2, \tau_3, T_3, \tau_4, T_4) = (r_1, r_2, r_3, r_4, r_5, r_6, r_7, r_8)^T, \quad (25)$$

with  $\tau_i$  denoting the specific volume in the  $i$ th inner state and  $r_j$  the  $j$ th residual. The residuals  $r_1, \dots, r_5$  are defined by considering integral conservation across each of the classical waves. For details on these we refer to the publication of Hitz et al. [25]. The residuals  $r_6, r_7, r_8$  concern the conditions at the phase interface. These have been altered slightly with respect to the original method, in order to include the evaporation model described in Sect. 4.1. The residuals are given by the integral jump

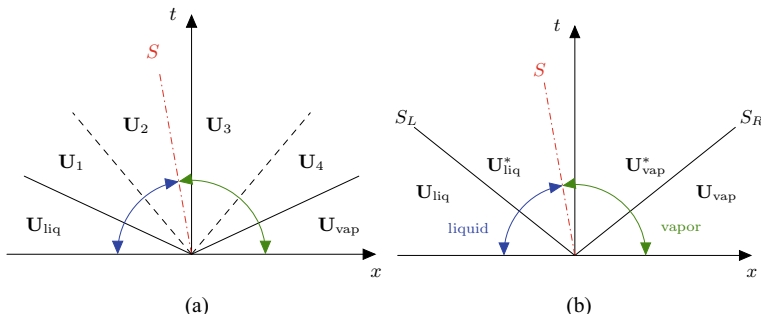


**Fig. 3** Wave fans of the Riemann solvers for the two-phase Riemann problem: **a** exact solver **b** HLLP solver

conditions for momentum and energy, as well as the kinetic relation and therefore read as

$$r_6 = \dot{m}(u_3 - u_2) + p_3 - p_2 - \Delta p \quad (26)$$

$$r_7 = \dot{m} \left( h_3 - h_2 + \frac{1}{2} \dot{m}^2 (\tau_3 - \tau_2) \right) + q_3 - q_2 \quad (27)$$

$$r_8 = \mathcal{K}_m. \quad (28)$$

The heat flux at the liquid side of the interface  $q_2$  is defined by ensuring the correct interfacial energy flux, given by Eq. (20):

$$q_2 = j_e - \dot{m} \left( h_2 + \frac{1}{2} \dot{m}^2 \tau_2 \right). \quad (29)$$

Since the thermal conductivity of the liquid is usually much higher than the thermal conductivity of the vapor phase, we assume that the heat of evaporation is predominantly provided by the liquid side and set

$$q_3 = 0. \quad (30)$$

We then solve the system  $\mathbf{G}_{TRP}$  with an eight-dimensional root-finding algorithm provided by the open-source libraries GSL(V2.1) and FGSL(V1.2.0). The solution of the Riemann problem provides the boundary conditions needed in the ghost fluid method. They are defined by the states left and right of the interface:

$$\hat{\mathbf{F}}_{\text{liq}}^* = \mathbf{F}_2 \quad \hat{\mathbf{F}}_{\text{vap}}^* = \mathbf{F}_3. \quad (31)$$

Note that the heat fluxes  $q_2$  and  $q_3$  are included in the flux.

#### 4.2.2 Approximate HLLP Riemann Solver

The downside of the exact solver is the immense computational cost due to the eight-dimensional root-finding algorithm. To reduce the complexity, we formulate an approximate HLLP Riemann solver, as proposed by Fechter et al. in [15]. Therein, the Riemann problem is solved for the simplified fan shown in Fig. 3b. This followed the ideas of the HLL and HLLC solver for single and multiphase situations [19, 27, 46]. The outer, non-linear waves are either shocks or rarefactions and the classical Rankine-Hugoniot jump conditions apply. The inner wave is the phase interface, for which the considerations from Sect. 4.1 are valid.

The solver is formulated as a one-dimensional iteration scheme, with the kinetic relation  $\mathcal{K}_m$  as the target function. Initially, the outer wave speeds are estimated by using

$$S_L = u_{\text{liq}} - a_{\text{liq}} \quad (32)$$

$$S_R = u_{\text{vap}} + a_{\text{vap}}, \quad (33)$$

with  $a$  being the speed of sound of the respective phase. Afterwards, the iteration procedure starts by calculating the inner states. They are given by a thermodynamically overdetermined state vector. The hydrodynamic components of the state vector  $\rho^*$ ,  $\mathbf{v}^*$ , and  $p^*$  can be calculated from the mass and momentum jump conditions across all three waves. The explicit formulas have been reported in [15]. The specific total energy in the inner states can be then calculated from the energy jump conditions across the two outer waves. Finally, the liquid heat flux can be calculated from the CIT and the vapor heat flux by fulfilling the energy jump condition across the interface:

$$q_{\text{liq}} = \dot{J}_e - \dot{m} \left( h_{\text{liq}}^* + \frac{1}{2} \dot{m}^2 \frac{1}{\rho_{\text{liq}}^*} \right), \quad (34)$$

$$q_{\text{vap}} = q_{\text{liq}} + \dot{m} \left( e_{\text{liq}}^* - e_{\text{vap}}^* \right) + \left( p_{\text{liq}}^* \mathbf{v}_{\text{liq}}^* \cdot \mathbf{n}^I - p_{\text{vap}}^* \mathbf{v}_{\text{vap}}^* \cdot \mathbf{n}^I \right) \quad (35)$$

In contrast to the exact solver, a local evaluation of the approximate Riemann solution is not used to calculate the interface flux since it is only valid in an integral sense. Hence, the boundary conditions for the ghost fluid method are calculated from the integral consistency conditions:

$$\hat{\mathbf{F}}_{\text{liq}}^* = \mathbf{F}_{\text{liq}} + S_L (\mathbf{U}_{\text{liq}}^* - \mathbf{U}_{\text{liq}}), \quad \hat{\mathbf{F}}_{\text{vap}}^* = \mathbf{F}_{\text{vap}} + S_R (\mathbf{U}_{\text{vap}}^* - \mathbf{U}_{\text{vap}}). \quad (36)$$

## 5 Numerical Results

In this section, we validate our numerical scheme by comparing it with data obtained from molecular dynamics simulations of *TP-B6*. In all our test cases, we considered the Lennard-Jones truncated and shifted fluid (LJTS). For this fluid, highly accurate EOS are available [20, 45], which makes a one-to-one comparison of the macroscopic and microscopic methods possible. We validated this kind of comparison in [24], where a shock tube scenario with a supercritical liquid and supercritical vapor, as well as an expansion into vacuum, were considered. Furthermore, we discussed a shock tube scenario with evaporation [25]. There, our numerical scheme showed promising results, however, deviations from the molecular dynamics data could be observed in the temperature. To validate the evaporation model presented above, we first revisit the evaporation shock tube presented in [25]. Afterwards, we show numerical results of a novel stationary evaporation case.

In all the results presented below, we have used the PeTS EOS [20] to simulate the LJTS fluid. The Onsager coefficients were set to  $L_{mm} = 1.05E - 2$ ,  $L_{me} = -0.6E - 2$  and  $L_{ee} = 0.8E - 2$  for both cases. For the thermal conductivity, the model of

Lautenschlaeger et al. [33] was used. All quantities were non-dimensionalized with respect to the reference length  $\sigma_{\text{ref}} = 1 \text{ \AA}$ , the reference energy  $\epsilon_{\text{ref}}/k_B = 1 \text{ K}$  and reference mass  $m_{\text{ref}} = 1 \text{ u}$  as follows

$$x = \frac{\hat{x}}{\sigma_{\text{ref}}}, \quad t = \frac{\hat{t}}{\sigma_{\text{ref}} \sqrt{m_{\text{ref}}/\epsilon_{\text{ref}}}}, \quad \rho = \frac{\hat{\rho}}{m_{\text{ref}}/\sigma_{\text{ref}}^3}, \quad u = \hat{u} \sqrt{m_{\text{ref}}/\epsilon_{\text{ref}}}, \quad T = \frac{\hat{T}}{\epsilon_{\text{ref}}/k_B},$$

where the dimensional quantities are indicated with a hat. The polynomial degree of the DGSEM was set to  $N = 3$ . In the bulk phases, the HLLC-Riemann solver was used to calculate the numerical fluxes. For time integration, a fourth-order Runge-Kutta scheme with five stages was used. In the one-dimensional test cases presented below, we advect the computational mesh with the interface velocity using the ALE method for DGSEM, cf., [25]. Thus, the interface is kept sharp and does not move with respect to the grid.

## 5.1 Evaporation Shock Tube

The evaporation shock tube scenario is taken from [25]. It is a Riemann problem type-case with piecewise constant initial data:

$$\mathbf{U}(x, 0) = \begin{cases} \mathbf{U}_{\text{liq}} & \text{for } x < 0 \\ \mathbf{U}_{\text{vap}} & \text{for } x > 0. \end{cases} \quad (37)$$

The liquid is initially given in a saturated state with a temperature of  $T = 0.9$ . The vapor initially has a temperature of  $T = 0.8$  and a density of 50% of its saturation density. The computational domain  $x \in [-400, 1500]$  was discretized into 200 grid elements.

The numerical results for both Riemann solvers are shown in Fig. 4, supplemented by the molecular dynamics data from [25] for  $t = 600$ . The sharp interface method is capable of reproducing the reference data. In density, velocity, and temperature a qualitative and quantitative agreement can be seen, which is an improvement with respect to the results shown in [25]. The remaining differences between the molecular dynamics data and the sharp interface method may be explained by the lack of an appropriate model for the Onsager coefficients. At the shock wave, the absence of viscous effects can be seen as well. Between the two Riemann solvers, slight deviations can be observed in the vicinity of the interface, where the HLLP solver leads to a slightly cooler freshly evaporated vapor. However, the approximate Riemann solver reduces the total computational time by about 70% compared to the exact solver.

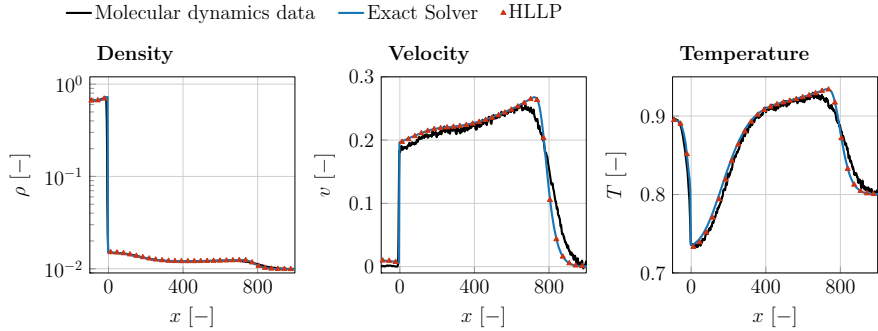


**Fig. 4** Evaporation shock tube with molecular dynamics data and results from the sharp interface method for different Riemann solvers

## 5.2 Stationary Evaporation

The stationary evaporation case is taken from the work of Heinen et al. [21]. It is less complex than the evaporation shock tube scenario described above since it only considers the sole interface. In this way, the modelling of the interface can be thoroughly investigated, as no other wave appears in the solution.

The domain is given by  $x \in [-12, 400]$ . The phase interface is positioned at  $x = 0$ . On the left boundary ( $x = -12$ ), liquid enters the domain at a temperature of  $T = 0.8$  and with a mass flux that equals the evaporation mass flux. On the other side ( $x = 400$ ), the velocity of the vapor is held constant at a value of  $u = 0.2$ . Initially, both liquid and vapor are saturated and have a temperature of  $T = 0.8$ . The liquid is at rest while the vapors initial velocity is  $u = 0.2$ . The simulation was run until  $t = 6000$ , where a stationary state was achieved. The domain was discretized with 100 elements and the HLLP solver was used as the interface solver.

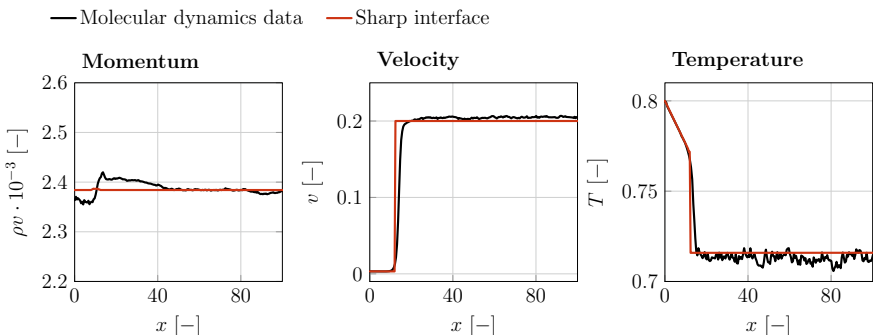


**Fig. 5** Comparison of molecular dynamics data and results by the sharp interface method for stationary evaporation case

Numerical results can be seen in Fig. 5, supplemented by the molecular dynamics data from [21]. In all three quantities, the sharp interface shows a very good agreement. Most notably, both the momentum and the temperature are predicted very well by our numerical method. We want to note that the same set of Onsager coefficients were chosen as in the evaporation shock tube case. Although only being an empirical fit against the data from [25], it shows accurate results for different test cases with a similar range of temperatures.

## 6 Conclusions

In this article, we surveyed the results of the subproject *TP-A2* whithin the Collaborative Research Center *SFB-TRR75*. The sharp interface method for droplet dynamics in high pressure and temperature environments and its extension to evaporation was considered. The method is based on a discontinuous Galerkin spectral element method, supplemented by finite-volume sub-cells. The interface tracking is done via a level-set method and the jump conditions across the phase interface are fulfilled via the use of special interface Riemann solvers. Evaporation is modeled via classical irreversible thermodynamics and linear constitutive laws. We discussed two different interface Riemann solvers: an exact solver which resolves the full wave fan of the two-phase Riemann problem, as well as an approximate HLLP Riemann solver with a reduced complexity of the wave fan.

Numerical results with the evaporation model were shown for an evaporation shock tube scenario as well as a stationary evaporation. Molecular dynamics data of *TP-B6* was used as a benchmark. In both cases, the numerical results showed a very good agreement with the reference data. The approximate Riemann solver showed only slight differences to the exact solver, while drastically reducing the computational effort.

The Onsager coefficients used in this work were fitted and not predicted by an appropriate model. Future investigations will focus on predictive models circumventing the need for an empirical fit. These shall be validated by a deepened discussion on the stationary evaporation for a variety of initial conditions in close cooperation with *TP-B6*. A comparison between our compressible framework and the incompressible one of *TP-B1* is planned as well. A next step will also be the use of our method in multi-dimensional applications.

**Acknowledgements** This work was supported by the German Research Foundation (DFG) through the Project SFB-TRR 75, Project number 84292822 - “Droplet Dynamics under Extreme Ambient Conditions”. The simulations were performed on the national supercomputer HPE Apollo (Hawk) at the High-Performance Computing Center Stuttgart (HLRS).

## References

1. Abeyaratne R, Knowles JK (1991) Kinetic relations and the propagation of phase boundaries in solids. *Arch Ration Mech Anal* 114(2):119–154. <https://doi.org/10.1007/BF00375400>
2. Aslam TD (2004) A partial differential equation approach to multidimensional extrapolation. *J Comput Phys* 193(1):349–355. <https://doi.org/10.1016/j.jcp.2003.08.001>
3. Bassi F, Rebay S (1997) A high-order accurate discontinuous finite element method for the numerical solution of the compressible Navier-Stokes equations. *J Comput Phys* 131(2):267–279. <https://doi.org/10.1006/jcph.1996.5572>
4. Beck AD, Bolemann T, Flad D, Frank H, Gassner GJ, Hindenlang F, Munz CD (2014) High-order discontinuous Galerkin spectral element methods for transitional and turbulent flow simulations. *Int J Numer Methods Fluids* 76(8):522–548
5. Bedeaux D, Kjelstrup S (1999) Transfer coefficients for evaporation 270:413–426
6. Bedeaux D, Kjelstrup S, Rubi JM (2003) Nonequilibrium translational effects in evaporation and condensation. *J Chem Phys* 119(17):9163–9170. <https://doi.org/10.1063/1.1613640>
7. Carpenter M, Kennedy C (1994) Fourth-order  $2N$ -storage Runge-Kutta schemes. Technical report, NASA Langley Research Center
8. Castro M, Gallardo J, Parés C (2006) High order finite volume schemes based on reconstruction of states for solving hyperbolic systems with nonconservative products. applications to shallow-water systems. *Math Comput* 75(255):1103–1134
9. Dietzel D, Hitz T, Munz CD, Kronenburg A (2019) Numerical simulation of the growth and interaction of vapour bubbles in superheated liquid jets. *Int J Multiph Flow* 121:103112. <https://doi.org/10.1016/j.ijmultiphaseflow.2019.103112>
10. Dietzel D, Hitz T, Munz CD, Kronenburg A (2019) Single vapour bubble growth under flash boiling conditions using a modified HLLC Riemann solver. *Int J Multiph Flow* 116:250–269. <https://doi.org/10.1016/j.ijmultiphaseflow.2019.04.010>
11. Dumbser M, Loubère R (2016) A simple robust and accurate a posteriori sub-cell finite volume limiter for the discontinuous Galerkin method on unstructured meshes. *J Comput Phys* 319:163–199. <https://doi.org/10.1016/j.jcp.2016.05.002>
12. Fechter S, Jaegle F, Schleper V (2013) Exact and approximate Riemann solvers at phase boundaries. *Comput Fluids* 75:112–126
13. Fechter S, Munz CD (2015) A discontinuous Galerkin-based sharp-interface method to simulate three-dimensional compressible two-phase flow. *Int J Numer Meth Fluids* 78(7):413–435
14. Fechter S, Munz CD, Rohde C, Zeiler C (2017) A sharp interface method for compressible liquid-vapor flow with phase transition and surface tension. *J Comput Phys* 336:347–374. <https://doi.org/10.1016/j.jcp.2017.02.001>
15. Fechter S, Munz CD, Rohde C, Zeiler C (2018) Approximate Riemann solver for compressible liquid vapor flow with phase transition and surface tension. *Comput Fluids* 169:169–185. <https://doi.org/10.1016/j.compfluid.2017.03.026>
16. Fedkiw RP, Aslam T, Merriman B, Osher S (1999) A non-oscillatory Eulerian approach to interfaces in multimaterial flows (the ghost fluid method). *J Comput Phys* 152(2):457–492. <https://doi.org/10.1006/jcph.1999.6236>
17. Föll F, Hitz T, Müller C, Munz CD, Dumbser M (2019) On the use of tabulated equations of state for multi-phase simulations in the homogeneous equilibrium limit. *Shock Waves*. <https://doi.org/10.1007/s00193-019-00896-1>
18. Hantke M, Thein F (2019) On the impossibility of first-order phase transitions in systems modeled by the full Euler equations. *Entropy* 21(11):1039. <https://doi.org/10.3390/e21111039>
19. Harten A, Lax PD, van Leer B (1983) On upstream differencing and Godunov-type schemes for hyperbolic conservation laws. *SIAM Rev* 25(1):35–61. <https://doi.org/10.1137/1025002>
20. Heier M, Stephan S, Liu J, Chapman WG, Hasse H, Langenbach K (2018) Equation of state for the Lennard-Jones truncated and shifted fluid with a cut-off radius of 2.5 sigma based on perturbation theory and its applications to interfacial thermodynamics. *Mol Phys* 116(15–16):2083–2094. <https://doi.org/10.1080/00268976.2018.1447153>

21. Heinen M, Vrabec J (2019) Evaporation sampled by stationary molecular dynamics simulation. *J Chem Phys* 151(4). <https://doi.org/10.1063/1.5111759>
22. Hempert F, Boblest S, Ertl T, Sadlo F, Offenhäuser P, Glass CW, Hoffmann M, Beck A, Munz CD, Iben U (2017) Simulation of real gas effects in supersonic methane jets using a tabulated equation of state with a discontinuous Galerkin spectral element method. *Comput Fluids* 145:167–179. <https://doi.org/10.1016/j.compfluid.2016.12.024>
23. Hindenlang F, Gassner GJ, Altmann C, Beck A, Staudenmaier M, Munz CD (2012) Explicit discontinuous Galerkin methods for unsteady problems. *Comput Fluids* 61:86–93. <https://doi.org/10.1016/j.compfluid.2012.03.006>
24. Hitz T, Heinen M, Vrabec J, Munz CD (2020) Comparison of macro- and microscopic solutions of the Riemann problem I. Supercritical shock tube and expansion into vacuum. *J Comput Phys* 402:109077. <https://doi.org/10.1016/j.jcp.2019.109077>
25. Hitz T, Jöns S, Heinen M, Vrabec J, Munz CD (2021) Comparison of macro- and microscopic solutions of the Riemann problem II. Two-phase shock tube. *J Comput Phys* 429:110027. <https://doi.org/10.1016/j.jcp.2020.110027>
26. Hitz T, Keim J, Munz CD, Rohde C (2020) A parabolic relaxation model for the Navier-Stokes-Korteweg equations. *J Comput Phys* 109714. <https://doi.org/10.1016/j.jcp.2020.109714>
27. Hu X, Adams N, Iaccarino G (2009) On the HLLC Riemann solver for interface interaction in compressible multi-fluid flow. *J Comput Phys* 228(17):6572–6589. <https://doi.org/10.1016/j.jcp.2009.06.002>
28. Safari P, Masoudi A, Irajizad P, Nazari M, Kashyap V, Eslami B, Ghasemi H (2018) Evaporation mass flux: a predictive model and experiments. *Langmuir* 34(39):11676–11684. <https://doi.org/10.1021/acs.langmuir.8b02289>
29. Jiang GS, Peng D (2000) Weighted ENO schemes for Hamilton-Jacobi equations. *SIAM J Sci Comput* 21(6):2126–2143. <https://doi.org/10.1137/s106482759732455x>
30. Jöns S, Müller C, Zeifang J, Munz CD (2020) Recent advances and complex applications of the compressible ghost-fluid method. In: SEMA SIMAI Springer Series. *Proceedings of Numhyp 2019*. Springer accepted
31. Kopriva DA (2009) Spectral element methods. In: *Scientific computation*. Springer, The Netherlands, pp 293–354. [https://doi.org/10.1007/978-90-481-2261-5\\_8](https://doi.org/10.1007/978-90-481-2261-5_8)
32. Krais N, Beck A, Boemann T, Frank H, Flad D, Gassner G, Hindenlang F, Hoffmann M, Kuhn T, Sonntag M, Munz CD (2020) FLEXI: A high order discontinuous Galerkin framework for hyperbolic-parabolic conservation laws. *Comput Math with Appl*. <https://doi.org/10.1016/j.camwa.2020.05.004>
33. Lautenschlaeger MP, Hasse H (2019) Transport properties of the Lennard-Jones truncated and shifted fluid from non-equilibrium molecular dynamics simulations. *Fluid Phase Equilib* 482:38–47. <https://doi.org/10.1016/j.fluid.2018.10.019>
34. Le Métayer O, Massoni J, Saurel R (2005) Modelling evaporation fronts with reactive Riemann solvers. *J Comput Phys* 205:567–610. <https://doi.org/10.1016/j.jcp.2004.11.021>
35. Lebon G, Jou D, Casas-Vázquez J (2008) Understanding non-equilibrium thermodynamics. Springer, Berlin. <https://doi.org/10.1007/978-3-540-74252-4>
36. Menikoff R, Plohr BJ (1989) The Riemann problem for fluid flow of real materials. *Rev Mod Phys* 61(1):75–130. <https://doi.org/10.1103/RevModPhys.61.75>
37. Merkle C, Rohde C (2007) The sharp-interface approach for fluids with phase change: Riemann problems and ghost fluid techniques. *ESAIM: Math Model Numer Anal* 41(06):1089–1123. <https://doi.org/10.1051/m2an:2007048>
38. Müller C, Hitz T, Jöns S, Zeifang J, Chiocchetti S, Munz CD (2020) Improvement of the level-set ghost-fluid method for the compressible Euler equations. In: Lamanna G, Tonini S, Cossali GE, Weigand B (eds) *Droplet interaction and spray processes*. Springer, Heidelberg, Berlin
39. Persson PO, Peraire J (2006) Sub-cell shock capturing for discontinuous Galerkin methods. In: 44th AIAA aerospace sciences meeting and exhibit. American Institute of Aeronautics and Astronautics. <https://doi.org/10.2514/6.2006-112>
40. Rohde C, Zeiler C (2015) A relaxation Riemann solver for compressible two-phase flow with phase transition and surface tension. *Appl Numer Math* 95:267–279. <https://doi.org/10.1016/j.apnum.2014.05.001>

41. Rohde C, Zeiler C (2018) On Riemann solvers and kinetic relations for isothermal two-phase flows with surface tension. *Z Angew Math Phys* 69(3):76. <https://doi.org/10.1007/s00033-018-0958-1>
42. Simões-Moreira JR, Shepherd JE (1999) Evaporation waves in superheated dodecane. *J Fluid Mech* 382:63–86. <https://doi.org/10.1017/S0022112098003796>
43. Sonntag M, Munz CD (2016) Efficient parallelization of a shock capturing for discontinuous Galerkin methods using finite volume sub-cells. *J Sci Comput* 70(3):1262–1289. <https://doi.org/10.1007/s10915-016-0287-5>
44. Sussman M, Smereka P, Osher S (1994) A level set approach for computing solutions to incompressible two-phase flow. *J Comput Phys* 114(1):146–159. <https://doi.org/10.1006/jcph.1994.1155>
45. Thol M, Rutkai G, Span R, Vrabec J, Lustig R (2015) Equation of state for the Lennard-Jones truncated and shifted model fluid. *Int J Thermophys* 36(1):25–43. <https://doi.org/10.1007/s10765-014-1764-4>
46. Toro EF, Spruce M, Speares W (1994) Restoration of the contact surface in the HLL-Riemann solver. *Shock Waves* 4(1):25–34. <https://doi.org/10.1007/BF01414629>
47. Zeifang J (2020) A discontinuous Galerkin method for droplet dynamics in weakly compressible flows
48. Zeiler C (2016) Liquid vapor phase transitions: modeling, Riemann solvers and computation. PhD Thesis, University of Stuttgart, Stuttgart

**Open Access** This chapter is licensed under the terms of the Creative Commons Attribution 4.0 International License (<http://creativecommons.org/licenses/by/4.0/>), which permits use, sharing, adaptation, distribution and reproduction in any medium or format, as long as you give appropriate credit to the original author(s) and the source, provide a link to the Creative Commons license and indicate if changes were made.

The images or other third party material in this chapter are included in the chapter's Creative Commons license, unless indicated otherwise in a credit line to the material. If material is not included in the chapter's Creative Commons license and your intended use is not permitted by statutory regulation or exceeds the permitted use, you will need to obtain permission directly from the copyright holder.



# Analysis and Numerics of Sharp and Diffuse Interface Models for Droplet Dynamics



Jim Magiera and Christian Rohde

**Abstract** The modelling of liquid–vapour flow with phase transition poses many challenges, both on the theoretical level, as well as on the level of discretisation methods. Therefore, accurate mathematical models and efficient numerical methods are required. In that, we focus on two modelling approaches: the sharp-interface (SI) approach and the diffuse-interface (DI) approach. For the SI-approach, representing the phase boundary as a co-dimension-1 manifold, we develop and validate analytical Riemann solvers for basic isothermal two-phase flow scenarios. This ansatz becomes cumbersome for increasingly complex thermodynamical settings. A more versatile multiscale interface solver, that is based on molecular dynamics simulations, is able to accurately describe the evolution of phase boundaries in the temperature-dependent case. It is shown to be even applicable to two-phase flow of multiple components. Despite the successful developments for the SI approach, these models fail if the interface undergoes topological changes. To understand merging and splitting phenomena for droplet ensembles, we consider DI models of second gradient type. For these Navier–Stokes–Korteweg systems, that can be seen as a third order extension of the Navier–Stokes equations, we propose variants that are more accessible to standard numerical schemes. More precisely, we reformulate the capillarity operator to restore the hyperbolicity of the Euler operator in the full system.

## 1 Introduction

In this contribution we consider the compressible flow of homogeneous fluids that occur in two phases: a liquid and a vapour phase. We focus on a spatial scale such that the phase boundaries exist as isolated flow patterns, i.e. single droplets are fully resolved in the model. For the mathematical modelling of a compressible fluid with liquid–vapour phase transitions one can then use either models which represent the

---

J. Magiera (✉) · C. Rohde  
Institute of Applied Analysis and Numerical Simulation (IANS), University of Stuttgart,  
Stuttgart, Germany  
e-mail: [jim.magiera@ians.uni-stuttgart.de](mailto:jim.magiera@ians.uni-stuttgart.de)

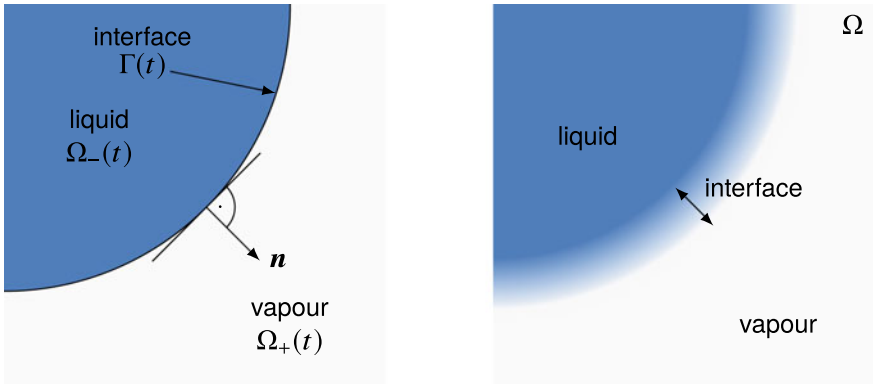


**Fig. 1** Graphical representation of a sharp interface (left) and a diffuse interface (right)

phase boundary as a codimension-1 manifold (Sharp-Interface (SI) approach) or as a steep but continuous transition zone (Diffuse-Interface (DI) approach), see Fig. 1 for an illustration. Both concepts are related via a SI-limit. This means, that a sequence of solutions of the DI model converges to a solution of the SI model for vanishing diffuse-interface parameter.

The thermodynamical setting is summarised in Sect. 2. We proceed with the SI concept in Sect. 3. The mathematical model can then be seen as a free boundary value problem that consists of appropriate coupling conditions across the interface, and evolution equations in the bulk domains. We shortly review the one-dimensional case, which amounts (in the absence of viscous forces) to solving a Riemann problem. Notably, the phase boundary shows up as a discontinuous wave, similar to a shock wave. Since exact Riemann solvers are not available for arbitrary thermodynamical settings we develop in the in the SFB–TRR 75 a new multiscale approach. This method determines the speed of a phase boundary locally by solving a molecular-dynamical problem. In Sect. 4 we present some results of the research on DI models. After a short review of the classical Navier–Stokes–Korteweg system we give a sketch for a new model. This model relies on a nonlocal free-energy formulation that has been previously suggested to describe two-phase equilibria in solid mechanics. The special structure of the resulting capillarity tensor can be exploited to compensate for the occurrence of a spinodal region in two-phase thermodynamics. As a consequence the resulting model can be solved numerically in a straightforward way using standard CFD codes for compressible flow. We conclude with some numerical experiments on droplet ensembles with various phase transition phenomena.

This article bases largely on the publications of the authors and (former) members of the working group that have been involved in the SFB–TRR 75. It contains results of the PhD thesis of the first author [25].

## 2 Thermodynamics of Compressible Two-Phase Flow

A central role in modelling two-phase flow plays the accurate representation of the thermodynamic properties of fluids. For this purpose, *equations of state* (EOS) are prescribed that put thermodynamic quantities in relation. Typically, an equation of state contains a function  $\psi(\rho, T)$  that determines the specific Helmholtz free energy  $\psi$  from the fluid density  $\rho$  and the fluid temperature  $T$ . From this dependency the fluid pressure  $p$  and specific Gibbs free energy  $\mu$  can be inferred for temperature  $T > 0$  via

$$p = p(\rho) = \rho^2 \frac{d}{d\rho} \psi(\rho), \quad (1)$$

$$\mu = \mu(\rho) = \psi(\rho) + \frac{p(\rho)}{\rho}. \quad (2)$$

In what follows, we consider for the sake of simplicity the case of constant temperature  $T = T_{\text{ref}}$  (with the exception of Sect. 3.2). A prototypical example for an isothermal two-phase flow model is the van der Waals-fluid, for which one considers the pressure function

$$p(\rho) := \frac{RT_{\text{ref}}\rho}{1 - b\rho} - a\rho^2, \quad (3)$$

with some constants  $R, a, b > 0$ , and the reference temperature  $T_{\text{ref}} > 0$ . For temperatures  $T_{\text{ref}}$  below the critical temperature  $T_{\text{crit}} = \frac{8a}{27Rb}$ , the pressure function becomes non-monotone, see Fig. 2. The interval where the pressure is decreasing, i.e.  $\mathcal{A}_{\text{spin}} = (\rho_+^{\max}, \rho_-^{\min}) = \{\rho \in (0, \frac{1}{b}) : p'(\rho) < 0\}$  is called spinodal region. In this region, the liquid is in a meta-stable state, and the system (4) below is not hyperbolic anymore. For that reason, we define the admissible density intervals  $\mathcal{A}_+ = (0, \rho_+^{\max})$

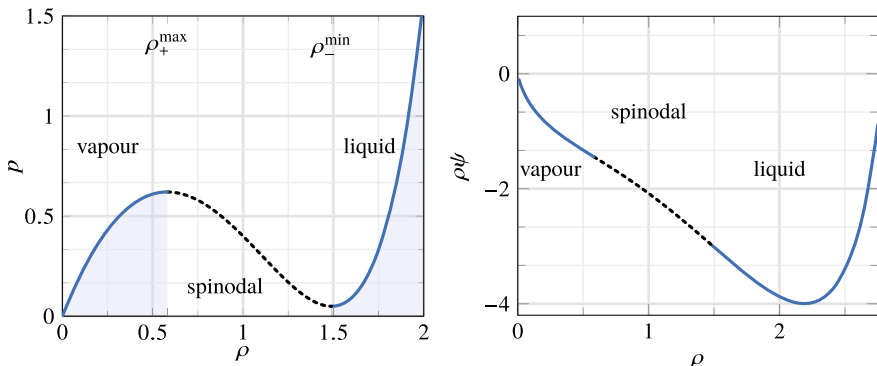


**Fig. 2** The van der Waals pressure  $p(\rho)$  and free Helmholtz energy density  $\rho\psi(\rho)$  for  $T_{\text{ref}} < T_{\text{crit}}$  as a prototypical example to describe a liquid with two phases

and  $\mathcal{A}_- = (\rho_-^{\min}, \frac{1}{b})$ . These intervals can be associated with the two fluid phases, which means  $\mathcal{A}_+$  indicates the density interval for the vapour phase, and  $\mathcal{A}_-$  for the liquid phase.

### 3 Sharp-Interface Modelling

This section is devoted to SI models that incorporate the well-known transmission conditions at liquid–vapour interfaces [4]. The focus is on ideal fluids and the development of interface Riemann solvers for the description of phase boundary dynamics. We do not consider viscous fluids, which would not be accessible by self-similar solutions in a conservation law framework.

In this article, we provide a summary of a multiscale approach that allows to access complex scenarios like temperature-dependent flow and multi-component flow. For project-related results within the SFB–TRR 75, we refer for the basic two-phase Riemann solvers and the free boundary value problem to [23, 31–33]. In collaboration with sub-project A2 within SFB–TRR 75, the ghost-fluid method and two-phase Riemann solvers were further developed and applied in existing CFD-code, see [16–18] Concerning two-phase multiscale modeling, we refer to e.g. [25, 32] and for the related work about constraint-aware surrogate solvers to [26]. A sharp interface approach in the framework of the Stefan problem is pursued in [12].

#### 3.1 Isothermal Two-Phase Flow

For the sharp-interface representation of two-phase flow, we consider a domain  $\Omega \subset \mathbb{R}^d$  that is split into two open, disjoint, time-dependent subdomains  $\Omega_+(t)$ ,  $\Omega_-(t)$ ,  $t \in (0, t_{\text{end}})$ , by a  $(d - 1)$ -dimensional manifold  $\Gamma(t)$ , see Fig. 1. It is assumed that in each subdomain  $\Omega_+(t)$ ,  $\Omega_-(t)$  only one phase is present. Furthermore, we assume that in both domains, the fluid flow is described by the same set of PDEs. Neglecting external forces, inviscid two-phase flow is governed for constant temperature by the isothermal Euler equations

$$\begin{aligned} \partial_t \rho + \nabla \cdot (\rho \mathbf{v}) &= 0, \\ \partial_t (\rho \mathbf{v}) + \nabla \cdot (\rho \mathbf{v} \otimes \mathbf{v} + p \mathbf{I}) &= \mathbf{0}, \end{aligned} \quad \text{in } \Omega_{\pm}(t) \text{ for } t \in (0, t_{\text{end}}). \quad (4)$$

In (4),  $\rho = \rho(\mathbf{x}, t)$  denotes the fluid density,  $\mathbf{v} = \mathbf{v}(\mathbf{x}, t)$  the fluid velocity,  $\mathbf{I}$  the  $d$ -dimensional identity matrix. The pressure  $p = p(\rho)$  is defined by an equation of state; we refer to the discussion in Sect. 2. The system (4) is supplemented by appropriate initial conditions. Additionally, we assume no-flow boundary conditions on  $\partial\Omega$ .

For a fixed point  $\xi \in \Gamma(t)$  on the interface, the normal vector (pointing into the vapor region  $\Omega_+(t)$ ) is denoted by  $\mathbf{n} = \mathbf{n}(\xi, t) \in \mathbb{S}^{d-1}$  and the speed of the interface  $\Gamma(t)$  in normal direction is indicated by  $s = s(\xi, t) \in \mathbb{R}$ .

We assume that the interface  $\Gamma(t)$  does not store any mass, and impose a momentum balance involving curvature effects. For constant surface tension  $\sigma \in \mathbb{R}$ , this implies a no-slip condition for the tangential velocities (see [2] for a rational derivation of balance laws for interfacial transport). Altogether, we have

$$\begin{aligned}\llbracket \rho(\mathbf{v} \cdot \mathbf{n} - s) \rrbracket &= 0, \\ \llbracket \rho(\mathbf{v} \cdot \mathbf{n} - s)\mathbf{v} \cdot \mathbf{n} + p(\rho) \rrbracket &= (d-1)\kappa\sigma, \\ \llbracket \mathbf{v} \cdot \mathbf{t} \rrbracket &= 0, \quad \forall \mathbf{t} \perp \mathbf{n},\end{aligned}\tag{5}$$

with  $\kappa = \kappa(\xi, t) = -\nabla_{\Gamma(t)} \cdot \mathbf{n}(\xi, t)$  denoting the mean curvature of the interface, given by the negative surface divergence of  $\mathbf{n}$  on the interface  $\Gamma(t)$ . The jump operator  $\llbracket \cdot \rrbracket$  computes the difference between vapour and liquid phase quantities at the interface  $\Gamma$ . For an arbitrary function  $a : \mathbb{R}^d \rightarrow \mathbb{R}$  it is defined by

$$\llbracket a \rrbracket := \bar{a}_+ - \bar{a}_-, \text{ with } \bar{a}_{\pm} := \lim_{\substack{\epsilon \rightarrow 0 \\ \epsilon > 0}} a(\xi \pm \epsilon \mathbf{n}).\tag{6}$$

In order to obtain a well-posed model, an additional condition at the interface is required, that determines the mass transfer across the interface. A direct prescription of it might not be consistent with the second law of thermodynamics. Therefore, we follow the ansatz in [1, 36] and formulate an algebraic equation at the interface—the so-called kinetic relation that specifies the entropy dissipation at the interface. For this purpose, let a driving force  $\mathcal{K} : \mathbb{R} \rightarrow \mathbb{R} : j \mapsto \mathcal{K}(j)$  be given that depends on the relative mass flux  $j$  across the interface, i.e.

$$j = \rho_{\pm}(\mathbf{v}_{\pm} \cdot \mathbf{n} - s).\tag{7}$$

In the isothermal case, a kinetic relation takes the following form

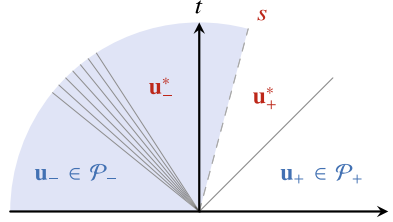
$$\llbracket \mu(\rho) + \frac{j^2}{2\rho^2} \rrbracket = -\mathcal{K}(j).\tag{8}$$

To see the thermodynamical significance of (8), let us assume for the moment that  $(\rho, \rho\mathbf{v})$  is a classical solution of Eqs. (4) in both bulk phases  $\Omega_{\pm}(t)$  fulfilling the interface conditions (5) and the kinetic relation (8) with a driving force  $\mathcal{K}(j)$ . In this case, if the driving force upholds

$$j\mathcal{K}(j) \geq 0, \quad \text{for all } j \in \mathbb{R},\tag{9}$$

it can be shown that the solution satisfies the second law of thermodynamics. This means, the solution dissipates the energy at the interface, i.e. it holds

**Fig. 3** Exemplary wave pattern of an isothermal two-phase Riemann solution



$$-s [E] - s(d-1)\kappa\sigma + [(E+p(\rho))\mathbf{v} \cdot \mathbf{n}] = -j\mathcal{K}(j) \leq 0. \quad (10)$$

For classical solutions in both bulk phases  $\Omega_{\pm}(t)$  and closed interfaces  $\Gamma(t)$  we deduce the energy inequality

$$\frac{d}{dt} \left( \int_{\Omega} \rho \psi(\rho) + \frac{1}{2} \rho |\mathbf{v}|^2 d\mathbf{x} + \sigma I[\Gamma(t)] \right) \leq 0. \quad (11)$$

For static solutions we infer that the sharp-interface solutions minimize the functional

$$F^{\text{SI}}[\rho] := \int_{\Omega} \rho \psi d\mathbf{x} + \sigma I[\Gamma], \quad (12)$$

where  $I[\Gamma]$  is the  $(d-1)$ -dimensional surface measure of the interface  $\Gamma$ .

In our project, we developed a Riemann solver for two-phase flow that is applicable to a wide range of kinetic relations [32, 37]. That means in particular, that we are able to compute two-phase Riemann solutions that are consistent with the second law of thermodynamics. For details on the Riemann solvers we refer to [32]. For numerical simulations it suffices to know that the Riemann solver is a mapping of the following form

$$\mathcal{R}: \mathcal{P}_- \times \mathcal{P}_+ \rightarrow \mathcal{P}_- \times \mathcal{P}_+ \times \mathbb{R}: (\mathbf{u}_-, \mathbf{u}_+) \mapsto (\mathbf{u}_-^*, \mathbf{u}_+^*, s). \quad (13)$$

It takes the liquid state  $\mathbf{u}_- \in \mathcal{P}_- \subset \mathbb{R}^{d+1}$  and the vapour state  $\mathbf{u}_+ \in \mathcal{P}_+ \subset \mathbb{R}^{d+1}$  directly at the phase boundary and returns the wave speed  $s \in \mathbb{R}$  of the phase boundary wave, as well as the adjacent wave states  $\mathbf{u}_-^*$ ,  $\mathbf{u}_+^*$ , see Fig. 3.

In Fig. 4 we show exemplary Riemann solutions computed by the aforementioned Riemann solver [32] for three kinetic relations and the corresponding Liu entropy solution. All choices lead to a three-wave solutions consisting of two bulk-phase shock waves and a subsonic phase-boundary wave (with attached rarefaction due to loss of genuine nonlinearity). The terms  $\mathcal{K}_1$  and  $\mathcal{K}_3$  are the lowest-order polynomial choices that ensure (10) via the monotonicity condition (9), i.e.

$$\mathcal{K}_1(j) = j, \quad \mathcal{K}_3(j) = \text{sign}(j)j^2. \quad (14)$$

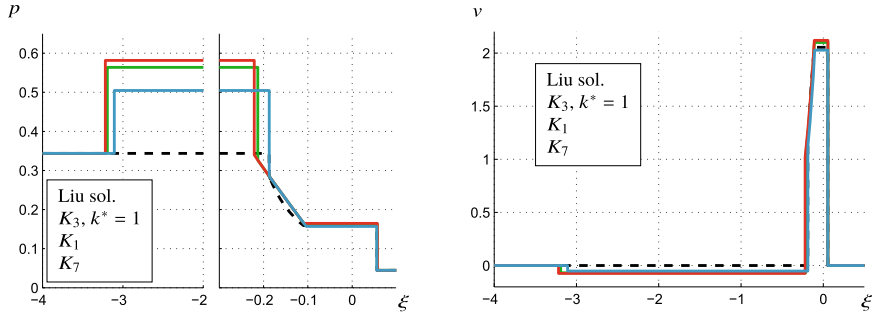


**Fig. 4** Riemann solutions for isothermal liquid–vapour flow for three different kinetic relations compared to the corresponding Liu entropy solution (dashed line). The Riemann solver [32] was used to compute the solutions. The left figure shows the fluid pressure, the right figure the fluid velocity. Both are plotted with respect to the Lagrangian space variable at time  $t = 1$  (Source [32], reprinted with permission from Springer Nature under No. 5039260679728)

These choices lead to a positive entropy dissipation. The function  $\mathcal{K}_7$  denotes a limit relation, as it admits only phase boundaries connecting the Maxwell states, i.e. the entropy dissipation is zero. For the sake of comparison we added the so-called Liu-solution. The Liu solution is the classical Riemann solution of the isothermal Euler equations (4) when the free energy  $\rho\psi(\rho)$  is substituted by its convex envelope, which leads to a non-decreasing pressure function.

### 3.2 Temperature-Dependent Two-Phase Flow

Up to now, we have focused on isothermal two-phase flow. Most application-relevant processes, however, are temperature-dependent. For example, latent heat can have a strong influence on the local temperature distribution. Therefore, we turn to the temperature-dependent Euler equations

$$\begin{aligned} \partial_t \rho + \nabla \cdot (\rho \mathbf{v}) &= 0, \\ \partial_t (\rho \mathbf{v}) + \nabla \cdot (\rho \mathbf{v} \otimes \mathbf{v} + p \mathbf{I}) &= \mathbf{0}, \quad \text{in } \Omega_{\pm}(t) \text{ for } t \in (0, t_{\text{end}}), \\ \partial_t E + \nabla \cdot ((E + p)\mathbf{v}) &= 0 \end{aligned} \quad (15)$$

with the total energy density  $E = E(\mathbf{x}, t)$  satisfying  $E = \rho\varepsilon + \frac{1}{2}\rho|\mathbf{v}|^2$ , with  $\varepsilon$  denoting the specific internal energy. The fluid state variables of Eq. (15) are also written in the form of a state vector  $\mathbf{u} = (\rho, \rho\mathbf{v}, E)$ . For the system given by Eq. (15), we have to specify equations of state, that put in relation the pressure  $p = p(\rho, T)$ , the specific internal energy  $\varepsilon = \varepsilon(\rho, T)$ , and the temperature  $T > 0$ .

In [37] the aforementioned isothermal Riemann solver is extended to the temperature-dependent case. Unfortunately, finding an appropriate kinetic relation is

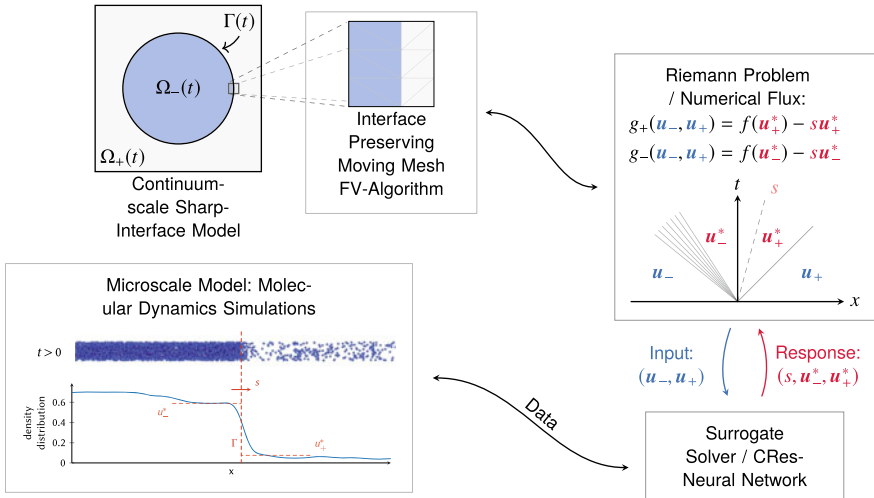


**Fig. 5** Graphical representation of the multiscale scheme illustrating its modules [25]

a non-trivial problem and the corresponding Riemann solutions may exhibit overly large temperature jumps. As a matter of fact, and as discussed in [21], it appears that the classical approach (using kinetic relations, and in absence of heat flux) is unable to reproduce physically consistent behaviour. To circumvent this problem one might model the heat flux across the interface. Yet this introduces new challenges and requires further closure relations, which are difficult to obtain.

Therefore, we propose a novel approach to model the interface dynamics, that is based on the microscopic dynamics of the fluid molecules at the interface. On this scale, only the interactions between the fluid molecules have to be modelled, and continuum-scale properties such as mass or heat flux emerge naturally. The multiscale model consists of several modules, namely

- a continuum-scale sharp-interface two-phase model,
- the interface-preserving finite-volume algorithm on moving meshes (IPFV-algorithm),
- the microscale interface solver, based on molecular dynamics simulations,
- constraint-aware neural networks, that account for underlying physical properties.

A schematic representation of the multiscale model and the aforementioned modules is shown in Fig. 5.

To set up the multiscale model, we consider on the continuum scale the system (15). Note that the EOS on the continuum scale has to be consistent with the microscale MD system—in our case we apply the EOS for the Lennard–Jones fluid presented in [35].

For the discretisation of the sharp-interface continuum-scale two-phase flow, we apply an interface preserving finite volume method on moving meshes [7]. It has the advantage, that the sharp interface is resolved within the mesh and the fluid phases

are strictly separated, which means that on the discretisation-level fluid states are not mixed across the phases. Moreover, this method enables us to use a dedicated interface solver directly at the interface.

This microscale interface solver  $\mathcal{R}_{\text{MD}}$  is of the same type as  $\mathcal{R}$  in (13), i.e.

$$\mathcal{R}_{\text{MD}} : \mathcal{P}_- \times \mathcal{P}_+ \rightarrow \mathcal{P}_- \times \mathcal{P}_+ \times \mathbb{R} : (\mathbf{u}_-, \mathbf{u}_+) \mapsto (\mathbf{u}_-^*, \mathbf{u}_+^*, s). \quad (16)$$

Instead of determining the interface speed  $s$  and wave states  $\mathbf{u}_-^*$ ,  $\mathbf{u}_+^*$  analytically,  $\mathcal{R}_{\text{MD}}$  determines them via molecular dynamics (MD) simulations. This means that large particle systems are considered, consisting of symmetric mono-atomic particles that interact via the Lennard–Jones potential. Now, evaluating  $\mathcal{R}_{\text{MD}}$  corresponds to simulate one large MD simulation that is set up analogously to a continuum-scale Riemann problem. More specifically, we divide the MD simulation-domain into two parts: the liquid phase and the vapour phase. In each phase, we set up particle distributions that correspond to continuum-scale fluid states at the phase boundary. Note that in the current implementation the interface curvature is not considered in the MD simulations. Therefore, surface tension effects are also neglected on the continuum scale. Starting from these Riemann problem-like initial data, we perform the MD simulation and obtain the interface position and speed  $s$ , as well as the interface wave states  $\mathbf{u}_-^*$ ,  $\mathbf{u}_+^*$  via local averaging on the MD scale.

To reduce the computational complexity of performing an MD simulation at every single time step during the continuum-scale simulation, we employ a machine-learned surrogate solver substituting  $\mathcal{R}_{\text{MD}}$ . For this purpose, we apply constraint-resolving neural networks [26] that satisfy mass conservation at the phase boundary.

For a fully detailed description of the multiscale scheme we refer to the PhD-thesis of the first author [25].

### 3.3 Numerical Simulation Results

In the following, we present numerical simulation results of the multiscale model. In Fig. 6 we present a one-dimensional continuum-scale multiscale solution overlaid over the corresponding MD Riemann solution. In this simulation, a vapour wave hits the liquid, and increases the temperature near the phase boundary. We observe that the multiscale solution is quantitatively consistent with the microscale MD solution, up to some diffusive effects that are present only in the particle model.

The two-dimensional simulation shown in Fig. 7 illustrates, that the multiscale scheme can be successfully applied to more complex situations. In this simulation, a liquid droplet oscillates and gets hit by a vapour wave. The need for a surrogate solver becomes evident. If we had to run a MD simulation—taking roughly 5 min—for each of the approximately 200 interface edges in each of the 1000 time steps, the whole simulation would have taken at least 16,000 h which is clearly unfeasible. By employing the surrogate solver, we can reduce the computational time for the simulation to roughly 15 h.

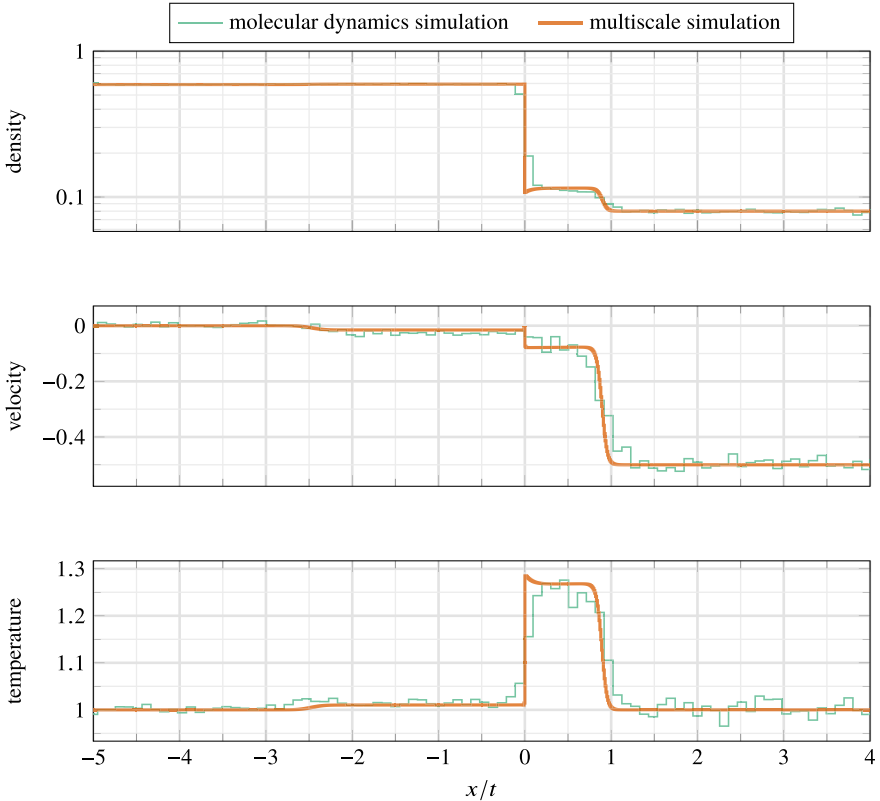


**Fig. 6** Multiscale simulation for the temperature-dependent two-phase flow model in one space dimension and the corresponding MD simulations (a binned statistic is shown, averaged over 50 MD simulations) [25]. The initial data  $\rho_- = 0.58$ ,  $v_- = 0$ ,  $T_- = 1.0$ ,  $\rho_+ = 0.05$ ,  $v_+ = -0.5$ ,  $T_+ = 1.0$  is chosen in such a way that a vapour phase wave hits the liquid phase

### 3.4 Isothermal Two-Component Two-Phase Flow

An advantage of the multiscale model is that it is straightforward to consider more complex fluids and fluid mixtures. Isothermal two-component flow can be modelled, for example, with the continuum-scale, multi-component model derived in [6], which has the following form for each component  $i$

$$\begin{aligned} \partial_t \rho_i + \nabla \cdot (\rho_i \mathbf{v}_i) &= 0, \\ \partial_t (\rho_i \mathbf{v}_i) + \nabla \cdot (\rho_i \mathbf{v}_i \otimes \mathbf{v}_i) &= -\rho_i \nabla \mu_i - T \sum_j f_{ij} \rho_i \rho_j (\mathbf{v}_i - \mathbf{v}_j), \end{aligned} \quad (17)$$

in  $\Omega_{\pm}(t)$  for  $t \in (0, t_{\text{end}})$ . The primary variables are the partial mass densities  $\rho_i$  and the partial velocities  $\mathbf{v}_i$ . The friction factor  $f_{ij} = f_{ji} > 0$  between the components  $i$

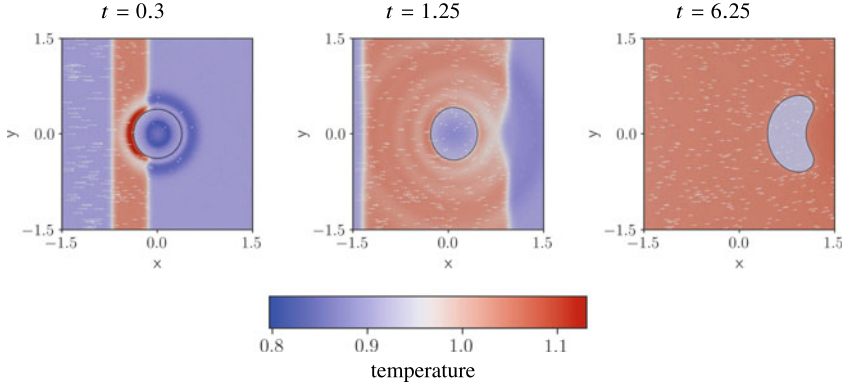


**Fig. 7** Two-dimensional multiscale simulation of the temperature-dependent two-phase flow model. Initially the liquid droplet and the vapour atmosphere are not in equilibrium, resulting in oscillations. Then a wave hits the liquid droplet, that increases the fluid temperature and deforms the droplet [25]

and  $j$  is proportional to the reciprocal of the Maxwell–Stefan diffusion coefficients  $\mathfrak{D}_{ij}$ . The chemical potential of component  $i$  with respect to mass is denoted by  $\mu_i$ , and given by the EOS. We decided to apply the PC-SAFT EOS [20] as it is in good agreement with our MD results.

To test the multiscale model, we consider a mixture of the two components argon and methane, i.e.  $i \in \{\text{Ar}, \text{Me}\}$ . The structure of the corresponding molecules is simple enough to be approximated by basic Lennard–Jones particles, only the parameters of the interaction potential need to be adapted.

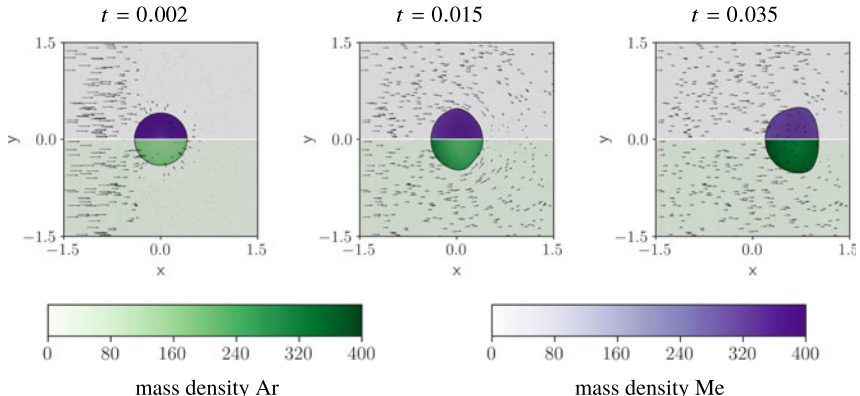


**Fig. 8** Two-dimensional multiscale simulation of two-component, two-phase flow model for an argon–methane mixture. A gaseous wave consisting mostly of argon hits a liquid droplet that consists primarily of methane. The upper part of each sub-figure shows  $\rho_{\text{Me}}, v_{\text{Me}}$  for methane, and the lower part  $\rho_{\text{Ar}}, v_{\text{Ar}}$  for argon [25]

The basic principle of the multiscale model does not change compared to the single-component case—for all details we refer to [25].

In Fig. 8 two-dimensional simulation results are shown for a two-phase argon–methane mixture. In it, a liquid droplet, consisting mostly of methane, is hit by a vapour wave, that is composed mostly of argon. The droplet in turn deforms and is pushed through the fluid domain, while evaporating methane into and accumulating argon from the vapour atmosphere.

## 4 Diffuse-Interface Modelling

The SI approach from Sect. 3 is physically well-grounded as long as the interfaces are separated. However, it comes with a severe disadvantage if interfaces meet. Coalescence, splitting, formation or distinction events go along with singular curvature states, rendering the original approach to fail. For such reasons, diffuse-interface (DI) models have been suggested to describe the dynamics of a compressible fluid with liquid-vapour phase transition. The DI models split into at least two sub-groups. Whereas there are the widely-used phase-field models for compressible liquid-vapour flow (e.g. [3, 5, 29]), we favour a second-gradient approach which does not require to bind an artificial order parameter to the density determining the phase state. Precisely, we rely on models of the Navier–Stokes–Korteweg (NSK) class. As in Sect. 3 the phases are then uniquely determined by the density state (if temperature is kept constant). Starting with the work of [14] there is by now a vast amount on literature for the NSK equations concerning analysis as well as numerics (see e.g. the reviews [3, 30] for a partial overview). We will shortly review the classical NSK system in Sect. 4.1, and then report on new model variants that have been obtained within the SFB–TRR 75. In Sect. 4.2 we will then present numerical simulations for the new model approaches.

This part uses material that has already been published in [8–11, 13, 15, 22, 28].

### 4.1 Navier–Stokes–Korteweg (NSK) Equations for Two-Phase Flow

We keep the temperature fixed at  $T_{\text{ref}} < T_{\text{crit}}$ , such that a liquid and a vapour phase co-exist (see Fig. 2 for the corresponding pressure  $p = p(\rho)$  omitting the temperature dependence). For what follows, the unknowns will depend on a parameter  $\epsilon > 0$  governing the width of the diffuse interface. For  $\epsilon \rightarrow 0$  we expect under appropriate scaling of viscosity and capillarity parameters to recover certain solutions of models in Sect. 3. As initial conditions for density and velocity we then set

$$\rho^\epsilon(\cdot, 0) = \rho_0, \mathbf{v}^\epsilon(\cdot, 0) = \mathbf{v}_0 \text{ in } \Omega. \quad (18)$$

**The Classical Navier–Stokes–Korteweg Equations.** Let the capillarity parameter  $\gamma = \gamma(\epsilon) > 0$  and  $\mathbf{T}^\epsilon$  be the viscous part of the stress tensor, given for the dynamical shear viscosity  $\eta = \eta(\epsilon)$ , and the bulk viscosity  $\lambda = \lambda(\epsilon)$  with  $\eta \geq 0$ ,  $3\lambda + 2\eta \geq 0$  by

$$\mathbf{T}_{ij}^\epsilon[\mathbf{v}] := \lambda(\nabla \cdot \mathbf{v})\delta_{ij} + 2\eta \mathbf{D}_{ij}[\mathbf{v}], \quad \mathbf{D}_{ij}[\mathbf{v}] = \frac{1}{2}(v_{j,x_i}^\epsilon + v_{i,x_j}^\epsilon), \quad (19)$$

for  $i, j \in \{1, \dots, n\}$ . For the unknowns, density  $\rho^\epsilon = \rho^\epsilon(\mathbf{x}, t) : \Omega \times [0, t_{\text{end}}] \rightarrow (0, 1/b)$ , velocity  $\mathbf{v} = \mathbf{v}(\mathbf{x}, t) : \Omega \times [0, t_{\text{end}}] \rightarrow \mathbb{R}^d$ , the classical NSK system extends the Navier–Stokes system and reads as [14]

$$\begin{aligned} \partial_t \rho^\epsilon + \nabla \cdot (\rho^\epsilon \mathbf{v}^\epsilon) &= 0, \\ \partial_t(\rho^\epsilon \mathbf{v}^\epsilon) + \nabla \cdot (\rho^\epsilon \mathbf{v}^\epsilon \otimes \mathbf{v}^\epsilon + p(\rho^\epsilon) \mathbf{I}) &= \nabla \cdot (\mathbf{T}^\epsilon[\mathbf{v}^\epsilon]) + \gamma \rho^\epsilon \nabla \Delta \rho^\epsilon, \end{aligned} \quad (20)$$

in  $\Omega \times (0, t_{\text{end}})$ . Besides the initial conditions (18), we fix, for  $\mathbf{n}_\Omega \in \mathbb{S}^{d-1}$  being the outer normal of  $\partial\Omega$ , the boundary conditions

$$\mathbf{v}^\epsilon(\cdot, t) = \mathbf{0}, \quad \mathbf{n}_\Omega \cdot \nabla \rho^\epsilon(\cdot, t) = 0 \quad \text{on } \partial\Omega. \quad (21)$$

This choice induces a 90°-degree contact angle between the phases at the solid wall boundary. The model is thermodynamically consistent, i.e. using (1), classical solutions of (18), (20), (21) satisfy for all  $t \in (0, t_{\text{end}})$  and  $\lambda, \eta$  as above

$$\begin{aligned} \frac{d}{dt} \left( \int_\Omega \frac{1}{2} \rho^\epsilon(\mathbf{x}, t) |\mathbf{v}^\epsilon(\mathbf{x}, t)|^2 + \rho^\epsilon(\mathbf{x}, t) \psi(\rho^\epsilon(\mathbf{x}, t)) + \frac{\gamma}{2} |\nabla \rho^\epsilon(\mathbf{x}, t)|^2 d\mathbf{x} \right) \\ \leq - \int_\Omega 2\eta \mathbf{D}[\mathbf{v}^\epsilon(\mathbf{x}, t)] : \mathbf{D}[\mathbf{v}^\epsilon(\mathbf{x}, t)] + \lambda(\nabla \cdot (\mathbf{v}^\epsilon(\mathbf{x}, t)))^2 d\mathbf{x} \leq 0. \end{aligned} \quad (22)$$

The energy inequality (22) is the DI analogue to the SI energy inequality (11). Let us consider static equilibrium solutions for (20). The generalized energy in (22) reduces then to the van der Waals energy

$$F^{\text{DI-NSK}}[\rho^\epsilon] := \int_\Omega \rho^\epsilon(\mathbf{x}) \psi(\rho^\epsilon(\mathbf{x})) + \frac{\gamma}{2} |\nabla \rho^\epsilon(\mathbf{x})|^2 d\mathbf{x}. \quad (23)$$

In other words, the density component of the time-asymptotic limit of solutions of the Eqs. (18), (20), (21) can be expected to minimize the functional  $F^{\text{DI-NSK}}$ . For the scaling  $\gamma(\epsilon) = O(\epsilon^2)$ , minimizers of (23) approach minimizers of the SI functional  $F^{\text{SI}}$  in (12) (see e.g. [27]). Additionally, with  $\lambda(\epsilon), \eta(\epsilon) = O(\epsilon)$  one recovers for  $\epsilon \rightarrow 0$  solutions of Eqs. (4), (5), (8) with  $\sigma = 0$  (see [13] for formal asymptotic analysis results in this direction including alternative scalings).

**The Relaxed Navier–Stokes–Korteweg Equations.** The classical NSK system involves third-order derivatives, which makes it numerically quite complicated. Moreover, the Euler-type operator in Eq. (20) is of mixed hyperbolic–elliptic type,

i.e. the flux Jacobian has complex eigenvalues for densities in the spinodal region (see Fig. 2). As one practical consequence, it is not possible to extend modern numerical methods for the Navier–Stokes equations because these require the hyperbolicity. Therefore, we aim at developing alternative formulations of the NSK system (20) that avoid this difficulty. First, one can substitute the Laplacian in the momentum balance of Eq. (20) by a convolution term (see [8, 28]) that relies on analytical arguments from [9]. This approach necessitates the solution of an extra elliptic equation. As a second approach we re-formulate the ansatz leading to a hyperbolic–parabolic system that is solvable for any standard solver for the Navier–Stokes equations.

To be precise, for a relaxation parameter  $\alpha > 0$  we consider the relaxed NSK system, given by

$$\begin{aligned} \partial_t \rho^{\epsilon,\alpha} + \nabla \cdot (\rho^{\epsilon,\alpha} \mathbf{v}^{\epsilon,\alpha}) &= 0, \\ \partial_t (\rho^{\epsilon,\alpha} \mathbf{v}^{\epsilon,\alpha}) + \nabla \cdot (\rho^{\epsilon,\alpha} \mathbf{v}^{\epsilon,\alpha} \otimes \mathbf{v}^{\epsilon,\alpha} + p(\rho^{\epsilon,\alpha}) \mathbf{I}) &= \nabla \cdot (\mathbf{T}^\epsilon[\mathbf{v}^{\epsilon,\alpha}]) \\ &\quad + \alpha \rho^{\epsilon,\alpha} \nabla(c^{\epsilon,\alpha} - \rho^{\epsilon,\alpha}), \\ \beta c_t - \gamma \Delta c^{\epsilon,\alpha} &= \alpha(\rho^{\epsilon,\alpha} - c^{\epsilon,\alpha}) \end{aligned} \quad (24)$$

in  $\Omega \times (0, t_{\text{end}})$ . Here,  $\beta = \beta(\alpha)$  is a mobility parameter. The system (24) extends the classical NSK system by a heat equation for the relaxation quantity  $c^{\epsilon,\alpha} = c^{\epsilon,\alpha}(\mathbf{x}, t) \in \mathbb{R}$ . The unknown  $c$  should be close to  $\rho^{\epsilon,\alpha}$  such that the initial conditions are chosen as

$$\rho^{\epsilon,\alpha}(\cdot, 0) = c^{\epsilon,\alpha}(\cdot, 0) = \rho_0, \quad \mathbf{v}^{\epsilon,\alpha}(\cdot, 0) = \mathbf{v}_0 \quad \text{in } \Omega. \quad (25)$$

Note that Eq. (24) does not contain higher derivatives on  $\rho^{\epsilon,\alpha}$ . The boundary conditions from Eq. (21) with a Neumann condition on  $\rho^{\epsilon,\alpha}$  transfer to

$$\mathbf{v}^{\epsilon,\alpha}(\cdot, t) = \mathbf{0}, \quad \mathbf{n}_\Omega \cdot \nabla c^{\epsilon,\alpha}(\cdot, t) = 0 \quad \text{on } \partial\Omega. \quad (26)$$

Local well-posedness of classical solutions for the Eqs. (24), (25), (26) can be derived with standard contraction techniques. Before we go on to discuss the relation between the relaxed NSK system and the NSK system (20) let us note that it is a straightforward computation to verify that (24) is thermodynamically consistent. Classical solutions  $(\rho^{\epsilon,\alpha}, \mathbf{v}^{\epsilon,\alpha}, c^{\epsilon,\alpha})$  of Eqs. (24), (25), (26) obey for  $t \in [0, t_{\text{end}}]$  the inequality

$$\begin{aligned} \frac{d}{dt} \mathcal{E}^{\epsilon,\alpha}(t) &:= \frac{d}{dt} \left( \int_\Omega \frac{1}{2} \rho^{\epsilon,\alpha}(\mathbf{x}, t) |\mathbf{v}^{\epsilon,\alpha}(\mathbf{x}, t)|^2 + \rho^{\epsilon,\alpha}(\mathbf{x}, t) \psi(\rho^{\epsilon,\alpha}(\mathbf{x}, t)) \right. \\ &\quad \left. + \frac{\alpha}{2} (\rho^{\epsilon,\alpha}(\mathbf{x}, t) - c(\mathbf{x}, t))^2 + \frac{\gamma}{2} |\nabla c(\mathbf{x}, t)|^2 d\mathbf{x} \right) \\ &= - \int_\Omega 2\eta \mathbf{D}[\mathbf{v}^{\epsilon,\alpha}(\mathbf{x}, t)] : \mathbf{D}[\mathbf{v}^{\epsilon,\alpha}(\mathbf{x}, t)] \\ &\quad + \lambda (\nabla \cdot (\mathbf{v}^{\epsilon,\alpha}(\mathbf{x}, t)))^2 + \beta (c_t(\mathbf{x}, t))^2 d\mathbf{x} \\ &\leq 0. \end{aligned} \quad (27)$$

Static equilibrium solutions of Eq. (24) are provided by minimizers of the functional

$$\begin{aligned} F^{\text{DL-rNSK}}[\rho^{\epsilon,\alpha}, c^{\epsilon,\alpha}] := \\ \int_{\Omega} \rho^{\epsilon,\alpha}(\mathbf{x}) \psi(\rho^{\epsilon,\alpha}(\mathbf{x})) + \frac{\alpha}{2} (\rho^{\epsilon,\alpha}(\mathbf{x}) - c^{\epsilon,\alpha}(\mathbf{x}))^2 + \frac{\gamma}{2} |\nabla c^{\epsilon,\alpha}(\mathbf{x})|^2 \, d\mathbf{x}. \end{aligned} \quad (28)$$

One observes that minima of the Van-der-Waals functional (23) are (formally) recovered when considering the Korteweg limit  $\alpha \rightarrow \infty$  for a sequence of minimizers of Eq. (28) (see [34] for rigorous results, always keeping  $\epsilon$  fixed). Likewise, we have achieved analytical and numerical evidence that solutions of the relaxed NSK system (24) with  $\beta = O(\epsilon\alpha^{-1})$  converge for  $\alpha \rightarrow \infty$  to solutions of the NSK system (20) [10, 15, 28], that have been extended later in e.g. [19]. In turn, keeping  $\alpha$  fixed and scaling  $\gamma(\epsilon) = O(\epsilon^2)$ ,  $\lambda(\epsilon)$ ,  $\eta(\epsilon) = O(\epsilon)$  we conjecture that the SI limit  $\epsilon \rightarrow 0$  equals the ones for Eqs. (23), (20), respectively.

## 4.2 Numerical Simulations for the Relaxed NSK System

Based on the analysis of the Korteweg limit  $\alpha \rightarrow \infty$  for the relaxed NSK problem (24)–(26) as described in Sect. 4.1, we view it as an approximation of the original NSK problem (18), (20), (21). We have developed several numerical schemes to solve the relaxed problems focusing on the Local Discontinuous-Galerkin method that appears to be most flexible for this type of equations. For details we refer to [11, 22, 28]. Before we conclude this section with a series of numerical experiments let us clarify why the relaxed system is more appropriate for the numerical discretisation.

First, the relaxed NSK system contains only *second-order* and *local* differential operators as compared to the third-order system (20). Note that solving the additional equation for the relaxation unknown  $c^{\epsilon,\alpha}$  is not a problem. This equation is a simple linear heat equation, which can be solved extremely efficiently. But there is another issue which makes Eq. (24) attractive. Neglecting the viscous part of the stress tensor in Eq. (24) the momentum balance can be re-written in the form

$$\partial_t(\rho^{\epsilon,\alpha} \mathbf{v}^{\epsilon,\alpha}) + \nabla \cdot (\rho^{\epsilon,\alpha} \mathbf{v}^{\epsilon,\alpha} \otimes \mathbf{v}^{\epsilon,\alpha} + p_\alpha(\rho^{\epsilon,\alpha}) \mathbf{I}) = \alpha \rho^{\epsilon,\alpha} \nabla c, \quad (29)$$

using the re-defined pressure

$$p_\alpha(\rho) := p(\rho) + \frac{\alpha}{2} \rho^2. \quad (30)$$

One readily observes that for  $\alpha \gg 1$ , the function  $p_\alpha$  is monotonically increasing. Then the entire Euler operator in Eq. (24) (, i.e., substituting  $p$  by  $p_\alpha$  in Eq. (24)) becomes hyperbolic. In turn the relaxed NSK system is accessible to standard methods for hyperbolic-parabolic equations of Navier–Stokes type. In the sequel we report

on two examples from [22], which have been computed by an extension of the CFD-code FLEXI [24].

**Merging of multiple droplets, Ostwald ripening, and trend to equilibrium (from [22]).** For the first example, we start in  $t = 0.0$  with an ensemble of droplets in  $\Omega = (0, 1)^2$ , as displayed in the upper-left box in Fig. 9. The initial velocity vanishes and for the parameters in Eq. (24) we make the choices

$$\lambda = -\frac{2}{3}\epsilon, \eta = \epsilon, \beta = \epsilon\alpha^{-1}, \gamma = \epsilon^2, \epsilon = 0.01, \alpha = 100.$$

As pressure, the van der Waals function (3) is chosen with  $a = 1/b = 3, R = 8/3$  and  $T_{\text{ref}} = 0.85$ . The results of the simulation can be seen in Fig. 9. One observes several phase transition effects. Smaller droplets merge and unite to a bigger one which is

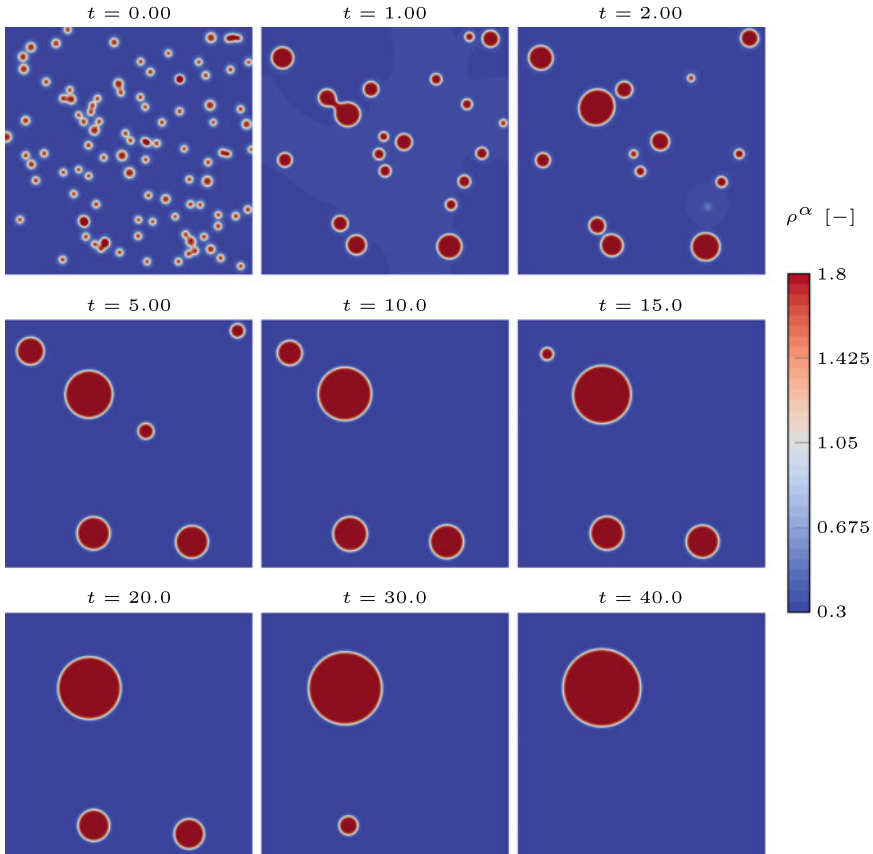


**Fig. 9** Evolution of a droplet ensemble and trend to (spherical) equilibrium (Source [22], reprinted with permission from Elsevier under No. 5039260334246)

driven into spherical (quasi-)equilibrium. Notably, there is also Ostwald ripening taking place: droplets get smaller and vanish without contact to other droplets. For this slow process the liquid mass is transported through the surrounding low-density vapour phase. For the end of the simulation, one sees, that a spherical droplet remains, confirming the discussion of equilibria in Sect. 4.1.

**Head-on collisions and discrete energy dissipation (from [22]).** For the second example in  $\Omega = (0, 1)^3$ , we take all parameters as in the first one. The initial density field is arranged, such that there are two droplets with density  $\rho_l$  in a vapor atmosphere of density  $\rho_v$ , see the upper-left box in Fig. 10. The initial velocity is chosen such that the droplets are forced together. For the exact set-up we refer to [22, Sect. 4.3.2.]. The resulting collision scenario is shown in Fig. 10, where the contour surfaces for the mean value of  $\rho_l$  and  $\rho_v$  are plotted. The two droplets merge and result in one squashed droplet. This droplet oscillates, and finally evaporates completely. It is remarkable, that for this numerical simulation, there holds a discrete analogue of the energy decay as expressed in the relation (27). Its time evolution is tracked in Fig. 11. We employed a third-order version of the spectral element approach in FLEXI [24], with a spatial resolution of  $64^3$  elements, resulting in  $256^3$  degrees of freedom. For a complete study of head collisions with its various topological droplet scenarios we refer to [22].

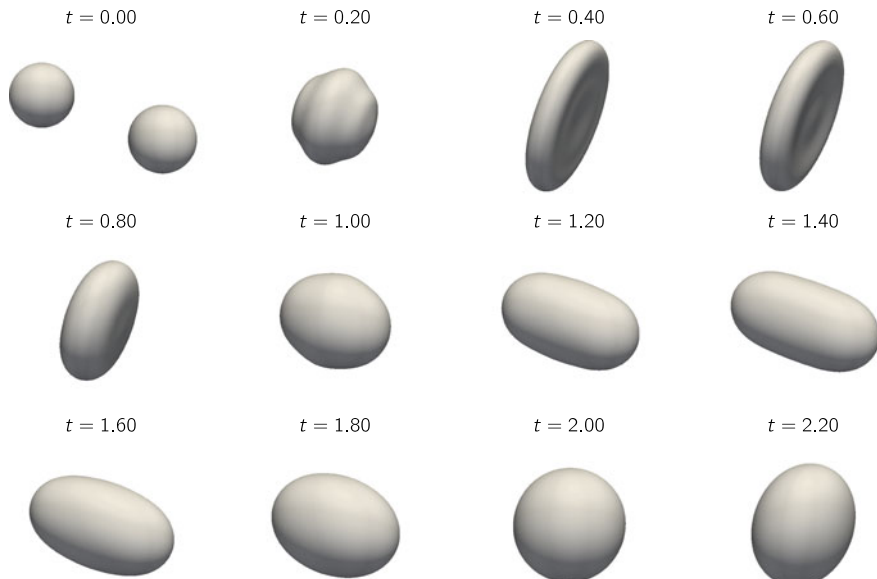
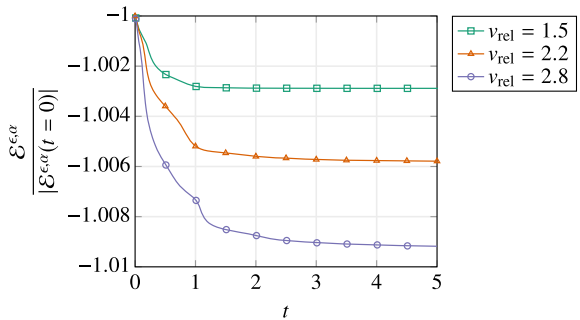


**Fig. 10** Evolution of two colliding droplets. The figures display representative contour surfaces of the density field at different times (Source [22], reprinted with permission from Elsevier under No. 5039260334246)

**Fig. 11** Time evolution of the discrete energy  $\mathcal{E}^{\epsilon,\alpha}(t)$  for different collision velocities  $v_{\text{rel}}$ . The plot at the top corresponds to the simulation shown in Fig. 10. Just as for the exact solution (see (27)), the discrete energy in the numerical simulations decreases monotonically. (Source [22])



## 5 Conclusions

In the course of the project, we have developed novel approaches to model and simulate two-phase flows.

For the SI modelling approach, an analytical two-phase solver was developed, that is applicable to a wide range of kinetic closure relations. Furthermore, a new multiscale model was designed, that does not need prescribed closure relations at the interface. Instead, the phase boundary dynamics are determined from MD simulations on a more fundamental level. The versatility of this approach is proven by the fact that even multi-component flow can be simulated.

Within the DI modelling framework, we considered a NSK-system, which, in its basic form, is quite expensive to solve. Thus, we proposed and investigated alternative formulations of the system, which are more efficient to simulate.

**Acknowledgements** This work was supported by the German Research Foundation (DFG) through project SFB–TRR 75 “Droplet dynamics under extreme ambient conditions” with the project number 84292822. The authors kindly acknowledge the financial support for the work by the DFG.

## References

1. Abeyaratne R, Knowles JK (2006) Evolution of phase transitions: a continuum theory. Cambridge University Press. <https://doi.org/10.1017/CBO9780511547133>
2. Alt HW (2009) The entropy principle for interfaces. Fluids and solids. Adv Math Sci Appl 19(2):585–663
3. Anderson DM, McFadden GB, Wheeler AA (1998) Diffuse-interface methods in fluid mechanics. Annu Rev Fluid Mech 30(1):139–165. <https://doi.org/10.1146/annurev.fluid.30.1.139>
4. Batchelor GK (1999) An introduction to fluid dynamics, paperback edn. Cambridge mathematical library. Cambridge University Press, Cambridge. <https://doi.org/10.1017/CBO9780511800955>
5. Blesgen T (1999) A generalization of the Navier-Stokes equations to two-phase flows. J Phys D Appl Phys 32(10):1119–1123. <https://doi.org/10.1088/0022-3727/32/10/307>
6. Bothe D, Dreyer W (2015) Continuum thermodynamics of chemically reacting fluid mixtures. Acta Mech 226(6):1757–1805. <https://doi.org/10.1007/s00707-014-1275-1>

7. Chalons C, Rohde C, Wiebe M (2017) A finite volume method for undercompressive shock waves in two space dimensions. *ESAIM Math Model Numer Anal.* <https://doi.org/10.1051/m2an/2017027>
8. Chertock A, Degond P, Neusser J (2017) An asymptotic-preserving method for a relaxation of the Navier-Stokes-Korteweg equations. *J Comput Phys* 335:387–403. <https://doi.org/10.1016/j.jcp.2017.01.030>
9. Corli A, Rohde C (2012) Singular limits for a parabolic-elliptic regularization of scalar conservation laws. *J Differ Equ* 253(5):1399–1421. <https://doi.org/10.1016/j.jde.2012.05.006>
10. Corli A, Rohde C, Schleper V (2014) Parabolic approximations of diffusive-dispersive equations. *J Math Anal Appl* 414(2):773–798. <https://doi.org/10.1016/j.jmaa.2014.01.049>
11. Diehl D, Kremser J, Kröner D, Rohde C (2016) Numerical solution of Navier-Stokes-Korteweg systems by local discontinuous Galerkin methods in multiple space dimensions. *Appl Math Comput* 272(part 2):309–335. <https://doi.org/10.1016/j.amc.2015.09.080>
12. Dragomirescu FI, Eisenschmidt K, Rohde C, Weigand B (2016) Perturbation solutions for the finite radially symmetric Stefan problem. *Int J Therm Sci* 104:386–395. <https://doi.org/10.1016/j.ijthermalsci.2016.01.019>
13. Dreyer W, Giesselmann J, Kraus C, Rohde C (2012) Asymptotic analysis for Korteweg models. *Interfaces Free Bound.* 14(1):105–143. <https://doi.org/10.4171/ifb/275>
14. Dunn JE, Serrin J (1985) On the thermomechanics of interstitial working. *Arch Rational Mech Anal* 88(2):95–133. <https://doi.org/10.1007/BF00250907>
15. Engel P, Viorel A, Rohde C (2013) A low-order approximation for viscous-capillary phase transition dynamics. *Port Math* 70(4):319–344. <https://doi.org/10.4171/PM/1937>
16. Fechter S, Jaegle F, Schleper V (2013) Exact and approximate Riemann solvers at phase boundaries. *Comput Fluids* 75:112–126. <https://doi.org/10.1016/j.compfluid.2013.01.024>
17. Fechter S, Munz CD, Rohde C, Zeiler C (2017) A sharp interface method for compressible liquid-vapor flow with phase transition and surface tension. *J Comput Phys* 336:347–374. <https://doi.org/10.1016/j.jcp.2017.02.001>
18. Fechter S, Munz CD, Rohde C, Zeiler C (2018) Approximate Riemann solver for compressible liquid vapor flow with phase transition and surface tension. *Comput Fluids* 169:169–185. <https://doi.org/10.1016/j.compfluid.2017.03.026>
19. Giesselmann J (2014) A relative entropy approach to convergence of a low order approximation to a nonlinear elasticity model with viscosity and capillarity. *SIAM J Math Anal* 46(5):3518–3539. <https://doi.org/10.1137/140951710>
20. Gross J, Sadowski G (2001) Perturbed-Chain SAFT: an equation of state based on a perturbation theory for chain molecules. *Ind Eng Chem Res* 40(4):1244–1260. <https://doi.org/10.1021/ie0003887>
21. Hantke M, Thein F (2019) On the impossibility of first-order phase transitions in systems modeled by the full Euler equations. *Entropy* 21(11):1039. <https://doi.org/10.3390/e21111039>
22. Hitz T, Keim J, Munz CD, Rohde C (2020) A parabolic relaxation model for the Navier-Stokes-Korteweg equations. *J Comput Phys* 421:109714. <https://doi.org/10.1016/j.jcp.2020.109714>
23. Kabil B, Rohde C (2014) The influence of surface tension and configurational forces on the stability of liquid-vapor interfaces. *Nonlinear Anal* 107:63–75. <https://doi.org/10.1016/j.na.2014.04.003>
24. Krais N, Beck A, Boermann T et al (2021) FLEXI: a high order discontinuous Galerkin framework for hyperbolic-parabolic conservation laws. *Comput Math Appl* 81:186–219. <https://doi.org/10.1016/j.camwa.2020.05.004>
25. Magiera J (2021) A molecular–continuum multiscale solver for liquid–vapor flow: Modeling and numerical simulation. PhD thesis, University of Stuttgart. <https://doi.org/10.18419/opus-11797>
26. Magiera J, Ray D, Hesthaven JS, Rohde C (2020) Constraint-aware neural networks for Riemann problems. *J Comput Phys* 409:109345. <https://doi.org/10.1016/j.jcp.2020.109345>
27. Modica L (1987) The gradient theory of phase transitions and the minimal interface criterion. *Arch Ration Mech Anal* 98(2):123–142. <https://doi.org/10.1007/BF00251230>

28. Neusser J, Rohde C, Schleper V (2015) Relaxation of the Navier-Stokes-Korteweg equations for compressible two-phase flow with phase transition. *Int J Numer Methods Fluids* 79(12):615–639. <https://doi.org/10.1002/fld.4065>
29. Ostrowski L, Massa FC, Rohde C (2020) A phase field approach to compressible droplet impingement. In: Lamanna G, Tonini S, Cossali GE, Weigand B (eds) *Droplet Interactions and Spray Processes*. Springer International Publishing, Cham, pp 113–126. [https://doi.org/10.1007/978-3-030-33338-6\\_9](https://doi.org/10.1007/978-3-030-33338-6_9)
30. Rohde C (2018) Fully resolved compressible two-phase flow: modelling, analytical and numerical issues. In: *New trends and results in mathematical description of fluid flows*, Nečas Center Ser. Birkhäuser/Springer, Cham, pp 115–181. [https://doi.org/10.1007/978-3-319-94343-5\\_4](https://doi.org/10.1007/978-3-319-94343-5_4)
31. Rohde C, Zeiler C (2015) A relaxation Riemann solver for compressible two-phase flow with phase transition and surface tension. *Appl Numer Math* 95:267–279. <https://doi.org/10.1016/j.apnum.2014.05.001>
32. Rohde C, Zeiler C (2018) On Riemann solvers and kinetic relations for isothermal two-phase flows with surface tension. *Z Angew Math Phys* 69(3):76. <https://doi.org/10.1007/s00033-018-0958-1>
33. Schleper V (2016) A HLL-type Riemann solver for two-phase flow with surface forces and phase transitions. *Appl Numer Math* 108:256–270. <https://doi.org/10.1016/j.apnum.2015.12.010>
34. Solci M, Vitali E (2003) Variational models for phase separation. *Interfaces Free Bound.* 5(1):27–46. <https://doi.org/10.4171/IFB/70>
35. Thol M, Rutkai G, Köster A, Lustig R, Span R, Vrabec J (2016) Equation of state for the Lennard-Jones fluid. *J Phys Chem Ref Data* 45(2):023–101. <https://doi.org/10.1063/1.4945000>
36. Truskinovsky L (1993) Kinks versus shocks. In: *Shock induced transitions and phase structures in general media*, IMA Vol Math Appl, vol 52. Springer, New York, pp 185–229. [https://doi.org/10.1007/978-1-4613-8348-2\\_11](https://doi.org/10.1007/978-1-4613-8348-2_11)
37. Zeiler C (2015) Liquid vapor phase transitions: modeling, Riemann solvers and computation. PhD thesis, Universität Stuttgart. <https://doi.org/10.18419/opus-8902>

**Open Access** This chapter is licensed under the terms of the Creative Commons Attribution 4.0 International License (<http://creativecommons.org/licenses/by/4.0/>), which permits use, sharing, adaptation, distribution and reproduction in any medium or format, as long as you give appropriate credit to the original author(s) and the source, provide a link to the Creative Commons license and indicate if changes were made.

The images or other third party material in this chapter are included in the chapter's Creative Commons license, unless indicated otherwise in a credit line to the material. If material is not included in the chapter's Creative Commons license and your intended use is not permitted by statutory regulation or exceeds the permitted use, you will need to obtain permission directly from the copyright holder.



# Stopping Droplet Rebound with Polymer Additives: A Molecular Viewpoint



Eunsang Lee, Hari Krishna Chilukoti, and Florian Müller-Plathe

**Abstract** The origin of rebound suppression of an impacting droplet by a small amount of polymer additive has been tentatively explained by various physical concepts including the dynamic surface tension, the additional energy dissipation by non-Newtonian elongational viscosity, the elastic force of stretched polymer, and the additional friction on a receding contact line. To better understand the role of polymer on a molecular level, we performed multi-body dissipative particle dynamics simulations of droplets impacting on solvophobic surfaces. The rebound suppression is achieved by the elastic force of stretched polymer during the hopping stage, and the additional friction on the contact line during the retraction stage. Both slow-hopping and slow-retraction mechanisms coexist in a wide range of simulation parameters, but the latter is prevailing for large droplets, and for the strong attraction strength between polymer and surface. The increased polymer adsorption, which maybe achieved by a higher polymer concentration or a larger molecular weight, stimulates both mechanisms. Also, the molecular evidence of the additional friction on the receding contact line is shown from the relation between the contact angle and the contact line velocity where the slope of the fitted line is an indication of the additional friction.

---

E. Lee (✉) · F. Müller-Plathe

Eduard-Zintl Institute for Inorganic and Physical Chemistry, Technical University of Darmstadt, Darmstadt, Germany

e-mail: [e.lee@theo.chemie.tu-darmstadt.de](mailto:e.lee@theo.chemie.tu-darmstadt.de)

F. Müller-Plathe

e-mail: [f.mueller-plathe@theo.chemie.tu-darmstadt.de](mailto:f.mueller-plathe@theo.chemie.tu-darmstadt.de)

H. Krishna Chilukoti

Department of Mechanical Engineering, National Institute of Technology Warangal, Warangal, India

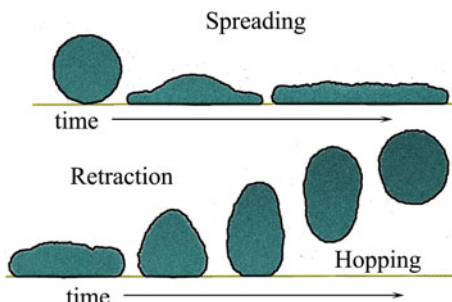
e-mail: [chk@nitw.ac.in](mailto:chk@nitw.ac.in)

## 1 Introduction

Dynamic wetting of a solid surface by impacting liquid droplets has gained a lot of attention due to its practical relevance in agriculture, coating, painting, ink-jet printing, etc.. [13, 17, 20, 53, 60]. When a droplet impacts on a solvophobic surface, it can deposit, splash (disintegrate), or rebound depending on liquid and solid properties [29]. After a droplet touches a surface, it spreads laterally. The spreading of Newtonian droplets is generally governed by their initial kinetic energy (impact velocity), the viscous energy dissipation of the liquid, and the surface tension of the droplet. Dimensionless Reynolds,  $Re = \rho v D / \eta$ , and Weber numbers,  $We = \rho v^2 D / \gamma$ , characterise the balance between them, where  $\rho$ ,  $v$ ,  $D$ ,  $\eta$ , and  $\gamma$  refer to the droplet mass density, the impact velocity, the initial droplet diameter, the shear viscosity of the liquid, and the droplet surface tension, respectively [1, 29, 38, 50]. For a droplet of small  $Re$ , much energy is dissipated by liquid viscosity, which leads to a small droplet diameter at maximum spreading. A small  $We$  refers to large surface tension, also resulting in small droplet diameter. The spreading is followed by splashing or retraction depending on the surface energy compared to the remaining kinetic energy. If the liquid-vapor surface tension is not large enough to store the remaining kinetic energy, the droplet splits into several sub-droplets. Otherwise, the droplet retracts as it minimises its surface area. The retraction of Newtonian droplets is controlled by the initial kinetic energy, the capillary force and the viscous dissipation, which is quantified by the dimensionless capillary number,  $Ca = \eta v / \gamma$ . A large  $Ca$  denotes a stronger viscous effect compared to an elastic effect of the surface, thus it makes the retraction velocity slow. The retraction is also affected by frictional energy dissipation at the liquid-solid interface, which is characterised either by surface wettability or the solid-liquid interfacial tension. As the latter is not easy to measure experimentally, equilibrium or dynamic contact angles are widely adopted in its place. If the kinetic energy is not sufficiently dissipated during the retraction, the remaining particle momentum is diverted to the surface normal, which results in droplet rebound (Fig. 1).

A droplet impacting on a solvophobic surface is very likely to bounce off it as the frictional energy dissipation at the liquid-solid interface during spreading and retraction is small. The unwanted droplet rebound may lead to reduced productivity

**Fig. 1** Schematic description of droplet impact process. A droplet first spreads laterally after touching the surface. After reaching maximum spreading, it retracts back to recover its spherical shape. If the initial kinetic energy is not fully dissipated, it rebounds off the surface



in many industrial processes including coating, painting and printing [2, 35, 57]. In agriculture, it is a challenging problem to suppress the bouncing of pesticide sprays for better efficiency without a large modification of the solution composition [62]. Among several strategies to suppress droplet rebound from a solvophobic surface [26, 30, 58], polymer additives are well-established. The first observation was that a few hundreds ppm of polyethylene oxide (PEO) in water suppresses the rebound when a droplet impacts on a hydrophobic leaf [6, 36, 54]. A droplet of an aqueous polymer solution in the dilute regime well below the overlap concentration has a liquid-vapor surface tension and the shear viscosity very similar to that of a pure water droplet, but it is able to suppress the rebound [4]. Since only considering We and Ca cannot explain the phenomenon, other, non-Newtonian properties are necessary to explain it.

Over three decades, scientists put efforts to find the mechanism of the polymer-induced anti-rebound. Many observations showed that the retraction velocity of a polymer-solution droplet is slower than that of a pure solvent droplet, but this has been interpreted in many different ways. In this article, we review some physical concepts of the existing explanations, and we provide a molecular picture of the droplet impact process in order to elucidate the polymer effect on the rebound using dissipative particle dynamics simulations.

## 1.1 Dynamic Surface Tension

An early attempt held the dynamic liquid-vapor surface tension of a droplet responsible for the rebound suppression. Mourougou-Candoni et al. [37] performed a droplet impact experiment of a surfactant solution onto a hydrophobic flat surface, and interpreted the different dynamics, particularly during retraction, in terms of the dynamic surface tension. Newtonian droplets have a homogeneous liquid-vapor interface, thus the surface tension under any deformation remains the same or very close to its equilibrium value. In contrast, a small amount of surfactant is heterogeneously distributed in the droplet, and the molecules are localised on a quickly expanding or shrinking surface. As the droplet is deformed, a surfactant molecule needs time to diffuse onto the new surface. The rate of the surfactant diffusion to the surface, typically called adsorption kinetics, depends on the type of surfactants and the deformation rate. Surfactants with fast adsorption kinetics quickly diffuse to the surface during spreading, so the dynamic surface tension at maximum spreading becomes small, leading to a low retraction force. The adsorption kinetics also affects the reduction of the surface tension during retraction. The slow retraction due to the small surface tension causes a fast reorganisation of surfactant molecules on the surface during retraction, leading to a further decrease of the surface tension. Therefore, surfactants having fast adsorption kinetics are expected to suppress the droplet rebound.

A later work done by Crooks et al. [16] followed a similar idea of the dynamic surface tension, but under restricted conditions. They found that the fluid's hydrodynamics is different for the droplet impact from that in the maximum bubble pressure

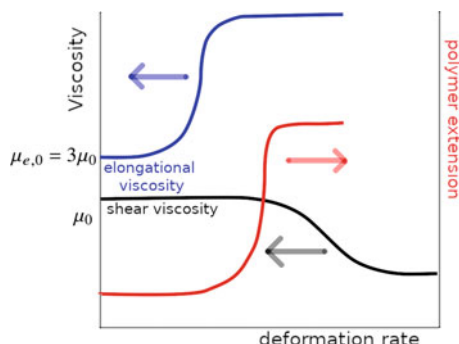
method (MBPM) which is a measurement technique for the dynamic surface tension. They alleged that the mechanism of the dynamic surface tension does not work below the critical micelle concentration of the surfactant when hydrodynamics critically influences to the surfactant diffusion. However, above the critical micelle concentration, demicellisation quickly supplies the surfactants to the surface. Because this process is not much affected by hydrodynamics, the dynamic surface tension observed from MBPM could explain the different retraction and rebound upon impact.

The idea of the reduced surface tension, however, cannot explain the rebound suppression by a polymer additive, e.g., PEO in water, as PEO has a very slow adsorption kinetics [24]. Moreover, a small amount of surface-stabilising surfactants substantially reduces an equilibrium surface tension, provoking fragmentation or splashing of the droplet after spreading, which worsens the problems beyond the droplet rebound in many applications.

## 1.2 Elongational Viscosity

When an elongational deformation is applied to a polymeric material, the polymer stretches in the direction of the elongation. The stretched polymer is entropically and sometimes energetically, too, unfavourable compared to its average equilibrium conformation. The tendency to recover its equilibrium coiled conformation generates a pulling force against elongation. If a polymer solution is deformed by flow, the polymer is elongated in the flow direction. As a consequence, the first normal stress difference,  $N_1 = \sigma_{zz} - \sigma_{xx}$ , becomes negative, where  $\sigma_{zz}$  and  $\sigma_{xx}$  refer to the diagonal stress tensor components in flow and in perpendicular directions, respectively. The elongational viscosity characterises the viscous energy dissipation by the first normal stress under elongation, written as  $\eta_e = -N_1/\dot{\epsilon}$ , where  $\dot{\epsilon}$  indicates the elongational flow rate. For moderate flow rates, the restoring force of the polymer is purely entropic and the elongational viscosity is strongly related to the amount of stretch of the polymer chains (Fig. 2). Due to the finite extensibility of chains, the elongational viscosity saturates at high elongation rates. The finite extensibility of the polymer

**Fig. 2** A typical schematic of shear (black) and elongational (blue) viscosities as a function of deformation rate of polymeric materials. A red line indicates an average polymer extension in the steady state as a function of the elongation flow rate



also makes it difficult to measure experimentally the elongational viscosity of a dilute polymer solution since the fluid easily breaks up under the large deformation. Figure 2 shows a typical dependence of the elongational viscosity of shear-thinning polymeric materials on the deformation rate. At low deformation rates, materials follow Newtonian behaviour with the relation  $\eta_e = 3\eta$  [9]. At high deformation rates, however, the Trouton ratio defined by the ratio between elongational and shear viscosities,  $\eta_e/\eta$ , raises to up to  $10^4$  for polymer solutions [47].

The concentration dependence of the elongational viscosity of polymer solution is stronger than of the shear viscosity. Even for dilute polymer solutions far below the overlap concentration, the elongational viscosity increases rapidly with increasing polymer concentration as the stretching amount is very sensitive to the elongation rate, while the shear viscosity is not [48]. The strongly concentration-dependent, non-Newtonian property made it an attractive candidate explanation for the slow droplet retraction caused by a tiny amount of polymer.

Bergeron et al. [3] proposed a relation between the reduction of the retraction velocity and the elongational viscosity of the fluid. They found that the retraction of a 100 ppm aqueous PEO droplet impacting on a hydrophobic spin-coated glass plate is five times slower than that of a pure water droplet, and consequently, the droplet does not rebound. The elongational viscosity was obtained using an opposing nozzle rheometer, and also by fitting the normal stress under shear with the finite extensible nonlinear elastic polymer (FENE-P) constitutive equation [9]. The authors claimed that the normal stress differences due to the elongated chains are the main channel for the additional energy dissipation during retraction. The capillary number typically governing the retraction velocity of Newtonian droplets also works for polymer solution droplets when it is re-written in terms of the elongational viscosity replacing shear viscosity,  $Ca = v_{ret}\eta_e/3\gamma$ .

A controversy about this work, however, debated the effect of the elongational viscosity being applied only to the retraction, but not to the spreading. In their publication, even for an impacting velocity high enough to make the liquid flow rate much faster than the polymer relaxation rate ( $We > 1$ ), the elongational viscous energy dissipation does not occur during the spreading, and the maximum spreading diameter does not change [6]. Furthermore, the calculated elongation is incorrect because the flow velocity is divided by the thickness of the droplet instead of the length of the droplet along the elongation direction, which is, by definition, a shear rate. The correct elongation rate would be an order of magnitude smaller than that reported, thus it is no longer constant with varying flow rate, and its accuracy is no longer reliable. The discrepancy of  $\eta_e$  of the same material in different publications from the same group also made it even more controversial [6, 34].

Recently, non-Newtonian liquid properties originating from polymer stretching were again studied in an experiment by Dhar et al. [18]. They impacted an aqueous solution droplet of polyacrylamid on a superhydrophobic surface, and observed the critical impact velocity above which the rebound is suppressed. It turned out to decrease with increasing polymer concentration. They argued that a deformation rate of the fluid faster than the rate of polymer relaxation, achieved by the high impact velocity, is necessary for the additional energy dissipation during retraction.

Although the fact that the additional energy dissipation by non-Newtonian behaviour of the droplet suppresses the droplet rebound aligns with the idea of Bergeron et al. [3], it would rather have to be interpreted as the behaviour of a non-Newtonian droplet whose shear viscosity is higher than that of a pure water droplet, because they used droplets of high polymer concentration and also the shear rate is used for the critical Weissenberg number.

While many simulations of the impact Newtonian droplets using molecular dynamics [23, 31], dissipative particle dynamics [56, 61], and numerical solutions of the Eulerian droplet model [14] have been published, very few studied dilute polymer solution droplets using field-based simulations of the FENE-Chilcott-Rallison (FENE-CR) model [28, 49]. This model can control non-Newtonian viscoelasticity of a droplet by an extra stress tensor, keeping the solvent viscosity constant. A study by Izbassarov et al. [28] found an enhanced rebound tendency of the viscoelastic droplet compared to a Newtonian one, when its equilibrium contact angle ranges from 50 to 120°. This result is opposed to many experimental findings of polymer-induced rebound suppression, which implies that elongational energy dissipation is not the source of rebound suppression. A later work by Tembely et al. [49] reproduced the rebound suppression of a viscoelastic droplet on a super-hydrophobic surface with an equilibrium contact angle of 154°. Unfortunately, molecular mechanisms or its physical origins are completely missing in this publication. Furthermore, the FENE-CR model showed that the behaviour during spreading, i.e. a maximum spreading factor defined by the maximum diameter divided by the initial droplet diameter, is also affected by viscoelastic properties, which is contrary to experimental observations.

The idea of the energy dissipation by non-Newtonian elongational viscosity receded from the mainstream, since several experiments provided evidence against it. Rozhkov et al. [40] performed an experiment of PEO solution droplets of various concentrations impacting on a small disk-like object whose diameter is comparable to the droplet's diameter. The purpose of impacting droplet on a very small object is to minimise the effect of surface wettability (liquid-surface interaction) on the droplet dynamics. They found that the maximum spreading factor and the retraction velocity do not depend on the PEO concentration, but that the shape of the spreading droplet does, which ruled out the possible role of the elongational viscosity as the source of energy dissipation during spreading and retraction. Another impact experiment of polymer solution droplets on a heated surface in which the liquid-surface interaction is negligible due to the vapor film above the surface (Leidenfrost phenomenon) also showed that polymer concentration does not alter the rebound tendency [4].

The fluid behaviour caused by polymer elongation was recently revisited in a different aspect by Chen et al. [15]. This work performed a droplet impact experiment of a dilute aqueous PEO solution on a superhydrophobic glass surface coated with cellulose stearoyl ester. They found a “beads-on-a-string” structure which is a thin liquid filament between the droplet and the substrate, when the droplet jumped from the surface. The filament can be thinner and longer before breaking up for higher polymer concentrations, and it applies an elastic elongation force against the rebound (Fig. 3a). Analysis of the droplet-height oscillation by fitting it with the equation for a damped harmonic oscillator (flatness factor,  $\xi$ ) shows a higher damp-

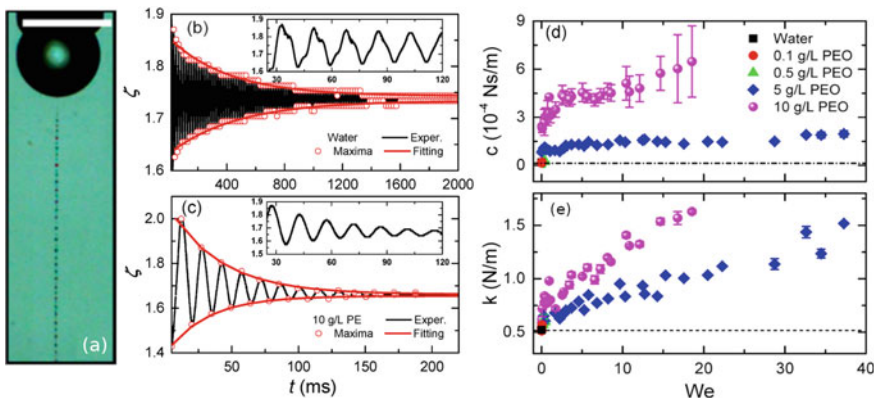


**Fig. 3** **a** Beads-on-a-spring structure in 5g/L PEO solution. Temporal evolution of the flatness factor  $\zeta$ , height divided by lateral radius, for **b** pure water and **c** 10g/L polymer solution droplets. **d** The damping coefficient and **e** the spring constant obtained by fitting data with the equation of a damped harmonic oscillator. Reprinted with permission from [15]. Copyright (2018) @ American Chemical Society

ing coefficient and a higher spring constant for higher polymer concentration (Fig. 3b–e). The formation of a thin neck in the course of the hopping was also observed in another experiment [18]. Although only macroscopic images were given without any molecular evidence, these works suggested a possible role of the elongation force of polymer not only during retraction, but also during the hopping stage after retraction.

### 1.3 Friction on Three Phase Contact Line

Most recently, the focus moved to more local effects of polymer additives, especially to their effect on the three-phase contact line (TPL). A study done by Bartolo et al. [2] showed an experiment of a polyacrylamid-solution droplet impacting on a hydrophobic parafilm surface. They stated that the additional energy dissipation by the normal stress at the TPL under the applied shear, which is known to increase quadratically with increasing shear rate, reduces the retraction velocity of the droplet. They also ruled out the possible roles of liquid-surface interaction and the polymer adsorption on the surface leading to the energy dissipation at the TPL. The established lubricant equation for thin films states that, for large dynamic contact angles, the retraction velocity is inversely proportional to the square root of the normal stress at the TPL. When the surface-adsorption effect is ignored as the authors intended, this statement is, however, contrary to the elastic effect of the elongation force from a molecular point of view. The net force due to the normal stress by elongation pulls the TPL in the same direction as the capillary force, which would have increased the retraction velocity. Furthermore, the typical shear rate of droplets of dilute polymer solution during retraction, calculated as the retraction speed divided by the height of the

droplet, is of the order of  $10^2 \text{ s}^{-1}$ . At this shear rate, the first normal stress difference of a bulk dilute polymer solution is negligible, as given by their experimental data. The polymer concentration in their experiments is above the overlap concentration. Therefore, influences other than the first normal stress, such as the shear viscosity and the surface tension cannot be simply ruled out as main contributors to the rebound suppression.

The most widely accepted explanation for the polymer-induced rebound suppression in recent years is the additional friction on the moving TPL. Using particle image velocimetry, Bertola et al. showed that the average velocities of all molecules inside droplets of rebounding water and non-rebounding polymer solution are quantitatively similar to each other even during retraction [42–44]. The main velocity difference is found locally at the TPL. The energy dissipation by the additional friction, which is quantified by the slip distance during the first contact angle oscillation, increases with polymer concentration. They also visualised stained  $\gamma$ -DNA added to a droplet which deposits behind the receding contact line (Fig. 4a). This finding directly indicates the change of surface properties by the polymer.

Their statement was also supported by the observation of dynamic contact angles [5–7, 45]. The apparent contact angle of the polymer solution droplet at the beginning of the retraction is much smaller than that of the water droplet, even though their behaviour during spreading is identical (Fig. 4b) [7]. The dynamic contact angle varying with the contact line velocity is interpreted either by viscous bending of the liquid-vapor interface in a mesoscopic region or by the kinetics of molecular adsorption/desorption to the surface [11]. Especially, the latter, often called Molecular Kinetic Theory (MKT) of dynamic wetting, explains contact angle dependence on the velocity of the TPL in terms of the surface wettability (an equilibrium contact angle). Therefore, the reduced contact angle during the retraction together with the decreasing retraction velocity can be interpreted by the additional friction by polymer on the TPL. It was also found that the concentration of polymer and the impact velocity affect the retraction as shown in Fig. 4c. The increasing polymer concentration leads to a decrease of the contact angle and in the TPL velocity, which is indicative of the increased friction on the TPL.

It is worth noting that the increasing impact velocity ( $We$ ) also decreases the contact angle and the TPL velocity, implying a large effective friction against the TPL movement. This result is consistent with the experiment by Dhar et al. [18] who interpreted the behaviour in a different way using the polymer relaxation time with respect to the shear rate. The same tendency was observed in another experiment for an impacting water droplet with PEO and nanoparticle additives [59]. This work argued that the impact velocity mainly affects the amount of polymer adsorption on the surface during spreading. For a high enough impact velocity, the droplet is highly deformed and then polymer accumulates on the substrate, which in turn, generates a strong friction at the liquid-solid interface. They showed, as an analogy to the decreasing contact angle during retraction, an increasing advancing contact angle upon impact on a tiled surface with the increasing impact velocity. However, again, no molecular evidence was provided in these works, which makes it difficult to find a concrete mechanism covering the impact dynamics of various types of material.

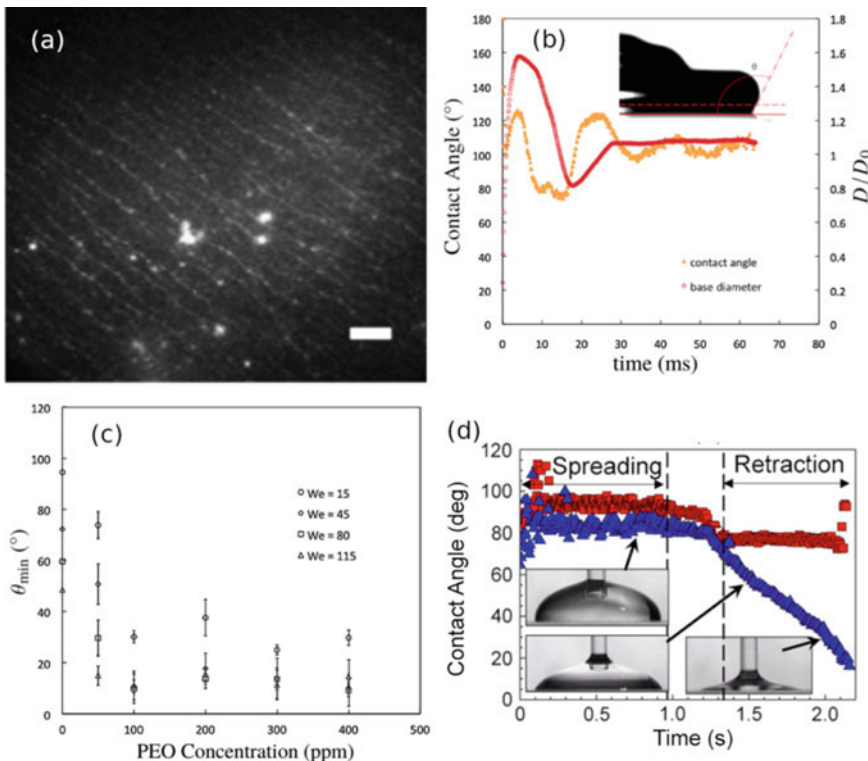


**Fig. 4** **a** Fluorescence microscope image of  $\gamma$ -DNA left behind on the surface after the droplet has retracted. Reprinted figure with permission from [43]. Copyright (2010) @ American Physical Society. **b** Apparent contact angle and the spreading factor of 50 ppm aqueous PEO solution impacting on the hydrophobic surface. Inset shows the definition of the apparent contact angle. **c** The minimum dynamic apparent contact angle for different polymer concentration and the different impact velocity. Reprinted figures from [7]. Copyright (2015) with permission from Elsevier. **d** Syringe-driven flow (square) water and (triangle) PEO solution droplets at flow rate  $485 \mu\text{L/s}^{-1}$ . Reprinted with permission from [45]. Copyright (2014) @ American Chemical Society

Another experiment obtained the dependency of the contact line velocity on the dynamic contact angle from a different experimental setup, so called forced dewetting [45]. This work measured the dynamic contact angle of a polymer solution droplet under the syringe-driven flow where the retraction velocity can be imposed by the rate of liquid suction (Fig. 4d). They found that the contact angle of the polymer solution droplet during the retraction is substantially smaller than that of a water droplet at the same retraction velocity. Furthermore, it continuously decreases as the TPL recedes with a constant velocity, which indicates an increasing frictional force in the course of retraction.

To establish the relation between the polymer concentration and the rebound tendency with the concept of the additional friction, a semimperical energy balance

equation was derived [27]. The equation shows the excess rebound energy in terms of the spreading factor, the equilibrium contact angle, and the capillary number. However, the capillary number used is written in terms of the shear viscosity of the polymer solution which, in the authors' intention, directly contributes to the additional energy dissipation at the TPL. Therefore, the behaviour of a dilute polymer solution, specifically the experimental observation of the polymeric effect only acting on the retraction not on the spreading, can not be explained by this model.

### 1.4 A Summary of the State of the Art

To sum up, the rebound suppression by a small amount of polymer additive has been explained broadly by different physical concepts: the dynamic surface tension depending on the adsorption kinetics, the elongation effect of the stretched polymer, and the additional friction on the three-phase contact line by polymer adsorption. The dynamic surface tension turned out to be inappropriate for the dilute polymer solution since it leads to a significantly reduced equilibrium surface tension, which is not found for dilute polymer solutions. The elongational viscosity was also debated, since the experiments with negligible surface-liquid interactions showed almost the same retraction behaviour irrespective of the presence of polymer in the droplet. However, a few works have focused on the different role of the elongation force as an elastic response, in which the liquid filament of the polymer solution actually pulls the droplet back when it tries to jump from the substrate. The concept most widely accepted in recent years is the additional friction on the TPL induced by polymer adsorbed on a surface. This idea was supported by the visible presence of a polymer deposit behind the receding contact line, and the substantial reduction of the receding contact angle for a polymer solution. Although the experimental findings clearly point out the increased friction on the TPL as the polymer contribution to the rebound suppression, a comprehensive understanding with a clear molecular picture is still incomplete, which raises the need of molecular simulation studies.

## 2 Elongation Force of Stretched Polymer during Hopping

Recently, we examined how the elastic force of elongated polymer reduces the rebound tendency using particle-based multi-body dissipative particle dynamics (MDPD) simulations [32]. This method allows mesoscale simulations with correct hydrodynamics using a soft-core interaction potential [21, 22, 25]. In particular, the density-dependent attractive force in MDPD makes it possible to sample phase coexistence for one-component systems, which is necessary for the droplet impact simulation [52]. Different adsorptivity of solvent and polymer beads to surface beads were suspected as a physical origin of the polymer effect as many experimental observations imply. The strength of the pairwise attractive force in MDPD is given by the

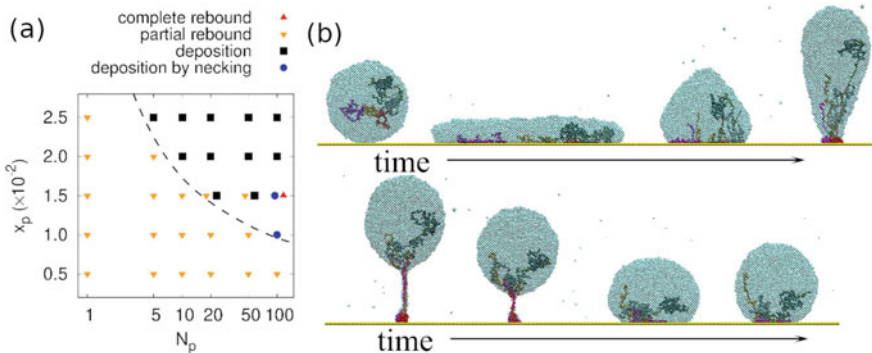


**Fig. 5** **a** The most probable outcomes are shown for different polymer molecular weight ( $N_p$ ) and concentration ( $x_p$ ). Two outcomes for a given  $N_p$  and  $x_p$  (for example, deposition and partial rebound for  $N_p = 20$ ,  $x_p = 0.015$ ) indicate that two outcomes are equally probable out of five independent trajectories. The black dashed line on the graph is a rough boundary between rebound and deposition. **b** Simulation snapshots of the outcome of deposition by polymer necking from side view. Solvent and substrate particles are coloured in cyan and yellow, respectively. Each polymer strand is depicted in different colour. Reprinted with permission from [32]. Copyright (2021) @ American Chemical Society

amplitude of a function which decays linearly with the distance between two beads, i.e.  $F = A(1 - r/r_c)$ , where  $A$ ,  $r$ , and  $r_c$  refer to the amplitude, the distance between two beads, and the cutoff distance beyond which the force is zero, respectively. A similar but shorter-ranged term accounts for pairwise repulsion. The repulsive potential parameters for all pairs are identical. We varied  $A$  between different bead types to model the different adsorptivity. Our choice of  $A$  for different pairs mimics a good solvent condition of the polymer solution, a solvophobic and polymerphilic surface with equilibrium contact angles of  $155^\circ$  for a pure solvent droplet, and of  $83^\circ$  for a pure polymer droplet. We investigated polymer-solution droplets for different polymer molecular weights and concentrations, where the concentration is always far below the overlap concentration. The zero-shear viscosity and the equilibrium liquid-vapor surface tension of the fluids were calculated separately. They turned out to be almost identical irrespective of the polymer content in this regime, where the Reynolds and the Weber numbers are  $Re = 35\text{--}42$  and  $We = 78\text{--}81$ .

The droplets (total number of particles =  $4 \times 10^4$ ) were shot towards the surface with a velocity  $v_{imp} = 2$  (in DPD reduced unit). We observed four characteristic outcomes of rebound, complete rebound (R), partial rebound (P), deposition (D) and deposition by necking (N), at different polymer composition (Fig. 5a). A higher polymer concentration and a larger molecular weight tend to suppress the rebound. Especially close to the boundary between rebound and deposition, a thin liquid filament, mainly composed of polymer chains, is observed which is in agreement with experimental images by high speed cameras [15, 18, 27]. On the molecular level, as the polymer preferably adsorbs on the surface, one of its ends is pinned on the surface and the other end is immersed in the droplet jumping from the surface.

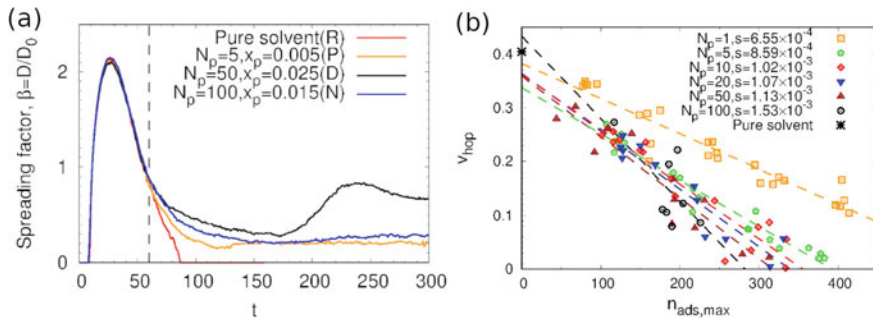


**Fig. 6** **a** Spreading factor as a function of time for droplets of different outcomes: complete rebound (R), partial rebound (P), deposition (D) and deposition by necking (N). The vertical dashed line indicates the beginning of a hopping stage. **b** Hopping velocity versus the maximum value of the number of adsorbed polymer beads for different  $N_p$  and  $x_p$ . Each  $v_{hop}$  is obtained from each trajectory in which the droplet rebounds. Fitted linear functions for each  $N_p$  ( $v_{hop} = -sn_{ads,max} + c$ ) are represented by dashed lines, where the fitted  $s$  are given in the legend. Reprinted with permission from [32]. Copyright (2021) @ American Chemical Society

Owing to the elastic elongation force of the stretched polymer originating from the tendency to recover its coiled structure, the polymer pulls the droplet back to the surface, leading to droplet deposition. A similar morphology of the liquid filament for viscoelastic polymer solutions has been observed not only in droplet impact experiments [15, 18, 27] but also in different experimental systems [19, 41, 46, 51] such as a droplet pinch-off in a T-shaped microfluidic junction [41]. In particular, the highly stretched polymer conformation within the “neck” is confirmed by a fluorescence image, which is a clear indication of the polymer contribution to the elasticity of the fluid.

The time evolution of the spreading factor in Fig. 6a shows that the maximum spreading factor does not depend on droplet properties as expected from similar Re and We numbers. Interestingly, all simulated droplets show almost identical retraction velocities, calculated by the slope of the spreading factor *versus* time during the retraction. This is contrary to many experimental observations in which the rebound suppression is attributed to a reduced retraction velocity. Our simulation rather showed that the polymer adsorption is more relevant for rebound suppression. The maximum number of adsorbed polymer beads during the whole impact,  $n_{ads,max}$ , is strongly (almost linearly) correlated with the hopping (rebound) velocity (Fig. 6b). A droplet of higher polymer concentration and larger molecular weight shows more polymer adsorption, which eventually leads to rebound suppression. The concentration effect on the polymer adsorption is obvious as more chains in the filament apply a stronger elastic force to the droplet. The observation that longer polymers suppress the rebound more effectively for droplets at the same  $n_{ads,max}$  can be understood by the fact that a longer polymer can exert the restoring force for longer time as the filament can be stretched longer [19].

This simulation work provided a clear picture of the so-called, slow hopping mechanism, induced by the elastic effect of the elongated polymer whose one end is pinned on the surface. However, the identical retraction velocity for different droplets observed in this work does not mean that slow hopping is the only mechanism responsible for the rebound suppression. Other scenarios like the slow retraction may prevail under different choice of simulation parameters (see the next section). This work rather states that the elongation force of polymer and the polymer-containing thin filament can be one reason of the rebound suppression by polymer additives.

### 3 Increasing the Contact Line Friction by Adsorbed Polymer

#### 3.1 Slow Retraction and Adsorbed Polymer

Our recent study using MDPD simulations of impacting droplet reproduced a second mechanism coexisting with the slow hopping, the so-called slow retraction mechanism [33]. It is a function of the polymer-solvent attraction strength,  $|A_{P/W}|$  (Fig. 7). In Fig. 7a, the retraction velocity initially decreases substantially ( $|A_{P/W}| < 90$ ), leading to rebound suppression (blue squares) as  $|A_{P/W}|$  increases. However, if  $|A_{P/W}|$  increases further beyond 90, the retraction velocity again increases due to complete deposition of the polymer behind the receding contact line. Moreover, the slow retraction velocity of  $|A_{P/W}| > 150$  is similar to that at  $|A_{P/W}| = 50$ . Thus, on its own, it can not suppress the droplet rebound without elongation force during the hopping stage. This indicates the coexistence of two mechanisms, the slow-hopping and the slow-retraction mechanisms.

We found that the retraction velocity is correlated, again, with the number of adsorbed polymer beads on the surface. As more polymer beads adsorb, the retraction is slowed down (Fig. 7b). The influence of the molecular weight on the retraction velocity is not as strong as on the hopping resistance (Fig. 6b). A noticeable difference in this work, which uses larger droplets (total number of particles =  $10^5$ ) than the former study [32], is that the retraction velocity at  $|A_{P/W}| = 30$  is also reduced despite the same simulation parameters except for the droplet size. This is attributed to the small surface-to-volume ratio of the large droplet in which the larger fraction of the solid-liquid interface is covered by polymer at the same bulk concentration.

The contribution of the adsorbed polymer to the slow retraction velocity is also confirmed by droplet impact simulations at different impact velocities. We found that the critical polymer concentration necessary to suppress the rebound decreases with increasing impact velocity, which is in agreement with experiments [18, 59]. The authors of the experiments stated that the shear rate being faster than the polymer relaxation is a key factor of the rebound suppression. However, our simulation provided a molecular picture completely different from this interpretation: the amount of adsorbed polymer determined by the impact velocity is a key of the slow retraction

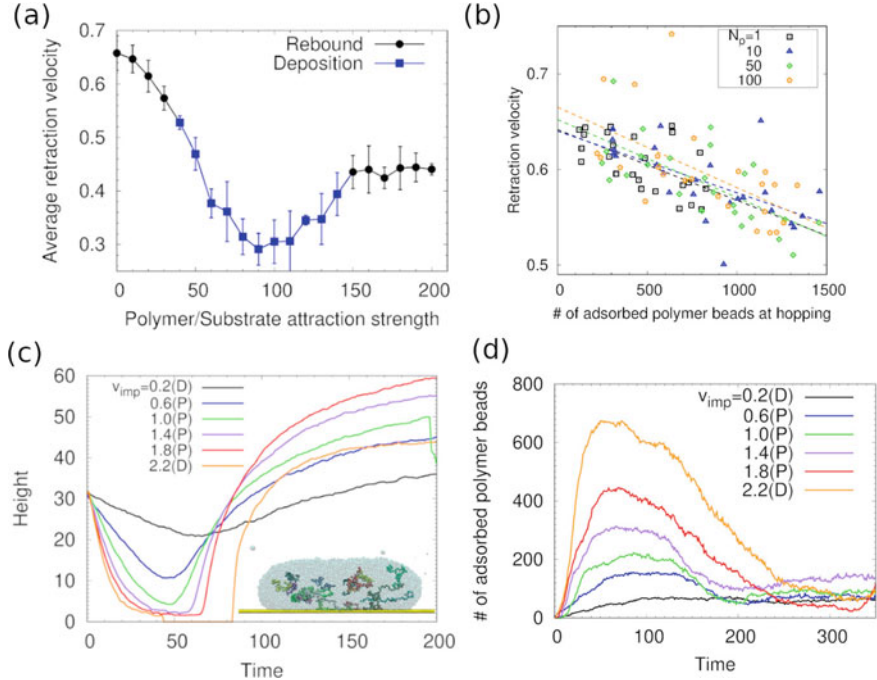


**Fig. 7** **a** The average retraction velocity of impacting droplets at different polymer-surface attraction strength,  $|A_{P/W}|$ . Black and blue points indicate rebounding and depositing droplets, respectively. **b** Retraction velocity of individual trajectory as a function of the number of adsorbed polymer beads at the beginning of the hopping stage. Dashed lines indicate the linear fitting of  $v_{ret}$  with  $n_{ads,hop}$ . Difference symbols represent different molecular weight. **c** Height and **d** the number of adsorbed polymer beads as a function of time for different impact velocities. Simulations snapshot of droplets at maximum spreading for  $v_{imp} = 0.6$  is given in the inset of (c)

(inset of Fig. 7c). We found that a smaller height of the laterally expanded droplet enables more polymer adsorption since the diffusion path from solution to surface is shorter (Fig. 7c and d). Such impact velocity-dependent rebound suppression was also shown in recent molecular dynamics simulation study [55]. Therefore, a droplet of low polymer concentration needs high impact velocity and strong droplet deformation into the thin pancake-like morphology in order to transfer a large amount of polymer to the surface.

### 3.2 Dynamic Contact Angle during Retraction

According to the Molecular Kinetic Theory (MKT) of dynamic wetting, the friction on the moving contact line determines the relation between its velocity and the dynamic contact angle [8, 10]. In this theory, the velocity of the moving contact line,

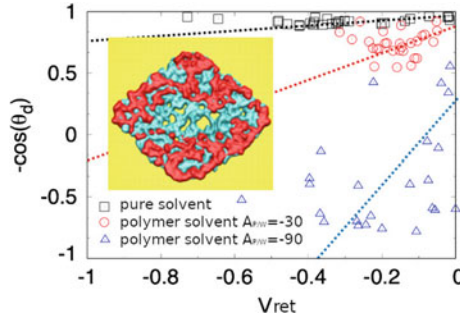


**Fig. 8** A scatter plot of the  $-\cos \theta_d$  as a function of  $v_{\text{ret}}$  for a pure solvent droplet, a polymer solution droplet with  $A_{\text{P/W}} = -30$ , and a polymer solution droplet with  $A_{\text{P/W}} = -90$ . Dashed lines represent fitted functions with line. Inset shows a simulation snapshot of the liquid particles on the first layer from the surface for 2500 ppm polymer solutions in the middle of the retraction stage

$v_{\text{cl}}$ , is calculated from the frequency of a random molecular displacement to the next nearest adsorption site,  $\kappa_0$ , thus it is given by

$$v_{\text{cl}} = 2\kappa_0 \lambda \sinh \left( \frac{\gamma(\cos \theta_0 - \cos \theta_d)}{2nkT} \right), \quad (1)$$

where  $\gamma$ ,  $\lambda$ ,  $\theta_0$ ,  $\theta_d$ , and  $n$  refer to the liquid-vapor surface tension, the distance between the adsorption sites, the equilibrium contact angle, the dynamic contact angle and the number of adsorption sites per unit area, respectively.  $k$  is the Boltzmann constant and  $T$  is the temperature. When the system is close to equilibrium or to the steady state, so as  $v_{\text{cl}}$  is close to zero, Eq. (1) reduces to

$$v_{\text{cl}} = \frac{\kappa_0 \lambda}{nkT} \gamma (\cos \theta_0 - \cos \theta_d). \quad (2)$$

On the right hand side of Eq. (2),  $\left( \frac{\kappa_0 \lambda}{nkT} \right)^{-1}$  is often defined as  $\zeta_{\text{cl}}$ , the coefficient of effective friction on the contact line. When the friction is strong (large  $\zeta_{\text{cl}}$ ),  $\cos \theta_d$  depends strongly on  $v_{\text{cl}}$ .

The additional friction by adsorbed polymer during retraction is, therefore, quantified by the relation between the dynamic contact angle ( $\theta_d$ ) and the retraction velocity ( $v_{\text{ret}} = v_{\text{cl}}$ ). Figure 8 shows a scatter plot of  $-\cos \theta_d$  as a function of  $v_{\text{ret}}$  for a pure solvent droplet (black squares), a polymer solution droplet with moderate polymer-surface attraction strength ( $A_{\text{P/W}} = -30$ , red circles), and a polymer solution droplet with strong polymer-surface attraction strength ( $A_{\text{P/W}} = -90$ , blue triangles). If we fit the data approximately with a line, the slope of the line increases as  $|A_{\text{P/W}}|$  increases. For the pure solvent droplet, the slope is small which means that  $\kappa_0$  is large and the friction,  $\zeta_{\text{cl}}$ , is small. Larger slopes are found for stronger polymer-surface attractions, which implies a larger effective friction on the contact

line. A simulation snapshot in the inset of Fig. 8 shows that the adsorbed polymer becomes more concentrated near the contact line as the contact line recedes during retraction. This is attributed to the slower surface diffusivity of polymers compared to solvent molecules. Therefore, even a tiny amount of polymer accumulates near the contact line during retraction, which leads to the substantial reduction of the retraction velocity.

## 4 Conclusions

We reviewed the state-of-the-art of the possible physical origins of the rebound suppression of an impacting droplet from a solvophobic surface by a small amount of polymer additive. We discussed several physical concepts, such as the dynamic surface tension, the additional energy dissipation by non-Newtonian elongational viscosity, the elastic force of the stretched polymer and the additional friction on the receding contact line. The explanation based on the dynamic surface tension and the elongational energy dissipation have become less persuasive, since contradictory evidence was reported. The additional friction on the contact line during retraction became more popular, but still lacked a comprehensive understanding. Our MDPD simulations traced the rebound suppression to both the slowing of droplet hopping by the restoring force of stretched polymer, and to the slowing of the droplet retraction by an additional friction on the contact line provided by the polymer adsorbed on the surface. Both mechanisms coexist over a wide range of simulation parameters, but the slow-retraction mechanism is prevailing for large droplets and for strong attraction between polymer and surface. Increasing the polymer adsorption by changing its polymer concentration, its molecular weight, or its interactions with the surface, stimulates both mechanisms; thus, the rebound is suppressed. Evidence of the additional friction on the receding contact line is inferred from the relation between the dynamic contact angle and the contact line velocity, as the slope of the fitted line is proportional to the friction.

The molecular mechanism can be roughly summarised: After impact, the droplet expands sideways. During this spreading phase, the flow is unhindered by the polymer, since its concentration is low enough to leave both the fluid viscosity and its surface tension unchanged. At the same time, however, polymer equilibrates between solvation and surface adsorption. This equilibration is aided by a shorter diffusion path, i.e. a flatter, more spread-out droplet, which in turn is brought about by a higher impact velocity. The adsorbed polymer, however, strongly influences the second phase, retraction. When the fluid is driven by its surface tension to retract, the polymer is unable to follow quickly enough due to its slow mobility on the surface. It remains partially attracted to the surface. Its other parts are dissolved in the solvent, which is as we recall, a good solvent. In its effort to stay solvated, it exerts a thermodynamic force, akin to an osmotic pressure, on the solvent molecules. Since, due to its slowness, the polymer is enriched near the contact line, the force counteracts the retraction of the contact line. This contact-line friction makes some of the kinetic

energy of the droplet dissipate. In phase three, hopping, the remaining kinetic energy is converted. Hopping is opposed by polymer chains that are attached to the surface with one end and dissolved in the solvent with the other. The chains stretch, as the droplet is trying to detach, and at a large enough concentration, they prevent hopping.

Our simulation studies clearly confirmed the qualitative origin of the polymer-induced anti-rebound on the molecular level. A quantitative understanding of the rebound tendency as a function of polymer composition is still poor since droplet impact is an extremely non-equilibrium process and not even close to the steady state. We expect that the physics of the moving contact line upon droplet impact can be quantitatively analysed by simulations of a capillary bridge under steady shear [12, 39] which give the velocity-angle relation of the contact line with better statistics. The effect of elastic elongation force of stretched polymer can also be studied by dynamics of polymer solution droplets, e.g., the droplet impact on wired surface [46], and a droplet detachment simulation from polymer-tethered surfaces.

**Acknowledgements** The authors acknowledge the financial support by the Deutsche Forschungsgemeinschaft (DFG) within the SFB-TRR 75, project number 84292822, of which this work was a major part in funding period 3. Calculations for this research were conducted on the Lichtenberg high performance computer of the TU Darmstadt and the GCS Supercomputer JUWELS at Jülich Supercomputing Centre (JSC).

## References

1. Attané P, Girard F, Morin V (2007) An energy balance approach of the dynamics of drop impact on a solid surface. *Phys Fluids* 19(1):012101
2. Bartolo D, Josserand C, Bonn D (2006) Singular jets and bubbles in drop impact. *Phys Rev Lett* 96(12):124501
3. Bergeron V, Bonn D, Martin JY, Vovelle L (2000) Controlling droplet deposition with polymer additives. *Nature* 405(6788):772–775
4. Bertola V (2009) An experimental study of bouncing leidenfrost drops: comparison between newtonian and viscoelastic liquids. *Int J Heat Mass Transf* 52(7–8):1786–1793
5. Bertola V (2010) Effect of polymer additives on the apparent dynamic contact angle of impacting drops. *Colloids Surf, A* 363(1–3):135–140
6. Bertola V (2013) Dynamic wetting of dilute polymer solutions: the case of impacting droplets. *Adv Colloid Interface Sci* 193–194:1–11
7. Bertola V, Wang M (2015) Dynamic contact angle of dilute polymer solution drops impacting on a hydrophobic surface. *Colloids Surf A Physicochem Eng Asp* 481:600–608
8. Bertrand E, Blake TD, De Coninck J (2009) Influence of solid–liquid interactions on dynamic wetting: a molecular dynamics study. *J Phys: Condens Matter* 21(46):464124
9. Bird RB, Armstrong RC, Hassager O (1987) Dynamics of polymeric liquids, vol 1. Fluid mechanics
10. Blake T, Haynes J (1969) Kinetics of liquidliquid displacement. *J Colloid Interface Sci* 30(3):421–423
11. Blake TD (2006) The physics of moving wetting lines. *J Colloid Interface Sci* 299(1):1–13
12. Blake TD, Fernandez-Toledano JC, Doyen G, De Coninck J (2015) Forced wetting and hydrodynamic assist. *Phys Fluids* 27(11):112101
13. Bonn D, Eggers J, Indekeu J, Meunier J, Rolley E (2009) Wetting and spreading. *Rev Mod Phys* 81(2):739

14. Bourgault Y, Habashi WG, Dompierre J, Baruzzi GS (1999) A finite element method study of Eulerian droplets impingement models. *Int J Numer Methods Fluids* 29(4):429–449
15. Chen L, Wang Y, Peng X, Zhu Q, Zhang K (2018) Impact dynamics of aqueous polymer droplets on superhydrophobic surfaces. *Macromolecules* 51(19):7817–7827
16. Crooks R, Cooper-White J, Boger DV (2001) The role of dynamic surface tension and elasticity on the dynamics of drop impact. *Chem Eng Sci* 56(19):5575–5592
17. De Gennes PG (1985) Wetting: statics and dynamics. *Rev Mod Phys* 57(3):827
18. Dhar P, Mishra SR, Samanta D (2019) Onset of rebound suppression in non-newtonian droplets post-impact on superhydrophobic surfaces. *Phys Rev Fluid* 4(10):103303
19. Dinic J, Sharma V (2019) Macromolecular relaxation, strain, and extensibility determine elastocapillary thinning and extensional viscosity of polymer solutions. *Proc Natl Acad Sci* 116(18):8766–8774
20. Dussan E (1979) On the spreading of liquids on solid surfaces: static and dynamic contact lines. *Annu Rev Fluid Mech* 11(1):371–400
21. Español P, Warren P (1995) Statistical mechanics of dissipative particle dynamics. *EPL* 30(4):191–196
22. Español P, Warren PB (2017) Perspective: dissipative particle dynamics. *J Chem Phys* 146(15):150901
23. Gentner F, Rioboo R, Baland J, De Coninck J (2004) Low inertia impact dynamics for nanodrops. *Langmuir* 20(11):4748–4755
24. Glass J (1968) Adsorption characteristics of water-soluble polymers. ii. poly (ethylene oxide) at the aqueous-air interface. *J Phys Chem* 72(13):4459–4467
25. Groot RD, Warren PB (1997) Dissipative particle dynamics: bridging the gap between atomistic and mesoscopic simulation. *J Chem Phys* 107(11):4423–4435
26. Hao C, Zhou Y, Zhou X, Che L, Chu B, Wang Z (2016) Dynamic control of droplet jumping by tailoring nanoparticle concentrations. *Appl Phys Lett* 109(2):021601
27. Huh HK, Jung S, Seo KW, Lee SJ (2015) Role of polymer concentration and molecular weight on the rebounding behaviors of polymer solution droplet impacting on hydrophobic surfaces. *Microfluid Nanofluidics* 18(5–6):1221–1232
28. Izbassarov D, Muradoglu M (2016) Effects of viscoelasticity on drop impact and spreading on a solid surface. *Phys Rev Fluids* 1(2):023302
29. Josserand C, Thoroddsen ST (2016) Drop impact on a solid surface. *Annu Rev Fluid Mech* 48:365–391
30. Jowkar S, Morad M (2019) Rebounding suppression of droplet impact on hot surfaces: effect of surface temperature and concaveness. *Soft Matter* 15(5):1017–1026
31. Koishi T, Yasuoka K, Zeng XC (2017) Molecular dynamics simulation of water nanodroplet bounce back from flat and nanopillared surface. *Langmuir* 33(39):10184–10192
32. Lee E, Chilukoti HK, Müller-Plathe F (2021) Rebound suppression of a droplet impacting on a supersolvophobic surface by a small amount of polymer additives. *ACS Macro Lett* 10:192–196
33. Lee E, Chilukoti HK, Müller-Plathe F (2021) Suppressing the rebound of impacting droplets from solvophobic surfaces by polymer additives: polymer adsorption and molecular mechanisms. *Soft Matter* 17:6952–6963
34. Lindner A, Vermant J, Bonn D (2003) How to obtain the elongational viscosity of dilute polymer solutions? *Phys A* 319:125–133
35. Mao T, Kuhn DC, Tran H (1997) Spread and rebound of liquid droplets upon impact on flat surfaces. *AIChE J* 43(9):2169–2179
36. Monteux C, Elmaaleem Y, Narita T, Lequeux F (2008) Advancing-drying droplets of polymer solutions: local increase of the viscosity at the contact line. *EPL* 83(3):34005
37. Mourougou-Candoni N, Prunet-Foch B, Legay F, Vignes-Adler M, Wong K (1997) Influence of dynamic surface tension on the spreading of surfactant solution droplets impacting onto a low-surface-energy solid substrate. *J Colloid Interface Sci* 192(1):129–141
38. Pasandideh-Fard M, Qiao YM, Chandra S, Mostaghimi J (1996) Capillary effects during droplet impact on a solid surface. *Phys Fluids* 8(3):650–659

39. Priezjev NV, Troian SM (2004) Molecular origin and dynamic behavior of slip in sheared polymer films. *Phys Rev Lett* 92(1):018302
40. Rozhkov A, Prunet-Foch B, Vignes-Adler M (2003) Impact of drops of polymer solutions on small targets. *Phys Fluids* 15(7):2006–2019
41. Sachdev S, Muralidharan A, Boukany PE (2016) Molecular processes leading to “necking” in extensional flow of polymer solutions: using microfluidics and single DNA imaging. *Macromolecules* 49(24):9578–9585
42. Smith M, Bertola V (2010) The anti-rebound effect of flexible polymers on impacting drops. In: Proceedings of 23rd annual conference liquid atomization spray systems Europe (ILASS-Europe), vol 124
43. Smith M, Bertola V (2010) Effect of polymer additives on the wetting of impacting droplets. *Phys Rev Lett* 104(15):154502
44. Smith M, Bertola V (2011) Particle velocimetry inside newtonian and non-newtonian droplets impacting a hydrophobic surface. *Exp Fluids* 50(5):1385–1391
45. Smith M, Sharp J (2014) Origin of contact line forces during the retraction of dilute polymer solution drops. *Langmuir* 30(19):5455–5459
46. Song M, Hu D, Zheng X, Wang L, Yu Z, An W, Na R, Li C, Li N, Lu Z (2019) Enhancing droplet deposition on wired and curved superhydrophobic leaves. *ACS Nano* 13(7):7966–7974
47. Sridhar T, Tirtaatmadja V, Nguyen D, Gupta R (1991) Measurement of extensional viscosity of polymer solutions. *J Non-Newton Fluid* 40(3):271–280
48. Stoltz C, de Pablo JJ, Graham MD (2006) Concentration dependence of shear and extensional rheology of polymer solutions: brownian dynamics simulations. *J Rheol* 50(2):137–167
49. Tembely M, Vadillo D, Soucemarianadin A, Dolatabadi A (2019) Numerical simulations of polymer solution droplet impact on surfaces of different wettabilities. *Processes* 7(11):798
50. Ukiwe C, Kwok DY (2005) On the maximum spreading diameter of impacting droplets on well-prepared solid surfaces. *Langmuir* 21(2):666–673
51. Wagner C, Amarouchene Y, Bonn D, Eggers J (2005) Droplet detachment and satellite bead formation in viscoelastic fluids. *Phys Rev Lett* 95(16):164504
52. Warren PB (2003) Vapor-liquid coexistence in many-body dissipative particle dynamics. *Phys Rev E* 68(6):066702
53. Werder T, Walther JH, Jaffe R, Halicioglu T, Koumoutsakos P (2003) On the water- carbon interaction for use in molecular dynamics simulations of graphite and carbon nanotubes. *J Phys Chem B* 107(6):1345–1352
54. Wirth W, Storp S, Jacobsen W (1991) Mechanisms controlling leaf retention of agricultural spray solutions. *Pestic Sci* 33(4):411–420
55. Yan HJ, Wan ZH, Qin FH, Sun DJ (2021) Origin of rebound suppression for dilute polymer solution droplets on superhydrophobic substrate. *Langmuir* 37(24):7565–7572
56. Yi G, Cai Z, Gao Z, Jiang Z, Huang X, Derksen JJ (2020) Droplet impingement and wetting behavior on a chemically heterogeneous surface in the beyond-cassie-baxter regime. *AIChE J* 66(8):e16263
57. Yokoi K, Vadillo D, Hinch J, Hutchings I (2009) Numerical studies of the influence of the dynamic contact angle on a droplet impacting on a dry surface. *Phys Fluids* 21(7):072102
58. Yun S, Hong J, Kang KH (2013) Suppressing drop rebound by electrically driven shape distortion. *Phys Rev E* 87(3):033010
59. Zang D, Wang X, Geng X, Zhang Y, Chen Y (2013) Impact dynamics of droplets with silica nanoparticles and polymer additives. *Soft Matter* 9(2):394–400
60. Zhang J, Leroy F, Müller-Plathe F (2014) Influence of contact-line curvature on the evaporation of nanodroplets from solid substrates. *Phys Rev Lett* 113(4):046101
61. Zhao J, Chen S, Liu Y (2017) Dynamical behaviors of droplet impingement and spreading on chemically heterogeneous surfaces. *Appl Surf Sci* 400:515–523
62. Zheng L, Cao C, Cao L, Chen Z, Huang Q, Song B (2018) Bounce behavior and regulation of pesticide solution droplets on rice leaf surfaces. *J Agric Food Chem* 66(44):11560–11568

**Open Access** This chapter is licensed under the terms of the Creative Commons Attribution 4.0 International License (<http://creativecommons.org/licenses/by/4.0/>), which permits use, sharing, adaptation, distribution and reproduction in any medium or format, as long as you give appropriate credit to the original author(s) and the source, provide a link to the Creative Commons license and indicate if changes were made.

The images or other third party material in this chapter are included in the chapter's Creative Commons license, unless indicated otherwise in a credit line to the material. If material is not included in the chapter's Creative Commons license and your intended use is not permitted by statutory regulation or exceeds the permitted use, you will need to obtain permission directly from the copyright holder.



# Modelling of Droplet Dynamics in Strong Electric Fields



Erion Gjonaj, Yun Ouedraogo, and Sebastian Schöps

**Abstract** We describe a modelling approach for the simulation of droplet dynamics in strong electric fields. The model accounts for electroquasistatic fields, convective and conductive currents, contact angle dynamics and charging effects associated with droplet breakup processes. Two classes of applications are considered. The first refers to the problem of water droplet oscillations on the surface of outdoor high-voltage insulators. The contact angle characteristics resulting from this analysis provides a measure for the estimation of the electric field inception thresholds for electrical discharges on the surface. The second class of applications consists in the numerical characterization of electrosprays. Detailed simulations confirm the scaling law for the first electrospray ejection and, furthermore, provide insight on the charge-radius characteristics for transient as well as steady state electrosprays.

## 1 Introduction

Applying electric fields to manipulate droplets, jets and sprays is an established technique used in various applications, including the development of microfluidic chips [1] and novel display technologies [2]. In more conventional fields such as electrostatic atomization, electric fields enable the generation of well-dispersed spray plumes with enhanced controllability of droplet size and spray angle as required, e.g., in industrial painting, electrowetting, ink-jet printing and coating applications.

Due to the vast range of applications, the electrohydrodynamic (EHD) modelling of droplet flows remains an important research subject. The interest in the topic is twofold. First, one is interested in the characterization of these flows for the purpose of design and optimization of specific technological processes. This includes,

---

E. Gjonaj (✉) · Y. Ouedraogo

Electromagnetic Field Theory Group (EMFT), TU Darmstadt, Darmstadt, Germany

e-mail: [erion.gjonaj@tu-darmstadt.de](mailto:erion.gjonaj@tu-darmstadt.de)

S. Schöps

Graduate School of Excellence Computational Engineering (CE), TU Darmstadt, Darmstadt, Germany

for example, the ability to control droplet positioning by electric fields generated by complex electrode arrangements in microfluidic devices or the optimization of electrospray properties for ink-jet applications. Second, the investigations aim at a better understanding of EHD phenomena. Analytical models are often not suitable for the description of practical problems, even for simplistic geometries and electric field configurations. A more appropriate means for investigating such problems is numerical simulation. However, also the numerical approach faces major difficulties. Despite the huge computational burden, numerical simulations often fail to capture all of the involved events due to neglecting or oversimplifying the underlying physics. This is the case, in particular, for droplet problems involving an interface between different fluid phases and fluid-solid phases. At such interfaces, the fluid and charge dynamics are determined by microscopic processes that on their turn strongly influence the behaviour of the macroscopic system [20].

Various EHD simulation models have been presented (cf. [29, 30]). An electro-quasistatic (EQS) model using a sharp interface approach for the simulation of droplet oscillations in electric fields was described by Songoro et al. [28]. Recently, more sophisticated models based on the diffuse-interface description have been introduced, taking into account charge relaxation effects by explicitly solving the charge conservation equation [16, 24]. Most of these works, however, focus on the electrokinetics of charged species in electrolytic solvents rather than on capillary droplet dynamics. Furthermore, contact line effects at solid interfaces are typically not considered. In the following, a EHD modelling approach including these effects is described. The model is, furthermore, applied in the analysis of droplet induced partial discharges on the surface of outdoor high-voltage (HV) insulators as well as in the investigation of transient and steady state electrospray atomization processes.

## 2 The Electrohydrodynamic Model

The electric fields involved in most EHD applications are considered to be slowly varying, therefore, a quasistatic approximation for the Maxwell's equations is sufficient. In the following, thermal diffusion, charge production in the bulk and interfacial charge layers are neglected. These assumptions are reasonable for typical applications with conductive droplets where the electrostatic screening length is much smaller than the characteristic size of the system [22]. Furthermore, the effect of Faradaic currents induced by electrochemical reactions on electrode surfaces is not taken into account. Under these assumptions, the EHD problem is well described by the Taylor-Melcher leaky dielectric model [18] that is summarized below.

## 2.1 Governing Equations

The fluid flow problem consists in the dynamics of an incompressible liquid (droplet) emerged in a gaseous phase (air), eventually interfacing a solid body (dielectric substrate or capillary). The Navier-Stokes equations read,

$$\frac{\partial \rho \mathbf{u}}{\partial t} + \nabla \cdot \rho \mathbf{u} \mathbf{u} = -\nabla p + \nabla \cdot (\mu [\nabla \mathbf{u} + \nabla \mathbf{u}^T]) + \rho \mathbf{g} + \mathbf{f}_s + \mathbf{f}_e, \quad (1)$$

$$\nabla \cdot \mathbf{u} = 0, \quad (2)$$

where  $\mathbf{u}$  denotes fluid velocity,  $\rho$  density,  $\mu$  dynamic viscosity and  $p$  pressure. The driving terms  $\mathbf{f}_s$  and  $\mathbf{f}_e$  are the surface tension force density and the electric force density, respectively. The former is derived from the surface force density given by the Young-Laplace equation,  $\hat{\mathbf{f}}_s = 2\gamma H \mathbf{n}$ , where  $\gamma$  is the surface tension,  $H$  is the mean curvature and  $\mathbf{n}$  the interface normal.

The total electric current in the liquid phase consists of a convective and a conductive contribution as,  $\mathbf{J} = \rho_e \mathbf{u} + \kappa \mathbf{E}$ , where  $\kappa$  is the Ohmic conductivity,  $\mathbf{E}$  the electric field strength and  $\rho_e$  the charge density associated with the free charge carriers in the liquid. The latter is related to electric field by Gauß's law,  $\rho_e = \nabla \cdot \varepsilon \mathbf{E}$ , where  $\varepsilon$  is the dielectric permittivity of the medium. Introducing an electric potential,  $\mathbf{E} = -\nabla \varphi$ , the charge conservation law in the flowing medium reads

$$\nabla \cdot \varepsilon \nabla \varphi = -\rho_e, \quad (3)$$

$$\frac{\partial \rho_e}{\partial t} + \nabla \cdot (\rho_e \mathbf{u}) = \nabla \cdot \kappa \nabla \varphi. \quad (4)$$

Note that the charge density can actually be eliminated from the system of equations. However, this results in a third order equation for the electric potential; a form which is less suitable for numerical calculations. In conductive solids ( $\mathbf{u} = \mathbf{0}$ ), the system of Eqs. (3)–(4) reduces to the conventional EQS formulation for low frequency fields in resting media. In nonconducting dielectrics ( $\mathbf{u} = \mathbf{0}, \kappa = 0$ ), the equations reduce to Laplace's equation for the electrostatic potential. Thus, the electric field problem is well posed in the fluid as well as in the solid phases provided that appropriate boundary and initial conditions are specified for the electric potential and charge density, respectively.

Finally, given the electric field distribution, the electric force density applied on the fluid can be obtained from the Maxwell stress tensor [18] as

$$\mathbf{f}_e = \nabla \cdot \left( \varepsilon \mathbf{E} \otimes \mathbf{E} - \frac{1}{2} \varepsilon E^2 \mathbf{I} \right), \quad (5)$$

where  $\mathbf{I}$  represents the third-order unit tensor.

## 2.2 Contact Line Model

Droplet dynamics is closely related to the properties of the three-phase contact line between the liquid droplet, surrounding air and a solid body. Along this line, the surface tension force is ill-defined. Therefore, the flow properties at the contact line must be imposed by a boundary condition that is typically obtained from experiments. A common boundary condition consists in prescribing the apparent contact angle,  $\theta$ , between the droplet surface and solid wall [8]. In static equilibrium, the contact angle attains a range of admissible values,  $\theta_{\text{rec}} < \theta < \theta_{\text{adv}}$ , where  $\theta_{\text{rec}}$  denotes the minimal contact angle required for a receding contact line motion and,  $\theta_{\text{adv}}$  is the maximal angle required for the contact line to perform an advancing motion. Within this range of contact angels, the droplet exhibits hysteretic motion with the position of the contact line remaining pinned on the solid wall.

In the dynamic case involving a moving contact line, the contact angle will generally depend on the local contact line velocity along the solid wall,  $u_{\text{cl}}$ . The dynamic contact angle model adopted in this paper is given by Kistler [13]:

$$\theta = f_{\text{H}}(C_a + f_{\text{H}}^{-1}(\theta_{\text{adv/rec}})) , \quad (6)$$

$$\text{with } f_{\text{H}}(x) = \arccos \left( 1 - 2 \tanh \left[ 5.16 \left( \frac{x}{1 + 1.31x^{0.99}} \right)^{0.706} \right] \right) . \quad (7)$$

In (6), the capillary number,  $C_a = \mu u_{\text{cl}} / \gamma$ , is a signed quantity. It is considered to be positive when the contact line is advancing and is otherwise negative. Similarly,  $\theta_{\text{adv/rec}}$  attains the value  $\theta_{\text{adv}}$  or  $\theta_{\text{rec}}$  depending on whether the contact line performs a receding or an advancing motion, respectively. Thus, the limiting contact angles,  $\theta_{\text{adv}}$  and  $\theta_{\text{rec}}$ , represent two model parameters that need to be determined experimentally. Note that these limiting angles are directly related to the wettability of the solid surface for the given liquid.

## 3 Numerical Implementation

Equations (1)–(2), (3)–(5) and (6), (7) provide a complete description of the EHD problem. We use the classical Volume of Fluid (VoF) method [12] for discretizing the equations, an iso-surface interface reconstruction approach for curvature and contact line dynamics and a dedicated mesh coupling procedure for transferring data between the fluid flow and electric field problems. These approaches are implemented in the computational framework OPENFOAM [21] as described in the following.

### 3.1 The Fluid Flow Problem

For the solution of the Navier-Stokes equations, (1)–(2), a diffuse-interface approach is adopted. The density of the liquid phase is represented on the mesh by the volume fraction,  $\alpha$ , obeying the transport equation,

$$\frac{\partial \alpha}{\partial t} + \nabla \cdot (\alpha [\mathbf{u} + \mathbf{u}_c]) = 0, \quad (8)$$

with  $\alpha \in [0, 1]$ , where  $\mathbf{u}_c$  is an artificial compression velocity pointing in the direction normal to the phase boundary. The effective fluid properties used in the discretization of (1)–(2) are determined as weighted averages with the volume fraction field,  $\alpha$ , on the mesh [12]. The diffuse-interface representation of the phase boundary allows to compute the surface tension force as [3],

$$\mathbf{f}_s = -\gamma \nabla \cdot \left( \frac{\nabla \alpha}{||\nabla \alpha||} \right) \nabla \alpha. \quad (9)$$

In order to apply the contact line model given by (6), (7) the velocity of the contact line along the solid wall must be evaluated numerically. In this work, we have adopted the scheme proposed in [15] where the contact line velocity is given by

$$u_{cl} = \frac{\mathbf{u}_w \cdot \mathbf{n}_i}{\sqrt{1 - (\mathbf{n}_w \cdot \mathbf{n}_i)^2}}, \quad (10)$$

where  $\mathbf{u}_w$  is the fluid velocity near the solid wall,  $\mathbf{n}_w$  is the normal vector to the wall and  $\mathbf{n}_i = \nabla \alpha / ||\nabla \alpha||$  is the normal to the diffuse interface. In order to account for contact line pinning, the volume fraction in the boundary cells is kept constant as long as the contact angle lies between its static limits  $\theta_{adv}$  and  $\theta_{rec}$ , respectively.

Given the above model for the phase boundary, the pressure-velocity Eqs. (1), (2) are solved numerically using the PISO algorithm implemented in the `interFoam` solver [21]. The handling of the contact line dynamics has been adopted from a specialized implementation of the code; the `interFoamExtended` solver developed at the Technical University of Darmstadt [25].

### 3.2 The Electric Field Problem

The solution of the electric field Eqs. (3) and (4) can be performed on the same footing with the flow problem using a VoF-scheme with the volume fraction (8). The electric potential and charge density are allocated at cell centres on the same computational mesh as the fluid flow quantities. At the diffuse electric interface between fluid phases 1 and 2, the effective dielectric permittivity and electric conductivity are computed as weighted harmonic averages,

$$\frac{1}{\varepsilon} = \frac{\alpha}{\varepsilon_1} + \frac{1-\alpha}{\varepsilon_2} \quad \text{and} \quad \frac{1}{\kappa} = \frac{\alpha}{\kappa_1} + \frac{1-\alpha}{\kappa_2}, \quad (11)$$

respectively. The choice of harmonic averaging in (11) has been shown to be numerically more accurate for strongly contrasting material properties [31] as is the case for a conductive droplet in an essentially nonconducting gaseous environment.

Equations (3), (4) are advanced in time by the staggered scheme,

$$\nabla \cdot \varepsilon^{n+1/2} \nabla \varphi^{n+1/2} = -\rho_e^{n+1/2}, \quad (12)$$

$$\frac{\rho_e^{n+1} - \rho_e^n}{\Delta t} + \nabla \cdot (\rho_e^{n+1/2} \mathbf{u}^{n+1/2}) = \nabla \cdot \kappa^{n+1/2} \nabla \varphi^{n+1/2}, \quad (13)$$

where  $\Delta t$  is the time step and  $n$  the time level. In addition, a fixed-point iteration is applied in every time step (cf. Fig. 1) in order to ensure numerical consistency between the charge density and electric potential solutions.

### 3.3 Coupling Procedure

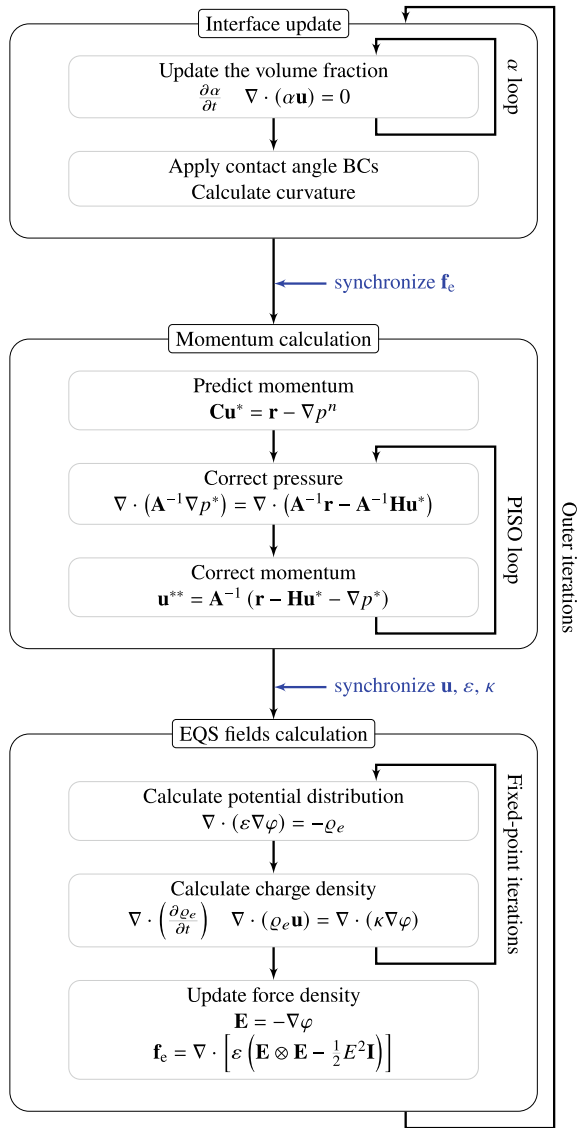
Most EHD problems include the presence of solid bodies such as dielectric substrates or electrode coatings. While these solids are irrelevant for the fluid flow problem, the solution of the EQS problem is often determined by their geometry and material properties. Since the solution domains for the fluid flow and EQS problems are generally not identical, a two-mesh coupling procedure is applied. The computational mesh for the EQS problem includes the fluid domains as well as eventually available dielectric solids. A second computational mesh for the flow problem is constructed as a subset of the EQS mesh by excluding solid parts. Index maps are used to transfer discrete fields from one mesh to the other. Hereby, no explicit interpolation is required since the field data reside on the same locations in the mesh.

The complete flow chart of the coupling scheme including the inner and outer fixed-point iteration loops is shown in Fig. 1. In addition to the depicted steps, a parallel adaptive mesh refinement procedure with dynamic load balancing is applied in every time step of the simulation. The reader is referred to [26] for a detailed description of the parallel mesh refinement procedure that we have omitted in this article for the sake of compactness.

## 4 Applications

The simulation model is applied in the study of two droplet problems of practical relevance. The first consists in the investigation of forced droplet oscillations on the surface of outdoor HV insulators for power line applications. The assessment of the dynamic droplet contact angle provides the starting point for an estimation

**Fig. 1** Flow chart of the time stepping scheme for the coupled fluid dynamics and electric field problems including the inner and outer iteration loops that ensure solution consistency in every time step of the simulation. For the notation used in the momentum calculation step, the user is referred to [21]. Adapted figure with permission from [22] under the Creative Common License (CC-BY-NC-ND 4.0 International)



of inception fields for the partial discharges caused by these droplets. The second application is the characterization of electrosprays in the cone-jet mode in terms of the relationship between droplet charge and its radius.

## 4.1 Sessile Droplets in HV Fields

Water droplets caused by rain or dew on the surface of HV outdoor equipment undergo a continuous oscillatory motion under the influence of AC electric fields. The sharp contact angle between droplet surface and insulating substrate results in a field singularity along the contact line that is responsible for electric field enhancement on the insulator surface. As a result, electrical discharge events occur that gradually damage the insulator surface [11].

We consider the experimental setup used in [19] and depicted in Fig. 2. It consists of a pair of cylindrical electrodes that are embedded in an silicone rubber substrate. A water droplet placed between the electrodes experiences a nearly homogeneous AC electric field that is oriented along the substrate surface. As seen in the Figure, the presence of a (static) droplet causes field enhancement at the droplet's contact line from which the partial discharge events are initiated.

### 4.1.1 Droplet Oscillation Modes

In the simulations, a  $20\ \mu\text{L}$  water droplet is considered with a peak voltage of 7 kV at frequency 27 Hz applied between the electrodes. The initial droplet shape is calculated semi-analytically by numerically integrating the Young-Laplace equilibrium equation according to the procedure described in [27]. The hysteresis range for water droplets on silicone rubber is obtained experimentally resulting in the limiting receding and advancing angles,  $\theta_{\text{rec}} = 60^\circ$  and  $\theta_{\text{adv}} = 140^\circ$ , respectively [19].

Experimental evidence shows that droplets on insulator surfaces under outdoor conditions may contain a certain amount of net charge that is due to surface con-

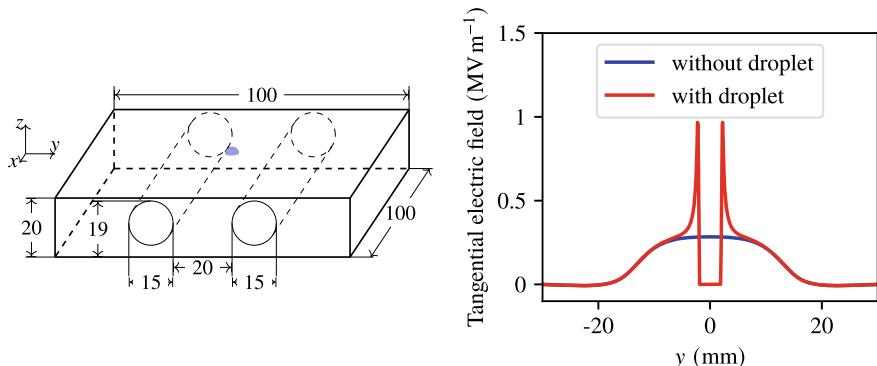


**Fig. 2** Left: simulation setup including HV electrodes and water droplet on the substrate. Right: electric field strength along the substrate surface parallel to the applied field. The field is singular at the contact line between droplet and substrate. For simplicity, the case of a static droplet is shown. Adapted figure with permission from [22] under the Creative Common License (CC-BY-NC-ND 4.0 International)

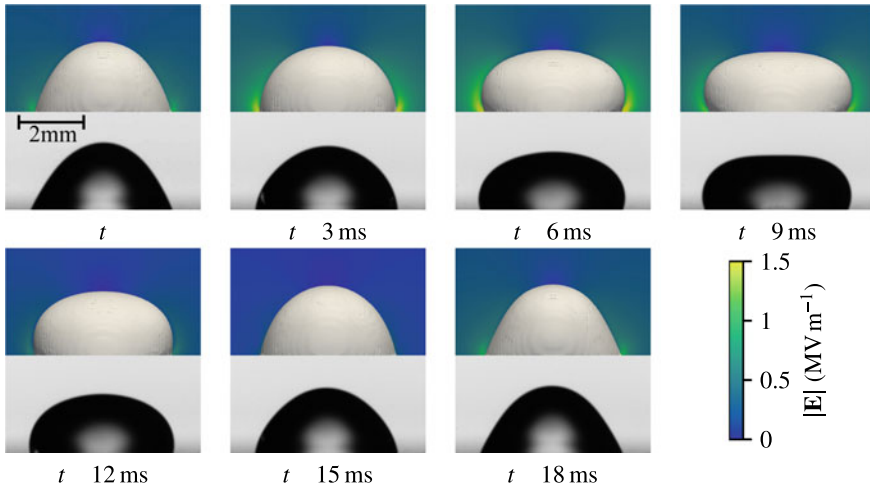
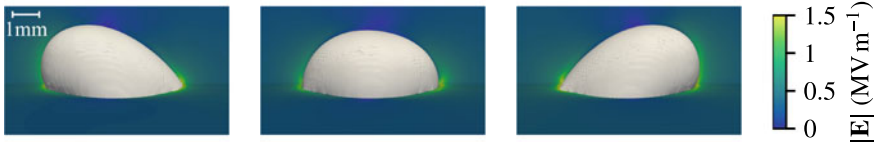


**Fig. 3** Motion of a  $20 \mu\text{L}$  droplet when a 7 kV peak voltage at 27 Hz is applied. The dynamics over half a period of the AC voltage is shown. First and third lines: simulation results. The colour map depicts electric field strength. Second and fourth lines: high-speed camera images obtained experimentally. Reprinted figure with permission from [22] under the Creative Common License (CC-BY-NC-ND 4.0 International)

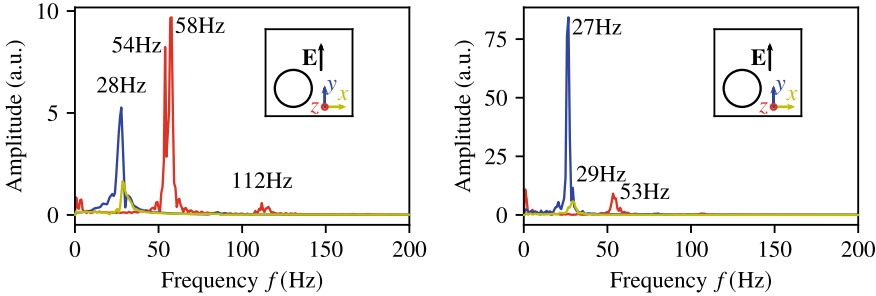
tamination or ionization events in air [5]. A droplet charge in the order of 100 pC, as suggested in [17], is quite significant compared to the displacement charge induced by the external field. This charge will have a strong impact on droplet's motion. Therefore, in the following, two droplet scenarios are considered. In the first scenario, an uncharged water droplet is considered. In the second one, a net charge of 100 pC is given to the droplet before the electric field is switched on. The initial charge distribution within the droplet is found from the steady state solution of the EHD problem in absence of external fields.

Figure 3 shows simulation results for the uncharged droplet. The oscillation pattern shown in the Figure is settled after a few periods of the applied voltage. The motion consists essentially in a forced vertical oscillation at twice the applied frequency. This is the expected behaviour, since the dominant driving force on the droplet is due to dielectric polarization. Also in the Figure, the simulation results are compared with droplet images obtained experimentally using a high-speed camera in the High Voltage Lab at the TU Darmstadt. The striking agreement between simulation and measurement demonstrates the reliability of the simulation model.

Figure 4 shows an analogous simulation for a charged droplet. The difference to the uncharged case is obvious. A horizontal mode in the direction of the applied field is excited with a considerably larger amplitude than in the charged case. In addition, the frequency of oscillation is nearly the same as that of the applied field. This indicates that the dominant driving force in the charged case is given by a monopole-type interaction of the external field with the net charge of the droplet in its centre of mass.



**Fig. 4** Oscillations of a charged droplet at 27 Hz. Droplet profiles at three time instants over half a period are shown. The colour map depicts electric field strength. Reprinted figure with permission from [22] under the Creative Common License (CC-BY-NC-ND 4.0 International)



**Fig. 5** Oscillating modes of a  $20\text{ }\mu\text{L}$  sessile droplet for an applied voltage at 27 Hz. The coordinate system is as in Fig. 2. Left: uncharged droplet. Right: droplet with a net charge of  $100\text{ pC}$ . Adapted figure with permission from [22] under the Creative Common License (CC-BY-NC-ND 4.0 International)

The above results can be quantified in terms of harmonic oscillation modes. For this purpose the motion of the droplet centre of mass in all three directions is considered. The spectral content of this motion is shown in Fig. 5. As observed, the dominant mode for the uncharged droplet is a vertical oscillation at  $\sim 58\text{ Hz}$ , that is slightly larger than double the frequency of the applied voltage. However, a horizontal oscillation of smaller amplitude is observed as well. The latter occurs at around the same frequency as the applied voltage. This is consistent with the finding in [4, 28] for uncharged droplets, where azimuthally degenerate droplet modes were found to oscillate at half the frequency of the driving force.

The case of the charged droplet is shown in Fig. 5 (right). The modal patterns and frequencies are essentially the same as in the uncharged case. However, the horizontal mode at the lower frequency,  $27\text{ Hz}$ , is clearly the dominant one. Thus, the dynamics of sessile droplets on insulator surfaces depends strongly on the net charge carried by the droplet. This behaviour has immediate consequences on the electric field threshold for partial discharge inception as discussed in the following.

#### 4.1.2 Inception Field Estimation

The basic assumption in the analysis is that partial discharges originate from the electric field enhancement at the droplet's contact line only. The field singularity at this location is essentially determined by the contact angle between droplet surface and dielectric substrate, where the strength of singularity is larger for smaller contact angles [22]. Thus, the discharge inception field may be estimated from the worst case scenario consisting in the smallest value of contact angle attained by the droplet at the peak applied voltage. This approach simplifies the analysis substantially by allowing to consider the droplet dynamics and the discharge inception problems one at a time.

The transient behaviour of the contact angle is shown in Fig. 6 for the two considered cases of an uncharged and a charged droplet, respectively. The thin grey lines in each of the graphs depict instantaneous contact angle values measured along the the y-direction over half a period of the applied field. Since droplet motion is quasiperiodic due to modal superposition, the contact angles over several periods will span a whole range of values. This range is described in the figure by the blue-shaded areas corresponding to the envelope of the contact angle curves recorded for different phases of the applied field.

As seen in Fig. 6, the contact angle range in the charged droplet case is substantially different from that of the uncharged one. In the uncharged case, the contact angles essentially follow the magnitude of the applied field. The worst case of a minimum contact angle is obtained at the zero-crossing of the applied voltage where a partial discharge is unlikely to occur. In all cases, however, the contact angle remains consistently within the hysteresis range given by the static receding and advancing angles,  $\theta_{\text{rec}} = 60^\circ$  and  $\theta_{\text{adv}} = 140^\circ$ , respectively. In other words, for the vertical mode excited in the uncharged case, the contact line remains pinned. Therefore, the

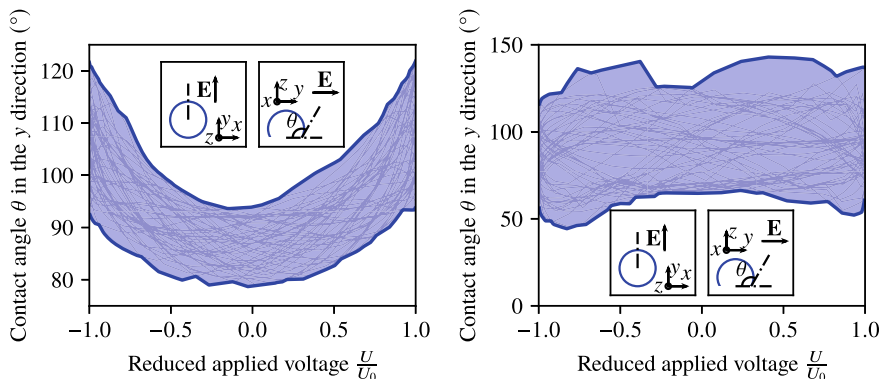


**Fig. 6** Range of contact angles in the direction parallel to the field vs. phase of the applied field for a 20  $\mu\text{L}$  droplet at 27 Hz. Left: uncharged droplet. Right: droplet with a net charge of 100 pC. Adapted figure with permission from [22] under the Creative Common License (CC-BY-NC-ND 4.0 International)

knowledge of the limiting receding angle for a given substrate wettability ( $60^\circ$  in this case) is fully sufficient to identify a worst case scenario for discharge inception from uncharged droplets.

The situation is significantly different in the case of a charged droplet featuring the horizontal oscillation mode seen in Fig. 5 (right). The range of attainable angles is nearly independent from the instantaneous applied voltage. The contact angles at the peak voltage span the full hysteresis range. Furthermore, contact angles beyond the limiting static values can be observed indicating that the contact line performs a stick-slip motion as it has been previously noted, e.g. in [9]. Thus, for charged droplets the discharge inception field is expected to be substantially lower than for uncharged ones. Furthermore, the discharge inception depends not only on the wettability properties of the substrate surface, but also on the net charge carried by water droplets under atmospheric conditions.

The discharge inception fields can be quantified in the range of realistic droplet sizes and contact angles. For this purpose, the electric field distribution at power line frequency is computed numerically for a set of static droplets with different (but fixed) sizes and shapes. Hereby, droplet motion may be ignored, since only the worst case of the smallest attainable contact angle is of interest. Given a numerically computed field distribution, the corona discharge model introduced in [14] is applied for different droplet shapes and sizes using the commercial software Spark3D. The detailed procedure for extracting discharge inception fields is described thoroughly in [22]. In the following, we restrict the discussion to the main results of this study providing the link between the contact angles predicted by droplet dynamics simulations and the discharge characteristics on the surface. This is depicted in Fig. 7 (left), where the inception field is shown as a function of droplet volume for different contact angles assuming a fixed, axially symmetric droplet geometry. The inception field

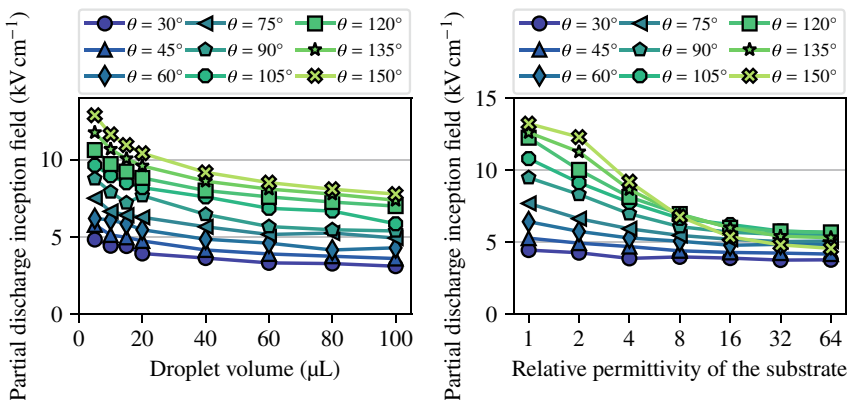


**Fig. 7** Left: discharge inception field vs. droplet volume for static droplets with different (but fixed) contact angles. Right: effect of substrate permittivity on partial discharge inception for a  $20\text{ }\mu\text{L}$  droplet for different values of the contact angle. Adapted figure with permission from [22] under the Creative Common License (CC-BY-NC-ND 4.0 International)

decreases, both, with increasing droplet volume and decreasing contact angle. Over the range of considered volumes, the contact angle causes the inception field to vary by more than a factor of two. The higher sensitivity is observed for small droplets whereas for larger ones the variation of the inception field with droplet volume is less pronounced. The complex relationship between discharge characteristics and problem parameters is demonstrated in Fig. 7 (right). Obviously, the inception field can be maximized by using an insulating substrate with small permittivity. However, this is no longer true for droplet oscillations featuring small contact angles as is the case for intrinsically charged droplets and surfaces with low wettability.

## 4.2 Electrosprays

Various efforts have been made for the characterization of electrosprays in order to predict the size and charge of the microdroplets produced by electrostatic atomization. Most prominently, Collins et al. [6] and later Gañán-Calvo et al. [10] have suggested the existence of universal scaling laws relating the charge to the radius of the very first ejected electrospray droplet. In the following, the simulation model is used for the investigation of the charge-radius characteristics in cone-jet electrosprays. Thereby, not only the first ejected droplet but rather the complete transient dynamics of electrospray including the steady state limit is considered.

### 4.2.1 First Electrospray Droplet

For the study of the first ejection, the onset of electrospray from a (large) sessile droplet placed between two plane electrodes is considered. In the simulations, axial symmetry is presumed. A voltage pulse is ramped up causing the droplet to deform to a conical shape, at the tip of which a jet streams, leading eventually to electrospray atomization. Simulation results for two different test liquids in the initial stage of electrospray are shown in Fig. 8. Clearly, the size (and charge) of the ejected droplets and also the time scales characterizing the process depend on liquid properties.

Visual inspection of Fig. 8 indicates that the very first ejected droplet is slightly larger than the succeeding ones. This indicates a different dynamical behaviour of this droplet compared to the rest of electrospray droplets. For this particular droplet, Collins et al. [6] postulate a universal scaling law that provides a liquid-independent relationship between the droplet charge,  $q$  and its radius,  $r$ . Given the characteristic viscous length  $l_\mu = \mu^2/\rho\gamma$  and the dimensionless droplet charge and radius defined as  $q^* = q/\sqrt{\varepsilon\gamma l_\mu^3}$  and  $r^* = r/l_\mu$ , respectively, the scaling law reads,  $q^* \propto (r^*)^{3/2}$ , where the proportionality constant is independent from liquid properties. Figure 9 depicts the computed correlation between the first droplet charge and radius for 21 different liquid mixtures spanning a large range of electrical and mechanical

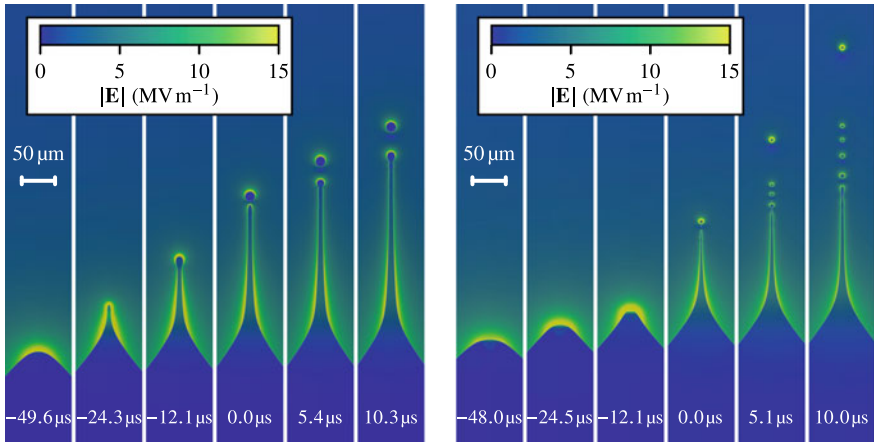


**Fig. 8** Onset of electrospray from a sessile droplet shown at different time instants including the ejection of the first few droplets. The origin of time is at the instant of first droplet ejection. The colour map depicts electric field strength. Left: methanol. Right: a heptane mixture (with  $\gamma = 21\text{mN/m}$ ,  $\kappa = 1.9\mu\text{S/m}$ ). The conductivity of the heptane mixture is nearly one order of magnitude smaller than that of methanol [22]. Adapted figure with permission from [23], Copyright 2020 by the IEEE

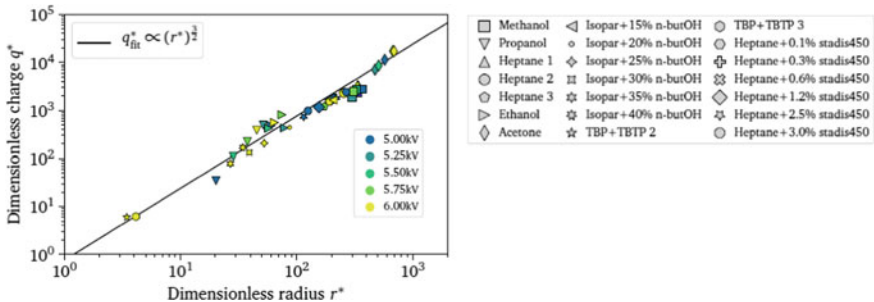


**Fig. 9** Charge-radius correlation for the first electrospray droplet for different applied voltages and a number of liquid mixtures with different electrical and mechanical properties. The black line represents the Collins's scaling law [6]. Adapted figure with permission from [23], Copyright 2020 by the IEEE

properties. The simulation results fit quite well to the predicted power law, thus, providing a numerical confirmation for the universal scaling suggested in [6].

#### 4.2.2 Transient Electrosprays

As the electrospray develops, the cone-jet dynamics will affect the ongoing atomization process. Thus, the size and charge of subsequent droplets are expected to differ from that of the first ejection (cf. Fig. 8). The question posed is, to what extent the

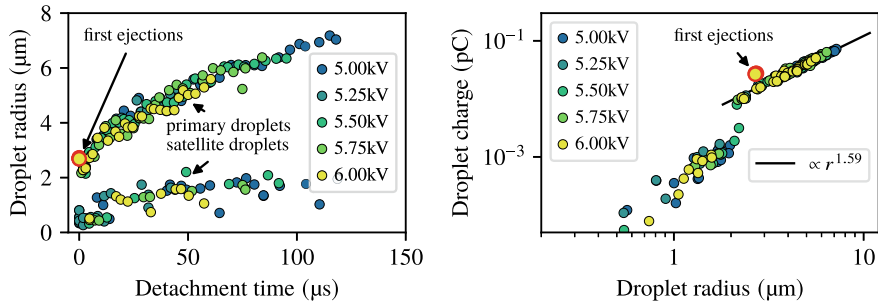


**Fig. 10** Left: droplet size vs. ejection time for a heptane mixture electrospray ( $\gamma = 21\text{mN/m}$ ,  $\kappa = 1.9\mu\text{S/m}$ ). Right: charge-radius correlation for different applied voltages. The red-framed circle depicts the first ejection. Adapted figure with permission from [23], Copyright 2020 by the IEEE

properties of these subsequent droplets in a transient electrospray process comply to the scaling law in Sect. 4.2.1. It is, furthermore, unclear whether the charge-radius correlation for longer time transients can be represented by a power law, as is the case for the first ejected droplet.

Figure 10 (left) shows the computed droplet radii vs. their breakup time for a heptane mixture. The droplets can be clearly classified into two groups referred to as primary and satellite droplets, respectively, where the radius of the latter is consistently smaller than  $2\mu\text{m}$ . The size of the first few primary droplets is smaller than that of the first ejection. However, the radius of subsequent ejections increases as the electrospray develops. This trend is the same for all considered voltages.

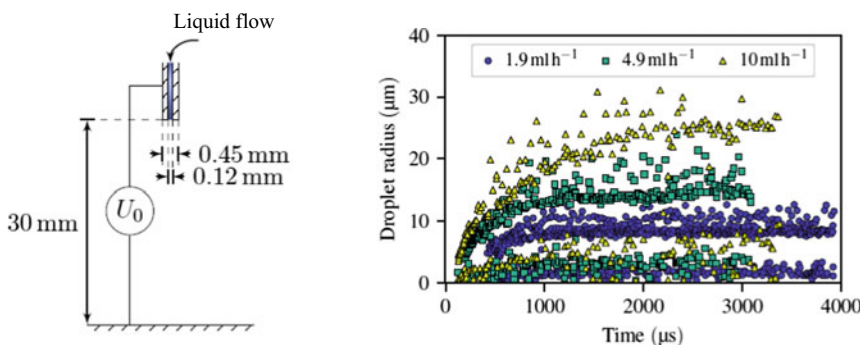
The charge-radius correlation for all produced droplets in the course of the transient process and for all applied voltages is depicted in Fig. 10 (right). For comparison, the first ejected droplet for each voltage is highlighted by a red-framed circle. Two scaling trends can be observed corresponding to primary and satellite droplets, respectively. Since satellites carry little charge compared to primary droplets, we restrict the discussion on the charge-radius correlation for primary droplets. Clearly, this correlation fits well to a power law. However, the scaling exponent (1.59) differs from that of the universal law for the first droplet. Interesting to note is that the charge density of the first ejection is always higher than that of all succeeding droplets. Detailed simulations with other liquids show that the charge-radius scaling is always consistent with a power law similar to the one obtained in [6] for the first ejection. However, the scaling exponents are different and do, in general, depend on the electrical and mechanical liquid properties. Explicit values of these exponents for acetone, methanol and various heptane mixtures with different electric conductivities are reported in [23].

### 4.2.3 Steady State Electrosprays

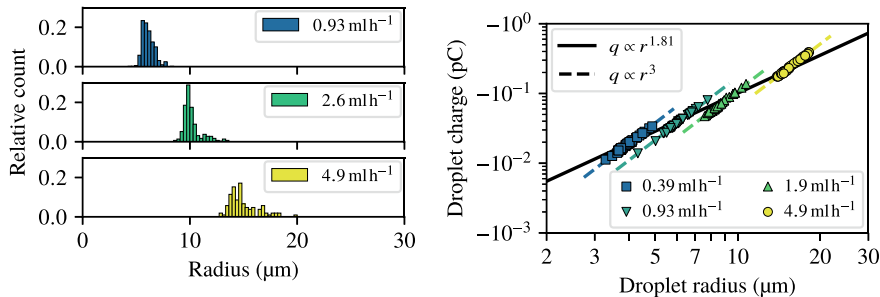
In most applications, electrosprays are applied in continuous-flow mode where a constant liquid flow is supplied in order to sustain a steady atomization process. In order to investigate steady state electrosprays, the simulation setup shown in Fig. 11 (left) is considered. The liquid is provided with different flow rates by means of a metallic capillary. The latter serves at the same time as driving electrode where a voltage of a few kilovolts is applied. The test liquid is heptane enriched with 0.3% stadis-450 ( $\gamma = 18.6 \text{ mN/m}$ ,  $\kappa = 1.4 \mu\text{S/m}$ ).

Figure 11 (right) depicts the electrospray dynamics for three different flow rates. A steady state situation with a nearly constant mean droplet size is reached in all three considered cases. However, the transition times as well as the resulting final droplet sizes are quite different, depending on the applied flow rates. In the case with the largest flow rate, steady state is reached after a few milliseconds corresponding to approximately 200 primary ejections. Note also that for each individual electrospray the two groups of primary and satellite droplets, respectively, can be clearly distinguished.

As seen in Fig. 11, droplet sizes and charges at steady state manifest a significant spread due to fluctuations of the jet profile and perturbations originating from prior ejections. The steady state distributions of primary droplet sizes for different flow rates are shown in Fig. 12 (left). In order to discard transient effects, in this representation, only late-time primary droplets are included that are produced after 200 ejections have already taken place. The relationship between primary droplet sizes and charges at steady state is depicted in Fig. 12 (right). Obviously, the scaling of the mean droplet size and charge at steady state seem to follow a power law when the flow rate is changed with a corresponding scaling exponent of 1.81 for the particular liquid used in the simulations.



**Fig. 11** Left: simulation setup for continuous-flow electrosprays. A voltage of 4 kV is applied between capillary and the ground plane. Right: droplet size vs. ejection time for the heptane mixture electrospray for three different flow rates. Adapted figure with permission from [22] under the Creative Common License (CC-BY-NC-ND 4.0 International)



**Fig. 12** Left: droplet size distributions at steady state for three different flow rates. Right: scatter plot of droplet charges and radii at steady state for each flow rate. For reference, the two characteristic scaling curves for steady state electrosprays are shown. Adapted figure with permission from [22] under the Creative Common License (CC-BY-NC-ND 4.0 International)

The other interesting observation concerns the relationship between droplet charge and size deviations from their respective mean values for any given electrospray at steady state. As seen in Fig. 12 (right), droplet charge deviations correlate proportionally to volume deviations. This is true for all three flow rates considered. This result is consistent with the experimental finding in [7], where it was observed that the droplet charge distribution at steady state exhibits a significantly larger spread than that of the corresponding size distribution. Furthermore, “...the mean charge  $q$  and diameter  $d$  associated with these sections are such that the charge density  $6q/(\pi d^3)$  varies little within the full range of drop volumes and charges produced by a given spray” [7]. A justification for this behaviour was offered in [7], where Rayleigh’s breakup theory for a cylindrical jet was applied assuming that electric charges are frozen on the jet surface during droplet breakup. Simulations do confirm this result while specifying that the correlation  $q \sim r^3$  refers to droplet charge and size deviations from their mean values for a given electrospray at steady state.

## 5 Conclusions

The strength of the modelling approach consists in the detailed description of contact angle dynamics as well as in the incorporation of electric field distributions resulting from complicated electrode and insulator geometries. This allows for accurate simulations of real world droplet dynamics problems. Two such applications are considered. In the case of water droplets on high-voltage insulators, the oscillations of uncharged and charged droplets are considered. A corona discharge model is applied to determine inception fields as a function of contact angle, droplet size and dielectric permittivity of the substrate. The second application concerns electrosprays. Simulations for an electrospray initiated from a sessile droplet as well as continuous flow electrosprays were performed. Despite the well-known charge-radius scaling of

the first droplet, simulations show that a similar scaling applies to the subsequently ejected droplets. The scaling exponent, however, depends on liquid properties. As the electrospray evolves to steady state, yet another characteristic scaling can be observed. It indicates that deviations of the droplet charge distribution from its mean value correlate proportionally with volume deviations. Furthermore, also the correlation of the mean droplet charges and radii at steady state for different flow rates fits well to a liquid specific power law. This latter observation, however, requires further investigations that will be presented in a forthcoming work.

**Acknowledgements** The authors gratefully acknowledge the German Research Foundation (DFG) for the financial support of the project SFB-TRR 75 under the project number 84292822.

## References

1. Aryasomayajula A, Bayat P, Rezai P, Selvaganapathy PR (2017) Microfluidic devices and their applications. In: Bhushan B (ed) Springer handbook of nanotechnology. Springer, Berlin Heidelberg, Berlin, Heidelberg, pp 487–536
2. Bartels F (2016) Droplet-driven electrowetting displays. In: Chen J, Cranton W, Fihn M (eds) Handbook of visual display technology. Springer International Publishing, Cham, pp 2459–2472
3. Brackbill J, Kothe D, Zemach C (1992) A continuum method for modeling surface tension. *J Comput Phys* 100(2):335–354
4. Chang CT, Bostwick JB, Steen PH, Daniel S (2013) Substrate constraint modifies the Rayleigh spectrum of vibrating sessile drops. *Phys Rev E* 88:023015
5. Choi D, Lee H, Im DJ, Kang IS, Lim G, Kim DS, Kang KH (2013) Spontaneous electrical charging of droplets by conventional pipetting. *Sci Rep* 3(1):2037–2037
6. Collins RT, Sambath K, Harris MT, Basaran OA (2013) Universal scaling laws for the disintegration of electrified drops. *Proc Natl Acad Sci* 110(13):4905–4910
7. de Juan L, Fernández de la Mora J (1997) Charge and size distributions of electrospray drops. *J Colloid Interface Sci* 186(2):280–293
8. Dussan EB (1979) On the spreading of liquids on solid surfaces: static and dynamic contact lines. *Annu Rev Fluid Mech* 11(1):371–400
9. Fayzrakhmanova IS, Straube AV (2009) Stick-slip dynamics of an oscillated sessile drop. *Phys Fluids* 21(7):072104
10. Gañán-Calvo A, López-Herrera J, Rebollo-Muñoz N, Montanero J (2016) The onset of electrospray: the universal scaling laws of the first ejection. *Sci Rep* 6
11. Gorur RS, Karady GG, Jagota A, Shah M, Yates AM (1992) Aging in silicone rubber used for outdoor insulation. *IEEE Trans Power Deliv* 7(2):525–538
12. Hirt C, Nichols B (1981) Volume of fluid (VOF) method for the dynamics of free boundaries. *J Comput Phys* 39(1):201–225
13. Kistler S (1993) Hydrodynamics of wetting. *Wettability* 6:311–430
14. Koufogiannis ID, Sorolla E, Mosig JR, Mattes M (2013) Analyzing corona breakdown with a finite element-based electromagnetic solver. In: 2013 7th European conference on antennas and propagation (EuCAP), pp 2312–2314
15. Linder N, Criscione A, Roisman IV, Marschall H, Tropea C (2015) 3d computation of an incipient motion of a sessile drop on a rigid surface with contact angle hysteresis. *Theoret Comput Fluid Dyn* 29(5):373–390
16. López-Herrera J, Gañán-Calvo A, Popinet S, Herrada M (2015) Electrokinetic effects in the breakup of electrified jets: a volume-of-fluid numerical study. *Int J Multiph Flow* 71:14–22

17. Löwe JM, Hinrichsen V, Roisman IV, Tropea C (2020) Behavior of charged and uncharged drops in high alternating tangential electric fields. *Phys Rev E* 101:023102
18. Melcher JR (1981) Continuum electromechanics. MIT Press
19. Nazemi MH (2016) Experimental investigations on water droplets on polymeric insulating surfaces under the impact of high electric fields. Ph.D. thesis, Technische Universität Darmstadt, Darmstadt
20. Omori T, Kajishima T (2017) Apparent and microscopic dynamic contact angles in confined flows. *Phys Fluids* 29(11):112107
21. Openfoam (2021). <https://openfoamwiki.net>
22. Ouedraogo Y (2020) Modelling of electrohydrodynamic droplet motion under the influence of strong electric fields. Ph.D. thesis, Technische Universität, Darmstadt. <https://tuprints.ulb.tu-darmstadt.de/14008/>
23. Ouedraogo Y, Gjonaj E, De Gersem H, Schoeps S (2020) Simulation of transient electrospray dynamics in conductive fluids. *IEEE Trans Magn* 56(3)
24. Pimenta F, Alves M (2019) A coupled finite-volume solver for numerical simulation of electrically-driven flows. *Comput Fluids* 193:104279
25. Rettenmaier D (2019) Numerical simulation of shear driven wetting. Ph.D. thesis, Technische Universität, Darmstadt
26. Rettenmaier D, Deising D, Ouedraogo Y, Gjonaj E, De Gersem H, Bothe D, Tropea C, Marschall H (2019) Load balanced 2D and 3D adaptive mesh refinement in openfoam. *SoftwareX* 10:100317
27. Saad SM, Neumann AW (2016) Axisymmetric drop shape analysis (ADSA): an outline. *Adv Coll Interface Sci* 238:62–87
28. Songoro H (2015) Electrohydrodynamic modeling of droplet vibrations under the influence of electric fields. Ph.D. thesis, Technische Universität, Darmstadt
29. Teigen KE, Munkejord ST (2009) Sharp-interface simulations of drop deformation in electric fields. *IEEE Trans Dielectr Electr Insul* 16(2):475–482
30. Tomar G, Gerlach D, Biswas G, Alleborn N, Sharma A, Durst F, Welch S, Delgado A (2007) Two-phase electrohydrodynamic simulations using a volume-of-fluid approach. *J Comput Phys* 227(2):1267–1285
31. Yang Q, Li BQ, Ding Y (2013) 3D phase field modeling of electrohydrodynamic multiphase flows. *Int J Multiph Flow* 57:1–9

**Open Access** This chapter is licensed under the terms of the Creative Commons Attribution 4.0 International License (<http://creativecommons.org/licenses/by/4.0/>), which permits use, sharing, adaptation, distribution and reproduction in any medium or format, as long as you give appropriate credit to the original author(s) and the source, provide a link to the Creative Commons license and indicate if changes were made.

The images or other third party material in this chapter are included in the chapter's Creative Commons license, unless indicated otherwise in a credit line to the material. If material is not included in the chapter's Creative Commons license and your intended use is not permitted by statutory regulation or exceeds the permitted use, you will need to obtain permission directly from the copyright holder.



# Modelling and Numerical Simulation of Binary Droplet Collisions Under Extreme Conditions



Johanna Potyka, Johannes Kromer, Muyuan Liu, Kathrin Schulte, and Dieter Bothe

**Abstract** The complexity of binary droplet collisions strongly increases in case of immiscible liquids with the occurrence of triple lines or for high energetic collisions, where strong rim instabilities lead to the spattering of satellite droplets. To cope with such cases, the Volume of Fluid method is extended by an efficient interface reconstruction, also applicable to multi-material cells of arbitrary configuration, as well as an enhanced continuous surface stress model for accurate surface force computations, also applicable to thin films. For collisions of fully wetting liquids, excellent agreement to experimental data is achieved in different collision regimes. High-resolution simulations predict droplet collisions in the spattering regime and provide detailed insights into the evolution of the rim instability. Another challenge is the numerical prediction of the collision outcome in the bouncing or coalescence region, where the rarefied gas dynamics in the thin gas film determines the collision result. To this end, an important step forward became possible by modelling the pressure in the gas film. With the introduction of an interior collision plane within the flow domain, it is now possible to simulate droplet collisions with gas film thickness reaching the physically relevant length scale.

## 1 Introduction

Binary droplet collisions play an important role in nature, science and technology, ranging from cloud dynamic processes to technical spray applications. The collision can result in coalescence or fragmentation of the droplets. The collision outcome strongly affects the resulting droplet size distributions. Consequently, any sound

---

J. Potyka · K. Schulte (✉)

Institute of Aerospace Thermodynamics, University of Stuttgart, Stuttgart, Germany

e-mail: [kathrin.schulte@itlr.uni-stuttgart.de](mailto:kathrin.schulte@itlr.uni-stuttgart.de)

M. Liu

School of Mechanics and Engineering, Southwest Jiaotong University, Chengdu, China

J. Kromer · D. Bothe

Mathematical Modeling and Analysis, Technical University of Darmstadt, Darmstadt, Germany

© The Author(s) 2022

127

K. Schulte et al. (eds.), *Droplet Dynamics Under Extreme Ambient Conditions*,

Fluid Mechanics and Its Applications 124,

[https://doi.org/10.1007/978-3-031-09008-0\\_7](https://doi.org/10.1007/978-3-031-09008-0_7)

description of droplet population dynamics is to be based on a fundamental understanding of (binary) droplet collisions as an elementary process. The main question here is which specific outcome a binary collision takes, depending on the specific dimensionless parameters of the process. Figure 1 displays some prototypical collision processes. Binary collision outcomes for identical droplets are mainly influenced by the Weber number ( $We$ ) and the impact parameter ( $B$ ; see Fig. 2) with

$$We = \frac{\rho_l U_{\text{rel}}^2 D_0}{\sigma} \quad \text{and} \quad B = \frac{b}{D_0}, \quad (1)$$

where  $\rho_l$  is the liquid density,  $U_{\text{rel}}$  the relative velocity,  $D_0$  the initial droplet diameter,  $\sigma$  the surface tension and  $b$  is the offset of the droplets' trajectories. Further parameters of influence are the Ohnesorge number ( $Oh$ ), as well as the ratios of density ( $\psi$ ) and the viscosity ( $\varphi$ ) with

$$Oh = \frac{\eta_l}{\sqrt{D_0 \rho_l \sigma}}, \quad \psi = \frac{\rho_l}{\rho_g} \quad \text{and} \quad \varphi = \frac{\eta_l}{\eta_g}, \quad (2)$$

where  $\eta$  denotes the viscosity and the subscript  $g$  (l) refers to the ambient gas (liquid). The Ohnesorge number could be replaced by the Reynolds number  $Re = \sqrt{We}/Oh$ , but the use of  $Oh$  is advantageous since the collision outcome is then only dependent on  $We$  and  $B$ , as long as the material parameters and the droplet size are fixed. Another dimensionless parameter used for the description of the temporal evolution of a droplet collision is the dimensionless time  $t^* = t U_{\text{rel}} / D_0$  with  $t^* = 0$  at the moment of initial contact.

In previous work [14, 28, 31], mainly on droplet collisions at low Weber numbers, distinct regimes of collision outcomes were characterized and condensed into a collision regime map. An adapted map is shown in Fig. 2. In the regime of low Weber numbers, four different collision outcomes are identified depending on the combination of  $We$  and  $B$ . These are: coalescence (I, III), bouncing (II), near head-on separation (IV) and off-center separation (V); the latter two are also called reflexive separation and stretching separation, respectively. The numbers in brackets are the corresponding section numbers in the regime map. For larger  $We$ , the rim of the collision complex becomes unstable, fingers are formed and partly ejected as satellite droplets. This collision outcome is named spatter (VI) or shattering (also splashing, in particular for droplets colliding with a wall). Going from left to right in Fig. 1, we see examples for these different collision outcomes, from (I) to (VI). Highly relevant and current topics are binary collisions of drops of different liquids, either miscible or immiscible. Droplet collisions of different, miscible liquids appear for instance in spray drying processes, where different droplets' flight history can lead to different liquid compositions [10]. This leads to Marangoni stress since the surface tension depends on the local composition [11]. This yields to changes of the boundaries in the collision regime map, cf. [1]. In the collision of droplets of immiscible liquids, which is important not only for pharmaceutical applications but also for modern combustion engines in which water is injected [3], the interfacial tensions deter-

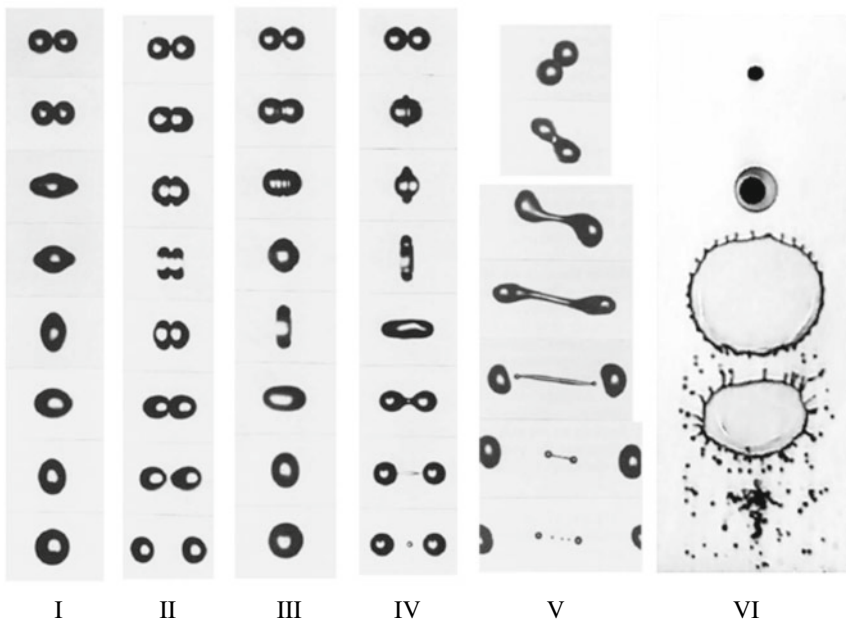


**Fig. 1** Prototypical collision processes (left to right, cf. Fig. 2 for the types I–VI): coalescence (I), bouncing (II), coalescence (III), near head-on separation (IV), off-center separation (V) (reproduced from [14] with permission, Copyright by Cambridge University Press) and spatter (VI) (reproduced from [34] with permission)

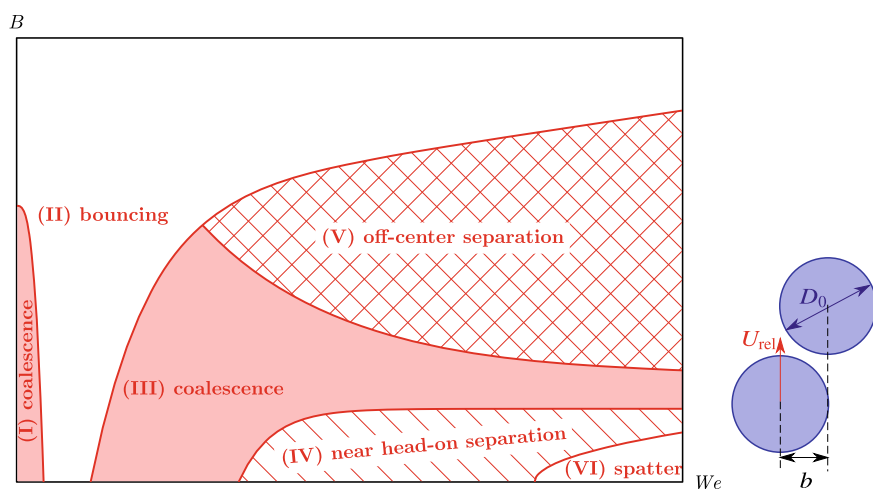


**Fig. 2** Regime map for binary droplet collision as a function of Weber number  $We$  and center offset  $B = \frac{b}{D_0}$ , adapted from [28]

mine the contact angle at the three-phase contact line. This can lead to a (partial) enclosure of the droplet of higher surface tension. Bouncing, coalescence, crossing and reflexive separation [3, 27] are possible outcomes of collisions of immiscible liquids. For partial wetting adhesive merging [40] and a retraction of the contact line after a full encapsulation [41] can occur additionally. Despite impressive experimental work such as, e.g., [14, 22, 23, 27, 28, 31, 42], a fundamental analysis of the local phenomena during (binary) droplet collisions requires full information of the instantaneous velocity and pressure fields within the liquid phase. This requires a computational approach, based on fully resolved, detailed numerical solution of the governing equations from continuum physics. This leads to deep insights into the local flow dynamics, a valuable input for model enhancement [26]. In the following, the results achieved in the sub-project A7 of the Collaborative Research Center SFB-TRR75 are presented.

## 2 Continuum Mechanical Model

The droplet collisions under consideration are modelled as incompressible (due to low Mach numbers), isothermal two-phase flows without phase change, where the two immiscible fluid phases are labelled by  $\pm$  and occupy the time-dependent domains  $\Omega^\pm(t)$ , such that  $\Omega$  is disjointly decomposed into  $\Omega = \Omega^+(t) \cup \Omega^-(t) \cup \Sigma(t)$ , where  $\Sigma(t)$  denotes the sharp interface. The velocity  $\mathbf{u}(t, \mathbf{x})$  and pressure  $p(t, \mathbf{x})$  are governed by the Navier-Stokes equations

$$\rho(\partial_t \mathbf{u} + (\mathbf{u} \cdot \nabla) \mathbf{u}) = -\nabla p + \eta \Delta \mathbf{u} + \rho \mathbf{g} \quad \text{and} \quad \nabla \cdot \mathbf{u} = 0, \quad (3)$$

where  $\mathbf{g}$ ,  $\rho$  and  $\eta$  denote the acceleration due to gravity, the phase-specific mass density and dynamic viscosity, respectively. The interface is assumed to carry no mass and admits no tangential slip of the adjacent velocity fields  $\mathbf{u}$ . With constant surface tension  $\sigma$ , one obtains the dynamic and kinematic jump conditions

$$[p\mathbf{I} - \eta(\nabla \mathbf{u} + \nabla \mathbf{u}^\top)]\mathbf{n}_\Sigma = \sigma \kappa_\Sigma \mathbf{n}_\Sigma \quad \text{and} \quad [\mathbf{u}] = \mathbf{0}, \quad (4)$$

where  $\mathbf{n}_\Sigma$  denotes the unit normal and the so-called *jump-bracket*

$$[\phi](t, \mathbf{x}) := \lim_{h \searrow 0} (\phi(t, \mathbf{x} + h\mathbf{n}_\Sigma) - \phi(t, \mathbf{x} - h\mathbf{n}_\Sigma)) \quad \text{for } \mathbf{x} \in \Sigma(t) \quad (5)$$

expresses the jump of a phase-specific quantity  $\phi$  across the interface  $\Sigma$ . Neglecting phase change, which is a valid assumption considering the small time-scales of droplet collision processes, the speed of normal displacement  $V_\Sigma$  of the interface fulfils the kinematic condition  $V_\Sigma = \langle \mathbf{u}, \mathbf{n}_\Sigma \rangle$ , i.e. the interface is passively advected by the flow.

### 3 Numerical Method

Due to the possible occurrence of topological changes during the droplet collision numerical methods with implicit treatment of the interface are advantageous. Since conservation of phase volume is also desired, the Volume of Fluid (VOF) method of [13] has been employed for direct numerical simulations within this project, using the in-house solver **Free Surface 3D** (FS3D), originally developed by [33]; cf. [7] for an overview. The volume indicator function

$$f(t, \mathbf{x}) := \begin{cases} 0 & \text{for } \mathbf{x} \in \Omega^+(t), \\ 1 & \text{for } \mathbf{x} \in \Omega^-(t), \end{cases} \quad (6)$$

encodes the assignment of a point  $\mathbf{x}$  to the respective phase, which is governed by

$$\partial_t f + \mathbf{u} \cdot \nabla f = 0, \quad (7)$$

see Fig. 3 for illustration. One thus obtains a one-field formulation of the two-phase Navier-Stokes equations, namely

$$\rho (\partial_t \mathbf{u} + (\mathbf{u} \cdot \nabla) \mathbf{u}) = -\nabla p + \eta \Delta \mathbf{u} + \rho \mathbf{g} + \mathbf{f}_\Sigma. \quad (8)$$

The volume specific forces due to surface tension  $\mathbf{f}_\Sigma$  enter the model either by using the continuous surface force (CSF) [2] or stress (CSS) [19] formulation, i.e.

$$\mathbf{f}_\Sigma^{\text{CSF}} = \sigma \kappa_\Sigma \mathbf{n}_\Sigma \delta_\Sigma \quad \text{or} \quad \mathbf{f}_\Sigma^{\text{CSS}} = -\sigma \nabla \cdot (\delta_\Sigma (\mathbf{I} - \mathbf{n}_\Sigma \otimes \mathbf{n}_\Sigma)), \quad (9)$$

where  $\delta_\Sigma$  denotes the surface Dirac distribution. The control volumes for the velocity and pressure, respectively, admit a staggered (MAC) arrangement in the Cartesian grid. Combining the pressure-projection of [4] with a first-order temporal discretization, the convective terms are semi-linearized by an alternating permutation of directionally split transport, which ensures second-order accuracy [39]. In order to obtain reliable results, it is crucial to maintain a sharp interface throughout the simulation. Thus, the passive advection of the volume fractions, i.e. the time-integration of Eq. (7), is carried out geometrically [32]. Since the accuracy of initial volume fractions crucially affects the simulation outcome, the algorithm of [16] is employed. The details of the interface reconstruction are deferred to Sect. 3.1. In the CSF formulation for the surface tension, cf. Eq. (9), the curvature  $\kappa_\Sigma$  is obtained from height functions [29]. Figure 4 contains a flowchart of the procedure.

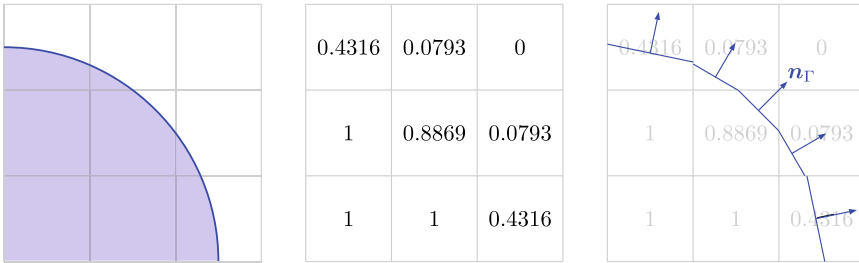


**Fig. 3** Physical phases on a Cartesian grid represented by volume fractions  $f$  with Piecewise Linear Interface Calculation (PLIC, [32])

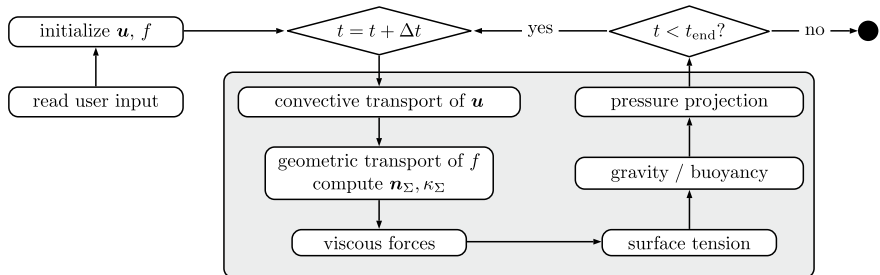


**Fig. 4** Schematic flowchart of solver Free Surface 3D

### 3.1 Efficient Interface Reconstruction

In geometric VOF methods, the interface reconstruction  $\Gamma$ , which is an approximation of the true interface  $\Sigma$  from volume fractions, constitutes a central element in terms of both accuracy of the method and consumption of computational resources. Since the physical phenomena under consideration feature highly dynamic deformations as well as a large amount of surface area, a robust and efficient method for the reconstruction of the interface from the volume fractions  $f$  is required. In the Piecewise Linear Interface Calculation (PLIC) approach, this task comprises the computation of the normal field and the positioning of a plane in each cell to match the associated volume fraction.

As observed in experiments and shown in Fig. 5, the presence of a third phase enriches the topological spectrum by thin films and contact lines, which requires a robust and efficient method to capture all possible topologies. In analogy to a liquid interacting with a solid particle, for the three-fluid configurations under consideration, the liquid with the lower surface tension (denoted *secondary*, index 2) towards the gaseous face always covers the one with the higher surface tension (denoted *primary*, index 1). Thus, a sequential reconstruction can be justified, i.e. the *primary* normal  $\mathbf{n}_{\Gamma,1}$  can be computed first and independently of the *secondary* normal  $\mathbf{n}_{\Gamma,2}$ , by resorting to the method of [43] employed for two-phase configurations. Figure 6



**Fig. 5** Results from an experimental study of the wetting behaviour reported in [41]. This study was performed in a cooperation of sub-projects A7, B1 and C4 together with D. Baumgartner and C. Planchette from TU Graz. 73% Glycerol- water solution (G73) (transparent) colliding with an other droplet (blue) of Bromonaphthalene (B) as a partially wetting liquid or Silicon Oil M5 (SOM5) as a fully wetting liquid. From left to right: G73 + B just before collision; G73 + SOM5 rim formation; G73 + B disc formation; G73 + B retraction of the contact line after collision (dewetting). The collisions finally show separation into two or multiple droplets

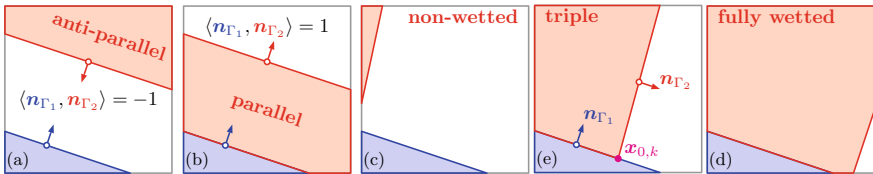


**Fig. 6** Three component topological configurations. From left to right: **a** anti-parallel, non-wetted interfaces, **b** parallel, fully-wetted interfaces, **c** independent non-wetted interfaces, **d** fully-wetted, layered interfaces, **e** interfaces with a contact line

illustrates the topological configurations, each of which is associated to a different scheme for the computation of the secondary normal  $\mathbf{n}_{\Gamma,2}$ . While the normal  $\mathbf{n}_{\Gamma,1}$  of the first component is obtained in the same way as in the two-phase case, the computation of  $\mathbf{n}_{\Gamma,2}$  is performed in a case-sensitive manner as follows [30]:

- Anti-parallel interfaces with a thin gas film in between:  $\mathbf{n}_{\Gamma,2} = -\mathbf{n}_{\Gamma,1}$
- Parallel interfaces, liquid film:  $\mathbf{n}_{\Gamma,2} = \mathbf{n}_{\Gamma,1}$
- Non-wetted, independent interfaces (gas film):  $\mathbf{n}_{\Gamma,2} = \nabla f_2$
- Fully wetted, layered interfaces (liquid film):  $\mathbf{n}_{\Gamma,2} = \nabla(f_1 + f_2)$
- Interfaces form a contact line with contact angle  $\theta$  (see [24]):

$$\mathbf{n}_{\Gamma,2} = \mathbf{n}_{\Gamma,1} \cos(\theta) + \frac{\nabla f_2 - (\mathbf{n}_{\Gamma,1} \cdot \nabla f_2) \mathbf{n}_{\Gamma,1}}{\|\nabla f_2 - (\mathbf{n}_{\Gamma,1} \cdot \nabla f_2) \mathbf{n}_{\Gamma,1}\|} \sin(\theta)$$

- Two component cells with liquid 1 truncating the liquid 2's reconstruction stencil: Treatment like three component cells (a-e).

A sequential positioning of the PLIC planes, which is described below, is performed such that the volume fractions are each enclosed. The correct orientation is determined in three steps:

1. The number of neighbouring cells are counted, in which an enclosed volume fraction as well as the true volume fraction  $f_2$  are 1. The enclosed volume fraction results from an extension of the PLIC plane in cell  $(i, j, k)$  to its neighbours. The orientation with the maximum count is chosen.
2. If two orientations have the same count in step 1, the minimum of

$$g_{i,j,k}(\mathbf{n}_{\Gamma,2}) = \sum_{i^*=i-1}^{i+1} \sum_{j^*=j-1}^{j+1} \sum_{k^*=k-1}^{k+1} (f_{2,i^*,j^*,k^*} - f_{p,i^*,j^*,k^*}(\mathbf{n}_{\Gamma,2}))^2 \quad (10)$$

is employed (similar to [25]) as a second criterion for the decision, which orientation yields the true topology. The predicted volume fraction  $f_p$  is again computed in all neighbouring cells.

3. A topology check is performed. If the topological properties are not as assumed, the orientation is not chosen.

This method of computing the interfaces normals is explicit, thus relatively fast, and allows the reconstruction of thin liquid or gas films. Before Eq. (10) can be evaluated, the secondary PLIC interface must be positioned to match the associated volume fraction. With the discrete fields of approximative normals  $\mathbf{n}_{\Gamma,i}$  at hand, positioning the PLIC planes in a cell translates to finding the unique root of a scalar monotonous function, namely the truncated cell volume. By exploiting the Gaussian divergence theorem in combination with a joint co-moving coordinate origin  $\mathbf{x}_0$ , the truncated volume is conveniently parametrized in terms of the signed distance as a sum of face-based quantities. This is favourable in terms of general applicability and allows to restrain from the costly extraction of topological connectivity at runtime. By assigning to each face (index  $k$ ) of the original cell an individual origin  $\mathbf{x}_{0,k}$  (co-moving with the intersection of the PLIC planes; cf. Fig. 6), the volume computation can be extended to the three-phase case, where the computational cells are truncated twice. The full mathematical details can be found in [18]. In both cases, the derivatives of the volume function, which are exploited in a higher-order root finding scheme, can be obtained at negligible cost. With the polyhedron truncation and volume computation being decisive for the computational effort, the developed approach was shown to be highly efficient. On average, only one to two truncations are required to position the plane, outperforming existing methods. Further information concerning the performance assessment for an extensive set of polyhedrons, volume fractions and normal orientations can be found in [17], along with comprehensive description of the algorithm. Ongoing research aims at embedding the developed volume computation into a minimization-based scheme to improve the estimation of the normal fields  $\mathbf{n}_{\Gamma}$  from volume fraction data  $f$ . The above described non-iterative topology-capturing algorithm for the orientation and the efficient positioning are the basis for simulations of immiscible liquids.

### 3.2 Surface Forces for the Collision of Immiscible Liquids

During the collision of immiscible liquids, thin films of the outer liquid 2 spread over the inner liquid 1 which has the higher surface tension  $\sigma_{13}$  towards the continuous phase 3, cf. Fig. 5. The wetting behaviour in droplet collisions of two immiscible liquids 1 and 2 is governed by the interfacial tensions and is described by the spreading parameter  $S = \sigma_{13} - \sigma_{23} - \sigma_{12}$  [27]. In case of  $S > 0$ , liquid 2 fully wets liquid 1, while partial wetting occurs if  $S < 0$ . In Sect. 3.1 it was already discussed that the reconstruction of various topologies of three-component situations are to be captured correctly in numerical simulations of collision processes of immiscible liquids. The modelling of the surface forces is equally affected, as the surface forces are modelled utilising the volume fractions' gradients which are truncated for liquid 2. The CSS model, cf. Eq. (9), employs the interface normals

$$\tilde{\mathbf{n}}_\Gamma = \frac{\nabla \tilde{f}}{||\nabla \tilde{f}||} \quad (11)$$

and the approximation of the surface Dirac distribution

$$\tilde{\delta}_\Gamma = ||\nabla \tilde{f}||. \quad (12)$$

The normals of the interfaces are approximated analogously to the two-phase PLIC algorithm, but applied to a quadratically smoothed volume fraction field  $\tilde{f}$ . Compared to calculations of the surface Dirac distributions from the PLIC planes' areas, much smoother results are obtained by the approximation according to Eq. (12), as the discretisation effect is lower, cf. [19]. The acceleration due to the surface forces, i.e.

$$(\partial_t \mathbf{u})_\Gamma = \frac{2}{\rho_1 + \rho_3} \mathbf{f}_\Gamma^{\text{CSS}}, \quad (13)$$

results from a scaling with the average density at the interface, which again avoids an influence of the discretisation. The use of a local density proved insufficient in multiple studies with FS3D. A physical reasoning for this might be that the surface force is acting very locally. This becomes important for the extension of the CSS model to immiscible liquids, cf. [30]. This extension is facilitated by introducing partial surface tensions  $\gamma_i$ , following the idea of [15, 38]. The interfacial tensions between component  $i$  and  $j$ ,

$$\sigma_{ij} = \gamma_i + \gamma_j, \quad (14)$$

are described as sums of the partial surface tensions  $\gamma_i$ . For the further discussion, index 1 denotes the inner liquid, 2 the covering liquid and 3 the gaseous continuous phase. For the superposition of the interfaces' contributions, the capillary pressure tensor, cf. [19],

$$\mathbf{T}_i = -\nabla \cdot (\tilde{\delta}_\Gamma (\mathbf{I} - \tilde{\mathbf{n}}_\Gamma \otimes \tilde{\mathbf{n}}_\Gamma)) \quad (15)$$

is computed for each component to retrieve the resulting acceleration

$$(\partial_t \mathbf{u})_\Gamma = \frac{1}{\rho} \sum_{i=1}^3 \gamma_i \mathbf{T}_i. \quad (16)$$

A virtual volume fraction field of liquid 2 is constructed in the vicinity of three component cells to obtain a sufficient stencil for the smoothing of the volume fractions. It is extrapolated from the PLIC interfaces at the contact line. The orientations  $\tilde{\mathbf{n}}_{\Gamma,i}$  and the approximated surface Dirac distributions  $\tilde{\delta}_{\Gamma,i}$  are computed with Eqs. (11) and (12) for the respective phase. The information of the interfaces present is necessary for the choice of the scaling density

$$\rho = \begin{cases} 0.5(\rho_1 + \rho_3) & \text{in 3 component cells in the smoothed field,} \\ 0.5(\rho_i + \rho_j) & \text{in 2 component cell with smoothed } i-j\text{-interface,} \end{cases} \quad (17)$$

employed to calculate the accelerations. As the topology information is not available inside the smoothed field, the information from the unsmoothed field is used to identify cells with a thin film. For all other cells, the information of the smoothed volume fractions is used to identify the interfaces present. This leads to a non-smoothing approach in cells with a thin film and is identical to the original CSS model everywhere else. Like for the reconstruction, additional modelling of the surface forces at thin liquid films is necessary. In cells with a thin film of liquid 2 covering liquid 1 and cells with a contact line, which is surrounded by such liquid film cells, the accelerations are chosen as

$$(\partial_t \mathbf{u})_{\Gamma,\text{film}} = \frac{2}{\rho_3 + \rho_1} (\gamma_1 + 2\gamma_2 + \gamma_3) \mathbf{T}_1, \quad (18)$$

assuming that the interfaces are parallel to each other and the film is very thin. The interface of the covering liquid reduces the interfacial tension compared to the two component case. The thin film does not act like a liquid-liquid interface yet. Therefore, the surface force scales with the inner liquid's density jump towards the gaseous phase 3. This choice of the density strongly affects the collision outcome of two immiscible liquid droplets. The choice of the density in three component cells according to Eq. (17) is motivated by the results presented in Sect. 4. The analysis for the collision of fully wetting liquids has shown that the modelling of the surface forces is very delicate. Simulations of the partial wetting behaviour qualitatively yield the expected behaviour with this choice of the scaling density. However, for partial wetting, no suitable experimental validation data could be found in the literature.

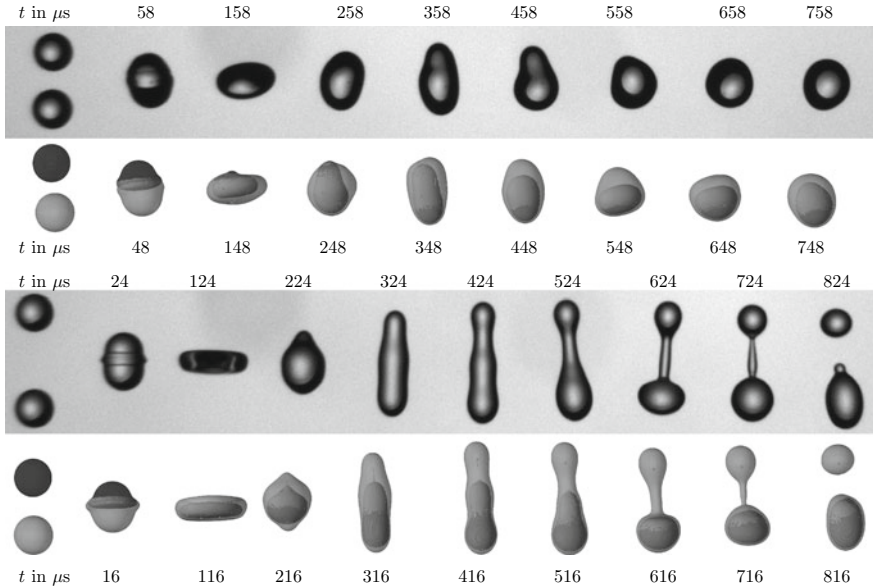


**Fig. 7** Simulation of the interaction of 50% glycerol solution (dark) and the silicon oil M5 (light) compared to experimental results [27]. Top: Coalescence:  $D_1 = 187 \text{ mm}$ ,  $B = 0.089$ ,  $U_{\text{rel}} = 1.98 \text{ m/s}$ ; Bottom: Crossing separation:  $D_1 = 189 \text{ mm}$ ,  $B = 0.014$ ,  $U_{\text{rel}} = 3.71 \text{ m/s}$ . Both:  $D_2 = 195 \text{ mm}$ ,  $6.25 \mu\text{m}/\text{cell}$ . Pictures of experiments by courtesy of C. Planchette

## 4 Droplet Collisions of Immiscible Liquids

In Sects. 3.1 and 3.2, a topology-capturing PLIC method as well as a film stabilisation CSS method were presented. With those new methods, numerical simulations of droplets of two immiscible liquids were enabled in FS3D. A comparison to experiments of near head-on coalescence as well as crossing separation of equally sized droplets of silicon oil M5 and a 50% glycerol-water solution are shown in Fig. 7. The visualisation of the PLIC interfaces was enabled by a Paraview plugin developed in sub-project A1, see Heinemann et al. [in this volume](#). Gravitation is omitted in the simulations due to limitations of the computational domain size at an adequate resolution. Both cases shown are near head-on collision, but no symmetry is imposed in the algorithm. The film stabilisation in both the reconstruction as well as the CSS model enable the simulation of fully wetting liquids, where a thin film of the outer liquid covers the inner liquid. The choice of the density, which scales the interfacial forces, is essential to capture the collision outcomes. Also the smoothing has to be done carefully: In the simulations shown in Fig. 7, one smoothing step was sufficient. With half the resolution, no smoothing at all showed the best results, but at a higher resolution, the number of smoothing steps had to be increased to counteract the refinement. A detailed analysis of this preliminary finding is necessary with further increase of the resolution enabled by parallelisation of the algorithm. The successful

comparison to experimental data shows that the methods utilised for the simulation of immiscible droplet collisions are valid. This enables future studies on the influence of the geometry parameters and fluid properties on the collision outcome of fully wetting immiscible liquid droplet collisions. According to [41], the influence of the wetting behaviour plays an important role for the collision morphology and outcome. Further investigations of the contact line modelling are therefore necessary for partially wetting droplets. This is planned as soon as sufficient experimental validation data is available across different collision regimes.

## 5 Bouncing Versus Coalescence

Under standard ambient conditions, the regime transition from bouncing to coalescence (II→III, cf. Fig. 2) occurs around the critical Weber number  $We_{\text{crit}} \approx 13.63$  [28]. The critical distance between the colliding droplets is in the order of 10 nm and the mean free path of gas molecules  $\lambda$  is about 100 nm.

Since the head-on collision process can be considered symmetrical, cf. Fig. 8, the computational effort can be significantly reduced by numerically replacing one of the droplets by a mirror droplet via a collision plane. With gas film thicknesses  $h \approx \lambda$  to be expected, however, a full spatial resolution of the problem remains infeasible due to the viscous time step limit. In order to correctly account for the effect of the thin gas film, a subgrid scale model was applied at the collision plane. Note that, while the thickness of the gas film between the droplets becomes very small during the collision process, the lateral film extension permits the application of a continuum model. Indeed, the so-called lubrication approximation is valid and was shown to accurately capture the relevant physics [12]. For a given film thickness  $h$ , the pressure  $p$  is governed by

$$\nabla \cdot \left( \left( \frac{h^3}{3} + C_1 \lambda h^2 + C_2 \lambda^2 h \right) \nabla p \right) = \eta \left( \partial_t h + \nabla \cdot (h \mathbf{u}^\Sigma) \right), \quad (19)$$

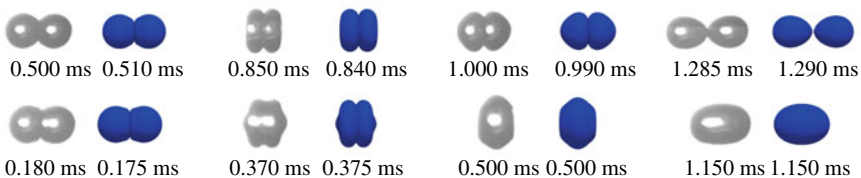


**Fig. 8** Comparison of experiments (gray, reproduced from [23] with permission, Copyright by AIP Publishing) and direct numerical simulation (blue, [21]) for bouncing (top row,  $We = 9.33$ ,  $Re = 110.36$ ) and coalescence (bottom row,  $We = 13.63$ ,  $Re = 134.24$ ) of binary droplets for varying time instances

where  $\mathbf{u}^\Sigma = [u^\Sigma, v^\Sigma]^\top$  denotes the lateral interface velocity and the coefficients  $C_i$  account for the slip of the lateral velocity at the collision plane [6]. At the lateral boundary of  $\Omega_{\text{gap}}$ , Dirichlet boundary conditions for the pressure are applied. The local film thickness  $h$  is obtained from the volume fractions in the three cell layers above the collision plane, and determines the dynamic extension of the lubrication domain. E.g., for a collision plane with normal  $\mathbf{e}_z$  and base point  $(0, 0, z_{\text{lub}})$ , one obtains

$$\Omega_{\text{gap}}(t; z_{\text{lub}}) := \{(x, y) \in \mathbb{R}^2 : (x, y, z_{\text{lub}}) \in \Omega \text{ and } h(t; x, y) \leq h_{\text{lub}}\}, \quad (20)$$

where  $h_{\text{lub}}$  is chosen to cover two to three layers of cells. The numerical investigations were conducted resorting to two realisations of the collision plane.

## 5.1 Collision with a Symmetry Plane

Aiming at the numerical prediction of transition, we have conducted numerical investigations for a series of Weber numbers between 7.77 and 18.8 [21]. As stated above, the binary collision numerically corresponds to a single droplet colliding with the domain boundary, where symmetry conditions were applied for the velocity. This approach was found to be very well suited for capturing the physics for prescribed collision outcome, cf. again Fig. 8. The procedure works as follows: once the film thickness  $h$  reaches a certain threshold ( $\approx 3$  cells), the surface forces exerted by the mirrored interface induce an artificial rupture of the gas film, yielding coalescence for all  $We$ . If the symmetry of the volume fraction field is replaced by a Dirichlet condition for the volume fractions, for analogous reasons, one always obtains only bouncing. Thus, switching between these two strategies at some user-defined time (if the gas film is sufficiently thin), allows to compute the desired outcome. For an unspecified collision outcome, however, no convergence with mesh refinement could be obtained. Above some threshold resolution, only bouncing was observed in the numerical simulations of configurations for which experiments show coalescence. It was found that the minimum gap height ( $\approx 200$  nm) did not reach physically reasonable levels ( $\approx 70$  nm), thus inhibiting coalescence. From a follow-up series of numerical experiments and comparison to [5], it was conjectured that this numerical artifact is caused by imposing symmetry boundary conditions at the collision plane, suggesting to shift the collision plane into the interior of the computational domain.

## 5.2 An Artificial Interior Collision Plane

For the collision with the domain boundary described above, the lubrication pressure was coupled to the flow solver in two steps: after the original time stepping scheme shown in Fig. 4 is performed, the bulk pressure at the boudary of  $\Omega_{\text{gap}}$  serves as a

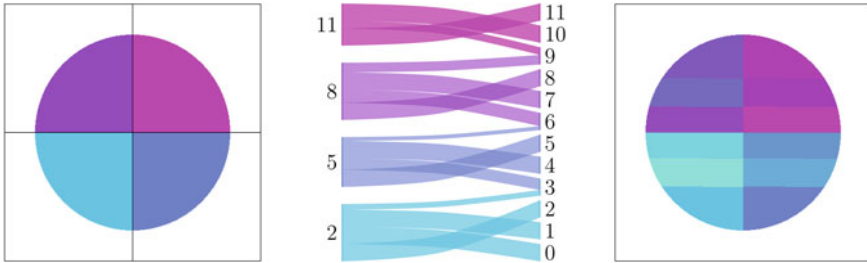


**Fig. 9** Initial distribution of degrees of freedom (left, involving only 4 of 12 processors), load balancing scheme and balanced distribution (involving all processors) (illustrated for the configuration of Fig. 10, where the colors correspond to the individual processors)

Dirichlet boundary condition for Eq. (19). Since  $\Omega_{\text{gap}} \subset \partial\Omega$ , the resulting lubrication pressure is then in turn applied as a boundary condition for the pressure projection in the bulk, such that applying the resulting gradient ensures a divergence-free velocity. An internal collision plane, i.e.  $\Omega_{\text{gap}} \not\subset \partial\Omega$  (left panel in Fig. 10), however, requires two modifications: firstly, the lubrication pressure cannot be prescribed as boundary condition for the bulk pressure. Instead, the lubrication pressure exerts a surface force (analogous to the CSF-model for the surface tension, cf. Sect. 3). Secondly, in preliminary numerical experiments, it was found that employing an intermediate bulk pressure as a local boundary condition for the lubrication equations induces numerical noise. In order to alleviate this influence, by taking into account the rotational symmetry, the local values are replaced by an average, say  $p_{\text{BC}}$ , over the boundary of  $\Omega_{\text{gap}}$ . Equation (19) translates into a linear system whose solution is computed by a standard GMRES scheme [35]. The drawing in Fig. 10 (top-left) illustrates that, as a result of the Cartesian domain decomposition of the flow solver FS3D, the collision plane only intersects a subset of the parallel processes. Furthermore, the domain  $\Omega_{\text{gap}}$ , within which the lubrication equation is solved, dynamically deforms along with the flattening of the droplet, implying potentially large spatial load imbalances. For an efficient solution, a load balancing scheme for deformable domain was designed and implemented. Figure 9 illustrates the concept. In comparison to the Gauss-Seidel-type approach of Sect. 5.1, the computational effort was reduced significantly.

While the droplet deformation in Fig. 10 qualitatively coincides with the top row in Fig. 8 (collision with domain boundary), the modified subgrid-scale model allows to additionally obtain physically reasonable minimum film thicknesses for an appropriate choice of  $p_{\text{BC}}$ , even for a very coarse spatial resolution; see the diagram in Fig. 10 (top-right). However, recall that the boundary condition  $p_{\text{BC}}$  resorts to the bulk pressure, whose absolute value does not necessarily carry any physical meaning for incompressible flows, since only the gradient is employed for the projection; cf. Fig. 4. Contrary, the lubrication pressure enters the model directly. Thus, any offset strongly influences the simulation outcome and a consistent intrinsic choice of  $p_{\text{BC}}$  is subject of ongoing research.

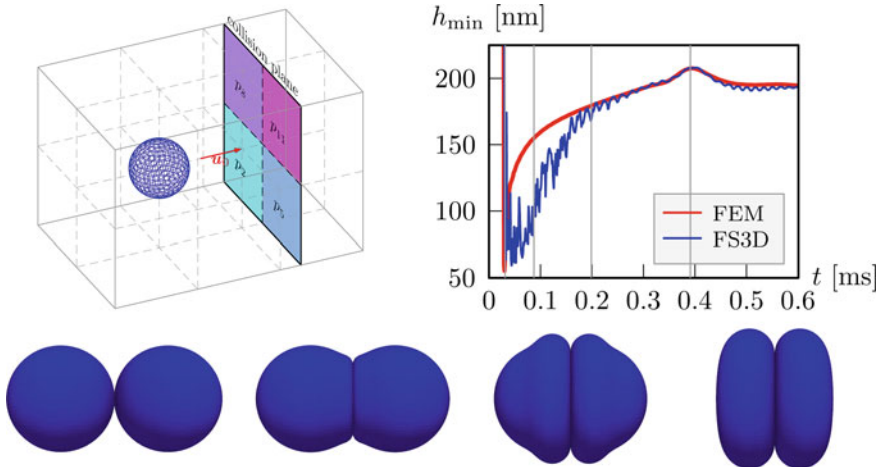


**Fig. 10** Illustration of interior collision plane with processors (left) and minimum film thickness over time (right;  $We = 3.47$ ; FEM: courtesy of M. Chubynsky) with vertical lines corresponding to the instants shown in the bottom row

## 6 Spattering Collisions at High Weber Numbers

In high energetic head-on collisions of two droplets with the same diameters and material properties ( $We \geq \mathcal{O}(100)$ ), the rim of the collision complex formed on the collision plane becomes increasingly unstable with increasing Weber numbers [34]. If the Weber number is high enough, it yields substantial disintegration into secondary droplets. In order to prevent the thin liquid lamella emerging at high energy collisions from unphysical rapture, the stabilisation method of [9] has been further improved [20]. With this approach, interface tension forces are correctly calculated also at liquid interfaces with a neighbouring, additional interface. Since the numerical simulation of binary droplet collisions at high Weber numbers requires a high grid resolution, a domain adjustment technique based on [8] can be used to reduce the computational effort. With a small white noise disturbance (1% of the initial relative velocity of the droplets) exerted to the initial velocity field, simulation results are in excellent agreement with the corresponding experiments for  $We = 443$  [20]. A comparison of the results is reproduced in Fig. 11. These high-resolution calculations offer detailed insights into areas of the collision complex that are not accessible with experimental methods. Furthermore, the comparison of a Fast-Fourier Transform analysis (FFT) combined with statistical techniques applied to the VOF simulation's results with theoretical predictions based on [44] revealed that the rim instability in binary droplet collisions is completely dominated by the Plateau-Rayleigh instability [20].

Simulations of binary droplet collisions at still higher Weber number ( $We = 805$  in the following) require even higher grid resolutions. Grid independence studies need to be performed to determine the necessary resolution. The white noise signal imposed

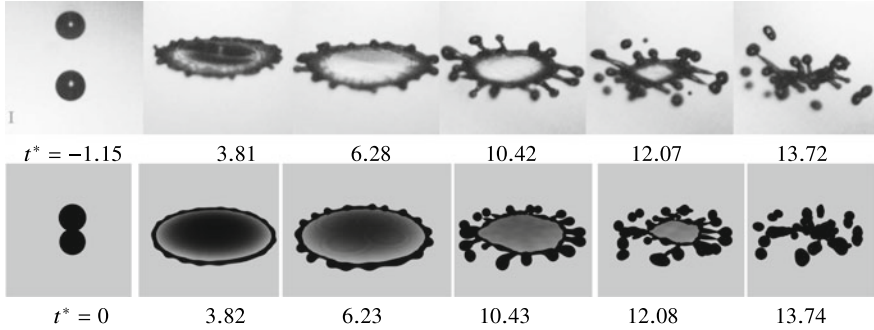


**Fig. 11** Comparison of experiment (top, [22]. Reprinted with permission, Copyright by the American Physical Society) and direct numerical simulation (bottom, [20]) for head-on collision of binary droplet at  $We = 443$  and  $Re = 6207.3$

on the velocity field as initial disturbance, however, is grid-dependent as higher frequencies are resolved on a finer grid. Therefore, a function for the description of the initial disturbance which can be transferred to equidistant grids of different resolution is constructed. This function should have the non-regular structure of a white or coloured noise signal and consider all spatial directions equally. In [36], a first idea of this function has been presented and is given here in more detail. The noise function, written exemplarily for the first component,

$$u_{\text{noise}}(\tilde{x}_1, \tilde{x}_2, \tilde{x}_3) = A \sum_{i=0}^{I_{\max}/3} \sum_{k=0}^5 \prod_{l=1}^3 \cos((3i + \pi_{k,l}) \Phi \tilde{x}_l (1 + a R_{6i+k}) + \omega_{6i+k}) \quad (21)$$

is imposed on each component of the velocity field, where  $\pi_{k,l}$  refers to the l-th component of the k-th permutation of (1,2,3). The spatial coordinates are normalised by multiplication with  $2\pi$  and division by the maximum length of the computational domain. The imposed disturbance is normalised by  $A := \frac{1}{2} \|\mathbf{u}_{\text{noise}}\|$ . Due to the multiplication with a random number  $R_k \in [-1, 1]$ , the summands are incommensurable with probability 1; thus, a regular structure of the noise signal is avoided. The factor  $a \in ]0, 1[$  prevents the suppression of individual frequencies, for example in case of  $R_k = -1$ . The addition with random numbers  $\omega_k \in [0, 2\pi]$  in the argument of the cosine function prevents a local amplification of the signal. The factor  $\Phi \in ]0, 1[$  allows the representation of intermediate frequencies. The maximum frequency that can be represented is determined by the cell width. According to sampling theory, to reproduce a signal with the maximum frequency  $f_{\max}$ , the sampling frequency must be more than twice as high [37]. Thus, the maximum representable frequency in the normalised domain  $f_{\max} \leq N/2$ , where  $N$  is the number of grid cells in the direction of the largest extension of the computational domain. The largest possible frequency in the argument of the cosine function is  $\bar{f}_{\max} = (I_{\max} + 2)\Phi(1 + a)$ . The upper limit of the sum (21) can thus be expressed as

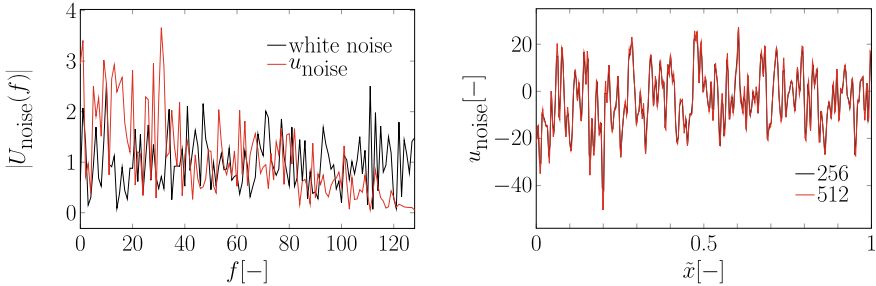


**Fig. 12** The noise signal  $u_{\text{noise}}(\tilde{x}_1, \tilde{x}_2, \tilde{x}_3)$  resolved on a  $256 \times 256 \times 64$  grid reveals a frequency spectrum which is comparable to the one of the white noise signal (left) and can be transferred to higher grid resolution,  $512 \times 512 \times 128$  (right); factor  $a = 0.95$ ,  $\Phi = 0.1$

$$I_{\max} \leq 3 \left\lfloor \frac{1}{3} \left( \frac{N}{2\Phi(1+a)} - 2 \right) \right\rfloor. \quad (22)$$

To evaluate the  $6I_{\max}/3$  summands per spatial direction,  $12I_{\max}$  random numbers are required. To validate the noise function, the comparison of the frequency spectrum of  $u_{\text{noise}}(\tilde{x}_1, \tilde{x}_2, \tilde{x}_3)$  with the spectrum of the previously used perturbation on a  $256 \times 256 \times 64$  grid is shown in Fig. 12 (left). The signal  $u_{\text{noise}}$  is normalised here by the factor  $u_{\text{var}}/\tilde{A}$ , where  $u_{\text{var}}$  is the variance of the original disturbance function,  $\tilde{A}$  the arithmetically averaged amplitude of the disturbance function  $u_{\text{noise}}$ . Furthermore, the noise signal with a maximum frequency corresponding to the grid resolution  $256 \times 256 \times 64$  is transferred to disturb the initial velocity field on a grid with twice as many nodes in each direction (cf. Fig. 12 (right)). The agreement between the two disturbance signals is excellent.

A grid convergence study was performed for droplet collisions with  $We = 805$ . Using symmetry conditions, the problem could be reduced to a quarter of a droplet. Its radius has been resolved by  $0.11N_x$  cells in a domain of  $N_x \times N_x \times N_x/4$ , where  $N_x \in (512, 1024, 2048)$ . However, the results do not yet show convergence. The collision complex initially spreads faster on grids with higher resolution. This finding indicates that there are additional physical effects on the smallest time scales that are not yet understood. One such effect might be the ageing of the interface. For further analysis we benefit from detailed insights into the evolution of the collision complex, the growth of liquid fingers on the rim and the detachment of secondary droplets. Figure 13 (left) shows the velocity field at time  $t = 0.54$  ms, where the first drops have already detached. Fluid is still flowing from the disc into the rim at high velocity. The detailed view of the rim region in Fig. 13 (center) illustrates that the viscous dissipation in the fluid is very high in a narrow transition region. The detailed view in Fig. 13 (right), which shows the pressure field in the area of the rim, confirms that fluid is flowing from the disc into the rim. The constrictions between two adjacent finger-forming structures are also characterised by a reduced pressure. This causes them to grow together, whereas the high pressure in the area of the depicted single finger structure increases its growth in subsequent timesteps.

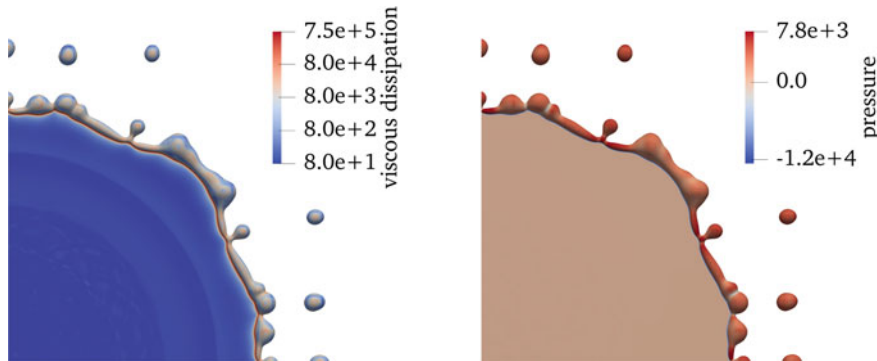


**Fig. 13** Top view on spreading collision complex at  $t = 0.54$  ms. The rate of local viscous dissipation ( $\text{kg m}^{-2} \text{s}^{-3}$ , left) and the pressure difference to the ambience ( $\text{kg m}^{-1} \text{s}^{-2}$ , right) are mapped onto the contour plot  $f = 0.5$

## 7 Conclusions

This project within the SFB-TRR75 was driven by the desire to understand small-scale phenomena in binary droplet collisions as a basis for new and improved multi-scale models of larger processes, which involve droplets under extreme conditions. The investigations' concern were droplet collisions with immiscible liquids, the rim instability during spattering collisions at high Weber numbers and the regime transition between bouncing and coalescence in head-on collisions. In each of these different scenarios, the collision process is of multi-scale nature in itself: For collisions of immiscible liquids, triple lines and thin films of the two interacting liquids and ambient gas are present. The local forces in the vicinity of the triple line determine the overall collision outcome. Looking at collisions at high Weber numbers a liquid rim develops corrugations, which grow into liquid fingers and eventually pinch off to form satellite droplets. At the same time the rim is contracted by the surface tension forces of the extremely thin liquid lamella. Droplets approaching each other at low Weber numbers expel the thin gas film in the gap between the droplets. Coalescence can only occur if the Van-der-Waals forces come into action at gap thicknesses below 100 nm, a scale at which the flow in the gas film can be described by the rarefied flow equations and slip between gas and liquid becomes relevant. To allow for valid and accurate numerical simulations of such collision processes, the capabilities of the Volume-of-Fluid method were enhanced with new approaches like an efficient and topology-capturing PLIC algorithm for three immiscible volume fractions, an enhanced lamella detection and stabilisation algorithm for head-on collisions as well as a subgrid-scale model for computing the pressure in thin gas films based on lubrication approximation. However, due to the multi-scale character of the phenomena during droplet collisions, sufficient grid resolution remains a challenge: The collision outcome for immiscible droplets strongly depends on the modelling of the surface forces, where the mesh resolution and the choice of the

scaling density proved to be important. However, the described methods enable a detailed calculation of droplet collisions of immiscible liquids also for asymmetric collisions. Also high energetic droplet collisions reveal a strong influence of the grid resolution. Direct Numerical Simulations were employed there to rigorously show that the Plateau-Rayleigh instability pattern dominates the rim instability - this is valuable for the development of analytical models for predicting the onset of spatter and the secondary droplets' spectrum. Moreover, experimentally inaccessible data such as the local dissipation rates in the liquid throughout the collision process were obtained. Some challenges remain, caused by the multi-scale and multi-physical character of droplet collisions under extreme conditions. Predicting the transition between bouncing and coalescence, rather than computing the fine details retrospectively, still requires a more consistent coupling between the different solvers for the different governing equations, and a two-phase subgrid-scale modelling seems promising. A challenge of general nature is the simulation of flow instabilities, since the latter act as amplification systems, highly sensitive to disturbances in the fields. At this point, the introduction of carefully computed artificial noise is a key step enabling further research. Last, but not least, numerical simulations are restricted to the physics included in the underlying mathematical models. Here, we found indications for additional dissipative mechanics, being present in the experiments but not in the numerical simulations. Such discrepancies occur, if new surface area is generated at high local rates. This poses another extreme condition which deserves further investigation. To conclude, analysing binary droplet collisions on the small scales enhances the understanding and modelling applied on larger scales which enable predictions ranging from spray processes to weather forecast.

**Acknowledgements** The authors gratefully acknowledge financial support provided by the German Research Foundation (DFG) within the scope of SFB-TRR 75 (project number 84292822). Some calculations for this research were conducted on the Lichtenberg high performance computer of the TU Darmstadt and on the national supercomputer HPE Apollo (Hawk) at the High-Performance Computing Center Stuttgart (HLRS) under the grant no. FS3D/11142. The authors kindly acknowledge the granted computational time and support.

## References

1. Al-Dirawi KH, Bayly AE (2020) An experimental study of binary collisions of miscible droplets with non-identical viscosities. *Exp Fl* 61:50
2. Brackbill J, Kothe D, Zemach C (1992) A continuum method for modeling surface tension. *J Comp Phys* 100:335–354
3. Chen RH, Chen CT (2006) Collision between immiscible drops with large surface tension difference: diesel oil and water. *Exp Fl* 41:453–461
4. Chorin A (1968) Numerical solution of the Navier-Stokes equation. *Math Comp* 22:745–762
5. Chubynsky M, Belousov K, Lockerby D, Sprittles J (2020) Bouncing off the walls: the influence of gas-kinetic and van der Waals effects in drop impact. *Phys R L* 124:084501
6. Dongari N, Agrawal A, Agrawal A (2007) Analytical solution of gaseous slip flow in long microchannels. *IJ Heat Mass Trans* 50(17):3411–3421

7. Eisenschmidt K, Ertl M, Gomaa H, Kieffer-Roth C, Meister C, Rauschenberger P, Reitzle M, Schlottke K, Weigand B (2016) Direct numerical simulations for multiphase flows: an overview of the multiphase code FS3D. *App Math Comp* 272:508–517
8. Focke C (2013) Direkte numerische simulation binärer kollisionen newtonscher und nichtnewtonscher tropfen. Ph.D. thesis, TU Darmstadt
9. Focke C, Bothe D (2011) Computational analysis of binary collisions of shear-thinning droplets. *J Non-Newton Fl Mech* 166:799–810
10. Focke C, Kuschel M, Sommerfeld M, Bothe D (2013) Collision between high and low viscosity droplets: direct numerical simulations and experiments. *DIJ Multi Fl* 56:81–92
11. Gao TC, Pu JY, Lin TH, Chen RH (2005) Collision between an ethanol drop and a water drop. *Exp Fl* 38:731–738
12. Hamrock BJ, Schmid SR, Jacobson BO (2004) Fundamentals of fluid film lubrication. Taylor & Francis
13. Hirt C, Nichols B (1981) Volume of Fluid (VOF) method for the dynamics of free boundaries. *J Comp Phys* 39:201–225
14. Jiang Y, Umemura A, Law C (1992) An experimental investigation on the collision behaviour of hydrocarbon droplets. *J Fl Mech* 234:171–190
15. Joubert N, Gardin P, Zaleski S, Popinet S (2020) Modelling of mass transfer in a steelmaking ladle. In: 14th international conference on CFD in oil & gas, metallurgical and process industries
16. Kromer J, Bothe D (2019) Highly accurate computation of volume fractions using differential geometry. *J Comp Phys* 396:761–784
17. Kromer J, Bothe D (2022) Face-based volume-of-Fluid interface positioning in arbitrary polyhedra. *J Comp Phys* 449:110776
18. Kromer J, Potyka J, Schulte K, Bothe D (2021) Efficient three-material PLIC interface positioning on unstructured polyhedral meshes. [arXiv:2105.08972](https://arxiv.org/abs/2105.08972)
19. Lafaurie B, Nardonne C, Scardovelli R, Zaleski S, Zanetti G (1994) Modelling, merging and fragmentation in multiphase flow with surfer. *J Comp Phys* 113:134–147
20. Liu M, Bothe D (2016) Numerical study of head-on droplet collisions at high Weber numbers. *J Fl Mech* 789:785–805
21. Liu M, Bothe D (2019) Toward the predictive simulation of bouncing versus coalescence in binary droplet collisions. *A Mech* 230(2):623–644
22. Pan KL, Chou PC, Tseng YJ (2009) Binary droplet collision at high weber number. *Phys R E* 80:036301
23. Pan KL, Law C, Zhou B (2008) Experimental and mechanistic description of merging and bouncing in head-on binary droplet collision. *J App Phys* 103(6):064901
24. Patel H, Das S, Kuipers J, Padding J, Peters E (2017) A coupled volume of fluid and immersed boundary method for simulating 3D multiphase flows with contact line dynamics in complex geometries. *Chem Eng Sci* 166:28–41
25. Pathak A, Raessi M (2016) A three-dimensional Volume-of-Fluid method for reconstructing and advecting three-material interfaces forming contact lines. *J Comp Phys* 307:550–573
26. Planchette C, Hinterbichler H, Liu M, Bothe D, Brenn G (2017) Colliding drops as coalescing and fragmenting liquid springs. *J Fl Mech* 814:277–300
27. Planchette C, Lorenceau E, Brenn G (2011) Binary collisions of immiscible liquid drops for liquid encapsulation. *FDMP* 7(3):279–301
28. Poo J, Ashgriz N (1990) Coalescence and separation in binary collisions of liquid drops. *J Fl Mech* 221:183–204
29. Popinet S (2009) An accurate adaptive solver for surface-tension-driven interfacial flows. *J Comp Phys* 228(16):5838–5866
30. Potyka J, Schulte K (2021) New approaches for the interface reconstruction and surface force computation for volume of fluid simulations of droplet interaction of immiscible liquids. [arXiv:2104.11108](https://arxiv.org/abs/2104.11108)
31. Qian J, Law CK (1997) Regimes of coalescence and separation in droplet collision. *J Fl Mech* 331:59–80
32. Rider W, Kothe D (1998) Reconstructing volume tracking. *J Comp Phys* 141:112–152

33. Rieber M (2004) Numerische Simulation der Dynamik freier Grenzflächen in Zweiphasenströmungen". Ph.D. thesis, Universität Stuttgart
34. Roth N, Rabe C, Weigand B, Feuillebois F, Male J (2007) Droplet collision outcomes at high Weber number. In: Proceedings of the 21st ILASS—Europe meeting. Mugla
35. Saad Y (2003) Iterative methods for sparse linear systems, 2nd edn. SIAM, Philadelphia, PA, USA
36. Schulte K, Weigand B, Tropea C (2018) Selected results of the collaborative research center "Droplet dynamics under extreme ambient conditions SFB-TRR 75". In: ICLASS 2018
37. Shannon C (1949) Communication in the presence of noise. Proc IRE 37(1):10–21
38. Smith K, Solis F, Chopp D (2002) A projection method for motion of triple junctions by level sets. Interface Free Bound 4:263–276
39. Strang G (1968) On the construction and comparison of difference schemes. SIAM J Num Anal 5:506–517
40. Wang C, Lin C, Hung WG, Huang WC, Law CK (2004) On the burning characteristics of collision-generated water/hexadecane droplets. Comb Sci Tech 176(1):71–93
41. Weigand B, Schulte K, Tropea C (2021) Selected results of the collaborative research center "Droplet dynamics under extreme ambient conditions SFB-TRR 75". In: ICLASS 2021
42. Yarin AL (2006) Drop impact dynamics: splashing, spreading, receding, bouncing. Ann R Fl Mech 38(1):159–192
43. Youngs D (1982) Time-dependent multi-material flow with large fluid distortion. Numerical methods for fluid dynamics, vol 24. Academic Press, New York, pp 273–285
44. Zhang L, Brunet P, Eggers J, Deegan R (2010) Wavelength selection in the crown splash. Phys Fl 22(12):122105–122109

**Open Access** This chapter is licensed under the terms of the Creative Commons Attribution 4.0 International License (<http://creativecommons.org/licenses/by/4.0/>), which permits use, sharing, adaptation, distribution and reproduction in any medium or format, as long as you give appropriate credit to the original author(s) and the source, provide a link to the Creative Commons license and indicate if changes were made.

The images or other third party material in this chapter are included in the chapter's Creative Commons license, unless indicated otherwise in a credit line to the material. If material is not included in the chapter's Creative Commons license and your intended use is not permitted by statutory regulation or exceeds the permitted use, you will need to obtain permission directly from the copyright holder.



# Investigation of the Behaviour of Supercooled Droplets Concerning Evaporation, Sublimation and Freezing Under Different Boundary Conditions



**Jonathan Reutzsch, Verena Kunberger, Martin Reitzle, Stefano Ruberto, and Bernhard Weigand**

**Abstract** Phase change processes of supercooled droplets at different boundary conditions are presented. This study is a summary of the current developments within subproject B1 of the SFB-TRR 75 with the focus on evaporation, sublimation, and freezing of supercooled droplets. To this end, new numerical methods to describe the phase transition were developed and novel strategies dealing with the challenges of droplets under extreme conditions are presented. The numerical solution procedure of all phase changes are summarized in a compact way within this work. In order to validate the numerical models, experiments were conducted. For this, new experimental setups and approaches were developed. These comprise a test chamber for optical levitation of supercooled droplets, which is able to trap a droplet by means of a laser beam at subzero temperatures and variable ambient humidity. Comparisons of the numerical simulations and the conducted experiments are presented for several phase change processes. The results are in very good agreement and proof the capability of the methods.

## 1 Introduction

Phase change processes in clouds are one of the most important driving factors of precipitation, such as rain or snow, and have a great influence on our daily weather. The understanding of these processes is crucial for the development of weather and climate models and of reliable weather forecasts [40]. Especially the small scales, such as droplets and their interactions in the atmosphere, strongly affect the behaviour of the macroscopic systems [5, 39]. However, there is still a lack of knowledge regarding the processes in clouds at high altitude [28, 62]. Within these, a range of phenomena are encountered which in turn are responsible for the evolution of the water cycle [64]. Among them are the freezing of supercooled droplets, collision and coalescence events, evaporation and sublimation processes, droplet growth due

---

J. Reutzsch (✉) · V. Kunberger · M. Reitzle · S. Ruberto · B. Weigand  
Institute of Aerospace Thermodynamics (ITLR), University of Stuttgart, Stuttgart, Germany  
e-mail: [jonathan.reutzsch@itlr.uni-stuttgart.de](mailto:jonathan.reutzsch@itlr.uni-stuttgart.de)

to condensation, or the formation of larger structures, such as snow or hail [25]. Acquiring a deeper understanding of those events as well as developing new models and strategies was the aim of this study.

The main focus is put on the behaviour of droplets in extreme conditions, particularly at low temperatures. In high altitudes, where the atmosphere cools down to less than  $-40^{\circ}\text{C}$  [77], liquid droplets are still present in a metastable state, which is termed *supercooled*. In an unsaturated ambiance evaporation processes can occur, whereas when the surrounding air is oversaturated condensation takes place. If droplets cool down even further, droplet freezing inevitably begins. Two different types of freezing processes exist. On the one hand, homogeneous freezing, when a sufficiently large nucleus is spontaneously generated, and on the other hand heterogeneous freezing, where a seed particle initiates the solidification [75]. In an analogous way, depending on the ambient conditions, the frozen droplets can subsequently grow even further due to deposition or decrease in size because of sublimation. The growth of ice strongly depends on the pressure and temperature boundary conditions in the surrounding and various crystallized structures can evolve [7].

In order to investigate supercooled droplets under extreme ambient conditions and to study the mentioned phase change processes, experimental and numerical methods are deployed in this work. The combination of both allows precise insight into the physics of droplets. Furthermore, the synergy of numerical simulations and experiments can provide detailed information about the phase change processes. The present work represents a summary of multiple studies within the third funding phase of the subproject B1 of the Collaborative Research Centre SFB-TRR 75. To classify the complete compilation and outcome of the project, a brief overview of previous works concerning phase change processes of droplets is given in the following. It is split into experimental and numerical studies and subdivided into the respective characteristics of phase change.

Many numerical studies focusing on multiphase flows exist in literature. Two approaches are prevalent, which are front-tracking [72] and front-capturing methods [20, 60]. A classification of both can be found in [33]. When dealing with evaporation, a lot of numerical approaches in the literature provide deep insight into its mechanisms [14, 18, 19, 46, 47, 68, 73]. The most promising approaches, which are also able to deal with complex three-dimensional structures as well as extreme conditions, are conducted using the Volume-of-Fluid (VOF) method [49, 58, 78]. The same accounts for investigations of solidification and melting processes, where auspicious results were obtained with this method in [32] and within the SFB-TRR 75 [42, 44]. Nevertheless, various other approaches exist, particularly for investigating crystal growth of water [1, 8, 10, 59, 67, 74]. In contrast to evaporation or freezing, numerical studies regarding sublimation are rare in literature. Besides large-scale investigations [30, 64] for geophysical models only a few small-scale approaches exist [27, 45, 70].

Various experiments were reported that study the supercooled environment in clouds. These were conducted in wind tunnels and cloud chambers, among others [38, 66]. In order to study the phase change of droplets more closely, experiments with single droplets were conducted. Several experimental studies have been performed

on the evaporation of droplets under ambient conditions in electrodynamic traps [24, 26] and by means of acoustic levitation [48] as well as on the evaporation of droplets at low Reynolds numbers [79]. Only few literature can be found concerning the investigation of the evaporation of supercooled water droplets (SWD) [51, 71]. More broadly investigated is the behaviour of ice crystals which included experimental studies on evaporation and melting of different shapes of ice crystals [36], sublimation [35, 65] and growth of ice crystals [65]. Furthermore, sublimation experiments with frozen droplets or spheres were conducted [52, 70]. Several works have focused on the freezing of droplets. The probabilities of freezing on contact was investigated [2] as well as heterogeneous nucleation and contact freezing of levitated droplets [13, 23, 37]. Additionally, studies were performed to determine the nucleation time and freezing behaviour of SWDs [11, 29, 52, 61].

The following sections will outline the numerical and experimental investigations of the evaporation, sublimation and freezing of droplets within the subproject B1 of the Collaborative Research Centre SFB-TRR 75.

## 2 Experimental Methods

### 2.1 Experimental Setup

The experiments are conducted with an optical levitation setup as described in Roth et al. [52] and Ruberto et al. [56]. The stable optical trapping through radiation pressure was first investigated by Ashkin [4]. Figure 1 shows the setup of the cooling chamber as well as the optical setup. A laser beam focused by a lens is directed through the levitation chamber. The droplet is levitated above the focus and the position of the droplet within the chamber can be varied when the lens is moved. The laser has a wavelength of 532 nm, that is hardly absorbed by water, so the droplet does not heat up during the experiments. The chamber can be cooled down to  $-40^{\circ}\text{C}$  by a cryostat. A U-shaped temperature profile develops in the chamber, that is qualitatively shown in Fig. 1 next to the experimental setup. Droplets were trapped in the region of constant temperature. As the droplet is cooled down to a metastable state, it is important to use purified water so that it does not freeze due to impurities. In order to avoid pollution of the atmosphere inside the chamber and convection from outside, a very slow flow of dry nitrogen (99,999%) passes through the chamber. It is controlled by precise mass flow meters. The volume flow rate is variable but chosen such that only low Reynolds numbers are reached. This flow is needed for achieving steady conditions in the chamber, so that evaporated mass from the droplet can be transported out and no saturation is reached inside the chamber. To study phase-change behaviours with different relative humidities, the nitrogen can be humidified in an appropriate setup. These conditions, relative humidity and temperature, are monitored before and after the experiment.

The droplets are produced by a droplet-on-demand generator which is driven by a piezo-electric ceramic. Recently, the in-house built generator was exchanged with

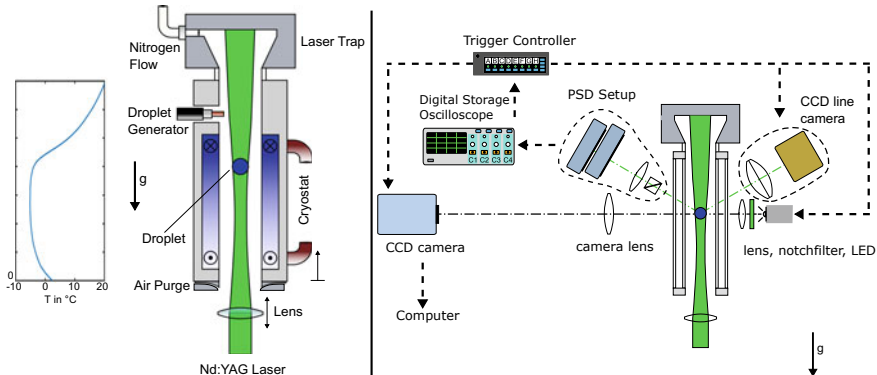


**Fig. 1** Left side: Schematic of the experimental setup, indicating the temperature profile along the chamber height. Right side: Optical setup to record the light scattering and shadowgraphy and signal path, adapted from [55]

a commercial one [69] which allows for more controllable conditions and increased repeatability for future experiments. As the droplet is levitated, it has to fall into the test chamber along the centre of the laser beam. Thus, the generator is mounted onto two precise linear position stages. The position of the levitated droplet is monitored by a position sensitive device (PSD). A second PSD sensor is mounted alongside the first. It monitors the split-beam of the scattered light after a Wollaston prism which will show the depolarisation of the light due to the freezing of the droplet. Once the droplet is levitated, the measurement starts with a delay in order to ensure that the droplet attained the ambient temperature.

## 2.2 Observation Techniques

The droplet inside the test chamber can be observed by two techniques. When the laser reaches the droplet, the light scatters. This light scattering in the forward hemisphere is recorded by a CCD line camera and is shown in Fig. 2. The light is collected by a lens in the focal plane of the camera so that a specific scattering angle is recorded on the same camera pixel. The recorded intensity distribution is converted to intensity over scattering angle. The scattering image is dependent on the droplet diameter which will show a smaller fringe spacing and higher number of maxima for a larger droplet diameter [15]. The following equation was used to determine the droplet diameter,  $D$ , for evaporating droplets [15]

$$D = \frac{2\lambda}{\Delta\Theta} \left( \cos\left(\frac{\Theta}{2}\right) + n \sin\left(\frac{\Theta}{2}\right) \left[ 1 + n^2 - 2n \cos\left(\frac{\Theta}{2}\right) \right]^{1/2} \right)^{-1} \quad (1)$$

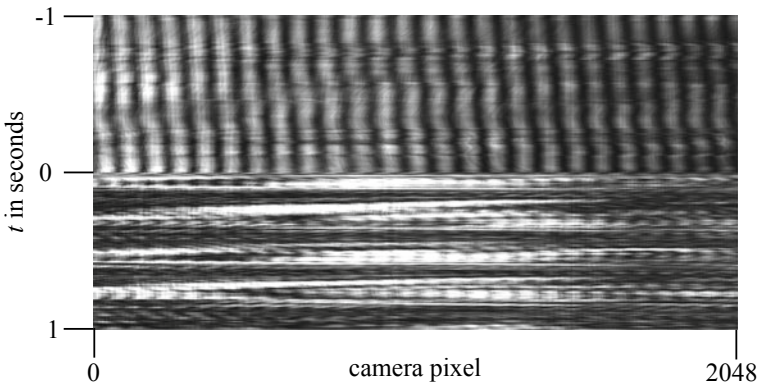


**Fig. 2** Light scattering recorded from a SWD, which froze at  $t = 0$  s. The intensity signal is plotted over the camera pixel

in which  $n$  is the refractive index,  $\lambda$  the laser wavelength in m,  $\Theta$  the camera mounting angle in  $^{\circ}$  and  $\Delta\Theta$  the angular fringe distance in  $^{\circ}$ . The refractive index was derived from a correlation as a function of the laser wavelength  $\lambda$  and the fluid temperature [16, 56]. The fringe distance is averaged over several maxima of a line. The accuracy of the measurements is about  $\pm 2\%$  for droplet diameters in the range of  $20 \mu\text{m} < D < 60 \mu\text{m}$  [56]. Below  $20 \mu\text{m}$ , the accuracy decreases as the intensity of the maxima is lower and, therefore, the noise increases. As mentioned above, the number of maxima decreases for lower droplet diameters which leads to larger uncertainties in  $\Delta\Theta$  [56]. As mentioned above, the number of maxima decreases for lower droplet diameters which leads to larger uncertainties in  $\Delta\Theta$  [56]. It is important that the image of the line camera is not overexposed as the position of the maxima is then lost [55]. The line camera was triggered with a frequency of 5000 Hz and for a period of 12 s. This method is mainly used for the observation of evaporating droplets and derivation of the evaporation rate. When the droplet freezes, the scattering image shows a dramatic difference and the pattern of the maxima becomes more indistinct and chaotic. Nevertheless, it was still possible to derive the sublimation rate from the scattering images by adapting the evaluation code. As mentioned above, the moment of freezing is detected by an increase of intensity on the PSD sensor after the Wollaston Prism. As the scattering image is chaotic, the droplet is also observed by shadowgraphy. A LED illuminates the droplet and the shadow is recorded by a CCD camera with a frequency of 2 Hz and a magnification of  $M = 36.4$  [54]. The size of the droplet can be derived from the shadow images by image processing. An algorithm identifies the size of the area of the shadow by the number of pixels that the droplet comprises or a circle can be computed that fits the area around the droplet. From the area and the circle around the droplet, its size and the decrease in diameter over time can be derived.

### 3 Numerical Methods

All developed methods and conducted numerical investigations are done using the in-house software package Free Surface 3D (FS3D) [12]. This Direct Numerical Simulation (DNS) code is based on the mentioned VOF method and solves the incompressible Navier-Stokes equations on a Marker and Cell (MAC) grid. In addition, the energy equation is included, which is mandatory when dealing with phase change processes. The interface reconstruction is achieved by applying the Piecewise Linear Interface Calculation (PLIC) scheme. The code is highly parallelized using MPI as well as OpenMP and is run on the High-Performance Computing Center (HLRS) in Stuttgart. Main focus from the numerical side is put on the three types of phase change: solidification, sublimation, and evaporation. The introduced new developed methods and approaches are based on works of Reitzle et al. [44, 45] (solidification and sublimation) as well as Reutzsch et al. [49] (evaporation).

#### 3.1 Conservation Equations

For all phase change algorithms the basic equations are similar. Several assumptions are made, such as neglecting radiation and viscous dissipation, pure substances, Newtonian insoluble fluids, and local thermodynamic equilibrium at the interface. Furthermore, a Fickian diffusion model is used for the diffusive fluxes. The mass conservation for every species  $j$  reads

$$\frac{\partial(\rho_p^j)}{\partial t} + \nabla \cdot (\rho_p^j \mathbf{u}) = \nabla \cdot (\bar{\rho} \mathfrak{D} \nabla X^j), \quad (2)$$

with the partial density  $\rho_p$ , average density  $\bar{\rho}$ , velocity  $\mathbf{u}$ , diffusion coefficient  $\mathfrak{D}$ , and the mass fraction  $X$ . For an incompressible, pure fluid within a Eulerian one-field formulation it simplifies to  $\nabla \cdot \mathbf{u} = 0$ . This can be used to formulate the momentum balance equation in differential form as

$$\frac{\partial(\rho \mathbf{u})}{\partial t} + \nabla \cdot (\rho \mathbf{u} \otimes \mathbf{u}) = -\nabla p + \nabla \cdot \mathbf{S} + \rho \mathbf{g}, \quad (3)$$

where  $p$  denotes the pressure,  $\mathbf{S} = \mu (\nabla \mathbf{u} + (\nabla \mathbf{u})^T)$  the viscous part of the stress tensor with the dynamic viscosity  $\mu$ , and  $\mathbf{g}$  the gravitational acceleration. Finally, the energy equation reads

$$\frac{\partial}{\partial t} (\rho c_p T) + \nabla \cdot (\rho c_p T \mathbf{u}) = \nabla \cdot (\lambda \nabla T) + \dot{q}'''. \quad (4)$$

Therein,  $c_p$  is the specific heat capacity at constant pressure,  $T$  the temperature,  $\lambda$  the thermal heat conductivity, and  $\dot{q}'''$  a volumetric heat source. A two-field approach

is used where an energy equation is solved for each phase. The balance equations are coupled at the interface with jump conditions as additional constraints in multiphase flows. In the following, we distinguish between the continuous phase (<sup>c</sup>) and the disperse phase (<sup>d</sup>). In addition, whenever necessary, a further differentiation is made regarding the phase change cases solidification (so), sublimation (su), and evaporation (ev). The mass jump condition can be written as

$$\dot{m}'' = \rho^c (\mathbf{u}^c - \mathbf{u}_\Gamma) \cdot \mathbf{n}_\Gamma = \rho^d (\mathbf{u}^d - \mathbf{u}_\Gamma) \cdot \mathbf{n}_\Gamma, \quad (5)$$

with the area-specific mass source  $\dot{m}''$ , the interface velocity  $\mathbf{u}_\Gamma$  and the respective normal vector  $\mathbf{n}_\Gamma$ . The disperse phase represents the solid for solidification and sublimation, and analogously the liquid for evaporation cases. The continuous phase is synonymous considered to the gaseous phase (<sup>gp</sup>) for sublimation and evaporation, and to the liquid phase for solidification. For sublimation and evaporation, the gaseous phase can be split further into inert gas (<sup>g</sup>) and vapour (<sup>v</sup>) and the interface velocity can be derived from the mass source (see [45]) as

$$V_\Gamma = -\frac{\rho_\Gamma^{gp}}{\rho^d} \mathfrak{D} \frac{1}{1 - X^v} \nabla X^v \cdot \mathbf{n}_\Gamma. \quad (6)$$

Note that in order to evaluate the term  $\nabla X^v \cdot \mathbf{n}_\Gamma$  information about the condition at the interface need to be known. For sublimation processes, an expression for the solid-gaseous equilibrium was derived [43, 45], whereas for evaporation the saturation condition for the pure substance was used. The momentum jump condition simplifies to the well-known Young-Laplace equation

$$p^d - p^c = \kappa \sigma, \quad (7)$$

where  $\kappa$  represents the interface curvature and  $\sigma$  the surface tension. The energy balance across the interface (see [43] for the contained simplifications and assumptions) yields

$$\dot{m}'' \Delta h = -\lambda^c \Delta T^c \cdot \mathbf{n}_\Gamma - \lambda^d \Delta T^d \cdot \mathbf{n}_\Gamma, \quad (8)$$

with the specific latent heat  $\Delta h$ , which obviously differs for all cases.

For solidification processes, containing liquid (<sup>l</sup>) and solid (<sup>s</sup>), the character of growth is of greater interest. The surface energy density determines strongly the morphology of a crystal. The boundary condition for the energy is computed with the Gibbs-Thomson equation in this case. Considering the anisotropic mean curvature  $H_\Gamma$  that contains information about the (possibly anisotropic) surface energy densities it reads

$$T_\Gamma = T_m \left[ 1 - \frac{1}{\rho \Delta h^s} (\sigma_0 H_\Gamma) \right] + \frac{(c_p^l - c^s)}{\Delta h^s} \left[ T_\Gamma \ln \left( \frac{T_\Gamma}{T_m} \right) - (T_m - T_\Gamma) \right], \quad (9)$$

with the interface temperature  $T_\Gamma$ , melting temperature  $T_m$ , and latent heat of fusion  $\Delta h^s$ . For detailed information the reader is referred to [45]. The energy equation for solidification at the interface, also known as Stefan condition, can be derived as

$$\dot{m}'' [\Delta h^s - (c_p^l - c^s) (T_m - T_\Gamma)] = -\lambda^l \Delta T^l \cdot \mathbf{n}_\Gamma + \lambda^s \Delta T^s \cdot \mathbf{n}_\Gamma. \quad (10)$$

Note that terms of higher order were neglected in this formulation. For the precise modelling of the local thermodynamic equilibrium at the interface, the anisotropic surface energy density, and a detailed derivation of all boundary conditions the reader is referred to already mentioned studies [44, 45, 49].

### 3.2 Numerical Approach

The complete basic numerical scheme of the used code is described in great detail in the work of Rieber [50] and several extensions are given by many other authors e.g. [12, 17, 41, 58]. Thus, only a brief overview of the necessary approaches is given here. Due to the formulation of the VOF method, additional scalar variables  $f_i$  are introduced, which contain information about the volume fraction within each cell. They are defined as

$$f_i(\mathbf{x}, t) = \begin{cases} 0 & \text{in the continuous phase,} \\ ]0; 1[ & \text{in interface cells,} \\ 1 & \text{in the disperse phase.} \end{cases} \quad (11)$$

Depending on the phase,  $f_i$  describes the fraction of the liquid ( $f_1$ ), the vapour ( $f_2$ ), or the solid ( $f_3$ ) phase. Due to the one-field character of the VOF method, material properties can be expressed using just one equation. Considering all volume fractions the density, for instance, reads

$$\rho(\mathbf{x}, t) = \sum_{i=1}^3 f_i(\mathbf{x}, t) \rho_{p,i} + \left( 1 - \sum_{i=1}^3 f_i(\mathbf{x}, t) \right) \rho^g. \quad (12)$$

The densities  $\rho_{p,i}$  refer to the partial densities of the liquid, vapour, and solid phase. The transport of the VOF variables is done via the equation

$$\frac{\partial f_i}{\partial t} + \mathbf{u} \cdot \nabla f_i = 0. \quad (13)$$

Note that diffusion is additionally considered for the transport of the vapour phase inside the inert gas. Advection is done using an operator-splitting technique [63], where the three dimensional transport is achieved by three single one-dimensional steps. Details regarding the necessary divergence corrections steps can be found in [50]. The fluxes are obtained in interfacial cells using the PLIC algorithm.

Furthermore, for phase change processes the movement of the interface is interpreted as a consequence of a flux. In contrast to previous approaches [42, 58] this leads to more stable simulations as well as circumvents complex redistribution. Hence, the movement of the interface is done using an additional transport equation, which reads

$$\frac{\partial f_i}{\partial t} + \nabla \cdot (f_i \mathbf{u}_\Gamma) = f_i \nabla \cdot \mathbf{u}_\Gamma . \quad (14)$$

The velocity field at the interface  $\mathbf{u}_\Gamma$  is related to the local interfacial velocity via  $V_\Gamma = \mathbf{u}_\Gamma \cdot \mathbf{n}_\Gamma$ . For the evaluation of the fluxes a geometrical unsplit advection scheme is applied [44]. The gradients of volume fractions, which serve as the basis to derive the interface velocity, are obtained by means of second order finite differences coupled with a tridiagonal interpolation scheme [42].

Taking the definition of the density and substituting it into the continuous and disperse part and considering the global mass conservation, an expression for the volume conserving velocity  $\mathbf{u}_{\text{vol}}$  depending on the mass source  $\dot{m}'''$  can be derived as

$$\nabla \cdot \mathbf{u}_{\text{vol}} = \dot{m}''' \left( \frac{1}{\rho^c} - \frac{1}{\rho^d} \right) . \quad (15)$$

Note that in case of solidification the difference in densities of the phases is neglected and, hence, a solenoidal velocity field is retained. For evaporation the possible movement of the liquid interface also has to be considered for the convective step. A mass averaged velocity is necessary which is a consequence of the solution of the momentum equations. Two methods to obtain the velocities for the gaseous and liquid phase were developed by Reutzsch et al. [49]. The basic idea is to split the parts into the respective amounts of vapour and inert gas and connect them with the mass source term. An averaging with the volume fractions as well as a more precise approach using cell wetting is proposed.

The momentum equations are solved in several steps. The detailed procedure is described in [50]. In a first step, the convective part is handled using the before mentioned operator-splitting method. The viscous part is discretized using central differences and a pressure projection scheme is applied in order to obtain a solenoidal velocity field [9]. For rigid bodies, which are relevant for solidification and sublimation cases, further treatment is necessary (see [42]).

The diffusive parts are solved using the newly developed approach by Reitzel et al. [45]. The energy equation is solved for all phase change processes, using a two-field approach in order to gain more precise values at the interface [43, 57]. Diffusive mass transfer is only considered for the vapour field in sublimation or evaporation simulations. The basic idea is to set Dirichlet boundary conditions on the

sharp interface for the concentration fields. The gradient is obtained by an accurate geometrical approach evaluating an inverse distance interpolation scheme in the vicinity of neighbouring cells. The resulting system of linear equations is finally solved with a Red-Black Gauss-Seidel algorithm.

The convective part of the energy equation is again solved using the splitting algorithm in a semi-implicit formulation. A TVD-limiter from van Leer [76] is used in order to interpolate the values onto the cell edges. The fluxes are obtained in a similar way as the VOF variables.

### 3.3 Solution Procedure

Due to the complexity of the code the complete time integration scheme is not presented here and the reader is referred to the afore mentioned literature for a detailed description. In general, it is possible to use first or second order accurate schemes within FS3D.

An abstracted, simplified sequence of steps for all possible phase change processes is shown in Fig. 3. Note that the depicted procedure gives only a rough overview and several steps are summed up within one sub-item. The new methods developed within this project dealing with solidification, sublimation, and evaporation were validated extensively. Due to the high complexity, multi-stage procedures were applied in order to validate not only the single terms and routines, but also their interactions for all kinds of setups. The respective simulations, evaluations and comparisons to experimental results or analytical models are not presented here. They can be found e.g. in the works of Reitzle et al. [43–45] and Reutzsch et al. [49] along with the complete, detailed description of all routines.

## 4 Results

### 4.1 Solidification Simulation

A three dimensional simulation for the hexagonal anisotropic growth of a water crystal has been conducted successfully. It is described in detail in [44], a short summary is presented in the following. The initial setup contains a spherical seed with a radius  $r_0 = 8.206 \mu\text{m}$  slightly larger than the stable radius in a liquid water environment with a supercooling of  $\Delta T = 10 \text{ K}$ . The cubic domain has a dimension of  $30r_0$ , where a Dirichlet boundary condition for the temperature is applied at a sphere with a radius of  $15r_0$  in order to minimize the influence of the cubic domain. The material properties of the solid were evaluated at the melting temperature, the liquid properties were taken at a reference temperature  $T = T_\infty$ , where  $T_\infty$  denotes the ambient temperature. In addition, a slight rotation of the prismatic energy was set

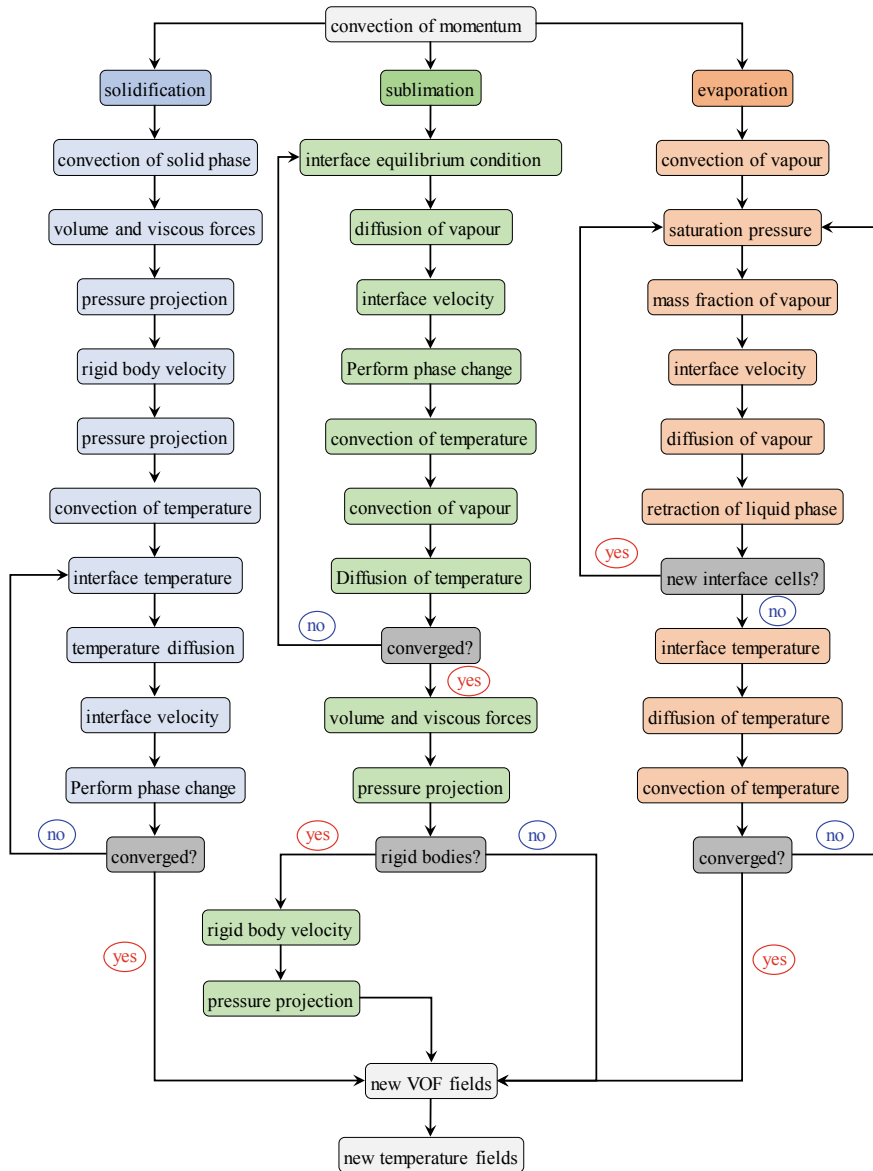


**Fig. 3** Simplified sequence of steps for all considered phase change processes

**Fig. 4** Temporal evolution of the solid particle represented by partly opaque PLIC surfaces

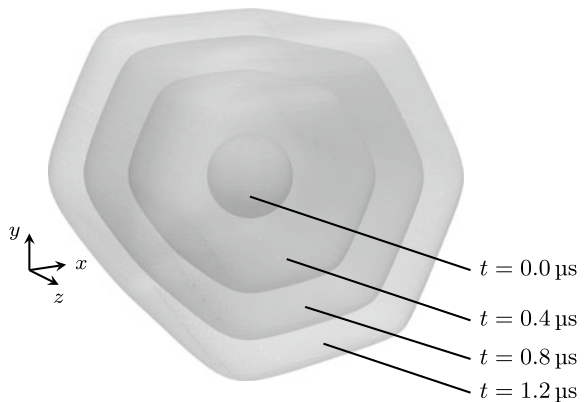


**Fig. 5** Rendered visualization based on PLIC surface data at  $t = 1.2 \mu\text{s}$



to ensure that no dendrite is directly aligned with any coordinate axis. The temporal evolution of the crystal growth from the spherical seed is shown in Fig. 4. In addition, the three-dimensional ice crystal after  $t = 1.2 \mu\text{s}$  is depicted in Fig. 5. The hexagonal structure as well as constrictions of the crystal in the prismatic planes are clearly visible. This behaviour is also observed in literature (cf. [6]). Furthermore, it leads to the evolution of crystal forms, such as capped-cylinders or hollow needles.

## 4.2 Sublimation Simulations and Experimental Results

Investigations concerning sublimation of frozen droplets were conducted numerically and experimentally. A detailed description of the numerical setup as well as the test chamber is given in [45]. An ice particle at 236.15 K with a diameter of 50  $\mu\text{m}$  in a slow air flow was investigated. Sublimation rates were measured and simulated at

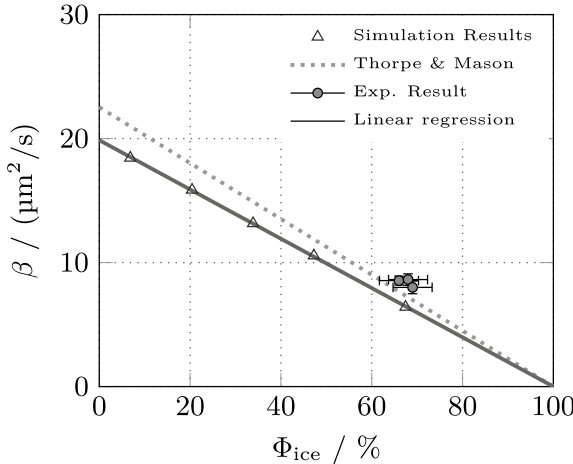


**Fig. 6** Comparison of experimentally (dots) and numerically (triangles) obtained rates of sublimation  $\beta$  over relative humidity  $\Phi_{\text{ice}}$  with respect to ice. A linear fit (solid line) to the experimental results was calculated using a forced constraint  $\beta(\Phi_{\text{ice}} = 100\%) = 0$ . The uncertainties in the experiments in the vertical direction incorporate the 95 % confidence level, whereas the uncertainty in the horizontal direction is due to the accuracy of the humidity sensor

varying ambient humidity  $\Phi$  and compared subsequently. The material properties for all components were obtained from literature [3, 31, 53]. A numerical setup with a spatial resolution of  $512^3$  grid cells was chosen that represents a small part of the experimental test chamber. The experiments were conducted at relative humidities with respect to ice of  $\Phi_{\text{ice}1} = 66\%$ ,  $\Phi_{\text{ice}2} = 69\%$ , and  $\Phi_{\text{ice}3} = 70\%$ . The results were obtained by averaging at least 10 independent measurements. Again, detailed values are presented in [45]. Whereas the experiments could not be conducted at a broad range of humidity, the simulations were performed between 0 and 80%. The sublimation rates  $\beta_{\text{su}}$  are compared and results are shown in Fig. 6. One can clearly see that there is a linear trend of the sublimation rate as was already assumed in literature (e.g. [70]). The comparison of numerical and experimental results shows that the numerical model is able to predict the sublimation rates very well. The remaining differences occur probably due to uncertainties in the boundary conditions and the remaining simplifications in the numerical model. The maximum sublimation rate at 0% was found as  $\beta_{\Phi=0} = 19.87 \mu\text{m s}^{-2}$ .

The experiments were conducted at around  $T_\infty = 236\text{ K}$  which was the temperature at which homogeneous nucleation occurred. At this temperature, it proved difficult to control and measure the humidity as the conditions inside the chamber were already supersaturated with the residual humidity and the humidities in Fig. 6 resulted from freezing at the chamber entry. Moreover, the accuracy of the humidity sensor was not high at such low temperatures and no dew point monitors could be used due to space restrictions in the chamber.

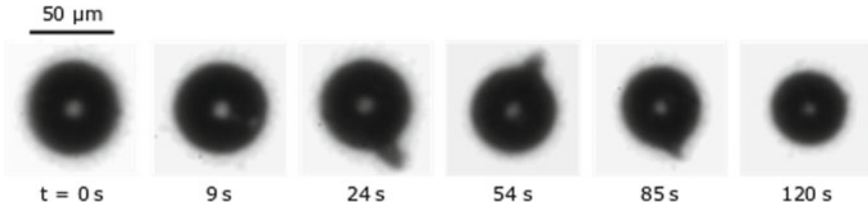


**Fig. 7** Time evolution of a levitated drop from the liquid to the frozen state showing a spike. After 120 s, the droplet shrank and the spike disappeared due to sublimation, leaving the droplet almost spherical again

In Fig. 7, shadow images of a first liquid and then frozen droplet are shown. In the experiments, when the droplet froze, it deformed and a spike appeared on the outside of the droplet. In literature, it is reported that this spike can eject ice particles or in case of larger droplets, the droplet can shatter due to high pressure inside [21, 66]. This is a very important process in cloud formation [22]. In comparison, the droplet is also shown after 120s when it is reduced in size and the spike has disappeared due to sublimation. The measurements of the ambient conditions and sublimation rate include some uncertainties. For the temperature, it was  $\pm \Delta T_\infty = 0.4\text{K}$  and  $\pm \Delta \phi = 4\%$  for the humidity over ice. The uncertainty in the sublimation rate was determined as the standard error of the mean with a 95% confidence interval.

### 4.3 Evaporation Simulations and Experimental Results

A similar procedure as for the before mentioned sublimation investigation was applied for the evaluation of evaporation of supercooled droplets. The experimental setup is described in detail by Ruberto et al. [55] whereas further information about the numerics can be found in Reutzsch et al. [49]. In contrast to sublimation, the control of the ambient conditions of the experimental setup was easier. Therefore, it was possible to conduct an expanded systematic study on the evaporation rates. Supercooled droplets were levitated at various temperature regimes. In addition, the ambient humidity could be varied in a larger range. Hence, measurements between  $T_\infty = 253.15\text{ K}$  and  $T_\infty = 268.15\text{ K}$  have been performed with a humidity between 25% and up to 95% and the corresponding evaporation rates  $\beta_{ev}$  were measured. The new evaporation model was applied to perform comparative simulations. The numerical setup was adapted to the experiments and is shown schematically in Fig. 8. The domain, consisting of the levitated droplet, an air flow from the left side, as well as several boundary conditions, has a resolution of  $512 \times 256 \times 256$  cells. Thus, the droplet is resolved with about 26 cells per diameter. Material properties were taken from the literature (cf. Sect. 4.2).

The results of the experiments as well as the simulations are depicted in Fig. 9. For three different ambient temperatures in the test chamber at  $T_\infty = 268.15\text{ K}$ ,

**Fig. 8** Numerical setup. The droplet, air flow, and the respective boundary conditions are highlighted

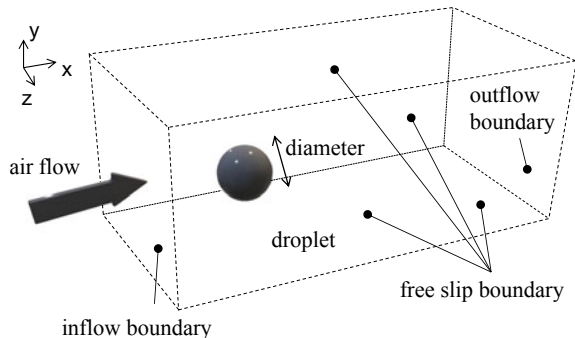
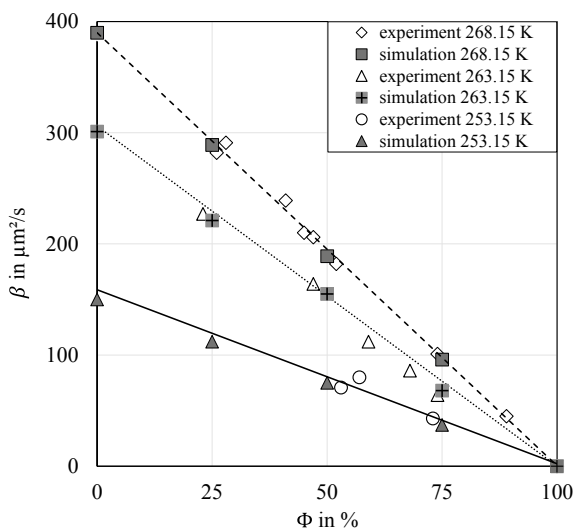


**Fig. 9** Experimental and numerical results at temperatures  $T_\infty = 268.15$ ,  $T_\infty = 263.15$ , and  $T_\infty = 253.15$  with varying humidity  $\Phi$ . The symbols represent the averaged measurements and simulations, respectively, the linear fits of the experiments are additionally highlighted with lines



$T_\infty = 263.15$  K, and  $T_\infty = 253.15$  K several points were measured and simulations have been conducted. The humidities, as mentioned before, were varied. In the frame of the numerical investigation, even a complete dry atmosphere, as well as a saturated ambiance were set up and simulated for each case. The experimental linear fit for all temperatures is also depicted with the respective lines. The results are in very good agreement for all cases. The maximum deviation between the linear fits and the simulations is about 5%. In addition, a comparison with the well known  $D^2$ -law [34] is promising. Worth mentioning is that also an older evaporation model of the authors was able to predict similar evaporation rates [55, 56]. However, the current evaporation model was mainly developed to cope with all ranges of extreme ambient condition, even with higher evaporation rates and strong surface deformations. The latter problems cannot be described with our previous models.

There are several uncertainties in the measurements. In case of the temperature the uncertainties originate from the accuracy of the thermocouple, an uncertainty due

to the droplet position in the chamber and the stability of the ambient temperature in the chamber [54]. Furthermore, a mean value as well as the standard error of the mean (SEM) were calculated from the measurements of the ambient conditions in the chamber for all of the measurements of a set temperature. This gave an uncertainty in the temperature of  $\Delta T_{\infty} \approx 0.4\text{K}$ . The SEM for the humidity was low and the uncertainty stems mostly from the probe with  $\Delta\Phi = \pm 6\%$  or lower. The SEM of the evaporation rate was calculated with a Student's factor for a 95% confidence interval [54].

## 5 Conclusions

The investigation of phase changes of and in supercooled droplets is of fundamental interest for the understanding of the processes in clouds at high altitudes and the development of modern climate models. The focus in this work lies on the phase transitions evaporation, sublimation, and freezing. Due to the metastable state of supercooled droplets, the extreme conditions and the complexity of this topic, several approaches to increase the knowledge within this field were considered and multiple studies have been conducted: On the one hand, numerical models were developed, which are capable of dealing with all three phase transitions mentioned above. These newly developed methods, which comprise fully consistent treatments of the processes, were summarized and the solution procedures were collated in a neat arrangement for the first time. On the other hand, experimental investigations were performed simultaneously. An experimental setup was built, which traps single droplets through optical levitation. The test chamber is able to realise conditions far below the freezing point of water and, thus, emulate the temperature encountered in clouds at high altitudes. Sublimation and evaporation rates of frozen and supercooled droplets were measured. Subsequently, they were compared with the simulation results gained by means of the developed numerical methods. The experimental and numerical results showed a very good agreement.

**Acknowledgements** The authors kindly acknowledge the financial support by the Deutsche Forschungsgemeinschaft (DFG) within the SFB-TRR75, project number 84292822. Furthermore, the authors kindly acknowledge the High Performance Computing Center Stuttgart (HLRS) for support and supply of computational time on the Cray XC40 platform under the Grant No. FS3D/11142.

## References

1. Al-Rawahi N, Tryggvason G (2004) Numerical simulation of dendritic solidification with convection: three-dimensional flow. *J Comput Phys* 194:677–696. <https://doi.org/10.1016/j.jcp.2003.09.020>
2. Alkezweeny AJ (1969) Freezing of supercooled water droplets due to collision. *J Appl Meteorol Climatol* 8(6):994–995. [https://doi.org/10.1175/1520-0450\(1969\)008<0994:FOSWDD>2.0.CO;2](https://doi.org/10.1175/1520-0450(1969)008<0994:FOSWDD>2.0.CO;2)

3. Aly FA, Lee LL (1981) Self-consistent equations for calculating the ideal gas heat capacity, enthalpy, and entropy. *Fluid Phase Equilib* 6(3):169–179. [https://doi.org/10.1016/0378-3812\(81\)85002-9](https://doi.org/10.1016/0378-3812(81)85002-9)
4. Ashkin A (1970) Acceleration and trapping of particles by radiation pressure. *Phys Rev Lett* 24:156–159. <https://doi.org/10.1103/PhysRevLett.24.156>
5. Bailey M, Hallett J (2004) Growth rates and habits of ice crystals between –20 and –70°C. *J Atmos Sci* 61(5):514–544 (01 Mar 2004)
6. Barrett JW, Garcke H, Nürnberg R (2012) Numerical computations of faceted pattern formation in snow crystal growth. *Phys Rev E* 86(1):011604. <https://doi.org/10.1103/PhysRevE.86.011604>
7. Bartels-Rausch T, Bergeron V, Cartwright JHE, Escribano R, Finney JL, Grothe H, Gutiérrez PJ, Haapala J, Kuhs WF, Pettersson JBC, Price SD, Sainz-Díaz CI, Stokes DJ, Strazzulla G, Thomson ES, Trinks H, Uras-Aytemiz N (2012) Ice structures, patterns, and processes: a view across the icefields. *Rev Mod Phys* 84(2):885–944. <https://doi.org/10.1103/RevModPhys.84.885>
8. Beckermann C, Diepers HJ, Steinbach I, Karma A, Tong X (1999) Modeling melt convection in phase-field simulations of solidification. *J Comput Phys* 154:468–496. <https://doi.org/10.1006/jcph.1999.6323>
9. Bell JB, Colella P, Glaz HM (1989) A second-order projection method for the incompressible Navier-Stokes equations. *J Comput Phys* 85(2):257–283
10. Chen S, Merriman B, Osher S, Smereka P (1997) A simple level set method for solving Stefan problems. *J Comput Phys* 135(1):8–29. <https://doi.org/10.1006/jcph.1997.5721>
11. Duft D (2011) Laborexperimente zur Mikrophysik der Wolken. Technische Universität Ilmenau, Doctoral thesis
12. Eisenschmidt K, Ertl M, Gomaa H, Kieffer-Roth C, Meister C, Rauschenberger P, Reitzle M, Schlottke K, Weigand B (2016) Direct numerical simulations for multiphase flows: an overview of the multiphase code FS3D. *J Appl Math Comput* 272(2):508–517. <https://doi.org/10.1016/j.amc.2015.05.095>
13. Ettner M, Mitra SK, Borrman S (2004) Heterogeneous freezing of single sulfuric acid solution droplets: laboratory experiments utilizing an acoustic levitator. *Atmos Chem Phys* 4(7):1925–1932. <https://doi.org/10.5194/acp-4-1925-2004>
14. Gibou F, Fedkiw R (2005) A fourth order accurate discretization for the laplace and heat equations on arbitrary domains, with applications to the stefan problem. *J Comput Phys* 202(2):577–601
15. Glantschnig WJ, Chen SH (1981) Light scattering from water droplets in the geometrical optics approximation. *Appl Opt* 20(14):2499–2509. <https://doi.org/10.1364/AO.20.002499>
16. Harvey AH, Gallagher JS, Sengers JMHL (1998) Revised formulation for the refractive index of water and steam as a function of wavelength, temperature and density. *J Phys Chem Ref Data* 27(4):761–774. <https://doi.org/10.1063/1.556029>
17. Hase M (2005) Numerische Berechnung dreidimensionaler Transportvorgänge an angeströmten, sich verformenden Tropfen. Ph.D. thesis, Universität Stuttgart
18. Haywood RJ, Renksizbulut M, Raithby GD (1994) Numerical solution of deforming evaporating droplets at intermediate Reynolds numbers. *Numer Heat Transf Part A-Appl* 26(3):253–272
19. Hernández J, López J, Gómez P, Zanzi C, Faura F (2008) A new volume of fluid method in three dimensions—part I: multidimensional advection method with face-matched flux polyhedra. *Int J Numer Meth Fluids* 58(8):897–921. <https://doi.org/10.1002/fld.1776>
20. Hirt CW, Nichols BD (1981) Volume of fluid (VOF) method for the dynamics of free boundaries. *J Comput Phys* 39(1):201–225. [https://doi.org/10.1016/0021-9991\(81\)90145-5](https://doi.org/10.1016/0021-9991(81)90145-5)
21. Hobbs PV, Alkezweeny AJ (1968) The fragmentation of freezing water droplets in free fall. *J Atmos Sci* 25(5):881–888. [https://doi.org/10.1175/1520-0469\(1968\)025<0881:TFOFWD>2.0.CO;2](https://doi.org/10.1175/1520-0469(1968)025<0881:TFOFWD>2.0.CO;2)
22. Hobbs PV, Rangno AL (1985) Ice particle concentrations in clouds. *J Atmos Sci* 42(23):2523–2549. [https://doi.org/10.1175/1520-0469\(1985\)042<2523:IPCIC>2.0.CO;2](https://doi.org/10.1175/1520-0469(1985)042<2523:IPCIC>2.0.CO;2)

23. Hoffmann N (2015) Experimental study on the contact freezing of supercooled micro-droplets in electrodynamic balance. Ph.D. thesis, Ruperto-Carola University of Heidelberg
24. Holyst R, Litniewski M, Jakubczyk D, Kolwas K, Kolwas M, Kowalski K, Migacz S, Palesa S, Zientara M (2013) Evaporation of freely suspended single droplets: experimental, theoretical and computational simulations. *Rep Prog Phys* 76(3). <https://doi.org/10.1088/0034-4885/76/3/034601>
25. Houze RA (1993) Cloud dynamics. International geophysics series, vol 53. Academic Press
26. Jakubczyk D, Zientara M, Kolwas K, Kolwas M (2007) Temperature dependence of evaporation coefficient for water measured in droplets in nitrogen under atmospheric pressure. *J Atmos Sci* 64(3):996–1004. <https://doi.org/10.1175/JAS3860.1>
27. Kaempfer TU, Plapp M (2009) Phase-field modeling of dry snow metamorphism. *Phys Rev E* 79(3):031502. <https://doi.org/10.1103/PhysRevE.79.031502>
28. Khain A, Ovtchinnikov M, Pinsky M, Pokrovsky A, Krugliak H (2000) Notes on the state-of-the-art numerical modeling of cloud microphysics. *Atmos Res* 55(3):159–224. [https://doi.org/10.1016/S0169-8095\(00\)00064-8](https://doi.org/10.1016/S0169-8095(00)00064-8)
29. Krämer B, Hübner O, Vortisch H, Wöste L, Leisner T, Schwell M, Rühl E, Baumgärtel H (1999) Homogeneous nucleation rates of supercooled water measured in single levitated micro-droplets. *J Chem Phys* 111(14):6521–6527. <https://doi.org/10.1063/1.479946>
30. Lehning M, Völksch I, Gustafsson D, Nguyen TA, Stähli M, Zappa M (2006) ALPINE3D: a detailed model of mountain surface processes and its application to snow hydrology. *Hydrol Process* 20(10):2111–2128. <https://doi.org/10.1002/hyp.6204>
31. Lemmon EW, Bell I, Huber ML, McLinden MO (2018) NIST standard reference database 23: reference fluid thermodynamic and transport properties-REFPROP, version 10.0. National Institute of Standards and Technology. <https://doi.org/10.18434/T4/1502528>
32. López J, Gómez P, Hernández J (2010) A volume of fluid approach for crystal growth simulation. *J Comput Phys* 229(19):6663–6672. <https://doi.org/10.1016/j.jcp.2010.05.026>
33. Marschall H, Boden S, Lehrenfeld C, Hampel U, Reusken A, Wörner M, Bothe D (2014) Validation of interface capturing and tracking techniques with different surface tension treatments against a Taylor bubble benchmark problem. *Comput Fluids* 102:336–352. <https://doi.org/10.1016/j.compfluid.2014.06.030>
34. Mills AF (2001) Mass transfer. Prentice Hall
35. Nelson J (1998) Sublimation of ice crystals. *J Atmos Sci* 55(5):910–919
36. Oraltay RG, Hallett J (1989) Evaporation and melting of ice crystals: a laboratory study. *Atmos Res* 24(1):169–189
37. Pander TJ (2015) Laboratory ice multiplication experiments in levitated microdroplets. Ph.D. thesis, Ruperto-Carola University of Heidelberg
38. Pflaus JC, Pruppacher HR (1979) A wind tunnel investigation of the growth of graupel initiated from frozen drops. *J Atmos Sci* 36(4):680–689. [https://doi.org/10.1175/1520-0469\(1979\)036<0680:AWTIOT>2.0.CO;2](https://doi.org/10.1175/1520-0469(1979)036<0680:AWTIOT>2.0.CO;2)
39. Pruppacher HR (1967) On the growth of ice crystals in supercooled water and aqueous solution drops. *Pure Appl Geophys* 68:186–195. <https://doi.org/10.1007/BF00874894>
40. Pruppacher HR, Klett JD (1997) Microphysics of clouds and precipitation. Kluwer Academic Publishers
41. Rauschenberger P, Schlottke J, Eisenschmidt K, Weigand B (2011) Direct numerical simulation of multiphase flow with rigid body motion in an Eulerian framework. In: ILASS—Europe 2011, 24th European conference on liquid atomization and spray systems, Estoril, Portugal
42. Rauschenberger P, Weigand B (2015) A Volume-of-Fluid method with interface reconstruction for ice growth in supercooled water. *J Comput Phys* 282:98–112. <https://doi.org/10.1016/j.jcp.2014.10.037>
43. Reitzle M (2020) A framework for the direct numerical simulation of phase change processes of water at low temperature and pressure. Dissertation, Universität Stuttgart
44. Reitzle M, Kieffer-Roth C, Garcke H, Weigand B (2017) A volume-of-fluid method for three-dimensional hexagonal solidification processes. *J Comput Phys* 339:356–369. <https://doi.org/10.1016/j.jcp.2017.03.001>

45. Reitzle M, Ruberto S, Stierle R, Gross J, Janzen T, Weigand B (2019) Direct numerical simulation of sublimating ice particles. *Int J Therm Sci* 145:105953. <https://doi.org/10.1016/j.ijthermalsci.2019.05.009>
46. Renksizbulut M, Bussmann M (1993) Multicomponent droplet evaporation at intermediate Reynolds-numbers. *Int J Heat Mass Transf* 36(11):2827–2835
47. Renksizbulut M, Yuen MC (1983) Numerical study of droplet evaporation in a high-temperature stream. *J Heat Transf-Trans Asme* 105(2):389–397
48. Rensink D (2004) Verdunstung akustisch levitierter schwingender tropfen aus homogenen und heterogenen medien. Doctoral thesis, Friedrich-Alexander-Universität Erlangen-Nürnberg (FAU)
49. Reutzsch J, Kieffer-Roth C, Weigand B (2020) A consistent method for direct numerical simulation of droplet evaporation. *J Comput Phys* 413:109455. <https://doi.org/10.1016/j.jcp.2020.109455>
50. Rieber M (2004) Numerische Modellierung der Dynamik freier Grenzflächen in Zweiphasenströmungen. Dissertation, Universität Stuttgart
51. Roth N, Anders K, Frohn A (1994) Determination of size, evaporation rate and freezing of water droplets using light scattering and radiation pressure. Part Part Syst Charact 11(3):207–211. <https://doi.org/10.1002/ppsc.19940110307>
52. Roth N, Frohn A (1998) Size and polarization behaviour of optically levitated frozen water droplets. *Atmos Environ* 32(18):3139–3143. [https://doi.org/10.1016/S1352-2310\(98\)00049-1](https://doi.org/10.1016/S1352-2310(98)00049-1)
53. Rowley RL, Wilding WV, Oscarson JL (2007) Database tools for evaluating thermophysical property data. *Int J Thermophys* 28(3):805–823. <https://doi.org/10.1007/s10765-007-0235-6>
54. Ruberto S (2020) Experimental investigation of the phase change of freely suspended supercooled water droplets. Dissertation, Universität Stuttgart
55. Ruberto S, Reutzsch J, Roth N, Weigand B (2017) A systematic experimental study on the evaporation rate of supercooled water droplets at subzero temperatures and varying relative humidity. *Exp Fluids* 58(5):55. <https://doi.org/10.1007/s00348-017-2339-5>
56. Ruberto S, Reutzsch J, Weigand B (2016) Experimental investigation of the evaporation rate of supercooled water droplets at constant temperature and varying relative humidity. *Int Commun Heat Mass Transfer* 77:190–194. <https://doi.org/10.1016/j.icheatmastransfer.2016.08.005>
57. Schlottke J, Rauschenberger P, Weigand B, Ma C, Bothe D (2011) Volume of fluid direct numerical simulation of heat and mass transfer using sharp temperature and concentration fields. In: ILASS—Europe 2011, 24th European conference on liquid atomization and spray systems, Estoril, Portugal
58. Schlottke J, Weigand B (2008) Direct numerical simulation of evaporating droplets. *J Comput Phys* 227(10):5215–5237. <https://doi.org/10.1016/j.jcp.2008.01.042>
59. Sethian JA, Strain J (1992) Crystal growth and dendritic solidification. *J Comput Phys* 98:231–253. [https://doi.org/10.1016/0021-9991\(92\)90140-T](https://doi.org/10.1016/0021-9991(92)90140-T)
60. Son G (2010) A level-set method for analysis of microdroplet evaporation on a heated surface. *J Mech Sci Technol* 24(4):991–997. <https://doi.org/10.1007/s12206-010-0206-x>
61. Stöckel P, Vortisch H, Leisner T, Baumgärtel H (2002) Homogeneous nucleation of supercooled liquid water in levitated microdroplets. *J Mol Liq* 96–97:153–175. [https://doi.org/10.1016/S0167-7322\(01\)00340-3](https://doi.org/10.1016/S0167-7322(01)00340-3) Physical Chemistry of Liquids
62. Straka JM (2009) Cloud and precipitation microphysics: principles and parameterizations. Cambridge University Press, Cambridge. <https://doi.org/10.1017/CBO9780511581168>
63. Strang G (1968) On the construction and comparison of difference schemes. *SIAM J Numer Anal* 5(3):506–517. <https://doi.org/10.1137/0705041>
64. Strasser U, Bernhardt M, Weber M, Liston GE, Mauser W (2008) Is snow sublimation important in the alpine water balance? *Cryosphere* 2(1):53–66. <https://doi.org/10.5194/tc-2-53-2008>
65. Swanson BD, Bacon NJ, Davis EJ, Baker MB (1999) Electrodynamic trapping and manipulation of ice crystals. *Q J R Meteorol Soc* 125(555):1039–1058. <https://doi.org/10.1002/qj.49712555514>

66. Takahashi C, Yamashita A (1970) Shattering of frozen water drops in a supercooled cloud. *J Meteorol Soc Jpn. Series II* 48(4):373–376. [https://doi.org/10.2151/jmsj1965.48.4\\_373](https://doi.org/10.2151/jmsj1965.48.4_373)
67. Tan L, Zabaras N (2006) A level set simulation of dendritic solidification with combined features of front-tracking and fixed-domain methods. *J Comput Phys* 211(1):36–63. <https://doi.org/10.1016/j.jcp.2005.05.013>
68. Tanguy S, Menard T, Berlemont A (2007) A level set method for vaporizing two-phase flows. *J Comput Phys* 221(2):837–853
69. microdrop Technologies GmbH: Tycho-Brahe-Kehre 1, D-22844 Norderstedt
70. Thorpe AD, Mason B (1966) The evaporation of ice spheres and ice crystals. *Br J Appl Phys* 17(4):541–548. <https://doi.org/10.1088/0508-3443/17/4/316>
71. Tong HJ, Ouyang B, Nikolovski N, Lienhard DM, Pope FD, Kalberer M (2015) A new electro-dynamic balance (EDB) design for low-temperature studies: application to immersion freezing of pollen extract bioaerosols. *Atmos Meas Tech* 8(3):1183–1195. <https://doi.org/10.5194/amt-8-1183-2015>
72. Tryggvason G, Bunner B, Esmaeeli A, Juric D, Al-Rawahi N, Tauber W, Han J, Nas S, Jan YJ (2001) A front-tracking method for the computations of multiphase flow. *J Comput Phys* 169(2):708–759
73. Tryggvason G, Lu J (2015) Direct numerical simulations of flows with phase change. *Procedia IUTAM* 15:2–13. <https://doi.org/10.1016/j.piutam.2015.04.002>. IUTAM symposium on multiphase flows with phase change: challenges and opportunities
74. Udaykumar H, Mittal R, Shyy W (1999) Computation of solid-liquid phase fronts in the sharp interface limit on fixed grids. *J Comput Phys* 153:535–574. <https://doi.org/10.1006/jcph.1999.6294>
75. Vali G (1996) Ice nucleation—a review. In: Nucleation and atmospheric aerosols 1996. Pergamon. <https://doi.org/10.1016/B978-008042030-1/50066-4>
76. van Leer B (1979) Towards the ultimate conservative difference scheme. V: a second-order sequel to Godunov's method. *J Comput Phys* 32(1):101–136. [https://doi.org/10.1016/0021-9991\(79\)90145-1](https://doi.org/10.1016/0021-9991(79)90145-1)
77. Walker J (1977) Evolution of the atmosphere. Macmillan
78. Welch SWJ, Wilson J (2000) A volume of fluid based method for fluid flows with phase change. *J Comput Phys* 160(2):662–682
79. Zhang S, Davis E (1987) Mass transfer from a single micro-droplet to a gas flowing at low Reynolds number. *Chem Eng Commun* 50(1–6):51–67. <https://doi.org/10.1080/00986448708911815>

**Open Access** This chapter is licensed under the terms of the Creative Commons Attribution 4.0 International License (<http://creativecommons.org/licenses/by/4.0/>), which permits use, sharing, adaptation, distribution and reproduction in any medium or format, as long as you give appropriate credit to the original author(s) and the source, provide a link to the Creative Commons license and indicate if changes were made.

The images or other third party material in this chapter are included in the chapter's Creative Commons license, unless indicated otherwise in a credit line to the material. If material is not included in the chapter's Creative Commons license and your intended use is not permitted by statutory regulation or exceeds the permitted use, you will need to obtain permission directly from the copyright holder.



# Experimental Investigations of Near-critical Fluid Phenomena by the Application of Laser Diagnostic Methods



Grazia Lamanna, Christoph Steinhausen, Andreas Preusche,  
and Andreas Dreizler

**Abstract** Physics of supercritical fluids is extremely complex and not yet fully understood. The importance of the presented investigations into the physics of supercritical fluids is twofold. First, the presented approach links the microscopic dynamics and macroscopic thermodynamics of supercritical fluids. Second, free falling droplets in a near to supercritical environment are investigated using spontaneous Raman scattering and a laser induced fluorescence/phosphorescence thermometry approach. The resulting spectroscopic data are employed to validate theoretical predictions of an improved evaporation model. Finally, laser induced thermal acoustics is used to investigate acoustic damping rates in the supercritical region of pure fluids.

## 1 Introduction

The physics of supercritical fluids is extremely complex and till today not fully understood. This is due to a number of concurrent factors, which are briefly discussed hereafter. First of all, a new theoretical framework is currently under development that links closely the dynamics and thermodynamics of supercritical fluids. This approach dates back to the pioneering work of Gorelli et al. [6, 7], who investigated the propagation of density fluctuations in supercritical fluids as a function of pressure and temperature. The authors found a direct correlation between the damping of acoustic waves and the occurrence of extrema in thermodynamic response functions (e.g. specific heat capacity  $c_p$ , thermal diffusivity  $D_T$  and kinematic shear  $\nu_s$  and volume  $\mu_b$  viscosities). It was found that the maxima of  $c_p$ , defining the so called Widom line, divide the supercritical region in a liquid-like and in a gas-like sub-region. In the gas-like area, the adiabatic propagation of sound waves was observed.

---

G. Lamanna (✉) · C. Steinhausen

Institute of Aerospace Thermodynamics (ITLR), University Stuttgart, Stuttgart, Germany  
e-mail: [grazia.lamanna@itlr.uni-stuttgart.de](mailto:grazia.lamanna@itlr.uni-stuttgart.de)

A. Preusche · A. Dreizler

Reactive Flows and Diagnostics (RSM), Technical University Darmstadt, Darmstadt, Germany

Instead, in the liquid-like region, positive sound dispersion was detected, as result of a complex interplay of acoustic and thermal waves [6]. Macroscopically, this occurs when the measured acoustic damping rate  $\Gamma$  deviates from the classical counterpart  $\Gamma_c$  due to non negligible volume viscosities, as typically found in liquids [17]. Second, reliable experimental data for the supercritical region are still missing, thus significantly hampering the validation of theoretical and thermodynamic models. This is particularly true with respect to the determination of fluid temperature and composition in two-phase mixing regimes. Third, the physical mechanisms controlling the transition from two-phase to single-phase mixing are still not understood. In our previous investigations [9, 10], we analysed different theoretical models and assessed their capability to predict the onset of single-phase mixing. The analysis clearly showed that, in presence of large temperature and/or concentration gradients, the role of evaporation cannot be neglected.

These preliminary considerations lie out the research path of the present work, which is summarised in the following sections. First, we have focused on the study of a single droplet at near-critical conditions. Contrary to sprays, droplets provide a simplified configuration, for which analytical solutions can be obtained to describe the simultaneous exchange of mass and energy at high-pressure conditions. Second, we have built a high-pressure, temperature-controlled test rig, equipped with an electrical droplet generator, to perform droplet experiments under controlled conditions. Third, several laser diagnostic methods have been developed and improved to enable the measurement of mean droplet temperatures and composition in the wake of an evaporating droplet. Moreover, laser induced thermal acoustics (LITA) has been extended to enable the measurement of the acoustic damping rates in the supercritical region of pure fluids. Following the approach proposed by Mysik [17], these measurements enable us, for the first time, to assess the importance of volume viscosity in the liquid-like supercritical region and may lead to improved closure models for modelling momentum transport and dissipation effects in supercritical fluids. Finally, the temperatures derived from non-resonant, spontaneous Raman scattering data and laser induced fluorescence and phosphorescence thermometry (LIFT) data provided by Preusche et al. [23] are employed to validate the theoretical prediction of an improved evaporation model. It is important to emphasise, that only the temporal evolution of the droplet temperature can be validated, since the presented measurements do not allow droplet size investigations. Additionally, the concentration field measured using non-resonant Raman scattering is compared to direct numerical simulation of a free falling evaporating droplet at high pressure and temperature conditions.

## 2 Experimental Setup

Experimental investigations are performed using two heatable high pressure, high temperature chambers. Two chambers are used since the investigations are performed at two different laboratories. One chamber is optimized for spectroscopic investigations, while the other is used for phenomenological investigations as well as measurements, using laser induced thermal acoustics. To distinguish between both chambers the first chamber located at the Technical University of Darmstadt (TUDA) is referred to as TUDA-chamber, whilst the second one located at the University of Stuttgart (US) is named US-chamber. Both chambers are designed for investigations of free-falling droplets in a near-critical environment. The droplet generator on top of the high pressure, high temperature chamber can be replaced with a closed lid for operation as homogeneous flow reactor for calibration purposes. The experimental setups are operated as continuous-flow reactors. The inlet mass flow is controlled using a Coriolis-based mass flow controller for carbon dioxide and carbon dioxide mixtures or a heat-capacity based mass flow controller for other fluids. Pressurized fluids are supplied through an annular orifice on top of the chambers. The pressure is controlled using a pneumatic valve at the system exhaust. The pressure inside the chamber is measured at the chamber exhaust by a temperature-compensated pressure transducer with an uncertainty rated at  $\pm 0.05$  MPa (US-chamber) or  $\pm 0.03$  MPa (TUDA-chamber). Temperature measurements inside the chamber are located at three different heights using resistance thermometers (US-chamber) or type-K thermocouples (TUDA-chamber) penetrating the metal core. Due to the temperature dependent uncertainty of the resistance thermometers the measurement uncertainties are calculated for each condition separately. The uncertainty of the type-K thermocouples is rated at  $\pm 1$  K. Both temperature and pressure are logged continuously. To ensure no contamination from previous investigations, the chamber is carefully evacuated before each set of experiments.

The US-chamber depicted in the upper part of Fig. 1 is built with heat-resistant stainless steel (EN-1.4913). It is designed for pressures up to 8 MPa and temperatures up to 773 K. For optical accessibility eight ultra-violet (UV)-transparent quartz windows are placed at two different heights with an angle of 90° to each other. The temperature is controlled using eight heating cartridges in the chamber body and a heating plate with four cartridges below the chamber. The temperature in the cartridges and the chamber body is hereby measured using type-K thermocouples. The chamber encloses a cylindrical core with a height of 240 mm and a diameter of 40 mm. A mineral-based silicate is used for thermal insulation. Additionally, the bottom of the heating plate is insulated using a vermiculite plate. The TUDA-chamber depicted in the lower part of Fig. 1 is designed for pressures up to 6 MPa and temperatures up to 553 K. The chamber is built with temperature-resistant stainless steel (EN-1.4571) and is optically accessible through four UV-transparent quartz windows placed at an angle of 90° to each other. The temperature is controlled using six heating cartridges in the chamber body. The temperature in the cartridges is hereby measured using type-J thermocouples. The elevated pressure chamber

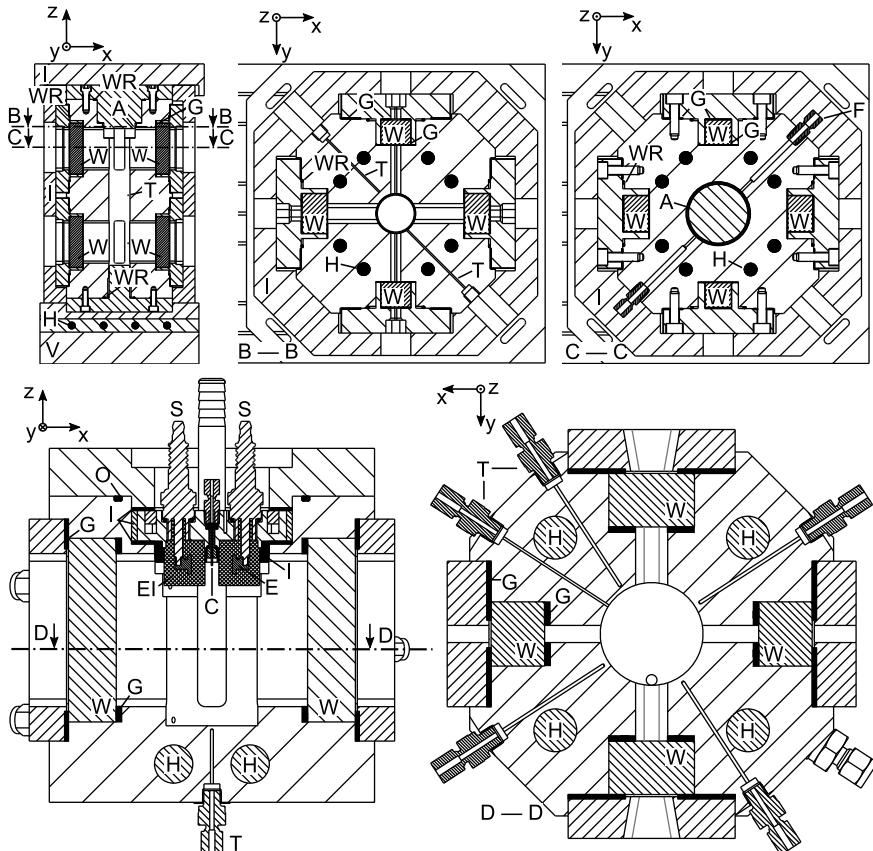


**Fig. 1** Horizontal and vertical sections of both chambers. **Upper left:** Vertical section through US-chamber. **Upper centre (section B—B):** Horizontal section through US-chamber at centre of first window. **Upper right (section C—C):** Horizontal section through US-chamber at fluid inlet and annular orifice. **Lower left:** Vertical section through TUDA-chamber. **Lower right (section D—D):** Horizontal section through TUDA-chamber at point of temperature measurement. A: annular orifice; EI: electrical insulation; F: fluid inlet; G: graphite gaskets; H: heating cartridges; I: thermal insulation; O: FFKM O-rings; S: spark plug; T: resistance thermometer; V: vermiculite plate; W: quartz windows; WR: Willis O-rings

encloses a cylindrical core with a height of 85 mm and a diameter of 48 mm. A detailed description of the droplet generator and its periphery as well as an investigation on the reproducibility of the droplet detachment, can be found in the works of Weckenmann et al. [32], Oldenhof et al. [18] and Lamanna et al. [9]. Ouedraogo et al. [20] presented a numerical study of the detachment principle as well as the underlying physics.

### 3 Experimental Methods

#### 3.1 2D Raman Spectroscopy for Mixture Fraction Determination

Spontaneous Raman scattering can be used to identify different substance molecules due to their spectral response to common incident light [5]. In order to measure the binary mixture fractions in the wake of the evaporating droplets, the Raman Stokes shift response of the involved substances is used. The liquid injected substances feature more complex Raman scattering responses compared to the ambient gas phase nitrogen ( $N_2$ ), which exhibits one vibrational stretching response at a wavenumber shift of around  $2330\text{ cm}^{-1}$ . However, only the carbon hydrogen (C-H) stretching region of their response is evaluated at a wavenumber shift in the region of around  $2700\text{--}3000\text{ cm}^{-1}$  for acetone, *n*-heptane, *n*-hexane and di-ethyl-ether. For the fluoroketone FK-5-1-12, the filters are changed to include the wavenumbers of  $400\text{--}1400\text{ cm}^{-1}$ , which includes the C-H<sub>2</sub> bending response. Generally, the spectral peaks are not temperature or pressure invariant and shift in their wavelength slightly with changes in those conditions (single digit wavenumbers) [30], but selecting broader filter and integration bands can mitigate this.

The detection system, starting from the pressure vessel, uses an achromatic lens, followed by a optic relay with two objective lenses. The relay is used to focus to infinity and parallelize the incoming light as much as possible to minimize angle dependent filtering. This leads into the filter section. First, the Rayleigh scattering at  $532\text{ nm}$  is blocked, subsequently the image is split spectrally by the image splitter. Two additional filters on the two camera paths each then restrict the remaining signals further spectrally, before they are imaged through objective lenses by two charge coupled devices (CCD) cameras. Due to the used binning, best possible resolution is approximately  $33\text{ }\mu\text{m}\times130\text{ }\mu\text{m}$  (vertical  $\times$  horizontal). A more detailed description of the optical setup is presented in [1]. The  $N_2$  and C-H filter regions are the integrated signals for two recording channels,  $S_{\text{sp}}$  and  $S_{\text{amb}}$ , that are used to measure the mixture fraction.

A pulsed neodymium-doped yttrium aluminium garnet (Nd:YAG) laser is used as illumination source. Two  $1\text{ }\mu\text{s}$  apart,  $7.5\text{ ns}$  long laser pulses are shaped into a  $130\text{ }\mu\text{m}$  thick ( $e^{-2}$ ),  $12\text{ mm}$  high vertical laser sheet. This sheet is subsequently trimmed by an aperture edge to a height of approximately  $7\text{ mm}$  and forms the image plane above the falling droplets as shown in Fig. 2. The intensity profile of the laser is changed to approximately ( $M^2$ ) of  $6\text{--}7$ , which produces a larger diffraction limited focus and prevents laser breakthroughs in the dense gas while simultaneously allowing a wider beam at the pressure vessel windows. The pulse energy is around  $300\text{ mJ}$  each.

The Raman cross-section of the substances represents an interaction probability of the photons scattering off the substance molecules. They vary between substances and their individual Raman response bands, as well as with changing temperature [14]. This necessitates calibration of the relevant mixture fractions at variable conditions, as the scattering intensities are proportional to the cross-sections. However, the

temperature range in the experiments is relatively low (393–553 K), and calibration results showed no discernible temperature and pressure dependence for mixing with nitrogen. The method is only shortly introduced. A more in depth explanation can be read in Bork et al. [1].

### 3.1.1 Evaluation

For calibration, the mixture fractions are set with mass flows and evaporated into the pressure vessel via an evaporator and temperature controlled tubing to prevent condensation. The target vapor mixture fraction inside the vessel can then be determined with [1, 2]

$$x_{\text{sp, set}} = \frac{N_{\text{sp}}}{N_{\text{sp}} + N_{\text{amb}}} = \frac{S_{\text{sp}}}{S_{\text{sp}}(1 - k_2) + k_1 S_{\text{amb}}}, \quad (1)$$

where  $x_{\text{sp, set}}$  is the mass flow determined molar mixture fraction of the injected fluid substance,  $N_{\text{sp}}$  is the molecule number density of the injected fluid substance and  $N_{\text{amb}}$  is the molecule number density of the ambient gas phase substance. The scattering intensity of nitrogen is proportional to its Raman cross-section, which differs from the other substances. In order to correlate the measured signals ( $S_{\text{sp}}$ ,  $S_{\text{amb}}$ ) to the number of molecules, a scaling factor is introduced between the measured injected substances and nitrogen,  $k_1$ . An additional factor,  $k_2$ , deals with the cross-talk between the two channels and is therefore subtracted proportionally with  $S_{\text{sp}}$  from the ambient signal. This is evaluated per image pixel to account for local deviations of the imaging system.

The two parameters  $k_1$  and  $k_2$  are fit to minimize deviations against  $x_{\text{set}}$  using non-linear least squares regression. The pressures 2, 4 and 6 MPa and variable temperatures ranging from 393 to 513 K (depending on substance) are calibrated, with mixture fractions increased until set point stability cannot be maintained or onset of condensation. Comparing the factors  $k_1$  between the substances with C-H stretching response shows that the scattering intensities are approximately proportional to the number of C-H bonds using this detection method [2].

Finally, during the measurement of evaporating droplets, the wakes are imaged identically to the calibration. The results are evaluated for  $x_{\text{sp}}$  and a modified mixture fraction result that is described in the following.

### 3.1.2 Relative Density and Adiabatic Mixing Temperature Estimation

The other way to interpret the wake behind the falling droplet involves the gas phase further away from the droplet wake, but still inside the imageable field of view. There, the mixture fraction of the injected liquid is very low or below the detection threshold. Due to the calibration of the parameter  $k_1$ , there is a correlation between

the signal strength of nitrogen and the injected fluid. Additionally, since the injected fluid presence is low, the cross-talk influence is low as well. These specific conditions are used to create an approximate maximum signal value of this fluid in the following way

$$S_{\text{sp,max}} = k_1 S_{\text{amb},x_{\text{sp}}=0}. \quad (2)$$

$S_{\text{sp,max}}$  is the approximate maximum count value in the image of the injected fluid, if it had the number density of the pure nitrogen that is actually imaged at that position. In other words, the pure nitrogen signal  $S_{\text{amb},x_{\text{sp}}=0}$  at the edges of the camera field of view is used to derive a pure injected fluid signal at this reference number density. Referring to Fig. 2, this information would be derived from beyond the left image border (from where the laser sheet enters), as the wake results are cropped to the droplet wake. With this information, the alternative mixture fraction value  $x_{\text{sp},l}$  is derived

$$x_{\text{sp},l} = \frac{S_{\text{sp}}}{S_{\text{sp,max}}}, \quad (3)$$

where the mixture fraction is calculated as the fraction of the injected fluid species signal  $S_{\text{sp}}$  and its' approximated maximum  $S_{\text{sp,max}}$ . This concentration result is erroneous, because the number density reference is that of pure nitrogen at the pressure vessel conditions. The fraction of the locally correct concentration and this result is used as a measure of number density increase due to mixing and temperature change

$$\frac{x_{\text{sp}}}{x_{\text{sp},l}} = \frac{N}{N_{\infty}}. \quad (4)$$

Using the Virial equation of state (EOS) together with Tsonopoulos' model for mixing and the second coefficient, as well as Orbey and Vera's model for the third coefficient [16, 19, 22, 31], the nitrogen and injected fluid mixture properties are derived using an adiabatic mixing approach from the respective pure substance data sourced from Refprop [12]. As reference points, the to be mixed pure nitrogen is always at the relevant conditions of the pressure vessel. The pressure of the injected substance is known, but not its temperature, since the injector temperature does not represent the true fluid temperature at the time of the wake recording.

Using non-linear least squares regression, the mixed fluid's relative number density is repeatedly re-evaluated as a function of mixture fraction using different starting enthalpies for the injected substance. This process finds a theoretical, pure liquid starting enthalpy, that minimizes the difference between modeled and the experimentally derived relative number density. The mixture is then adiabatically mixed using this pure liquid enthalpy and the enthalpy from the ambient gas at pressure vessel conditions. Finally, temperatures for each given mixture fraction can be approximated using the EOS. So there is a correlation between the mixture fraction  $x_{\text{sp}}$  and the temperature of the vapour in the droplet wake. This can be seen in Fig. 2 in Section

**4.1.** The actually measured vapour concentration never reaches the saturation condition, so temperatures for mole fractions past the measurement derived densities are extrapolated using these EOS results. An example can be seen in Fig. 5 in Section 5.

However, the found injected substance temperature is not physical with respect to the experiment, as the injection into the vessel is not an adiabatic process, furthermore this consideration neglects all dynamic processes [1, 10]. Rather, the intersection of the vapour-liquid equilibrium (VLE) of the mixtures and the adiabatic mixing line is used to estimate the liquid phase temperature. Since the third Virial coefficient derivation of Orbey and Vera [19] isn't valid for polar fluids, this method wasn't strictly suited for acetone mixing. Furthermore, the employed enthalpy mixing rule neglected excess enthalpy. To measure the liquid phase of the droplet independently from this extrapolation, laser-induced fluorescence and phosphorescence thermometry was attempted with acetone. Additionally, a different EOS is then used to account for polarity and excess mixing enthalpy.

### 3.2 *Laser Induced Fluorescence and Phosphorescence Thermometry*

The fluorescence of a substance is the emission of a photon after the absorption of another photon by the involved molecule. In contrast to scattering processes, the molecule is now resonant to the incoming photon and enters a higher energy state. In order to return to the ground state, the molecule may emit the photon from this higher state. The two radiative processes that can happen are the fluorescence and the phosphorescence. The fluorescence is a fast process, where the radiation is given off in the order of nanoseconds. The phosphorescence emits from an intermediate lower energy state. Time is needed to transition to this intermediate state and to emit the photon, which now has less energy and is therefore, in general, red-shifted compared to the fluorescence emission. The phosphorescence generally transpires in the range of  $10^{-6}$ – $10^0$  seconds. Acetone can be excited with UV light and then emits both fluorescence and phosphorescence as described. The spectral overlap between the two radiations is significant. The temporal overlap is small, and through time gating these two emissions can be separated sufficiently [2, 3, 24, 25].

In order to estimate the droplet temperature of acetone, the temperature dependent quenching of the phosphorescence is exploited. This is normalized with the combined fluorescence and phosphorescence response to reference the local UV energy area density inside the droplet. However, the phosphorescence signal is relatively weak, so the fluorescence signal is dominant in this normalization. The energy area density dependent emission of the fluorescence is linear with respect to the employed measurement energy ( $\geq 1.5 \text{ mJ cm}^{-2}$ ). The phosphorescence response, however, exhibits saturation effects starting below  $1 \text{ mJ cm}^{-2}$  [2, 3]. This necessitates an energy dependent calibration.

### 3.2.1 Evaluation

For calibration, the pressure vessel is filled with acetone and a vertical rectangular UV profile of approximately  $8\text{ mm} \times 2\text{ mm}$  is imaged into the acetone using an optic 4f relay and 320 nm dye laser emission source. The absorption cross-section of acetone is relatively low at this wavelength [34], which is advantageous due to the very low absorption in the vapour phase. The UV light is therefore negligibly absorbed in the nitrogen acetone vapour mixture towards the liquid droplet.

Similar to the Raman detection setup, a two CCD camera system is used. One camera records the combined non-intensified fluorescence and phosphorescence response and the other camera the intensified phosphorescence response, which is gated temporally from the fluorescence using the intensifier gate. A 650 nm short pass spectral filter is responsible for blocking the trigger laser (emitting at 675 nm), which is used to start the recording chain on droplet crossing. The image splitter is now a 30% transmission 70% reflection mirror. The stronger reflection signal is guided towards an objective lens with image intensifier for the phosphorescence signal. This reduces the necessary amplification. The fluorescence phosphorescence combination is imaged using the 30% transmission signal, now imaged by an identical objective lens and camera, but without image intensification. The time gate delay for the phosphorescence separation is set using the steep edge fall-off of the initial fluorescence signal. It is set to 20 ns after the 50% count level compared on the camera, compared to the maximum. This maximum is reached when the entire fluorescence peak is imaged from its beginning. A more detailed description of the setup is available in [23].

The acetone is now imaged in two different ways at variable temperatures and pressures. The temperature is limited by either evaporation, both in the calibration setup and when failing to generate droplets in the experiment, or the critical point around 508 K at 6 MPa. The acetone then becomes supercritical during calibration, which can not be achieved during droplet injection. Additionally, beyond 500 K the phosphorescence signal becomes very weak and imaging it becomes difficult even with an image intensifier. The measured pressures are chosen to reproduce those of the acetone and nitrogen droplet wake mixture fraction Raman experiment at 2, 4 and 6 MPa. First, the timing is set so that the phosphorescence is recorded separately, gated by the intensifier. This yields

$$V = \frac{\sum S_{\text{LIP,I},\text{ROI}}}{\sum S_{\text{LIP+LIF},\text{ROI}}} \quad (5)$$

Here, the images are summed across the pixels of the region of interest (ROI) which have count values above the background offset plus detection noise. The signal with the subscript LIP,I is the laser induced phosphorescence response alone imaged by the intensified camera, while LIP+LIF is both fluorescence and phosphorescence as recorded by the non-intensified camera. In order to mitigate intensifier amplification and liquid density based changes to the emission intensity, an amplification ratio between the two cameras is recorded with the time gating on the intensifier changed to include the entire fluorescence emission as well

$$V_{\text{amp}} = \frac{\sum S_{\text{LIP+LIF,I,ROI},i}}{\sum S_{\text{LIP+LIF,ROI},i}} \quad V_{\text{LIFP},i} = \frac{V_i}{V_{\text{amp}}}. \quad (6)$$

The amplification measurement is averaged over all frames  $i$  to generate the set-point amplification factor  $\bar{V}_{\text{amp}}$ . The calibration measurement value is  $V_{\text{LIFP},i}$  and the UV energy area density  $E_{\text{UV}}$ .  $V_{\text{LIFP},i}$  is fit with a first order polynomial against the energy area density for every pressure-temperature combination

$$V_{\text{LIFP,E}} = AE_{\text{UV}} + B \quad T_{\text{LIFP}} = \frac{CV_{\text{LIFP,E}}(E_{\text{UV}}) + D}{GV_{\text{LIFP,E}}(E_{\text{UV}})^2 + HV_{\text{LIFP,E}}(E_{\text{UV}}) + I}. \quad (7)$$

The fit parameters  $A$  and  $B$  are determined for every calibration set point. The non-linear fit parameters  $C, D, G, H, I$  are fit for each queried  $E_{\text{UV}}$ . The droplet measurement value of  $\bar{V}_{\text{LIFP},i}$  is then put into the equation for the estimated temperature using LIFP  $T_{\text{LIFP}}$ , with the fit parameters for an equivalent energy density  $E_{\text{UV}}$  to determine the temperature. This calibration method was found to be pressure independent within discernible precision and accuracy [23].

Note that the temperature is only evaluated for the average of 500 droplets. This is done to mitigate the influence of changing droplet topology and signal lensing of the liquid phase. Additionally, signals that cross certain count thresholds are discarded or lead to the entire image pair of the channels to be discarded. Otherwise, the lensing, leading to higher local excitation energy densities, introduces strong systematic errors into the temperature evaluation. The uncertainty was determined to be of the order of  $\pm 3 \text{ K}$  [23].

### 3.3 Laser Induced Thermal Acoustics

Laser induced thermal acoustics (LITA) also more generally known as laser induced (transient) grating spectroscopy (LIGS) utilizes the non-linear interaction of matter with an optical interference pattern to measure independently and simultaneously speed of sound, acoustic damping rates as well as thermal diffusivities. The optical interference pattern is generated by two short pulsed excitation laser beams from a pulsed Nd:YAG laser with an excitation wavelength  $\lambda_{\text{exc}} = 1064 \text{ nm}$ , a laser pulse length of  $\tau_{\text{pulse}} = 10 \text{ ns}$  and a  $30 \text{ GHz}$  line-width. The excitation beams are crossed with the same direction of linear polarization to produce a spatially periodic modulated polarization/light intensity distribution. A third input wave is provided using a continuous wave DPSS laser with a wavelength of  $\lambda_{\text{int}} = 532 \text{ nm}$  and a  $5 \text{ MHz}$  line-width to interrogate the resulting changes in the optical properties of the investigated fluids and is scattered by the spatially periodic perturbations within the measurement volume. All beams are focused into the probe volume using an AR-coated lens with a focal length of  $f = 1000 \text{ mm}$  at  $532 \text{ nm}$ . The scattered signal beam is spatially and spectrally filtered using a coupler and single-mode/multi-mode fibres and detected

by an avalanche detector. The voltage signal is logged with 20 GS/s by a 1 GHz bandwidth digital oscilloscope.

A detailed description of the optical arrangement used for the presented investigations as well as the spatial resolution of approximately 312 mm in diameter and less than 2 mm in length in the  $x$ -direction can be found in the work of Steinhausen et al. [28]. For a theoretical description of the generation of laser induced gratings the reader is referred to Cummings et al. [4], Schlamp et al. [26] as well as Stampanoni-Panariello et al. [27].

### 3.3.1 LITA Post-processing

The speed of sound can be extracted from a LITA signal using direct Fourier transformation (DFT). Note that the speed of sound data is hereby obtained from the frequency domain of the LITA signal using only geometrical parameters of the optical setup. Hence, no modelling assumptions or equations of states are necessary. As described by Hemmerling et al. [8] the speed of sound  $c_s$  can be estimated as follows

$$c_s = \frac{\nu \Lambda}{n}. \quad (8)$$

The dominating frequency of the LITA signal is  $\nu$  and the constant  $n$  indicates the resonant behaviour of the fluid. For resonant fluid behaviour  $n = 1$ , whereas in case of non-resonant fluid behaviour  $n = 2$ . The grid spacing of the optical interference pattern is denoted by  $\Lambda$  and is a calibration parameter for the optical setup.  $\Lambda$  can be expressed as referred in Stampanoni-Panariello et al. [27] as

$$\Lambda = \frac{\lambda_{exc}}{2 \sin(\Theta/2)}, \quad (9)$$

where  $\lambda_{exc}$  denotes the wavelength of the excitation beams and  $\Theta$  is the crossing angle of the excitation beams.

As described in our previous work [28] the evaluation of LITA signals proposed by Schlamp et al. [26] enables us after careful calibration to extract the speed of sound  $c_s$ , the acoustic damping rate  $\Gamma$  as well as the thermal diffusivity  $D_T$  from the shape of the LITA signal. Using the assumptions presented by Steinhausen et al. [28] the time-dependent diffraction efficiency  $\Psi(t)$  of a detected LITA signal shows the following dependencies

$$\Psi(t) = f(c_s, t, t_0, D_T, U_{eP}, U_\Theta, \bar{\eta}, \Lambda, \Gamma, \sigma, \omega), \quad (10)$$

where  $t_0$  indicates the time of the laser pulse,  $t$  the time,  $\bar{\eta}$  the beam misalignment in horizontal  $y$ -direction.  $U_\Theta$  and  $U_{eP}$  denote the approximate modulation depth of thermalisation and electrostriction gratings, respectively, and the Gaussian half-

width of the excitation and interrogation beam in the focal point is expressed as  $\omega$  and  $\sigma$ , respectively.

The calibration of the geometrical parameters of the optical arrangement, namely the grid spacing of the optical interference pattern  $\Lambda$  and the Gaussian half-width of the excitation beam  $\omega$ , is done in well-known quiescent conditions.  $\Lambda$  is hereby calculated using measurements in a pure nitrogen and pure argon atmosphere. A DFT together with a von Hann window and a bandpass filter is used together with Eq. (8). For the calibration of the Gaussian half-width of the excitation beam  $\omega$  only investigations in a pure argon atmosphere with pressures up to 4 MPa are utilised. Argon is chosen as the fluid for calibration because of two reasons. First, argon shows non-resonant fluid behaviour leading to a simplified model of the LITA signal independent from the thermal diffusivity (see [26, 28]). Second, for gaseous argon the volume viscosity is negligible compared to the shear viscosity (see [13, 15]). Therefore, the acoustic damping rate can be estimated using the expression for the classic acoustic damping rate shown in Li et al. [13]

$$\Gamma_c = \frac{1}{2\varrho} \left[ \frac{4}{3} \mu_s + (\gamma - 1) \frac{\kappa}{c_p} \right]. \quad (11)$$

The fluid density is indicated by  $\varrho$ ,  $\gamma$  is the specific heat ratio,  $\mu_s$  the shear viscosity,  $\kappa$  the thermal conductivity and  $c_p$  the specific isobaric heat capacity. Curve fitting of the LITA signal to the theoretical expression presented by Steinhause et al. [28] is achieved using a robust non-linear least-absolutes fit with the Levenberg–Marquardt algorithm. For this purpose, the non-linear fit in Matlab R2018a (MathWorks) with the robust option Least Absolute Residuals (LAR) is utilised.

## 4 Results

### 4.1 Raman Mixture Fractions

The results of the Raman campaign are quantitative mixture fractions in droplet wakes of the measured substances, as well as the temperature estimations derived from measurement number density considerations. Figure 2 shows examples for *n*-hexane droplets in nitrogen atmosphere.

The adiabatic mixing temperature  $T_{\text{ad,mix}}$  estimated from the experiment number density is put into context with the mixture VLE. The VLE is interpolated from isotherms calculated with the Peng-Robinson EOS, Huron-Vidal mixing rule, Mathias-Copeman alpha function and the non-random two liquid Gibbs free excess model (personal communication J. Vrabec, Thermodynamics and Thermal Separation Processes, University Berlin). The actual measured mixture fractions are always far below saturation in all conditions. In order to have temperature information beyond the actually measured mixture fractions, the EOS states are fitted to

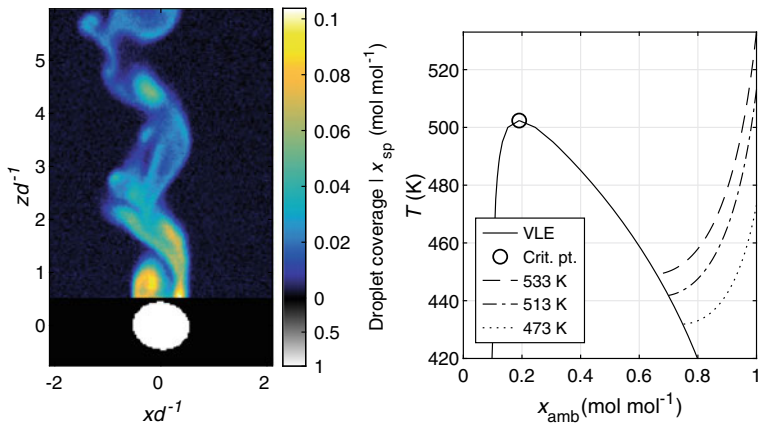


**Fig. 2** *n*-hexane droplets in nitrogen atmosphere. **Left:** single droplet mixture fraction result for nitrogen atmosphere temperature of  $T_{ch} = 533$  K, injector temperature of  $T_{inj} = 473$  K and pressure of  $p_{ch} = 6$  MPa. Horizontal  $x$  and vertical  $z$  distances are normalized to approximated droplet diameter  $d$ . **Right:** number density data estimated adiabatic mixing temperature curves dependent on mixture fraction. Varying ambient nitrogen temperature as shown, injector temperature fixed at 473 K and a pressure of 6 MPa

the experimental data and can be used as an extrapolation towards the dew line [1, 10]. Due to the involved assumptions and approximations, this temperature function becomes more erroneous with rising mixture fraction.

#### 4.2 Laser Induced Fluorescence and Phosphorescence Thermometry

The number density data from the Raman experiments was fitted to an adiabatic mixing model using the PC-SAFT EOS. This differs from the approach for other fluids than nitrogen and acetone, where the previously described Virial EOS is used for mixing. However, the potential is there to improve the other temperature approximations as well using more advanced EOS. The advantages for using this EOS were the inclusion of excess properties for the adiabatic mixing, in addition to the EOS being fitted to experimental and molecular simulation data for the polar acetone and nitrogen mixture. The results show agreement within 9 K and can be read in Preusche et al. [23].

### 4.3 Laser Induced Thermal Acoustics

The validation of the calibration process of the grid spacing is depicted in Fig. 3. The relative distribution of the ratio between the speed of sound data extracted from the LITA signal using Eq. (8) and theoretical values taken from the National Institute of Standards and Technology (NIST) database by Lemmon et al. [11] is shown. Since the ratio between the measured and the theoretical value is chosen, a ratio of 1 indicates a perfect validation. Note that we omitted the distinction between the fluids argon, nitrogen as well as the fluid mixtures for clarity.

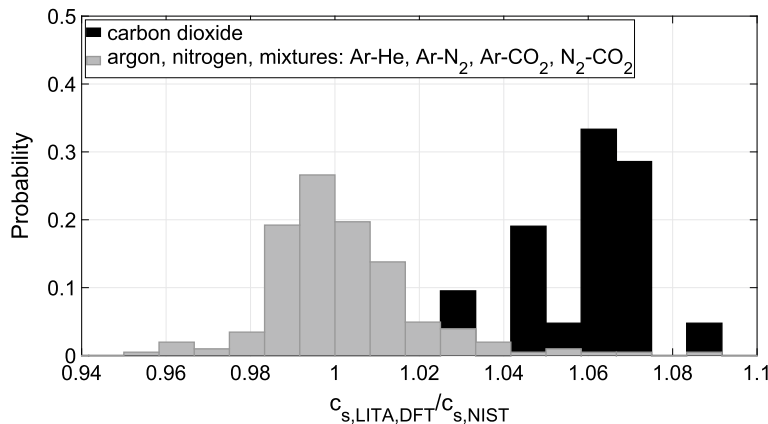


**Fig. 3** Relative distribution of the ratio between the measured speed of sound data and theoretical values for  $p_{\text{ch}} = 2$  to 8 MPa and temperatures up to  $T_{\text{ch}} = 700$  K (nitrogen –99.999% purity) and  $p_{\text{ch}} = 0.5$  to 8 MPa and temperatures up to  $T_{\text{ch}} = 600$  K (argon –99.998% purity and carbon dioxide –99.995% purity) as well as the investigated fluid mixtures argon-helium with mole fractions  $x_{\text{Ar}} = 0.9000$  and  $x_{\text{Ar}} = 0.2000$ , argon-nitrogen ( $x_{\text{Ar}} = 0.8000$ ), argon-carbon dioxide ( $x_{\text{Ar}} = 0.8000$ ) and nitrogen-carbon dioxide ( $x_{\text{N}_2} = 0.7999$ ) for  $p_{\text{ch}} = 0.5$  to 8 MPa and  $T_{\text{ch}} = 301$  K. The calibration resulted in a grid spacing of  $\Lambda = \Lambda_{\text{cal}} = 29.47 \pm 0.05$  mm. The speed of sound is calculated using a DFT with Eq. (8). Thermodynamic data for validation are taken from Lemmon et al. [11]

The observed offset in the distribution for carbon dioxide is a result of residual moisture in the experimental rig as discussed in Steinhausen et al. [28]. For all other fluids and fluid mixtures the distribution in Fig. 3 shows a good agreement between the measured speed of sound data and the theoretical values. Note that the measurement uncertainty using a confidence interval of 95% of the acquired speed of sound for all investigated fluids is below 2% while the width of the distribution is approximately 3%. Therefore we estimate that the speed of sound can be extracted with a relative uncertainty rated at 3% (95% confidence interval).

Figure 4 depicts acoustic damping rate ratios  $\Gamma_{\text{LITA}}/\Gamma_{c,\text{NIST}}$  for pure carbon dioxide (99.995% purity) at various temperatures for pressures between 0.5 and 8 MPa. For curve fitting the calibrated value for the grid spacing  $\Lambda = \Lambda_{\text{cal}} = 29.47$  mm as well as the calibrated values for the Gaussian beam width of the excitation beam

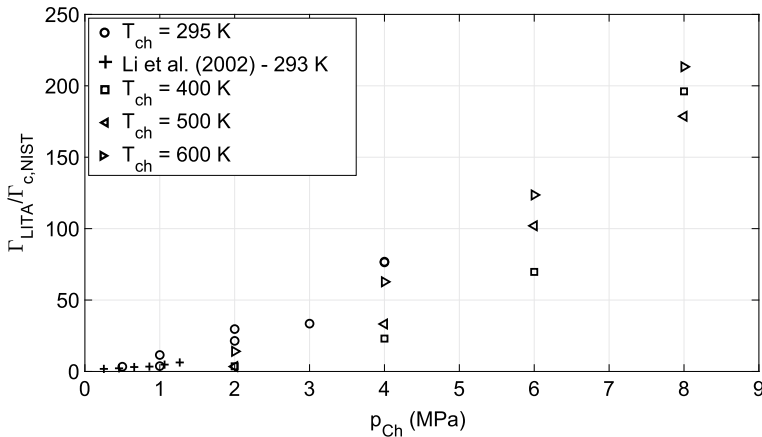


**Fig. 4** Acoustic damping rate ratio  $\Gamma_{LITA}/\Gamma_{c,NIST}$  over chamber pressure  $p_{ch}$  for pure carbon dioxide (99.995% purity) at temperatures up to 600 K temperature. Classical acoustic damping rates are estimated using NIST database by Lemmon et al. [11]. Experimental and theoretical data are taken from Li et al. [13]. Curve fitting input parameters:  $\Lambda = \Lambda_{cal} = 29.47\text{ mm}$ ;  $\sigma = \sigma_{th} = 177\text{ mm}$ ;  $\omega_{SM} = \omega_{SM,cal} = 254\text{ mm}$ ;  $\omega_{MM} = \omega_{MM,cal} = 225\text{ mm}$

$\omega_{SM} = \omega_{SM,cal} = 254\text{ mm}$ ;  $\omega_{MM} = \omega_{MM,cal} = 225\text{ mm}$  are used. For the latter a distinction between a single-mode fibre with diameter of 4 mm (SM) and a multi-mode fibre with diameter of 25 mm (MM) is implemented. The Gaussian beam width of the interrogation beam is set to the theoretical value based on the specification of the used laser source  $\sigma = \sigma_{th} = 177\text{ mm}$ . Values are compared to the experimental and theoretical investigations by Li et al. [13]. For pressures up to 1 MPa our experimental investigation shows good consensus with data by Li et al. [13]. At higher pressure the assumption of a linear pressure dependence seems to be not applicable and a monotonic increase in the acoustic damping rate ratios  $\Gamma_{LITA}/\Gamma_{c,NIST}$  is observed.

## 5 Discussion

The importance of volume viscosities for complex fluids, such as carbon dioxide, from sub- to supercritical fluid states is shown by the comparison of the measured acoustic damping rate  $\Gamma_{LITA}$  and the classic acoustic damping rate  $\Gamma_{c,NIST}$ , which neglects the contribution of the volume viscosity, shown in Fig. 4. For carbon dioxide this is also true at low pressure conditions. As depicted, the acoustic damping rate ratio shows a non-linear, monotonic increase. At near to supercritical pressures (6 to 8 MPa) the measured acoustic damping rate  $\Gamma_{LITA}$  exceeds the classic acoustic damping rate  $\Gamma_{c,NIST}$  by two orders of magnitude, which highlights the importance of the consideration of the volume viscosity in supercritical fluid physics.

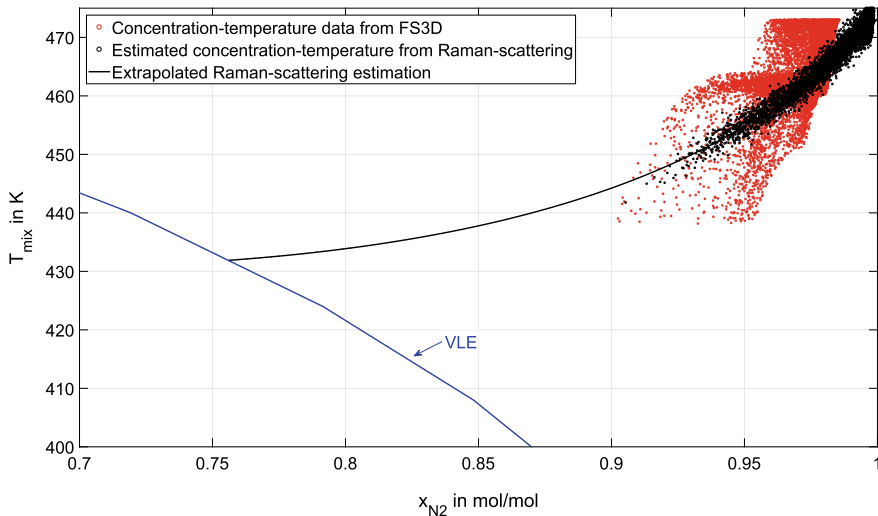


**Fig. 5** Comparison of Raman scattering, direct numerical simulation and theoretical concentration-temperature profiles; Black line: extrapolated curve fit of the experimental concentration-temperature data using an adiabatic mixing assumption together with the PC-SAFT EOS; Blue line: VLE; Ambient nitrogen temperature 473 K, injector temperature 473 K and pressure of 6 MPa. Droplet diameter at  $t = 0.5$  s is 1.25 mm. Image is taken from Steinhausen et al. [29]

The employed laser diagnostics methods, namely spontaneous Raman scattering and laser induced fluorescence and phosphorescence thermometry enable a quantitative comparison of droplet evaporation processes with theoretical evaporation models and direct numerical simulations. The Raman scattering investigations lead to a concentration-density field in the droplet wake. By applying the PC-SAFT EOS together with an adiabatic mixing assumption this concentration-density field can be used to estimate a concentration-temperature profile in the wake of the droplet. To compare the experimentally gained concentration-temperature profile of a n-hexane droplet in a nitrogen atmosphere with direct numerical simulations, we extracted the temperature and concentration of each numerical cell inside the region of interest from the numerical data; for more detail the reader is referred to Steinhausen et al. [29]. Figure 5 depicts the numerical data in red in a  $T,x$ -diagram. The concentration-temperature field estimated from the Raman scattering results are displayed in black. Furthermore, an extrapolated curve fit of the experimental concentration-temperature data is shown as a black line and the VLE is presented as a blue line. The latter is computed using the PC-SAFT EOS.

The presented comparison shows reasonably good agreement. Hence, our proposed method to extract temperature data from the Raman scattering results is supported by the direct numerical simulation. The extrapolated Raman temperature, proposed by Lamanna et al. [10], is the intersection of the PC-SAFT based fit of the experimental data with the VLE.

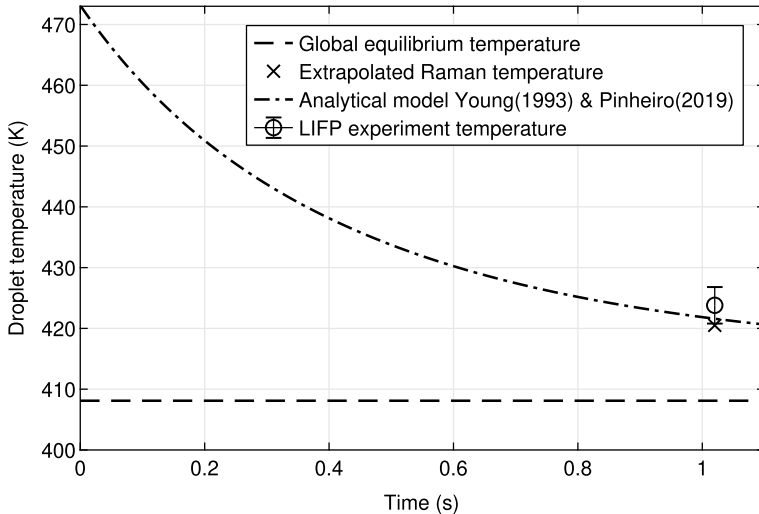


**Fig. 6** Comparison of the analytical model by Young [33] and modified Pinheiro et al. [21] with LIFP measurement, Raman extrapolated temperature and the theoretical global thermodynamic equilibrium. Ambient nitrogen temperature 513 K, injector temperature 473 K and pressure of 6 MPa. Droplet diameter at  $t = 1$  s is 1.35 mm

The performed spectroscopic investigations of free falling droplets are compared with the temperature evolution predicted by the evaporation model from Young [33]. In Fig. 6, the evolution of the droplet temperature of a preheated, free falling acetone droplet with an initial fluid temperature of 473 K in a nitrogen atmosphere with a temperature of 513 K at 6 MPa is depicted together with the estimated temperatures using LIFP and spontaneous Raman scattering. The temporal evolution is hereby estimated using an improved version of the evaporation model by Young [33]. To account for convective effects a convection correction from Pinheiro and Vedovoto [21] is applied. Additionally real gas effects are considered by taking the fugacity as well as solubility effects into account. Note that the evaporation model by Young [33] is a Langmuir type model following Onsager's theory and heat conduction within the liquid phase is not considered. Hence, the surface temperature of the droplet equals the liquid phase temperature. For a detailed description and discussion regarding the selection criteria of evaporation model as well as the importance of non-equilibrium models the reader is referred to Lamanna et al. [10]. The results show a good agreement between the Raman derived temperature estimation (extrapolated Raman temperature) and the LIFP temperature results measured with a droplet detachment frequency of 1 Hz and the analytical investigations. Note, that the evolution of the droplet temperatures, measured (circle and cross) or analytical (dash-dotted), are significantly above the global equilibrium temperature (dashed line) for the given conditions [23]. In case of an acetone droplet in nitrogen atmosphere, the droplets would reach a wet bulb temperatures above the global equilibrium tempera-

ture. The difference to the equilibrium is explained by the strong interdependencies of energy and mass fluxes at high pressures droplet evaporation as has been shown by Lamanna et al. [10]. Therefore, the evolution over time is strongly dependent on substance parameters and dynamic conditions such as the forced advection due to the fall velocity.

## 6 Conclusions

In the presented work, an experimental setup as well as three laser diagnostic techniques for the investigation of relaxation phenomena in supercritical fluids and near-critical droplet evaporation was introduced. By applying laser-induced thermal acoustics in pure fluids from sub- to supercritical fluid condition the importance of volume viscosities was assessed. The experimental results clearly indicate that volume viscosities should be considered when studying supercritical fluid phenomena. Using spontaneous Raman scattering the concentration-density field of a free falling evaporating droplet was measured and converted in a temperature-concentration field and an estimated droplet temperature. Comparisons between the extracted temperature-concentration field and a direct numerical simulation yields reasonably good agreement. The estimated Raman temperature was validated using direct LIFP thermography. Finally, both droplet temperatures measurements were utilised to validate the theoretical prediction of an improved evaporation model regarding the temporal evolution of the droplet temperature. The validation shows an excellent agreement between the direct droplet temperature measurement (LIFP), the estimated Raman temperature as well as the theoretical predictions by the improved evaporation model.

**Acknowledgements** The authors gratefully acknowledge the financial support by the Deutsche Forschungsgemeinschaft (DFG, German Research Foundation)—Project SFB–TRR 75, Project number 84292822.

## References

1. Bork B, Preusche A, Weckenmann F, Lamanna G, Dreizler A (2016) Measurement of species concentration and estimation of temperature in the wake of evaporating n-heptane droplets at trans-critical conditions. Proc Combust Inst. <https://doi.org/10.1016/j.proci.2016.07.037>
2. Bork BS (2017) Tropfenverdampfung in transkritischer Umgebung: Untersuchung mit laserspektroskopischen Methoden. PhD thesis, Technische Universität Darmstadt, Darmstadt, Germany
3. Charogiannis A, Beyrau F (2013) Laser induced phosphorescence imaging for the investigation of evaporating liquid flows. Exp Fluids 54(5):2179. <https://doi.org/10.1007/s00348-013-1518-2>
4. Cummings EB, Leyva IA, Hornung HG (1995) Laser-induced thermal acoustics (LITA) signals from finite beams. Appl Opt 34(18):3290–3302. <https://doi.org/10.1364/AO.34.003290>
5. Demiröder W (2007) Laserspektroskopie: Grundlagen und Techniken, 5th edn. Springer, Berlin, Heidelberg

6. Gorelli FA, Bryk T, Krisch M, Ruocco G, Santoro M, Scopigno T (2013) Dynamics and thermodynamics beyond the critical point. *J Phys Chem Lett* 3:1203. <https://doi.org/10.1038/srep01203>
7. Gorelli FA, Santoro M, Scopigno T, Krisch M, Bryk T, Ruocco G, Ballerini R (2009) Inelastic x-ray scattering from high pressure fluids in a diamond anvil cell. *Appl Phys Lett* 94:074102. <https://doi.org/10.1063/1.3076123>
8. Hemmerling B, Kozlov DN (1999) Generation and temporally resolved detection of laser-induced gratings by a single, pulsed Nd: YAG laser. *Appl Opt* 38(6):1001. <https://doi.org/10.1364/AO.38.001001>
9. Lamanna G, Steinhausen C, Weckenmann F, Weigand B, Bork B, Preusche A, Dreizler A, Stierle R, Gross J (2020) Laboratory experiments of high-pressure fluid drops: chapter 2. American Institute of Aeronautics and Astronautics (Hg.)—High-Pressure Flows for Propulsion Applications, pp 49–109. 10.2514/5.9781624105814.0049.0110
10. Lamanna G, Steinhausen C, Weigand B, Preusche A, Bork B, Dreizler A, Stierle R, Groß J (2018) On the importance of non-equilibrium models for describing the coupling of heat and mass transfer at high pressure. *Int Commun Heat Mass Transf* 98:49–58. <https://doi.org/10.1016/j.icheatmasstransfer.2018.07.012>
11. Lemmon EW, Bell IH, Huber ML, McLinden MO (2018) NIST standard reference database 23: reference fluid thermodynamic and transport properties-REFPROP, Version 10.0, National Institute of Standards and Technology. <https://doi.org/10.18434/T4JS3C>. <https://www.nist.gov/srd/refprop>
12. Lemmon EW, Huber ML, McLinden MO (2013) NIST standard reference database 23: reference fluid thermodynamic and transport properties-REFPROP. National Institute of Standards and Technology, Gaithersburg
13. Li Y, Roberts WL, Brown MS (2002) Investigation of gaseous acoustic damping rates by transient grating spectroscopy. *AIAA J* 40(6):1071–1077. <https://doi.org/10.2514/2.1790>
14. Magnotti G, KC U, Varghese PL, Barlow RS (2015) Raman spectra of methane, ethylene, ethane, dimethyl ether, formaldehyde and propane for combustion applications. *J Quant Spectrosc Radiat Transf* 163, 80–101 (2015). <https://doi.org/10.1016/j.jqsrt.2015.04.018>
15. Meier K, Laesecke A, Kabelac S (2005) Transport coefficients of the Lennard-Jones model fluid. III. Bulk viscosity. *J Chem Phys* 122(1), 14513 (2005). <https://doi.org/10.1063/1.1828040>
16. Meng L, Duan YY, Wang XD (2007) Binary interaction parameter  $k_{ij}$  for calculating the second cross-virial coefficients of mixtures. *Fluid Phase Equil* 260(2):354–358. <https://doi.org/10.1016/j.fluid.2007.07.044>
17. Mysik SV (2015) Analyzing the acoustic spectra of sound velocity and absorption in amphiphilic liquids. *St. Petersburg Polytech Univ J: Phys Math* 1(3):325–331 (2015). <https://doi.org/10.1016/j.spjpm.2015.12.003>
18. Oldenhof E, Weckenmann F, Lamanna G, Weigand B, Bork B, Dreizler A (2013) Experimental investigation of isolated acetone droplets at ambient and near-critical conditions, injected in a nitrogen atmosphere. *Progress in propulsion physics: 4–8 July 2011, St Petersburg, Russian*, vol 4, pp 257–270. <https://doi.org/10.1051/eucass/201304257>
19. Orbey H, Vera JH (1983) Correlation for the third virial coefficient using  $t_c$ ,  $p_c$  and  $\omega$  as parameters. *AIChE J* 29(1):107–113. <https://doi.org/10.1002/aic.690290115>
20. Ouedraogo Y, Gjonaj E, Weiland T, de Gersem H, Steinhausen C, Lamanna G, Weigand B, Preusche A, Dreizler A, Schremb M (2017) Electrohydrodynamic simulation of electrically controlled droplet generation. *Int J Heat Fluid Flow* 64:120–128. <https://doi.org/10.1016/j.ijheatfluidflow.2017.02.007>
21. Pinheiro AP, Vedovoto JM (2019) Evaluation of droplet evaporation models and the incorporation of natural convection effects. *Flow Turbul Combust* 102(3):537–558. <https://doi.org/10.1007/s10494-018-9973-8>
22. Poling BE, Prausnitz JM, O'Connell JP (2000) The properties of gases and liquids, 5th edn. McGraw-Hill, New York, London
23. Preusche A, Dreizler A, Steinhausen C, Lamanna G, Stierle R (2020) Non-invasive, spatially averaged temperature measurements of falling acetone droplets in nitrogen atmosphere at

- elevated pressures and temperatures. *J Supercrit Fluids* 166:105025. <https://doi.org/10.1016/j.supflu.2020.105025>
- 24. Renge I (2009) A solvent dependence of n-pi\* absorption in acetone. *J Phys Chem* 113(40):10678–10686. <https://doi.org/10.1021/jp9033886>
  - 25. Ritchie B, Seitzmann J (2004) Simultaneous imaging of vapor and liquid spray concentration using combined acetone fluorescence and phosphorescence. In: 42nd aerospace sciences meeting and exhibit
  - 26. Schlamp S, Cummings EB, Hornung HG (1999) Beam misalignments and fluid velocities in laser-induced thermal acoustics. *Appl Opt* 38(27):5724. <https://doi.org/10.1364/AO.38.005724>
  - 27. Stampaponi-Panariello A, Kozlov DN, Radi PP, Hemmerling B (2005) Gas phase diagnostics by laser-induced gratings I. theory. *Appl Phys B* 81(1), 101–111 (2005). <https://doi.org/10.1007/s00340-005-1852-z>
  - 28. Steinhausen C, Gerber V, Preusche A, Weigand B, Dreizler A, Lamanna G (2021) On the potential and challenges of laser-induced thermal acoustics for experimental investigation of macroscopic fluid phenomena. *Exp Fluids* 62(1) (2021). <https://doi.org/10.1007/s00348-020-03088-1>
  - 29. Steinhausen C, Reutzsch J, Lamanna G, Weigand B, Stierle R, Gross J, Preusche A, Dreizler A (2019) Droplet evaporation under high pressure and temperature conditions: a comparison of experimental estimations and direct numerical simulations. In: Proceedings ILASS-Europe 2019, 29th conference on liquid atomization and spray systems: 2–4 Sept 2019, Paris, France
  - 30. Sublett DM, Sendula E, Lamadrid H, Steele-MacInnis M, Spiekermann G, Burruss RC, Bodnar RJ (2020) Shift in the Raman symmetric stretching band of N<sub>2</sub>, CO<sub>2</sub>, and CH<sub>4</sub> as a function of temperature, pressure, and density. *J Raman Spectrosc* 51(3):555–568. <https://doi.org/10.1002/jrs.5805>
  - 31. Tsionopoulos C, Dymond JH (1997) Second virial coefficients of normal alkanes, linear 1-alkanols (and water), alkyl ethers, and their mixtures. *Fluid Phase Equilib* 133(1–2):11–34, 105025. [https://doi.org/10.1016/S0378-3812\(97\)00058-7](https://doi.org/10.1016/S0378-3812(97)00058-7)
  - 32. Weckenmann F, Bork B, Oldenhof E, Lamanna G, Weigand B, Böhm B, Dreizler A (2011) Single acetone droplets at supercritical pressure: droplet generation and characterization of PLIFP. *Zeitschrift für Physikalische Chemie* 225(11–12):1417–1431. <https://doi.org/10.1524/zpch.2011.0188>
  - 33. Young JB (1993) The condensation and evaporation of liquid droplets at arbitrary Knudsen number in the presence of an inert gas. *Int J Heat Mass Trans* 36(11):2941–2956. [https://doi.org/10.1016/0017-9310\(93\)90112-J](https://doi.org/10.1016/0017-9310(93)90112-J)
  - 34. Yujing M, Mellouki A (2000) The near-uv absorption cross sections for several ketones. *J Photochem Photobiol A: Chem* 134(1–2):31–36. [https://doi.org/10.1016/S1010-6030\(00\)00243-4](https://doi.org/10.1016/S1010-6030(00)00243-4)

**Open Access** This chapter is licensed under the terms of the Creative Commons Attribution 4.0 International License (<http://creativecommons.org/licenses/by/4.0/>), which permits use, sharing, adaptation, distribution and reproduction in any medium or format, as long as you give appropriate credit to the original author(s) and the source, provide a link to the Creative Commons license and indicate if changes were made.

The images or other third party material in this chapter are included in the chapter's Creative Commons license, unless indicated otherwise in a credit line to the material. If material is not included in the chapter's Creative Commons license and your intended use is not permitted by statutory regulation or exceeds the permitted use, you will need to obtain permission directly from the copyright holder.



# Modeling and Simulation of a Turbulent Multi-component Two-phase Flow Involving Phase Change Processes Under Supercritical Conditions



Dennis Kuetemeier and Amsini Sadiki

**Abstract** The present paper aims at developing a generally valid, consistent numerical description of a turbulent multi-component two-phase flow that experiences processes that may occur under both subcritical and trans-critical or supercritical operating conditions. Within an appropriate LES methodology, focus is put on an Euler-Eulerian method that includes multi-component mixture properties along with phase change process. Thereby, the two-phase flow fluid is considered as multi-component mixtures in which the real fluid properties are accounted for by a composite Peng-Robinson (PR) equation of state (EoS), so that each phase is governed by its own PR EoS. The suggested numerical modelling approach is validated while simulating the disintegration of an elliptic jet of supercritical fluoroketone injected into a helium environment. Qualitative and quantitative analyses are carried out. The results show significant coupled effect of the turbulence and the thermodynamic on the jet disintegration along with the mixing processes. Especially, comparisons between the numerical predictions and available experimental data provided in terms of penetration length, fluoroketone density, and jet spreading angle outline good agreements that attest the performance of the proposed model at elevated pressures and temperatures. Further aspects of transcritical jet flow case as well as comparison with an Eulerian-Lagrangian approach which is extended to integrate the arising effects of vanishing surface tension in evolving sprays are left for future work.

## 1 Introduction

Many industrial and engineering applications exploit thermo-fluid flow processes under thermodynamically subcritical, trans-critical, or supercritical regimes. As is well-known injection processes in transportation, propulsion, power generation and other high temperature applications are commonly used. Thereby, liquid fuels are

---

D. Kuetemeier · A. Sadiki (✉)

Technische Universität Darmstadt, Institute of Reactive Flows and Diagnostics,  
64287 Darmstadt, Germany  
e-mail: [amsini.sadiki@tu-darmstadt.de](mailto:amsini.sadiki@tu-darmstadt.de)

preferred as they feature high energy density (energy per unit volume), and thus mostly easy to store and transport. However, their use suffers from complex fuel atomization phenomena (primary and secondary breakup), evaporation and mixing that represent the major performance limiting factors of specific technologies in which these fuels are utilized.

A widespread tendency is to obviate this limitation by moving the operating conditions into supercritical state in which the fuel is able to evaporate directly without phase change. Such a behavior is due to the liquid surface tension and the latent heat which gradually diminish and even vanish when the ambient condition lies above the critical point of the injected fuel. In this way, a higher specific energy conversion can be achieved in combination with an improvement in the thermodynamic efficiency, or heat and mass transport can be enhanced along with reduction of harmful gas emissions (see [12, 26]). Examples of such techniques are found in propulsion rocket engines, modern gas turbines, diesel engines, and also in supercritical drying, cooling and cleaning, etc. Thereby, the majority of fuels reach supercritical conditions for pressures in the range of about 1.5–3 MPa. In modern aircraft combustors the pressure is now exceeding values of 2–2.5 MPa at cruise conditions and 5–6 MPa during ground power generation, takeoff, and landing, while even higher values are expected for the future generation of gas turbines. In a naturally aspirated diesel engine, air at close-to-atmospheric pressure is inducted during the intake stroke and then compressed to a pressure of about 5 MPa and temperature of about 900 K during the compression stroke [7].

In such applications, when the fuel is injected as a compact, continuous stream and not as a disperse cloud of individual droplets, dispersed droplets can also be observed under supercritical pressure conditions. In fact, Roy et al. [43] experimentally investigated an initially supercritical fluid injected into a supercritical pressure environment. The jet undergoes for sufficiently low ambient temperatures phase separation leading to the formation of droplets and ligaments in the jet. This mainly stems from the interaction between the injectant and the surrounding gas, see also [55]. For more details, the reader may refer to the works by Anitescu et al. [6], Chehroudi [12], Klima et al. [21], Oefelein [33], and therein included references. Additional observations have been reported in which the droplets undergo a gradual transition from subcritical evaporation to mixing regime at different pressure and temperature above the pure fuel critical point. This gives a hint to state that the fuel still stays in the subcritical two-phase state for some time before fully entering the diffusion mixing regime, and the transition time varies with fuel types and droplet size [14]. It turns out that in the whole injection process, the combination of classical evaporation regime for the main liquid core and transition to the dense gas mixing state is possible at high ambient temperature especially for the droplets formed by possible primary atomization near the nozzle or at the end of the injection events.

In a case of mixture evolving in a combustor that experiences a pressure above the critical value of the mixture, the investigated mixture will behave as a supercritical fluid. Since the critical pressure strongly depends on the composition of the mixture in presence, the critical pressure for hydrocarbon-gas mixtures, for example, can reach very high values beyond the application relevant pressure levels. Furthermore,

only in rare cases the liquid fuel is preheated to supercritical temperatures before injection into the combustion chamber. For hydrocarbons, these are in the range of 400-500 K [20]. After the injection, other processes may occur in the combustion chamber, such as heating by the combustion products and evaporative cooling. Therefore, the occurrence of subcritical and supercritical phenomena in combustion chambers might likely be expected in vicinity of the injector [14, 16, 26]. Due to the complexity of the evolving multi-scale and multi-physical processes, and to the urgent need of designing and improving the performance of the involved technologies, understanding and modelling of supercritical process or processes implying supercritical region of the fuel have become a relevant issue.

Focusing on numerically based investigations, various approaches for the spray simulation, namely the Eulerian-Lagrangian (EL) method, the Eulerian-Eulerian (EE) or multi-fluid approach and the Transported Probability Density Function (T-PDF), are usually applied. A recent review is provided by Ries and Sadiki [42].

Reported investigations of supercritical injection processes range from individual jets (e.g. [17, 24]) to sprays in the entire combustion chamber [50]. Mixing processes within such configurations were examined on different numerical scales by means of direct numerical simulations (DNS) [11, 27, 47], Large Eddy simulations (LES) [23, 33, 49] or Reynolds Averaged Numerical Simulation (here RANS) descriptions [10, 48]. Thereby, the main focus was on the mixture formation [23], the phase separation [39, 40] or the effects at the phase boundary [15, 28]. For the model validation in this class of investigations the detailed study by Chehroudi [12], who neatly generated and compared various experimental data from different liquid and gas jets as function of pressures, remains state of the art. The contribution by Mayer et al. [26] can be considered as standard configuration for non-reacting flow studies. The fuel flow system is usually described as a single phase dense gas with real gas effects within an Eulerian framework. This method, also known as single fluid mixing (SFM) model, corresponds to a so-called homogeneous EE model. As it is valid to decouple real and ideal fluid behavior, Banuti [8, 9] suggested an extension by considering a multi-fluid mixing (MFM) modeling.

Focusing on LES modeling, some studies report on a priori investigations that are based on a gaseous phase description while taking into account real gas properties. Two aspects are essentially addressed, namely the inclusion of necessary physics in subgrid scale (SGS) models into the governing filtered equations and into the real fluid EoS. First, the consistency of existing classic LES models primary designed for atmospheric environments was evaluated ([11, 27, 47]). Then, a posteriori validation has been reported. Finally, first comparisons with experimental data in the supercritical range were carried out by e.g. Miller et al. [27, 28], Petit et al. [38]. All these investigations were limited to comparisons of prediction obtained with different SGS models developed for subcritical flow situations in connection with various real gas descriptions. It turns out that LES modelling based on single-fluid mixture models is not able to provide a detailed description of all fluid states, such as liquid, gaseous, supercritical up to multi-phase mixtures including spray dynamics and phase changes. Furthermore, the consideration of SGS in dealing with the real fluid EoS has been often neglected as reviewed by Ries and Sadiki [42].

Despite the limitations observed with single fluid models, several researchers employed the pure Eulerian modeling within the framework of LES (e.g. [23, 28, 38, 46]). The broad consensus is that LES allows an accurate prediction of such supercritical fluid flows, whereby species mixing and combustion within supercritical injection conditions could be addressed in a satisfactory way (e.g. [18, 33, 51, 52]).

In the case of coexistence of supercritical states and multi-component subcritical two-phase states, Mattheis and Hickel [25] presented and evaluated a two-phase model for Eulerian LES of liquid-fuel injection and mixing at high pressure. This model is based on cubic EoS and VLE (vapor-liquid equilibrium) calculations via a homogeneous mixture approach. Such an approach holds only for dense and moderately dense high-pressure injection cases which feature typically high Weber number and low Stokes number. The droplet diameters are small and surface tension is low giving raise to droplet vaporization time scale and droplet inertial time scales sufficiently small compared to hydrodynamic time scales and of the order of the computational time step [25]. For liquid fuel injection which includes dilute spray region and intrinsically permits significant slip velocity between the dispersed liquid and the gas phase, the above pure Eulerian approach with a single-valued velocity for both phases is invalid.

A coupling between the Eulerian VLE-based two-phase model for the primary jet breakup and an appropriate subsequent approach to describe the evolvement of the spray is necessary. This allows to make a clear difference between the classical multifluid model (EE) family [45] which is rather well suitable to describe two-phase flow processes (see [22, 36]) and the pure Eulerian modeling appropriate for single phase multi-species mixing. Indeed, in the latter the thermodynamic mixing process is retrieved using either the SFM or the MFM models [9], whereas the multifluid (EE) methods offer a versatile framework to deal with two-phase flows, as different levels of disequilibrium between phases can be treated, and physical effects (e.g. surface tension, phase change) easily be integrated [36].

Accordingly, the EE-methods are able to treat formation and disappearance of interfaces, even though they may require several grid cells to capture the interface while being subject to progressive interface smearing. The review paper by Ries and Sadiki [42] and the comprehensive contribution by Pelletier [36] provide more description details. Ping et al. [57] suggested recently an EE- multicomponent real-fluid fully compressible four-equation model for two-phase flow with phase change. Thereby, the balance equations for distinct species in gas and liquid phases are considered, while a mixture momentum and mixture specific internal energy are solved. They are completed by real gas equations of state for both gas and liquid phases. As long as the multicomponent mixture is outside the vapor dome (i.e., single phase), the system of governing equations is closed by PR EoS. Once, the mixture is inside the vapor dome (i.e., two phase), the system is closed by the composite EoS connected with the set of algebraic equations for each phase (equilibrium connection constraints). In particular, in the composite EoS, each phase always follows its own EoS (here Peng-Robinson), and the equilibrium connection constraints ensure that the mixture speed of sound is always defined.

Under supercritical/transcritical conditions, the most comprehensive spray simulation following an EL framework as adopted by Oefelein [33] and Yang [56] represents an alternative to EE. Thereby both EE and EL methods adapted for supercritical conditions have been employed, see also [54]. Nishad et al. [32] investigated the effect of real gas behavior on the evaporation of isolated droplets subject to transcritical operating environments. Thereby, a multicomponent evaporation model has been developed and applied. The model includes following effects: (a) the gas solubility in the liquid phase; (b) the diffusion inside the droplet, including internal flow recirculation with effective thermal conductivity and mass diffusivity; (c) the gradients on the gas phase side by Nusselt and Sherwood numbers using the effective film method; (d) the real gas behavior in the gas and liquid phases by using the PR equation of state; (e) the spatial and temporal variation of the thermophysical properties. In particular, the impact of Nu- and She-number correlations has been appraised.

The present paper aims at developing a generally valid, consistent numerical description of a turbulent multi-component two-phase flow that experiences processes that may occur under both subcritical and trans-critical or supercritical operating conditions. Within an appropriate LES methodology, focus is put on an Euler-Eulerian description method suitable for trans- and supercritical sprays under consideration of multi-component mixture properties along with phase change process.

The paper is organized as follows. In Sect. 2, the LES-based numerical modelling approach adopted is outlined. Thereby, the governing filtered equations, the sub-grid scale models applied, the real fluid thermodynamic and transport models are introduced. Subsequently, the numerical procedure and the numerical setup are provided. In Sect. 3, the investigated configuration is outlined along with the computational domain and the inflow/boundary conditions. In Sect. 4 relevant results of this paper are presented and discussed before concluding and addressing open issues and challenges in the last section (Sect. 5)

## 2 Methods and Models

In this section, the required Favre-filtered governing equations for LES and the thermophysical models are briefly introduced. Subsequently the numerical procedure employed in this work is concisely described.

### 2.1 *Governing Filtered Equations and Modeling*

A Large Eddy Simulation (LES) framework with an incompressible low-Mach solver capable to simulate configurations with Mach-numbers up to 0.35 is utilized. In order to capture turbulent multiphase flow characteristics along with phase change processes, the original low-Mach approach in accordance to Ries et al. [41] and

Müller et al. [29], is developed and extended to obtain an Eulerian-Eulerian approach for multi-species mixtures under consideration of multicomponent aspects in line with [25, 44] and [57]. This results in the following set of governing filtered Eulerian-Eulerian equations for mass, momentum, species and sensible enthalpy, respectively, which is solved for the two phases considered as multi-species mixtures:

$$\frac{\partial \alpha_p \bar{\rho}}{\partial t} + \frac{\partial}{\partial x_j} (\alpha_p \bar{\rho} \tilde{u}_j) = 0 \quad (1)$$

$$\frac{\partial \alpha_p \bar{\rho} \tilde{u}_j}{\partial t} + \frac{\partial}{\partial x_j} (\alpha_p \bar{\rho} \tilde{u}_i \tilde{u}_j) = -\frac{\partial \alpha_p \tilde{p}}{\partial x_j} + \frac{\partial}{\partial x_j} (\alpha_p \bar{\tau}_{ij} - \alpha_p \bar{\rho} \tau_{ij}^{SGS}) \quad (2)$$

$$\frac{\partial \alpha_p \bar{\rho} Y_S}{\partial t} + \frac{\partial}{\partial x_j} (\alpha_p \bar{\rho} Y_S \tilde{u}_j) = -\frac{\partial}{\partial x_j} (\alpha_p j_{S,j} + \alpha_p^- \rho j_{S,j}^{SGS}) \quad (3)$$

$$\frac{\partial \alpha_p \bar{\rho} \tilde{h}}{\partial t} + \frac{\partial}{\partial x_j} (\alpha_p \bar{\rho} \tilde{u}_j \tilde{h}) = -\frac{\partial}{\partial x_j} (\alpha_p q_j + \alpha_p \bar{\rho} q_j^{SGS}) \quad (4)$$

In these equations and throughout the paper, filtered variables are denoted by  $(\tilde{*})$  while  $(*^{SGS})$  represents sub-grid-scale quantities. In Eqs. (1)–(4) the phase fractions  $\alpha_p$  of the mixture are calculated by  $\alpha_p = \frac{\partial V_p}{\partial V}$  with  $\sum \alpha_p = 1$ , where the index  $p$  (with  $p = \text{liquid, gas}$ ) denotes the phase state. It is worth noting that once Eq. 1 is written for each phase, the phase change terms denoted as  $\pi_{p,S_k}$  appear, but are constrained by  $\sum_p \pi_{p,S_k} = 0$  for the whole mixture. On the left hand side of the equations,  $t$  represents time and  $\bar{\rho}$  the density with  $\bar{\rho} = \sum \alpha_p \bar{\rho}_p$ . In particular,  $\tilde{u}_i$  represents the mixture velocity components with  $i = 1, 2, 3$  denoting the Cartesian coordinates,  $\tilde{h}$  the sensible enthalpy and  $Y_S$  the volume fraction of each specie. According to the low Mach approach,  $\tilde{p}$  is the modified thermodynamic pressure in which sub-grid-scales are not accounted for.

On the right hand side of these equations appear several flux terms, namely molecular contribution and its SGS counterpart for the stress tensor  $\tau_{ij}$ ,  $\tau_{ij}^{SGS}$ , the heat flux  $q_j$ ,  $q_j^{SGS}$  and the mass flux of species  $j_{S,j}$ ,  $j_{S,j}^{SGS}$ , in Eqs. (2), (3) and (4), respectively. These quantities are very complex and need to be modelled.

Dealing with Newtonian fluid flows, the molecular stress tensor obeys the Newtonian law given as

$$\tau_{ij} = -\nu \left( \frac{\partial \tilde{u}_i}{\partial x_j} + \frac{\partial \tilde{u}_j}{\partial x_i} - \frac{2}{3} \frac{\partial \tilde{u}_k}{\partial x_k} \delta_{ij} \right), \quad (5)$$

where  $\delta_{ij}$  is the Kronecker-delta function. The mixture viscosity  $\nu$  is determined by means of the correlations of Chung et al. [13]:

$$\nu = \nu_p + \nu_k, \quad (6)$$

consisting of a temperature and a pressure depending viscosity  $\nu_k$  and  $\nu_p$  given as:

$$\nu_k = \nu_0 \left[ \frac{1}{G_2} + A_6 Y \right], \quad \nu_p = \left[ 36.344 \cdot 10^6 \frac{(MT_c)^{\frac{1}{2}}}{V_c^{\frac{2}{3}}} \right], \quad (7)$$

respectively. In these expressions,  $\nu_0$  is the dilute gas viscosity,  $T_c$  the critical temperature of the mixture and  $V_c$  the critical volume.  $M$ ,  $A_n$ ,  $G_o$  and  $Y$  represent linear functions depending on a set of empirical linear equations. Further information regarding Chung et al. correlations can be found in [13].

As pointed out in [34, 42] and elsewhere, the molecular flux vectors for the system consisting of multiple species  $S_\kappa$ ; ( $\kappa \in [1, N - 1]$ ;  $N$  : number of species) can have very complex forms based on the full matrices of mass-diffusion coefficients and thermal-diffusion factors with consideration of the Soret and Dufour effects. As for the viscosity, the thermal conductivity are computed using mixture rules. In this paper, such molecular fluxes are simply modeled according to [34] as:

$$j_{S_\kappa, j} = - \left[ j'_{S_\kappa, j} + (\alpha_{IK} - \alpha_h) Y_{S_\kappa} Y_{S_\gamma} \frac{\rho D}{T} \frac{\partial T}{\partial x_j} \right], \quad (8)$$

where  $\alpha_{IK}$  and  $\alpha_h$  are transport coefficients associated to molar and heat fluxes. The diffusion factor  $D$  is derived from  $Sc = \nu \alpha_D D$ , with mass diffusion factor  $\alpha_D$ , and

$$j'_{S_\kappa, j} = \bar{\rho} D \left[ \alpha_D \frac{\partial Y_{S_\kappa}}{\partial x_j} + \frac{Y_{S_\kappa} Y_{S_\gamma}}{R T} \frac{m_{S_\kappa} m_{S_\gamma}}{m_m} \left( \frac{v_{S_\kappa}}{m_{S_\kappa}} - \frac{v_{S_\gamma}}{m_{S_\gamma}} \right) \frac{\partial p}{\partial x_j} \right]. \quad (9)$$

In this Eq. (9)  $R$  stands for the universal gas constant, the quantity  $m_z$ ; ( $z = \kappa, \gamma$ ) are the molar mass of species  $S_z$  and  $m_m$  the molar mass of the mixture, while  $v_{S_z}$  expresses the partial molar volume of species  $z$  with  $v_{S_z} = (\partial v / \partial X_{S_z})$  and  $X_{S_z}$  the molar fraction of species  $S_z$  given as  $X_{S_z} = m_m Y_{S_z} / m_{S_z}$ ). Relying on the low-Mach solver approach, the quantity  $\partial p / \partial x_j$  is negligibly small. The heat flux vector is modeled as:

$$q_j = -\lambda \frac{\partial T}{\partial x_j} - \alpha_{IK} R T \frac{m}{m_{S_1} m_{S_2}} j'_{S_1, j}, \quad (10)$$

where  $\lambda$  is the thermal conductivity.

Concerning the SGS counterparts, various modelling approaches and their consistency have been discussed in Ries and Sadiki [42]. The modeling approach used in the present paper follows the outcome from [42] by applying the simplest consistent reduced framework provided by the zero-equation approach. Correspondingly, the simple gradient approach is used for both the SGS stress tensor, the mass flux and heat flux vectors as:

$$\tau_{ij}^{SGS} = -\nu^{SGS} \left( \frac{\partial \tilde{u}_i}{\partial x_j} + \frac{\partial \tilde{u}_j}{\partial x_i} - \frac{2}{3} \frac{\partial \tilde{u}_k}{\partial x_k} \delta_{ij} \right) \quad (11)$$

with  $\nu^{SGS}$  the SGS kinematic viscosity expressed by the Smagorinsky SGS approximation. Accordingly

$$\nu^{SGS} = C \Delta^2 \sqrt{2 \bar{S}_{ij} \bar{S}_{ij}} = C \Delta^2 |\bar{S}| , \quad (12)$$

where  $\Delta$  represents the filter width of the underlying numerical domain, and  $\bar{S}_{ij} = \frac{1}{2} \left( \frac{\partial \bar{u}_i}{\partial x_j} + \frac{\partial \bar{u}_j}{\partial x_i} \right)$  stands for the rate-of-strain tensor.  $C$  is a constant model coefficient calculated here according to  $C = \frac{1}{\pi} \left( \frac{2}{3\alpha_S} \right)^{\frac{3}{4}}$ . With the Kolmogorov constant  $\alpha_S = 1.5$  this leads to  $C = 0.173$ . The mass and the heat flux vectors are modelled as

$$j_{S,j}^{SGS} = - \frac{\nu^{SGS}}{Sc^{SGS}} \frac{\partial Y_{S_k}}{\partial x_j}, \quad q_j^{SGS} = - \frac{\nu^{SGS}}{Pr^{SGS}} \frac{\partial \tilde{h}}{\partial x_j}, \quad (13)$$

respectively, where  $Sc^{SGS}$  is the SGS Schmidt number and  $Pr^{SGS}$  the SGS Prandtl number.

## 2.2 Thermodynamic and Transport Models

In the present study a heat transfer fluid [53] and more exotic fire extinguishing fluid (see, e.g. [30]), fluoroketone is investigated under supercritical conditions. As already pointed out above, constitutive equations or closures for  $\rho$ ,  $\mu$ ,  $\lambda$ ,  $Cp$  and  $h$  as functions of local temperature and pressure are required. Once under supercritical conditions, non-ideal gas behavior must be accounted for. The commonly used Peng-Robinson equation of state (PR-EOS) [37] is employed in the present study. With supercritical conditions are meant pressure levels above the mixtures critical pressure as well as temperature higher than the mixture critical temperatures. To remedy the limitations of the PR-EOS at operation conditions near the critical point, a generalized volume translation method proposed by Abudour et al. [5] can be applied. Non-ideal corrections of  $c_p$  and  $h$  are thus expressed in terms of departure functions derived from the PR-EOS, where the contributions from the hypothetical, ideal gas are calculated using the 7-coefficients NASA polynomials. Regarding transport properties, the correlations of Chung [13], applicable for dilute and dense fluids, are utilized for  $\mu$  and  $\lambda$  as outlined above. Indeed, dealing with two-phase flow considered as multicomponent mixtures, the Peng-Robinson equation of state is applied separately for each phase of the multi-species mixture:

$$p = \frac{RT}{\tilde{v} - b_m} - \frac{(\alpha a)_m}{\tilde{v}^2 + 2b\tilde{v} - b^2} \quad (14)$$

with

$$\alpha = \left[ 1 + (0.37464 + 1.54226\omega - 0.26992\omega^2) \left( 1 - \sqrt{\frac{T}{T_c}} \right) \right]. \quad (15)$$

**Table 1** Operating conditions of fluoroketone and helium

Quantity	Fluoroketone	Helium
$T_c$ in K	441.81	5.1953
$P_c$ in $N/m^2$	$18.646 \cdot 10^6$	$0.22746 \cdot 10^6$
$\omega$	0.471	-0.382
$u_i$ in $m/s$	0.55	0.0
$Ma$	$\ll 0.1$	-
$T$ in K	468.32	459.48
$p$ in $N/m^2$	$25.17 \cdot 10^6$	$25.17 \cdot 10^6$

In this equation,

$$a = 0.45724 \frac{(R T_c)^2}{P_c}, \quad b = 0.0778 \frac{R T_c}{P_c} \quad (16)$$

where  $T_c$  expresses the critical temperature,  $P_c$  the critical pressure and  $\omega$  the acentric factor. The mixture parameters  $(\alpha a)_m$  and  $b_m$  are defined by means of the Van-der-Waals mixing rules:

$$(\alpha a)_m = \sum_{\kappa} \sum_{\gamma} X_{\kappa} X_{\gamma} (\alpha a)_{\kappa\gamma}, \quad (\alpha a)_{\kappa\gamma} = \sqrt{(\alpha a)_{\kappa} (\alpha a)_{\gamma}} (1 - k_{\kappa\gamma}),$$

$$b_m = \sum_{\kappa} X_{\kappa} b_{\kappa},$$

where  $k_{\kappa\gamma}$  is representing the binary interaction parameter.

Table 1 summarizes the initial critical and flow properties of fluoroketone and helium under consideration in the investigated configuration in Sect. 3. The simulation conditions are far from the vicinity of the critical point for helium. Fig. 1 shows that the thermodynamic and transport models are in good agreement with the reference data owing to the fact that helium is by far more volatile in comparison to fluoroketone.

It is worth mentioning that in subcritical conditions, the cubic Peng-Robinson equation EOS is first solved resulting in three roots. The smallest positive one is calculated to obtain the liquid molar volume. The remaining roots of the Peng-Robinson EOS are used to determine the gas molar volume, which corresponds to the larger root. Under single-phase conditions, the Peng Robinson EOS is calculated only once and the real positive root is considered to obtain the molar volume. When the phase molar volume is known, other values including phase density and mixture density can be calculated. The phase composition can then be used for the calculation of the thermal properties of each phase. In supercritical conditions the process follows the same procedure with respect to the critical point of species and mixtures.

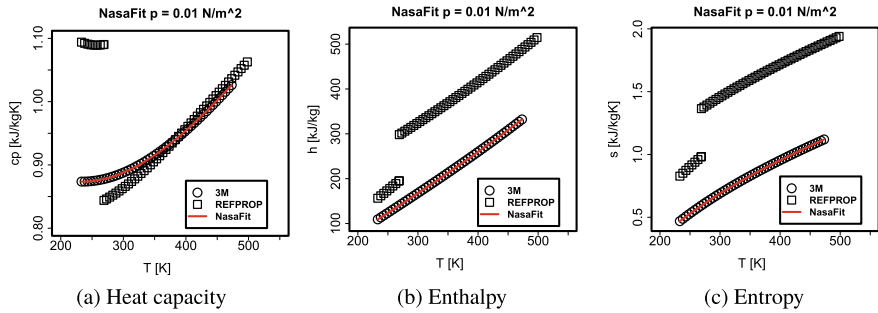
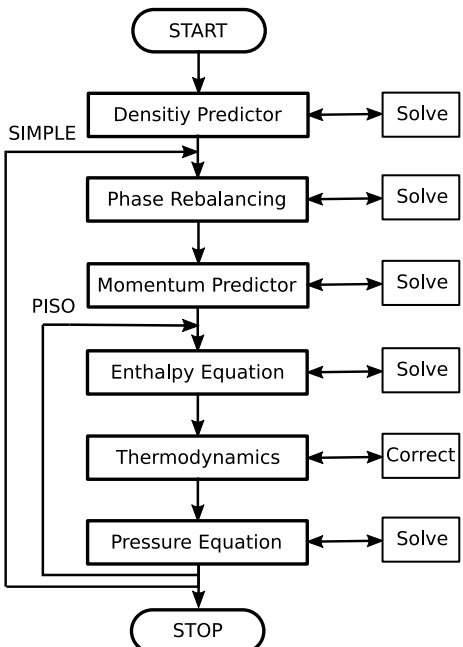


**Fig. 1** NASA fitted curves of relevant thermodynamic data in respect to data sets obtained from REFPROP [4] and 3M [1]

### 2.3 Numerical Procedure and Setup

The governing filtered Eulerian-Eulerian low-Mach equations (Eqs. 1–4) are phase dependent solved by calculating a chain of predictor-corrector steps. A combination of PISO [19] and SIMPLE [35] algorithms is applied for coupling phase velocities and pressure. A schematic representation of the solution algorithm is depicted in Fig. 2.

**Fig. 2** Flow chart of the low Mach Eulerian-Eulerian PISO-SIMPLE algorithm



Beginning in the global SIMPLE loop, a density predictor is solved by means of the continuity equation. Next, the phases in the simulation domain are rebalanced according to thermodynamic states. Then, momentum is predicted using previous iteration field variables. Moving into the PISO loop, the enthalpy equation is calculated and temperature is iteratively derived. Then, the thermodynamic pressures and temperatures are updated and eventually, the pressure equation is solved and the velocity is corrected. The whole process is iteratively repeated in the related SIMPLE and PISO loops until convergence is reached.

Regarding temporal as well as spatial discretization, a central differencing scheme of second order is utilized for the convection terms. In addition a conservative second order scheme is used for the Laplacian terms. The time derivative terms are solved by a second order backward integration method. A preconditioned conjugate gradient solver is deployed for the density predictor and geometric algebraic multi grid solvers are utilized for pressure, momentum and enthalpy equations in order to increase computation speed by multi grid resolutions. Details about the discretization procedure and the numerical schemes can be found in the OpenFOAM programmers guide [3].

This Eulerian-Eulerian algorithm is implemented in the OpenSource computational fluid dynamics software framework, OpenFOAM Version 7.0 [2].

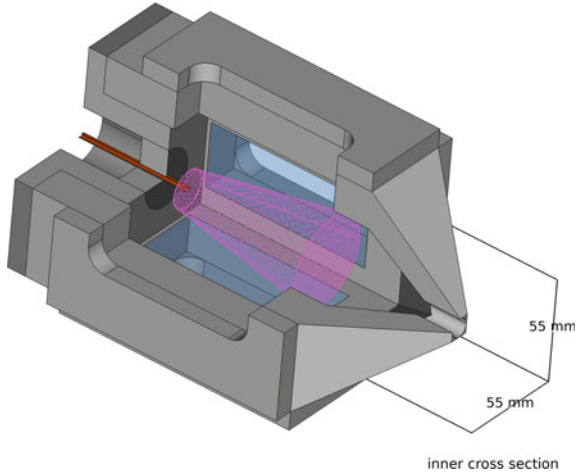
### 3 Investigated Configuration

The configuration under study corresponds to the experimentally investigated jet of fluoroketone by Muthukumaran et al. [30, 31]. Fluoroketone finds applications as a heat transfer fluid in cooling applications [53] and as fire extinguishing fluid.

#### 3.1 Experimental Reference

In [30, 31] a supercritical elliptical jet of fluoroketone is injected into a high pressure and temperature chamber, see Fig. 3. The chamber design is based on the experimental study of Roy et al. [43]. It features a 55 mm square cross section and a chamber length of 190.5 mm. On each side a window in the chamber provides a field of observation of 22 mm width and 86 mm length. The injector orifice is of elliptic shape with a 4 to 1 mm ratio. The elliptic inlet orifice is intentionally used to detect effects of surface tension in the experiment. In the presence of surface tension the initial elliptic jet is forced from the elliptic surface into a round surface. The chamber is initially filled with helium at supercritical pressure and temperature. Finally the elliptic jet of supercritical fluoroketone is injected into the chamber. The elliptic jet evolves from a fully developed elliptic pipe flow with a hydraulic diameter of  $d_H \approx 1.45$  mm, a corresponding Reynolds number of  $Re \approx 13000$  and a inlet Mach-number  $Ma << 0.1$ .

**Fig. 3** Computational domain embedded in a drawing which corresponds to the experimental setup used in [30, 43]

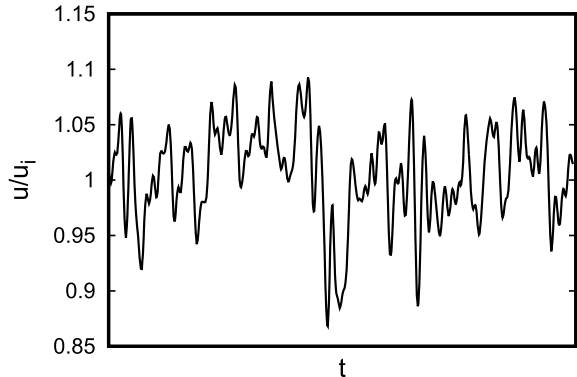


### 3.2 Computational Domain, Initial and Boundary Conditions

In order to increase the computational efficiency and to avoid unnecessary computational costs, only a conical cutout of the experimental chamber, representing the primary region of interest, is considered in the present study. By maintaining a sufficient distance of the numerical domain to the walls present in the experimental setup and under consideration of the fact that the ambient fluid in the chamber is a quiescent medium of very low density, the effect of the wall is neglected in the simulation domain. The chamber simulation domain consists of a conical domain with a length of 90 mm and a  $5 d_H$  diameter at the narrow inlet side gradually increasing to a  $10 d_H$  diameter at the outlet end. A three-dimensional, block structured numerical grid consisting of  $\approx 3$  million numerical control volumes, is employed after a preliminary grid resolution study. The numerical grids finest solution is located at the inlet walls and slightly spreads out radial and downstream in control volume dimensions. The mentioned inlet data simulation numerical grid fits exactly to the inlet of the jet injection simulation domain in order to avoid any numerical disturbances.

In particular a full simulation of the injector pipe was conducted to generate proper inlet data for the jet injection case. For that purpose a elliptic pipe of  $20 d_H$  length was utilized. By applying recycling boundary conditions at the pipe inlet/outlet a numerically infinite elliptic pipe corresponding to the given diameters is simulated and slices of the flow field are extracted from the middle section of the pipe. The pressure gradient along the pipe flow direction, that drives the flow, is adjusted dynamically to maintain a constant mass flux for the resulting inlet data. The latter is recorded after two full passes of fluid through the simulation domain in order to avoid artificial numerical artifacts in the inlet data that may result from minor fluctuating inaccuracies in the initial conditions of the pipe simulation. In this elliptical cross section a velocity field data set is subsequently stored in a database at each relevant

**Fig. 4** Inlet velocity fluctuations  $u_{mean}$  normalized by injection velocity  $u_i$  in m/s on the inlet pipe centerline



time step, see Fig. 4. This inlet data set is interpolated with second order accuracy in space and time in order to match the inlet of the jet and utilized as inflow conditions of the jet simulation. On the outlet and conical domain shell surface, a velocity inlet/outlet boundary condition is imposed to enable fluctuating fluxes of fluid from the surrounding domain. Thereby, the incoming velocity is calculated from the internal cell value. In the opposite direction a Neumann condition is applied in the case of outflow. At the walls next to the inlet orifice, a no-slip condition is utilized. In the case of temperature boundary conditions, a Dirichlet condition is set for the inlet, while Neumann conditions are imposed at the outflow and domain shell.

## 4 Results and Discussions

First, turbulent flow dynamics and thermal properties are examined in order to identify the distinctive features of the jet disintegration process under the operating supercritical thermodynamic conditions.

Figure 5 depicts a spatial representation of the simulated elliptical fluoroketone jet injection. The foreground contour represents the medium temperature, while the turquoise colored contour is wrapping the main core of the jet. Moving downstream, the jet begins to disintegrate and the main core vanishes. On the back plane the mean temperature of the jet is shown. The increasing widening in the direction of flow, as well as the slowly decreasing temperature profile of the jet is clearly visible. On the lower plane an instantaneous image of the temperature is given. In contrast to the mean temperature field, turbulent structures are clearly visible. In terms of the temperature field, it ranges from high values at the core of the jet to small values in the ambient helium. However no sharply defined interface exists in the temperature distribution of the jet. Close to the inlet, the elliptic jet surface is nearly unaffected by the surrounding. Further downstream, turbulent and diffusive effects begin to influence the jet and lead to an increasing jet disintegration. Due to the absence of surface tension in supercritical environments, finger-like structures begin to stretch

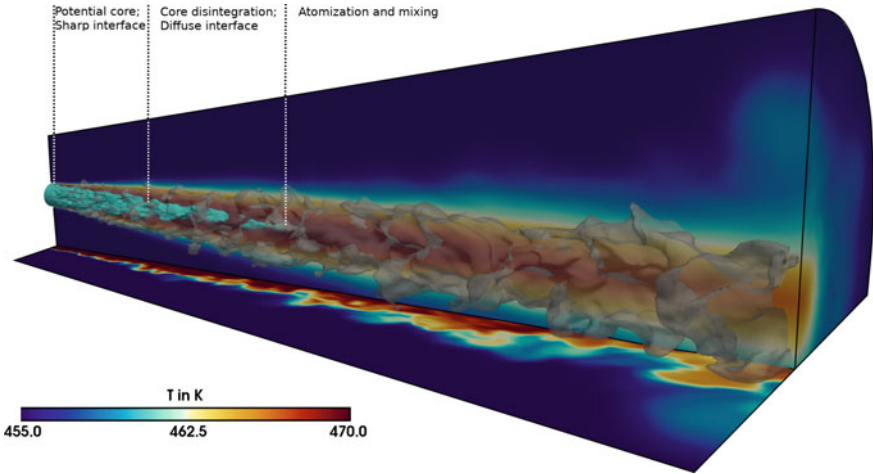


**Fig. 5** Representation of the medium temperature of the simulated jet (Contour in foreground). Back plane: Mean temperature in  $K$ . Horizontal plane: Instantaneous temperature in  $K$ . Turquoise contour: Potential core

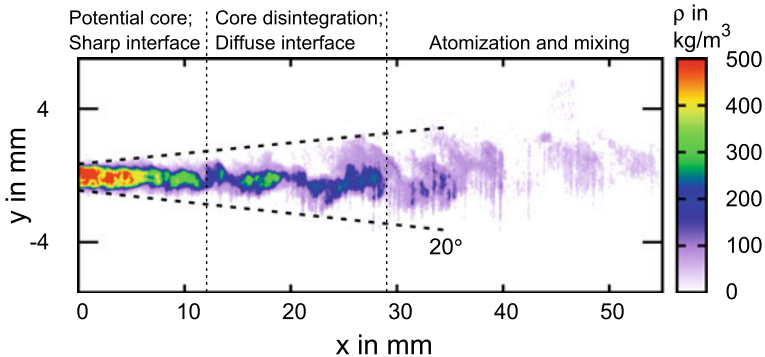


**Fig. 6** Experiment: Density of the fluoroketone jet in  $kg/m^3$  in the centerline axial plane, according to [30]

out of the jet interface into the ambient helium atmosphere. Finally these structures dissolve and accelerate the disintegration process of the temperature interface.

Figure 6 depicts the experimental result of an instantaneous shot of an elliptical jet injection of fluoroketone into a helium environment. Some scattering effects due to the utilized measurement methods are visible in the resulting density fields. The jet has a visible length of  $x \approx 60$  mm and is fully disintegrating in the observation area. The main core of the jet breaks up at  $x \approx 12$  mm downstream. It further disintegrates and begins to fall apart at  $\approx 28$  mm. The main core maximum density is  $478 \frac{kg}{m^3}$  while the spreading angle of the jet in between the two dashed lines amounts  $20^\circ$ .

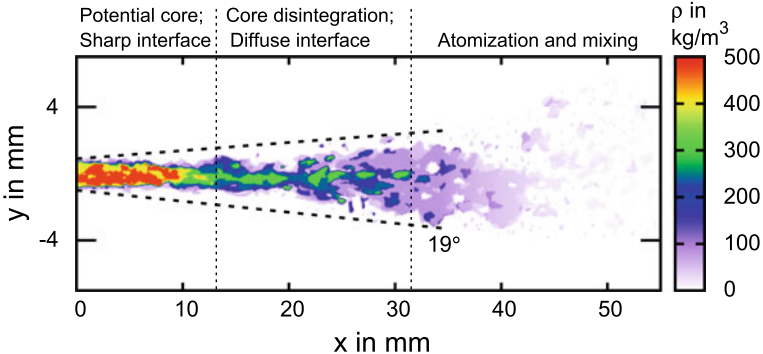


**Fig. 7** Simulation: Density of the fluoroketone jet in  $kg/m^3$  in the centerline axial plane

**Fig. 8** Comparison of density profile along centerline of the fluoroketone jet

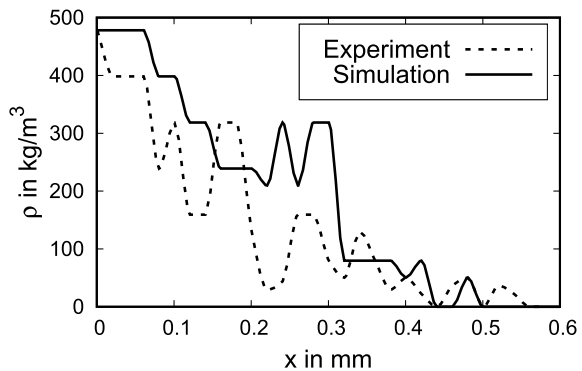
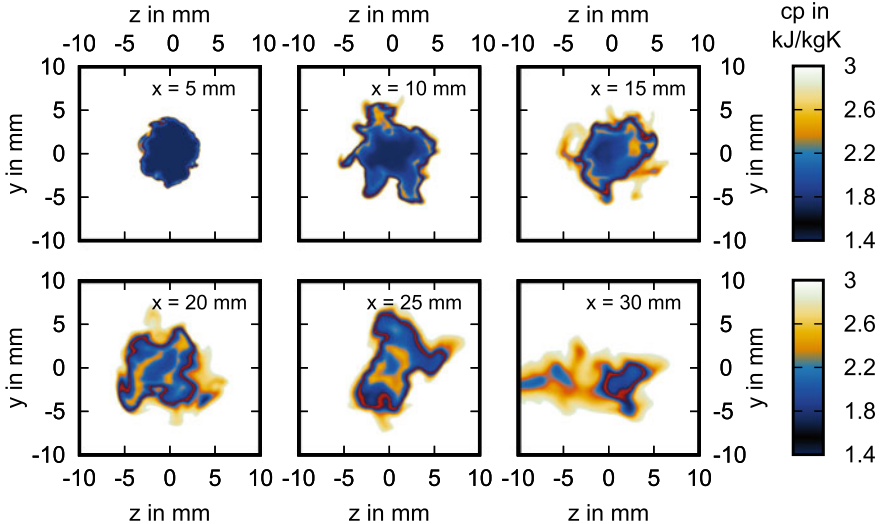


Figure 7 shows an instantaneous shot of an elliptical jet simulation on the center plane and the obtained jet spreading angle of 19 degrees. This value is slightly narrower than in the experiment, suggesting that the velocity in downstream direction is a little elevated in comparison to the experiment. The main core has a slightly higher density of  $493 \frac{kg}{m^3}$  in comparison to experimental data. One can observe a constriction of the main core of the jet at  $x \approx 13 \text{ mm}$  downstream. This fits very well to the primary main core breakup in the experimental data from Fig. 6. A temporal observation of the primary breakup shows that this point fluctuates from  $x \approx 11$  to  $13 \text{ mm}$ , and the secondary breakup fluctuates subsequently from  $x \approx 29$  to  $34 \text{ mm}$ . It turns out that the secondary breakup is numerically well reproduced and the pseudo-liquid pockets are more visible in contrast to the experiment. This is also depicted in Fig. 8 which compares the density profiles along the centerline in experiment and simulation. Thereby it is visible that the simulated density result is following the global trend of the experimental data.

As pointed out above, some minor density aggregations are observable downstream the secondary breakup in contrast to measurement result. This indicates a slightly over prediction and delayed full dilution of the mixture density in the wake



**Fig. 9** Isobaric mixture heat capacity at six different downstream cross sections, representing the main core disintegration. (Red area: Disintegration interface)

flow as already seen in Fig. 8. This prediction divergence might be due to the still coarser mesh resolution downstream and the more sensitive numerical capturing of density fragments in comparison to the low experimental resolution under high pressure conditions. Finally, to note is that the liquid jet is not forced into a round shape; it rather preserves an elliptical shape until the disintegration process is completed.

Figure 9 displays the isobaric heat capacity of the mixture at six different downstream cross sections. Close to the injection ( $x = 5 \text{ mm}$ ), the jet is expanding out of the elliptic injection outline, due to the injection velocity differences across the injection cross section. The velocity is significantly larger in the inner section and therefore the jet expands from the narrow diameter in radial direction. Further downstream the main core becomes subject to turbulent and thermodynamic mixing processes and thereby varies considerably in its shape, with a clearly defined interface. The interfaces fades out and finally disappears while the processes of turbulent mixing and resulting jet disintegration take place.

To get further insights into the turbulent fluctuations, the flow field is examined. Even though experimental data is not available, Figs. 10 and 11 allow to gain a view of the velocity field. Figure 10 shows an instantaneous view of the velocity  $u/u_i$  of the fluoroketone jet in the main cross section, ranging up to a ratio of  $\approx 1.1$  in good agreement with Fig. 4. One can recognize that tiny turbulent disturbances in the sharp interface region ( $x \approx < 12 \text{ mm}$ ) modulate the turbulent turn over in the further downstream region and thereby initialize the turbulent mixing.

Figure 11 illustrates the fluctuations of velocity of the jet in terms of  $u'/u_{\text{mean}}$  which indicates areas of high turbulent effects penetrating the jet interface. In the sharp interface region these disturbing effects are more concentrated leading to the

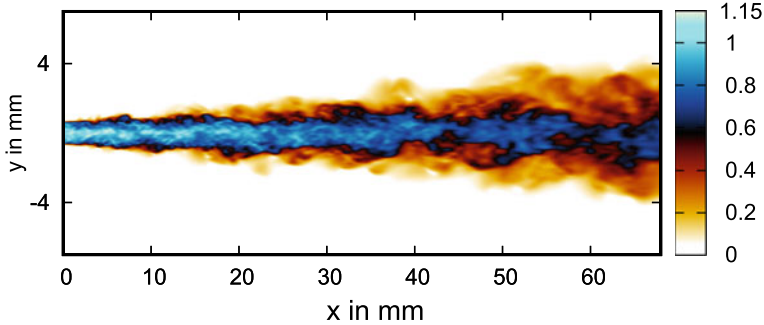


**Fig. 10** Instantaneous velocity field  $u$  of the fluoroketone jet, in the centerline axial plane, normalized by  $u_i$

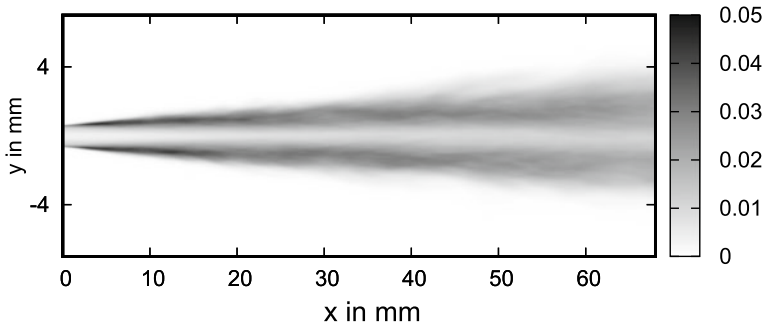


**Fig. 11** Fluctuations of velocity  $u'$ , of the fluoroketone jet, in the centerline axial plane, normalized by  $u_{mean}$

relatively intense breakup of the main core further downstream. It appears clearly that under trans- and supercritical conditions very complex thermodynamic processes occur in the fluid systems in which the fluid properties vary significantly. In particular, the changes in entropy production are very large, so that an analysis using the second law of thermodynamics appears essential in order to delimit sub-processes and identify the causes of possible inefficiencies of these sub-processes. Such an approach has been utilized, and results have already been reported by Ries and Sadiki [42] for similar configurations as investigated in the present paper.

## 5 Conclusions

Relying on a low-Mach Eulerian-Eulerian based real fluid system modelling, an LES approach has been developed which is able to describe turbulent two-phase flow fluids with phase change as multi-component mixtures in which the real fluid properties are accounted for by a composite Peng-Robinson equation of state. Thereby each phase is

governed by its own PR EoS. The numerical model allowed to perform qualitative and quantitative analyses. The results showed significant coupled effect of the turbulence and the thermodynamic on the jet disintegration along with the mixing processes of a supercritical jet of fluoroketone fluid injected into an environment of helium.

To appraise the prediction capability of the model suggested, comparisons of the achieved numerical results with available experimental data have been carried out. The numerical simulations could reproduce correctly the jet disintegration regimes as observed experimentally in terms of penetration length, fluoroketone mass density and jet spreading angle. In addition, the effect chain of the evolving processes was especially consistently reproduced under such operating conditions.

The prediction evaluation of the validated model needs to be further assessed. For that purpose, simulations of trans-critical jet injection are being carried out. A comparison of the expected results with those obtained from an Euler-Lagrangian approach which is extended to integrate the arising effects of vanishing surface tension is left for future work.

**Acknowledgements** The authors kindly acknowledge the financial support by the Deutsche Forschungsgemeinschaft (DFG) within the SFB-TRR 75, project number 84292822. The authors of this work gratefully acknowledge Prof. Dr.-Ing. Johannes Janicka for his valuable and fruitful participation in this project during the first two funding periods as one of the principal investigators.

## References

1. 3M (2021). <https://multimedia.3m.com/mws/media/604395O/3mtm-novectm-649-engineered-fluid.pdf>
2. OpenFOAM 7 (2021). <https://openfoam.org/version/7/>
3. OpenFOAM Programmers Guide (2021). <https://openfoam.org/guides/>
4. RefProp (2021). <https://refprop-docs.readthedocs.io>
5. Abudour A, Mohammad SR Jr, Gasem K (2012) Volume-translated peng-robinson equation of state for saturated and single-phase liquid densities. *Fluid Phase Equilibr* 335:74–87
6. Anitescu G, Bruno T, Tavlarides L (2012) Dieseline for supercritical injection and combustion in compression-ignition engines: volatility, phase transitions, spray/jet structure, and thermal stability. *Energy Fuels* 26:6247–6258
7. Heywood JB (2018) Internal combustion engine fundamentals. McGraw-Hill Education
8. Banuti D (2015) Crossing the widom-line-supercritical pseudo-boiling. *J Supercrit Fluid* 98:12–16
9. Banuti D, Hannemann V, Weigand B (2016) An efficient multi-fluid-mixing model for real gas reacting flows in liquid propellant rocket engines. *Combust Flame* 168:98–112
10. Banuti D, Raju M, Ma P, Ihme M, Hickey J (2017) Seven questions about supercritical fluids towards a new fluid state diagram. No AAIA 2017–1106 in 55th AIAA aerospace sciences meeting. AIAA SciTech Forum
11. Bellan J (2017) Direct numerical simulation of a high-pressure turbulent reacting mixing layer. *Combust Flame* 176:245–262
12. Chehroudi B, Cohn R, Talley D (2002) Cryogenic shear layers: experiments and phenomenological modeling of the initial growth rate under subcritical and supercritical conditions. *Int J Heat Fluid Flow* 23(5):554–563

13. Chung T, Ajlan M, Lee L, Starling K (1988) Generalized multiparameter correlation for non-polar and polar fluid transport properties. *Ind Eng Chem Res* 27:671–679
14. Crua C, Heikal M, Gold M (2015) Microscopic imaging of the initial stage of diesel spray formation. *Fuel* 157:140–150
15. Dahms R, Oefelein J (2015) Non-equilibrium gas-liquid interface dynamics in high-pressure liquid injection systems. *Proc. Combust. Inst.* 35(2):1587–1594
16. De Boer C, Bonar G, Sasaki S, Shetty S (2013) Application of supercritical gasoline injection to a direct injection spark ignition engine for particulate reduction. *SAE technical paper* (2013-01-0257)
17. Falgout Z, Rahm M, Sedarsky D, Linne M (2016) Gas/fuel jet interfaces under high pressures and temperatures. *Fuel* 168:14–21
18. Huo H, Yang V (2013) Sub-grid scale models for large-eddy simulation of supercritical combustion. In: 51st, AIAA aerospace sciences meeting including the new horizons forum and aerospace exposition
19. Issa RI (1985) Solution of the implicitly discretised fluid flow equations by operator-splitting. *J Comput Phys* 62(1):40–65
20. Jofre L, Urzay J, Mani A, Moin P (2015) On diffuse-interface modeling of high-pressure transcritical fuel sprays. *Center Turbul Res Ann Res Briefs* 2015:55–64
21. Klima T, Peter A, Riess S, Wensing M, Braeuer A (2020) Quantification of mixture composition, liquidphase fraction and -temperature in transcritical sprays. *J Supercrit Fluid* 159(104777)
22. Kokh S, Lagoutière F (2010) An anti-diffusive numerical scheme for the simulation of interfaces between compressible fluids by means of a five-equation model. *J Comput Phys* 229:2273–2809
23. Lacaze G, Misdariis A, Ruiz A, Oefelein C (2015) Analysis of high-pressure diesel fuel injection processes using les with real-fluid thermodynamics and transport. *Proc Combust Inst* 35(2):1603–1611
24. Manin J, Picket L, Bardi M, Dahms R, Oefelein J (2014) Microscopic investigation of the atomization and mixing processes of diesel sprays injected into high pressure and temperature environments. *Fuel* 134:531–543
25. Mattheis J, Hickel S (2018) Multi-component vapor-liquid equilibrium model for les of high-pressure fuel injection and application to ECN spray. *Int J Multiph Flow* 99:294–311
26. Mayer W, Tamura H (1996) Propellant injection in a liquid oxygen/gaseous hydrogen rocket engine. *J Propuls Power* 12(6):1137–1147
27. Miller RS, Harstad KG, Bellan J (2001) Direct numerical simulations of supercritical fluid mixing layers applied to heptane-nitrogen. *J Fluid Mech* 436:1–39
28. Mueller H, Niedermeier C, Mattheis J, Pfitzner M, Hickel S (2016) Large eddy simulation of nitrogen injection at trans- and supercritical conditions. *Phys Fluids* 28(015102)
29. Müller H, Pfitzner M, Mattheis J, Hickel S (2015) Large-eddy simulation of coaxial ln2/gh2 injection at trans- and supercritical conditions. *J Propuls Power* 32(1):46–56
30. Muthukumaran CK, Vaidyanathan A (2015) Experimental study of elliptical jet from supercritical to subcritical conditions using planar laser induced fluorescence. *Phys Fluids* 27(034109)
31. Muthukumaran CK, Vaidyanathan A (2016) Initial instability of round liquid jet at subcritical and supercritical environments. *Phys Fluids* 28(074104)
32. Nishad K, Shevchuk I, Sadiki A, Weigand B, Vrabec J, Janicka J (2017) Effect of nu- and sh-number correlations on numerical predictions of droplet evaporation rate under transcritical conditionos. *MCS* 10
33. Oefelein J, Lacaze G, Dahms G, Ruiz A (2014) Effects of real-fluid thermodynamics on high-pressure fuel injection processes. *SAE Int J Engines* 7(2014-01-1429):1125–1136
34. Okong'o N, Harstad K, Bellan J (2002) Direct numerical simulations of o/h temporal mixing layers under supercritical conditions. *AIAA J* 40(5):914–926
35. Patankar S, Spalding D (1972) A calculation procedure for heat, mass and momentum transfer in three-dimensional parabolic flows. *Int J Heat Mass Trans* 15(10):1787–1806
36. Pelletier M (2019) Diffuse interface models and adapted numerical schemes for the simulation of subcritical to supercritical flows. PhD thesis, University Paris-Saclay, Ecole CentraleSupupe

37. Peng D, Robinson D (1976) A new two-constant equation of state. *Ind Eng Chem Fundamen* 15:59–64
38. Petit X, Ribert G, Lartigue G, Domingo P (2013) Large-eddy simulation of supercritical fluid injection. *J Supercrit Fluids* 84:61–73
39. Qiu L, Reitz R (2014) Simulation of supercritical fuel injection with condensation. *Int J Heat Mass Trans* 79:1070–1086
40. Qiu L, Reitz R (2015) An investigation of thermodynamic states during high-pressure fuel injection using equilibrium thermodynamics. *Int J Multiph Flow* 72:819–834
41. Ries F, Obando P, Shevchuck I, Janicka J, Sadiki A (2017) Numerical analysis of turbulent flow dynamics and heat transport in a round jet at supercritical conditions. *Int J Heat Fluid Flow* 66:172–184
42. Ries F, Sadiki A (2020) Supercritical and transcritical turbulent injection processes: consistency of numerical modeling. *At Sprays*
43. Roy A, Joly C, Segal C (2013) Disintegrating supercritical jets in a subcritical environment. *J Fluid Mech* 717:193–202
44. Sanjosé M, Senoner J, Jaegle F, Cuenot B, Moreau S, Poinsot T (2011) Fuel injection model for euler-euler and euler-lagrange large-eddy simulations of an evaporating spray inside an aeronautical combustor. *Int J Multiph Flow* 37:514–529
45. Saurel R, Abgrall R (1999) A multiphase godunov method for compressible multifluid and multiphase flows. *J Comput Phys* 150:425–467
46. Schmitt T (2020) Large-eddy simulations of the mascotte test cases operating at supercritical pressure. *Flow Turbul Combust* 105:159–189
47. Selle L, Okong'o N, Bellan J, Harstad K (2007) Modelling of subgrid-scale phenomena in supercritical transitional mixing layers: an a priori study. *J Fluid Mech* 593:57–91
48. Sierra-Pallares J, Garcia del Valle J, Garcia-Carrascal P, Castro Ruiz R (2016) Numerical study of supercritical and transcritical injection using different turbulent prandlt numbers: a second law analysis. *J Supercrit Fluids* 115:86–98
49. Srivastava S, Jaberi F (2017) Large eddy simulations of complex multicomponent diesel fuels in high temperature and pressure turbulent flows. *Int J Heat Mass Trans* 104:819–834
50. Sun M, Zhong Z, Liang J, Wang H (2016) Experimental investigation on combustion performance of cavity-strut injection of supercritical kerosene in supersonic model combustor. *Acta Astronautica* 127:112–119
51. Tramecourt N, Menon S, Amaya J (2004) Les of supercritical combustion in a gas turbine engine. In: 40th, AIAA/ASME/SAE/ASEE joint propulsion conference and exhibit: joint propulsion conferences
52. Traxinger C, Pfitzner M, Baab S, Lamana G (2019) Experimental and numerical investigation of phase separation due to multicomponent mixing at high-pressure conditions. *Phys Rev Fluids* 4(074303)
53. Tuma PE (2008) Fluoroketone  $C_2F_5C(O)CF(CF_3)_2$  as a heat transfer fluid for passive and pumped 2-phase applications. In: Annual IEEE semiconductor thermal measurement and management symposium
54. Wehrfritz A, Vuorinen V, Kaario O, Larmi M (2013) Large eddy simulation of high-velocity fuel sprays: studying mesh resolution and breakup model effects for spray a. *At Spray* 23:419–442
55. Wensing M, Vogel T, Götz G (2015) Transition of diesel spray to a supercritical state under engine conditions. *Int J Engine Res* 17(1):108–119
56. Yang S, Gao Y, Deng C, Xu B, Ji F, He F (2016) Evaporation and dynamic characteristics of a high-speed droplet under transcritical conditions. *Adv Mech Eng* 8(4):1–12
57. Yi P, Yang S, Habchi C, Lug R (2019) A multicomponent real-fluid fully compressible four-equation model for two-phase flow with phase change. *Phys Fluids* 31

**Open Access** This chapter is licensed under the terms of the Creative Commons Attribution 4.0 International License (<http://creativecommons.org/licenses/by/4.0/>), which permits use, sharing, adaptation, distribution and reproduction in any medium or format, as long as you give appropriate credit to the original author(s) and the source, provide a link to the Creative Commons license and indicate if changes were made.

The images or other third party material in this chapter are included in the chapter's Creative Commons license, unless indicated otherwise in a credit line to the material. If material is not included in the chapter's Creative Commons license and your intended use is not permitted by statutory regulation or exceeds the permitted use, you will need to obtain permission directly from the copyright holder.



# Experimental Investigation of Transient Injection Phenomena in Rocket Combusters at Vacuum with Cryogenic Flash Boiling



Andreas Rees and Michael Oschwald

**Abstract** The substitution of the toxic hydrazine in current high-altitude rocket engines like upper stages or reaction control thrusters by green propellants is a major key driver in the current technology development of rocket propulsion systems. Operating these kind of rocket engines at high-altitude leads to a sudden pressure drop in the liquid propellants during their injection into the combustion chamber with a near-vacuum atmosphere prior to ignition. The resulting superheated thermodynamic state of the liquid causes a fast and eruptive evaporation which is called flash boiling. The degree of atomisation is important for a successful ignition and a secure operation of the rocket engine. The development and operation of a cryogenic high-altitude test bench at DLR Lampoldshausen enables the systematical experimental characterization of cryogenic flash boiling due to its ability to adjust and control the injection parameters like temperature, pressure or geometry. Several test campaigns with liquid nitrogen (LN<sub>2</sub>) were performed using two optical diagnostic methods: First, flash boiling LN<sub>2</sub> spray patterns were visualised by means of high-speed shadowgraphy and, secondly, we determined the droplet size and velocity distributions in strongly superheated LN<sub>2</sub> sprays with the help of a laser-based Phase Doppler system (PDA). The experimental data generated within these measurement campaigns provide defined boundary conditions as well as a broad data base for the numerical modelling of cryogenic flash boiling like e.g. the publications [8, 9].

## 1 Introduction

One of the key elements in the current technology development of rocket propulsion systems typical for cryogenic upper stage rocket engines like, e.g., the Vinci engine of Ariane 6, for cryogenic reaction and control system thrusters or for orbital and

---

A. Rees (✉) · M. Oschwald

Institute of Rocket Propulsion, German Aerospace Center (DLR), Lampoldshausen, Germany  
e-mail: [andreas.rees@dlr.de](mailto:andreas.rees@dlr.de)

M. Oschwald

Institute of Jet Propulsion and Turbomachinery, RWTH Aachen University, Aachen, Germany

manoeuvring system engines is the substitution of toxic propellants like hydrazine by green propellants as well as the introduction of advanced ignition technologies like laser ignition [17]. These kind of rocket engines are all operating at high-altitude conditions. Hence, the used propellants are injected into a low-pressure atmosphere within the combustion chamber prior to ignition due to the vacuum of space. This means that the ambient pressure  $p_\infty$  is below the saturation pressure  $p_{sat}(T_{inj})$  at the corresponding injection temperature  $T_{inj}$  of the injected liquid fuel. During this sudden pressure drop the liquid gets into a metastable thermodynamic state called superheated. As a consequence of the superheated state, the liquid jet evaporates eruptively and expands fastly, which is called flash boiling. The evaporation chills down the two-phase flow and raises the pressure inside the combustor until the equilibrium or the desired operation pressure immediately before ignition is reached. An effective determination of ignition parameters for a secure operation of the rocket engine without any destructive pressure peaks requires to know the actual conditions of the propellants in the combustion chamber in terms of phase, temperature distribution, atomisation behaviour and species.

## 1.1 Flash Boiling

The injection temperature  $T_{inj}$  and the chamber or back pressure  $p_{ch}$  are the dominating injection parameters for flash boiling in a given liquid. The degree of superheat of a superheated liquid can be defined by those two parameters as the pressure ratio

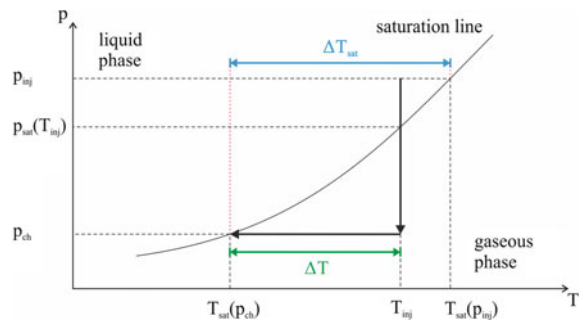
$$R_p = \frac{p_{sat}(T_{inj})}{p_{ch}} \quad (1)$$

or as the ratio of the temperature differences

$$\Delta T^* = \frac{\Delta T}{\Delta T_{sat}} = \frac{T_{inj} - T_{sat}(p_{ch})}{T_{sat}(p_{inj}) - T_{sat}(p_{ch})} \quad (2)$$

with the saturation temperatures  $T_{sat}(p_{ch})$  and  $T_{sat}(p_{inj})$  at the chamber pressure  $p_{ch}$  and at the injection pressure  $p_{inj}$ , respectively, according to Fig. 1. For high degrees of superheat the injected jet is atomising close to or already in the injector which leads to the generation of a fine and wide-opened spray consisting of small droplets. According to reference [40] aerodynamical effects on the jet break-up can be neglected in flash boiling sprays. A new equilibrium state is reached after the chill-down of the two-phase system to the saturation state at  $T_{sat}(p_{ch})$  due to evaporation and expansion. Some authors even observed solidification of storable propellants during high-altitude injection due to strong chill-downs below the triple point [34]. Due to the complex nature of these non-equilibrium processes during the transient start-up phase of cryogenic rocket engines at high-altitude conditions, detailed experimental data is required.

**Fig. 1** p-T phase diagram of a superheated liquid injected into a low-pressure atmosphere with adiabatic depressurization



## 1.2 State of Research

Liquid jet atomisation by the process of flash boiling is known since the beginning of the 20th century [18, 36]. Within the automotive industry, flash boiling of storable fluids like gasoline, diesel or similar substitute fuels were investigated in the last three decades [1–3, 10, 29, 30]. An increase of engine efficiency and a reduction of the exhaust emissions was reached by a stronger atomisation of the fuel due to an artificial superheated state by its pre-heating. [30]. Flash boiling due to nucleation within the liquid jet was observed as the predominant fuel atomisation mechanism while cavitation in the injector can be neglected [1]. Two different kinds of nucleation processes can occur which depend on the degree of superheat, the initial fuel temperature, the ambient pressure, the fuel's critical temperature and the geometry [19, 31, 35]. The two types differ from each other by their mechanism and place of origin: The so-called homogeneous nucleation takes place within the bulk liquid itself, whereas the heterogeneous nucleation process needs a foreign phase like, e.g., at the interface between the nozzle wall and the liquid. The atomisation of a fuel can be enhanced by forced flash boiling after mixing the fuel with low boiling liquids of low concentrations [10]. Araneo and Dondè studied the injection of hydrocarbon sprays generated by a multi-hole injector [2]. They found a relation between the spray angle and the injection conditions by the analysis of backlight shadowgraphy images. Phase Doppler Anemometry (PDA) measurements in hydrocarbon sprays were performed by the same authors to show a similar break-up behavior of jets with dissolved air compared to superheated jets [3]. Several models were developed for the determination of the average spray droplet diameters in superheated water sprays [32], to predict nucleation rates and droplet sizes in flash boiling hydrocarbon sprays [29] or for the prediction of superheat within water sprays during a depressurization transient [7]. In the context of process safety in other industrial sectors like nuclear, chemical or process technology, studies about flash boiling of the storable liquids water, refrigerants like R-134A, ethanol or further hydrocarbons were published [4, 7, 28, 33, 39]. It was found that the injection conditions like the injection pressure and the diameter of the injector orifice influence the intensity of flash boiling besides the degree of superheat [39]. By shadowgraph imaging the region of the actual axial

and radial jet break-up was identified as remaining liquid core within the flash boiling spray close to the injector orifice [28, 33]. Three characteristic break-up modes of flash boiling water sprays were found and differentiated into an aerodynamical break-up region, a fully flashing region and a transition region between both. These regions were empirically quantified by the usage of the dimensionless Weber and Jakob numbers derived from the injection conditions [4, 37]. The resulting correlations were found to be valid also for the superheated fluids acetone, ethanol and iso-octane within study [13]. In the same study an onset criterion basing on the classical nucleation theory for the inception of flash boiling as well as a model for the prediction of the spray angle close to the injector orifice depending on the degree of superheat and the dimensionless surface tension were developed. The difficult operating conditions due to the cryogenic as well as the high-altitude environments are the reason for only few experimental studies concerning cryogenic sprays atomised by flash boiling compared to storable fluids. In one of those few studies liquid nitrogen (LN2) sprays with about 10 s injection duration and varying injection conditions were visualised by means of high-speed shadowgraphy [16]. Besides maximum spray angles of about 140°, the study revealed that the influence of the injection geometry and the injection pressure on the spray angle evolution is negligible and that the LN2 sprays are cooling down below the triple point why solidification occurs at temperature measurement sensors which were positioned along the spray's central axis. An experimental study about laser ignition of a coaxially with gaseous hydrogen injected superheated liquid oxygen (LOX) jet was performed at test bench M3.1 at DLR Lampoldshausen within a model rocket combustion chamber under high-altitude conditions [5]. However, the co-flow of the gaseous hydrogen suppressed the spray widening and significantly narrower spray angles were observed compared to flash boiling sprays of mono-component jets. During the first two funding periods of the SFB TRR75 project the influence of two different injection configurations on the flash boiling process of LOX jets was investigated at the same test bench facility. A comparison of the results with the data of storable fluids in study [12] revealed similar spray morphologies despite the strongly varying physical properties of the used fluids. However, the injection system of test bench M3.1 is limited in terms of controlling and adjusting the desired injection temperature since only the two different temperature levels  $T_{\text{inj}} = 94 \text{ K}$  and  $T_{\text{inj}} = 113 \text{ K}$  were achieved. Furthermore, these temperatures were measured about 200 mm away from the actual injector and they were very sensitive to ambient conditions because the injection system was not thermally insulated from the atmosphere around the test bench.

In this chapter we provide a summary about the behaviour of flash boiling LN2 sprays in respect of their degrees of superheat and their injection conditions. With the experimental data of these sprays we generate a comprehensive data base for further numerical investigations about cryogenic flash boiling, like e.g. in the studies [8, 9].

## 2 Experimental Set-Up

Since the adjustment and control of the injection temperature  $T_{inj}$ , especially, was partly limited in the few experimental studies about cryogenic flash boiling and this temperature is the dominating parameter for the flash boiling process besides the back pressure  $p_{ch}$ , these two parameters have to be adjustable, controllable during the injection period and reproducible for a systematic experimental investigation. Hence, we are operating the newly built test bench M3.3 at DLR Lampoldshausen [22, 25].

### 2.1 Cryogenic Test Bench M3.3

This test bench which is depicted in Fig. 2, can be divided into its three subsystems media supply and pressurization system, a cryogenic temperature adjustment and injection system (CTAIS) and a vacuum system. The first one serves as an interface between the gas infrastructure of DLR Lampoldshausen and the test bench to distribute and pressurize all gases (nitrogen, helium, oxygen) needed for the operation of the CTAIS, the second subsystem of the test bench. Basically, this system consists of an inner pressure tank with the actual test fluid LN2 or LOX within an outer one filled with the cooling agent liquid and gaseous nitrogen (GN2). The double-walled and vacuum-insulated casing of the outer pressure tank can be seen in Fig. 2 on the left and right. The temperature of the cooling agent within this tank is controlled by evacuating or pressurizing the GN2 phase depending on whether the fluid has to be cooled down or heated up, respectively: To reach a new saturation state after evacuation, LN2 vaporizes and the latent heat of vaporization necessary for this phase change causes a loss of heat of the two-phase nitrogen system and consequently to a decrease of its temperature. In the case of pressurization the new saturation state is achieved by condensation of the gaseous nitrogen phase which releases its latent heat of condensation and heats up the two-phased nitrogen. The inner pressure tank, also called run-tank, with a volume of 0.5 L is much smaller and quickly reaches the temperature of the surrounding cooling fluid. Apart from the run-tank, the injector unit with a pneumatic run valve and an injector nozzle, a coriolis mass flowmeter and piping in-between complete the test fluid feed and injection system, as can be seen in the middle of Fig. 2. Hence, the whole feed and injection system is surrounded by the cooling agent LN2/GN2 which ensures a homogeneous temperature distribution from the run-tank to the injector nozzle. For the secure operation of the CTAIS, for its temperature control and adjustment as well as to know the injection parameters of the test fluid, the CTAIS is equipped with various temperature and pressure sensors. Especially close to the injector a Pt100 temperature sensor as well as a dynamic pressure sensor of the type 601A by Kistler are installed not further than about 30 mm upstream of the injector nozzle exit. For safety reasons the cable ducts of the sensor cables inside the outer pressure tank are pressurized by gaseous helium which

is also used as working fluid for the pneumatically triggered axial run valve of the type Axius by Stöhr Armaturen. The supply pipes for helium, for the test fluid and for the cooling agent as well as the sensor cables are connected to the media supply and pressurization system by a hand hole positioned at the top of the outer pressure tank. The third sub-system, i.e. the vacuum system, consists of a cylindrical chamber with an outer diameter of 360 mm, an inner diameter of 300 mm and a height of 225 mm from the injector nozzle exit to the bottom of the chamber. Four windows, installed at an angle of 90° to each other, with a diameter of 100 mm each provide an optical access to the interior of the vacuum chamber for spray visualisation and optical measurement techniques. Because of the cryogenic operation conditions the humidity of the ambient atmosphere condensates and freezes on the test bench's surfaces. This is why we are operating a window heating with warm GN2 to prevent icing of the optical accesses. The copper pipes of the heating system can be seen on the right-hand side of Fig. 2 below and besides the cylindrical window. The near-vacuum atmosphere within the vacuum chamber for the high-altitude requirement is generated by a vacuum pump with a pumping speed of 87.5 m<sup>3</sup>/h attached to the chamber. To get rid of the humidity within the CTAIS, all its pipes, tanks and vessels have to be evacuated before starting the chill-down process with LN2. The latter takes, e.g., about 90 minutes until a target test fluid temperature of 90 K is reached [24]. During the chill-down the gaseous test fluid nitrogen is filled into the run-tank and gets liquefied in the meantime. In our study [24] we show that the CTAIS allows a constant injection temperature  $T_{inj}$  during the whole injection time of about 2 s without significantly being affected by ambient conditions surrounding the test facility. In contrast to the former injection system at test bench M3.1, the CTAIS of test bench M3.3 enables the adjustment of the injection temperature within the range of 77 K ≤  $T_{inj}$  ≤ 96 K with a reproducibility of ±0.6 K for each test run and a homogeneous temperature distribution in the whole feed line systems [21, 22, 25].

## 2.2 Injection Conditions

In our first measurement campaign we generate about 120 superheated LN2 sprays with varying injection parameters and visualise these sprays with the help of high-speed shadowgraph imaging. The respective temperature and pressure values are listed in Table 1. The injector with a sharp edge, a length-to-diameter ratio of  $L/D = 2.9$  and a diameter of  $D_{inj} = 1$  mm is used during the whole measurement campaign. Further details about the injector can be found in references [23, 26]. From the total amount of the generated sprays we are analysing 22 of them more closely. Their injection conditions and  $R_p$ -values are listed in Table 2. Other parameters of those sprays like their degrees of superheat  $\Delta T$  and  $\Delta T^*$  or their dimensionless numbers like the Weber numbers  $We_{g,l} = \rho_{g,l} u_{inj}^2 D_{inj} / \sigma$  for the gaseous and liquid phase, the Reynolds number  $Re = \rho_l u_{inj} D_{inj} / \eta$ , the Ohnesorge number  $Oh = \sqrt{We}/Re$  and the Jakob number  $Ja = \rho_l c_{p,l} \Delta T / \rho_g \Delta h_{vap}$  can be found in our study [26]. For their evaluation



**Fig. 2** Main sub-systems of DLR test bench M3.3: media supply and pressurization system, opened CTAIS, vacuum system (left); opened CTAIS with test fluid feed and injection system, i.e. run-tank, injector unit and sensors in-between (middle); chilled-down test bench during operation (right) [23]

**Table 1** Range of the injection parameters of the generated LN<sub>2</sub> sprays for high-speed shadowgraphy; republished with permission of Begell House Inc., from reference [26], permission conveyed through Copyright Clearance Center, Inc

Parameter	Value	Tolerance range
Inject. temperature $T_{inj}$	76.6–95.6 K	$\pm 0.6$ K
Inject. pressure $p_{inj}$	240–1210 kPa	$\pm 30$ kPa
Back pressure $p_{ch}$	2.8–192.1 kPa	$\pm 3.3$ kPa
Injector diameter $D_{inj}$	$1 \cdot 10^{-3}$ m	$\pm 5 \cdot 10^{-5}$ m
Length to diameter $L/D$	2.9	$\pm 0.2$
Inject. velocity $u_{inj}$	3.9–33.3 m/s	$\pm 3$ m/s
Degree of superheat $R_p$	1.4–191.4	$\pm 30$

we are using the density  $\rho_g$  and  $\rho_l$  of the gaseous and liquid phase, respectively, the velocity of the liquid within the injector  $u_{inj}$ , its diameter  $D_{inj}$ , the liquid's surface tension  $\sigma$ , heat capacity  $c_{p,l}$ , heat of vaporization  $h_{vap}$  and dynamic viscosity  $\eta$ . The investigated 22 LN<sub>2</sub> sprays are generated within the ranges of  $4 < We_g < 856$  for the gaseous Weber number,  $1.73 \cdot 10^4 < We_l < 8.30 \cdot 10^4$  for the liquid Weber number,  $3 < Ja < 2001$  for the Jakob number,  $8.19 \cdot 10^4 < Re < 1.82 \cdot 10^5$  for the Reynolds number and  $1.45 \cdot 10^{-3} < Oh < 1.74 \cdot 10^{-3}$  for the Ohnesorge number.

In a second measurement campaign we generate LN<sub>2</sub> sprays with a high degree of superheat of  $R_p \approx 60$  to determine their droplet behaviour. Since the laser-based PDA measurement technique is a point measuring method instead of a global one, we set constant injection parameters for all of the sprays and the same injector as in the first measurement campaign is used. The respective parameter values are listed in Table 3. For comparison reasons we are using the definition of the degree of superheat  $R_p$  according to Eq. (1) despite its obviously big tolerance range in our

**Table 2** Injection parameters of the 22 LN2 sprays for the high-speed shadowgraphy campaign

#	$T_{\text{inj}}$ [K]	$p_{\text{inj}}$ [kPa]	$p_c$ [kPa]	$R_p$ [-]
1	82.9	816	61	3.0
2	82.7	808	51	3.5
3	82.9	815	46	4.1
4	82.6	803	41	4.4
5	82.7	802	32	5.7
6	82.9	802	26	7.0
7	82.3	805	15	12.0
8	81.9	810	6	28.4
9	82.6	404	60	3.0
10	82.1	397	54	3.2
11	82.9	408	45	4.2
12	82.7	404	41	4.4
13	81.9	400	30	5.5
14	82.7	407	26	7.0
15	82.7	409	14	12.7
16	83.2	403	4	52.3
17	86.2	420	7	39.2
18	84.8	390	3	74.3
19	84.7	400	3	80.0
20	89.4	610	3	108.3
21	95.6	620	3	191.4
22	86.6	800	192	1.4

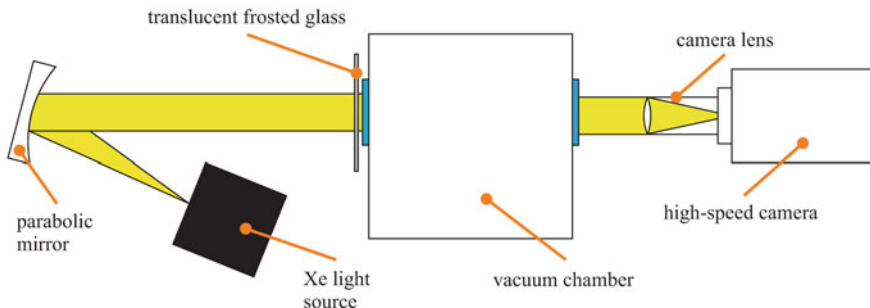
analysed sprays. The huge range can be explained by deviations of the back pressure  $p_{ch}$  which strongly affects the degree of superheat.

### 2.3 High-Speed Shadowgraphy

A high-speed shadowgraphy set-up with backlight illumination is used to visualise the flash boiling LN2 sprays [25–27]. According to the scheme in Fig. 3, we illuminate the generated sprays from one side of the chamber. The light of a xenon light source is bundled and directed by a parabolic mirror to one of the chamber windows in front of which we are using a translucent frosted glass for a homogeneous spray background. On the opposite side of the chamber we set-up the high-speed camera with its focus on the central plane of the injector. The camera Photron Fastcam SA-X is set to a frame rate of 10000 fps, a pixel resolution of  $1024 \times 1024$  pixels and a spatial

**Table 3** Injection conditions of the used LN<sub>2</sub> sprays for PDA

Parameter	Value	Tolerance range
Inject. temp. $T_{inj}$	89.7 K	$\pm 0.6$ K
Inject. pressure $p_{inj}$	$4.4 \cdot 10^5$ Pa	$\pm 0.4 \cdot 10^5$ Pa
Back pressure $p_{ch}$	$73 \cdot 10^2$ Pa	$\pm 27 \cdot 10^2$ Pa
Inject. diameter $D_{inj}$	$1 \cdot 10^{-3}$ m	$\pm 0.05 \cdot 10^{-3}$ m
Length-to-diameter $L/D$	2.9	$\pm 0.2$
Inject. velocity $u_{inj}$	18.1 m/s	$\pm 3$ m/s
Chamber wall temp. $T_w$	196.6 K	$\pm 3.0$ K
Degree of superh. $R_p$	60	$\pm 30$
Degree of superh. $\Delta T^*$	0.91	$\pm 0.04$
Weber number $Weg$	21	$\pm 10$
Jakob number $Ja$	746	$\pm 395$
Reynolds number $Re$	131952	$\pm 22165$

**Fig. 3** High-speed backlight shadowgraphy set-up at test bench M3.3; republished with permission of Begell House Inc., from reference [26], permission conveyed through Copyright Clearance Center

resolution of 0.02 mm/pixel. For further details about this optical set-up as well as for the post-processing of the raw images we refer to our work [26]. In that study, we also show that steady-state spray conditions are reached after a period of about  $100 \text{ ms} < t_{inj} < 120 \text{ ms}$  after triggering the start of the injection process. Hence, we choose  $t_{inj} = 120 \text{ ms}$  as steady-state evaluation time and all of the investigated sprays are analysed at this time, except spray #8 which is optically too dense at  $t_{inj} = 120 \text{ ms}$  and is analysed at  $t_{inj} = 100 \text{ ms}$  instead.

## 2.4 Phase Doppler System

We set-up the PDA system by the manufacturer Dantec Dynamics in a so-called 2D fibre configuration which allows the simultaneous measurement of the vertical and

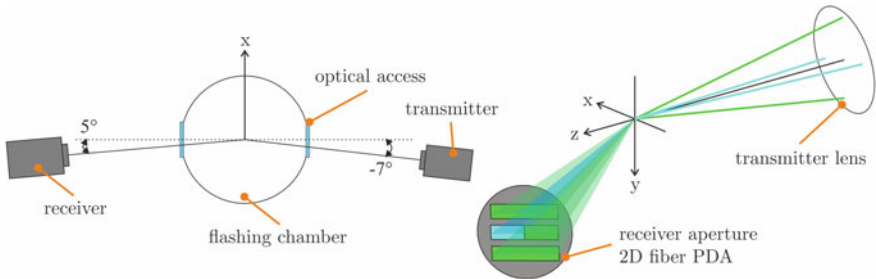


**Fig. 4** Optical alignment of the 2D Fibre PDA system at test bench M3.3 (left) and used aperture of the receiver probe (right) [23]

horizontal components of the droplet velocity and the droplet diameter distributions, which is depicted in Figs. 4 and 5 (left). By moving the optical components, namely the transmitter and the receiver probes, with the help of the 2D-traverse system various measurement positions in axial and radial directions within the sprays can be set. The geometrical alignment of the transmitter and the receiver probe to each other is depicted on the left of Fig. 4. The given geometry of the vacuum chamber in terms of its optical accesses allows a maximum intensity of scattering light by the dominant first order refraction for an off-axis angle of  $\varphi = 12^\circ$  between both PDA probes. Tilting not only the receiver but also the transmitter with  $\varphi_{\text{reci}} = 5^\circ$  and  $\varphi_{\text{trans}} = 7^\circ$ , respectively, expands the maximum field of view which is limited by the diameter and frame structures of the optical accesses. Basing on this field of view we can specify the measurement position matrix according to the right-hand side of Fig. 5. For each position of this matrix we generate at least one single wide flashing LN2 spray and record the data for a time of 12 s. Hence, we can not exclude small shot-to-shot variations between each test run at a certain measurement position. The data recording is synchronized with the trigger signal for the start of the injection process. As mentioned in Sect. 2.3, the steady-state of the injection process starts at  $t_{\text{inj}} = 120$  ms and, according to our study [24], ends after  $t_{\text{inj}} = 220$  ms. Consequently, the detected Doppler signals are evaluated within this duration by the calculation of their arithmetical mean values. Two diode pumped solid state (DPSS) lasers with a wavelength of 488 nm and 514 nm, respectively, are used within the PDA system. We are operating both lasers at a power of approximately 9 mW, each measured at the position of the measurement volume prior to the first test run. The receiver probe is equipped with a spatial filter in terms of a 100  $\mu\text{m}$  slit. We can quantify a systematical measurement error of  $\pm 26\%$  for the diameter determination as well as the maximum statistical errors  $\Delta U = \pm 6.1$  m/s,  $\Delta V = \pm 8.0$  m/s and  $\Delta D = \pm 3.3$   $\mu\text{m}$ . For further details about the set-up, calibration and adjustment procedures as well as error estimation we refer to our work [23].

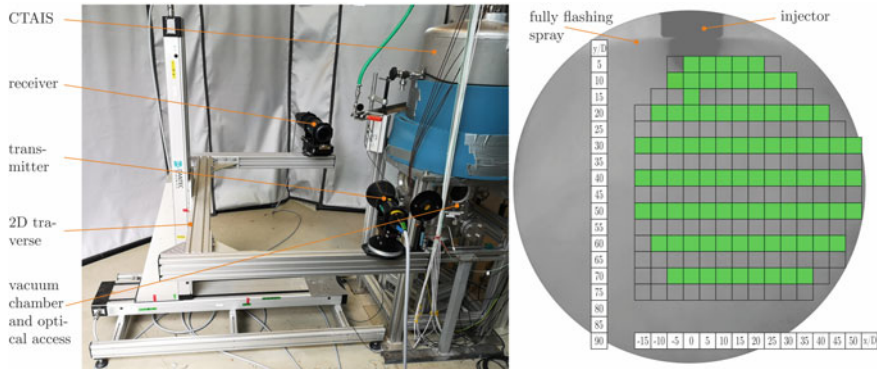


**Fig. 5** 2D Fibre PDA system at test bench M3.3 (left) and position matrix of measurement points in wide flashing LN<sub>2</sub> sprays (right) [23]

### 3 Results and Discussion

#### 3.1 Shadowgraph Images Analysis

The shadowgraph images of a test series containing the 16 sprays #1 to #16 with varying degrees of superheat from  $3.0 \leq R_p \leq 52.3$  but at a constant injection temperature of  $T_{inj} = 82.5 \pm 0.6$  K are depicted in Fig. 6. The first two rows of shadowgraph images with the sprays #1 to #8 show the influence of a growing degree of superheat  $R_p$  on the spray morphology by a gradual reduction of the back pressure  $p_{ch}$  from 60 to 3.6 kPa. Their injection pressure is kept constant at  $p_{inj} = 800 \pm 30$  kPa. Lowly superheated sprays with  $R_p \approx 3$  still show aerodynamical break-up patterns like large liquid ligaments. An example of the latter is highlighted on the left-hand side of Fig. 7. Here, the relative motion of the surrounding chamber atmosphere with the surface of the liquid jet is still a dominant factor for the break-up of the jet. With growing degrees of superheat the jet collapse gets more and more eruptive and produces sprays with wider opening angles due to the decreasing influence of the chamber atmosphere and the simultaneous increase of internal energy in the liquid jet. This energy dissipates by enhanced vaporization. A further increase of superheat by back pressure reduction culminates in the heavily flash boiling sprays #7 and #8 with a bell-shaped spray pattern and opening angles of almost 180°. Especially in the highly superheated spray #8 with a degree of superheat of  $R_p = 28.4$ , the liquid jet breaks up already at the injector outlet around a liquid core in axial and radial direction. Such a liquid core is exemplarily shown on the right-hand side of Fig. 7. A detailed analysis and model about the relation between these remaining liquid cores and the degree of superheat is discussed in our publication [27]. Apart from these liquid cores, no other liquid structures with a magnitude of one millimetre or more remain in that highly superheated sprays. As discussed in our publication [26] the heterogeneous nucleation is the predominant process of nucleation compared to the

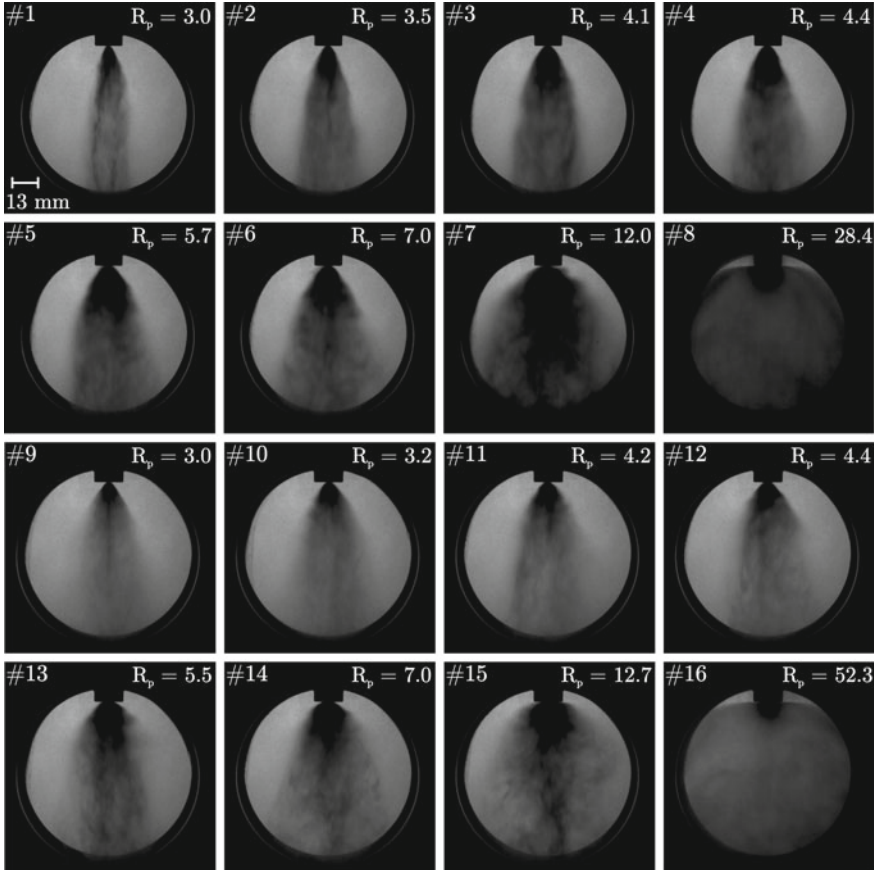
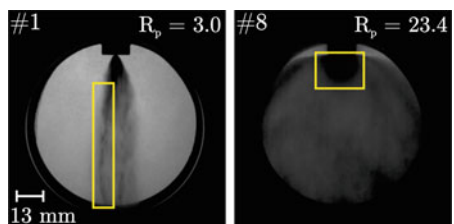


**Fig. 6** Shadowgraph images of LN2 sprays #1-16 with varying degrees of superheat from  $3.0 \leq R_p \leq 52.3$  at  $T_{inj} = 82.5\text{ K}$

**Fig. 7** Shadowgraph images of LN2 spray #1 with highlighted liquid ligament (left) and of spray #8 with highlighted remaining liquid core (right)



homogeneous one for the sprays #1-#22 due to lower injection temperatures than the minimum necessary temperature for the inception of homogeneous nucleation according to references [6, 15, 19, 20].

The third and fourth rows of shadowgraph images in Fig. 6 with the sprays #9 to #16 show the effect of the injection pressure  $p_{inj}$  on the spray pattern of flash

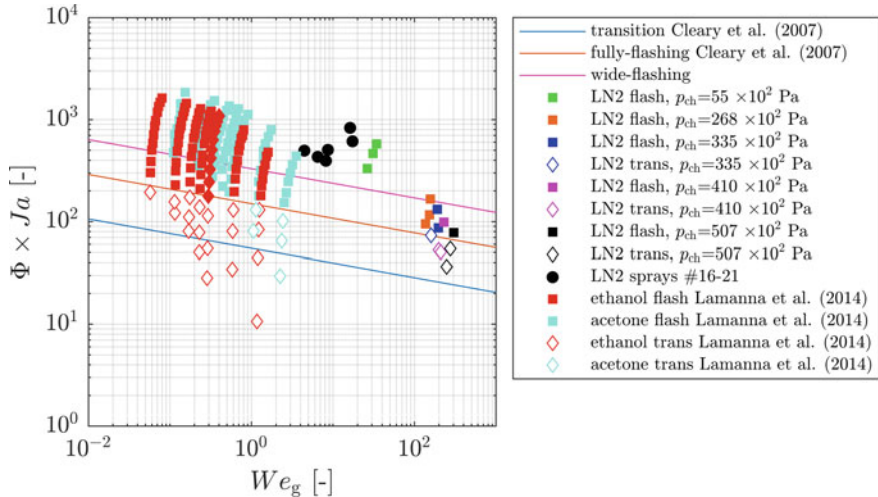


**Fig. 8** Experimental data of superheated acetone and ethanol by the study of Lamanna et al. [13] as well as data of several LN2 sprays with respect to the break-up regime correlations from studies [4, 37]; republished with permission of Begell House Inc., from reference [26], permission conveyed through Copyright Clearance Center

boiling LN2 sprays. Here, the pressure is reduced by half to a value of  $p_{\text{inj}} = 400 \pm 20$  kPa. The other injection parameters like the temperature  $T_{\text{inj}}$  as well as the gradual reduction of the back pressure  $p_{\text{ch}}$  are the same as in the case of the sprays #1 to #8. Obviously, the general trend of the spray evolution with increasing degrees of superheat does not change significantly compared to the sprays #1 to #8, i.e. a decline of larger liquid structures due to enhanced evaporation and a widening of the spray. However, at low degrees of superheat the sprays #9 to #12 with the lower injection pressure are wider than the sprays #1 to #4. The lower injection pressure leads to weaker flow-dynamic effects of the chamber atmosphere on the surface of the LN2 jet because of a lower flow velocity  $u_{\text{inj}}$  in the injector and therefore a less pronounced relative motion between the two phases [26]. Furthermore, the residence time of the LN2 within the injector is higher, and therefore also the nucleation rate, as a consequence of the lower injection pressure. Hence, the ratio between flash boiling and aerodynamical break-up is shifted towards the more dominant flash boiling process already at low degrees of superheat. For higher degrees of superheat of  $R_p \geq 12$  the jet break-up is solely driven by flash boiling why the influence of the different relative flow dynamics in the chamber nearly disappears and the spray patterns look very similar to the ones at the higher injection pressure.

In Fig. 8 the dimensionless numbers  $We_g$  and  $Ja$  of superheated acetone and ethanol sprays from reference [13] are depicted with respect to the three different break-up regimes *aerodynamical break-up*, *transition* and *fully-flashing* according to the studies [4, 37]. Taking into account our data about superheated LN2 like the sprays #16 to #21 as well as some more LN2 sprays with varying injection temperatures of

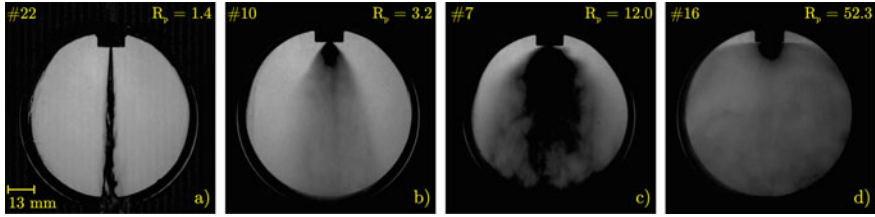


**Fig. 9** Four exemplary superheated LN2 sprays (#22, #10, #7 and #16) to demonstrate the classic break-up regimes **a** aerodynamical break-up, **b** transition regime and **c** fully flashing regime according to study [4] and the new **d** wide flashing regime [26]

$81 \text{ K} < T_{\text{inj}} < 93 \text{ K}$  demonstrates that our LN2 measurement campaign extends the validity range of the break-up regime correlations by two orders of magnitude towards higher Weber numbers. The LN2 sprays #22, #10 and #7 are depicted exemplarily in Fig. 9a–c to demonstrate the validity of the three break-up regimes *aerodynamical break-up*, *transition regime* and *fully-flashing regime*, originally derived for storable fluids, also for the cryogenic fluid LN2. Further details can be found in our work [26].

Determining the spray angles at the axial distance  $L/D = 1$  from the injector orifice by analysis of the shadowgraph images reveals spray angles of  $\theta > 170^\circ$  for LN2 sprays with very high degrees of superheat in the range of  $18 \leq R_p \leq 192$  like the sprays #8 and #16 to #21. In our work [26] we show that above a threshold angle of  $\theta_{\text{thresh}} \approx 160^\circ$  the spray patterns look the same as, e.g., the one of spray #16 and do not significantly change any more despite increasing degrees of superheat. We call the break-up mechanism of these wide-opened and very highly superheated sprays *wide flashing* with the corresponding analytical correlation in terms of the Weber and the Jakob number

$$Ja \Phi = 330 We_g^{-\frac{1}{7}} \quad (3)$$

with the Jakobs number  $Ja$ , the Weber number of the gaseous phase  $We_g$  and the factor

$$\Phi = 1 - \exp \left[ -2300 \frac{\rho_g}{\rho_l} \right]. \quad (4)$$

This curve is depicted as pink line in Fig. 8 and represents the transition from the fully flashing regime according to reference [4] into the newly introduced wide flashing regime [26]. A respective wide flashing LN2 spray is shown exemplarily in Fig. 9d).

### 3.2 PDA Results

As listed in Table 3 in Sect. 2.2, the used wide flashing LN2 sprays for the PDA measurement campaign are highly superheated with an injection temperature of  $T_{\text{inj}} = 89.7 \text{ K}$  and a resulting degree of superheat of  $R_p = 60$ . Their injection pressure is held constant at  $p_{\text{inj}} = 4.4 \cdot 10^5 \text{ Pa}$ . The spatial distributions of the two mean velocity components vertical velocity  $U$  (left) and horizontal velocity  $V$  (right) as well as the droplet mean diameter  $D_{10}$  in these LN2 sprays are depicted in Fig. 10. Here, each data circle represents one single injection event and includes a colour code for the velocity value while the circle size represents the mean diameter of the droplet set at this position. The respective scales can be found in the figure. In the near-injector region with  $-10 \leq x/D \leq 10$  and  $10 \leq y/D \leq 20$  the highest vertical droplet velocities with values of  $U = 50 - 70 \text{ m/s}$  are measured. Since these droplets are moving at significantly higher vertical velocities than the flow velocity within the injector with a value of  $u_{\text{inj}} = 18.1 \text{ m/s}$ , the explosive acceleration of the droplets due to evaporation and their subsequent expansion due to the flash boiling process is demonstrated. With growing radial direction the vertical droplet velocities are decreasing strongly because of the dominant radial momentum in the spray expansion from positions with  $x/D \geq 15$ . The pronounced change of the velocity magnitude between the spray's central axis and its periphery is the result of a complex interaction between non-equilibrium fluid transition effects and gas dynamics: Due to the high degree of superheat the liquid nitrogen nucleates within the injector and bubbles are generated already inside of it. As a consequence, the flow within the injector becomes choked and the speed of sound of the two-phased LN2 flow is reduced significantly. This leads to an under-expanded two-phase jet behaviour with a Prandtl-Mayer expansion flow at the exit of the injector [8, 11, 13]. Multiple characteristic expansion waves around the spray axis lead to the strong acceleration in this region while towards the spray edges only a few of them contribute to a significantly lower acceleration of the flow. After a vertical distance of  $y/D \geq 30$  from the injector exit after which the Mach disc is passed, the measured vertical velocities  $U$  are getting considerably smaller and the deviation to the vertical droplet velocities at the spray's radial edges nearly disappears. This is due to a flattening of the vertical velocity profile as a consequence of the normal shock uniformly decelerating the flow in the radial direction. The right-hand side of Fig. 10 with the spatial profiles of the mean horizontal velocities  $V$  is consistent with these considerations since the measured horizontal droplet velocities at positions  $y/D > 40$  become more and more uniform and homogeneous because of the Prandtl-Mayer expansion system with the decelerating normal shock [23]. The spatial distributions of both velocity components reveal that the near-injector region is the zone with the highest droplet velocities. Here, the transformation of the internal energy within the LN2 jet into kinetic one takes place. [23].

Concerning the droplet mean diameters  $D_{10}$ , this near-injector region reveals small droplets with diameters as small as  $D_{10} = 6.5 \mu\text{m}$  with no clear trend especially at the position  $y/D = 5$  according to Fig. 10. However, the limitations of optical diag-

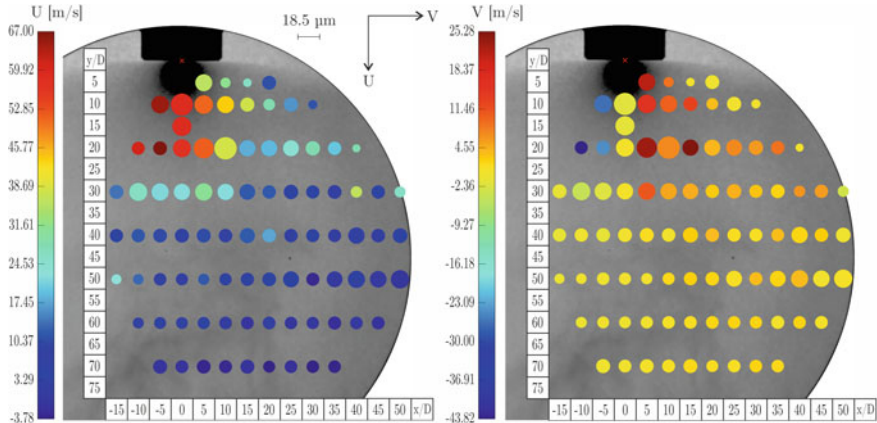
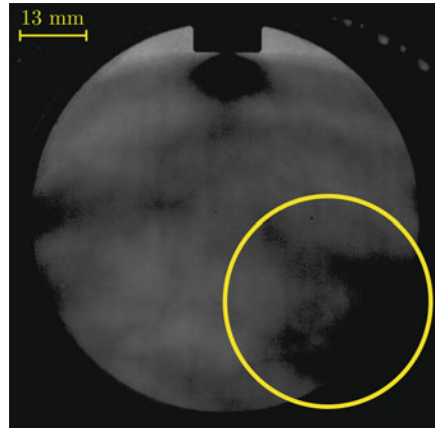


**Fig. 10** Spatial distributions of the mean vertical velocity  $U$  (left), the mean horizontal velocity  $V$  (right) and of the droplet mean diameter  $D_{10}$  in wide flashing LN2 sprays [23]

nostic techniques like PDA in these optically dense regions is repeatedly observed in literature [4, 14, 38]. Especially, the extensive presence of non-spherical particles and ligaments leads to low validation rates and biases the determination of the droplet diameters. Downstream in the region  $10 \leq y/D \leq 30$  the biggest mean diameters with values between  $14 \mu\text{m}$  and  $18.5 \mu\text{m}$  are measured within the centre of the spray. Laterally, the droplets are getting smaller with measured mean diameters of  $D_{10} \leq 10 \mu\text{m}$ . In line with the velocity measurements, the droplet size distribution gets more and more uniform with mean diameters of  $D_{10} = 8 - 10 \mu\text{m}$  at positions  $y/D > 40$ . Reaching this monodisperse-like droplet diameter distribution shows that the upstream existing non-spherical liquid particles disintegrate by further evaporation and expansion during the flash boiling process. However, at the edges of the spray at positions of  $x/D > 30$  we observe an unsteady distribution with even increasing droplet diameters. As can be seen in Fig. 11, at these spray positions flow interactions between the LN2 spray and the window margins of the vacuum chamber occur which affects the diameter measurement and leads to an increase in diameter. These effects including recirculation flows are discussed in detail in our publication [23].

The analysis of the PDA measurement data reveals two separate droplet populations at certain measurement positions within the LN2 sprays. The major distinctive factor of the two populations is a high mean vertical velocity of about  $U = 40 \text{ m/s}$  for the so-called upper, or Hi-population while the one of the lower Lo-population is much lower with values even below zero. This is exemplarily shown on the left of Fig. 12 for the spray position  $x/D = 0$  and  $y/D = 30$ . In contrast, however, the measurement data of the horizontal velocity does not show any distinguishable droplet populations. According to our data, we empirically choose a threshold value of  $U_{\text{thresh}} = 5 \text{ m/s}$  for the separation of the Hi-population with vertical mean velocity values of  $U > U_{\text{thresh}} = 5 \text{ m/s}$  from the Lo-population with velocities below the threshold. Besides the quite low vertical velocity range of  $-25 \text{ m/s} < U_{\text{Lo}} < 5 \text{ m/s}$

**Fig. 11** Flow interactions between a highly superheated LN<sub>2</sub> spray and the window margins of the vacuum chamber



of the Lo-population, its droplet diameters are slightly smaller than the ones of the Hi-population. As shown in detail in our work [23], the range of the Hi-population with  $10 \text{ m/s} < U_{\text{Lo}} < 70 \text{ m/s}$  is much higher and strongly depends on the axial distance from the injector. The measurement position matrix of Fig. 5 from Sect. 2.4 is depicted on the right of Fig. 12 to show the local occurrence of the two droplet populations: At every blue coloured measurement position both populations are clearly distinguishable from each other. Furthermore, these positions coincide with flow recirculation zones caused by the shock systems mentioned above and observed in our studies [23, 26]. That allows us to conclude that the upstream direction of motion of the droplets in the Lo-population is due to these recirculation zones and the droplets' capability to follow the gas flow of the wide flashing LN<sub>2</sub> sprays. The bigger droplets of the Hi-population, however, do not seem to be affected by those zones of high-dynamic gas flows. Instead, their higher inertia ensures that they flow along the initial flow trajectories which are characterized by the injection conditions prior and during the injection.

## 4 Conclusions

With the analysis of more than 200 superheated flash boiling liquid nitrogen (LN<sub>2</sub>) sprays by the optical measurement techniques high-speed shadowgraphy and laser-based Phase-Doppler droplet diagnostics (PDA) we generated a comprehensive data base about flash boiling LN<sub>2</sub> sprays at high-altitude conditions which facilitates further numerical modelling. The closer examination of 22 of those LN<sub>2</sub> sprays revealed an illustrative evolution of lowly superheated sprays with a narrow and turbulent shape to highly superheated ones with big opening angles and fine droplets depending on the injection conditions. Small changes like halving the injection pressure, e.g., did primarily affect only lowly superheated sprays in terms of wider spray

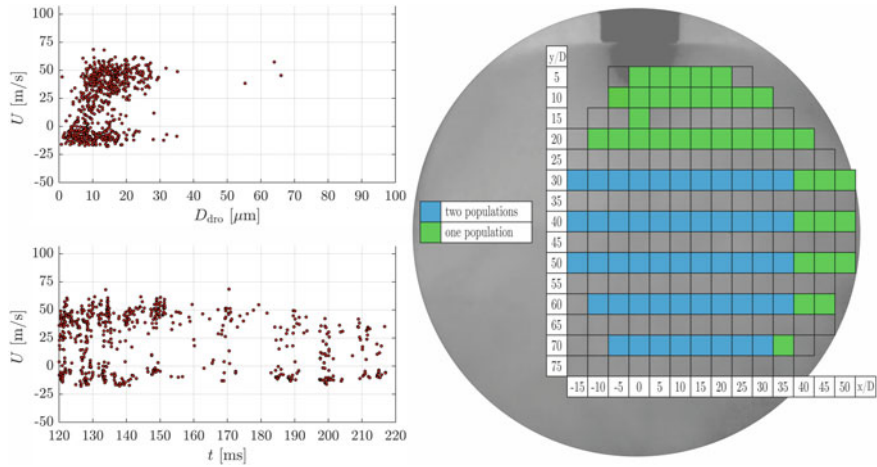


**Fig. 12** Two droplet populations at the spray position  $x/D = 0$  and  $y/D = 30$  with their measured vertical velocities  $U$  as functions of the time  $t$  and of the measured droplet diameter  $D_{\text{dro}}$  (left) [22]; measurement position matrix in wide flashing LN<sub>2</sub> sprays with local occurrence of Hi- and Lo-populations (right) [23]

cones due to enhanced nucleation within the injector compared to the ones with a higher injection pressure. With increasing degrees of superheat, these influences got negligible due to the growing dominance of flash boiling. We successfully applied correlations about break-up regimes derived for storable fluids on our test fluid LN<sub>2</sub>, extended the validity range of these correlations by about two orders of magnitude and introduced a new break-up regime called *wide flashing regime* for highly superheated jets. The droplet velocity and diameter measurements in wide flashing LN<sub>2</sub> sprays by PDA revealed maximum vertical and horizontal mean velocities in the highly energetic near-injector region. Here, the transformation of the liquid's internal energy into kinetic one takes place and the spray expands as a consequence of the evaporation processes. Due to the common known limitation of the PDA technique in the near-injector region the measured droplet diameters in this region are statistically not very reliable. However, the data rate increases drastically with growing axial distance to the injector and an almost monodisperse spray pattern develops with a homogeneous droplet distribution. Furthermore, at certain spray positions we observed the existence of two separate droplet populations which are distinguishable from each other mainly by the velocity magnitude, the direction of motion and also slightly by the diameters of their respective droplets. The separation is caused by recirculation zones due to the typical shock systems in flash boiling sprays and due to spray interaction with the structure of the vacuum chamber.

**Acknowledgements** The authors kindly acknowledge the financial support by the Deutsche Forschungsgemeinschaft (DFG) within the SFB-TRR 75, project number 84292822.

## References

1. Aleiferis PG, Serras-Pereira J, Augoye A, Davies TJ, Cracknell RF, Richardson D (2010) Effect of fuel temperature on in-nozzle cavitation and spray formation of liquid hydrocarbons and alcohols from a real-size optical injector for direct-injection spark-ignition engines. *Int J Heat Mass Trans* 53(21–22):4588–4606. <https://doi.org/10.1016/j.ijheatmasstransfer.2010.06.033>
2. Araneo L, Dondè R (2017) Flash boiling in a multihole G-DI injector—effects of the fuel distillation curve. *Fuel* 191:500–510. <https://doi.org/10.1016/j.fuel.2016.11.104>
3. Araneo L, Dondè R (2019) Atomization of a G-DI spray with air dissolved in gasoline and mono-component fuels. In: 29th ILASS-Europe conference, Paris, France. <https://ilass19.sciencesconf.org/251396>
4. Cleary V, Bowen P, Witlox H (2007) Flashing liquid jets and two-phase droplet dispersion: I. Experiments for derivation of droplet atomisation correlations. *J Hazard Mater* 142(3):786–796. <https://doi.org/10.1016/j.jhazmat.2006.06.125>
5. De Rosa M, Sender J, Zimmermann H, Oschwald M (2006) Cryogenic spray ignition at high altitude conditions. In: 42nd AIAA/ASME/SAE/ASEE JPC, Sacramento, CA. <https://doi.org/10.2514/6.2006-4539>
6. Eberhart JG, Schnyders HC (1973) Application of the mechanical stability condition to the prediction of the limit of superheat for normal alkanes. *Ether Water J Phys Chem* 77(23):2730–2736. <https://doi.org/10.1021/j100641a004>
7. Elias E, Chambré PL (1993) Flashing inception in water during rapid decompression. *J Heat Trans* 115(1):231–238. <https://doi.org/10.1115/1.2910654>
8. Gärtnner JW, Kronenburg A, Rees A, Sender J, Oschwald M, Lamanna G (2020) Numerical and experimental analysis of flashing cryogenic nitrogen. *Int J Multiph Flow* 130:1–13. <https://doi.org/10.1016/j.ijmultiphaseflow.2020.103360>
9. Gärtnner JW, Rees A, Kronenburg A, Sender J, Oschwald M, Loureiro D (2019) Large eddy simulation of flashing cryogenic liquid with a compressible volume of fluid solver. In: 29th ILASS-Europe, Paris, France. <https://ilass19.sciencesconf.org/246753>
10. Gemci T, Yakut K, Chigier N, Ho TC (2004) Experimental study of flash atomization of binary hydrocarbon liquids. *Int J Multiph Flow* 30(4):395–417. <https://doi.org/10.1016/j.ijmultiphaseflow.2003.12.003>
11. Kurschat T, Chaves H, Meier GEA (1992) Complete adiabatic evaporation of highly superheated liquid jets. *J Fluid Mech* 236:43–59. <https://doi.org/10.1017/S0022112092001332>
12. Lamanna G, Kamoun H, Weigand B, Manfletti C, Rees A, Sender J, Oschwald M, Steelant J (2015) Flashing behavior of rocket engine propellants. *At Spray* 25(10):837–856. <https://doi.org/10.1615/AtomizSpr.2015010398>
13. Lamanna G, Kamoun H, Weigand B, Steelant J (2014) Towards a unified treatment of fully flashing sprays. *Int J Multiph Flow* 58:168–184. <https://doi.org/10.1016/j.ijmultiphaseflow.2013.08.010>
14. Lecourt R, Barricau P, Steelant J (2009) Spray velocity and drop size measurements in flashing conditions. *At Sprays* 19(2):103–133. <https://doi.org/10.1615/AtomizSpr.v19.i2.10>
15. Levy M, Sher E (2010) Transition from heterogeneous to homogeneous nucleation in a simple structure flash-boiling atomizer. *At Spray* 20(10):905–907. <https://doi.org/10.1615/AtomizSpr.v20.i10.60>
16. Luo M, Haidn OJ (2016) Characterization of flashing phenomena with cryogenic fluid under vacuum conditions. *J Propul Power* 32(5):1253–1263. <https://doi.org/10.2514/1.B35963>
17. Manfletti C (2014) Laser ignition of an experimental 400 N cryogenic reaction and control thruster: pre-ignition conditions. *J Propul Power* 30(4):925–933. <https://doi.org/10.2514/1.B35115>
18. Meyer J (1911) Zur Kenntnis des negativen Drucks in Flüssigkeiten. *Abh Dtsch Bunsen-Ges Phys Chem* 3(1):1–53
19. Moshkovich Y, Levy Y, Sher E (2019) Theoretical criteria for homogeneous flash boiling atomization. *Chem Eng Sci* 206:471–475. <https://doi.org/10.1016/j.ces.2019.06.001>

20. Polanco G, Holdø AE, Munday G (2010) General review of flashing jet studies. *J Hazard Mater* 173:2–18. <https://doi.org/10.1016/j.jhazmat.2009.08.138>
21. Rees A (2020) Experimentelle Untersuchung der Flashverdampfung infolge der Einspritzung von kryogenem Stickstoff unter Höhenbedingungen. PhD thesis, RWTH Aachen University. <https://publications.rwth-aachen.de/record/807914>
22. Rees A, Araneo L, Salzmann H, Kurudzija E, Suslov D, Lamanna G, Sender J, Oschwald M (2019) Investigation of velocity and droplet size distributions of flash boiling LN<sub>2</sub>-Jets with phase doppler anemometry. In: 29th ILASS-Europe conference, Paris, France. <https://ilass19.sciencesconf.org/286174>
23. Rees A, Araneo L, Salzmann H, Lamanna G, Sender J, Oschwald M (2020) Droplet velocity and diameter distributions in flash boiling liquid nitrogen jets by means of phase doppler diagnostics. *Exp Fluids* 61(182). <https://doi.org/10.1007/s00348-020-03020-7>
24. Rees A, Oschwald M (2022) Cryogenic test bench for the experimental investigation of cryogenic injection in rocket combustors under high-altitude conditions. *IOP Conf Ser Mater Sci Eng* 1240:012103
25. Rees A, Salzmann H, Sender J, Oschwald M (2019) Investigation of flashing LN<sub>2</sub>-Jets in terms of spray morphology, droplet size and velocity distributions. In: 8th EUCASS conference, Madrid, Spain. <https://doi.org/10.13009/EUCASS2019-418>
26. Rees A, Salzmann H, Sender J, Oschwald M (2020) About the morphology of flash boiling liquid nitrogen sprays. *At Sprays* 30(10):713–740. <https://doi.org/10.1615/AtomizSpr.2020035265>
27. Rees A, Salzmann H, Sender J, Oschwald M (2021) The evolution of the liquid cores in flash boiling LN<sub>2</sub> sprays. In: 7th space propulsion 2020+1 conference, Estoril, Portugal (virtual)
28. Reitz RD (1990) A photographic study of flash-boiling atomization. *Aerosol Sci Technol* 12(3):561–569. <https://doi.org/10.1080/02786829008959370>
29. Senda J, Hojyo Y, Fujimoto H (1994) Modeling on atomization and vaporization process in flash boiling spray. *JSAE Rev* 15(4), 291–296. <https://www.sciencedirect.com/science/article/pii/0389430494902097>
30. Senda J, Wada Y, Kawano D, Fujimoto H (2008) Improvement of combustion and emissions in diesel engines by means of enhanced mixture formation based on flash boiling of mixed fuel. *Int J Engine Res* 9(1):15–27. <https://doi.org/10.1243/14680874JER02007>
31. Sher E, Bar-Kohany T, Rashkovian A (2008) Flash-boiling atomization. *Prog Energy Combust Sci* 34(4):417–439. <https://doi.org/10.1016/j.pecs.2007.05.001>
32. Sher E, Elata C (1977) Spray formation from pressure cans by flashing. *Ind Eng Chem Process Des Dev* 16(2):237–242. <https://doi.org/10.1021/i260062a014>
33. Simões-Moreira JR, Vieira MM, Angelo E (2002) Highly expanded flashing liquid jets. *J Thermophys Heat Trans* 16(3):415–424. <https://doi.org/10.2514/2.6695>
34. Simmons JA, Gift RD, Spurlock JM, Fletcher RF (1968) Reactions and expansion of hypergolic propellants in a vacuum. *AIAA J* 6(5):887–893. <https://doi.org/10.2514/3.4614>
35. Skripov VP (1974) Metastable liquids, 1st edn. Wiley, New York
36. Wismer KL (1921) The pressure-volume relation of super-heated liquids. *J Phys Chem* 26(4):301–315. <https://doi.org/10.1021/j150220a001>
37. Witlox H, Harper M, Bowen P, Cleary V (2007) Flashing liquid jets and two-phase droplet dispersion: II. Comparison and validation of droplet size and rainout formulations. *J Hazard Mater* 142(3):797–809. <https://doi.org/10.1016/j.jhazmat.2006.06.126>
38. Yildiz D, Beeck JPAJV, Riethmüller ML (2004) Feasibility exploration of laser-based techniques for characterization of a flashing jet. *Part Part Syst Charact* 21(5):390–402. <https://doi.org/10.1002/ppsc.200400834>
39. Yildiz D, Rambaud P, Van Beeck J, Buchlin JM (2002) A study on the dynamics of a flashing jet. *Final Contract Res Rep EAR0030, VKI*
40. Zeng Y, Lee CFF (2001) An atomization model for flash boiling sprays. *Combust Sci Tech* 169(1):45–67. <https://doi.org/10.1080/00102200108907839>

**Open Access** This chapter is licensed under the terms of the Creative Commons Attribution 4.0 International License (<http://creativecommons.org/licenses/by/4.0/>), which permits use, sharing, adaptation, distribution and reproduction in any medium or format, as long as you give appropriate credit to the original author(s) and the source, provide a link to the Creative Commons license and indicate if changes were made.

The images or other third party material in this chapter are included in the chapter's Creative Commons license, unless indicated otherwise in a credit line to the material. If material is not included in the chapter's Creative Commons license and your intended use is not permitted by statutory regulation or exceeds the permitted use, you will need to obtain permission directly from the copyright holder.



# Modelling and Simulation of Flash Evaporation of Cryogenic Liquids



Jan Wilhelm Gärtner, Daniel D. Loureiro, and Andreas Kronenburg

**Abstract** Rocket engine manufacturers attempt to replace toxic, hypergolic fuels by less toxic substances such as cryogenic hydrogen and oxygen. Such components will be superheated when injected into the combustion chamber prior to ignition. The liquids will flash evaporate and subsequent mixing will be crucial for a successful ignition of the engine. We now conduct a series of DNS and RANS-type simulations to better understand this mixing process including microscopic processes such as bubble growth, bubble-bubble interactions, spray breakup dynamics and the resulting droplet size distribution. Full scale RANS simulations provide further insight into effects associated with flow dynamic such as shock formation behind the injector outlet. Capturing these gas dynamic effects is important, as they affect the spray morphology and droplet movements.

## 1 Introduction

Recent developments of orbital manoeuvring systems and upper rocket stages, such as the cryogenic Ariane 6 Vinci engine, aim to replace the conventional propellant hydrazine with environmentally more friendly and operationally safer substitutes. Such a substitute can be a conventional fuel such as hydrogen, methane or kerosene. The replacement of hypergolic with conventional fuels requires a better understanding of the process of injection and ignition under the extreme conditions that prevail in space. Due to the near vacuum conditions in space, the typically cryogenic fuel and oxidizer are injected into a superheated state, which leads to a rapid and strong evaporation. This process of nearly instant evaporation of the liquid is called flash boiling or flash evaporation. Understanding this process and subsequent mixing of the two reactants is paramount to develop a stable and reliable ignition. Therefore, a holistic approach is needed to numerically and experimentally investigate this process since bubble nucleation at a nanometer scale, growth, breakup, coalescence at a

---

J. W. Gärtner · D. D. Loureiro · A. Kronenburg (✉)

Institute for Combustion Technology (ITV), University of Stuttgart, Stuttgart, Germany  
e-mail: [kronenburg@itv.uni-stuttgart.de](mailto:kronenburg@itv.uni-stuttgart.de)

macroscale and lastly the evaporation of droplets at a micrometer scale impose a wide range of scales that cannot easily be covered by conventional methods [35, 40]. Here, we use in a first attempt the unsteady Reynolds averaged Navier Stokes equations (RANS) to compute the complete injection process and direct numerical simulations (DNS) to analyse the microscale processes, bubble growth, interaction, and spray breakup. For large eddy simulations (LES) or RANS two general approaches exist to model two phase flows. One possibility is to treat the continuous phase in an Eulerian framework and the dispersed phase as Lagrangian particles. However, this poses the problem that prior to spray breakup the continuous phase represents the liquid and the vapour bubbles are treated as Lagrangian particles, while after spray breakup the attribution of the two phases to the Eulerian and Lagrangian frameworks needs to be reversed. Alternatively, both phases are treated in an Eulerian framework. Then, the full set of mass, momentum, and energy equations are solved for each phase individually and coupled with each other through exchange terms. The two phases are distinguished by a mass or volume fraction with a transport equation that has to be solved additionally to the other conservation equations [4]. Assuming that the two phases are closely coupled and hence move at the same velocity allows to reduce the set of equations to one common momentum and mass transport equation, the so-called one-fluid approach. This simplification of the equation system requires the assumption of zero slip velocity between the two phases and that both phases experience a common pressure [7]. The one-fluid approach has already been successfully applied to simulate flashing sprays by several authors [19, 26, 30, 33, 34] and is therefore used for all large scale simulations of this work.

In RANS or LES, the nucleation, bubble growth, and formed droplets have to be modelled at the sub-grid scale. One commonly used model to describe flash evaporation on the sub-grid scale is the homogeneous relaxation model (HRM). This model considers the thermal non-equilibrium state of the flashing liquid by introducing a relaxation time and relating the evaporation rate to the deviation of the current mass fraction from an equilibrium value [3]. Finding a suitable description for the relaxation time is a challenging task, yet the model of Downar-Zapolski et al. [12], which is an empirical fit to flashing water experiments, has shown a general applicability to several fluids and injection conditions [18, 26, 29, 30]. Nevertheless, the model coefficients may require case specific adaptations which cannot be directly determined a priori and thus, model verification is required for each case [20, 33]. Approaches that attempt to model the effects at the phase interface, such as the Hertz-Knudsen model or momentum conservation like the Rayleigh-Plesset equation are also used to describe the bubble growth for flashing sprays [9]. Yet, these models only consider a singular bubble in an infinite liquid medium, neglecting the strong interaction of bubbles in flashing flows [10]. Further, these models require the knowledge of either the bubble number or the current mean diameter, which is typically unknown for large scale LES or RANS simulations. Due to these reasons there is a need for further investigation of the bubble growth and interaction of flashing sprays to improve the current models. One possible strategy to investigate the flashing process in detail, and to create a database is the use of DNS simulations.

Further modelling challenges arise due to shock structures that accompany the injection of highly superheated liquid into the combustion chamber. Shocks in flashing flows have been first associated with retrograde fluids [21, 39] and recently have also been observed in non-retrograde fluids, such as ethanol, acetone [23] or propane [31]. In the case of multi-hole injectors these shock structures can lead to severe changes of the spray morphology e.g. spray collapse [15, 19, 31] and therefore it is important to capture this phenomenon correctly. This highlights the complexity of simulating flashing processes which require knowledge of the thermodynamic processes on the smallest scales such as nucleation and bubble growth as well as capturing macroscopic effects as shocks which affect the spray shape.

The chapter is organized as follows: Sect. 2 introduces fully compressible DNS simulations that are used to deduce surface specific evaporation rates and to identify important simplifications with respect to domain size that bubble-bubble interactions induce. Section 3 provides DNS data on droplet size distributions after jet breakup and suggests a simple correlation for the interface generation during the flash-evaporation process. RANS simulations of the entire flash evaporation process including the injector and combustion chamber are then presented in Sect. 4. For all simulations, the computational setup mimicks conditions of the flash evaporation experiments conducted at the German Aerospace Center (DLR) Lampoldshausen [32]. There, liquid nitrogen with temperatures between 80 and 120 K is injected into a low pressure chamber with ambient pressures between 1000 and 1E+5.

## 2 DNS Simulation of Vapour Bubble Growth and Interaction

To investigate the behaviour of bubble growth and bubble-bubble interaction in detail, the vapour bubble growth is simulated with a DNS approach. A fully compressible two phase DNS code with a discontinuous Galerkin spectral element method is used [11] together with an approximative Riemann solver [14]. Further detail about the numerical framework can be found in Dietzel et al. [11] and Fechter et al. [14].

Accurate DNS simulations resolving all relevant scales, however, is extremely challenging and two important aspects are highlighted in the following: First, the DNS code has to account for compressibility effects to accurately capture the early stages of flash evaporation. As the vapour density and evaporation rate are directly linked to the local pressure it is important to include local pressure fluctuations induced by neighbouring evaporating bubbles. Secondly, direct simulation of the phase change term is unfeasible as it requires resolution on a molecular scale and thus the phase change terms appear in an unclosed form and require modelling. One possible model to describe the phase change at the interface is the Hertz-Knudsen model,

$$\dot{m}'' = \sqrt{\frac{1}{2\pi R}} \left( \lambda_e \frac{p_s(T)}{\sqrt{T_L}} - \lambda_c \frac{p_G}{\sqrt{T_G}} \right), \quad (1)$$

with the two coefficients  $\lambda_e$  and  $\lambda_c$  that are case specific. Therefore, these coefficients have to be determined for the case of flashing cryogenic liquid. This is done by simulating the growth of a single vapour bubble [11] and then applying the results to bubble arrays [10].

## 2.1 Single Vapour Bubble Growth

To calibrate the Hertz-Knudsen model (HKM) such that it can be used in a full 3D DNS simulation with multiple bubbles, the growth of a single bubble is compared first with the solution of the coupled Rayleigh-Plesset and energy equations [25]. A direct calibration of the two parameters  $\lambda_c$  and  $\lambda_e$  in the HKM is difficult and it is therefore conventional to set  $\lambda_c = 0.99\lambda_e$ . The slight reduction of the condensation coefficient is introduced to stabilize the simulation at the early stages of bubble growth while the effect on the entire time interval is negligible. Further, as the early bubble growth stage has only a negligible contribution to the overall volume change, and as the bubble growth rate can vary over several magnitudes the parameter  $R_0^*$  is introduced to speed up the simulations. This parameter relates the starting radius of the bubble,  $R_0$ , in the 3D simulation to the critical radius  $R_{\text{crit}}$  with,

$$R_0^* = \frac{R_0}{R_{\text{crit}}}. \quad (2)$$

The critical radius equals the smallest radius for a stable nuclei and can be calculated from [5],

$$R_{\text{crit}} = \frac{2\sigma}{p_{\text{sat}}(T_{\infty}) - p_L}. \quad (3)$$

This gives the three independent simulation parameters: the pressure  $p$ , liquid temperature  $T_L$  and starting radius  $R_0^*$ . It is more conventional to characterize flashing flows by a superheat ratio  $R_p = p_{\text{sat}}/p$  (substituting  $p$ ) and  $\lambda_e$  is then calibrated as a function of superheat ratio, liquid temperature and starting radius.

The results show that the HKM can be calibrated to match the Rayleigh-Plesset solution within 10% of the integrated mass flux. The difference in mass flux, however, is also due to minor density changes between the two models. Even though the Hertz-Knudsen model can be calibrated for each computed single bubble case, the evaporation coefficient is case dependent and a simple functional expression with the input parameters,  $R_p$ ,  $T$ , and  $R_0^*$  seems elusive [11]. This is due to the high non-linearity of the growth rate over the bubbles growth history and the changing driving forces for bubble growth. Early growth is dominated by inertia effects while later stages are dominated by heat diffusion. However, as indicated above, the later stages of the growth process determine the volumetric expansion (and thus spray breakup) and a representative  $\lambda_e$  can be approximated by

$$\lambda_e = \lambda_{e,RPE} 1.27 (1 - \exp(-0.0086 R_{end}^*))^{0.61} \quad \text{with} \quad \lambda_{e,RPE} = \frac{\dot{m}''(R_{end})\sqrt{2\pi R}}{\frac{P_{sat}}{\sqrt{T_L}} - 0.99 \frac{P_v}{\sqrt{T_v}}} \quad (4)$$

and  $R_{end}^* = 10R_0^*$  [11]. Note that  $R_{end}^*$  denotes the bubble radius when the bubbles start to merge and is related to the nucleation rates. This will be further discussed in Sect. 3.

## 2.2 Bubble Interaction

In the previous section we have introduced a suitable calibration for the Hertz-Knudsen model that can now be applied to full 3D DNS simulations of multiple growing bubbles within a superheated jet. The initial conditions of the setup mirror the relevant conditions of the flash boiling experiments conducted at the German Aerospace Center (DLR) in Lampoldshausen using cryogenic liquids injected into chambers at near vacuum conditions. Resolving the injector would require at least 2000 cells for the radius alone, thus rendering a full scale simulation unfeasible. Consequently, the bubble growth and interaction is studied with a simplified setup that considers only the tip of the jet. A comparison of 1D bubble columns, 2D liquid jet slices, and 3D simulation of the jet tip showed that the simplified 2D simulation captures the bubble dynamics, interactions and jet expansion sufficiently accurate [10]. For all simulations the bubble spacing is set to 10 times the starting radius  $R_0^*$  as the last decade of bubble growth determines 99.9% of the volumetric expansion. Thus,  $R_0^*$  determines the bubble size when bubbles coalesce and the jet breaks up and it is directly related to the bubble density (or nucleation rate). We note here that no expression exists that would allow for an accurate estimate of the nucleation rate as known expressions can differ by more than 5 orders of magnitude. It is thus justified to impose a nucleation rate (or  $R_0^*$  or  $R_{end}^*$ ) in the DNS and use it as the only free parameter in RANS or LES to match full scale simulations with experiments.

For illustration, the simulation results are shown in Fig. 1 for a 3D reference case utilizing two symmetry planes and one dimension of freedom with the initial temperature of 120 K, superheat  $R_p = 5$  and radius  $R_0^* = 50$ . The liquid is located in the lower two-thirds of the column, the jet's interface is indicated by the pale blue rectangle and symmetry boundary conditions are used at the bottom of the domain. It is immediately apparent that the outer most bubbles grow magnitudes faster than the inner bubbles. This is due to pressure variations in the bubble column. The bubble expansion induces pressure waves yielding much higher pressures when moving away from the jet's interface and thus reducing evaporation rates and bubble growth for the inner bubbles. This finding is quantified in Fig. 2 with a series of 3D simulation with up to 125 bubbles. The figure shows normalized bubble growth as function of their dimensionless distance to the jet surface  $x/D_{bub}$ . The normalization factor is the bubble growth of a single bubble. We note that even the expansion of the first bubble,

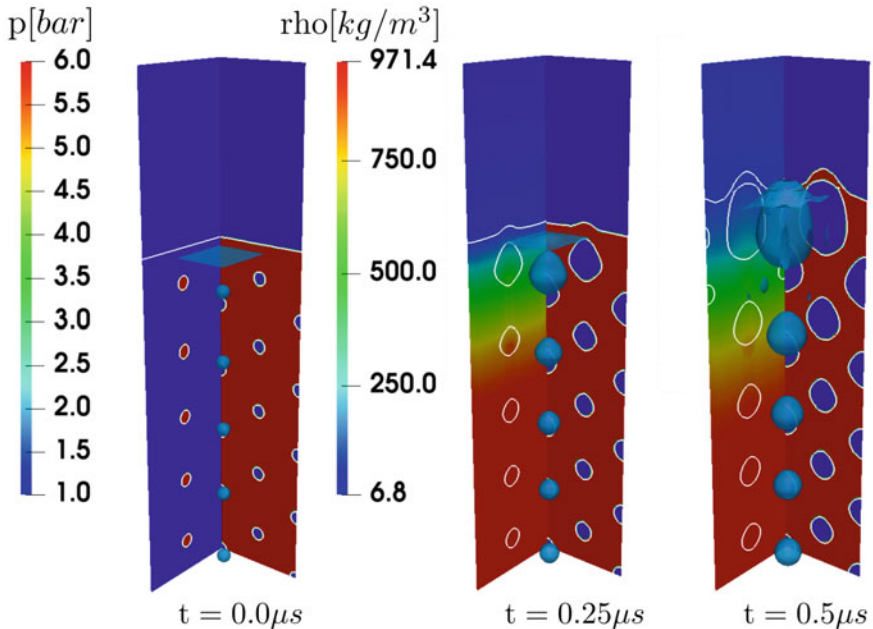
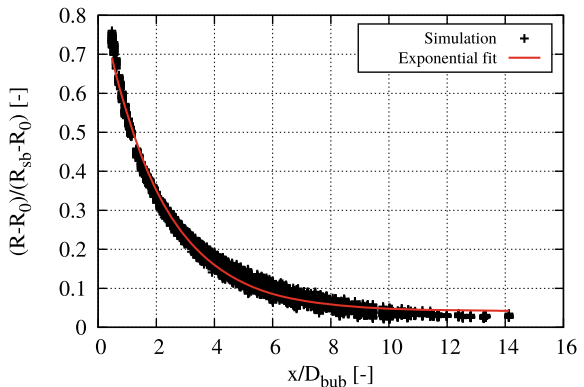


**Fig. 1** Contour plots of the bubble column test case for three different time steps with five bubble rows along the x-direction. The left and right planes show the time averaged pressure and the density fields, respectively. The blue coloured iso-surfaces indicate the interfaces between bubbles and superheated liquid. Adapted from [10] with permission from Elsevier

**Fig. 2** Bubble expansion in 3D compared to the single bubble growth ( $R_{sb}$ ) in respect to their normalized distance to the jet surface. Adapted from [10] with permission from Elsevier



as seen from the jet surface, is reduced by more than 20% and that radial growth of a bubble in the “fifth row” is reduced by 90 %. The importance of this finding cannot be sufficiently stressed: bubbles that are further away than  $x/D_{bub} \approx 5 - 10$  from the jet surface at time of jet breakup have hardly grown and do not need to be considered for the jet breakup dynamics [10].

### 3 Spray Break-up

The simulations in Sect. 2 demonstrate that analysis of small bubble configurations is sufficient to analyse breakup and subsequent droplet formation. The compressible DNS cannot, however, capture the final stages of breakup and droplet formation and additional DNS are needed. These final stages are likely to be within the inertia driven stage [28] and are dominated by the dynamics at the time of the first bubble coalescence when liquid structures burst and the first droplets form. It is therefore justified to calibrate the fluid properties as well as the bubble growth rate towards this instance in time and use an incompressible, multiphase solver such as Free-Surface 3D - FS3D [13] as only the efficiency of the incompressible treatment allows for the entire breakup dynamics and sufficient resolution of satellite droplets and droplet distributions. It follows that—similar to the DNS presented in Sect. 2—the ambient pressure  $p$ , liquid temperature  $T$ , and final bubble merging radius  $R_{end}$  (or nucleation rate) determine the numerical setup. Details on the setup and also limitations of the setup are discussed in Loureiro et al. [28].

#### 3.1 Test Case Setup

The test cases examine a liquid blob that either represents an outer layer of the liquid jet or has detached from the jet at the injector exit where a sudden pressure drop occurs. In that location high superheat ratios are reached which lead to high nucleation rates and bubble growth. A first study [28] where a regular cubic lattice distribution of the vapour bubbles was investigated, identified the three distinct breakup regimes that were labelled “retracting liquid” ( $We \leq 2$ ), “ligament stretching” ( $2 < We \leq 20$ ), and “thin lamella” ( $We \geq 20$ ) regimes. These regimes are categorized by the characteristic Weber and Ohnesorge numbers,

$$We = \frac{2R_{end}\rho_L \dot{R}^2}{\sigma} \quad \text{and} \quad Oh = \frac{\mu}{\sqrt{2R_{end}\rho_L \sigma}}.$$

Here,  $\sigma$  is the surface tension and  $\dot{R}$  the bubble growth rate determined by the Rayleigh-Plesset solution as a function of  $\dot{R} = f(p, T, R_{end})$ .

The regular cubic lattice arrays provide a unique characterization of droplet distance, they lead however, to a typically bi-disperse droplet size distribution with the larger droplet size being imposed by the interstitial volume and the smaller one by ligament shedding and local surface tension. Here, we therefore distribute the bubbles randomly to prevent any systematic bias for the droplet size. An example of the spray breakup process in the ligament stretching regime with 512 initial bubbles is shown in Fig. 3.

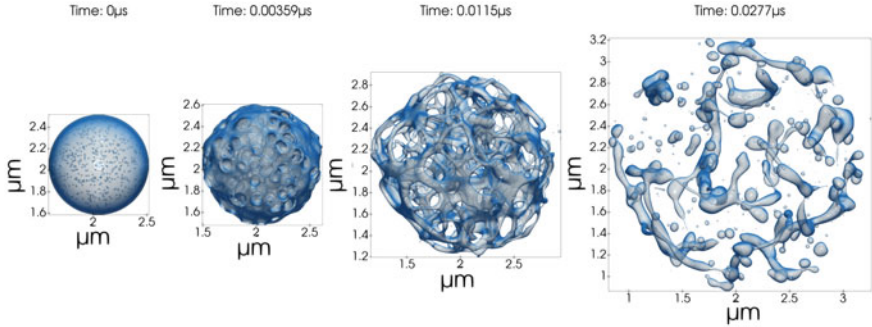


**Fig. 3** Time sequence of the spray breakup process and droplet generation. Break-up in the ligament stretching regime with conditions  $T_L = 120\text{K}$ ,  $R_f^* = 5$ ,  $\text{We} = 3.62$ ,  $\text{Oh} = 0.104$

### 3.2 Droplet Size Distribution

The process of bubble coalescence, pinching, ligament stretching and retraction to form satellite droplets is qualitatively similar to the process observed for the cubic lattice array [28] and thus confirms the regime classification. A typical droplet distribution is shown in Fig. 4. Across the parameter range investigated here, we note that the mean diameter is still close to the value that would be imposed by the interstitial volume but subsequent pinching, stretching and retraction leads to a more realistic, much wider distribution that can be approximated by a Gaussian. Note that the area weighted (Sauter) diameters are shown. This reduces the effect of the very small droplets that are generated when stretched ligaments pinch. This droplet size will be determined by the cell size and is likely to be a numerical artefact. However, their mass is negligible and they will contribute very little to any subsequent combustion process. The figure further includes an analytical approximation for the droplet diameter,  $D_{\text{ref}}$ , that is based on the relation of the kinetic energy in the liquid to the droplets volumetric surface energy. It is given by

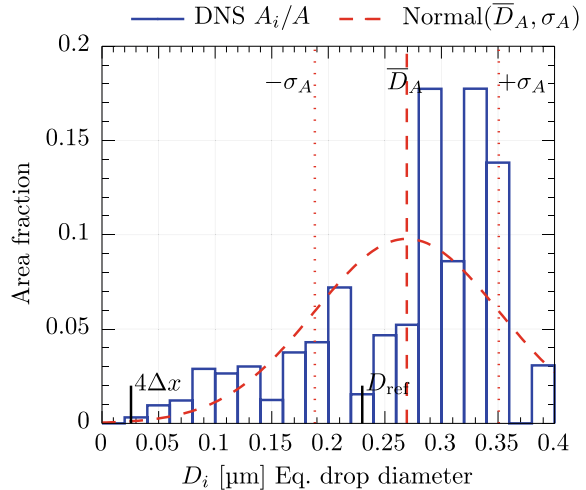
$$D_{\text{ref}} = \frac{8\sigma}{\rho_L R^2} = \frac{16}{\text{We}} R_{\text{end}}. \quad (5)$$

A comparison with the computed Sauter mean diameter allows to derive an exponential fit based on a linear least-square regression of  $\log(\overline{D}_A/D_{\text{ref}})$ ,

$$\frac{\overline{D}_A}{D_{\text{ref}}} \approx 0.294 \sqrt{\text{We}}. \quad (6)$$

This expression provides an estimate of the droplet size which is only based on the geometric setup and the fluid properties.

**Fig. 4** ( $T_L = 120K$ ,  $R_f^* = 16$ ,  $We = 13.38$ ,  $Oh = 0.05$ ): Area weighted droplet size distribution. The limit of the mesh resolution of 4 cells for a droplet is marked by the line  $4\Delta x$



Further analysis of the DNS (not shown here) provides an evolution for the surface area of the interface between liquid and vapour phase. Loureiro et al. [27] observed that (i) surface density is largely determined by bubble density (i.e. nucleation rate) and Weber number and (ii) stays relatively constant after the majority of bubbles have started to coalesce as surface creation by ligament pinching and surface destruction by ligament contraction seem to balance. A functional dependence for the specific surface area as function of time and We could be derived.

## 4 RANS Simulation of Flashing Sprays

The simulation of the entire injection process of flashing cryogenic liquids with resolved interfaces is still unfeasible due to the wide range of scales involved. Therefore, RANS or LES are a suitable alternative to get engineering relevant and yet accurate information, but bubble growth and bubble/droplet dynamics occur at sub-grid scale and need to be modelled. Models can be based on the findings highlighted in Sects. 2 and 3 or on standard closures that use empirical fitting constants. As outlined in the introduction, the present simulations of the complete injection process following the fluid from a high-pressure reservoir, through the injector, to the combustion chamber are based on an Euler-Euler approach. To simulate the cryogenic flash boiling a new solver has been developed in OpenFOAM [17, 36].

## 4.1 Governing Equations

The governing equations for volume fraction, momentum and energy transport are solved. In contrast to pure one-fluid solvers the energy equation is solved for each phase separately, hence allowing a temperature difference between the two phases at a single location. The choice to model the energy equation for both phases separately is motivated by the assumption, that the vapour is generated at the saturation conditions of the local pressure, thus the temperature of the liquid is much higher than that of the vapour. As the evaporation rate model depends on the liquid temperature alone, representation of the correct temperature difference is important [17]. Further, real gas effects that appear in the modelling of the heat flux are not accounted for as the very low pressure of the vapour justifies ideal gas assumptions. All other fluid properties, such as saturation conditions, liquid density or viscosity are determined using the thermodynamic library CoolProp [2]. To reduce the computational time the thermodynamic properties are calculated in advance and tabulated, such that required properties can be looked up during the run time of the simulation. More detailed information about the derivation of the governing equations can be found in Gärtner et al. [17].

### 4.1.1 Compressibility Modelling

Modelling the compressibility for the simulation of flashing flows is important, as higher superheated sprays exhibit behaviours similar to under-expanded gaseous jets with the same shock patterns [22, 31]. Typically, supersonic jets are simulated by solving for the density field and obtaining the pressure with an appropriate equation of state. Yet, this kind of solvers is not well suited for all Mach number conditions, as would be present for the simulation of flashing sprays. Therefore, a pressure based approach is chosen [8]. The pressure equation, as combination of momentum and mass conservation, can then be written as

$$\frac{\partial \psi p}{\partial t} + \nabla \cdot \left( \psi p \frac{H(U)}{a_p} \right) - \nabla \cdot \left( \frac{\rho}{a_p} \nabla p \right) = 0, \quad (7)$$

where  $\psi$  is the compressibility of the fluid,  $a_p$  are the coefficients of the velocity matrix and  $H(U)$  represents the discretized momentum equation except for the pressure gradient. For supercritical flows this is a suitable way as vapour and liquid densities can be expressed with  $\rho = \psi p$  [37], but it is no longer suitable for cryogenic liquids. Further, the solution of this equation gives a mass flux whereas the transport of the volume fraction requires a volume flux. Therefore, with the goal of preserving the volume change in flashing flows which is responsible for the large spray angles, the pressure equation of the developed solver is derived by first extracting the density from the convective term of the continuity equation giving,

$$\frac{D\rho}{Dt} + \rho \nabla \cdot (\mathbf{u}) = 0, \quad (8)$$

$$\frac{D\rho}{Dt} + \rho \nabla \cdot \left( \frac{H(U)}{a_p} \right) - \rho \nabla \cdot \left( \frac{\nabla p}{a_p} \right) = 0. \quad (9)$$

The material derivative of density can be replaced by the total derivative of density as a function of mass fraction,  $\chi$ , pressure  $p$ , and enthalpy  $h$ ,

$$\frac{D\rho}{Dt} = \underbrace{\left( \frac{\partial \rho}{\partial \chi} \right)_{p,h} \frac{D\chi}{Dt}}_{\text{evaporation}} + \underbrace{\left( \frac{\partial \rho}{\partial p} \right)_{\chi,h} \frac{Dp}{Dt}}_{\text{compressibility}} + \underbrace{\left( \frac{\partial \rho}{\partial h} \right)_{\chi,p} \frac{Dh}{Dt}}_{\text{heat expansion}}. \quad (10)$$

The compressibility of the vapour-liquid mixture is much higher than that given by the pure phase values and can be expressed by an inversely density weighted average [4]. In analogy, the change of density with respect to enthalpy can be described and finally combining the changes due to pressure and enthalpy gives

$$\frac{D\rho}{Dt} = \left( \frac{\partial \rho}{\partial \chi} \right)_{p,h} \frac{D\chi}{Dt} + \rho \left( \frac{\alpha_L}{\rho_L} \frac{D\rho_L}{Dt} + \frac{\alpha_G}{\alpha_G} \frac{D\psi_G p}{Dt} \right). \quad (11)$$

Here,  $\alpha_L$  denotes the liquid volume fraction,  $\alpha_L = V_L/V$ . Note that the density of the liquid is not replaced to avoid any numerical instabilities caused by the very low compressibility of the liquid. This leaves the first term of Eq. (11) to be modelled.

The turbulent contributions arising from the Reynolds averaging of the governing equations are modelled with a  $k-\omega$  SST model for the momentum transport and with the Reynolds analogy for the turbulent diffusion of the scalar and energy transport equations. Further details can be found in Gärtner et al. [17].

#### 4.1.2 Phase Change Models

Several models to predict the phase change in flashing flows exist. We first introduce the homogeneous relaxation model (HRM) as the standard model that is used to compute a reference case and to analyse the general structure of the flashing spray. The HRM model relates the rate of phase change to the deviation of the mass fraction from the local equilibrium value,

$$\frac{D\chi}{Dt} = -\chi \frac{h_L(p, T) - h_{SL}(p)}{h_{SG}(p) - h_{SL}(p)} \frac{1}{\Theta} = \frac{\dot{m}_L}{\rho}, \quad (12)$$

with  $h$  denoting the enthalpies of liquid, the saturation state and the latent heat (depending on its subscript). The model was originally proposed by Bilicki and Kestin [3] and a formulation for the relaxation time,  $\Theta$ , was found by Downar-

Zapolski et al. [12]. In their work the authors derived a high and low pressure fit of the relaxation time based on flashing water experiments,

$$\text{low pressure fit: } \Theta = \Theta_0 \epsilon^\beta \left( \frac{p_{\text{sat}}(T_L) - p}{p_{\text{sat}}} \right)^\lambda, \quad (13)$$

$$\text{high pressure fit: } \Theta = \Theta_0 \epsilon^\beta \left( \frac{p_{\text{sat}}(T_L) - p}{p_c - p_{\text{sat}}} \right)^\lambda. \quad (14)$$

Here,  $\epsilon$  is the void fraction,  $p_{\text{sat}}(T_L)$  the saturation pressure based on the liquid temperature,  $p_c$  the pressure at the critical point and  $\Theta_0$ ,  $\beta$ , and  $\lambda$  are empirical coefficients. Despite being fitted to flashing water experiments, the description of the relaxation time derived by Downar-Zapolski et al. [12] have shown a wide range of applicability for several technical applications, fluids, and thermodynamic conditions. Because of these reasons, the HRM model is applied for all LES/RANS simulations to model the evaporation rate.

An alternative model could be derived from the DNS in Sects. 2 and 3. The calibrated Hertz-Knudsen model provides an expression for the surface specific evaporation rate of the bubble. The phase interface is, however, not resolved in RANS or LES and requires modelling itself. Transport equations for the volume specific interface surface exist, they are commonly referred to as Euler-Lagrange spray atomisation models (ELSA) [1, 24] and are available in OpenFOAM. Existing closure for the transport equation of the sub-grid surface area employ source terms for interface generation that account for turbulent liquid jet breakup due to viscous effects at the interface, but they do not include surface generation through bubble growth and coalescence that govern the dynamics of flash atomization processes. Here, the correlations developed in Sect. 3 could be used. In addition, droplet size distribution would need to be specified after local disintegration of the jet and could also be deduced from the DNS introduced in the same section. However, a reference solution is sought first and results from the HRM model will be shown in Sect. 4.3.

## 4.2 Numerical Methods

The system of equations is solved by a combined semi-implicit method for pressure linked equations (SIMPLE) and a pressure implicit with splitting operator (PISO) loop called PIMPLE. The discretization schemes are run time selectable. Typically, total variation diminishing (TVD) schemes such as van Leer limiter or OpenFOAM's limited linear are chosen for problems involving two phase flows. However, despite having formal second order accuracy they cannot achieve this accuracy in real applications [6, 38]. Further, the implemented schemes in OpenFOAM do not guarantee proper resolution of the shock front for all cases [17]. To solve problems with discontinuities while maintaining a high order of accuracy, weighted essential non-oscillating (WENO) schemes are a suitable choice. To include this scheme in OpenFOAM a

computationally improved version was developed in Gartner et al. [16] and is used here for the momentum, enthalpy, and kinetic energy transport. Lastly, the volume fraction transport is solved with a multi-dimensional limited with explicit solution (MULES) procedure, which is an effective method to guarantee the boundedness of the volume fraction. As the current work focuses on quasi stationary states, a first order in time Euler integration is applied.

### 4.3 Shock Structure

The solver's capability to resolve low and high Mach number regimes in flashing flows has been validated by comparison with experiments of flashing acetone sprays where the shock structures were visualized and where unambiguous measurements of the shocks' positions exist [23]. Gartner et al. [17] demonstrated that the computed lateral expansion of the shocks is accurate and that the solver is capable to predict the shock size and position well.

After validating the solvers capability to capture supersonic conditions accurately, the two cryogenic nitrogen sprays presented in Table 1 are simulated and compared to shadowgraph images provided by DLR Lampoldshausen [17]. The simulation domain consists of a two dimensional wedge of the injector geometry and the attached vacuum chamber with a minimum cell size of 10  $\mu\text{m}$ .

A comparison of the velocity magnitude and the density gradient between simulation and the shadowgraph images is presented in Fig. 5. Here, the characteristic bow shock of an under-expanded jet is visible. In addition, a region with low velocity is observed about 20 to 30 jet diameters downstream of the injector. This region of low velocity is caused by the relative high velocity of the slip stream and the low velocity in the core of the spray, which causes a shear layer that leads to a recirculation zone in that region. Even though no velocity data is available from the experiments, the shadowgraph images indicate the presence of such a recirculation zone by nearly motionless or slightly upstream floating dark structures. This is visualized in more detail for case LN2-2 in Fig. 6, where the velocity direction is marked by vectors and the recirculation zone of the experiment is marked by a yellow square. Within this recirculation zone droplets can accumulate and cause the dark structures visible in the shadowgraph images. In conclusion, the recirculation zone visible in the numerical results gives an explanation for the observed structures in the shadowgraph images and reinforces the importance to include the compressible effects.

Additional to the shadowgraph images, the mass flow rate is provided and can be used to validate the evaporation rate inside the injector. A comparison of the mass flow rate of the simulation and experiment show that the mass flow rate predicted by the simulation is within the experimental uncertainty, see Table 1. Further, the results confirm the simulation data that the liquid nitrogen already evaporates within the injector, thus causing the pressure to increase and reducing the mass flow compared to a non-flashing flow. Hence, including the injector and the upstream conditions is important to capture the spray conditions correctly.

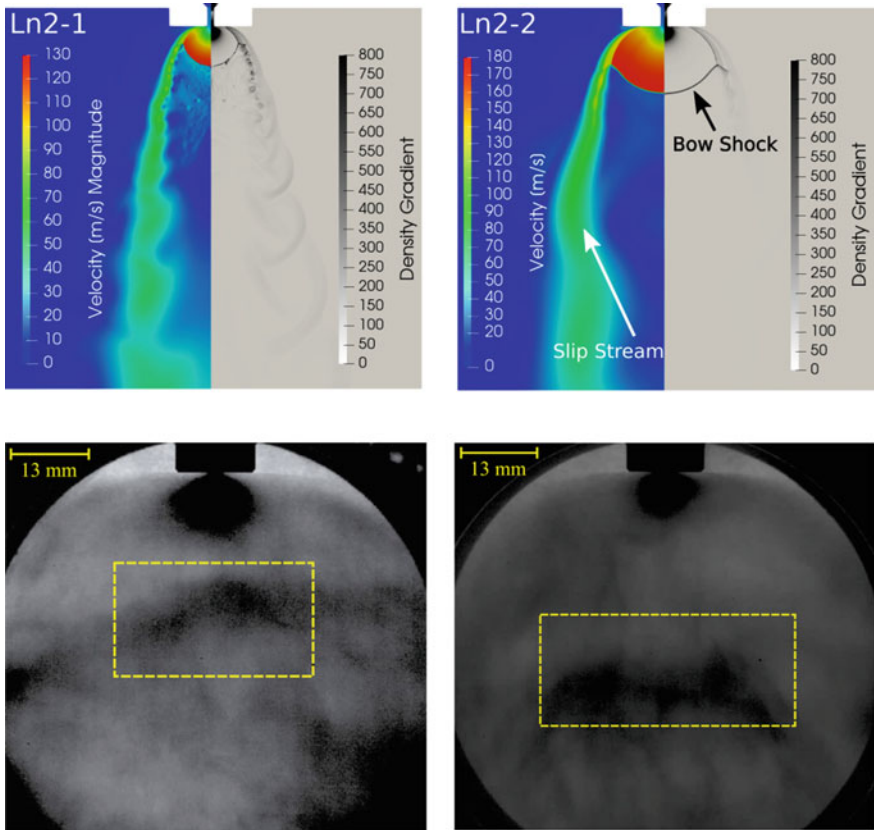


**Fig. 5** Velocity magnitude and magnitude of the vapour density gradient for the flashing liquid nitrogen cases compared to the shadowgraph images. The location of the nearly motionless structures are marked with a yellow square. Adapted from Gärtner et al. [17] with permission from Elsevier

## 5 Conclusions

Flash evaporation of cryogenic liquids is investigated numerically using DNS and RANS approaches. DNS simulations of the vapour bubble growth, interaction and succeeding spray breakup were performed to gain a detailed insight into the bubble and droplet dynamics. In addition, RANS simulations featuring the full injection process of the flow through the injector and in the combustion chamber have been realized. Details on the numerics have been published in previous work [10, 11, 15, 17, 27, 28].

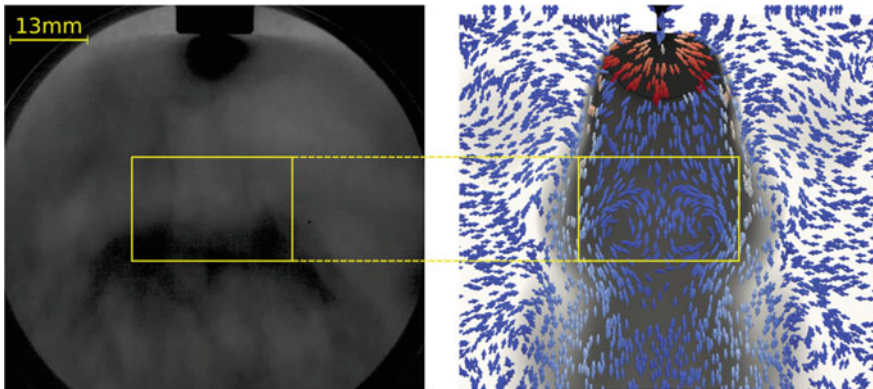


**Fig. 6** Shadowgraph image of case LN2-2 compared to the mass fraction field and the velocity vectors coloured in respect to their velocity magnitude. The recirculation zone is marked with a yellow box in the shadowgraph and simulation image. Adapted from Gärtner et al. [17] with permission from Elsevier

**Table 1** Boundary conditions of flashing cryogenic nitrogen sprays

Case	$T_{\text{inj}}$ [K]	$p_{\text{inj}}$ [bar]	$p_{ch}$ [mbar]	$R_p$ [-]	$\dot{m}_{\text{Exp}}$ [g/s]	$\dot{m}_{\text{Sim}}$ [g/s]
LN2-1	89.7	4.4	73	48.1	10.6 ( $\pm 1.8$ )	10.6
LN2-2	95.6	6.2	30	188.6	12.3 ( $\pm 1.8$ )	11.1

The key results are:

- The Hertz-Knudsen model can predict the volume change of a growing bubble in 3D simulations.
- Only bubbles close to the jet surface grow significantly as the bubble expansion causes pressure increases and thus reduced superheat and growth rates in the interior of the jet. Bubbles at distances that are more than 10 bubble diameters away from the jet interface can be neglected as they do not contribute to the jet expansion and breakup.
- The characteristics of the spray breakup depend on the Weber and Ohnesorge number and fall in regimes that can be labelled retracting liquid, ligament stretching, and thin lamella regime.
- The order of magnitude of the resulting mean droplet diameter can be estimated by a simple kinematic relationship.
- The mean Sauter diameter is largely determined by the interstitial space between the bubbles at time of coalescence and the droplet size distribution is close to Gaussian.
- Surface area generation by bubble growth and spray breakup is largely determined by bubble number density and We. Secondary breakup leads to slow changes in surface area only.

- A RANS based solver has been developed and validated. Shock structures can be well captured.
- Simulations and experiments agree with respect to the major flow features.

Future work will provide more quantitative comparison (e.g. droplet velocities and sizes) between simulations and experiments. The simple HRM model may not allow to extract such information. An LES code with a one-fluid two-equation model for the two-phases (one for the volume fraction and one for the surface area) exists. The DNS results will need to be exploited to develop and implement a suitable source term for the surface area transport equation that accounts for the specific characteristics of flash atomization. Dietzel et al. [10] provide the surface area specific growth rates as functions of local (LES-filtered) pressures and the DNS by Loureiro et al. [27] provide surface generation terms due to the dynamics of the breakup process.

**Acknowledgements** The authors thank the German Research Foundation (DFG) for financial support of the project within the collaborative research center SFB-TRR 75, Project number 84292822. The authors also are grateful for the access to the supercomputers HPE Hawk system of the High Performance Computing Center Stuttgart (HLRS) and ForHLR funded by the Ministry of Science, Research and the Arts Baden-Württemberg and by the Federal Ministry of Education and Research.

## References

1. Anez J, Ahmed A, Hecht N, Duret B, Reveillon J, Demoulin FX (2019) Eulerian-Lagrangian spray atomization model coupled with interface capturing method for diesel injectors. *Int J Multiph Flow* 325–342
2. Bell IH, Wronski J, Quoilin S, Lemort V (2014) Pure and pseudo-pure fluid thermophysical property evaluation and the open-source thermophysical property library CoolProp. *Ind Eng Chem Res* 53(6):2498–2508
3. Bilicki Z, Kestin J (1990) Physical aspects of the relaxation model in two-phase flow. *Proc R Soc London Ser A* 428(1875):379–397
4. Brennen CE (2005) Fundamentals of multiphase flow. Cambridge University Press
5. Brennen CE (2014) Cavitation and bubble dynamics. Cambridge University Press
6. Cao Y, Tamura T (2015) Assessment of unstructured les with both structured LES and experimental database: flow past a square cylinder at  $Re = 2.2e+4$ . In: The 29th computational fluid dynamics symposium
7. Carey VP (2018) Liquid-vapor phase-change phenomena: an introduction to the thermophysics of vaporization and condensation processes in heat transfer equipment. CRC Press
8. Denner F, Xiao CN, van Wachem BG (2018) Pressure-based algorithm for compressible interfacial flows with acoustically-conservative interface discretisation. *J Comput Phys* 367:192–234
9. Devassy B, Benkovic D, Petranovic Z, Edelbauer W, Vujanovic M (2019) Numerical simulation of internal flashing in a GDI injector nozzle. In: 29th European conference on liquid atomization and spray systems
10. Dietzel D, Hitz T, Munz CD, Kronenburg A (2019) Numerical simulation of the growth and interaction of vapour bubbles in superheated liquid jets. *Int J Multiph Flow* 103:112
11. Dietzel D, Hitz T, Munz CD, Kronenburg A (2019) Single vapour bubble growth under flash boiling conditions using a modified HLLC Riemann solver. *Int J Multiph Flow* 116:250–269
12. Downar-Zapolski P, Bilicki Z, Bolle L, Franco J (1996) The non-equilibrium relaxation model for one-dimensional flashing liquid flow. *Int J Multiph Flow* 22(3):473–483
13. Eisenschmidt K, Ertl M, Gomaa H, Kieffer-Roth C, Meister C, Rauschenberger P, Reitzle M, Schlotte K, Weigand B (2016) Direct numerical simulations for multiphase flows: an overview of the multiphase code FS3D. *Appl Math Comput* 272:508–517

14. Fechter S, Munz CD, Rohde C, Zeiler C (2018) Approximate riemann solver for compressible liquid vapor flow with phase transition and surface tension. *Comput Fluids* 169:169–185.
15. Recent progress in nonlinear numerical methods for time-dependent flow & transport problems
15. Gärtnner JW, Feng Y, Kronenburg A, Stein OT (2021) Numerical investigation of spray collapse in GDI with OpenFOAM. *Fluids* 6(3)
16. Gärtnner JW, Kronenburg A, Martin T (2020) Efficient WENO library for OpenFOAM. *SoftwareX* 12:100611
17. Gärtnner JW, Kronenburg A, Rees A, Sender J, Oschwald M, Lamanna G (2020) Numerical and experimental analysis of flashing cryogenic nitrogen. *Int J Multiph Flow* 130:103360
18. Guo H, Li Y, Wang B, Zhang H, Xu H (2019) Numerical investigation on flashing jet behaviors of single-hole GDI injector. *Int J Heat Mass Trans* 130:50–59
19. Guo H, Nocivelli L, Torelli R (2021) Numerical study on spray collapse process of ECN spray G injector under flash boiling conditions. *Fuel* 290:119961
20. Guo H, Nocivelli L, Torelli R, Som S (2020) Towards understanding the development and characteristics of under-expanded flash boiling jets. *Int J Multiph Flow* 129:103315
21. Kurschat T, Chaves H, Meier G (1992) Complete adiabatic evaporation of highly superheated liquid jets. *J Fluid Mech* 236:43–59
22. Lamanna G, Kamoun H, Weigand B, Manfletti C, Rees A, Sender J, Oschwald M, Steelant J (2015) Flashing behavior of rocket engine propellants. *At Sprays* 25(10)
23. Lamanna G, Kamoun H, Weigand B, Steelant J (2014) Towards a unified treatment of fully flashing sprays. *Int J Multiph Flow* 58:168–184
24. Lebas R, Menard T, Beau P, Berlemont A, Demoulin F (2009) Numerical simulation of primary break-up and atomization: DNS and modelling study. *Int J Multiph Flow* 35(3):247–260
25. Lee HS, Merte H (1996) Spherical vapor bubble growth in uniformly superheated liquids. *Int J Heat Mass Trans* 39(12):2427–2447
26. Lee J, Madabhushi R, Fotache C, Gopalakrishnan S, Schmidt D (2009) Flashing flow of superheated jet fuel. In: PCIRC2, vol 32, pp 3215–3222
27. Loureiro DD, Kronenburg A, Reutzsch J, Weigand B, Vogiatzaki K (2021) Droplet size distributions in cryogenic flash atomization. *Int J Multiphase Flow*. p submitted
28. Loureiro DD, Reutzsch J, Kronenburg A, Weigand B, Vogiatzaki K (2020) Primary breakup regimes for cryogenic flash atomization. *Int J Multiph Flow* 132:103405
29. Lyras K, Dembele S, Vyazmina E, Jallais S, Wen J (2017) Numerical simulation of flash-boiling through sharp-edged orifices. *Int J Comput Methods Exp Meas* 6:176–185
30. Mohapatra CK, Schmidt DP, Sforozzo BA, Matusik KE, Yue Z, Powell CF, Som S, Mohan B, Im HG, Badra J, Bode M, Pitsch H, Papoulias D, Neroorkar K, Muzaferija S, Martí-Aldaraví P, Martínez M (2020) Collaborative investigation of the internal flow and near-nozzle flow of an eight-hole gasoline injector (Engine Combustion Network Spray G). *Int J Engine Res*
31. Pourasadegh F, Lacey JS, Brear MJ, Gordon RL, Petersen P, Lakey C, Butcher B, Ryan S, Kramer U (2018) On the phase and structural variability of directly injected propane at spark ignition engine conditions. *Fuel* 222:294–306
32. Rees A, Araneo L, Salzmann H, Kurudzija E, Suslov D, Lamanna G, Sender J, Oschwald M (2019) Investigation of velocity and droplet size distributions of flash boiling LN<sub>2</sub>-jets with phase doppler anemometry. In: ILASS-Europe 2019, 29th annual conference on liquid atomization and spray systems
33. Saha K, Som S, Battistoni M (2017) Investigation of homogeneous relaxation model parameters and their implications for gasoline injectors. *At Sprays* 27(4):345–365
34. Schmidt D, Gopalakrishnan S, Jasak H (2010) Multidimensional simulation of thermal non-equilibrium channel flow. *Int J Multiph Flow* 36:284–292
35. Sher E, Bar-Kohany T, Rashkovian A (2008) Flash-boiling atomization. *Prog Energy Combust Sci* 34(4):417–439
36. The OpenFOAM Foundation Ltd: OpenFOAM (2021). <https://openfoam.org/>
37. Traxinger C, Zips J, Banholzer M, Pfitzner M (2020) A pressure-based solution framework for sub- and supersonic flows considering real-gas effects and phase separation under engine-relevant conditions. *Comput Fluids* 202:104452

38. Tsang CW, Rutland C (2016) Effects of numerical schemes on large eddy simulation of turbulent planar gas jet and diesel spray. *SAE Int J Fuels Lubr* 9(1):149–164
39. Vieira MM, Simoes-Moriera JR (2007) Low-pressure flashing mechanisms in iso-octane liquid jets. *J Fluid Mech* 572:121–144
40. Witlox H, Harper M, Bowen P, Cleary V (2007) Flashing liquid jets and two-phase droplet dispersion: II. Comparison and validation of droplet size and rainout formulations. *J Hazard Mater* 142(3):797–809. Papers Presented at the 2005 Symposium of the Mary Kay O'Connor Process Safety Center

**Open Access** This chapter is licensed under the terms of the Creative Commons Attribution 4.0 International License (<http://creativecommons.org/licenses/by/4.0/>), which permits use, sharing, adaptation, distribution and reproduction in any medium or format, as long as you give appropriate credit to the original author(s) and the source, provide a link to the Creative Commons license and indicate if changes were made.

The images or other third party material in this chapter are included in the chapter's Creative Commons license, unless indicated otherwise in a credit line to the material. If material is not included in the chapter's Creative Commons license and your intended use is not permitted by statutory regulation or exceeds the permitted use, you will need to obtain permission directly from the copyright holder.



# Mass Transport Across Droplet Interfaces by Atomistic Simulations



Matthias Heinen, Simon Homes, Gabriela Guevara-Carrion,  
and Jadran Vrabec

**Abstract** Due to availability of powerful computers and efficient algorithms, physical processes occurring at the micrometer scale can nowadays be studied with atomistic simulations. In the framework of the collaborative research center SFB-TRR75 “Droplet dynamics under extreme ambient conditions”, investigations of the mass transport across vapour-liquid interfaces are conducted. Non-equilibrium molecular dynamics simulation is employed to study single- and two-phase shock tube scenarios for a simple noble gas-like fluid. The generated data show an excellent agreement with computational fluid dynamics simulations. Further, particle and energy flux during evaporation are sampled and analysed with respect to their dependence on the interface temperature, employing a newly developed method which ensures a stationary process. In this context, the interface properties between liquid nitrogen and hydrogen under strong gradients of temperature and composition are investigated. Moreover, the Fick diffusion coefficient of strongly diluted species in supercritical CO<sub>2</sub> is predicted by equilibrium molecular dynamics simulation and the Green-Kubo formalism. These results are employed to assess the performance of several predictive equations from the literature.

## 1 Introduction

Since 1953, molecular modelling and simulation has contributed substantially to thermodynamics and materials science as a numerical approach to investigate the thermo-physical behaviour of matter. It is based on the interactions between molecules that are described by force fields and are modeled today on the basis of quantum chemical data. This approach rests on statistical mechanics, which postulates that a macroscopic thermodynamic state in the sense of classical thermodynamics is represented by the sum of its underlying microstates. In other words, when studying a microscopic system by sampling a sufficient number of microstates under appropriate boundary

---

M. Heinen · S. Homes · G. Guevara-Carrion · J. Vrabec (✉)

Thermodynamics and Process Engineering, Technical University of Berlin, Berlin, Germany  
e-mail: [vrabec@tu-berlin.de](mailto:vrabec@tu-berlin.de)

conditions, all thermophysical properties of the corresponding macroscopic system can be determined. The accessibility of physical properties with atomistic simulations has been extended by the development of computer hardware and sampling algorithms [4]. For instance, transport properties like the Fick diffusion coefficient matrix of multicomponent mixtures, which are hardly measurable with experiments, can be determined with equilibrium molecular dynamics (EMD).

Due to the fact that the interactions are considered for every molecule individually, the computational effort remains an issue for atomistic simulations. Although the number of calculations can be reduced by considering the interactions only within a certain cutoff radius, the effort is still large, which limits the accessible length and time scales. The length scale is related to the atomic radius of the elements, i.e. a molecular system consisting of a few thousand particles, a typical size for EMD simulations, has an extent of a few nanometers only. The time scale is related to the propagation speed of molecules, which for moderate temperatures is on the order of a few hundred meters per second, depending of the molecular weight. To perform a stable molecular dynamics (MD) simulation, the trajectory of every individual molecule has to be followed with a sufficient temporal resolution. Consequently, a time step on the order of a femtosecond is needed.

Systems consisting of a few hundred molecules, which are small from today's perspective, were a challenge in the past even for the most advanced computers. Due to the exponential growth of computational resources and the development of highly parallelised code [20], however, the accessible length and time scales were significantly extended so that simulations of molecular systems on the micrometer and microsecond scales are feasible today. These orders of magnitude are sufficiently large to obtain results that are directly comparable with computational fluid dynamics (CFD) simulations. Especially due to the limitation of the accessible time scale with atomistic simulations, such direct comparisons with CFD are particularly tractable in situations where rapid physical processes are investigated. This condition was favourable for the research topic of the collaborative research center SFB-TRR75 "Droplet dynamics under extreme ambient conditions". Direct comparisons to models on a coarser level were a central element of the investigations of our group, with the overarching goal to bring insights obtained on the microscopic scale to the macroscopic scale. The aim was to improve the assumptions that have to be made in continuum methods, especially when considering multiphase systems in the presence of interfaces. In the following, a selection of this work is presented, starting with the investigation of single- and two-phase shock tube scenarios, considering a simple noble gas-like fluid in Sect. 2. Next, investigations of stationary evaporation across a planar interface of pure fluids are described in Sect. 3. In Sect. 4, a more complex scenario is discussed, where liquid nitrogen evaporates into a hydrogen gas phase. Finally, selected results on the Fick diffusion coefficient of supercritical fluids are presented in Sect. 5.

## 2 Shock Tube

The finite volume (FV) scheme is a numerical method for the discretization of the Navier-Stokes equations. Due to its conservative properties, allowing for discontinuities between the grid cells, it is widely used in CFD codes. The flux between grid cells is nowadays determined by the solution of the Riemann problem. This idea was proposed by Godunov in his pioneering work. Since then, the so-called Riemann solvers have been continuously developed so that modern methods reduce the computational effort by approximate solutions, while preserving the advantageous properties of the Godunov scheme.

The most simple example for a Riemann problem is a classical shock tube scenario, consisting of two homogeneous gas phases on different pressure levels that are initially separated by a diaphragm. Once the diaphragm is ruptured, a shock wave is exerted by the high pressure region and propagates through the low pressure region. The Riemann problem solution for this scenario is well known. Hence, it was used as a starting point for the present study, before considering the more challenging case of a two-phase shock tube scenario, where the high pressure gas phase of the classical single-phase shock tube is replaced with a liquid phase and the adjacent gas phase has a pressure below the saturation pressure of the liquid.

The treatment of this case with CFD is much more complex, since the solution structure of the Riemann problem has to be extended accordingly. The solution of the Riemann problem with phase transition, starting from initial data for the interacting phases, must find a path through the two-phase region, wherein the isotherm and isentrope exhibit a Maxwell loop that entails an imaginary speed of sound. This has mathematical consequences in the form that the hyperbolicity of the Euler equations is lost and the partial differential equations become hyperbolic-elliptic. Further implications are discussed in Ref. [12].

Since no analytical solution for the two-phase shock tube exists and open questions with respect to both the modelling and the numerical treatment remain, it was particularly interesting to generate a reference data set with NEMD simulation for this case. The study was divided into two parts. First, two single-phase shock tube scenarios were investigated to assess the general concept of a direct comparison between NEMD and CFD simulations: A classical shock tube scenario with two supercritical gas phases at different pressure levels and the expansion of one supercritical gas phase into vacuum. Second, the more complex case of the two-phase shock tube was investigated. Before selected results are presented in the following, some common features are addressed.

In the according NEMD simulations, a simple molecular model, i.e. the truncated and shifted Lennard-Jones (LJTS) potential, was used. It can be parametrized such that it nicely mimics the thermophysical properties of the noble gases and methane [23]. This model is computationally cheap in MD simulations and two accurate equations of state for its thermophysical properties exist, which were used as an input for the CFD simulations so that both the microscopic (MD) and the macroscopic (CFD) solutions considered exactly the same fluid.

During NEMD simulations, spatially resolved temperature  $T$ , density  $\rho$  and hydrodynamic velocity  $v$  profiles were sampled by employing a classical binning scheme. To capture the dynamics of the shock tube processes, these profiles were averaged over comparatively short time intervals of  $\Delta t = 10$  (20 ps for argon) to avoid blurring the rapidly changing profiles. The evolution of these profiles over time was compared to the profiles obtained from CFD simulations. To achieve a good statistical quality despite the short sampling time intervals, comparatively large interface areas were considered by NEMD, yielding configurations comprising a total of up to  $3 \cdot 10^8$  particles. Moreover, the statistical quality was raised by a factor of two by exploiting the spatial symmetry of the systems.

The macroscopic CFD solutions were obtained by solving the conservation equations with a discontinuous Galerkin spectral element method (DGSEM) [10], which was implemented in the open source code *FLEXI*<sup>1</sup>. The associated work was done by Munz and coworkers. Detailed comparisons between MD and CFD have recently been published in Refs. [11, 12].

Results for the single-phase shock tube scenario are shown in Fig. 1, covering the well known characteristics of this case, i.e. a shock wave, delimited by a shock front, propagating into the low pressure region, followed by a material boundary with lower propagation speed that initially separated the high and low pressure regions as well as a rarefaction wave that travels in opposite direction into the high pressure region. The comparison between results from MD and CFD simulations showed an almost perfect agreement, which was a good motivation for the consideration of the more complex scenario. Figure 2 shows results for one of the investigated two-phase shock tube scenarios. The snapshots together with the density and velocity profiles illustrate major aspects of the system behaviour. By colouring of the particles and sampling partial density profiles, the spontaneously evaporated matter (red) can be determined.

From the velocity profiles, it can be seen that this matter accelerated the initially resting vapour phase (green) and thereby induced a shock wave. The magnitude of the shock wave, i.e. the compression of the vapour phase, is weak compared to the one observed in the single-phase scenario (note that the left plot of Fig. 2b shows only the range of the vapour density). The shock front and the material boundary, where the latter can be identified at the point where the partial density profiles cross, smear out during their propagation because of diffusion.

A comparison of the results from NEMD and CFD simulations is given in Fig. 3. It clearly shows that the homogeneous equilibrium method simulation failed to reproduce the results from NEMD, whereas results from the sharp interface method show a very good agreement, covering all characteristics of the density, velocity and temperature profiles obtained from NEMD simulation. The temperature profiles, however, revealed that reproducing the evaporative cooling effect by CFD remains an issue. The NEMD results show a much more pronounced temperature drop at the vapour-liquid interface. Consequently, also a deviation for the vapour density close to the liquid phase was found.

---

<sup>1</sup> <https://www.flexi-project.org/>.

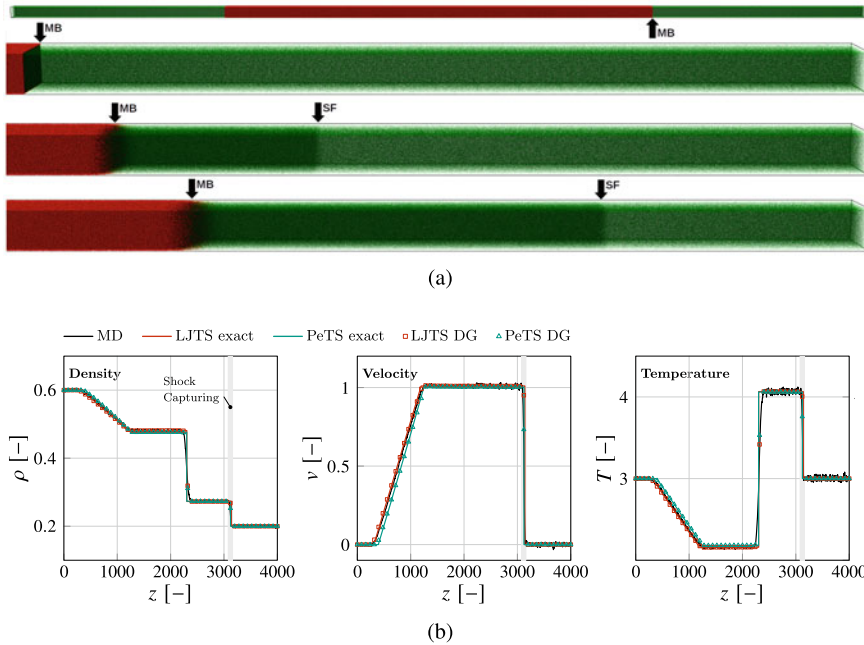


**Fig. 1** Results for the supercritical shock tube problem. **a** Snapshots of the MD system, rendered by *MegaMol* [5], at three instances of time  $t = 0, 182$  and  $364$  with an overall view of the initial configuration (top) followed by magnified views on the right interface and low pressure region. Particles constituting the initial high and low pressure regions are coloured red and green, respectively. Black arrows mark the material boundary (MB) and the shock front (SF). **b** Comparison of the results from MD simulations, the exact solution of the corresponding macroscopic Riemann problem and the approximate solution by the DGSEM scheme. The Riemann problem was solved with the LJTS or the PeTS equation of state. The grey rectangle indicates the region where shock capturing was active [12]

### 3 Evaporation of a Pure Fluid

To gain further insight into evaporation processes, the evaporative mass transfer of the pure LJTS fluid across a planar vapour-liquid interface was investigated. The focus of the present study [13] laid on the influence of the liquid region. The bulk liquid temperature as well as the thermal resistance were varied and their impact on the evaporation process was analysed by carrying out large NEMD simulations with up to  $8.4 \cdot 10^6$  particles using the software *lsl mardyn* [20].

A common method to investigate evaporation processes harnesses a symmetrical molecular system. Such a system consists of two vapour phases surrounding a liquid phase, cf. Fig. 4a. Besides imposing periodic boundary conditions at the volume faces that are perpendicular to the interface, a vacuum is used to enforce a driving gradient for evaporation. Since particles are deleted in the vacuum region, the total number of particles in the system decreases, leading to a receding interface, which entails

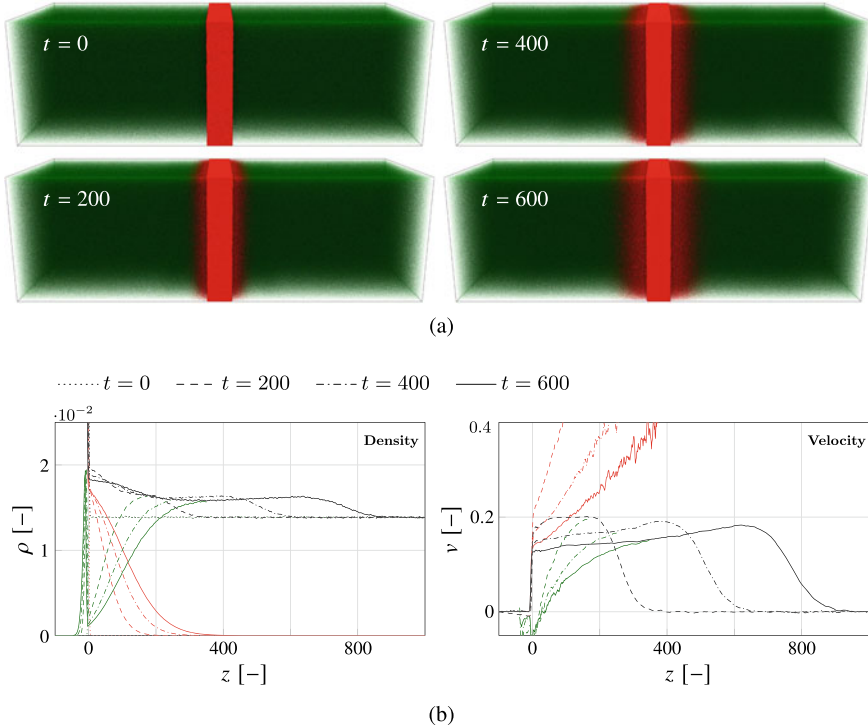


**Fig. 2** Results for a two-phase shock tube scenario obtained from NEMD simulation. **a** Snapshots [5] of the MD system at four instances of time  $t = 0, 200, 400$  and  $600$ . Particles that were initially constituting the liquid and vapour phase are coloured red and green, respectively. **b** Evolution of density  $\rho$  and hydrodynamic velocity  $v$  profiles depicted at the same time instances as the snapshots. Partial density and partial velocity profiles were sampled considering only particles that were initially constituting the liquid (red) or the vapour (green), respectively. The total density and velocity profiles (black) are the weighted sum of the partial ones

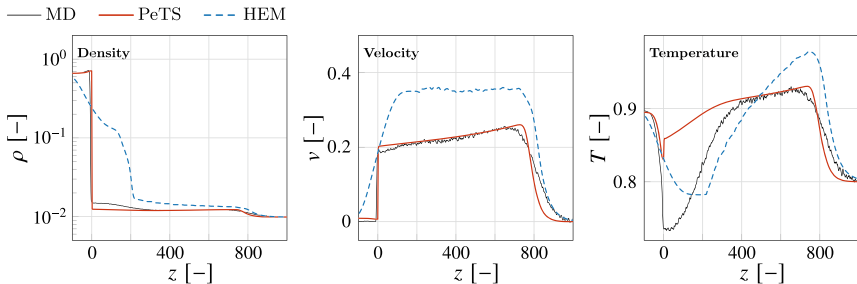


**Fig. 3** Density  $\rho$ , velocity  $v$  and temperature  $T$  profiles at time  $t = 600$  obtained from NEMD and CFD simulations with both approaches, the sharp interface method (PeTS) and the homogeneous equilibrium method (HEM). The initial conditions of the depicted case refer to the strongest non-equilibrium considered in Ref. [12]

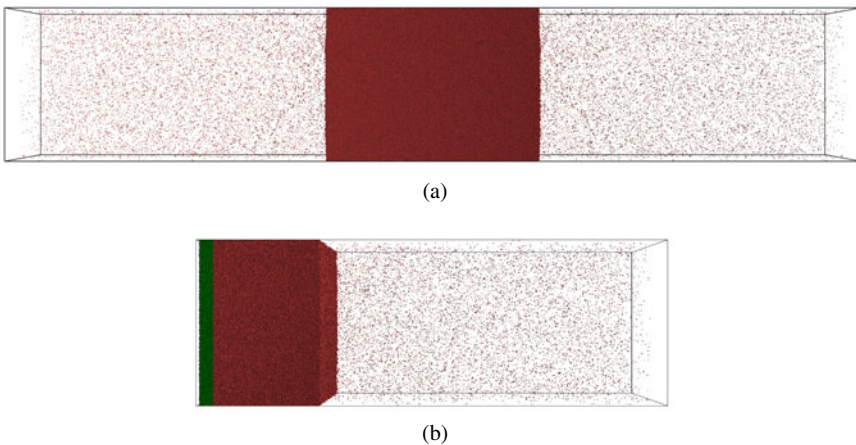


**Fig. 4** Snapshots [5] of systems for the investigation of evaporation. **a** Symmetrical method with two vapour and one liquid phase as it is commonly used. **b** Present method to maintain stationary conditions

several disadvantages. The receding interface allows only for a limited sampling duration, since the liquid phase vanishes at some point in time. Moreover, it is not possible to simulate very large systems because they require a long time to reach quasi-stationarity.

In order to overcome these challenges, our collaborating partner Müller-Plathe and coworkers [31] developed two methods to simulate stationary evaporation, which are based on sophisticated algorithms for particle insertions to replenish the liquid. They showed that those algorithms could be used successfully in situations with high evaporation rates and also for more complex molecules such as ethanol. To guarantee smooth insertions, however, a few control parameters have to be specified in a careful manner. Hence, for the specific case of stationary evaporation across a planar interface a new method was developed that works without the need of any parameters [9]. As shown in Fig. 4b, the system is constituted by one liquid and one vapour phase. There is still a vacuum on the right-hand side, where particles are deleted, but in contrast to the common method, these are replaced by a slab of liquid that is pushed into the system at its left boundary. Hence, the total number of particles within the system remains constant. Since the liquid slab is continuously replenished, stationary conditions are guaranteed, facilitating arbitrarily long simulation runs.

This method is suited for the present parameter study, since systems with a large number of particles were investigated. Besides the vacuum at the right boundary, a thermostat in the bulk liquid constrained the system. In that thermostated region, the velocity of the particles was scaled such that a specified bulk liquid temperature  $T_{\text{liq}}$  was maintained. The second quantity which was varied in this study was the distance  $L_n$  between the thermostat and the interface. After reaching stationary conditions, all desired quantities, like density, temperature and velocity profiles, were sampled

for about  $10^6$  time steps. The sampling was performed in bins with a width of  $1/4$  particle diameters. Further details on the methodology can be found in Ref. [13].

A stationary simulation is characterised by several quantities. The present study focused on the particle flux  $j_p$  and energy flux  $j_e$  that are constant over the simulation volume under stationary conditions. Both fluxes were not sampled directly, but calculated during post-processing. Quantities which were sampled directly include the hydrodynamic velocity  $v_z$ , density  $\rho$  and temperature  $T$ . Those profiles were combined as follows to yield the particle flux  $j_p$

$$j_p = \rho v_z.$$

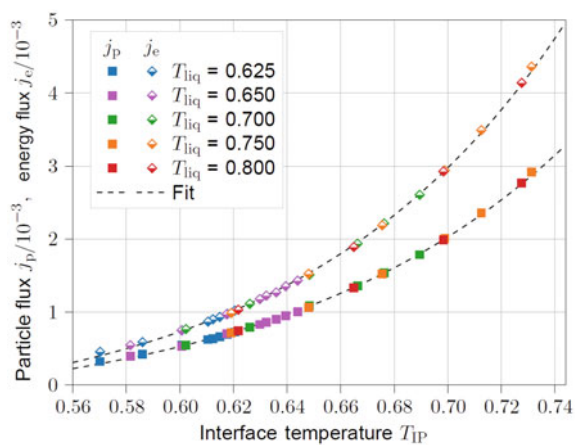
While the particle flux rises with increasing bulk liquid temperature, it decreases for a larger distance between the thermostated region and the interface  $L_n$ . Furthermore, an asymptotic behaviour was observed, as the particle flux reaches a certain value  $j_p^\infty$  for a distance  $L_n$  extrapolated to infinity.

In analogy with the particle flux, the energy flux  $j_e$  was calculated by post-processing using the directly sampled profiles. The following equation was used

$$j_e = (h + e_{\text{kin}}) j_p + \dot{q},$$

in which  $h$  is the enthalpy,  $e_{\text{kin}}$  the kinetic energy and  $\dot{q}$  the heat flux. In order to obtain the enthalpy  $h$ , an equation of state [8] was utilised to compute the enthalpy as a function of temperature and density. The kinetic energy  $e_{\text{kin}}$  was derived straightforwardly from the directly-sampled hydrodynamic velocity. The heat flux  $\dot{q}$  was determined with Fourier's law for which the thermal conductivity was taken from two correlations [15, 16] and the directly sampled temperature and density profiles as input parameters.

**Fig. 5** Particle flux  $j_p$  and energy flux  $j_e$  over the interface temperature  $T_{\text{IP}}$  for all conducted simulations



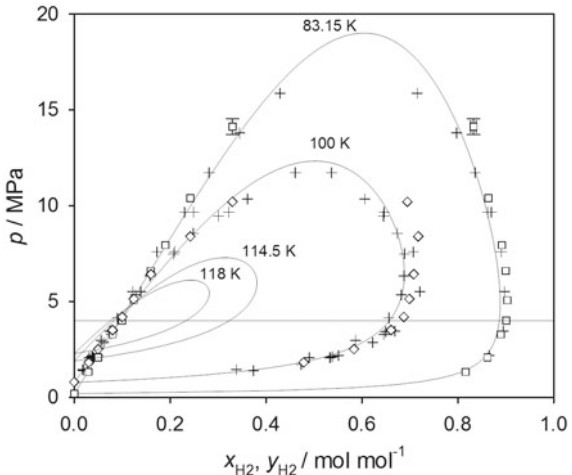
Similar to the fluxes, the interface temperature  $T_{IP}$  depends on the bulk liquid temperature  $T_{liq}$  as well as on the distance between thermostat and interface  $L_n$ . Nevertheless, when investigating the dependence of the fluxes on the interface temperature, it turns out that both the particle flux and the energy flux depend under the given boundary conditions solely on the interface temperature, cf. Fig. 5. Regardless of the initial parameters, like bulk liquid temperature and distance between thermostat and interface, simulations yield the same fluxes when their interface temperature is the same. Under the present boundary conditions, this holds for the entire investigated temperature range.

## 4 Evaporation of Liquid Nitrogen into Hydrogen

The injection process in liquid propellant rocket engines is a prominent example of extreme conditions, which are characterised by high pressures and cryogenic injection temperatures. While the chamber pressure often exceeds the critical pressure of the injected fluid, the injection temperature of one or both propellants is usually below or close to the critical temperature of the pure fluid so that they are in a trans- or supercritical state. Especially due to the high operating pressure, the experimental conditions are very challenging and therefore the process-relevant quantities are difficult to access metrologically. Moreover, a better understanding of the atomisation process is of great scientific and also economic interest due to the savings potential through possible optimisations.

An early experimental work on this topic was carried out by Oschwald et al. [22], where coaxial injection processes of liquid nitrogen ( $\text{LN}_2$ ) into gaseous hydrogen ( $\text{H}_2$ ) at supercritical pressure were studied with Raman scattering. Nitrogen was used as a substitute for oxygen in order to allow for an isolated observation of the mixing processes with the exclusion of chemical reactions. Avoiding experimental challenges, Müller et al. [19] investigated two of the test cases (D4 and E4) of Ref. [22] with large-eddy simulations. For the transcritical injection conditions (E4), the simulation results showed that thermodynamic states occur in the shear layer that lie in the two-phase region, as indicated by a vapour-liquid equilibrium calculation. These results, however, contradicted the findings of Dahms and Oefelein [3], who proposed a model to predict the operating pressure where classical sprays transition to dense-fluid mixing, based on a Knudsen number criterion using the interface thickness as the representative physical length scale. While a lively discussion on this topic continued in the rocket combustion community, Traxinger et al. [28] extended the thermodynamic framework used in Ref. [19] to additionally account for multicomponent phase separation by means of a vapour-liquid equilibrium model. Employing this extended framework for the case of n-hexane injected into a chamber containing nitrogen in a combined experimental and numerical study, results from both were in good agreement, showing phase separation and the transition from a dense-gas to a spray-like jet for the test cases where the a priori calculation predicted a two-phase flow.

**Fig. 6** Isothermal phase diagram of the binary mixture  $\text{H}_2 + \text{N}_2$  obtained by molecular simulation (squares and diamonds), Peng-Robinson equation of state (solid lines) and experiment (crosses) [14]. The horizontal line marks the pressure  $p = 4 \text{ MPa}$  of the low pressure case NEMD simulation



Contributing to the understanding of such processes, three NEMD simulations were conducted in the present study, investigating a  $\text{LN}_2/\text{H}_2$  interface exposed to strong temperature and composition gradients, considering similar conditions as test case E4 of Ref. [22]. The force fields selected to model the molecular interactions of hydrogen and nitrogen have shown their validity in a prior study where the phase behaviour of this binary mixture was investigated by EMD simulations, cf. Fig. 6.

While maintaining the same temperature and composition gradient for all three NEMD simulations, the system pressure was varied  $p = 4, 12$  and  $20 \text{ MPa}$ . Since the two highest pressures showed qualitatively similar results, the terms ‘*low pressure case*’ ( $p = 4 \text{ MPa}$ ) and ‘*high pressure case*’ ( $p = 12$  or  $20 \text{ MPa}$ ) are used in the following. Figure 7a shows a snapshot of the system’s initial configuration in the low pressure case, consisting of two homogeneous and pure phases ( $\text{LN}_2$  and  $\text{H}_2$ ) in physical contact through a comparatively large planar interface with an area of  $(85 \text{ nm})^2$  to obtain sampling results with a high statistical quality. Hence, a configuration comprised a total of  $\sim 10^7$  molecules. The  $\text{LN}_2$  and  $\text{H}_2$  phases had a width of 50 nm and 140 nm, respectively, yielding an overall extent of the system of 190 nm in  $z$  direction.

Before these phases were brought into contact, they were both thoroughly equilibrated by EMD simulation in the canonic ensemble. The liquid slab of  $\text{LN}_2$  had a temperature of  $T_{\text{N}2} = 118 \text{ K}$  and the  $\text{H}_2$  gas phase had a temperature of  $T_{\text{H}2} = 270 \text{ K}$ . Once the initial configurations were prepared, NEMD simulations were conducted to follow the temporal evolution of the system, in particular the vapour-liquid interface. During these simulations, the state of the bulk phases  $\text{LN}_2$  and  $\text{H}_2$  was controlled within control volumes (CV) at the outer limits of the system in  $z$  direction, cf. Fig. 7a. In both CV, the composition was controlled to maintain the fluids in their pure state. This was achieved by identity change, i.e. hydrogen molecules entering the CV in the liquid phase were substituted by nitrogen molecules and nitrogen molecules entering

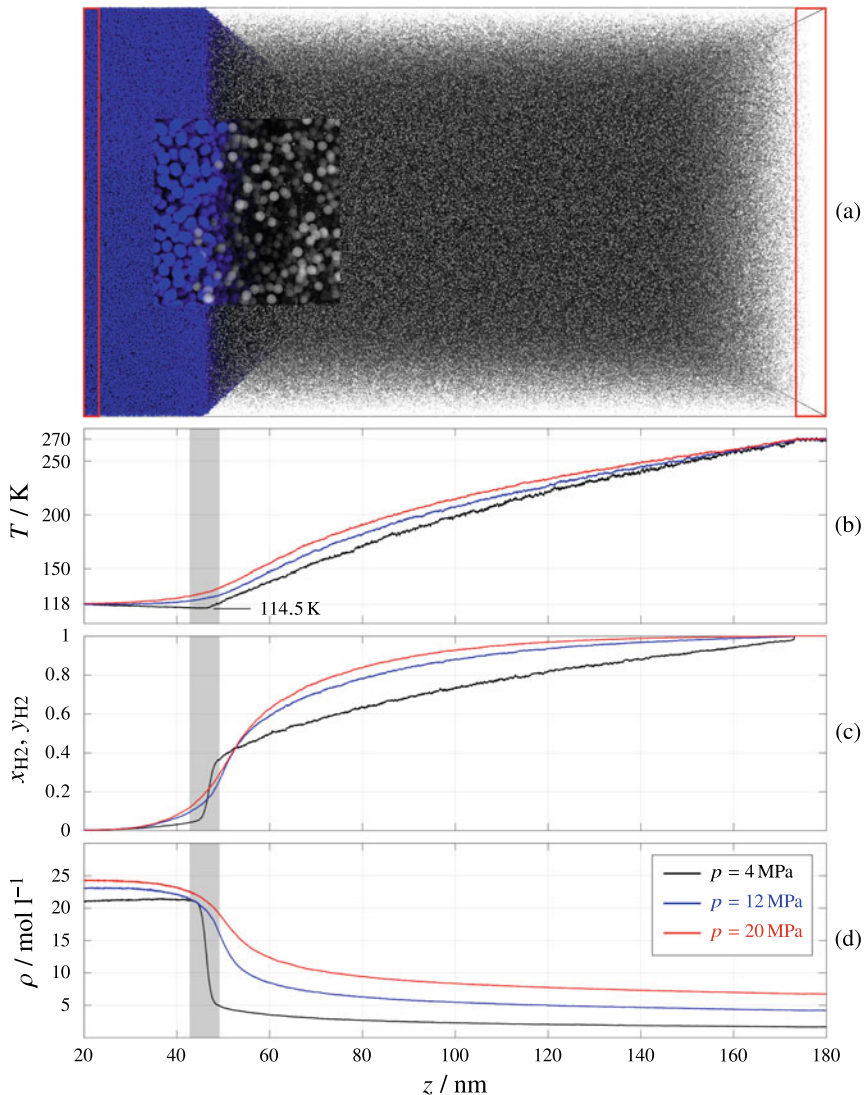


**Fig. 7** **a** Snapshot [5] of the initial configuration of the low pressure case ( $p = 4 \text{ MPa}$ ), consisting of a liquid nitrogen LN<sub>2</sub> phase at a temperature of  $T_{\text{N}2} = 118 \text{ K}$  on the left and a supercritical hydrogen H<sub>2</sub> phase at a temperature of  $T_{\text{H}2} = 270 \text{ K}$  on the right side. The inset shows a magnified view on the interface. Two control volumes (CV), in which the boundary conditions in  $z$  direction were maintained, are marked by red rectangles. Temperature  $T$ , mole fraction of hydrogen  $x_{\text{H}2}$ ,  $y_{\text{H}2}$  and density  $\rho$  profiles are shown in panels **b-d** for the three pressure cases:  $p = 4 \text{ MPa}$  (black),  $p = 12 \text{ MPa}$  (blue) and  $p = 20 \text{ MPa}$  (red). The grey area marks the interface region of the low pressure case

the CV in the gas phase were substituted by hydrogen molecules. The temperatures  $T_{N2} = 118$  K and  $T_{H2} = 270$  K were controlled in the CV by velocity scaling. Moreover, the desired system pressure was maintained indirectly by imposing a constant density within the gas phase CV by particle deletion. Finally, the liquid phase was replenished from a liquid reservoir to maintain stationary conditions, cf. Ref. [9].

To investigate the system behaviour, the temperature  $T$ , hydrogen mole fraction  $x_{H2}$ ,  $y_{H2}$  and density  $\rho$  profiles were sampled by NEMD simulation employing a classical binning scheme. Because of the strong thermodynamic non-equilibrium between the two phases in the initial configuration, a rapid transition from the step-wise profiles to the profiles under stationary conditions was observed, cf. Fig. 7b-d. These were attained after a time period of approximately 3 ns in all pressure cases. One of the striking features of the density profiles is that with increasing pressure not only the gas density of the  $H_2$  bulk phase increased (almost linearly), but also the density of the  $LN_2$  phase increased, indicating a compressible liquid. However, this is not surprising since  $T_{N2} = 118$  K is close to the critical temperature of nitrogen  $T_{c,N2} = 126$  K. Considering the transition from liquid to gas, a clear difference between the pressure cases can be noticed. In the low pressure case, a sharp interface with a thickness of only a few nanometers was observed, whereas the high pressure cases show much broader and comparatively smooth transitions that span over tens of nanometers, which can be identified as dense-fluid mixing. A similar observation was made for the mole fraction profile  $x_{H2}$ ,  $y_{H2}$ . The low pressure case shows a steep gradient at the interface, which can be interpreted as a resistance for hydrogen to dissolve into the  $LN_2$  phase, whereas the higher pressure cases show much broader and comparatively smooth transitions, similar to the density profile. The temperature profiles exhibit an overall similar course. However, a particular characteristic was revealed at the interface. In the low pressure case, a temperature decrease towards the interface was observed, leading to a minimum of 114.5 K. This means that despite a much higher temperature of the gas phase, a part of the enthalpy of evaporation was supplied by the liquid phase. Conversely, in the high pressure cases, the liquid phase was heated up, despite the evaporative cooling effect. This can be explained by the much more intense thermal coupling between the liquid and gas phase at higher pressure, predominantly due to the higher gas density.

To further asses these results, they were compared to an isothermal phase diagram of the binary mixture  $H_2 + N_2$  [14], cf. Fig. 6. The diagram shows the vapour pressure over the hydrogen mole fraction  $x_{H2}$ ,  $y_{H2}$  for four isotherms. Since the critical temperature of hydrogen is  $T_{c,H2} = 33$  K, all isotherms are tied up to the vapour pressure of pure nitrogen only. With increasing temperature, the two-phase region becomes much smaller and recedes toward pure nitrogen so that at a certain temperature limit the mixture is found to be supercritical at any pressure and composition. Considering a pressure of  $p = 4$  MPa (low pressure case), a stable vapour-liquid equilibrium can be found for all depicted isotherms, where with decreasing temperature the critical point of the mixture becomes more distant to the 4 MPa line. That means that the evaporative cooling effect, leading to a decreased interface temperature of 114.5 K, stabilises the presence of the interface when assuming local equilibrium conditions. Conversely, the increased interface temperature due to enhanced thermal coupling of

the liquid and gas phase, as observed in the NEMD simulations of the high pressure cases, leads to a reduced critical pressure of the mixture and thereby to a weakened interface.

## 5 Diffusion in the Supercritical Region

Diffusion is one of the key processes in the context of mass transfer across interfaces. For instance, evaporation of liquids into a vapour phase driven by a chemical potential gradient is often rate-limited by diffusion [2]. Mass transport of one component in the presence of a stagnant gas, known as Stefan diffusion, often occurs during adsorption and condensation operations [27]. Analyses of evaporation experiments in a Stefan tube require the Fick diffusion coefficient near the infinite dilution limit, since the evaporating species is present in extremely low concentrations at the top of the tube. Therefore, it is important to identify adequate procedures to obtain reliable diffusion coefficient data under these conditions.

This work focuses on the prediction of the Fick diffusion coefficient of various solutes diluted in supercritical carbon dioxide ( $\text{CO}_2$ ), which is an environmentally friendly solvent employed in various industrial processes [21]. The measurement of diffusion coefficients in supercritical  $\text{CO}_2$  is experimentally challenging and many techniques still require improvement to reach an adequate accuracy. Data availability is thus limited, especially in the extended critical region. Driven by the lack of experimental data, many models and correlations, mainly based on the Stokes-Einstein equation or the rough-hard-sphere model, have been developed to predict the Fick diffusion coefficient. An overview of the proposed predictive equations with their strengths and shortcomings can be found in recent reviews [17, 26].

On the other hand, EMD simulation offers a physically sound route not only to predict diffusion data, but also to gain an insight into the underlying molecular mechanisms. Therefore, EMD simulation and the Green-Kubo formalism were employed here to predict Fick diffusion coefficients of methane ( $\text{CH}_4$ ), benzene ( $\text{C}_6\text{H}_6$ ) and toluene ( $\text{C}_7\text{H}_8$ ) diluted in supercritical  $\text{CO}_2$  under near-critical conditions. The simulation results were subsequently compared with several predictive equations from the literature.

Rigid, non-polarizable, Lennard-Jones (LJ) based force fields were chosen. If required, superimposed point quadrupoles were used to account for the electrostatic interactions. The description of the force fields and the corresponding parameters can be found in Refs. [6, 18, 29]. To specify the unlike interactions between LJ sites, a modification of the Lorentz-Berthelot combining rules given by  $\sigma_{ab} = (\sigma_{aa} + \sigma_{bb})/2$  and  $\epsilon_{ab} = \xi \sqrt{\epsilon_{aa}\epsilon_{bb}}$ , was employed. The parameter  $\xi$  was obtained by adjusting the sampled vapour-liquid equilibrium to experimental data for each binary mixture.

One way to obtain the Fick diffusion coefficient  $D_{ij}$  is to calculate it from the sampled Maxwell-Stefan (MS) diffusion coefficient  $\mathcal{D}_{ij}$  employing the relation

$$D_{ij} = \mathcal{D}_{ij} \cdot \Gamma , \quad (1)$$

where  $\Gamma$  is the so-called thermodynamic factor, which is given by

$$\Gamma = \frac{x_1}{k_B T} \left( \frac{\partial \mu_1}{\partial x_1} \right)_{T,p}. \quad (2)$$

Therein,  $x_1$  and  $\mu_1$  are the mole fraction and the chemical potential of component 1, respectively, and  $k_B$  is the Boltzmann constant.

The thermodynamic factor is usually obtained from an equation of state or an excess Gibbs energy model fitted to experimental phase equilibrium data. However, it can also be estimated by molecular simulation, either by sampling the chemical potential or Kirkwood-Buff integrals. In this work, the chemical potential was sampled with Widom's test particle method and the right-hand side of Eq. (2) was then approximated by numerical differentiation.

The thermodynamic factor is defined to be unity at the infinite dilution limit where both MS and Fick diffusion coefficients are equivalent. In the case of dense liquids, the thermodynamic factor is usually approximated by unity near the infinite dilution limit. However, in the extended critical region, the thermodynamic factor can largely differ from unity even for strongly diluted mixtures.

Intra-, MS and Fick diffusion coefficients of methane, benzene and toluene diluted in supercritical CO<sub>2</sub> were sampled in the temperature range between 295 and 335 K along the isobar  $p = 9$  MPa. The corresponding equations have been reported previously, e.g. in Ref. [6], and are not repeated here. Figure 8 shows the temperature dependence of the different diffusion coefficients predicted for the three diluted mixtures with a CO<sub>2</sub> mole fraction of  $x_{\text{CO}_2} = 0.99 \text{ mol}\cdot\text{mol}^{-1}$ . The MS diffusion coefficient predicted with Darken's equation is also shown. As expected, the intra-diffusion coefficient of CO<sub>2</sub> is lower than that of methane and higher than that of benzene and toluene because of the differing molecular mass. Further, Darken's equation is consistent with the predicted MS diffusion coefficient for all regarded mixtures, which suggests the presence of rather unspecific intramolecular interactions between unlike species. In general, the diffusion coefficients increase with temperature. Note that between 308 and 320 K, intra- and MS diffusion coefficients show a significant step-wise variation with temperature, which is related to the likewise strong change of the mixtures' density in this temperature range.

On the other hand, the Fick diffusion coefficient shows a different behaviour, which can be clearly observed for the mixtures with benzene and toluene, cf. Fig. 8. An anomalous decrease of the Fick diffusion coefficient with rising temperature was found, which can be explained on the basis of Eq. (1). The Fick diffusion coefficient consists of two contributions, the hydrodynamic represented by the MS diffusion coefficient  $D_{ij}$  and the thermodynamic contribution given by  $\Gamma$ . Although the MS diffusion coefficient increases strongly with temperature, the thermodynamic factor reaches values far below unity due to the proximity of the critical point. The combination of both effects yields the observed behaviour of the Fick diffusion coefficient.

A number of different expressions to predict the temperature dependence of the Fick diffusion coefficient for strongly diluted binary mixtures is available in the

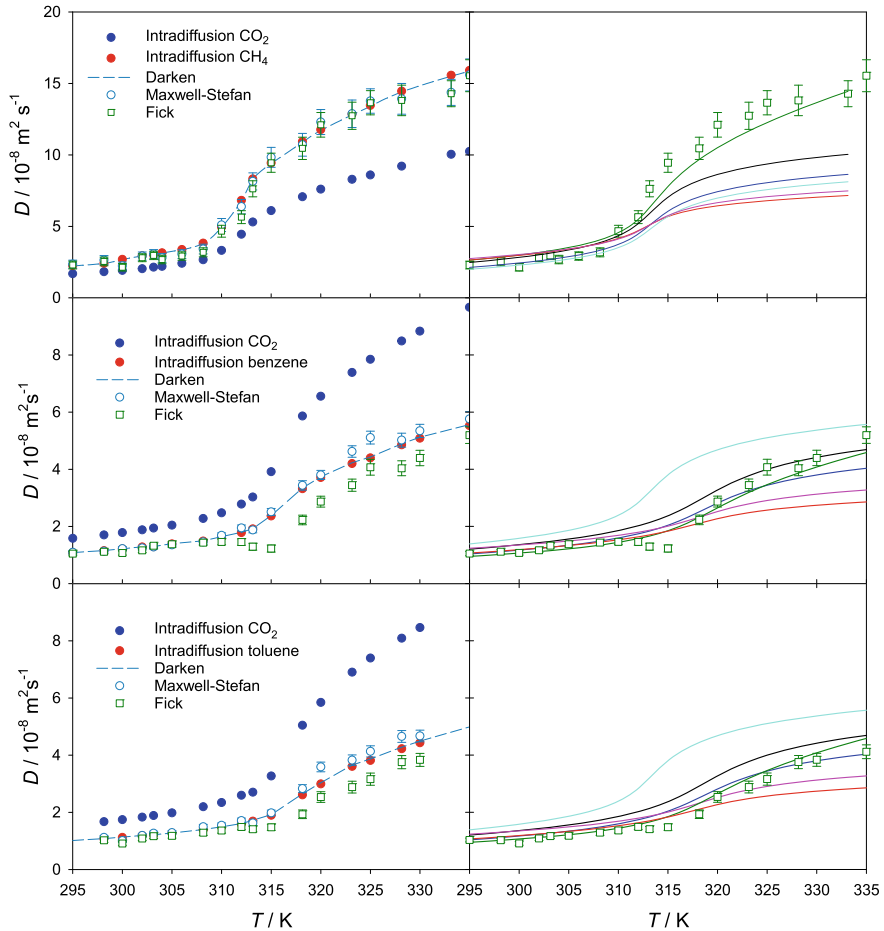


**Fig. 8** (left) Temperature dependence of the intra-, Maxwell-Stefan and Fick diffusion coefficients for the mixtures (top)  $\text{CH}_4 + \text{CO}_2$ , (center)  $\text{C}_6\text{H}_6 + \text{CO}_2$  and (bottom)  $\text{C}_7\text{H}_8 + \text{CO}_2$  at  $p = 9 \text{ MPa}$  and  $x_{\text{CO}_2} = 0.99 \text{ mol mol}^{-1}$ . (right) Simulation results for the Fick diffusion coefficient (green squares) are compared with predictive equations (lines) by Sassi et al. [24] (black), Wilke and Chang [30] (blue), Catchpole and King [1] (green), He and Yu [7] (red) and Scheibel [25] (cyan)

literature, many of which were developed exclusively for supercritical  $\text{CO}_2$  mixtures. Figure 8 shows the predicted Fick diffusion coefficient for the studied mixtures employing the equations by Sassi et al. [24], Scheibel [25], Wilke and Chang [30], Catchpole and King [1] as well as He and Yu [7]. Further equations are not shown for the sake of clarity. As can be seen, these equations yield significantly different values for the Fick diffusion coefficient at temperatures above 315 K. Generally, the equation proposed by Catchpole and King [1] yields the best agreement with present simulation results for all mixtures in the regarded temperature range. Other predictive equations show an acceptable agreement with simulation only for temperatures below

315 K, e.g. the well-known Wilke-Chang equation [30]. In general, it was observed that the predictive equations which explicitly include the solvent density perform better. However, it is clear that a trustworthy equation to predict the Fick diffusion coefficient under conditions regarded in this work is still to be developed.

## 6 Conclusions

With the overarching goal of transferring insight from the microscopic to the macroscopic scale, different studies were conducted by atomistic simulations to investigate mass transport across vapour-liquid interfaces under various conditions related to engineering applications.

Classical single-phase and two-phase shock tube scenarios were investigated using a model fluid (LJTS). As a reference data set, results of NEMD simulations were compared with those obtained from CFD simulations, for which the collaborating partner Munz and coworkers developed a new Riemann solver. By means of an accurate equation of state for the LJTS fluid as input for the CFD simulations, a direct comparison with the NEMD results became feasible. It showed an excellent agreement for the single-phase shock tube scenario and also very good agreement for the much more complex two-phase shock tube scenario.

The LJTS fluid was considered again for the investigation of the evaporation process across a planar interface. With a newly developed method, which allows to maintain stationary conditions for an arbitrarily long simulation time, it was possible to study large systems of up to  $8.4 \cdot 10^6$  particles of the LJTS fluid. Quantities like the hydrodynamic velocity, temperature and density were sampled directly and used to calculate further properties like the particle flux and the energy flux. Under the given boundary conditions, it was shown that both fluxes solely depend on the interface temperature.

The evaporation process across a planar interface was also studied for a more complex case, i.e. the binary mixture of liquid nitrogen and gaseous hydrogen. The conditions in the bulk phases were specified to correspond to the extreme conditions encountered in liquid propellant rocket engines, i.e. with strong temperature and composition gradients across the interface. The study focused on the question, under which conditions the atomisation process transitions from a classical spray to dense-fluid mixing. For this purpose, NEMD simulations were performed at three different pressure levels. At the lowest pressure level, the interface remained stable, whereas at the higher pressure levels, diffuse mixing was observed.

A detailed description of diffusion is important for the study of evaporation processes. Intra-, Maxwell-Stefan and Fick diffusion coefficients of methane, benzene and toluene diluted in supercritical carbon dioxide were predicted by equilibrium molecular dynamics simulation and the Green-Kubo formalism. Under near-critical conditions, it was observed that the Fick diffusion coefficient exhibits an anomalous behaviour, which was explained by the decrease of the thermodynamic factor. Further, several predictive equations for the Fick diffusion coefficient were compared

with present simulation results. Although some equations were able to reasonably predict the temperature dependence of the Fick diffusion coefficient at the studied conditions, none of the studied equations could be established as reliable.

**Acknowledgements** The authors kindly acknowledge the financial support by the Deutsche Forschungsgemeinschaft (DFG) within the SFB-TRR 75, project number 84292822. The simulations were performed on the national supercomputer HPE Apollo (Hawk) at the High Performance Computing Center Stuttgart (HLRS) as well as on the cluster Cray CS500 (Noctua) at the Paderborn Center for Parallel Computing (PC<sup>2</sup>) and the supercomputer SuperMUC-NG at the Leibniz Supercomputing Centre Garching (LRZ).

## References

1. Catchpole OJ, King MB (1994) Measurement and correlation of binary diffusion coefficients in near critical fluids. *Ind Eng Chem Res* 33:1828–1837
2. Chatwell RS, Heinen M, Vrabec J (2019) Diffusion limited evaporation of a binary liquid film. *Int J Heat Mass Transf* 132:1296–1305
3. Dahms RN, Oefelein JC (2015) Atomization and dense-fluid breakup regimes in liquid rocket engines. *J Propuls Power* 31:1221–1231
4. Fingerhut R, Guevara-Carrion G, Nitzke I, Saric D, Marx J, Langenbach K, Prokopev S, Celný D, Berreuther M, Stephan S, Kohns M, Hasse H, Vrabec J (2021) ms2: a molecular simulation tool for thermodynamic properties, release 4.0. *Comput Phys Commun* 262:107860
5. Grottel S, Krone M, Muller C, Reina G, Ertl T (2015) MegaMol—a prototyping framework for particle-based visualization. *IEEE Trans Vis Comput Graph* 21:201–214
6. Guevara-Carrion G, Janzen T, Munoz-Munoz YM, Vrabec J (2016) Mutual diffusion of binary liquid mixtures containing methanol, ethanol, acetone, benzene, cyclohexane, toluene, and carbon tetrachloride. *J Chem Phys* 144:124501
7. He CH, Yu YS (1998) New equation for infinite-dilution diffusion coefficients in supercritical and high-temperature liquid solvents. *Ind Eng Chem Res* 37:3793–3798
8. Heier M, Stephan S, Liu J, Chapman WG, Hasse H, Langenbach K (2018) Equation of state for the Lennard-Jones truncated and shifted fluid with a cut-off radius of 2.5 sigma based on perturbation theory and its applications to interfacial thermodynamics. *Mol Phys* 116:2083–2094
9. Heinen M, Vrabec J (2019) Evaporation sampled by stationary molecular dynamics simulation. *J Chem Phys* 151:044704
10. Hindenlang F, Gassner GJ, Altmann C, Beck A, Staudenmaier M, Munz CD (2012) Explicit discontinuous Galerkin methods for unsteady problems. *Comput Fluids* 61:86–93
11. Hitz T, Heinen M, Vrabec J, Munz CD (2020) Comparison of macro- and microscopic solutions of the Riemann problem I. Supercritical shock tube and expansion into vacuum. *J Comput Phys* 402:109077
12. Hitz T, JÄüns S, Heinen M, Vrabec J, Munz CD (2021) Comparison of macro- and microscopic solutions of the Riemann problem II. Two-phase shock tube. *J Comput Phys* 429:110027
13. Homes S, Heinen M, Vrabec J, Fischer J (2021) Evaporation driven by conductive heat transport. *Mol Phys* 119(15–16):e1836410
14. Köster A, Thol M, Vrabec J (2018) Molecular models for the hydrogen age: hydrogen, nitrogen, oxygen, argon, and water. *J Chem Eng Data* 63:305–320
15. Lautenschlaeger MP, Hasse H (2019) Transport properties of the Lennard-Jones truncated and shifted fluid from non-equilibrium molecular dynamics simulations. *Fluid Phase Equilib* 482:38–47
16. Lemmon EW, Jacobsen RT (2004) Viscosity and thermal conductivity equations for nitrogen, oxygen, argon, and air. *Int J Thermophys* 25:21–69

17. Medina I (2012) Determination of diffusion coefficients for supercritical fluids. *J Chromatogr A* 1250:124–140
18. Merker T, Engin C, Vrabec J, Hasse H (2010) Molecular model for carbon dioxide optimised to vapour-liquid equilibria. *J Chem Phys* 132:34512
19. Müller H, Pfitzner M, Mattheis J, Hickel S (2016) Large-eddy simulation of coaxial LN<sub>2</sub>/GH<sub>2</sub> injection at trans- and supercritical conditions. *J Propuls Power* 32:46–56
20. Niethammer C, Becker S, Bernreuther M, Buchholz M, Eckhardt W, Heinecke A, Werth S, Bungartz HJ, Glass CW, Hasse H, Vrabec J, Horsch M (2014) ls1 mardyn: The massively parallel molecular dynamics code for large systems. *J Chem Theory Comput* 10:4455–4464
21. Nikolai P, Rabiyat B, Aslan A, Ilmutdin A (2019) Supercritical CO<sub>2</sub>: properties and technological applications—a review. *J Thermal Sci* 28:394–430
22. Oschwald M, Schik A, Klar M, Mayer W (1999) Investigation of coaxial LN<sub>2</sub>/GH<sub>2</sub>-injection at supercritical pressure by spontaneous raman scattering. In: 35th joint propulsion conference and exhibit
23. Rutkai G, Thol M, Span R, Vrabec J (2016) How well does the Lennard-Jones potential represent the thermodynamic properties of noble gases? *Mol Phys* 115:1104–1121
24. Sassié PR, Mourier P, Caude MH, Rosset RH (1987) Measurement of diffusion coefficients in supercritical carbon dioxide and correlation with the equation of Wilke and Chang. *Anal Chem* 59:1164–1170
25. Scheibel EG (1954) Liquid diffusivities. *Ind Eng Chem* 46:2007–2008
26. Suarez JJ, Medina I, Bueno JL (1998) Diffusion coefficients in supercritical fluids: available data and graphical correlations. *Fluid Phase Equilib* 153:167–212
27. Taylor R, Krishna R (1993) Multicomponent mass transfer. Wiley, New York
28. Traxinger C, Pfitzner M, Baab S, Lamanna G, Weigand B (2019) Experimental and numerical investigation of phase separation due to multicomponent mixing at high-pressure conditions. *Phys Rev Fluids* 4:074303
29. Vrabec J, Stoll J, Hasse H (2001) A set of molecular models for symmetric quadrupolar fluids. *J Phys Chem B* 105:12126–12133
30. Wilke CR, Chang P (1955) Correlation of diffusion coefficients in dilute solutions. *AIChE J* 1:264–270
31. Zhang J, Müller-Plathe F, Yahia-Ouahmed M, Leroy F (2013) A steady-state non-equilibrium molecular dynamics approach for the study of evaporation processes. *J Chem Phys* 139:134701

**Open Access** This chapter is licensed under the terms of the Creative Commons Attribution 4.0 International License (<http://creativecommons.org/licenses/by/4.0/>), which permits use, sharing, adaptation, distribution and reproduction in any medium or format, as long as you give appropriate credit to the original author(s) and the source, provide a link to the Creative Commons license and indicate if changes were made.

The images or other third party material in this chapter are included in the chapter's Creative Commons license, unless indicated otherwise in a credit line to the material. If material is not included in the chapter's Creative Commons license and your intended use is not permitted by statutory regulation or exceeds the permitted use, you will need to obtain permission directly from the copyright holder.



# Numerical Simulation of Heat Transfer and Evaporation During Impingement of Drops onto a Heated Wall



Henrik Sontheimer, Christiane Schlawitschek, Stefan Batzdorf,  
Peter Stephan, and Tatiana Gambaryan-Roisman

**Abstract** In this study, hydrodynamics and heat transport during the impact of single and multiple drops onto a hot wall are studied numerically. The heat transfer in the vicinity of the three-phase contact line, where solid, liquid and vapour meet, contributes significantly to the global heat transfer. The microscale processes in the region of the three-phase contact line are analysed using a lubrication approximation. The results in the form of correlations are integrated into an overall model. The impingement of drops on a macro scale is simulated using a numerical model developed within the OpenFOAM library. The influence of dimensionless parameters, i.e., the Reynolds, Weber, Bond, Prandtl and Jakob numbers, as well as the influence of pressure, on the transport phenomena is discussed. The analysis of the influence of drop frequency and substrate thickness during the vertical coalescence and the influence of the drop spacing during the horizontal coalescence of drops on the hot surface complete the study. The results contribute to a better understanding of the complex mechanisms of spray cooling.

## 1 Introduction

Spray cooling is a very promising technology for the cooling of electronic devices. The hydrodynamic and heat transport processes that occur during the impact of a spray onto a hot wall are very complex. The first step towards an understanding of spray cooling mechanisms is the investigation of single and multiple drops impacting onto hot walls. The impact of single and multiple drops onto hot walls is also relevant to numerous additional industrial applications, such as falling-film evaporators, drop impingement onto steam turbine blades, metal quenching and direct-fuel injection [17, 18].

---

H. Sontheimer (✉) · C. Schlawitschek · S. Batzdorf · P. Stephan · T. Gambaryan-Roisman  
Institute for Technical Thermodynamics (TTD), Technical University of Darmstadt, Darmstadt,  
Germany  
e-mail: [sontheimer@ttd.tu-darmstadt.de](mailto:sontheimer@ttd.tu-darmstadt.de)

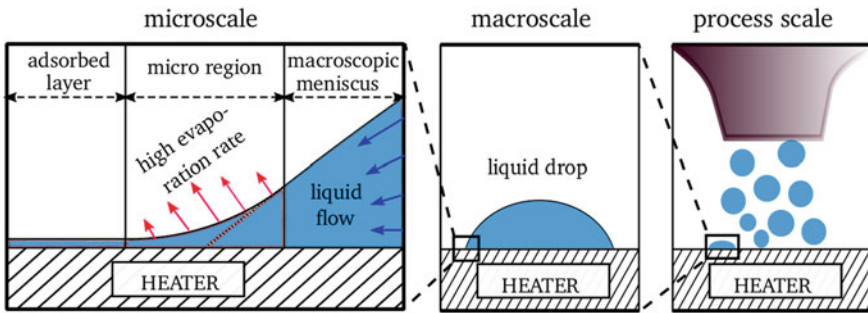


**Fig. 1** Different length scales of relevant hydrodynamic and heat transport processes during the impact of a spray onto a superheated wall

If a drop impacts onto a superheated wall, strong temperature gradients and extremely high local heat fluxes occur in the vicinity of the three-phase contact line, where solid, liquid and vapour meet. The hydrodynamics and heat transport at the macroscopic scale are influenced by the transport processes in the vicinity of the three-phase contact line. To understand the complex mechanisms during the drop impact, it is necessary to analyse the processes occurring at both the micro and the macro scales (see Fig. 1).

Comprehensive reviews of current experimental, numerical and analytical studies on the impact of a single drop onto non-heated walls are presented in [14, 19, 21, 23, 27]. Depending on the impact parameters, material properties and surface roughness, six characteristic impingement scenarios have been identified: drop deposition, prompt splash, corona splash, receding breakup, and partial and full rebound. If the wall is heated above the saturation temperature, the outcome additionally depends strongly on the wall superheat. Liang and Mudawar [17] identified four distinct scenarios: film evaporation, nucleate boiling, transition boiling and film boiling. Additionally, Breitenbach et al. [4] identified the thermal atomization regime. The focus of the present work is on the drop impingement at moderate Reynolds, Weber and Jakob numbers in the drop deposition and film evaporation regimes. Evaporation into a pure vapour atmosphere is considered.

In this study, numerical simulations are used to study the impact of single and multiple drops onto a hot wall with special consideration of the processes in the vicinity of the three-phase contact line (micro region). The hydrodynamic and heat transport processes in the micro region are analysed by means of a one-dimensional lubrication model and direct numerical simulations. On the macro scale, hydrodynamics and heat transfer during the drop impact over a wide range of dimensionless parameters are studied. Both a compressible and an incompressible solver are used to study the drop impact at different pressures. Furthermore, the influence of substrate thickness and drop frequency during the vertical coalescence of multiple successive impacting drops is analysed. Lastly, the horizontal coalescence of two simultaneously impacting drops is studied. The numerical results are compared with experimental results (see Gholijani et al. [in this volume](#)).

## 2 Overview of the Numerical Model

The impact phenomena considered in this study take place on a millimetre scale. The transport processes in the micro region are determined on a submicrometre scale. This scale difference necessitates a modular modelling approach, in which the micro region phenomena are considered separately, and the results are incorporated into the macroscale model (see Fig. 1) in the form of correlations. A lubrication approximation is used to simulate the micro region, and computational fluid dynamics simulations are used for the overall macroscale model. Additionally, a full-scale numerical simulation of the micro region has been used to determine the validity limits of the lubrication approximation for the micro region description. Beyond the applicability limits of the lubrication approximation, the full-scale numerical simulation can be used for the description of transport processes in the micro region.

Most simulations presented here use the refrigerant perfluorohexane (FC-72) at saturation conditions as a working fluid. The drop impinges onto a superheated calcium fluoride glass ( $\text{CaF}_2$ ), allowing the simulation results to be directly linked and compared with associated experimental results (see Gholijani et al. [in this volume](#)).

## 3 Modelling of the Micro Region

In this section, the micro region model in the framework of one-dimensional lubrication theory is briefly described and results using this model are presented. The influence of governing parameters on the output of the micro region model is analysed. Furthermore, a direct full-scale numerical simulation of the micro region is performed.

### 3.1 One-Dimensional Lubrication Model

Potash and Wayner [20] assumed in their concept of the contact line in an evaporating perfectly wetting liquid that a thin adsorbed film of fluid molecules covers the apparently dry wall (see Fig. 1). They suggested that the heat and mass flow at the apparent contact line are determined by the film thickness distribution in a micro region, or the region between the adsorbed film with thickness  $\delta_{\text{ad}}$  and the macroscopic meniscus. Stephan and Busse [26] have used the micro region approach to predict the evaporation rate from a groove at the heat pipe evaporator. Herbert et al. [12] and Schlawitschek [24] extended this model to account for the contact line velocity within a moving reference frame, the effect of recoil pressure, and the Kapitza resistance (a thermal resistance at the solid–liquid interface). A detailed and comprehensive description as well as the discussion of the assumptions made during the derivation of this model can be found in [1, 24]. Steady-state, incompressible Navier-Stokes

equations and the energy conservation equation are used to model the micro region. By using the one-dimensional lubrication approximation, a system of four coupled first order ordinary, non-linear differential equations can be derived.

Thermal resistances at the solid–liquid interface ( $R_{\text{Kap}}$ ), within the liquid ( $R_{\text{liq}}$ ) and at the liquid–vapour interface ( $R_{\text{int}}$ ) are taken into account. Furthermore, the effect of the augmented capillary pressure, which includes the vapour recoil and the disjoining pressure, is included. The model allows for the computation of the apparent contact angle  $\theta$ , the film thickness distribution, and the integrated heat flux  $\dot{Q}_{\text{mic}}$  as functions of the wall superheat,  $\Delta T = T_{w,\text{mic}} - T_{\text{sat}}$ , and the contact line velocity  $u_{\text{cl}}$ . The model is restricted to perfectly wetting fluids and small contact angles.

### 3.2 Influence of Contact Line Velocity and Local Wall Superheat

The integrated heat flux and the apparent contact angle predicted by the one-dimensional lubrication model of the micro region are depicted in Fig. 2 as functions of contact line speed and local wall superheat. The apparent contact angle increases with increasing wall superheat. This can be explained by the increasing evaporation rate, which is balanced by the enhanced liquid flow from the macroscopic meniscus. The enhanced flow is possible due to the higher film thickness gradients. The numerical predictions agree well with the experimentally observed static contact angle of less than  $3^\circ$  under isothermal conditions and about  $35^\circ$  for a wall superheat of  $\Delta T = 10 \text{ K}$  [12]. The increasing wall superheat also leads to an increase in integrated heat flux. The apparent contact angle increases with the contact line speed. This can be explained by the fact that, in the reference frame fixed at the advancing

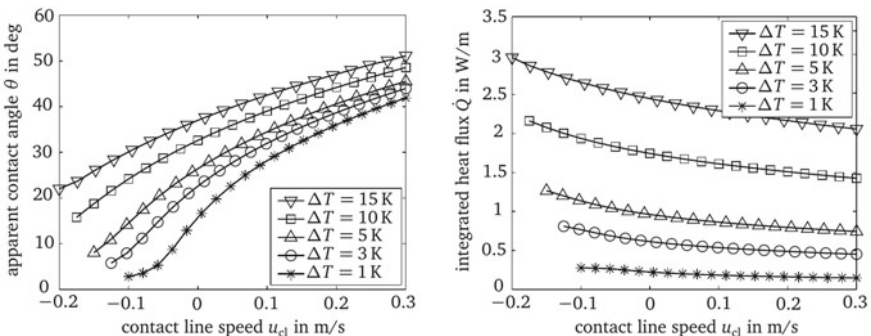


**Fig. 2** Influence of the contact line velocity  $u_{\text{cl}}$  and wall superheat  $\Delta T$  on the apparent contact angle  $\theta$  (left) and integrated heat flux  $\dot{Q}_{\text{mic}}$  (right). The Kapitza resistance is neglected in this study [1]

contact line, the moving wall transports liquid out of the micro region. The pressure difference between the macroscopic meniscus and the adsorbed layer is fixed by the wall superheat. As a result, the required liquid flow rate from the macroscopic meniscus is reached by an increase in the cross-sectional area. The concomitant increase in film thickness and of the thermal resistance of the liquid layer leads to a decrease in integrated heat flux.

### 3.3 Influence of Material Properties and Pressure

It can be observed in Fig. 3 that the contact angle and integrated heat flux in the micro region are very sensitive to changes in material properties. Material properties might change with changing pressure or by using a different fluid. The variation of liquid viscosity  $\nu_l$  and thermal conductivity  $k_l$  by an order of magnitude or more has a strong influence both on the apparent contact angle and integrated heat flux. However, this is only relevant if a different fluid is chosen, since these properties only moderately depend on pressure. In contrast, the saturated vapour density  $\rho_v$ , surface tension  $\sigma$  and latent heat of vaporisation  $\Delta h_v$  strongly depend on the ambient pressure and have a strong influence on the apparent contact angle as well as the integrated heat flux. Furthermore, the figure illustrates that small changes in material properties resulting from possible measurement uncertainties have a weak influence on the apparent contact angle and integrated heat flux.

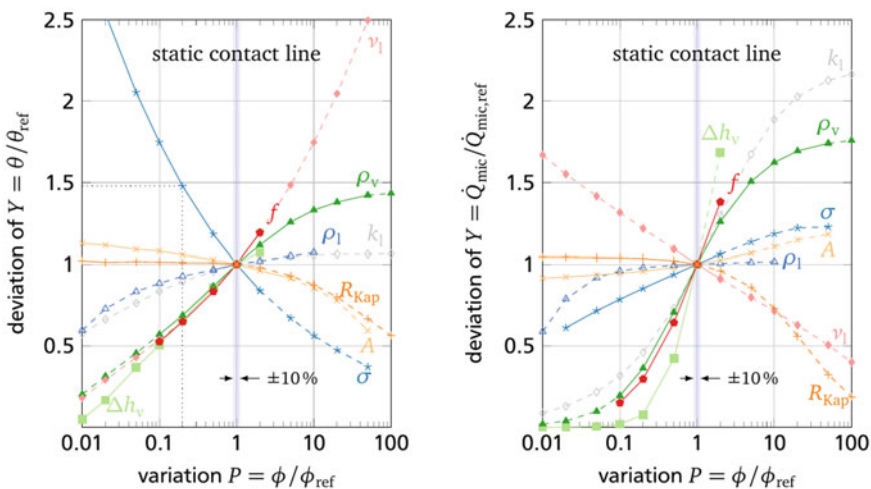


**Fig. 3** Sensitivity of the apparent contact angle  $\theta$  (left) and integrated heat flux  $\dot{Q}_{\text{mic}}$  (right) in dependency of the material properties  $\phi$ , exemplary for a static contact line and a wall superheat of  $\Delta T = 5 \text{ K}$ . Solid lines indicate a variation within the available data range in the literature; dashed lines indicate additional variations [24]

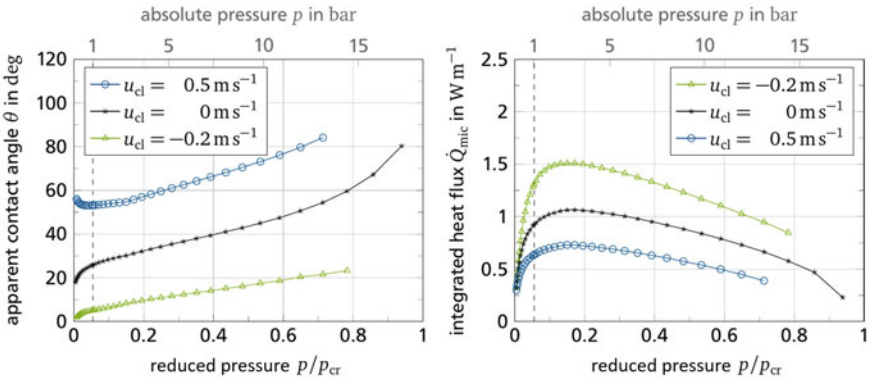


**Fig. 4** Influence of the pressure  $p$  on the apparent contact angle  $\theta$  (left) and integrated heat flux  $\dot{Q}_{\text{mic}}$  (right) for a receding, static and advancing contact line [24]

The influence of the ambient pressure on the apparent contact angle and integrated heat flux is shown in Fig. 4 and can be attributed to the change in the material properties. For static and receding contact lines, the apparent contact angle increases with pressure. For advancing contact lines, a local minimum of the apparent contact angle at approximately 1 bar is predicted. One of the significant factors affecting the increasing contact angle with pressure is the decreasing surface tension. The integrated heat flux depends on pressure non-monotonically. This behaviour is determined by a combined effect of simultaneously changing different material properties. In particular, the integrated heat flux decreases with increasing thermal resistance, which is a combination of the resistance at the liquid–vapour interface, the resistance of the liquid layer and the Kapitza resistance. The influence of pressure on the total average thermal resistance as well as on its components is illustrated in Fig. 5. For low pressures the thermal resistance at the liquid–vapour interface dominates, and at high pressures the thermal resistance within the liquid dominates. The Kapitza resistance has been calculated by Han et al. [10] for the combination of FC-72 and chromium using molecular dynamics simulations. It has been found that the Kapitza resistance is independent of pressure in the relevant range and is small compared to the total resistance over the entire pressure range. The total thermal resistance reaches a minimum in the pressure range corresponding to the maximum integrated heat flux.

### 3.4 Full-Scale Numerical Simulation of the Transport Processes in the Micro Region

Stationary, incompressible, three-dimensional Navier-Stokes equations and the energy balance equation are solved numerically using the OpenFOAM library. The momentum balance contains terms accounting for adhesion forces. Gravity is

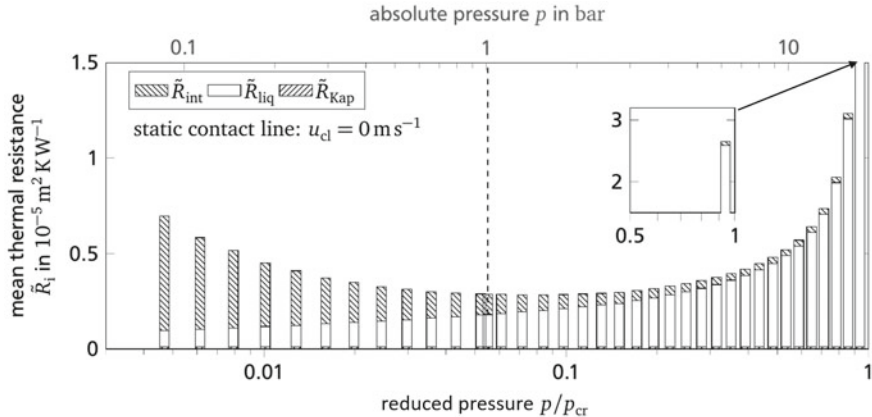


**Fig. 5** Different thermal resistances of the micro region averaged over the length of the micro region for different pressures, exemplary for a static contact line and a wall superheat of  $\Delta T = 5$  K [24]

neglected. In contrast to the one-dimensional lubrication model, the full scale numerical model is valid for apparent contact angles up to  $90^\circ$ . For larger apparent contact angles, the computational domain and the boundary conditions would have to be changed. A complete description of the numerical model can be found in [1, 3].

In [3], results of the direct numerical simulation are analysed and compared with results from the one-dimensional lubrication model. A parabolic velocity profile and a nearly linear temperature profile within the micro region for moderate wall superheats is shown in the results of the direct numerical simulation. The calculated apparent contact angle and integrated heat flux agree well with the results from the one-dimensional lubrication model up to the apparent contact angle of  $40^\circ$ . However, the direct numerical simulation predicts slightly higher heat flux values than the one-dimensional lubrication model, especially at high wall superheats. It has been shown that the deviation between the results of the full-scale numerical simulations and the lubrication model are mainly attributed to the assumption of one-dimensional heat conduction.

The errors in the evaluation of integrated heat flux are acceptable for moderate apparent contact angles, and the use of the lubrication approximation is justified, taking into account the significant reduction of computational efforts in comparison with the full-scale numerical simulation.

In addition, the full-scale numerical simulation has been used to study the micro region evaporation on a nanostructured wall consisting of periodically arranged cubes with a side length of 5 nm. This side length is comparable to the adsorbed film thickness. A part of the evaporating film near the curvilinear non-evaporating adsorbed film is shown in Fig. 6. In [3], it is shown that the apparent contact angle is slightly smaller for the structured wall than for the smooth wall. However, almost no change in the integrated heat flow is observed. Hence, for a static contact line, the structure

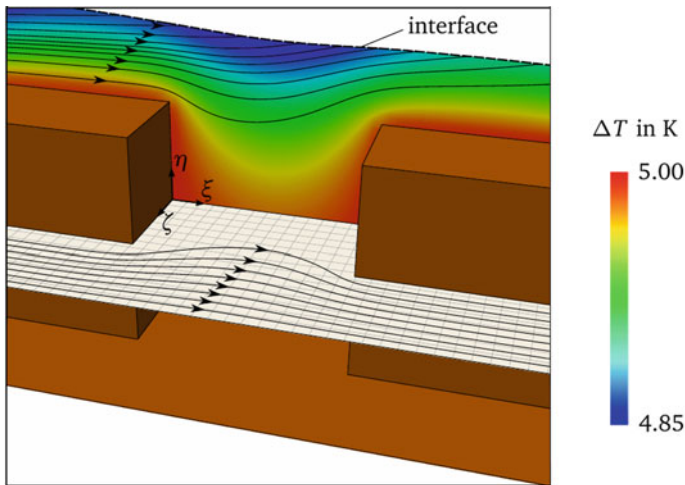


**Fig. 6** Streamlines and temperature profile in the micro region close to the adsorbed film layer for a static contact line and a wall superheat of  $\Delta T = 5$  K on a nanostructured wall. Reprinted from [3] with permission from ASME

of the wall can be neglected, as long as the length scale of the structure is on the order of the adsorbed film layer or smaller. More details on the investigation of the micro region using the full-scale numerical simulations can be found in [1, 3].

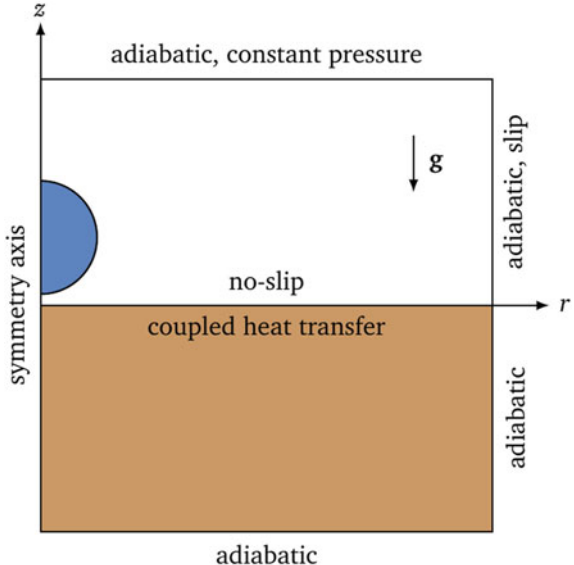
## 4 Macroscale Model

In this section, a macroscale model for simulation of a single drop impact onto a smooth, hot wall is presented. The numerical model developed within the OpenFOAM library is based on the interFoam solver. Hydrodynamics and heat transport phenomena are described, and the influence of dimensionless parameters and of system pressure on transport processes is analysed. Second, the macroscale model is applied to study the impact of multiple drops and their coalescence on a smooth, hot wall. Illustrative videos for different drop impact scenarios can be found in [25].

### 4.1 Model Description

The numerical model is based on the works of Kunkelmann [15] and Batzdorf [1]. Batzdorf [1] has applied the model to the description of the drop impact onto a smooth, hot wall. For a complete, comprehensive overview of the solver for incompressible flow, the reader is referred to [1]. More information on the solver for compressible flow developed by Schlawitschek [24] is given in Sect. 4.2.3.

**Fig. 7** Computational domain and boundary conditions for the 2D axis-symmetric grid. The opening angle of the wedge is  $5^\circ$ . A thermal boundary layer in the vapour region close to the wall is initialised prior to the simulation. Dimensions of the domain are chosen such that boundary conditions do not influence the drop impingement process [1]



It is shown in associated experiments in [6, 7] that no three-dimensional effects (like splash) are observed for the investigated parameter range. Hence, a static, structured 2D axis-symmetric grid with local grid refinement at the solid-fluid interface is chosen. Only for the case of the horizontal coalescence (Sect. 4.3.2), a dynamically refined 3D grid is chosen. In Fig. 7 the computational domain and the boundary conditions are illustrated.

The governing equations in the fluid region describe the conservation of mass, momentum and energy. Source terms ( $\Sigma_V$ ,  $\Sigma_e$ ) are added to the mass and energy equations to account for heat and mass transfer at the interface. Gravitational and surface tension forces ( $\rho g$ ,  $f_\sigma$ ) are included in the momentum equation. The system of transport equations has the form:

$$\nabla \cdot \mathbf{u} = \Sigma_V \quad (1)$$

$$\rho \left[ \frac{\partial \mathbf{u}}{\partial t} + (\mathbf{u} \cdot \nabla) \mathbf{u} \right] = \nabla \cdot \left[ -p - \frac{2}{3} \mu (\nabla \cdot \mathbf{u}) \mathbf{I} + \mu (\nabla \mathbf{u} + (\nabla \mathbf{u})^T) \right] + \rho \mathbf{g} + \mathbf{f}_\sigma \quad (2)$$

$$\frac{\partial (\rho c T)}{\partial t} + \nabla \cdot (\rho c \mathbf{u} T) = \nabla \cdot (k \nabla T) + \Sigma_e \quad (3)$$

In the solid region, only the energy conservation equation is solved:

$$\frac{\partial (\rho c T)}{\partial t} = \nabla \cdot (k \nabla T) \quad (4)$$

An explicit Dirichlet-Neumann algorithm is used to couple the solid and fluid regions. The volume-of-fluid method is used to track the interface. An additional compressive term counteracting the numerical diffusion is included in the transport equation for the volume fraction field  $F$ :

$$\frac{\partial F}{\partial t} + \nabla \cdot (\mathbf{u} F) + \nabla \cdot [c_F |\mathbf{u}| |\mathbf{n}_{\text{int}}| (1 - F) F] = \Sigma_v F \quad (5)$$

By considering the iso-surface of  $F = 0.5$ , the interface is reconstructed continuously. The evaporation model was developed by Kunkelmann and Stephan [16] and further developed by Herbert et al. [12]. At the interface, the saturation temperature is assumed to hold for both liquid and vapour. Temperature gradients normal to the interface are used to calculate the heat fluxes. The method developed by Hardt and Wondra [11] is used to enhance numerical stability. The results of the one-dimensional lubrication model of the micro region introduced in Sect. 3.1 are incorporated into the macroscale simulation using parametrised regressions to accurately calculate the contact angle  $\theta$ , integrated heat flux  $\dot{Q}_{\text{mic}}$  and film thickness  $\delta$  in dependency of wall superheat  $\Delta T$  and contact line velocity  $u_{\text{cl}}$  in the range of  $5 \text{ K} \leq \Delta T \leq 20 \text{ K}$  and  $-0.1 \text{ ms}^{-1} \leq u_{\text{cl}} \leq 2 \text{ ms}^{-1}$ , respectively.

## 4.2 Single Drop Impact

A detailed description and validation of the model describing the single drop impact onto a smooth, hot wall at ambient pressure, including the mesh independence study, is given in [1].

### 4.2.1 Basic Hydrodynamic and Heat Transport Phenomena

The numerical prediction of the evolution of spreading radius  $R_{\text{cl}}$  and of solid-drop heat flow  $\dot{Q}$ , which is validated by comparison with experimental data, is shown in Fig. 8. Details of the experimental setup and procedure can be found in [5, 12]. The impingement process can be divided into three phases: spreading phase (I), receding phase (II) and sessile drop phase (III). The kinetic energy of the impacting drop leads to quick spreading on the surface. Kinetic energy is then partly converted into surface energy and partly dissipated. After reaching the maximum contact line radius, surface tension forces the drop to recede, and the kinetic energy rises again. After the receding phase, the drop oscillates around its stationary state with decreasing amplitude.

During the spreading phase, the heat flow is dominated by convection due to high spreading velocities. The maximum heat flow is reached before the maximum contact line radius due to decreasing spreading velocities. The role of evaporation

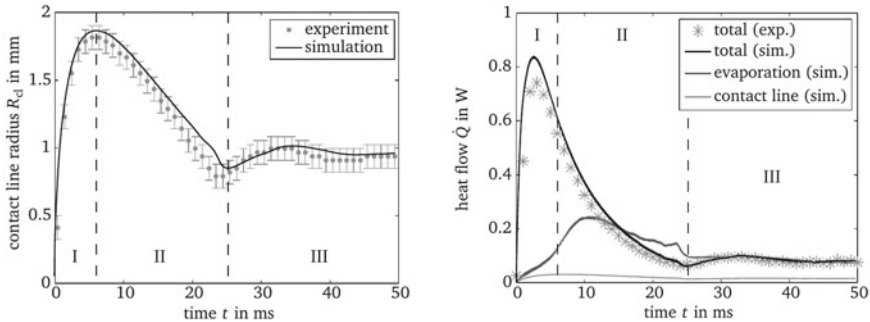


**Fig. 8** Contact line radius  $R_{cl}$  (left) and heat flow  $\dot{Q}$  (right) over time for the impact of a single drop ( $D_0 = 0.977$  mm,  $u_0 = 0.584$  ms $^{-1}$ ) onto a smooth, hot wall ( $\Delta T = 17.4$  K,  $\dot{q}_{\text{heater}} = 9500$  W m $^{-2}$ ). The total heat flow describes the heat transferred from the wall to the drop, the evaporation heat flow describes the heat transfer by evaporation, and the contact line heat flow describes the heat transfer in the vicinity of the three-phase contact line [1]

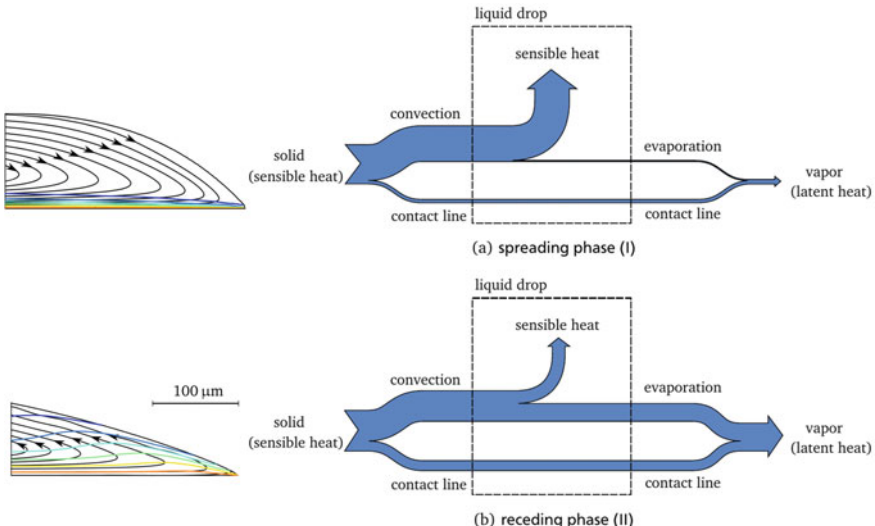


**Fig. 9** Exemplary heat transfer paths during the **a** spreading phase and **b** receding phase. The thickness of the paths shows the proportion of the heat transferred. The corresponding isotherms with a spacing of  $\Delta T = 2$  K and streamlines are shown in a moving reference frame close to the contact line [1]

increases during the receding phase. Especially at low velocities, the evaporation at the three-phase contact line can contribute up to 50% of the overall heat transfer [12].

The role of heat transfer mechanisms during the spreading and receding phases is illustrated in Fig. 9. During the spreading phase, the vortex in the vicinity of the apparent contact line transports the cold liquid towards the wall. This enhances the

convective heat transport. During the receding phase, the vortex changes its direction and transports hot liquid from the wall to the liquid–vapour interface. This effect leads to a decrease in the convective transport and to the enhancement of evaporation.

#### 4.2.2 Influence of Dimensionless Parameters

In this section, the influence of dimensionless parameters, i.e., the Reynolds ( $Re$ ), Weber ( $We$ ), Bond ( $Bo$ ), Prandtl ( $Pr$ ) and Jakob ( $Ja$ ) numbers, on the evolution of the spreading ratio (the relation between the drop footprint diameter and the initial drop diameter,  $S$ ) and the evolution of dimensionless cumulative heat transported from the solid to the drop,  $E^*$ , during the single drop impact onto a hot wall, is presented. Detailed discussions of the results can be found in [1, 13]. The significant influence of the Reynolds number on the maximum spreading shown in Fig. 10 is attributed to the competition between the inertial and friction forces during the spreading phase. The amplitude of drop oscillations before reaching the mechanically stable sessile shape increases with increasing  $Re$ . An increase in the Weber number leads to significant

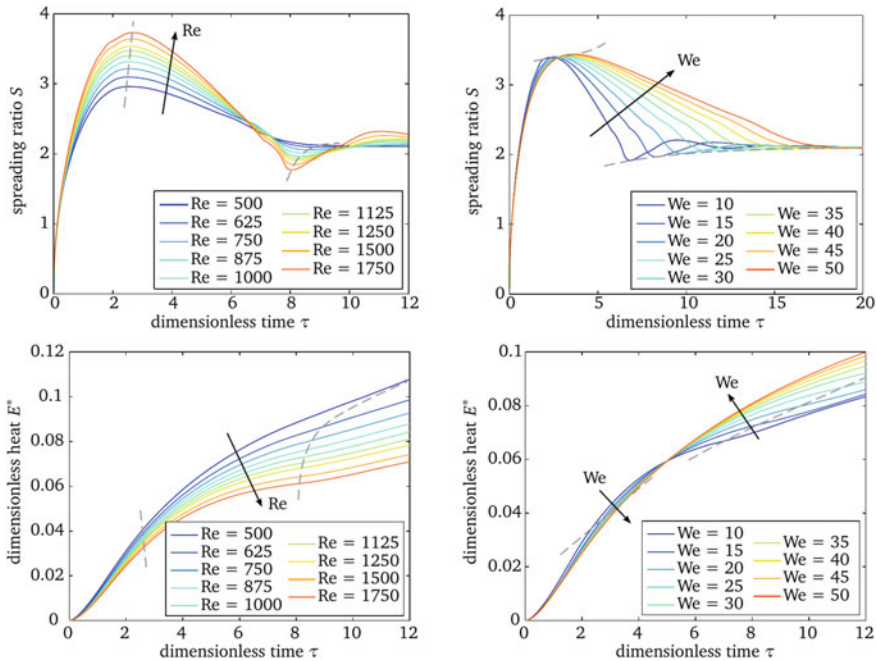


**Fig. 10** Influence of Reynolds ( $Re = \rho_l D_0 u_0 \mu_l^{-1}$ , left) and Weber ( $We = \rho_l D_0 u_0^2 \sigma^{-1}$ , right) numbers on the spreading ratio ( $S = D_{cl} D_0^{-1}$ ) and dimensionless heat ( $E^* = 6Q(\pi \rho_l D_0^3 h_{lv})^{-1}$ ) for the single drop impact onto an isothermal, hot wall ( $\Delta T = 10$  K). Results are obtained by changing the initial drop diameter  $D_0$ , impact velocity  $u_0$  and gravitational acceleration  $g$ , and keeping all other dimensionless numbers constant [1]

prolongation of the receding phase, since the role of surface tension, which is the driving force for the drop receding, decreases in comparison to inertia with increasing  $We$ .

Despite an increase in the maximum spreading ratio and thus the wetted area, the dimensionless cumulative heat decreases with increasing  $Re$ , since increasing  $Re$  at constant  $We$  corresponds to larger drop volume (the denominator in the definition of  $E^*$ ). Increasing  $We$  leads to decreasing  $E^*$  during the spreading phase and increasing  $E^*$  during the receding phase, which decelerates with increasing  $We$ .

Higher Bond numbers lead to higher maximal spreading and enhanced heat transfer. Increasing the Prandtl number increases the spreading ratio as well, but leads to a decrease in cumulative heat transfer. Increasing the Jakob number by increasing the wall superheat leads to an increase in the apparent contact angle and, consequently, to a decrease in the maximum spreading ratio and deceleration of the receding phase. The transferred heat increases with increasing Jakob numbers. The dependence of dimensionless parameters on the maximum spreading ratio and dimensionless heat transfer has been summarised in the form of correlations [1].

#### 4.2.3 Influence of Ambient Pressure

The analysis in this work is limited to reduced pressures of up to  $P^* = pp_{\text{crit}}^{-1} = 0.5$ . The solver of the macroscale model has been extended to account for compressibility effects and validated by Schlawitschek [24]. The governing equations in the fluid region (Eq. 1–3) have been modified: a source term has been added to the mass conservation equation to account for compressibility effects; the momentum and energy balance equations have been modified to account for the variable density. The density is calculated with a linearised Peng–Robinson equation of state. A complete, comprehensive description of the compressible solver is given in [24].

In the study on low and high ambient pressure presented in Fig. 11, all impact parameters are kept constant. The Reynolds, Weber, Bond and Jakob numbers increase with increasing pressure, while the Prandtl number decreases with increasing pressure. The maximum spreading ratio slightly increases with increasing pressure, which can be attributed to the dominant role of the Reynolds number. The dimensionless cumulative heat increases with increasing pressure, although the dimensional cumulative heat decreases with increasing pressure [24]. However, the drop mass and the latent heat of evaporation, which constitute the denominator in the definition of  $E^*$ , decrease at higher pressures stronger than  $Q$ . Further details related to the influence of pressure on hydrodynamics and heat transfer during single drop impingement onto a hot surface can be found in [24].

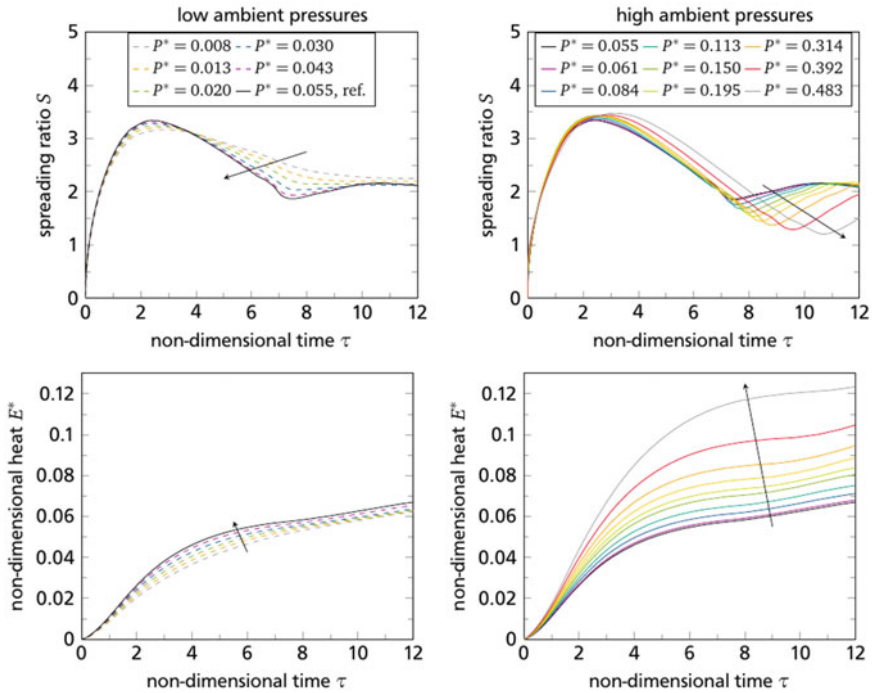


**Fig. 11** Influence of low (left) and high (right) ambient pressure ( $P^* = pp_{\text{crit}}^{-1}$ ) on the spreading ratio ( $S = D_{\text{cl}}D_0^{-1}$ ) and dimensionless heat ( $E^* = 6Q(\pi\rho_1D_0^3h_{\text{lv}})^{-1}$ ) for the single drop impact ( $D_0 = 1.0241 \text{ mm}$ ,  $u_0 = 0.2735 \text{ ms}^{-1}$ ) onto an isothermal, hot wall ( $\Delta T = 10 \text{ K}$ ) [24]

### 4.3 Multiple Drop Impact

In the spray cooling process, many drops impact successively and simultaneously onto a hot wall. The interaction between the drops governs the hydrodynamics and heat transport phenomena during spray cooling. In this chapter, the vertical and horizontal coalescence of drops over a hot surface are studied numerically.

#### 4.3.1 Vertical Coalescence

In this section, the impingement of chains of drops with identical impact parameters onto the same location is studied numerically. The predicted evolution of the contact line radius for the case of an impact of consequent drops onto a sessile drop has been compared with experimental results and shows good agreement (see Fig. 12). The experimental setup and procedure are described in [6, 7]. After the impact and coalescence of two drops, the combined drop spreads. The maximum spreading

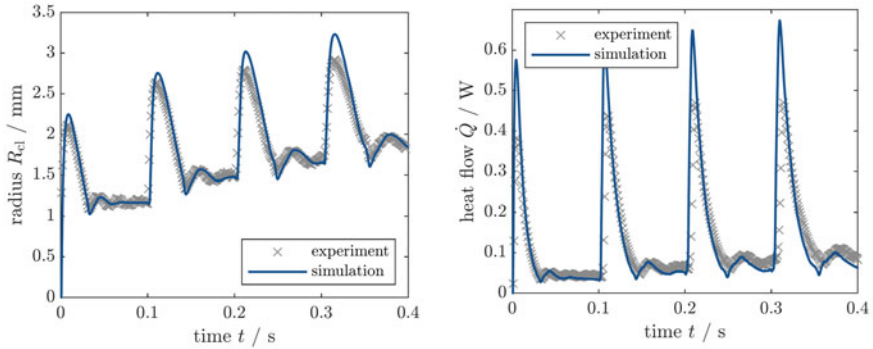


**Fig. 12** Contact line radius  $R_{\text{cl}}$  and heat flow  $\dot{Q}$  from the wall to the drop over time for four successively impacting drops ( $D_0 = 1.14 \text{ mm}$ ,  $u_0 = 0.54 \text{ ms}^{-1}$ ) onto a smooth, hot wall ( $\Delta T = 9.8 \text{ K}$ ,  $\dot{q}_{\text{heater}} = 2900 \text{ W m}^{-2}$ )

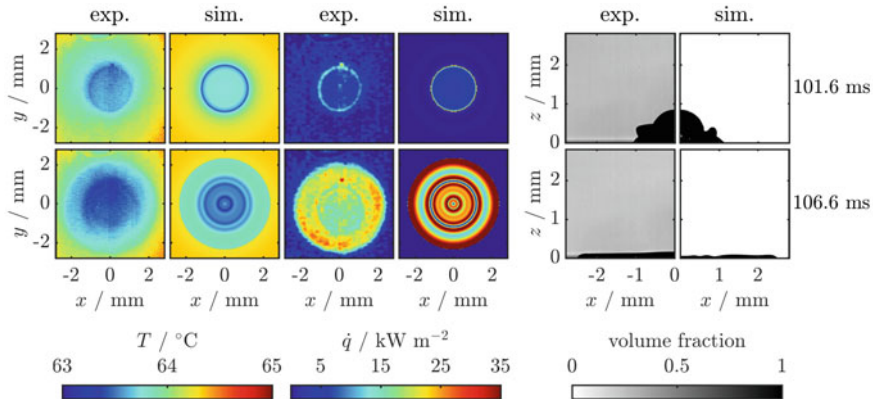


**Fig. 13** Comparison between experiments (exp.) and simulations (sim.) of temperature ( $T$ ) and heat flux ( $\dot{q}$ ) fields at the drop footprint as well as the side (exp.) and cross-sectional (sim.) views during the vertical coalescence onto a sessile drop ( $D_0 = 1.14 \text{ mm}$ ,  $u_0 = 0.54 \text{ ms}^{-1}$ ,  $\Delta T = 9.8 \text{ K}$ ,  $\dot{q}_{\text{heater}} = 2900 \text{ W m}^{-2}$ )

radius increases with each subsequent drop impact, and the oscillations preceding the sessile drop phase are more pronounced with each subsequent drop impact.

In Fig. 13, the snapshots of drop shape, wall temperature and wall heat flux distributions at two time instants (the first around one millisecond after the impact of second drop and the second close to end of the spreading phase) are shown. During the advanced spreading phase, several rings of high heat flux are observed in both experiments and simulations. The inner ring-shaped high heat flux region can be explained by the formation of a wave-like flow within the liquid leading to enhanced convective mixing of the liquid.

Guggilla et al. [8] reported a lower heat flow peak during the impact of a drop onto a sessile drop compared to the first drop impact. In their experimental work, a 25 mm

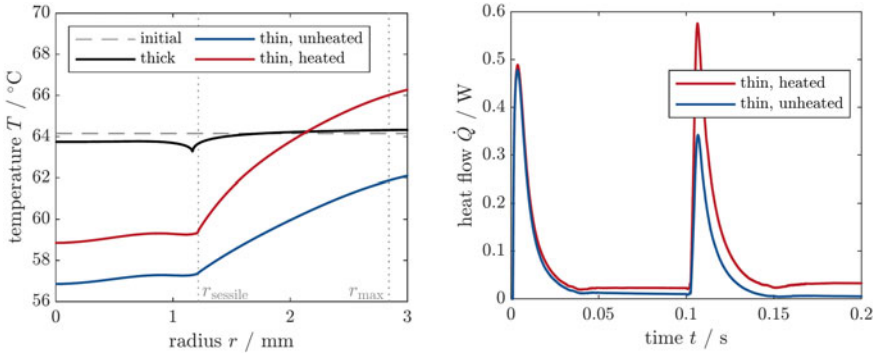


**Fig. 14** Left: Comparison of radial temperature profiles on the wall surface at the time just prior to the drop impact onto a sessile drop ( $D_0 = 1.14$  mm,  $u_0 = 0.54$  ms $^{-1}$ ). A thick substrate (4 mm) is compared to a thin substrate (24 mm), both heated ( $\Delta T = 9.8$  K,  $\dot{q}_{\text{heater}} = 2900$  Wm $^{-2}$ ) and unheated ( $\Delta T = 9.8$  K,  $\dot{q}_{\text{heater}} = 0$  Wm $^{-2}$ ). Right: Corresponding heat flow from the wall to the drop

thin steel foil heated by electrical current was used as a substrate, and the impact frequency was 20 drops per minute. In contrast, Gholijani et al. [6] reported a higher heat flow peak after each consequent impact; their experiments were performed with a heated, 4 mm thick calcium fluoride substrate, and the drop frequency was varied between 6 and 10 Hz. To explain this apparent contradiction, the developed numerical model has been used to study the influence of the substrate thickness on heat transfer by using identical thermal properties of the substrate (see Fig. 14). For the thick substrate, the input heat flux in the experiments of  $\dot{q}_{\text{heater}} = 2900$  Wm $^{-2}$  is chosen such that the dry substrate maintains a constant surface temperature. However, non-constant surface temperatures are expected when imposing this input heat flux to the thin substrate. Hence, for the thin substrate, a heated ( $\dot{q}_{\text{heater}} = 2900$  Wm $^{-2}$ ) and unheated ( $\dot{q}_{\text{heater}} = 0$  Wm $^{-2}$ ) substrate is studied numerically. The corresponding input heat flux to maintain a constant surface temperature on the dry, thin substrate is expected to be somewhere between these two limits. As shown in Fig. 14, the substrate temperature decreases significantly after the first drop impingement due to the low thermal inertia of the thin substrate. As a result, the second drop spreads, depending on the input heat flux of the heater, either on a warmer or a cooler surface. Hence, the peak in the heat flow of the second drop can be significantly higher or lower than the peak of the first drop. Further numerical studies reveal that this effect is more pronounced for lower impact frequencies. Similar conclusions have been drawn in a numerical study by Guggilla et al. [9].

Finally, the effect of the time interval between the first and the second impact on spreading radius and heat flow has been studied and compared with the impact of a single drop with double volume. The interval between the impacts has been chosen in such a way that the second drop impacts onto the first drop during the spreading, receding and sessile phases. As shown in Fig. 15, the highest maximal spreading

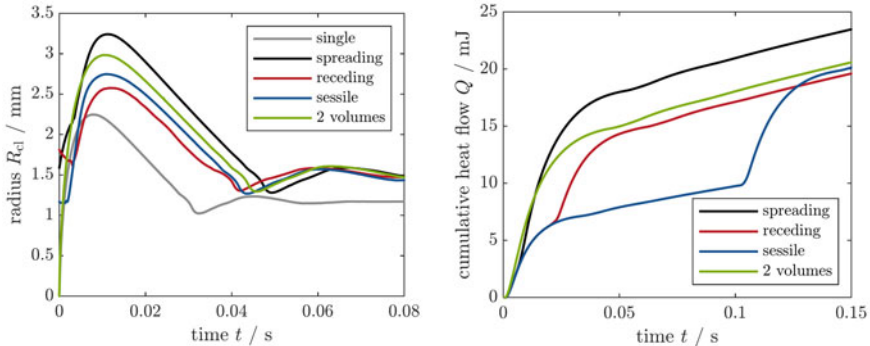


**Fig. 15** Contact line radius  $R_{cl}$  and cumulative heat flow  $Q$  from the wall to the drop over time for the impact of the second drop during different impingement phases of the initial drop ( $D_0 = 1.14$  mm,  $u_0 = 0.54$  ms $^{-1}$ ,  $\Delta T = 9.8$  K,  $\dot{q}_{\text{heater}} = 2900$  W m $^{-2}$ ). In the figure showing the radius, time  $t = 0$  s is set as the time just before the collision with the first drop or the wall occurs

radius is observed for the impact during the spreading phase of the first drop and the lowest for the impact during the receding phase. The flow field within the first drop at the instant of impact of the second drop has a significant influence on the spreading behaviour. The highest heat is transferred during the impact in the spreading phase. For all other studied cases, almost the same heat is transferred at 150 ms after the impact of the first drop.

Furthermore, a drop chain consisting of five drops impacting during the spreading phase of the previous drop has been studied. It has been found that the drop chain transfers more heat than a single drop of a fivefold volume.

#### 4.3.2 Horizontal Coalescence

For spray cooling, in addition to the vertical coalescence, the horizontal coalescence is also of great importance. The simultaneous impact of two identical drops onto two close locations of a hot substrate and the subsequent horizontal coalescence has been simulated using a structured 3D grid. Due to the symmetry of the geometry, the computational domain includes only a half of a droplet. A dynamic mesh refinement with load balancing [22] has been used to refine the mesh locally near the moving interface.

Figure 16 shows the impact of two drops with a small spacing onto a smooth, hot wall. Shortly after the collision of the drops' spreading fronts ( $t = 2$  ms), an uprising planar jet forms between the drops. Afterwards (starting at  $t = 3$  ms), a sideward flow of liquid leads to the thickening of a neck between the drops. The liquid flow far away from the location of collision is not influenced by the presence of a second drop. Later, the jet collapses and the two drops form a single sessile drop.

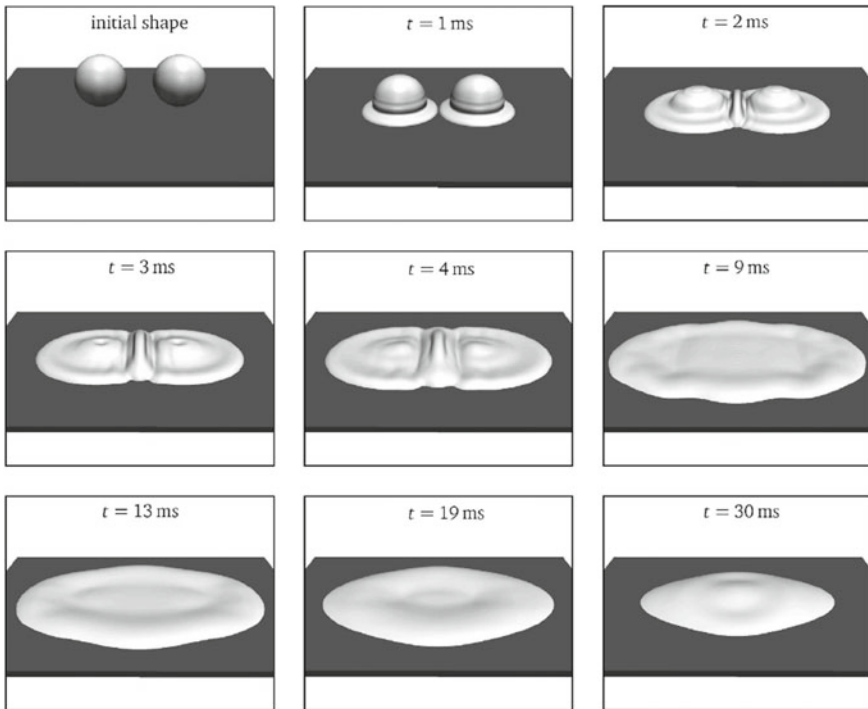


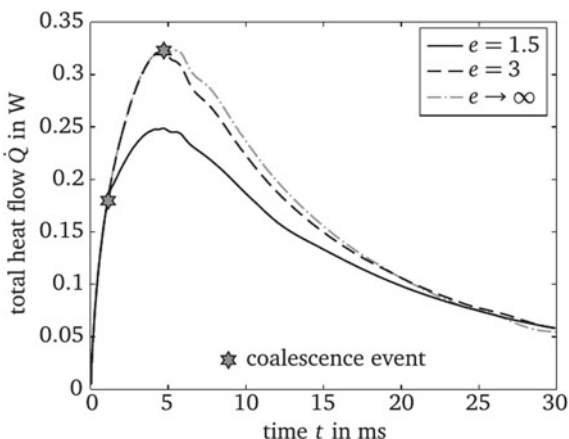
**Fig. 16** Horizontal coalescence of two drops with a spacing of  $e = d/D_0 = 1.5$ .  $d$  denotes the initial distance between the centres of the drops. Reprinted from [2] with permission from Elsevier

For different spacing parameters  $e$ , Fig. 17 shows that the heat flow from the wall deteriorates as soon as the drops coalesce in comparison to the case of two non-interacting drops. After the coalescence event, both the wetted area and the local flow velocity decrease resulting in a lower heat transfer compared to the case of two non-interacting drops. Hence, the outcome of the simultaneous impact of two drops strongly depends on the spacing between the drops. More details on the numerical investigation of the horizontal coalescence and a comparison with an analytical model can be found in [1, 2].

## 5 Conclusions

The numerical study of the impact of single and multiple drops onto hot walls significantly contributes to the understanding of the complex hydrodynamic and heat transport processes during spray cooling. In this study, the drop impact has been studied at moderate Reynolds, Weber and Jakob numbers in the drop deposition and film evaporation regime.

**Fig. 17** Total heat flow  $\dot{Q}$  from the wall to the drop over time during the horizontal coalescence of two drops with different spacing parameters  $e = d/D_0$ .  $d$  denotes the initial distance between the centres of the drops.  $e \rightarrow \infty$  labels the simultaneous impact of two non-interacting drops [1]



Almost 50% of the global heat transfer can be observed in the vicinity of the evaporative three-phase contact line. A one-dimensional lubrication model describes the hydrodynamic and heat transport processes in a micro region at the three-phase contact line. The results from this model are in good agreement in the chosen parameter range with results from a full-scale direct numerical simulation of the micro region.

A numerical model developed within the OpenFOAM library is used to study the drop impact on a macro scale. The results of the micro region model have been incorporated into the macroscale model in the form of correlations. It has been found that convective heat transfer is dominant during the spreading phase of the drop. However, during the receding and sessile drop phases, evaporation at the liquid-vapour interface and at the three-phase contact line play the main role. An extensive parameter study of the governing dimensionless numbers, i.e., the Reynolds, Weber, Bond, Prandtl and Jakob numbers, has been performed. The influence of pressures on hydrodynamics and heat transfer behaviour has been studied. Finally, the impact of multiple drops on the hot surface has been studied. The drop frequency is found to have a major influence on hydrodynamics and heat transport during the impingement process. Furthermore, it is shown that during the vertical coalescence of two successive impacting drops the peak in the heat flow can either be higher or lower for the second drop in comparison to the first drop, in dependency on the substrate thickness. The outcome of the horizontal coalescence of two simultaneously impacting drops is determined by the spacing between the drops.

**Acknowledgements** We kindly acknowledge the financial support of the Deutsche Forschungsgemeinschaft (DFG, German Research Foundation)—Project SFB-TRR 75, Project number 84292822. Calculations for this research were conducted on the Lichtenberg high-performance computer at the Technical University of Darmstadt.

## References

1. Batzdorf S (2015) Heat transfer and evaporation during single drop impingement onto a superheated wall. Ph.D. thesis, Technische Universität, Darmstadt. <http://tubiblio.ulb.tu-darmstadt.de/73268/>
2. Batzdorf S, Breitenbach J, Schlawitschek C, Roisman IV, Tropea C, Stephan P, Gambaryan-Roisman T (2017) Heat transfer during simultaneous impact of two drops onto a hot solid substrate. *Int J Heat Mass Transf* 113:898–907
3. Batzdorf S, Gambaryan-Roisman T, Stephan P (2017) Direct numerical simulation of the microscale fluid flow and heat transfer in the three-phase contact line region during evaporation. *J Heat Transf* 140(3):032401. <https://doi.org/10.1115/1.4038191>
4. Breitenbach J, Roisman IV, Tropea C (2018) From drop impact physics to spray cooling models: a critical review. *Exp Fluids* 59(3):55 <https://doi.org/10.1007/s00348-018-2514-3>
5. Fischer S, Herbert S, Gambaryan-Roisman T, Stephan P (2013) Local heat flux investigation during single drop impingement onto a heated wall. In: ILASS-Europe
6. Gholjani A, Gambaryan-Roisman T, Stephan P (2020) Experimental investigation of hydrodynamics and heat transport during vertical coalescence of multiple successive drops impacting a hot wall under saturated vapor atmosphere. *Exp Therm Fluid Sci* 118:110145 [www.sciencedirect.com/science/article/pii/S0894177719321120](http://www.sciencedirect.com/science/article/pii/S0894177719321120)
7. Gholjani A, Schlawitschek C, Gambaryan-Roisman T, Stephan P (2020) Heat transfer during drop impingement onto a hot wall: the influence of wall superheat, impact velocity, and drop diameter. *Int J Heat Mass Transf* 153:119661. [www.sciencedirect.com/science/article/pii/S0017931019353694](http://www.sciencedirect.com/science/article/pii/S0017931019353694)
8. Guggilla G, Narayanaswamy R, Pattamatta A (2020) An experimental investigation into the spread and heat transfer dynamics of a train of two concentric impinging droplets over a heated surface. *Exp Therm Fluid Sci* 110:109916. <https://doi.org/10.1016/j.expthermflusci.2019.109916>. [www.sciencedirect.com/science/article/pii/S0894177719304984](http://www.sciencedirect.com/science/article/pii/S0894177719304984)
9. Guggilla G, Narayanaswamy R, Stephan P, Pattamatta A (2021) Influence of flow rate and surface thickness on heat transfer characteristics of two consecutively impinging droplets on a heated surface. *Int J Heat Mass Transf* 165:120688. [www.sciencedirect.com/science/article/pii/S0017931020336243](http://www.sciencedirect.com/science/article/pii/S0017931020336243)
10. Han H, Schlawitschek C, Katyal N, Stephan P, Gambaryan-Roisman T, Leroy F, Müller-Plathe F (2017) Solid-liquid interface thermal resistance affects the evaporation rate of droplets from a surface: a study of perfluorohexane on chromium using molecular dynamics and continuum theory. *Langmuir* 33(21):5336–5343
11. Hardt S, Wondra F (2008) Evaporation model for interfacial flows based on a continuum-field representation of the source terms. *J Comput Phys* 227(11):5871–5895. [www.sciencedirect.com/science/article/pii/S0021999108001228](http://www.sciencedirect.com/science/article/pii/S0021999108001228)
12. Herbert S, Fischer S, Gambaryan-Roisman T, Stephan P (2013) Local heat transfer and phase change phenomena during single drop impingement on a hot surface. *Int J Heat Mass Transf* 61:605–614. [www.sciencedirect.com/science/article/pii/S0017931013001129](http://www.sciencedirect.com/science/article/pii/S0017931013001129)
13. Herbert S, Gambaryan-Roisman T, Stephan P (2013) Influence of the governing dimensionless parameters on heat transfer during single drop impingement onto a hot wall. *Colloids SurfS A: Phys Chem Eng Asp* 432:57–63. [www.sciencedirect.com/science/article/pii/S092775713003932](http://www.sciencedirect.com/science/article/pii/S092775713003932)
14. Josserand C, Thoroddsen ST (2016) Drop impact on a solid surface. *Annu Rev Fluid Mech* 48:365–391
15. Kunkelmann C (2011) Numerical modeling and investigation of boiling phenomena. Ph.D. thesis, Technische Universität, Darmstadt. <http://tuprints.ulb.tu-darmstadt.de/2731/>
16. Kunkelmann C, Stephan P (2010) Numerical simulation of the transient heat transfer during nucleate boiling of refrigerant HFE-7100. *Int J Refrig* 33(7):1221–1228. [www.sciencedirect.com/science/article/pii/S0140700710001593](http://www.sciencedirect.com/science/article/pii/S0140700710001593)
17. Liang G, Mudawar I (2017) Review of drop impact on heated walls. *Int J Heat Mass Transf* 106:103–126. [www.sciencedirect.com/science/article/pii/S0017931016324097](http://www.sciencedirect.com/science/article/pii/S0017931016324097)

18. Liang G, Mudawar I (2017) Review of spray cooling-part 1: single-phase and nucleate boiling regimes, and critical heat flux. *Int J Heat Mass Transf* 115:1174–1205
19. Marengo M, Antonini C, Roisman IV, Tropea C (2011) Drop collisions with simple and complex surfaces. *Curr Opin Colloid Interface Sci* 16(4):292–302
20. Potash M, Wayner P (1972) Evaporation from a two-dimensional extended meniscus. *Int J Heat Mass Transf* 15(10):1851–1863. [www.sciencedirect.com/science/article/pii/0017931072900580](http://www.sciencedirect.com/science/article/pii/0017931072900580)
21. Rein M (1993) Phenomena of liquid drop impact on solid and liquid surfaces. *Fluid Dyn Res* 12(2):61–93. <https://doi.org/10.1016/0169-598328932990106-k>
22. Rettenmaier D, Deising D, Ouedraogo Y, Gjonaj E, Gersem HD, Bothe D, Tropea C, Marschall H (2019) Load balanced 2D and 3D adaptive mesh refinement in OpenFOAM. *SoftwareX* 10:100317. [www.sciencedirect.com/science/article/pii/S2352711018301699](http://www.sciencedirect.com/science/article/pii/S2352711018301699)
23. Rioboo R, Tropea C, Marengo M (2001) Outcomes from a drop impact on solid surfaces. *Atomization Sprays* 11(2):155–165
24. Schlawitschek C (2020) Numerical simulation of drop impact and evaporation on superheated surfaces at low and high ambient pressures. Ph.D. thesis, Technische Universität, Darmstadt. <http://tuprints.ulb.tu-darmstadt.de/11800/>
25. Sontheimer H, Stephan P, Gambaryan-Roisman T (2021) Videos of the numerical simulation of drop impact onto heated walls. <https://doi.org/10.48328/tudatalib-578>. <https://tudatalib.ulb.tu-darmstadt.de/handle/tudatalib/2850>
26. Stephan P, Busse C (1992) Analysis of the heat transfer coefficient of grooved heat pipe evaporator walls. *Int J Heat Mass Transf* 35(2):383–391. [www.sciencedirect.com/science/article/pii/001793109290276X](http://www.sciencedirect.com/science/article/pii/001793109290276X)
27. Yarin A (2006) Drop impact dynamics: Splashing, spreading, receding, bouncing.... *Annu Rev Fluid Mech* 38(1):159–192. <https://doi.org/10.1146/annurev.fluid.38.050304.092144>

**Open Access** This chapter is licensed under the terms of the Creative Commons Attribution 4.0 International License (<http://creativecommons.org/licenses/by/4.0/>), which permits use, sharing, adaptation, distribution and reproduction in any medium or format, as long as you give appropriate credit to the original author(s) and the source, provide a link to the Creative Commons license and indicate if changes were made.

The images or other third party material in this chapter are included in the chapter's Creative Commons license, unless indicated otherwise in a credit line to the material. If material is not included in the chapter's Creative Commons license and your intended use is not permitted by statutory regulation or exceeds the permitted use, you will need to obtain permission directly from the copyright holder.



# High Resolution Measurements of Heat Transfer During Drop Impingement onto a Heated Wall



Alireza Gholijani, Sebastian Fischer, Tatiana Gambaryan-Roisman, and Peter Stephan

**Abstract** Drop impact on a hot surface heated above the saturation temperature of the fluid plays an important role in spray cooling. The heat transferred from the wall to the fluid is closely interrelated with drop hydrodynamics. If the surface temperature is below the Leidenfrost temperature, the heat transport strongly depends on the transport phenomena in the vicinity of the three-phase contact line. Due to extremely high local heat flux, a significant fraction of the total heat flow is transported through this region. The local transport processes near the three-phase contact line, and, therefore, the total heat transport, are determined by the wall superheat, contact line velocity, system pressure, fluid composition, surface structure and physical properties on the wall. The effect of the aforementioned influencing parameters on fluid dynamics and heat transport during evaporation of a single meniscus in a capillary slot are studied in a generic experimental setup. The hydrodynamics and evolution of wall heat flux distribution during the impact of a single drop onto a hot wall are also studied experimentally by varying the impact parameters, wall superheat, system pressure, and wall topography. In addition, the fluid dynamics and heat transport behavior during vertical and horizontal coalescence of multiple drops on a heated surface are studied experimentally.

## 1 Introduction

Spray cooling is one of the most efficient methods for heat removal in applications, which range from the cooling of electronic devices to metal quenching. Heat transfer by spray cooling is governed by the transport processes during the impact of multiple drops onto a hot surface (see Fig. 1, right). Understanding the multiple drop impacts

---

A. Gholijani · S. Fischer · T. Gambaryan-Roisman (✉)

Institute for Technical Thermodynamics (TTD), Technical University of Darmstadt, Darmstadt, Germany

e-mail: [pstephan@ttd.tu-darmstadt.de](mailto:pstephan@ttd.tu-darmstadt.de)

A. Gholijani

e-mail: [gholijani@ttd.tu-darmstadt.de](mailto:gholijani@ttd.tu-darmstadt.de)

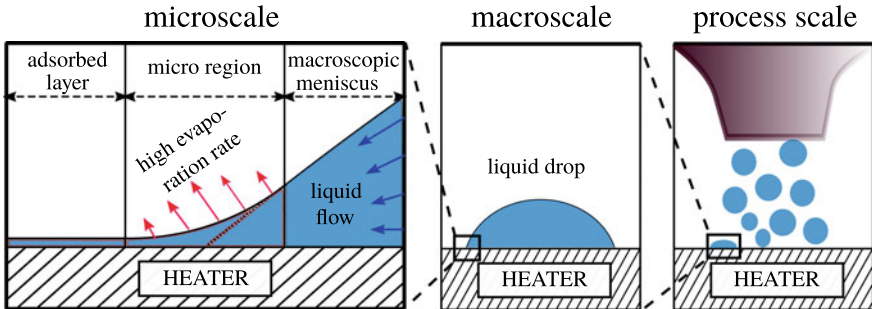


**Fig. 1** Sketch of spray cooling process (right), evaporating liquid drop (middle) and three-phase contact line (left)

necessitates a detailed investigation of transient processes accompanying the single drop impact (see Fig. 1, middle).

In a non-isothermal drop impact, the wall temperature affects both the hydrodynamics and heat transport. According to [2, 3, 16], five heat transfer regimes can be distinguished: (i) evaporation below the onset of bubble nucleation, which is also known as the film evaporation [16]; (ii) nucleate boiling; (iii) transition boiling; (iv) thermal atomization; and (v) film boiling. The impact regime is determined by the impact Reynolds and Weber numbers, properties of the substrate and the liquid, and wall temperature.

Numerical simulations [11, 12, 21] and experimental studies [8, 11] reveal that, if the drop impinges an impermeable and rigid substrate in drop deposition (in the absence of splashing and bouncing phenomena) and film evaporation regimes, its evolution can be subdivided into three subsequent phases: (i) the drop spreading phase, in which the contact line advances radially outwards due to action of inertia; (ii) the drop receding phase, in which the contact line moves inwards due to surface tension; and (iii) the phase of sessile drop evaporation, in which the drop is at a state of mechanical equilibrium. During all three phases, heat is transferred by conduction, convection, and evaporation. The contribution of each of these heat transfer mechanisms differs during the various phases. In many spray cooling regimes, the multiple impacting drops wet isolated parts of the surface. In these cases, the cooling efficiency significantly depends on the cumulative length of the contact lines which separate the wetted parts from dry patches [26]. This can be explained by strong heat flux maxima existing in the vicinity of the three-phase contact lines [13–15, 22] (see Fig. 1, left). Herbert et al. [11] and Batzendorf [21] have shown by numerical simulation of a drop impact and evaporation on a heated wall that the heat transported in the proximity of the three-phase contact line amounts to almost 50% of the total heat transfer during the sessile drop evaporation phase.

If the spray is not extremely dilute, the heat transport during spray cooling is governed not by the impacts of separate drops onto a hot wall, but by an interaction of multiple impacting drops with each other or with a liquid film covering the wall. The

heat transport mechanisms related to interaction between the drops on hot walls are very complex and not yet sufficiently understood. In order to reduce the complexity pertinent to the spray impact at applications-relevant conditions, the interactions drops can be studied in generic configurations, such as interaction between several drops simultaneously impacting onto different locations [1, 20] or an interaction between drops successively impacting onto the same location [5, 7, 9, 10, 17].

The present work aims at enhancing the understanding of non-isothermal drop-wall interactions in an atmosphere of a pure vapor and at a wall superheat (the difference between the temperature of the wall and the saturation temperature) below 18 K. A special attention is paid to detailed investigation of the contact line movement and heat transfer in the vicinity of the contact line. High resolution experimental studies have been performed for two configurations: single meniscus evaporation in a capillary gap, and impact of one drop or multiple drops onto a hot substrate. A parameter study has been conducted, in which, among others, the wall superheat and impact parameters have been systematically varied. The experimental results, together with a predictive model described in Chapter “[Numerical Simulation of Heat Transfer and Evaporation During Impingement of Drops onto a Heated Wall](#)”, contribute to better insights into the mechanisms of spray cooling and potential improvements of spray cooling systems.

## 2 Experimental Method

This section outlines the experimental apparatus employed for the single meniscus and the drop impact studies followed by a brief description of the data reduction and measurement uncertainties. The single meniscus experiment is designed in such a manner that allows a specific and generic investigation of the heat transfer phenomena in the direct vicinity of a moving three-phase contact line. The drop impact experiments, on the other hand, are designed to study the hydrodynamics and heat transfer phenomena on the larger and fully dynamic drop impact scale.

### 2.1 *Experimental Setups*

Figures 2 and 3 demonstrate the core parts of the single meniscus evaporation and drop impact experimental setups, respectively. The core component of both setups are sealed temperature-controlled test cells filled with pure vapor. Both setups utilize a high-temperature thermostat to pass heated liquid through the thermalization channels drilled in the walls of the cells to establish and control the fluid temperature and accordingly the system pressure.

The refrigerant FC-72 has been used as a working fluid. This refrigerant possesses a relatively low saturation temperature at atmospheric pressure (56.6 °C), which, together with the dielectric property of FC-72, makes it suitable for ther-

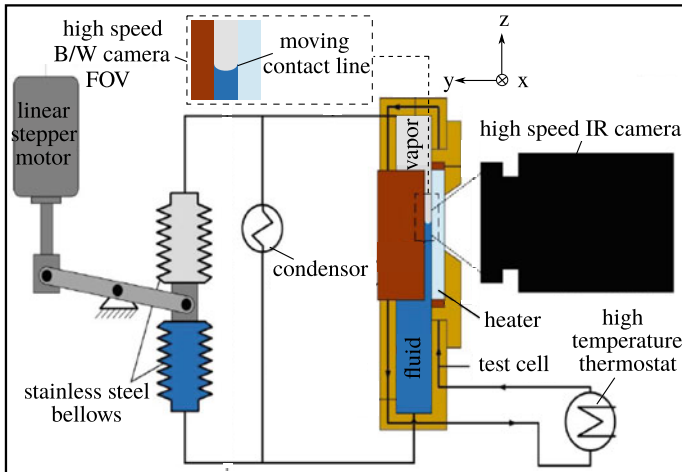


**Fig. 2** Schematic of single meniscus experimental setup

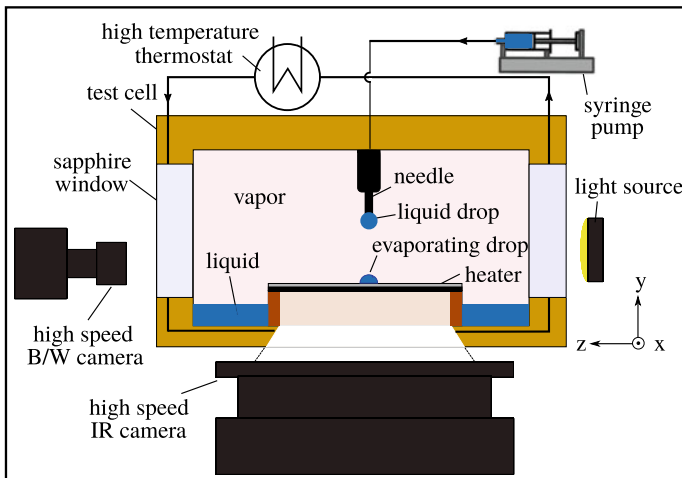


**Fig. 3** Schematic of drop impact experimental setup

mal management of electronic devices. Prior to filling the test cell with the working fluid, the non-condensable gases were extracted from the liquid using a degassing setup described in [22]. Afterward, the gas in cell was evacuated and filled with the degassed working fluid to establish pure saturation conditions.

In the single meniscus experimental setup (see Fig. 2), a single meniscus is formed in a vertical flat gap between the heater plate and a copper plate kept at the system set-point temperature. The meniscus can be moved in a direction normal to the straight contact line by a volume shift in the stainless steel bellows controlled by the stepper

motor. This allows the investigations of advancing (wetting) and receding (dewetting) contact lines.

In the experimental setup for investigation of drop impact (Fig. 3), the drops are generated by pumping the working fluid from a reservoir into the cell using a syringe pump. The drop size at the moment of detachment is governed by the balance between the gravity and surface tension forces and is therefore highly reproducible. To vary the impact velocity and the drop impact diameter, the height of the needle over the substrate and the needle diameter have been varied, respectively. In this study, the investigations are not limited to single drop impingement. Multiple drops are created by either variation of the dispensing volume flow rate of the pump (successive drop impingement) or by mounting an additional syringe pump unit parallel to the main unit (simultaneous drop impingement).

In both setups, a high-speed black/white camera is placed at the side of the cell for optical observation of the moving meniscus or of the dynamic drop shape evolution during its impact. The B/W images are post-processed in order to determine the liquid–vapor interface velocity and the apparent contact angle during single meniscus evaporation experiments, as well as the drop diameter, impact velocity, and time difference between two impacts during drop impact experiments.

An infrared (IR) camera having high spatial resolution and high frame rate is employed to record the temperature field at the solid–fluid interface. The spatial resolution of the IR camera is  $29.27 \mu\text{m}/\text{pixel}$  and the frame rate is 1 kHz. During the drop impact experiments, in order to fit the largest drop or two simultaneously impacting drops in the field of view (FOV) of the IR camera, its spatial resolution has been set to  $40.82 \mu\text{m}/\text{pixel}$ . After the experimental run was finished, the IR signal has been calibrated in-situ versus temperature for each pixel within FOV. The calibration has been accomplished by pressing a copper block with a known temperature against the substrate and recording IR images for different temperatures.

The heated substrate is comprised of an IR-transparent  $\text{CaF}_2$  glass plate with a thickness of 4 mm coated with a 400-nm-thick chromium nitride ( $\text{CrN}$ ) black layer with high emissivity and a 400-nm-thick chromium layer, which is used for Joule heating. These layers are deposited by employing the physical vapor deposition method [25]. The thermal diffusivity of the substrate material is close to the thermal diffusivity of the stainless steel alloys, which find application in many technical systems. The input heat flux and accordingly the wall superheat have been varied through the electrical power delivered to the chromium layer.

## 2.2 Data Reduction

The time-dependent distribution of the heat flux at the interface between the solid substrate and the working fluid is the central outcome of the experimental investigations. The heat flux distribution at the solid–fluid interface is computed from the

transient temperature field recorded with the IR camera. This is done by solving a transient three-dimensional equation of heat conduction within the substrate. The heat conduction equation is solved using the finite volume method. The details of the above procedure for determination of heat flux distribution and its accuracy are discussed in [8, 22].

In single meniscus evaporation experiments, the heat flux field has been averaged along the horizontal direction, and the resulting heat flux line profile along the vertical direction has been analyzed. The contact line position has been determined by searching for the local maximum of the heat flux line profile.

In drop impact experiments, the impact diameter, impact velocity, and time interval between the impact of drops are derived by post-processing of B/W images. The drop diameter is computed by applying a three-dimensional volume integration method. This method is based on the fact that the images of the drops which are captured by the black/white camera with a telecentric lens are orthogonal projections of the drop. The position of the contact line is derived via post-processing of the IR images. It has been assumed that the drops are symmetric in respect to the vertical axis. The effect of deviations from symmetry is marginal. The total heat flow at each time instant is calculated by integrating the heat flux over the whole footprint of the drop. The details of data reduction are given in [8].

### 2.3 Measurement Uncertainties

The uncertainties of the measured temperature arise from the noise level of the chip detector within the infrared camera. This noise level, which is also known as the noise-equivalent temperature difference (NETD), depends both on the temperature and on the optical setup. The NETDs values reported by the IR camera manufacturers are valid for a certain given temperature level. The noise-equivalent heat flux difference (NEHFD) related the heat flux uncertainty can be computed on the basis of NETD. The methods applied for determination of NETD and NEHFD for different temperatures are described in [22]. The uncertainty of the total heat flow is determined both by the uncertainties of the evaluation of the boundaries of the drop footprint and by the uncertainty of the the heat flux field. The drop footprint uncertainty is governed by the size of two pixels of the infrared image. The maximum uncertainty of the total heat flow occurs at the instant of maximal drop spreading. The vapor temperature inside the cell has been measured with an uncertainty of 0.6 K.

## 3 Results and Discussion

This section briefly addresses the main outcomes obtained from single meniscus experiments based on [22]. Subsequently, the results of single drop impact and multiple drops impact experiments are reviewed in detail.

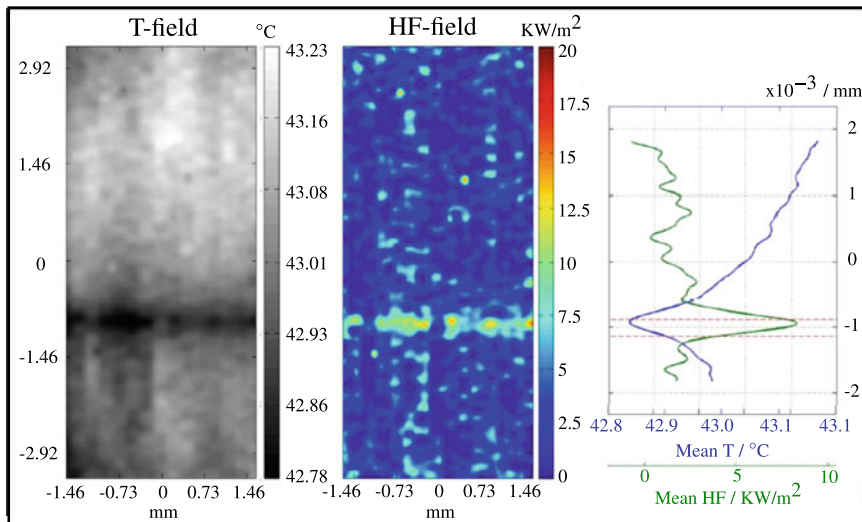
### 3.1 Single Meniscus Experiment

Figure 4 shows the temperature field (left), heat flux field (middle), and the corresponding temperature and heat flux line profiles (right) during the evaporation of a single meniscus. The temperature minimum and heat flux maximum in the vicinity of the three-phase contact line can be explained by an extremely small local thickness of the liquid film, which leads to a very low local thermal resistance of this film.

The **influence of contact line velocity and movement direction** on heat transport has been investigated. The heat flux peak at the spreading contact line has been found to be up to twice as high as at the receding case. The peak heat flux increases with an increase in the advancing contact line velocity. This is due to the stronger microconvection close to the contact line. This effect is absent for a receding contact line, resulting in the independence of the heat flux peak from the velocity [22].

The increasing **system pressure** leads to a decrease in the heat flux peak near the contact line for static, advancing, and receding contact lines. This is explained by the reduction in latent heat of vaporization at elevated pressures.

The heater substrate has been coated with a nanofiber mat generated through electrospinning of 5 wt% polyacrylonitrile solution (PAN;  $M_w = 150$  kDa) in N,N-dimethylformamide (DMF) to investigate the **influence of surface structure**. It has been found that the local heat flux in proximity of a stationary apparent contact line increases by 60% if the substrate is coated by the nanofiber mat. In the case of a receding meniscus, the heat transfer is enhanced due to formation of an extended region, in which the pores within the nano-textured mat are partially filled with evaporating liquid [4].



**Fig. 4** Temperature field (left), heat flux field (middle), and temperature and heat flux line profiles (right) at  $\Delta T = 3.4$  K and  $p = 0.57$  bar

A mixture of FC-3284 and FC-84 fluids has been used to study the **influence of fluid composition** on the local heat flux. It has been shown that in binary mixtures the local evaporation rate and heat flux peak are lower compared to the pure fluids. This effect can be explained by the influence of the mixture on the phase equilibrium, the local variation of the evaporation rates of various components and the local differences in concentration.

### 3.2 Drop Impact Experiment

This section contains the results corresponding to the impact of a single drop (Sect. 3.2.1) and multiple drops (Sect. 3.2.2) onto a heated surface.

#### 3.2.1 Single Drop Impact Experiment

This section addresses the influence of wall superheat, impact velocity, drop size, system pressure, and surface structure on hydrodynamics and heat transport during a single drop impact onto a heated surface. The side view of the drop captured by the B/W camera at different time instants and the temporal evolution of the heat flux distribution at the solid–fluid interface determined from the IR images are presented in Fig. 5. At the initial stages of impact, the maximal heat flux is detected at the center of the drop footprint. At this stage, a high, uniform heat flux around the central part of the footprint decreases radially outwards near the drop periphery. The heat is transported from the wall to the fluid mainly by conduction and convection. At  $t = 4$  ms, shortly before the drop reaches its maximum spreading radius, the highest local heat flux is observed near the contact line. Starting from this instant, the heat flux in proximity of the contact line is larger than near the center, indicating that the evaporation in the vicinity of the contact line is an important heat transfer mechanism at this stage. At  $t = 7$  ms, the contact line radius reaches its maximum and (i) the drop spreading phase ends. Then, (ii) the drop receding phase begins and the contact line moves inwards until  $t = 25$  ms. From this moment on, the drop reaches a

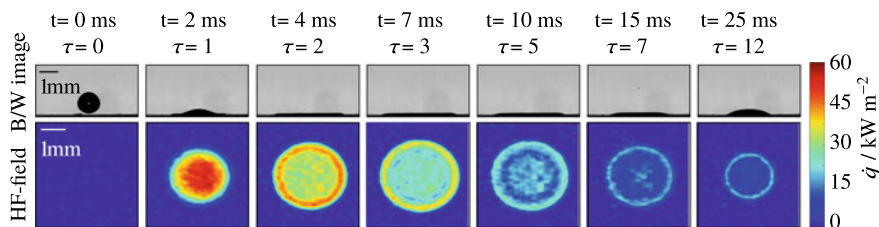


**Fig. 5** B/W images and heat flux fields during the impact of a drop onto a heater for 25 ms after impact ( $Re = 1450$ ,  $We = 34$ ,  $D_0 = 0.93$  mm,  $u_0 = 0.44$  m s $^{-1}$ ,  $\Delta T = 9.5$  K, and  $p = 0.9$  bar) [8]

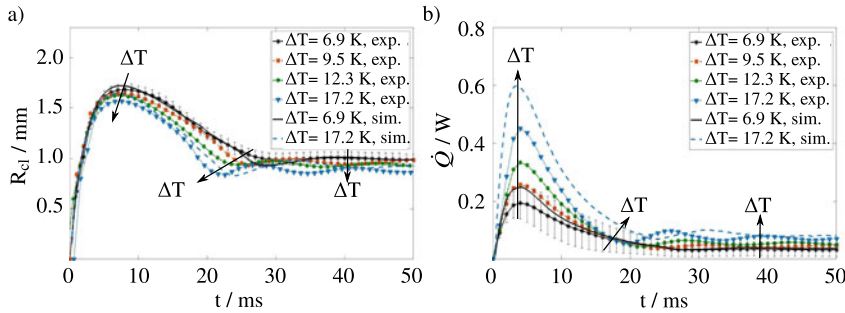


**Fig. 6** Temporal evolution of the **a** contact line radius and **b** heat flow during the impact of a single drop onto a bare heater for various wall superheats ( $Re = 1450$ ,  $We = 34$ ,  $D_0 = 0.93$  mm,  $u_0 = 0.44$  m s $^{-1}$ , and  $p = 0.9$  bar) [8]

state at which the drop footprint stays approximately constant, corresponding to (iii) the sessile drop evaporation phase. A qualitatively similar evolution of the contact line radius and heat flux distribution have been observed over the entire parameter range.

### Influence of Wall Superheat

The experimental results and numerical predictions of the contact line radius,  $R_{cl}$ , and the heat flow,  $\dot{Q}$ , for different wall superheats ranging from 6.9 to 17.2 K are shown in Fig. 6a and b, respectively. As depicted in Fig. 6a, increasing wall superheat leads to a decrease in maximum contact line radius and the duration of spreading and receding phases. This can be explained by the higher evaporation rate in proximity of the three-phase contact line and concomitant higher apparent contact angle [18]. Increasing the wall superheat leads to stronger oscillations before the beginning of the sessile drop evaporation phase. In addition, the drop footprint radius at the sessile drop evaporation phase decreases with increasing of the superheat. The experimental findings have been compared with numerical predictions showing a good agreement [8]. The heat transfer increases with increasing wall superheat, but the dependence is weaker than linear. The deviation between the measured and numerically predicted heat flow can be attributed to the limited spatial resolution of the IR camera.

### Influence of Drop Impact Velocity

Figures 7a and b show the experimental and numerical results on the contact line radius and heat flow for the impact velocities range from 0.33 to 0.57 m s $^{-1}$ .

The higher impact velocities and accordingly spreading velocities lead to the shorter duration of the spreading phase and the larger maximum contact line radius. The maximal contact line radius determined from these experimental data scales

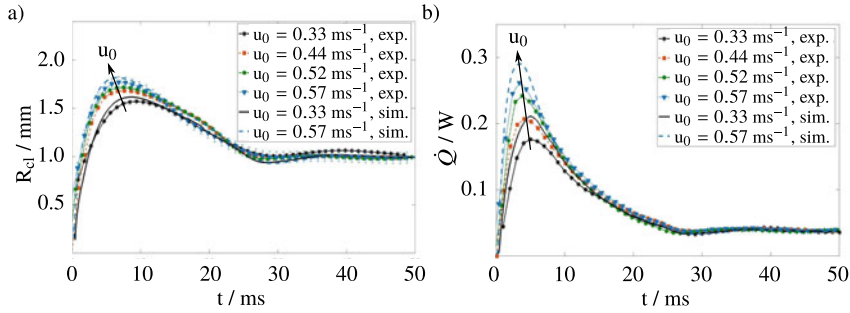


**Fig. 7** Temporal evolution of the **a** contact line radius and **b** heat flow during the impact of a single drop onto a bare heater for various impact velocities ( $1073 \leq \text{Re} \leq 1905$ ,  $20 \leq \text{We} \leq 59$ ,  $D_0 = 0.93 \text{ mm}$ ,  $\Delta T = 6.3 \text{ K}$ , and  $p = 0.9 \text{ bar}$ ) [8]

as  $R_{\text{cl,max}} \propto u_0^{0.208}$ . This is in good agreement with the scaling  $R_{\text{cl,max}} \propto u_0^{0.2}$  based on the balance between the initial kinetic energy and the viscous dissipation for isothermal impacts [12].

Increasing impact velocity leads to prolongation of the receding phase. The final radius of the sessile drop reached at the beginning of the sessile drop evaporation phase does not depend on the impact velocity. The shape of the sessile drop is determined by the balance between the surface tension and gravity (depending on the Bond number) for the given drop volume and static contact angle.

During the spreading phase, the heat flow reaches its maximum earlier with increasing the impact velocity. Heat flow increases with the impact velocity during both spreading and receding phases. However, the maximum of heat flow appears at a higher dimensionless time [8]. At the sessile drop evaporation phase, the heat flow, as well as the drop shape, is independent of the impact velocity. Experimental and simulation data are in good qualitative and quantitative agreement [8].

## Influence of Drop Size

The experimental and numerical data on the contact line radius and heat flow during the impact of liquid drops with sizes ranging from 0.97 to 1.60 mm are depicted in Fig. 8a and b, respectively. In these experiments, the spatial resolution of the IR camera is set to  $40.82 \mu\text{m}/\text{pixel}$ . This leads to lower measurement accuracy and a larger deviation between experimental and simulated curves.

It can be seen in Fig. 8a that the impact of larger drops is accompanied by the prolongation of both drop spreading and receding phases. Additionally, the maximum spreading radius strongly increases with the increase of the drop diameter. The heat flow during all phases increases with the increase of drop diameter, one of the reasons being the increased wetted area (see Fig. 8b).

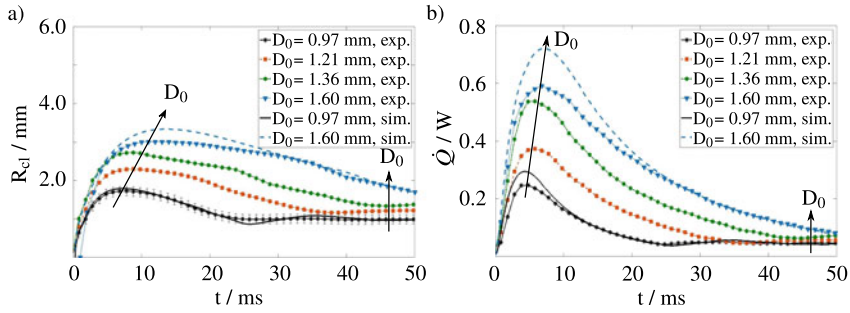


**Fig. 8** Temporal evolution of the **a** contact line radius and **b** heat flow during the impact of a single drop onto a bare heater for various impact diameters ( $1520 \leq Re \leq 2500$ ,  $37 \leq We \leq 61$ ,  $u_0 = 0.44 \text{ m s}^{-1}$ ,  $\Delta T = 6.9 \text{ K}$ , and  $p = 0.9 \text{ bar}$ ) [8]

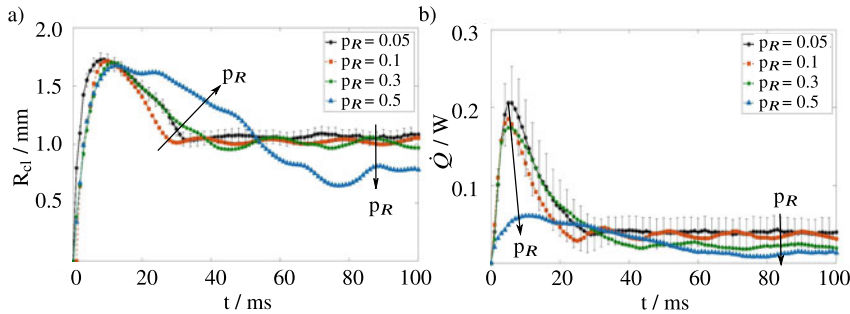


**Fig. 9** Temporal evolution of the **a** contact line radius and **b** heat flow during the impact of a single drop onto a bare heater for various system pressures ( $1220 \leq Re \leq 1530$ ,  $23 \leq We \leq 53$ ,  $D_0 = 0.94 \text{ mm}$ ,  $u_0 = 0.34 \text{ m s}^{-1}$ , and  $\Delta T = 6.5 \text{ K}$ )

## Influence of System Pressure

Figure 9a, and b present the temporal evolution of the contact line radius and heat flow during drop impact at reduced pressures (ratios of system pressure and critical pressure) ranging from 0.05 to 0.5, respectively. As depicted in Fig. 9a, the maximum of the contact line radius is similar for all four pressures. However, the duration of the spreading and particularly receding phases is increased at elevated pressures. This is attributed to the slight decrease of kinetic energy due to the lower liquid density and a significant decrease of surface tension caused by an increase in cell pressure. The drop footprint during the sessile drop evaporation phase decreases with increasing pressure. This is due to the decrease in latent heat of vaporization, which leads to a higher evaporation rate in proximity of the three-phase contact line and a higher apparent contact angle. The observed behavior agrees qualitatively with the numerical results of Schlawitschek [24].

The maximum heat flow decreases with increasing pressure, which can be attributed to the decreasing thermal effusivity of the liquid. The heat flow during the

sessile drop evaporation phase also decreases with increasing pressure (see Fig. 9b). This can be explained by a decrease in latent heat of vaporization at elevated pressures, which is supported by the results of the single capillary slot experiment.

## Influence of Surface Structure

This section is devoted to the influence of a porous coating on hydrodynamics and heat transport during a single drop impact onto a heated surface. To generate a porous coating, the heater substrate is covered with a nanofiber mat with a thickness of 22  $\mu\text{m}$  consisting of randomly oriented nanofibers generated through electrospinning of 5 wt% polyacrylonitrile solution (PAN;  $M_w = 150 \text{ kDa}$ ) in N,N-dimethylformamide (DMF). The mat thickness was measured using confocal microscopy.

An exemplary temporal evolution of heat flux distribution evaluated from the IR images in the presence and absence of nanofiber mat is presented in Fig. 10. Similar to the bare surfaces, inertia force leads to drop spreading over the nanofiber-coated surface at the early stages of impact. However, the spreading velocity is slower compared to the uncovered substrate. In addition, the heat flux during the spreading phase is significantly lower for the coated surface compared to the bare surface. After the maximal spreading radius is reached, the contact line remains pinned. The receding phase is suppressed. Moreover, spots of high heat flux appear at the periphery of the wetted region.

The presence of a nanofiber mat prevents direct contact between the liquid and the heater surface at the early stages of impact. The cold liquid impacts first onto the top surface of the hot nanofiber mat and is decelerated. The vapor entrapped inside the pores in between the Cr surface and the bulk liquid plays the role of heat-insulating layer. This phenomenon, which is referred to as the “skeletal” Leidenfrost effect, weakens the heat flux tremendously [27]. The drop cools down the nanofibers first,

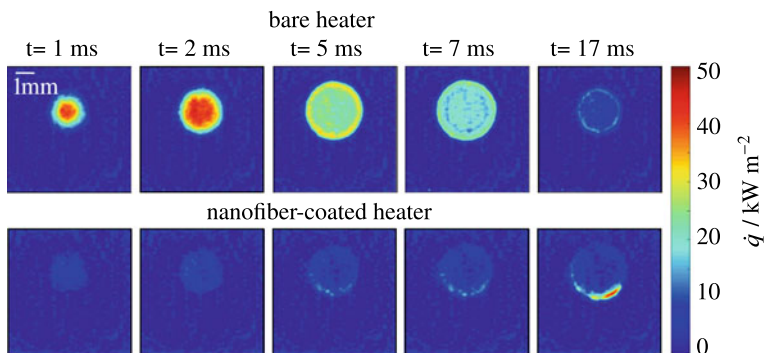


**Fig. 10** Heat flux fields for a duration of 17 ms after the impact of a drop onto a bare (top) and nanofiber-coated (bottom) heater ( $Re = 1500$ ,  $We = 37$ ,  $D_0 = 0.95 \text{ mm}$ ,  $u_0 = 0.45 \text{ m s}^{-1}$ , and  $\Delta T = 14.6 \text{ K}$ )

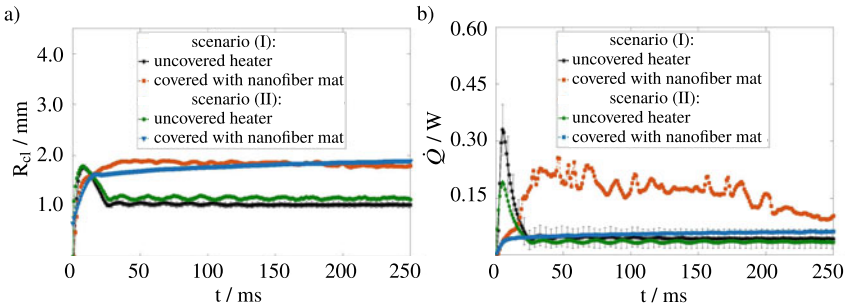


**Fig. 11** Temporal evolution of the **a** contact line radius and **b** heat flow during the impact of a single drop onto a bare and a nanofiber-coated heater ( $D_0 = 0.95$  mm,  $p = 0.9$  bar,  $h_{mat} = 22$   $\mu$ m, for scenario (I):  $Re = 1920$ ,  $We = 60$ ,  $u_0 = 0.58$  m  $s^{-1}$  and  $\Delta T = 9.6$  K; for scenario (II):  $Re = 1500$ ,  $We = 37$ ,  $u_0 = 0.45$  m  $s^{-1}$ , and  $\Delta T = 7.0$  K)

and heat is removed from the heater mainly through the nanofiber skeleton. At this stage, the heat transport is determined by the thermal conductivity of the nanofibers, which is  $0.02\text{--}0.05$  W  $m^{-1}$   $K^{-1}$  [23].

After several milliseconds, two scenarios might occur depending on wall superheat and impact velocity. Scenario (I): the liquid drop penetrates entirely through the pores of the nanofiber mat and reaches the solid heater surface. This phenomenon takes place at low wall superheats and high impact velocities and leads to the appearance of multiple regions of high heat flux. Scenario (II): the vapor entrapped inside the pores seems to prevent direct contact of the liquid with the substrate. In this scenario, the low kinetic energy of the impacting drop prevents the liquid drop from displacing the generated vapor inside the pores of the nanofiber mat radially outwards. Therefore, the heat flux around the center of the impact location stays at a low level.

Figure 11a and b compare the contact line radius and heat flow between scenarios (I) and (II) during drop impact onto a heater covered with nanofiber mat. For better comparability of the results, the data for drop impact onto a bare heater at the same impact parameters and wall superheats are plotted in the same figures.

If the heater is covered with a nanofiber mat, the drop evolution, regardless of the scenario, starts from an initial inertia-driven drop spreading, which is in both cases slower than for the bare substrates. Furthermore, the surface tension-driven receding phase observed for the drops on bare substrates is suppressed for both scenario (I) and scenario (II). The drop evolution in scenario (I) is characterized by a faster initial spreading and by a slow decreasing of the footprint radius after reaching the maximal spreading, which can be attributed to the effect of evaporation. Scenario (II) is characterized by a slower initial spreading velocity. At  $t = 14$  ms, the spreading velocity decreases considerably. It is suggested that imbibition is responsible for the second spreading phase, which is not completed after 250 ms. The dynamics of second spreading phase is strongly affected by the wettability of the fibers. Initially (during the spreading and a large part of the receding phase for the drops on a bare substrate) the total heat flow on the bare substrate is significantly higher than on

the coated substrate. However, starting from the time instant about 25 ms after the impact (sessile drop evaporation phase for drops on a bare substrate) the heat flow on a coated substrate is higher than that on a bare substrate. This can be attributed to the larger footprint of the drop. In scenario (I), the heat flow transported from the heated wall in this phase is very high. We assume that this is explained by the intensive evaporation of liquid at multiple liquid-solid contact spots appearing after the penetration of liquid through the mat. The fast evaporation at this phase leads to the observed slight shrinkage of the drop footprint.

### 3.2.2 Multiple Drop Impact Experiment

The present section addresses the cumulative effect of the impact of multiple drops onto a heated wall. With this objective, the hydrodynamic and heat transport behavior during vertical and horizontal coalescence of multiple drops on a heated surface is presented.

#### Vertical Coalescence

Figure 12 shows the side view of the drop recorded by the B/W camera and the temporal evolution of the heat flux distribution obtained by post-processing of the IR images. The behavior of the drop shape and heat flux for the first drop follows the trend presented in Sect. 3.2.1. At  $t = 102$  ms, the second drop impacts vertically onto the first drop. It is clearly seen on the side view images that, similar to the findings reported in literature [5, 17], the impact of the second drop is followed by swelling up of the bottom part of this drop ( $t = 102$  ms), by formation of a crown ( $t = 103$  ms) and by increasing of the footprint of the combined drop (from  $t = 103$  ms to  $t = 120$  ms). The heat flux within the drop footprint rises shortly after the impact of the second drop ( $t = 103$  ms). However, the level of maximal heat flux measured after the impact of the first drop ( $t = 4$  ms) is not reached. This is caused by the pre-cooling of the substrate by the first drop and by the fact that the direct contact between the liquid drop and the substrate is prevented due to the presence of the liquid layer on the substrate. At the time instants  $t = 105$  ms and  $t = 106$  ms two ring-shaped regions of high heat fluxes can be observed: the radius of the first region is close to the contact radius of the first drop prior to the second impact; the second region is at the contact line of the combined drop.

As presented in Chapter “[Numerical Simulation of Heat Transfer and Evaporation During Impingement of Drops onto a Heated Wall](#)”, the formation of the inner ring with high heat flux can be explained by the locally low thickness of the liquid film, which corresponds to the low local thermal resistance of the liquid layer. Moreover, a high local flow velocity in this region is observed, which leads to extensive mixing of the liquid. The spreading phase is followed by the receding phase (starting at  $t = 120$  ms), in which the contact line radius decreases. Finally, the sessile drop evaporation phase is reached. The footprint area of the combined drop at this stage

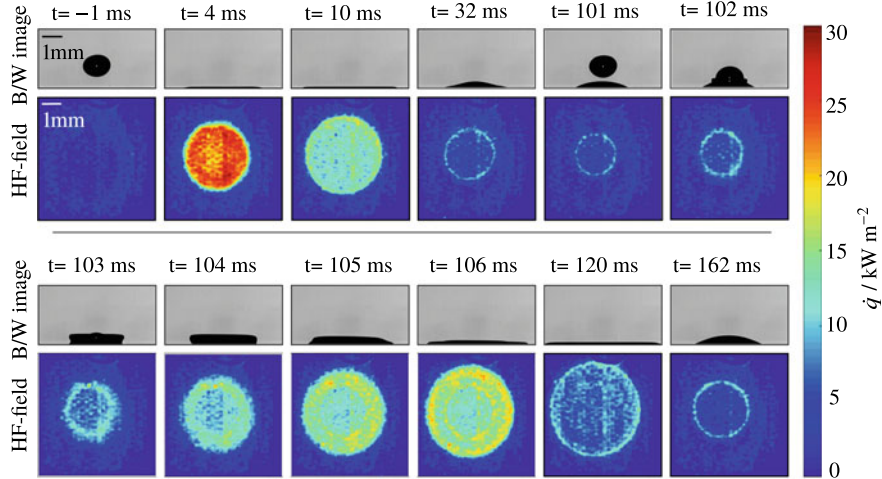


**Fig. 12** B/W images and heat flux fields for vertical coalescence of two successive drops impinging onto a bare heater ( $\text{Re} = 2160$ ,  $\text{We} = 64$ ,  $D_0 = 1.14 \text{ mm}$ ,  $u_0 = 0.54 \text{ m s}^{-1}$ ,  $\Delta T = 7.6 \text{ K}$ ,  $p = 0.9$  bar, and  $f = 10 \text{ Hz}$  [7])

is larger than that after the impact of the first drop, which is explained by a bigger volume contained in the combined drop.

Figure 13a and b illustrate the contact line radius and heat flow following the impacts of four successive drops with the frequency of 10 Hz, respectively. The contact line radius and the heat flow are shown as functions of time elapsed after the last impact event. As depicted in Fig. 13a, the duration of the spreading phase, and particularly, the receding phase, increases after each impact. Additionally, the maximum contact line radius rises after the second and the third impacts. This behavior, which is in qualitative agreement with the findings of Guggilla et al. [9], can be explained by the larger mass of the liquid wetting the substrate. The relative increase of the maximum spreading radius is less significant after the third impact, and the maximum spreading radius after the fourth impact stays the same as after the third one. At the end of the receding phase following each impact, oscillations of contact radius and heat flow are observed, whereas the oscillation frequency increases and its amplitude decreases with the increasing sequential number of drop.

Despite a lower maximal heat flux during the spreading phase initiated by the second impact, the maximum heat flow increases with increasing of the drop sequential number (see Fig. 13b). This is associated with the larger footprint of the drop (see Fig. 13a), which effect is more significant than a decrease of the heat flux. A weak increase in the maximum heat flow is observed after the third impact. The maximum heat flow after the fourth impact is nearly the same as after the third impact, in agreement with the trend of maximum spreading radius. The oscillations in the heat flow before the onset of the sessile drop evaporation phase are caused by the oscillations of the contact line radius.

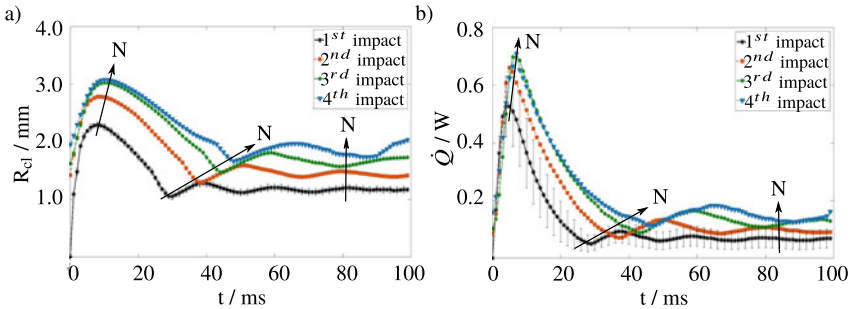


**Fig. 13** Temporal evolution of the **a** contact line radius and **b** heat flow during the vertical coalescence of four successive drops impinging onto a bare heater ( $Re = 2160$ ,  $We = 64$ ,  $D_0 = 1.14$  mm,  $u_0 = 0.54$  m s $^{-1}$ ,  $\Delta T = 12.4$  K,  $p = 0.9$  bar, and  $f = 10$  Hz) [7]

## Horizontal Coalescence

Figure 14 shows the side view of the drop recorded with the high-speed B/W camera and heat flux distribution, which was determined by postprocessing of the IR images, at different time instants after the nearly simultaneous impact of two drops. In this experiment, the difference in impact time between two drops is about 1 ms, which corresponds to the time resolution of the camera recordings. The wall superheat and the spacing parameter,  $e$ , which is the ratio of the distance between the impact locations to the drop diameter, are set to 7.3 K and 2.15, respectively. Similar to single drop impact, high local and overall heat fluxes are transferred to the liquid in the first few milliseconds when both drops spread over the heated surface.

At the time interval between 2 and 3 ms after the beginning of recording, the rims of both drops come into contact, and the coalescence of the drops starts. A stagnation flow is formed at the position where two spreading fronts meet. As a result, the liquid flow is redirected sideways and upwards, which leads to the emergence of a bump between the drops ( $t = 3$  ms). A similar phenomena has been observed in [1, 19, 20]. The wetted area and the heat flux distribution far from the region where the droplet coalescence takes place are not influenced by the interaction between the drops. Similar to the single drop impact, a region with high heat fluxes in proximity of the three-phase contact line of the combined drop can be examined. The spreading process of the combined drop ends due to the dissipation of kinetic energy ( $t = 8$  ms). The combined drop then starts to shrink, driven by the surface tension force. From this time on, low heat flux at the liquid–solid interface is observed everywhere, apart from the apparent three-phase contact line. After some time ( $t = 60$  ms), the combined drop reaches the equilibrium state, forming a single sessile drop.

Figure 15a and b present the the heat flow and cumulative heat transport as functions of time during the nearly simultaneous impact of two drops onto a heated surface for different spacing parameters. The impact with spacing parameters of 1.18 and 2.15 result in horizontal drop coalescence over the heater substrate. The spacing parameter of  $\infty$  stands for the impact of two drops that are so far from

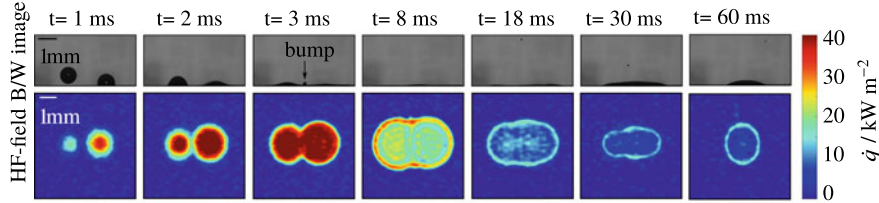


**Fig. 14** B/W images and heat flux fields during the horizontal coalescence of two drops over a bare heater ( $Re = 1750$ ,  $We = 50$ ,  $D_0 = 0.93$  mm,  $u_0 = 0.53$  m s $^{-1}$ ,  $\Delta T = 7.3$  K,  $p = 0.9$  bar, and  $e = 2.15$ ) [6]

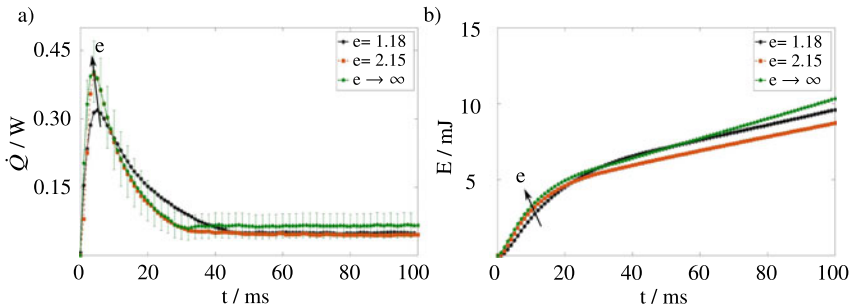


**Fig. 15** Temporal evolution of the **a** heat flow and **b** cumulative heat flow during simultaneous impact of two drops onto a bare heater for various spacing parameters;  $e \rightarrow \infty$  represents the non-coalescence case ( $Rec = 1750$ ,  $We = 50$ ,  $D_0 = 0.93$  mm,  $u_0 = 0.53$  m s $^{-1}$ ,  $\Delta T = 7.3$  K, and  $p = 0.9$  bar) [6]

each other that no interactions takes place between them. The corresponding heat flow is equivalent to twice the heat flow of a single drop impact. The experimental results show that the heat flow is not affected by the presence of a neighbouring drop as long as the the wetted regions corresponding to these drops stay separated from each other. Once the drops start to coalesce, the heat flow during the spreading and receding phases of  $e = 2.15$  is relatively similar to the case of two independent drops ( $e \rightarrow \infty$ ). However, for the case  $e = 1.18$  the heat flow during the spreading phase (including the maximal heat flow) is lower, and during the receding phase, is higher than for  $e \rightarrow \infty$  and  $e = 2.15$ . These results are in good agreement with the numerical simulations presented in [1].

At the late stages of the impact in which a single sessile drop is formed, the heat flow through the liquid–solid interface transferred to the combined drop is independent of the spacing parameter and is lower compared to the case of two independent drops. This observation is attributed to the smaller cumulative liquid–solid contact area and shorter cumulative length of the three-phase contact line of the combined sessile drop compared to two sessile drops with the same cumulative volume.

## 4 Conclusions

This study is devoted to experimental investigations on fluid dynamics and heat transport during the impact of a single drop and multiple drops onto a heated surface. In addition, transport phenomena associated with a single evaporating contact line under well-controlled conditions have been studied in a dedicated experimental environment. In the scope of this work, the influences of wall superheat, contact line velocity and its direction, system pressure, fluid composition, and surface structure on fluid dynamics and heat transport during moving contact line and drop impact were investigated.

The experimental results of single drop impact revealed that increasing the wall superheat, impact velocity, and drop diameter, as well as decreasing system pressure, results in increased heat flow to the drop after the impingement. The maximum spreading radius after impingement increases with the increase of impact velocity and impact diameter and decreases with the increase of wall superheat and system pressure. The experimental results at atmospheric pressure were compared against the available numerical model developed in [11, 21]. A good agreement between measurements and model predictions was observed. In addition, the impact of a drop onto a surface with a porous coating is accompanied by lower heat flow at the early stages of impact, while it leads to enhancement of the heat flow at the late stages of impact. The heat flow enhancement is due to the large solid–liquid contact area caused by the drop pinning effect. A significant heat transfer enhancement has been observed for the scenario in which the kinetic energy of the drop was sufficient to completely penetrate through the coating.

The last part of this study focuses on the impingement of multiple drops onto a moderately heated wall as an important step towards understanding the mechanisms of spray cooling. Hydrodynamics and heat transport behavior during vertical and horizontal coalescence of multiple drops over a heated surface are addressed. The investigations revealed that the solid–liquid contact area, and, accordingly, heat flow, rise after successive impacts. Horizontal drop coalescence leads to lower heat flow in comparison to non-coalescence cases, especially during the sessile drop evaporation phase.

**Acknowledgements** The authors kindly acknowledge the financial support by the Deutsche Forschungsgemeinschaft (DFG) within the SFB-TRR75, project number 84292822.

## References

1. Batzdorf S, Breitenbach J, Schlawitschek C, Roisman I, Tropea C, Stephan P, Gambaryan-Roisman T (2017) Heat transfer during simultaneous impact of two drops onto a hot solid substrate. *Int J Heat Mass Transf* 113:898–907
2. Bernardin J, Stebbins C, Mudawar I (1996) Effects of surface roughness on water droplet impact history and heat transfer regimes. *Int J Heat Mass Transf* 40(1):73–88. [https://doi.org/10.1016/S0017-9310\(96\)00067-1](https://doi.org/10.1016/S0017-9310(96)00067-1). [www.sciencedirect.com/science/article/pii/S0017931096000671](http://www.sciencedirect.com/science/article/pii/S0017931096000671)

3. Breitenbach J, Roisman I, Tropea C (2018) From drop impact physics to spray cooling models: a critical review. *Exper Fluids* 59(3). <https://doi.org/10.1007/s00348-018-2514-3>. <http://tubiblio.ulb.tu-darmstadt.de/96387/>
4. Fischer S, Sahu R, Sinha-Ray S, Yarin A, Gambaryan-Roisman T, Stephan P (2017) Effect of nano-textured heater surfaces on evaporation at a single meniscus. *Int J Heat Mass Transf* 108:2444–2450
5. Fujimoto H, Ogino T, Takuda H, Hatta N (2001) Collision of a droplet with a hemispherical static droplet on a solid. *Int J Multiph Flow* 27(7):1227–1245
6. Gholijani A, Gambaryan-Roisman T, Stephan P, Experimental investigation of hydrodynamics and heat transport during horizontal coalescence of two drops impinging a hot wall. *Exp Therm Fluid Sci* 131:110520
7. Gholijani A, Gambaryan-Roisman T, Stephan P (2020) Experimental investigation of hydrodynamics and heat transport during vertical coalescence of multiple successive drops impacting a hot wall under saturated vapor atmosphere. *Exp Therm Fluid Sci* 118:110145
8. Gholijani A, Schlawitschek C, Gambaryan-Roisman T, Stephan P (2020) Heat transfer during drop impingement onto a hot wall: the influence of wall superheat, impact velocity, and drop diameter. *Int J Heat Mass Transf* 153:119661
9. Guggilla G, Narayanaswamy R, Pattamatta A (2020) An experimental investigation into the spread and heat transfer dynamics of a train of two concentric impinging droplets over a heated surface. *Exp Therm Fluid Sci* 110:109916
10. Guggilla G, Pattamatta A, Narayanaswamy R (2018) Numerical investigation into the evaporation dynamics of drop-on-drop collisions over heated wetting surfaces. *Int J Heat Mass Transf* 123:1050–1067
11. Herbert S, Fischer S, Gambaryan-Roisman T, Stephan P (2013) Local heat transfer and phase change phenomena during single drop impingement on a hot surface. *Int J Heat Mass Transf* 61:605–614. <https://doi.org/10.1016/j.ijheatmasstransfer.2013.01.081>. [www.sciencedirect.com/science/article/pii/S0017931013001129](http://www.sciencedirect.com/science/article/pii/S0017931013001129)
12. Herbert S, Gambaryan-Roisman T, Stephan P (2013) Influence of the governing dimensionless parameters on heat transfer during single drop impingement onto a hot wall. *Colloids Surf A Physicochem Eng Asp* 432:57–63. <https://doi.org/10.1016/j.colsurfa.2013.05.014>. [www.sciencedirect.com/science/article/pii/S092775713003932](http://www.sciencedirect.com/science/article/pii/S092775713003932)
13. Höhmann C, Stephan P (2002) Microscale temperature measurement at an evaporating liquid meniscus. *Exp Therm Fluid Sci* 26(2–4):157–162
14. Ibrahem K, Abd Rabbo M, Gambaryan-Roisman T, Stephan P (2010) Experimental investigation of evaporative heat transfer characteristics at the 3-phase contact line. *Exp Therm Fluid Sci* 34(8):1036–1041
15. Kunkelmann C, Stephan P (2009) Cfd simulation of boiling flows using the volume-of-fluid method within openfoam. *Numer Heat Transf A* 56(8):631–646
16. Liang G, Mudawar I (2017) Review of drop impact on heated walls. *Int J Heat Mass Transf* 106:103–126. <https://doi.org/10.1016/j.ijheatmasstransfer.2016.10.031>. [www.sciencedirect.com/science/article/pii/S0017931016324097](http://www.sciencedirect.com/science/article/pii/S0017931016324097)
17. Minamikawa T, Fujimoto H, Hama T, Takuda H (2008) Numerical simulation of two droplets impinging successively on a hot solid in the film boiling regime. *ISIJ Int* 48(5):611–615
18. Raj R, Kunkelmann C, Stephan P, Plawsky J, Kim J (2012) Contact line behavior for a highly wetting fluid under superheated conditions. *Int J Heat Mass Transf* 55(9–10):2664–2675
19. Raman K, Jaiman R, Lee T, Low H (2017) Dynamics of simultaneously impinging drops on a dry surface: role of impact velocity and air inertia. *J Colloid Interface Sci* 486:265–276
20. Roisman I, Prunet-Foch B, Tropea C, Vignes-Adler M (2002) Multiple drop impact onto a dry solid substrate. *J Colloid Interface Sci* 256(2):396–410
21. S B (2015) Heat transfer and evaporation during single drop impingement onto a superheated wall. PhD thesis, TU Darmstadt, Germany. <http://tuprints.ulb.tu-darmstadt.de/4542/>
22. S F (2015) Experimental investigation of heat transfer during evaporation in the vicinity of moving three-phase contact lines. PhD thesis, TU Darmstadt, Germany

23. Sabetzadeh N, Bahrambeygi H, Rabbi A, Nasouri K (2012) Thermal conductivity of polyacrylonitrile nanofibre web in various nanofibre diameters and surface densities. *Micro & Nano Lett* 7(7):662–666
24. Schlawitschek C (2020) Numerical simulation of drop impact and evaporation on superheated surfaces at low and high ambient pressures. PhD thesis, TU Darmstadt, Germany
25. Slomski E (2012) Funktionsorientierte mikrostrukturierung von chromnitrid-beschichtungen mittels hybrider pvd-technologie. PhD thesis, TU Darmstadt, Germany
26. Sodtke C, Stephan P (2007) Spray cooling on micro structured surfaces. *Int J Heat Mass Transf* 50(19):4089–4097. <https://doi.org/10.1016/j.ijheatmasstransfer.2006.12.037>. [www.sciencedirect.com/science/article/pii/S0017931007001858](http://www.sciencedirect.com/science/article/pii/S0017931007001858)
27. Srikar R, Gambaryan-Roisman T, Steffes C, Stephan P, Tropea C, Yarin A (2009) Nanofiber coating of surfaces for intensification of drop or spray impact cooling. *Int J Heat Mass Transf* 52(25–26):5814–5826

**Open Access** This chapter is licensed under the terms of the Creative Commons Attribution 4.0 International License (<http://creativecommons.org/licenses/by/4.0/>), which permits use, sharing, adaptation, distribution and reproduction in any medium or format, as long as you give appropriate credit to the original author(s) and the source, provide a link to the Creative Commons license and indicate if changes were made.

The images or other third party material in this chapter are included in the chapter's Creative Commons license, unless indicated otherwise in a credit line to the material. If material is not included in the chapter's Creative Commons license and your intended use is not permitted by statutory regulation or exceeds the permitted use, you will need to obtain permission directly from the copyright holder.



# Impact of Supercooled Drops onto Cold Surfaces



Mark Gloerfeld, Markus Schremb, Antonio Criscione, Suad Jakirlic,  
and Cameron Tropea

**Abstract** Ice accretion resulting from the impact of supercooled water drops is a hazard for structures exposed to low temperatures, for instance aircraft wings and wind turbine blades. Despite a multitude of studies devoted to the involved phenomena, the underlying physical processes are not yet entirely understood. Hence, modelling of the conditions for ice accretion and prediction of the ice accretion rate are presently not reliable. The research conducted in this study addresses these deficiencies in order to lend insight into the physical processes involved. While presenting an overview of results obtained during the first funding periods of this project, new results are also presented, relating to the impact of supercooled drops onto a cold surface in a cold air flow. The experiments are conducted in a dedicated icing wind tunnel and involve measuring the residual mass after impact of a liquid supercooled drop exhibiting corona splash as well as the impact of dendritic frozen drops onto a solid surface.

## 1 Introduction

Icing of surfaces due to the impact of water drops at subfreezing temperatures, so-called supercooled large drops (SLD), poses a severe problem for transportation systems, as it may result in ice accretion on aircraft and roadways. This is also a frequent problem for power lines and wind turbines. Iced surfaces not only affect the proper and reliable function of the respective system; they can also represent a serious danger, since aircraft may crash, ships can capsize, iced roads result in traffic accidents and power lines and wind turbines may collapse as a consequence of additional loading by ice accretion. It is therefore of eminent importance that

---

M. Gloerfeld · M. Schremb · A. Criscione · S. Jakirlic · C. Tropea (✉)  
Institute of Fluid Mechanics and Aerodynamics (SLA), Technical University of Darmstadt,  
Darmstadt, Germany  
e-mail: [tropea@sla.tu-darmstadt.de](mailto:tropea@sla.tu-darmstadt.de)

M. Gloerfeld  
e-mail: [gloerfeld@sla.tu-darmstadt.de](mailto:gloerfeld@sla.tu-darmstadt.de)

the physics of drop solidification upon impact onto surfaces are understood and are predictable in order to properly model the phenomenon in numerical simulations and to design surfaces and/or means to reduce or eliminate icing.

However, the problem is complex. For one, solidification is initiated by nucleation, which in itself is inherently complex and normally treated in a stochastic manner. Then there is a complex interaction between thermodynamics and hydrodynamics, involving conjugate heat transfer with the substrate and wetting phenomena with material properties which are temperature dependent. Furthermore, these processes can involve mixed phases in which liquid, liquid with dendrites and ice are all present. Finally, the state of the substrate must also be considered. If the impact target is already covered with ice, then the entire solidification process can occur instantaneously upon impact, without exhibiting any freezing delay.

All of these complexities have been the focus of research in this project over the past 12 years at the Institute of Fluid Mechanics and Aerodynamics at the Technical University of Darmstadt within the framework of the CRC-TRR 75. The present article attempts to summarize the results of this work, divided into two main chapters: Chapter “[Interactive Visualization of Droplet Dynamic Processes](#)”, dealing with work performed during the first two funding periods from 2010 until 2017 and Chapter “[Development of Numerical Methods for the Simulation of Compressible Droplet Dynamics Under Extreme Ambient Conditions](#)”, dealing with on-going research until the completion of the CRCTR 75 in 2021. Further review articles of the work performed in the framework of this project can be found in [1, 2].

## 2 Nucleation and Freezing of Supercooled Large Drops (SLD)

The impact of a supercooled large drop (SLD) onto a surface is largely unaffected by the temperature of the substrate before nucleation occurs, exhibiting only minor dependencies related to the change of viscosity at low temperature [34]. Thus, a large body of literature addressing the hydrodynamics of drop impact onto dry surfaces with no phase change is directly applicable [27, 42]. However, once nucleation occurs, the rapid propagation of dendrites within the drop inhibits further hydrodynamic spreading and/or receding. Therefore, the nucleation instant and the associated freezing delay is of utmost importance in defining the final iced area and is an essential ingredient into any physics-based model describing ice accretion.

Once solidification starts as a result of the nucleation of ice embryos, a fast propagation of a cloud of dendrites throughout the bulk occurs, during which the remaining liquid portion of the drop warms to the freezing temperature. This rapid propagation of dendrites is followed by a slower, planar solidification corresponding to the Stefan problem. This process of solidification is depicted in Fig. 1. In the framework of this project, these phenomena have been examined in detail, experimentally, numerically and theoretically. Numerous articles summarize the main developments achieved,

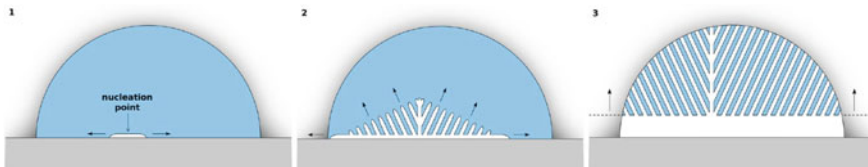


**Fig. 1** Three stages of solidification of a supercooled drop in the vicinity of a solid wall: (1) heterogeneous nucleation and spreading of a thin ice layer on the substrate, (2) dendritic freezing of the bulk liquid, (3) freezing of the remaining water at  $T_m$ . Note that the orientation of the dendrites in 2 and 3 is only schematically represented. Reprinted with permission from [35]. Copyright 2017 by the American Chemical Society

and two topics illustrating the main physical phenomena will be discussed in this Chapter: nucleation and freezing delay; and the three stages of solidification within the drop. The reader is referred to the other published material from this project for further details [1, 4, 5, 18, 19, 24, 29, 33–37].

## 2.1 Nucleation and Freezing Delay

The random nature of nucleation suggests that a statistical model should be possible to formulate by observing nucleation over a large number of identical experiments. Such a model for heterogeneous nucleation has been developed, based on a large number of impact experiments using double-distilled water drops and substrates at temperatures between +17 and –17°C. Denoting  $J_s(t)$  as the instantaneous rate of nucleation per unit area, the total average number of nucleation sites per drop can be estimated as

$$\lambda(t) = \int_0^{A_c(t)} \left( \int_{t_w(A_c)}^t J_s dt \right) dA, \quad (1)$$

where  $A_c(t)$  is the wetted surface area at time  $t$  and  $t_w$  is the instant when the given area element is wetted by the spreading drop for the first time. For long times after impact,  $t \gg t_w$ , the time of drop spreading can be neglected in comparison to the total time of nucleation and the expression for the average number of nucleation sites reduces to

$$\lambda(t) \approx \int_0^t J_s dt. \quad (2)$$

Since the process of nucleation is completely random, the statistics of the number of active nucleation sites follows a Poisson distribution. Considering statistics of  $N_0$  initially liquid drops impacting onto a cold substrate, the time at which the first nucleus appears in each drop is denoted  $t_n$  and can be determined from the

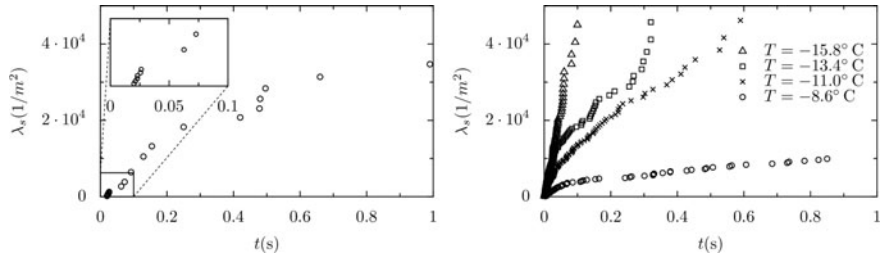


**Fig. 2** Average number of nucleation sites per unit area as a function of time. Left graph: water drops at  $14.3^\circ\text{C}$  impacting onto a cold, polished, aluminum substrate at  $-17.0^\circ\text{C}$ . Drop diameter is 3.09 mm and the impact velocity is 4.09 m/s. The impact angle is  $30^\circ$ . The contact temperature  $T_c = -14.7^\circ\text{C}$  is estimated using theory [28]. Right graph: supercooled water drops impacting onto a cold, sandblasted, glass substrate. The temperature of the substrate and the drop are the same. Drop diameter is 3.2 mm and the impact velocity is 2.2 m/s. The impact angle is  $90^\circ$ . Reprinted with permission from [37]. Copyright 2017 by the American Physical Society

experiments. The number of all the liquid drops  $N_{\text{liq}}(t)$ , whose nucleation time is larger than  $t$  continuously reduces in time. The above analysis yields the following remote asymptotic relation between the relative number of liquid drops and the nucleation rate

$$\lambda_s(t) \equiv \int_0^t J_s dt = \frac{1}{A_c(t)} \ln \frac{N_0}{N_{\text{liq}}(t)} \quad (3)$$

for times much longer than the time of drop spreading, where  $\lambda_s(t)$  is the average number of nucleation sites per unit area.

The values of  $\lambda_s(t)$  estimated from the experiments using the approximate expression (3) are shown in Fig. 2 for the impact of warm drops (left graph) and for impacts of supercooled drops (right graph) with various initial temperatures. In all cases, a time-dependent nucleation rate is observed. For the case of supercooled drops, the nucleation rate is relatively high during the first 35 ms after drop impact and is smaller for longer times. Moreover, a clear time lag for nucleation of approximately 20 ms is observed for oblique impact of warm drops (see the insert in Fig. 2 (left graph)).

Omitting further details which can be found in the cited literature, the surface temperature is found to be crucial for the nucleation rate. For low substrate temperatures, the contact area and contact time between the liquid and the substrate are increased as a consequence of varying liquid properties; especially the liquid viscosity exhibits a significant increase for temperature below  $0^\circ\text{C}$ . A more viscous flow leads to increased contact time, resulting in a higher nucleation probability. Concluding, the nucleation rate depends on time and is highest in the short phase immediately after impact. Further experiments performed with double-distilled degassed water drops exhibit a clear dependence of the nucleation rate on the liquid gas content, revealing another influence independent of the surface temperature [37].

## 2.2 Three Stages of Solidification within the Drop

To investigate the freezing process within a SLD in contact with a cold surface, a unique Hele-Shaw facility was conceived, constructed and proven to represent well the freezing of a sessile drop [38]. This facility is pictured in Fig. 3, illustrating the possibility of observing the freezing process through the acrylic glass plates using a high-speed video camera. The Hele-Shaw cell is placed on a cooling plate which maintains a specific temperature down to  $-30^{\circ}\text{C}$  using an external chiller. A typical freezing process of a water drop in this facility is shown in Fig. 4, indicating the three stages of freezing, with distinctly different time scales.

In the first stage, heterogeneous nucleation at the wall is followed by the tangential growth of a thin ice layer spreading over the metal substrate/water interface with a constant speed, which depends on supercooling. This initial ice layer has been well documented in [35] with comparison to existing studies [39]. In the second stage, the growth of dendrites arising from the layer instability is observed. While single dendrites are observed for smaller supercooling, the dendrite density increases with increasing supercooling, resulting in a dense front of dendrites for large supercooling. The spreading of the initial ice layer on the bottom locally causes solidification of

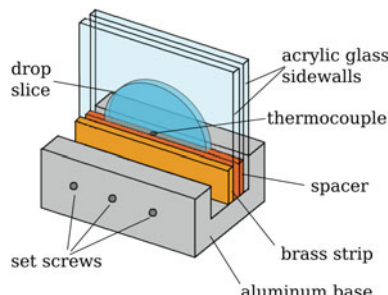


**Fig. 3** Schematic of the Hele-Shaw cell with an inserted drop. Reprinted with permission [35]. Copyright 2017 American Chemical Society

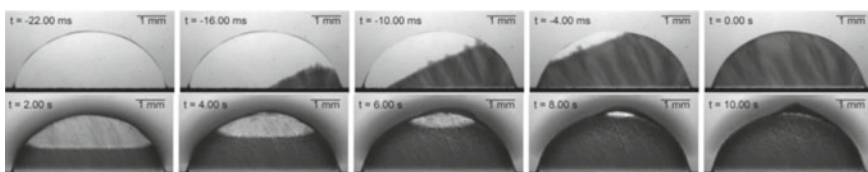


**Fig. 4** Observations of freezing process using Hele-Shaw cell. Top row—first two stages of solidification, supercooled to approx.  $-15.8^{\circ}\text{C}$ . Bottom row—Third stage of solidification of drop in top row. Approx. 19% of the liquid is already frozen at the beginning of this stage. Reprinted with permission [35]. Copyright 2017 American Chemical Society

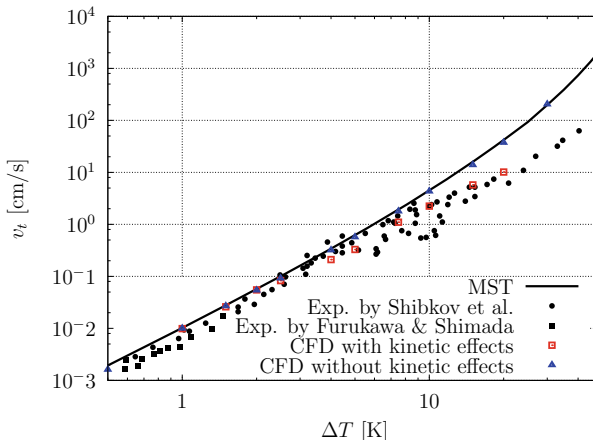


**Fig. 5** Steady state tip velocity,  $v_t$ , dependence on initial supercooling  $\Delta T$  for  $\lambda_s/\lambda_f = 1$ : computational versus MST-theoretical and experimental results; the results obtained by present empirical model accounting for kinetic undercooling at the solid-liquid interface exhibit good agreement with reference experiments over the entire range of initial supercooling. Reproduced from [6]. Copyright 2015 Elsevier Masson SAS. All rights reserved

the meta-stable liquid, leading to an asymmetric propagation of the dendrite front, as shown in the top row of images in Fig. 4 between  $t = -16\text{ ms}$  and  $t = -10\text{ ms}$ .

At the end of the second stage ( $t = 0$ ) only a portion of the initially supercooled drop is frozen and a lattice of dendritic ice fills the entire drop. The latent heat released during solidification has warmed up the water/ice mixture to thermodynamic equilibrium at the melting temperature. In the third stage ( $t > 0$ ) a stable freezing of the remaining water occurs. The freezing front in this stage moves in the opposite direction of the applied heat flux. This stage can be observed in the lower row of images in Fig. 4.

Although the final two stages of freezing have been previously identified experimentally [12], the modelling of these stages was unclear until recently. Building on the morphological instability of the initial tangential ice layer introduced by [22, 23], the analytic solution for the steady-state tip velocity and radius of growing dendrites from [10], as well as the principles governing the tip shape using Marginal Stability Theory (MST) introduced by [15–17], a unique tip growth velocity as a single valued function of the supercooling can be calculated. However, for larger supercooling the theory overpredicts the growth rate of dendrites, as shown in Fig. 5. Therefore an empirical model for the kinetic coefficient was developed, as outlined in the following. It represents a revised version of the model derived in [5].

In order to quantify the model term mimicking the kinetics-limited growth, the theoretical and experimental results displayed in Fig. 5 are comparatively analyzed. First of all, it is assumed that the steady-state dendrite tip velocity determined experimentally in [39],  $v_{n,\text{exp}}$ , is directly proportional to  $\Delta T$

$$v_{n,exp} \propto \Delta T_T, \quad (4)$$

with  $\Delta T_T$  representing the total undercooling (consisting of viscous and kinetic fractions,  $\Delta T_v$  and  $\Delta T_{kin}$  respectively) at the solid-liquid interface, which is defined as

$$\Delta T_T = \Delta T_v + \Delta T_{kin}. \quad (5)$$

In the analytical MST solution, the viscous undercooling is accounted for. In order to account for the kinetic undercooling, the ratio of the theoretical steady-state velocity  $v_{MST}$  (related to the viscous undercooling only) to the experimentally determined one  $v_{n,exp}$  (influenced in addition also by the kinetic undercooling),  $|\tilde{v}_n| = v_{MST}/v_{n,exp}$ , is computed assuming its proportionality to the ratio of the viscous (capillary) undercooling to the total undercooling

$$\Delta T_T = \frac{\Delta T_v}{|\tilde{v}_n|}. \quad (6)$$

Inserting it into Eq. (5) and adopting a linear function for the kinetic undercooling, the following expression for the kinetic coefficient is obtained

$$k_{kin} = \frac{|\tilde{v}_n| v_{MST} L \rho}{(1 - |\Delta v_n|) \kappa \sigma T_m}. \quad (7)$$

Here,  $\sigma$  and  $\kappa$  describe the interfacial energy of water and the curvature of the surface area, respectively.  $T_m$  denotes the melting temperature of water and  $L$  represents its latent heat of fusion. The density of ice and water is assumed to be equal and is given by  $\rho$ . The preliminary results obtained at high supercooling degrees by accounting for the kinetic undercooling in the present computational model exhibit good agreement with the experimental data. The only limitation when using Eq. (7) is that the kinetic coefficient is directly dependent on the theoretical steady-state velocity; hence, on the initial supercooling degree. In order to find a coefficient value valid for all supercooling degrees considered, the relation between the kinetic coefficient and the theoretical steady-state velocity is introduced by applying the following relation:

$$k_{kin} = \xi (v_{MST})^{\frac{2}{3}}. \quad (8)$$

The value of the coefficient  $\xi$  representing a pre-exponential factor, is calibrated by reference to the experiment by [39] (see Fig. 5), amounts to  $(\pi/11)^{2/3}$ . Accordingly, the coefficient  $\xi$  represents a dimensional quantity whose units corresponds to  $m^{1/3}/(s^{1/3}K)$ . The kinetic undercooling can be formulated as follows:

$$\Delta T_{kin} = \frac{v_n}{k_{kin}}. \quad (9)$$

Assuming that the solid-liquid interface velocity,  $v_n$ , corresponds to the theoretical value  $v_{MST}$  obtained by neglecting the kinetic effects, the kinetic undercooling can be redefined, yielding in following equation:

$$\Delta T_{\text{kin}} = \frac{(v_{\text{MST}})^{\frac{1}{3}}}{\xi}. \quad (10)$$

Thus, the appropriate quantification of the kinetic undercooling influence on the dendrite growth in the high supercooling range is provided. After accounting for the kinetic effects by considering the present approach, the computational results at high supercooling degrees follow closely the experimental results, Fig. 5. Further details of the numerical procedure used can be found in [5, 6].

### 3 Impact of Supercooled Large Drops Superimposed with a Cold Air Flow

Further investigations were devoted to the investigation of supercooled drops impacting under the influence of a cold air flow. These investigations involve fluid drops impacting with a corona splash as well as drops which have completed the second solidification stage (growth of dendrites in the bulk) before impact. The associated experiments have been conducted in a newly developed icing wind tunnel which is described in detail in the following section, followed by sections describing the experimental results and analyses.

#### 3.1 Test Facility

The wind tunnel is a vertical open return blower wind tunnel placed inside a cooling chamber, as depicted in Fig. 6. After passing the inlet section and nozzle, the flow enters a square test section with a side length of 140 mm, before entering a diffusor leading to a radial fan. The flow exits the fan into the cooling chamber. The velocity profile across the test section is highly uniform, reaching velocities up to  $U_{\text{air}} = 40$  m/s with a turbulence intensity of  $Tu = 0.5\%$ .

Supercooled drops are generated from above the tunnel inlet using a syringe needle inside of the wind tunnel and protected from the airflow by a shroud pipe. In order to minimize the probability of solidification inside of the water supply, the drops are produced from de-ionized water (*Milipore* ®). After detaching from the syringe, the drops accelerate due to gravity until entering the air flow, where they are further accelerated by the air flow. In the test section, the drops impact onto a surface placed horizontally in the wind-tunnel. The impact is captured using a high-speed camera (*Photron SA-X2*) with background illumination.

**Fig. 6** Icing wind tunnel placed inside of a cold chamber for investigating the impact of supercooled water drops. Some components are not shown to scale.  
Reprinted from [7]

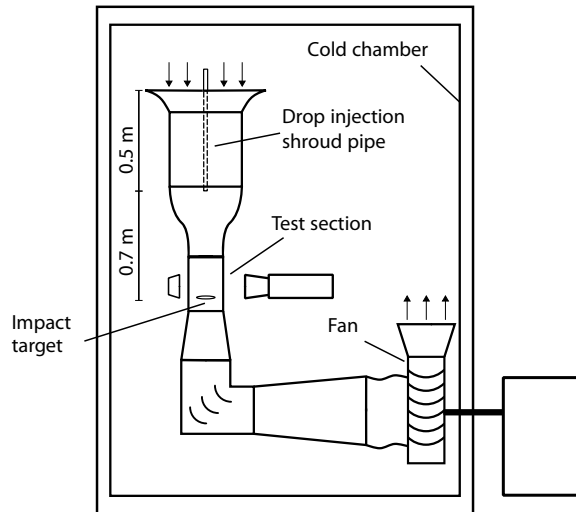
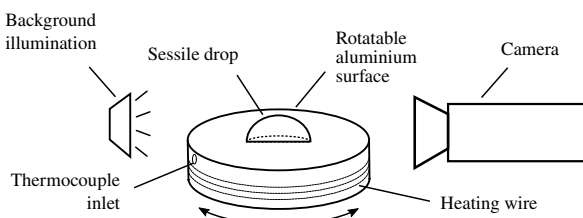


**Fig. 7** Rotatable impact surface for the investigation of residual mass, enabling multiple viewing angles.  
Reprinted from [7]



The cooling chamber maintains ambient temperatures down to  $T_{\text{amb}} = -20^{\circ}\text{C}$ ; thus determining the temperature of the airflow, the drops and the impact target. All temperatures range within  $\pm 1.5^{\circ}\text{C}$  of the chamber temperature. Furthermore, the ambient air is fully saturated, avoiding any temperature variation due to drop evaporation. In order to quantify the supercooling of the drops, the temperature is continuously measured by a thermocouple inside of the syringe needle. Additionally, the temperatures of the surface and the air flowing through the test section are monitored during the experiments.

The drop impacts onto a flat aluminum target. To examine the deposited liquid or ice on the surface after drop impact, some additional features have been incorporated into the target, as depicted in Fig. 7. A heating wire wraps around the cylindrical aluminum target in order to melt any residual ice remaining on the target. This is especially helpful in retroactively determining the volume/mass of the deposited fluid, since after heating the possibly frozen drop it becomes a sessile, liquid drop. To examine the residual ice and/or sessile drop in more detail, the target can be rotated, during which images from numerous viewing angles are captured. This technique, employing multiple views, yields a high precision measurement of the remaining liquid volume, elaborated in more detail below.

### 3.2 Impact of *Mushy* Frozen Drops

Supercooled drops are in a meta-stable state and their freezing depends on the occurrence of nucleation sites. An analysis of the nucleation probability after impact conducted previously [37] indicated that the highest nucleation probability occurred shortly after impact. However, the number of drops with a distinct freezing delay remains non-negligible. Thus, different icing scenarios have to be considered.

An onset of freezing long after the impact results in a solid spherical cap (truncated sphere) with an elevated top due to freezing expansion, arising from the solidification of the receded, sessile drop. The influence of fluid temperature and surface properties were investigated for this case in previous studies [6, 38]. However, if a shorter delay arises between impact and solidification, other freezing scenarios are possible. One frequent scenario is solidification shortly after impact. A freezing during the receding of the drop fixes the fluid in its current position and leads to a larger surface area covered with ice. The solidified area is therefore strongly linked to the impact hydrodynamics and the surface properties as described in [42]. In fact, dendritic solidification of the drop might occur even before impact if nucleation arises due to contaminants or disturbances beforehand. The short timescale of the first dendritic solidification stage and the significantly slower second stage then lead to an impact of a mushy, frozen drop. Moreover, the dendritic freezing may occur for supercooled liquid remaining on the surface after impact, which also yields a mushy phase. The impact and spreading of a ‘mushy’ phase, or dendritic frozen drop, remains unexplored to date and is one focus of the present study.

Although to the authors’ knowledge no study has addressed the impact of dendritic frozen drops, the impact of two-phase drops has been the topic of several investigations in the recent past. A review of compound drop impact is found in [2], although the investigated drops mainly involved two liquid phases. A study of the impact of a sand/water mixture drop was conducted in [20]. A more recent study from [14] is devoted to the impact of a partially frozen binary drop composed of hexadecane and diethylether. However, the solidification of these drops occurs uniformly from the outside to the centre during their descent.

In the present study, the impact of dendritic frozen drops is examined, whereby their ice fraction is varied systematically by the degree of supercooling of the initially liquid drop. In order to characterize the plastic flow behaviour of the impact, an existing model for the impact of a semi-brittle sphere is adapted [31]. Using this model and information gained from the high-speed recordings—the residual height after the impact of the mushy drop, the impact velocity and the ice fraction—the yield strength of the mushy phase is estimated. The results of this study can be found in [8].

### 3.2.1 Method

The drops used in this study all had a diameter of  $D_0 = 3\text{ mm}$  and their impact velocity was varied in the range  $3.8\text{--}5.6\text{ ms}^{-1}$  by varying the flow velocity in the wind tunnel. The initial supercooling of the drops was varied in the range  $-11.5$  to  $-7\text{ K}$ . To promote and ensure dendritic freezing before impact, several small ice crystals were pinned to the end of the shroud pipe. Since the typical time for dendritic freezing of the drop,  $\mathcal{O}(10\text{ ms})$ , is much shorter than the time it takes the drop to reach the impact target,  $\mathcal{O}(100\text{ ms})$  after nucleation, all drops in the present study have finished the dendritic stage of supercooled solidification upon impact. Hence, all impacting drops exhibit a temperature of  $0^\circ\text{C}$ , since thermodynamic equilibrium has been reached.

In order to determine the volume ratio of ice in the drop, the ice fraction  $\xi_{\text{ice}}$  is obtained from an energy balance in the drop [9]. Considering the temperature dependent properties of the fluid, the ice fraction is obtained from the initial supercooling after [33] as

$$\xi_{\text{ice}} = \frac{\rho_w c_{p,w} \Delta T}{\rho_{\text{ice}} L + \Delta T (\rho_w c_{p,w} - \rho_{\text{ice}} c_{p,\text{ice}})}. \quad (11)$$

Here,  $\Delta T$  represents the initial supercooling of the liquid in Kelvin and  $L$  the latent heat of fusion. Furthermore,  $\rho_w$  and  $c_{p,w}$  are the density and heat capacity of the supercooled liquid respectively, and correspondingly,  $\rho_{\text{ice}}$  and  $c_{p,\text{ice}}$  the properties of ice at  $0^\circ\text{C}$ . The ice fraction of the mushy drops used in the experiments ranges between  $\xi_{\text{ice}}(11.5\text{ K}) = 15.0\%$  and  $\xi_{\text{ice}}(7\text{ K}) = 9.4\%$ . The specific heat capacity at constant pressure ( $c_p$ ) is used instead of the specific heat capacity at constant volume ( $c_v$ ), since during freezing the pressure remains constant, but not the volume.

One quantity characterizing the mushy phase of drops with various dendritic ice fractions is the yield strength of the ice/water mixture. To estimate the yield strength, a model describing the impact and fragmentation of ice particles is adapted from [31]. The particle is considered as a semi-brittle sphere being crushed upon impact. The yield strength is obtained from a force balance normal to the surface and the dimensions of the crushed particle when it comes to rest. Throughout the impact event of a mushy frozen drop, the yield strength  $Y$  is assumed to be constant. This way, it is related to the impact velocity and the remaining height of the particle by

$$\frac{1}{Y} = -\frac{2}{\rho U_0^2} \ln \left[ \frac{(2 - \delta_{\max})^2 (1 + \delta_{\max})}{4} \right], \quad (12)$$

with  $\rho$  being the density of the particle and  $U_0$  its impact velocity. The remaining dimension in the vertical direction is denoted by the maximum of a dimensionless displacement  $\delta_{\max}$ . It is obtained from the particle height  $h_{\max}$  and the initial radius  $R_0$  as  $\delta_{\max} = 2 - (h_{\max}/R_0)$ . A more detailed derivation of the model is given in [31].

### 3.2.2 Results and Discussion

The ice dendrites developing inside the drop during the first freezing stage cause a significant change of its material properties and its impact behaviour. A pure liquid drop upon impact forms a thin lamella spreading over the surface [42]. In contrast, the flow in a mushy frozen particle corresponds more to a plastic flow behaviour, with an increased deceleration of the flow during impact. For the investigated mushy frozen particles, the deceleration is sufficient to cause a nearly cone-shaped ice agglomeration at the impact position when the mixture comes to rest. This behaviour is visible in the image sequence shown in Fig. 8.

In the first image before the impact occurs, the dendritic state of the drop is already noticeable. The first-order refracted light from the background illumination passing through a pure liquid drop would form a bright spot in the middle of the drop. However, the dendrites in the mushy particle cause a diffuse light scattering within the drop, resulting in an evenly dark appearance of the drop. In the first instance after the impact, small fragments leave the spreading mushy frozen particle, similar to the prompt splash of a liquid drop. However, their appearance suggests a mixture of water and broken dendrites, i.e., ice. Subsequently, the above-mentioned deceleration of the ensuing ice/water mixture initiates an accumulation of the mushy phase in the center. Eventually, the mushy phase comes to rest and forms a shape similar to a cone, as shown in the last two images of Fig. 8. The shape remains undisturbed on the surface while the remaining fluid in the mixed phase finishes its solidification.

The dimensions of the remaining cone are obtained from images captured while rotating the target. The analysis of the resulting geometry indicate two main dependencies. First, a higher impact velocity leads to a decreasing height of the remaining shape due to higher inertial forces during impact. Second, the height of the remaining shape alters with the initial supercooling of the drop, which corresponds to different ice fractions according to Eq. (11). This influence suggests a change of the mushy particle properties. With regard to the model of [31], this change manifests itself in a different yield strength of the mushy phase. With the aid of Eq. (12), a yield

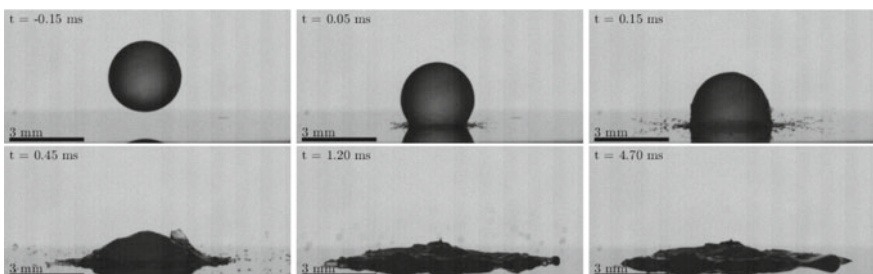


**Fig. 8** Image sequence of a mushy particle impacting with  $U_0 = 4.2 \text{ m/s}$  originating from a drop with an initial supercooling of  $\Delta T_0 = 9.2 \text{ K}$

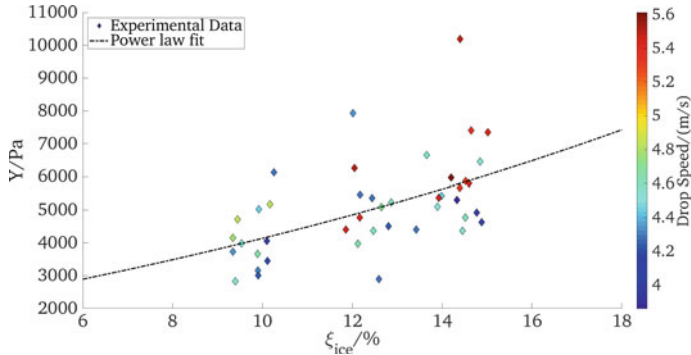


**Fig. 9** Yield strength determined from the experimental results for residual height plotted over the ice fraction of the corresponding mushy particle. The drawn line indicates the general trend

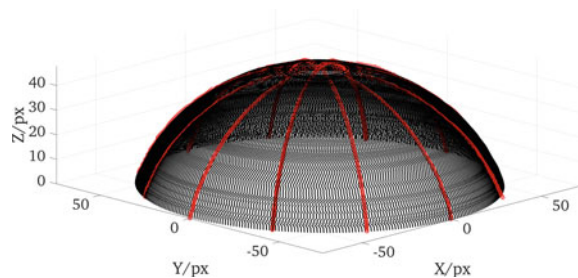
strength  $Y(U_0, \delta_{\max})$  for each impacting particle as a function of its impact velocity and residual height is obtained. In Fig. 9, this yield strength is plotted over the volume ice fraction  $\xi_{\text{ice}}$ .

The experiments reveal a clear tendency towards higher values of  $Y$  for increasing ice fraction; however, the scatter of the data indicates significant uncertainty in the exact value of  $Y$  and a larger amount of data would contribute to improvement of the predictive capability indicated by the data. Nevertheless, this data presents a novel step in understanding the physics and dynamics related to the impact of mushy frozen drops and their properties.

### 3.3 Residual Mass of Drops Impacting with a Corona Splash

The impact of a supercooled drop on a surface increases the probability of solidification of the fluid [37]; however, as long as the drop is not contaminated before impact it usually remains liquid during the impact. Considering the timescales of the kinematic and spreading phase of the impact [26] and the propagation of dendrites in the initial solidification stage [39], in general the impact stages are significantly faster. Hence, the first stages of a supercooled drop impacting as a liquid are not affected directly by the solidification of the fluid at the beginning. However, the flow following the first contact determines the distribution of fluid on the surface and influences where it eventually solidifies. Hence, the following section deals with the spreading dynamics of a liquid drop impacting with a co-flow and the mass remaining on the surface for situations in which a splash occurs.

**Fig. 10** Point cloud of drop (black) reconstructed from the framework of points (red) obtained from multiple viewing angles



### 3.3.1 Materials and Methods

Using the icing wind tunnel described above, experiments have been carried out with drop impact velocities in the range  $U_0 = 0$  to 10.5 m/s at supercoolings in the range  $\Delta T_0 = -5$  to  $-13$  K, keeping the drop diameter constant at  $D_0 = 3$  mm.

To conduct the measurement of deposited mass, the target is first heated to melt any ice which had formed after the splash. When melted, the liquid recedes into a spherical cap. Several images of this sessile drop are then captured from different viewing angles by rotating the target; hence, any deviations from axisymmetry or off-centering can be detected and accounted for, increasing the precision of the determined volume. The images are used for a three-dimensional reconstruction of the drop shape. This reconstruction is visualized in Fig. 10. The red lines in this figure correspond to elliptic contours obtained from different viewing angles; the black dots lie on the interpolated surface. From this point cloud, a triangulation of the enclosed volume is performed. The images are calibrated using metal spheres exhibiting a precision of  $<0.01$  mm in diameter. During the calibration, a reconstruction of the sphere volume with a maximum deviation of  $0.2 \mu\text{l}$  is achieved. Thus, the method enables a reconstruction of drop volumes with an uncertainty of  $\pm 0.2 \mu\text{l}$ .

### 3.3.2 Results and Discussion

Considering the impact of a drop with a superimposed co-flow, the flow of the impacting fluid is also affected by a deformation of the drop as it approaches the surface. An example of drop deforming in an airflow with  $U_{\text{air}} = 25$  m/s is shown in the right image of Fig. 11. In comparison to a spherical drop (left image), the drop exhibits a flattening of its front close to the surface. This deformation is most likely attributed to co-flow stagnation pressure arising on the target surface.

In order to investigate the effect of the deformation on the flow developing on the surface, the curvature of the drop needs to be quantified. For this purpose, the curvature of the drop front,  $\kappa$ , is determined from the inverse of the average radius in the immediate vicinity of the first point of contact before impact. Hence, a flattened drop front leads to an increase of average radius and to smaller values of  $\kappa$ . Furthermore, the spreading lamella flow on the surface is considered in terms of the evolution of

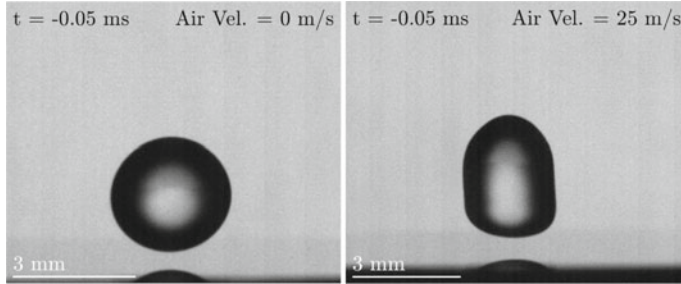


**Fig. 11** Drop deformation before impact due to acceleration in the surrounding air flow. The left drop impacts without a co-flow. The right drop is accelerated by an air flow with  $U_{\text{air}} = 25 \text{ m/s}$ . Both drops are of the same volume ( $V_0 \approx 14.1 \mu\text{l}$ ) [7]

the wetted area as introduced by [26]. In this work, the time dependent evolution of the radius of wetted area  $r$  is found to grow proportional to  $\sqrt{t}$ , resulting in an expression for the dimensionless radius of the wetted area  $r^+ = r/R_0$  as

$$r^+ = b\sqrt{t^+}. \quad (13)$$

Here,  $t^+ = tU_0/D_0$  denotes the dimensionless time and  $b$  a dimensionless proportionality constant. In the investigated drop impacts of the present study, the radius of the wetted area is tracked by an image recognition software. Assuming a correlation according to Eq. 13, the proportionality constant  $b$  is determined from a least squares fit to the obtained data for each impact. The resulting values are plotted in Fig. 12 with regard to the corresponding values of dimensionless curvature  $\kappa R_0$ . It is apparent that the values of  $b$  increase with decreasing curvature. Thus, a flattened drop front (smaller  $\kappa$ ) causes a faster spreading of the fluid on the surface, i.e. an increased spreading velocity of the fluid on the surface.

This perception leads to the hypothesis that the flow during the kinematic impact phase is not dependent on the average radius  $R_0$ , but on the curvature  $\kappa$ . Replacing  $R_0$  in Eq. 13 leads to a correction of the proportionality constant given by

$$b = \frac{b_0}{\sqrt{\kappa R_0}}. \quad (14)$$

Here  $b_0$  denotes the constant for a spherical drop ( $\kappa R_0 = 1$ ) which is marked in Fig. 12 with a dashed line. The solid line in the same figure represents a least squares fit of Eq. 14, which exhibits good agreement with the experimental data. The value of  $b_0$  for a spherical drop is determined as  $b_0 = 2.12$ , which agrees well with the value obtained by [26], being  $b_0 = 2.05$ . Note that the original value given in their work is obtained with a different scaling, which requires a conversion of the value with the factor  $1/\sqrt{2}$  in order to compare it to the findings of the present study. The curvature correction enables the incorporation of drop deformation effects in

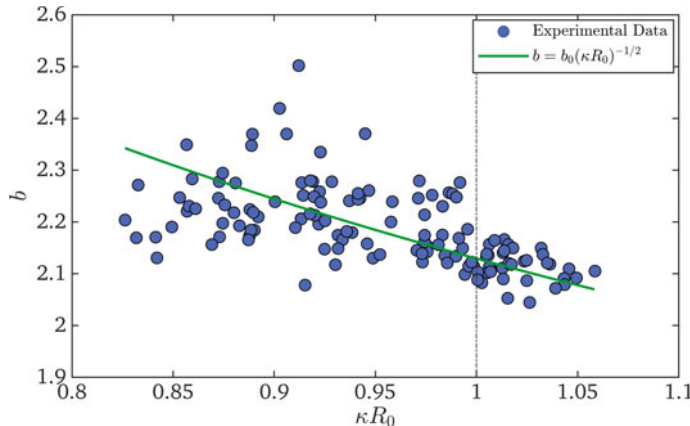


**Fig. 12** Proportionality constant  $b$  as a function of the dimensionless curvature ( $\kappa R_0$ ) of the impacting drops lower surface [7]

models describing the flow developing during impact, for instance with respect to the splashing of a drop as in [25]. A detailed description of the adaption of this model with regard to drop deformation can be found in [7].

Besides the drop spreading on the surface, some liquid will splash. This re-emitted liquid will end up somewhere else, possibly not even on the target [42]. The amount of deposited mass is of particular interest, since this directly influences the amount of ice accretion. Splashing of a drop impacting onto a dry surface has been a topic of exhaustive reviews in the past [11, 41, 42]; however, little work has succeeded in quantifying the ejected and/or deposited mass during the splash event. Some studies have attempted to estimate the mass of secondary drops emitted during impact of a spray. For instance, in [13] experiments were conducted using a phase Doppler system to measure this quantity. A summary of empirical models devoted to the ejected secondary droplet mass is given in [21]. In the present study, the deposited mass after impact of a supercooled drop undergoing corona splash is experimentally determined using the technique of melting the residual ice and viewing the resulting sessile drop involving several camera images.

A water drop at 20°C impacting with a velocity and diameter considered in this study would deposit on the surface without a splash. However, supercooled drops exhibit a significant change in fluid viscosity; more precisely, the viscosity increases by a factor of 3.3 for a temperature change between 20 and -15°C. This increase leads to a corona splash of the drop upon impact. According to [30], the threshold of this regime is defined by a critical Ohnesorge number  $Oh_{crit} = 0.0044$  ( $Oh = \mu / \sqrt{D_0 \rho \sigma}$ ), whereby a corona splash is predicted for values larger than  $Oh_{crit}$ . Considering the change in fluid properties due to supercooling, this condition is fulfilled for all investigated drops. Since the Ohnesorge number is independent of the impact velocity, this transition to the corona splash regime is solely accountable for by the fluid properties and the drop diameter. Considering splashing of super-

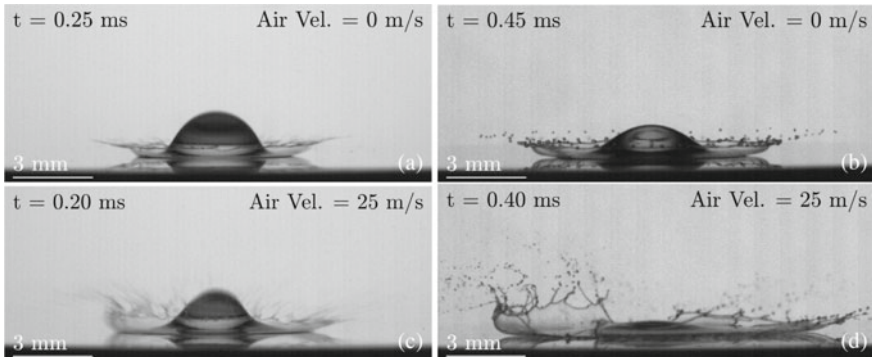


**Fig. 13** Comparison of the corona extent in the incident before break up from four drops ( $D_0 = 3 \text{ mm}$ ) with different drop temperatures and impact velocities. **a**  $U_0 \approx 4.2 \text{ m/s}$ ,  $\Delta T_0 \approx -5^\circ\text{C}$ ; **b**  $U_0 \approx 10.5 \text{ m/s}$ ,  $\Delta T_0 \approx -5^\circ\text{C}$ ; **c**  $U_0 \approx 4.2 \text{ m/s}$ ,  $\Delta T_0 \approx -13^\circ\text{C}$ ; **d**  $U_0 \approx 10.5 \text{ m/s}$ ,  $\Delta T_0 \approx -13^\circ\text{C}$

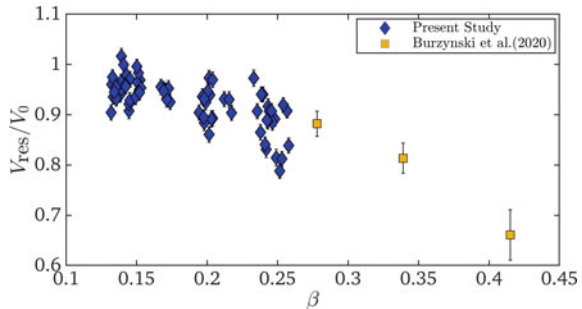
cooled water drops ( $T < 0^\circ\text{C}$ ), drops smaller than  $D_0 = 2.2 \text{ mm}$  will always exhibit a corona splash. Moreover, larger droplets will transition to this regime for a relatively small increase in supercooling.

Although all observed drops impact with a corona splash, the extent of the splash differs with temperature and air flow velocity, i.e. impact velocity. This change is already observable qualitatively from the high-speed recordings. Figure 13 shows the instant before the thin film of the corona breaks up for the highest and lowest temperatures and impact velocities respectively. Considering the two upper images, a slight influence of the temperature on the splash is noticeable. The crown of the corona extends farther away from the impact position just before breakup. With respect to the time of the breakup after impact, the increased extent can presumably be explained by a more stable film during crown formation. The stabilization of the film is most likely caused by the increased viscosity due to the lower drop temperature.

A higher impact velocity will increase the extent of the corona distinctly. When comparing the two images on the left of Fig. 13, a change due to an increased impact velocity is observable. For the higher velocity the film of the corona spreads faster. Note, the asymmetry of the corona is most likely caused by the air flow onto the surface and the drop deformation before impact. An additional increase of supercooling increases the spreading of the corona even more. Again, the uprising film is stable for a longer period of time, providing more time for its expansion.

The changes apparent from the qualitative analysis suggest that for higher supercooling more fluid enters the film during splash; hence, a subsequent breakup would result in more mass being ejected from the drop. In order to experimentally verify this hypothesis, the fluid volume remaining on the surface after impact is quantified with the drop size estimation method described above. Since the qualitative analysis suggests a residual volume change related to the film thickness of the corona splash, the origin of the film (lamella) lifting of the substrate surface is assumed to be a crucial influencing factor for the residual volume  $V_{\text{res}}$  on the surface.

**Fig. 14** Residual volume in relation to original drop volume plotted over the splashing parameter  $\beta$  defined after [25]. The impact parameters account for splashing well in the corona splashing regime ( $\text{Oh} > 0.0055$ )



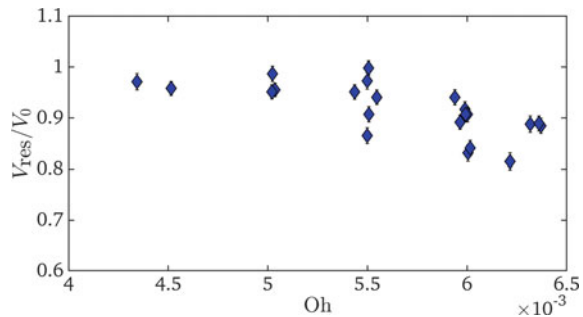
To describe the lamella lift-off, the model of [25] considers a force balance of the aerodynamic lift force acting on the lamella and the surface tension of the fluid. This ratio is introduced as the dimensionless parameter  $\beta > \beta^*$ , where  $\beta^*$  describes the critical value for the occurrence of a splash. While the value of  $\beta$  in the definition by [25] depends on the Reynolds number, Ohnesorge number, the mean free path of the surrounding gas and the average radius  $R_0$  of the drop before impact, the values presented in the following are obtained with an adaption to the model due to drop deformation before impact as described above. For a detailed description of the deformation, their consequences for the liquid flow on the surface and the adaption in the model, reference is made to [7].

Considering the residual volume  $V_{\text{res}}$  of a single impact with regard to the corresponding values of  $\beta$ , a clear trend is visible when considering drop impacts with a well-developed corona splash ( $\text{Oh} > 0.0055$ ). As shown in Fig. 14, the residual volume decreases with increasing values of  $\beta$ . The trend agrees well with values obtained in [3] marked with squared symbols in the figure. Hence, considering that  $\beta$  monotonically increases with the impact velocity  $U_0$ , the drop diameter  $D_0$  and the fluid viscosity  $\eta_l$ , an increase in each of these quantities will lead to a decrease in residual volume  $V_{\text{res}}$  on the surface after a corona splash. Here, the influence of  $U_0$  is the strongest factor with  $\beta \propto U_0^2$  in the range of the present values. Despite the visible trend in the data, the physical scatter in the data suggests some missing or unaccounted for influence in the parameter  $\beta$ .

A consideration of the residual volume obtained for a constant value of  $\beta$  confirms this interpretation of the results. In Fig. 15, the data determined for impacts with  $\beta \approx 0.24$  are shown as a function of the Ohnesorge number  $\text{Oh}$ . The decreasing trend of  $V_{\text{res}}$  with higher  $\text{Oh}$  suggests an underrepresented influence of the viscous forces ( $\sigma \approx \text{const.}$  in the present study) in the parameter  $\beta$  in order to predict the remaining fluid after the splash. Since the determination of  $\beta$  is mainly based on the hydrodynamics at the very beginning of the splash, the missing viscosity influence possibly takes effect at later stages of the splash, where the lifted film is already developing into a corona.

Especially a combination of viscous effects with the overriding air flow, which is in no way captured in the quantity  $\beta$ , seems likely. The highest  $\beta$  values correspond to the highest impact velocities  $U_0$ , which are themselves linked to the air flow

**Fig. 15** Residual volume in relation to original drop volume plotted over Oh for a constant value of the splashing parameter  $\beta \approx 0.24$



velocity. Hence, the asymmetric splashing for high air flow velocities (see Fig. 13) suggests an influence of the air flow, a supposition which requires further investigation. Nevertheless, the quantification of the residual volume and the dependence on the splashing parameter  $\beta$  represents a significant step towards measuring the mass remaining on the surface after a supercooled drop impacts on a dry surface.

## 4 Conclusion

The results presented above address the multitude of physical phenomena related to the impact and solidification of supercooled large drops onto cold surfaces. These results are particularly relevant to ice accretion in the aviation industry, but they elucidate fundamental phenomena which can be found in many other icing situations. The ultimate goal of this research is to improve predictive capability of ice accretion, and for this the experimental observations made in this study have been used to develop physics based models describing the respective hydrodynamics and thermodynamics involved.

The freezing of supercooled large drops occurs in three stages—nucleation, dendritic freezing, bulk freezing—whereby a significant freezing (nucleation) delay can occur even after impact onto a substrate. Depending on the freezing stage upon impact, the hydrodynamics of drop spreading can be strongly affected, influencing the area over which the ice is formed on the surface. Of particular importance for predicting ice accretion is to know the amount of volume of liquid and/or ice left on the surface, after some portion is splashed. For this, a novel method of experimentally determining this residual volume has been introduced. The experimental results obtained using this method were then used to adapt an existing model for residual mass, leading to a new theoretical relation between residual mass and impact parameters. Future work will expand the range of impact parameters experimentally investigated and consider necessary modifications to the derived models.

**Acknowledgements** The authors kindly acknowledge the financial support by the Deutsche Forschungsgemeinschaft (DFG) within the SFB-TRR 75, project number 84292822.

## References

- Berberović E, Schremb M, Tuković Ž, Jakirlić S, Tropea C (2018) Computational modeling of freezing of supercooled water using phase-field front propagation with immersed points. *Int J Multiph Flow* 99:329–346. <https://doi.org/10.1016/j.ijmultiphaseflow.2017.11.005>
- Blanken N, Saleem MS, Thoraval MJ, Antonini C (2021) Impact of compound drops: a perspective. *Curr Opin Colloid Interface Sci* 51:101389. <https://doi.org/10.1016/j.cocis.2020.09.002>
- Burzynski DA, Roisman IV, Bansmer SE (2020) On the splashing of high-speed drops impacting a dry surface. *J Fluid Mech* 892:A2. <https://doi.org/10.1017/jfm.2020.168>
- Criscione A, Jakirlić S, Tukovic Z, Roisman I, Tropea C (2015) Surface energy influence on supercooled water crystallization: a computational study. Technical report SAE Technical Paper (2015). <https://doi.org/10.4271/2015-01-2115>
- Criscione A, Kintea D, Tuković Ž, Jakirlić S, Roisman I, Tropea C (2013) Crystallization of supercooled water: a level-set-based modeling of the dendrite tip velocity. *Int J Heat Mass Transf* 66:830–837. <https://doi.org/10.1016/j.ijheatmasstransfer.2013.07.079>
- Criscione A, Roisman IV, Jakirlić S, Tropea C (2015) Towards modelling of initial and final stages of supercooled water solidification. *Int J Therm Sci* 92:150–161. <https://doi.org/10.1016/j.ijthermalsci.2015.01.021>
- Gloerfeld M, Roisman IV, Hussong J, Tropea C (2021) Measurements and modelling of the residual mass upon impact of supercooled liquid drops. *Exp Fluids* 62(10):4520. <https://doi.org/10.1007/s00348-021-03292-7>
- Gloerfeld M, Schremb M, Roisman I, Tropea C, Hussong J (2021) Impact of mushy frozen water particles onto a cold surface. In: 15th Triennial international conference on liquid atomization and spray systems, Edinburgh, UK, 29 Aug–2 Sept 2021
- Huppert HE (1990) The fluid mechanics of solidification. *J Fluid Mech* 212:209–240. <https://doi.org/10.1017/S0022112090001938>
- Ivantsov G (1947) The temperature field around a spherical, cylindrical, or pointed crystal growing in a cooling solution. *Dokl Akad Nauk SSSR* 58:567–569
- Josserand C, Thoroddsen ST (2016) Drop impact on a solid surface. *Annu Rev Fluid Mech* 48(1):365–391. <https://doi.org/10.1146/annurev-fluid-122414-034401>
- Jung S, Tiwari MK, Doan NV, Poulikakos D (2012) Mechanism of supercooled droplet freezing on surfaces. *Nat Commun* 3:615. <https://doi.org/10.1038/ncomms1630>
- Kalantari D, Tropea C (2007) Phase Doppler measurements of spray impact onto rigid walls. *Exp Fluids* 43(2–3):285–296. <https://doi.org/10.1007/s00348-007-0349-4>
- Kant P, Müller-Groeling H, Lohse D (2020) Pattern formation during the impact of a partially frozen binary droplet on a cold surface. *Phys Rev Lett* 125(18):184501. <https://doi.org/10.1103/PhysRevLett.125.184501>
- Langer J, Müller-Krumbhaar H (1977) Stability effects in dendritic crystal growth. *J Cryst Growth* 42:11–14. [https://doi.org/10.1016/0022-0248\(77\)90171-3](https://doi.org/10.1016/0022-0248(77)90171-3)
- Langer J, Müller-Krumbhaar H (1978) Theory of dendritic growth—I. Elements of a stability analysis. *Acta Metall* 26(11):1681–1687. [https://doi.org/10.1016/0001-6160\(78\)90078-0](https://doi.org/10.1016/0001-6160(78)90078-0)
- Langer J, Müller-Krumbhaar H (1988) Theory of dendritic growth—II. instabilities in the limit of vanishing surface tension. In: Dynamics of curved fronts. Elsevier, pp 289–295
- Linder N, Criscione A, Roisman IV, Marschall H, Tropea C (2015) 3D computation of an incipient motion of a sessile drop on a rigid surface with contact angle hysteresis. *Theor Comput Fluid Dyn* 29(5):373–390. <https://doi.org/10.1007/s00162-015-0362-9>
- Mandal DK, Criscione A, Tropea C, Amirkazli A (2015) Shedding of water drops from a surface under icing conditions. *Langmuir* 31(34):9340–9347. <https://doi.org/10.1021/acs.langmuir.5b02131>
- Marston JO, Mansoor MM, Thoroddsen ST (2013) Impact of granular drops. *Phys Rev E Stat Nonlin Soft Matter Phys* 88(1):010201. <https://doi.org/10.1103/PhysRevE.88.010201>

21. Moreira A, Moita AS, Panão MR (2010) Advances and challenges in explaining fuel spray impingement: how much of single droplet impact research is useful? *Prog Energy Combust Sci* 36(5):554–580. <https://doi.org/10.1016/j.pecs.2010.01.002>
22. Mullins WW, Sekerka RF (1963) Morphological stability of a particle growing by diffusion or heat flow. *Int J Appl Phys* 34(2):323–329. <https://doi.org/10.1063/1.1702607>
23. Mullins WW, Sekerka RF (1964) Stability of a planar interface during solidification of a dilute binary alloy. *Int J Appl Phys* 35(2):444–451. <https://doi.org/10.1063/1.1713333>
24. Rauschenberger P, Criscione A, Eisenschmidt K, Kintea D, Jakirlić S, Tuković Ž, Roisman I, Weigand B, Tropea C (2013) Comparative assessment of volume-of-fluid and level-set methods by relevance to dendritic ice growth in supercooled water. *Comput Fluids* 79:44–52. <https://doi.org/10.1016/j.compfluid.2013.03.010>
25. Riboux G, Gordillo JM (2014) Experiments of drops impacting a smooth solid surface: a model of the critical impact speed for drop splashing. *Phys Rev Lett* 113(2):024507. <https://doi.org/10.1103/PhysRevLett.113.024507>
26. Rioboo R, Marengo M, Tropea C (2002) Time evolution of liquid drop impact onto solid, dry surfaces. *Exp Fluids* 33(1):112–124. <https://doi.org/10.1007/s00348-002-0431-x>
27. Roisman I (2009) Inertia dominated drop collisions. II. An analytical solution of the navier-stokes equations for a spreading viscous film. *Phys Fluids* 21(5):052104. <https://doi.org/10.1063/1.3129283>
28. Roisman IV (2010) Fast forced liquid film spreading on a substrate: flow, heat transfer and phase transition. *J Fluid Mech* 656:189. <https://doi.org/10.1017/S0022112010001126>
29. Roisman IV, Criscione A, Tropea C, Mandal DK, Amirkazli A (2015) Dislodging a sessile drop by a high-reynolds-number shear flow at subfreezing temperatures. *Phys Rev E* 92(2):023007. <https://doi.org/10.1103/PhysRevE.92.023007>
30. Roisman IV, Lembach A, Tropea C (2015) Drop splashing induced by target roughness and porosity: the size plays no role. *Adv Colloid Interface Sci* 222:615–621. <https://doi.org/10.1016/j.cis.2015.02.004>
31. Roisman IV, Tropea C (2015) Impact of a crushing ice particle onto a dry solid wall. *Proc Math Phys Eng Sci* 471(2183):20150525. <https://doi.org/10.1098/rspa.2015.0525>
32. Roisman IV, Tropea C (2020) Wetting and icing of surfaces. *Curr Opin Colloid Interface Sci* 53:101400. <https://doi.org/10.1016/j.cocis.2020.101400>
33. Schremb M (2018) Hydrodynamics and thermodynamics of ice accretion through impact of supercooled large droplets: experiments, simulations and theory. Dissertation, Technische Universität Darmstadt, Darmstadt
34. Schremb M, Borchart S, Berberovic E, Jakirlic S, Roisman IV, Tropea C (2017) Computational modelling of flow and conjugate heat transfer of a drop impacting onto a cold wall. *Int J Heat Mass Transf* 109:971–980. <https://doi.org/10.1016/j.ijheatmasstransfer.2017.02.073>
35. Schremb M, Campbell JM, Christenson HK, Tropea C (2017) Ice layer spreading along a solid substrate during solidification of supercooled water: experiments and modeling. *Langmuir: ACS J Surf Colloids* 33(19):4870–4877. <https://doi.org/10.1021/acs.langmuir.7b00930>
36. Schremb M, Roisman IV, Tropea C (2017) Normal impact of supercooled water drops onto a smooth ice surface: experiments and modelling. *J Fluid Mech* 835:1087–1107. <https://doi.org/10.1017/jfm.2017.797>
37. Schremb M, Roisman IV, Tropea C (2017) Transient effects in ice nucleation of a water drop impacting onto a cold substrate. *Phys Rev E* 95(2–1):022805. <https://doi.org/10.1103/PhysRevE.95.022805>
38. Schremb M, Tropea C (2016) Solidification of supercooled water in the vicinity of a solid wall. *Phys Rev E* 94(5–1):052804. <https://doi.org/10.1103/PhysRevE.94.052804>
39. Shikov AA, Golovin YI, Zheltov MA, Korolev AA, Leonov AA (2003) Morphology diagram of nonequilibrium patterns of ice crystals growing in supercooled water. *Phys A* 319:65–79. [https://doi.org/10.1016/S0378-4371\(02\)01517-0](https://doi.org/10.1016/S0378-4371(02)01517-0)
40. Tropea C, Schremb M, Roisman IV (2017) Physics of SLD impact and solidification. In: Proceedings of the 7th European conference for aeronautics and space sciences, Milan, Italy. EUCASS

41. Yarin AL (2006) Drop impact dynamics: splashing, spreading, receding, bouncing. ... Annu Rev Fluid Mech 38(1):159–192. <https://doi.org/10.1146/annurev.fluid.38.050304.092144>
42. Yarin AL, Tropea C, Roisman I (2017) Collision phenomena in liquids and solids. Cambridge University Press, Cambridge

**Open Access** This chapter is licensed under the terms of the Creative Commons Attribution 4.0 International License (<http://creativecommons.org/licenses/by/4.0/>), which permits use, sharing, adaptation, distribution and reproduction in any medium or format, as long as you give appropriate credit to the original author(s) and the source, provide a link to the Creative Commons license and indicate if changes were made.

The images or other third party material in this chapter are included in the chapter's Creative Commons license, unless indicated otherwise in a credit line to the material. If material is not included in the chapter's Creative Commons license and your intended use is not permitted by statutory regulation or exceeds the permitted use, you will need to obtain permission directly from the copyright holder.



# Interaction of Drops and Sprays with a Heated Wall



Johannes Benedikt Schmidt, Jan Breitenbach, Ilia V. Roisman,  
and Cameron Tropea

**Abstract** Spray-wall interactions take place in many technical applications such as spray cooling, combustion processes, cleaning, wetting of surfaces, coating and painting, etc. The outcome of drop impact onto hot surfaces depends on a variety of parameters like for example material and thermal properties of the liquid and wall, substrate wetting properties, surrounding conditions which determine the saturation temperature, spray impact parameters and surface temperature. The aim of the current project is to improve knowledge of the underlying physics of spray-wall interactions. As an important step towards spray impact modeling first a single drop impact onto hot substrates is considered in detail. Various regimes of single drop impact, such as *thermal atomization*, *magic carpet breakup*, *nucleate boiling* and *thermosuper-repellency*, observed at different wall temperatures, ambient pressures and impact velocities, have been investigated experimentally and modelled theoretically during the project period. The heat flux, an important parameter for spray cooling, has been modeled not only for single drop impacts but also for sprays within many regimes. The models show a good agreement with experimental data as well as data from literature.

## 1 Introduction

The impact of drops with a solid surface is a widely studied phenomenon of interest not only for engineering applications, but also in many other fields, even extending into the natural and life sciences. However, the particular situation of impact onto a hot surface is much more specific and especially for surfaces at high temperatures, the heat transfer and thermodynamics of the wall-fluid interaction begin to significantly influence the hydrodynamics of drop impact, making the physics much more complex and challenging to predict. On the other hand, this is a common and key phenomenon,

---

J. B. Schmidt · J. Breitenbach · I. V. Roisman · C. Tropea (✉)  
Institute of Fluid Mechanics and Aerodynamics, Technical University of Darmstadt,  
Darmstadt, Germany  
e-mail: [tropea@sla.tu-darmstadt.de](mailto:tropea@sla.tu-darmstadt.de)

in particular for spray cooling, but also for many other applications. During the course of this project extending from 2010 until 2021, the strategy has been to investigate single drop impact onto hot surfaces under varying ambient conditions (pressure, surface temperature, etc.), with the aim to first develop models which are more physics-based than existing models, to describe the hydrodynamics and thermodynamics of the interaction. Once having developed these models, the next step is to extend these to the case of higher drop flux densities, eventually reaching conditions typical of spray impact onto hot surfaces. The overarching aim is to provide reliable models and predictive tools for design of such systems, in dependence of the boundary and operating conditions at hand. In many respects this goal has been achieved and both past results and on-going research will be summarized below.

It is not possible to recap all of the research conducted within the framework of this project and carried out at the Institute of Fluid Mechanics and Aerodynamics at the Technical University of Darmstadt, and therefore a selection has been made as to which topics to highlight. Nevertheless, more details can be found in the extensive literature published during the course of the project [3–7, 9, 14, 17, 22, 25].

Principally however, it is important to distinguish the boundary conditions imposed on any particular problem and these must also be reflected in the experimental, numerical and theoretical treatment of the problem. Although this statement appears trivial, it is of particular significance to the present physical problem, since the question immediately arises whether the hot surface is in an equilibrium state, for instance constant temperature or heat flux, or whether the surface is continually being cooled during interaction with liquid drops. This is important in two respects. For one, the material properties of the liquid are temperature dependent and if the surface changes temperature over time, this must be accounted for in the hydrodynamic treatment of the problem. Second, the problem may be a conjugate heat transfer problem, depending on the time scales involved, in which case also the thermal boundary layer and heat flux within the surface become an integral and very influential part of the problem. To the most extent, the results presented in Sect. 2 will relate to the case of the surface being in thermal equilibrium; however, also the case of transient cooling has been extensively investigated and the reader is referred to the appropriate literature for more details [27]. In Sect. 3 transient cooling of the substrate will also be addressed.

## 2 Heat Transfer Models in Various Drop Impact Regimes

This chapter begins with an overview of drop-wall regimes according to wall temperature and then proceeds with two sections addressing the selected cases of nucleate boiling and the strategy of extending single drop results to spray-wall interaction.

The impact of a drop onto a hot wall is usually subdivided into regimes according to the heat flux achieved at the wall, which is immediately reflected in the hydrodynamic behaviour upon impact and on total lifetime of the drop before complete evaporation. Figure 1 summarizes typical impact outcomes with representative photographs (on

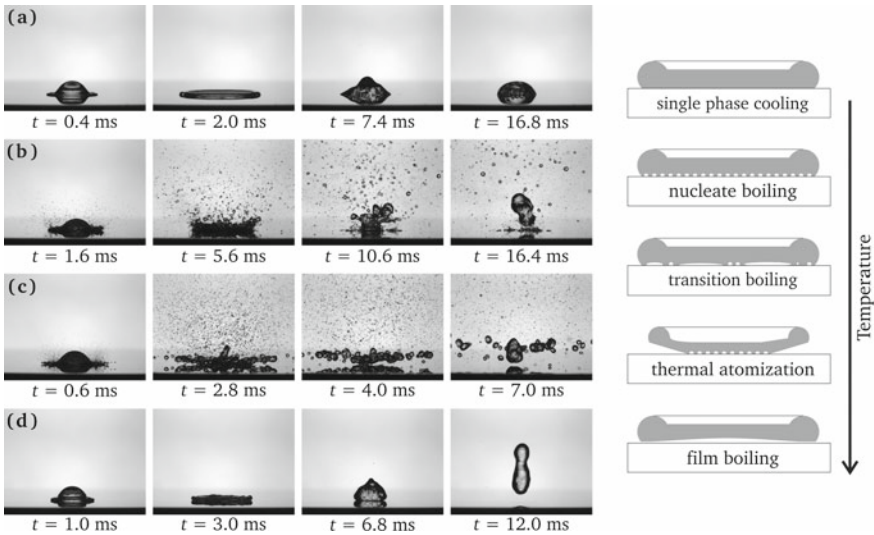


**Fig. 1** Thermally induced outcomes/regimes of drop impact onto a hot substrate. Left, from top to bottom: **a** drop deposition ( $T_{w0} = 120^\circ\text{C}$ ,  $V_0 = 1.5 \text{ m/s}$ ,  $D_0 = 2.2 \text{ mm}$ ), **b** drop dancing ( $T_{w0} = 170^\circ\text{C}$ ,  $V_0 = 0.7 \text{ m/s}$ ,  $D_0 = 2.2 \text{ mm}$ ), **c** thermal atomization ( $T_{w0} = 260^\circ\text{C}$ ,  $V_0 = 1.7 \text{ m/s}$ ,  $D_0 = 2.2 \text{ mm}$ ), **d** drop rebound ( $T_{w0} = 280^\circ\text{C}$ ,  $V_0 = 0.7 \text{ m/s}$ ,  $D_0 = 2.2 \text{ mm}$ ). Right, sketches of the typical mechanisms of the boiling regimes. (Adapted from [7], with permission of Springer, Copyright 2018)

the left side) and a pictorial representation of the liquid/wall contact encountered in each regime (on the right side). The heat flux associated with each regime is given in Fig. 2, whereby the exact demarcation and definition of regime boundaries can vary among authors. In the framework of this study a main achievement was to capture the heat flux in theoretical expressions for each of the various regimes dependent on the material and operating parameters. This then allowed estimation of the drop lifetime. One such expression, that for nucleate boiling, will be described below in the following section. More details of these expressions and their derivation can be found in the respective publications for: drop deposition [3]; nucleate boiling [5]; thermal atomization [4, 22]; and film boiling [6].

## 2.1 Drop Impact in the Nucleate Boiling Regime

At the instant of drop impact, heat begins to flow from the substrate to the drop; in the substrate this is pure conduction. The overall energy balance of heat transfer from the evaporating sessile drop and the heat flux from the substrate is given by

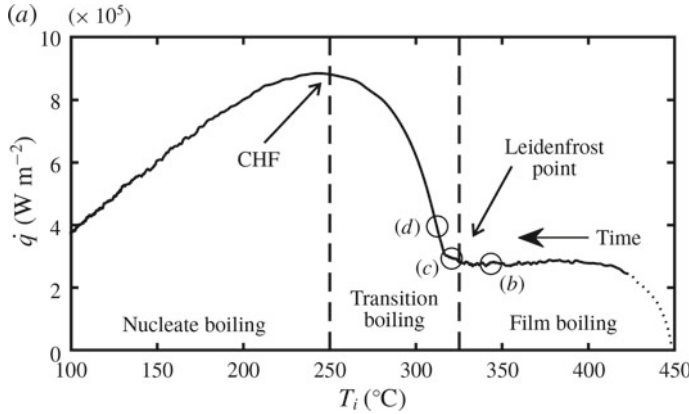


**Fig. 2** Measured heat flux  $\dot{q}$  as a function of surface temperature  $T_i$ . (Adapted from [27], with permission of Cambridge University Press, Copyright 2019)

$$\int_0^{t_c} A_c(t) \dot{q}(t) dt = \rho_l L \frac{\pi D_0^3}{6} \quad (1)$$

where  $t_c$  is the contact time until the entire drop is evaporated,  $A_c$  is the contact area,  $\dot{q}$  is the heat flux density at the solid/liquid interface,  $D_0$  is the initial drop diameter,  $\rho_l$  and  $L$  are the density and the latent heat of evaporation of the liquid, respectively.

At the first instant of drop contact a thermal boundary layer develops in the substrate. The thickness of the thermal boundary layer is  $h_{bl} \sim \sqrt{\alpha_w t}$ , where  $\alpha_w$  is the thermal diffusivity of the wall material. Since the thickness of the boundary layer is much smaller than the drop diameter, the heat conduction in the substrate can be approximated by a one-dimensional model. The temperature at the solid/liquid interface is not uniform. It is influenced by the appearance and growth of the bubbles initiated by heterogeneous nucleation at the substrate surface. The temperature at the contact line of each bubble is equal to the saturation temperature. The bubble contact lines move on the substrate, since the bubble diameter changes in time: periodically increasing due to evaporation until the drop detaches [10]. The wall superheat  $\Delta T = T_w - T_{sat}$  required for nucleation is in the order of 10 K. Therefore, to roughly estimate the heat flux it is possible to approximate the interface temperature by the saturation temperature,  $T_{sat}$  for  $T_0 - T_{sat} \gg 10$  K.

The geometry and the definition of the coordinate system are shown schematically in Fig. 3. At  $t = 0$  the liquid is placed in contact with a semi-infinite wall  $z < 0$  at the initial temperature  $T_0$ . The heat conduction equation in the wall,

$$\frac{\partial T_w}{\partial t} - \alpha_w \frac{\partial^2 T_w}{\partial z^2} = 0, \quad (2)$$

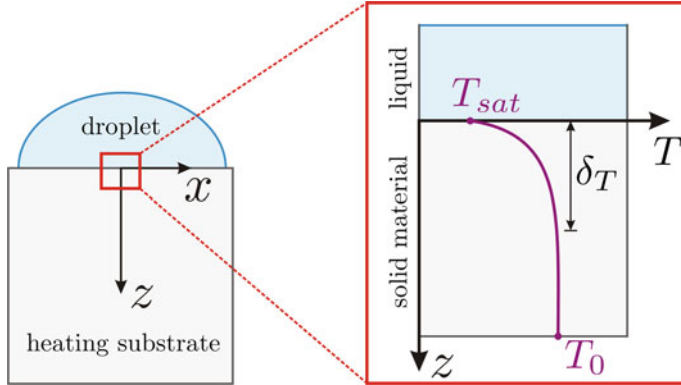


**Fig. 3** Sketch of the temperature distribution within the solid material due to the contact of the liquid to the substrate. The solid/liquid interface is located at  $z = 0$ . (Reprinted from [5], with permission of American Physical Society, Copyright 2017)

has to be solved subject to the boundary conditions

$$T_w = T_{\text{sat}} \quad \text{at } z = 0; \quad T_w \rightarrow T_0 \quad \text{at } z \rightarrow \infty, \quad (3)$$

where  $T_w(z, t)$  is the temperature in the wall region. The similarity solution of Eqs. (2)–(3) is well-known [21]

$$T_w(z, t) = T_{\text{sat}} + (T_0 - T_{\text{sat}}) \operatorname{erf}\left(\frac{z}{2\sqrt{\alpha_w t}}\right). \quad (4)$$

The heat flux density at the solid/liquid interface can be expressed with the help of Eq. (4) as

$$\dot{q}(t) \equiv \lambda_w \frac{\partial T_w}{\partial z} \Big|_{z=0} = \frac{e_w \Delta T_w}{\sqrt{\pi} \sqrt{t}}, \quad (5)$$

where  $\lambda_w$  is the thermal conductivity of the wall material,  $e_w$  is the thermal effusivity  $e_w = \sqrt{\lambda_w \rho_w c_p}$ , and  $\Delta T_w = T_0 - T_{\text{sat}}$  is the overall temperature difference in the wall (see Fig. 3).

The contact area  $A_c(t)$  changes during drop spreading and receding. However, since the contact time  $t_c$  in the nucleate boiling regime is much longer than the observed impact time ( $t_{imp} \sim D_0/V_0$ , where  $V_0$  is the impact velocity), the contact area can be estimated in the form

$$A_c \approx k_w \pi D_0^2, \quad (6)$$

where the coefficient  $k_w$  is determined primarily by the surface structure and wettability. The coefficient  $k_w$  accounts also for the effective drop growth due to bubble

expansion. This coefficient is of order unity and can be determined from the experiments. Substituting expressions (4), (5) and (6) into the energy balance Eq. (1) yields

$$t_c = \pi \left[ \frac{\rho_l L^* D_0}{12 k_w e_w \Delta T_w} \right]^2. \quad (7)$$

It is important to note that the obtained dependence  $t_c \sim \Delta T_w^{-2}$  is in good agreement with the experimental results. Introducing the scaled wall temperature and dimensionless time in the form

$$\Theta = \frac{T_0 - T_{\text{sat}}}{T_{\text{sat}} - T_l}, \quad \tau = \frac{t}{\pi} \left[ \frac{12 e_w (T_{\text{sat}} - T_l)}{\rho_l L^* D_0} \right]^2, \quad (8)$$

allows the contact time to be given in dimensionless form

$$\tau_c = \frac{1}{k_w^2 \Theta^2}. \quad (9)$$

The contact times from this study and those found in literature from Abu-Zaid [1], Buchmüller [8], Itaru and Kunihide [15] and Tartarini et al. [26] are compared with the theoretical prediction (9) in Fig. 4. The agreement is good for all the cases when the adjustable coefficient is set to  $k_w = 1.6$ . This parameter is the same for all the substrates used in the experiments, since their wettability properties are similar.

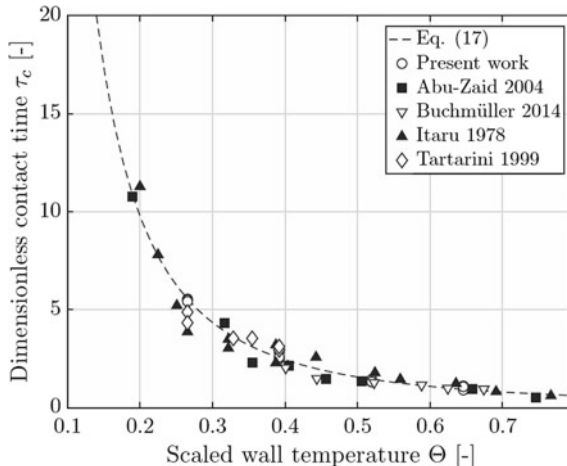


**Fig. 4** Dimensionless contact time from this study for water drops and existing literature data [1, 8, 15, 26] as a function of dimensionless time, in comparison with the theoretical prediction defined in (9) and in Eq. (17) in [5]. The initial drop diameter in the experiments ranges from 2.1 to 4.6 mm and the wall materials are aluminum, carbon steel and stainless steel. (Reprinted from [5], with permission of American Physical Society, Copyright 2017)

## 2.2 From Drop Impact to Spray Impact in the Film Boiling Regime

In this section the application of heat flux expressions for single drops to the case of sprays will be addressed for the particular condition of film boiling. In Sect. 3.4 the transition from drops to sprays will be examined for other heat transfer regimes. In film boiling a vapour layer arises between the liquid and hot wall such that the heat flux reduces to very low levels, as indicated in Fig. 2. This leads to the hydrodynamic behavior pictured in Fig. 1d, in which drops rebound completely from the surface. Thus, the heat transfer is only momentary and through the vapour layer. In [6] an expression for the total heat transferred during an impact event has been theoretically derived and experimentally validated. Accordingly, this amount can be expressed as:

$$Q_{\text{single}} = \frac{4.63 D_0^{5/2} G e_w (T_0 - T_{\text{sat}})}{V_0^{1/2} (K + 2G)} \quad (10)$$

where  $D_0$  and  $V_0$  are the drop diameter and velocity upon impact,  $T_0$  and  $T_{\text{sat}}$  are the wall temperature and liquid saturation temperature,  $e_w$  is the thermal effusivity of the wall material and  $G$  and  $K$  are given by the relations:

$$K = \sqrt{(B - G)^2 + \frac{4G}{\sqrt{\pi}}} - B - G, \quad (11)$$

with

$$G = \frac{\sqrt{\pi} \lambda_v \rho_f L}{2 (T_0 - T_{\text{sat}}) e_w^2}; \quad B = \frac{\sqrt{5} (T_{\text{sat}} - T_{D_0}) e_f}{\sqrt{\pi} (T_0 - T_{\text{sat}}) e_w}. \quad (12)$$

In the case of sparse sprays, each drop and its associated heat transfer would be independent of all other drop impacts, since the drops immediately leave the surface. Thus the heat flux can be computed as the superposition of many individual drops. However, at higher mass fluxes of drops, the probability of drops interacting with one another must be taken into consideration, which can be done on the basis of Poisson statistics. Once drop interaction occurs, for instance the spreading of one drop interacts with the spreading of a neighbour drop (in time and space), then a decrease in the overall heat flux must be accounted for, as outlined in [3]. Doing this, and using previous results for the spreading diameter and time of single drops given in [28], the heat flux coefficient for dense sprays can now be obtained

$$\alpha_{\text{ht}} = 8.85 \chi \frac{\dot{m} G e_w (T_0 - T_{\text{sat}})}{\rho_f \Delta T (K + 2G) D_0^{1/2} V_0^{1/2} \eta_{\text{wet}}}, \quad (13)$$

where  $\eta_{\text{wet}}$  is the correction factor for the relative wetted area estimated using the assumption of randomly distributed drop impacts on the substrates in space and

time, which can be described by the Poisson distribution. The cumulative wetted area  $\gamma$  on the surface

$$\gamma = \frac{2.1\dot{m}}{\rho_f V_0} (1 + 0.36We^{0.48})^2 \quad (14)$$

is expressed accounting for the superposition of all the drops impacting onto a unit area per unit time. Here  $\dot{m}$  is the mass flux in the spray and  $\rho_f$  is the fluid density. The Weber number is defined as  $We = \rho_f V_0 D_0^2 / \sigma$ , where  $\sigma$  is the surface tension. Therefore, the correction factor which accounts for the drop interactions at the substrate is

$$\eta_{\text{wet}} = \frac{1 - e^{-\gamma}}{\gamma}. \quad (15)$$

The dimensionless constant  $\chi$  accounts for the heat flux during the later stages of drop spreading, which is not considered in the present analysis. Since the heat flux density sharply reduces at large times, the value of  $\chi$  should be approximately unity. The coefficient  $\chi$  can be estimated by fitting to the experimental data.

This expression proves to predict very well past measurement of the heat transfer coefficient for dense sprays impacting on substrates at temperature above the Leidenfrost point. This is illustrated in Fig. 5. In the left plot of this figure, using a coefficient  $\chi = 3.2$  derived by fitting to the data from [18] and kept constant for all other comparisons, excellent agreement is found between theory and experiments for the heat transfer coefficient. Similarly, good agreement is found for varying operating conditions, in particular for largely differing average drop sizes and velocities, as shown in the right plot of Fig. 5.

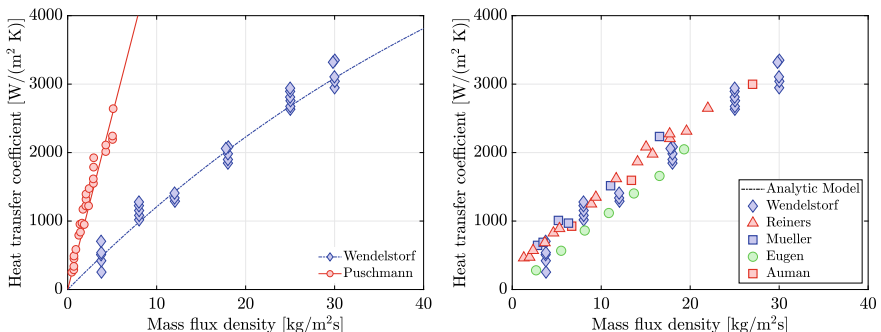


**Fig. 5** Heat transfer coefficient for water spray in the film boiling regime as a function of the mass flux densities of the spray  $\dot{m}$ . Comparison of the theoretical prediction (Eq. (13)) with existing experimental data from: Left plot—[2, 12, 16, 19, 29] for approximately the same operational conditions:  $\Delta T = 700^\circ\text{C}$ ,  $D_0 = 350 \mu\text{m}$ ,  $V_0 = 14 \text{ m/s}$ ; Right plot—for  $\Delta T = 700^\circ\text{C}$ ,  $D_0 = 350 \mu\text{m}$ ,  $V_0 = 14 \text{ m/s}$  from [29] and  $\Delta T = 550^\circ\text{C}$ ,  $D_0 = 18 \mu\text{m}$ ,  $V_0 = 27 \text{ m/s}$  from [18] (Adapted from [6], with permission of Elsevier, Copyright 2017)

### 3 Measurement of the Heat Flux

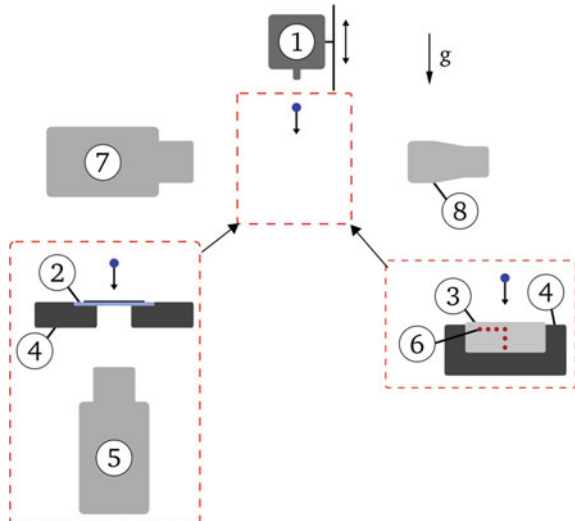
The focus of the current work is placed on the measurement of the heat flux during single drop impacts and the transfer of these results to sprays. Therefore single drop experiments as well as drop chain experiments have been performed.

#### 3.1 Experimental methods

The experimental setup comprises a drop generator, an impact target embedded in a heating system, a high-speed video system for viewing from the side and a high-speed mid-wave infrared (MWIR) camera system to measure the emitted infrared radiation of the hot surface during drop impact. The experimental setup is shown in Fig. 6. Drops with a diameter of  $D_0 = 2.2$  mm drip off a needle. The needle is fed with double-distilled water. By applying a constant volume flow a drop chain is generated with a drop frequency of 0.9 Hz up to 5.7 Hz. The impact velocity can be varied in the range of  $0.4\text{--}2\text{ m s}^{-1}$  by changing the height of the needle above the impact surface.

The drops impact onto a interchangeable hot surface. An IR transparent sapphire substrate is used as an impact target, enabling measurement of the surface temperature during drop impact with a high temporal and spatial resolution. The sapphire window has a thickness of 3 mm. The upper surface of the window is coated with a 600 nm thick CrN PVD layer. The coating is highly infrared emissive, while the sapphire window is transparent for MWIR radiation. The window is placed in a

**Fig. 6** Sketch of the experimental setup with the drop generator (1), sapphire window with CrN PVD coating (2) or metal substrate (3) as impact target, heating system (4), high-speed IR camera (5), thermocouples (6), high-speed camera with telecentric lens (7) and telecentric background light source (8)



heater with optical access in the center. The heating system controls the temperature of the sapphire window from 100 to 400 °C. The emitted infrared radiation from the CrN coating is captured from below using a high-speed MWIR camera. An in-situ calibration is performed to calculate the surface temperature based on the measured radiation and to take optical errors into account.

Different metal substrates of aluminium (EN AW 7075), copper (CW004A) and stainless steel (1.4841) have been used in the experiments as the impact substrates. The impact surface of the metal substrates are mirror polished. The metal substrates can be heated up to 550 °C. The temperature of the substrate is measured with thermocouples type J, placed 1 mm below the surface. The stainless steel target is equipped with 11 thermocouples to measure the temperature distribution inside the substrate during the impact of a drop chain.

The drop impact is observed from the side using a high-speed camera and with background lighting (shadowgraphy).

For the single drop experiments the substrate is heated to a certain surface temperature. After the system reaches steady state, the single drop experiments are performed. The side view observations are used to measure the impact parameters and residence time of the drops on the surface and to observe the drop impact regime. The IR camera is used to measure the temperature distribution close to the liquid-solid interface.

The drop impact lowers the contact temperature at the liquid-solid interface, leading to a three-dimensional temperature gradient inside the substrate. The temperature gradient inside is described by the heat conduction equation

$$\frac{\partial T_w}{\partial t} - \alpha_w \frac{\partial^2 T_w}{\partial z^2} = 0 \quad (16)$$

where  $T_w$  is the wall temperature,  $t$  is time and  $\alpha_w$  the thermal diffusivity of the wall.

The heat flux removed during a single drop impact is obtained by numerically solving the heat conduction equation inside the sapphire substrate. In Fig. 7 the mesh of the numerical calculation is shown. Close to the liquid-solid interface, the temperature gradient is very steep, thus, the mesh is refined in this area. The temperature distribution captured by the IR camera is used as a boundary condition at the upper surface. All other boundaries are considered to be adiabatic. The heat conduction equation is solved using the computational fluid dynamic solver OpenFOAM, as described in [13, 23].

For the drop chain experiments the substrate is initially heated up to 550 °C. After the system reaches steady state, the heater is switched off and the drop chain is applied to the surface. The impacting drop chain causes a transient cooling of the substrate and a growing thermal boundary layer, as described by Eq. (16). The thermal boundary is measured inside the stainless steel target using the thermocouples. Based on the thermal gradient orthogonal to the surface, the heat flux removed from the substrate is calculated using an analytical solver provided by Woodfield et al. [30].

The temporal resolution of the thermocouples is significantly lower than that of the IR camera. For this reason the IR camera is used to measure the heat flux removed

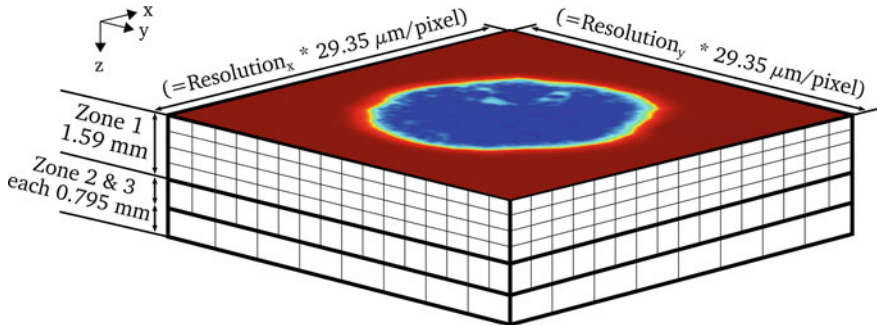


**Fig. 7** Computational mesh of the sapphire window. The mesh is refined closer to the impact surface. The temperature distribution, measured by the IR camera, is used as a boundary condition on the upper side

from single drops. Since the resistance of sapphire against thermal shocks is limited, it is not possible to resolve the transient heat transfer during the impact of the drop chain or during spray cooling of a sapphire window. For this reason a combination of both described measurement techniques is used, depending on the scope of the experiment.

### 3.2 Heat Flux During a Single Drop Impact

The heat flux removed from a substrate by single impacting droplets is addressed in the following section. The three drop impact phenomena, drop deposition with and without nucleate boiling and thermal atomization, have been observed using single drop experiments on the sapphire window. First the heat flux within the single regimes is described. Afterwards a two-dimensional heat flux model is introduced, valid for thermal atomization.

#### 3.2.1 Observations

**Drop evaporation** The heat flux removed from a hot surface depends on the drop impact regime. For low surface superheat the drop deposits on the surface and evaporates slowly without nucleate boiling. Figure 8 illustrates the heat flux removed from a hot surface during a drop impact in this regime. The initial surface temperature is 123 °C. The impacting drop leads to a temperature drop in the newly wetted area, causing a strong temperature gradient inside the substrate and a high heat flux removed from the substrate. The highest heat flux can be observed in the newly wetted areas and close to the three-phase contact line. After some time an

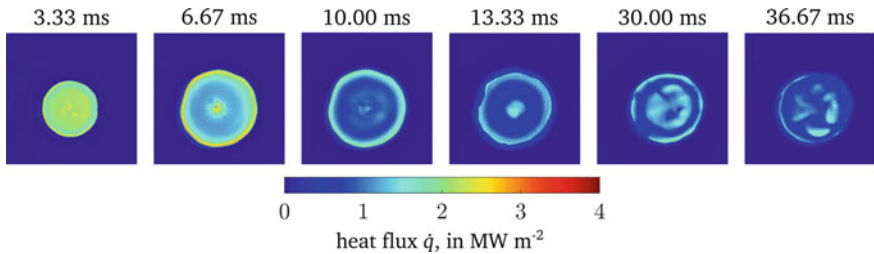


**Fig. 8** Heat flux measurements during drop impact on a sapphire substrate at 123 °C with an impact velocity of  $0.34 \text{ m s}^{-1}$ . The drop deposits and slowly evaporates without nucleate boiling

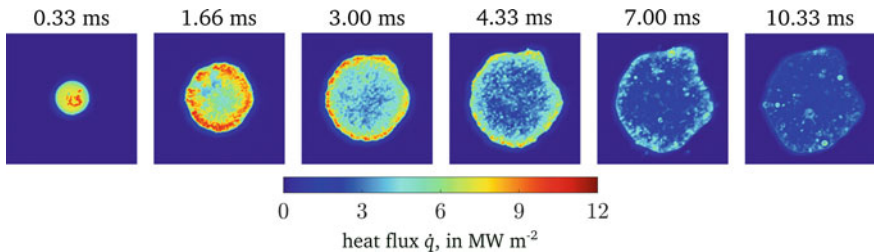


**Fig. 9** Heat flux measurements during drop impact onto a sapphire substrate at 166 °C with an impact velocity of  $0.45 \text{ m s}^{-1}$ . The drop deposits and nucleate boiling can be observed

ongoing convection can be observed inside the sessile drop, leading to heat flux rates comparable to the heat flux at the three-phase contact line.

**Nucleate boiling** At higher surface temperatures the drop deposition is accompanied by nucleate boiling. Figure 9 shows the heat flux during a drop impact onto a 166 °C hot surface in the nucleate boiling regime. Small areas with stronger temperature drops and high heat flux are observed, especially in newly wetted areas. The heat flux is less uniform compared to the drop evaporation regime. At later times the heat flux becomes more uniform, while a high heat flux at the three-phase contact line of growing bubbles remains. Early after the drop impact only small droplets and bubbles can be observed from the side. This leads to the assumption that many small microbubbles lead to the high, irregular heat flux at the beginning.

**Thermal atomization** At high surface temperatures the drop impacts and the drop rebounds or the drop atomizes. The heat flux measurements in this thermal atomization regime is shown in Fig. 10 for a drop impact onto a 345 °C hot surface. The thermal atomization regime is characterized by initial direct contact between the liquid and solid, leading to strong ongoing nucleate boiling with many small secondary droplets. Starting from the rim, the lamella starts to levitate away from the surface. The heat flux distribution in Fig. 10 shows a very high heat flux at the beginning. Later the heat flux decreases. After 2.05 ms the area of a high heat flux decreases, while the drop is still spreading. The decreasing heat flux area indicates that the liquid lamella, starting from the rim, has detached from the surface.

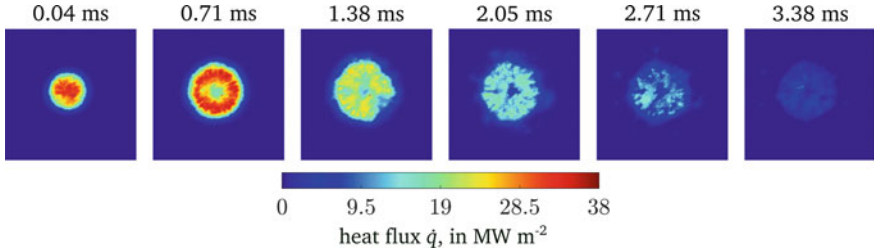


**Fig. 10** Heat flux measurements during drop impact in the thermal atomization regime. The sapphire substrate has a initial surface temperature of 345 °C. The drop impacts with an impact velocity of  $1.15 \text{ m s}^{-1}$

The heat flux inside the substrate is described by Eq. (16). Since the liquid and solid are in direct contact in the thermal atomization regime, the contact temperature at the interface is assumed to be at the liquid saturation temperature, while the substrate is still wetted. A thermal boundary layer grows inside the solid material as well as inside the liquid. Both are described by  $\sqrt{\alpha t}$ , with  $\alpha$  being the thermal diffusivity of the solid material or liquid. An exact solution of this problem is provided in [20, 21]. The heat flux removed from the substrate is obtained in the form

$$\dot{q}(r, t) = \frac{e_l e_w (T_{w0} - T_{l0})}{(e_l + e_w \mathcal{J}(Pr)) \sqrt{\pi t} \sqrt{1 - \bar{r}^2}} \quad (17)$$

in which  $e_w$  is the thermal effusivity of the wall,  $e_l$  the thermal effusivity of the liquid,  $T_{w0}$  the initial temperature of the wall,  $T_{l0}$  the initial temperature of the liquid. The factor  $\bar{r}$  is the dimensionless radius

$$\bar{r} = r/a(t), \quad a(t) \approx \sqrt{D_0 V_0 t} \quad (18)$$

with  $a$  being the contact radius.

Figure 11 compares the analytic model of Eq. (17) to the experimental data shown in Fig. 10 for  $r = 0$ . The analytic model exhibits good agreement with the experimental data. After 3.5 ms the liquid lamella levitates and the boundary condition and model are no longer valid.

In Fig. 12 the spatial distribution of heat flux is shown for  $t = 1.377$  ms after the impact, again a comparison between the analytical model and the experimental data. The experimental data is averaged over all cells with the same distance from the center of the lamella. The error bars represent the scatter by one standard deviation. In the center the experimental data exhibit a higher heat flux with low scatter. From  $r = 0.5 \text{ mm}$  to  $1.5 \text{ mm}$  the heat flux and scatter of the experimental data is higher. This is caused by the strong nucleate boiling in this area, leading to a higher heat flux compared to the pure conduction as assumed in Eq. (17). From  $r \approx 1.6 \text{ mm}$  onward the experimental data shows a decrease of heat flux, since the lamella starts

**Fig. 11** Heat flux of a drop impact in the thermal atomization regime. The drop impacted with  $1.15 \text{ m s}^{-1}$  at the  $345^\circ\text{C}$  hot substrate. The line shows the analytic model of Eq. (17) in the center of the lamella ( $r = 0$ ) as a function of time. The stars show the experimental data

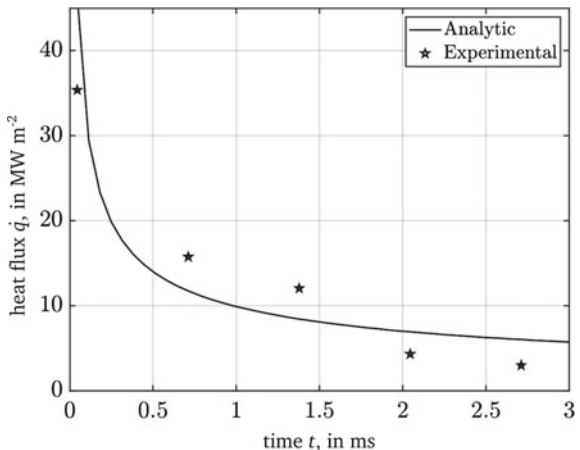
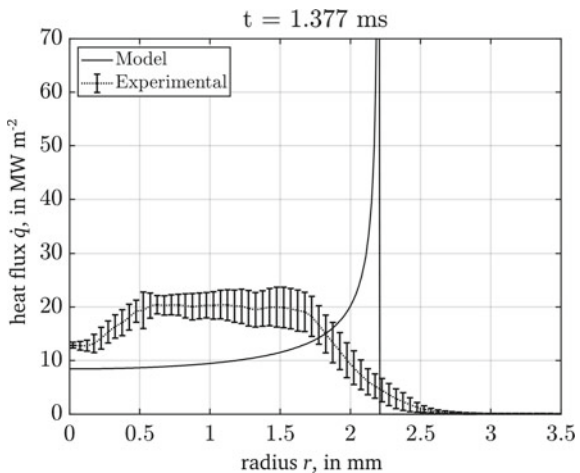


**Fig. 12** Heat flux of a drop impact in the thermal atomization regime. The impact velocity is  $1.15 \text{ m s}^{-1}$  and the initial surface temperature  $345^\circ\text{C}$ . The line shows the analytic model of Eq. (17) 1.377 ms after impact as a function of the radius. The experimental data are averaged over the radius and the error bars indicate one standard deviation of the measured fluctuations



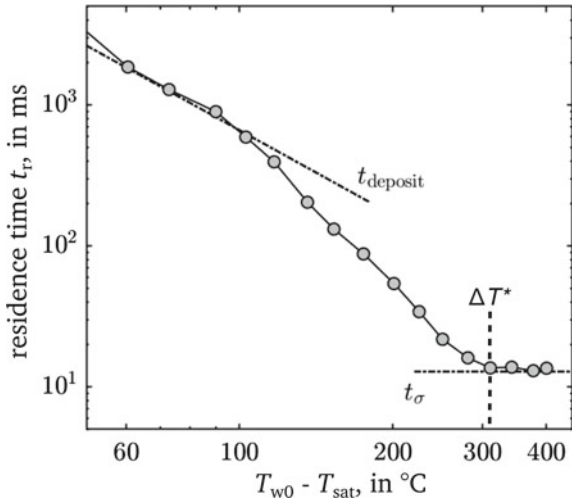
to levitate, beginning from the rim. For  $r = a$  the analytical model has a singularity, which is non-physical.

The experimental measured heat flux is in most cases higher than the predicted heat flux by conduction. This indicates that the liquid is in contact with the substrate without any isolating vapour layer, even if the surface temperature is very high.

### 3.3 Thermosuperrepellency

The transition between different drop impact regimes is important information for modeling as well as for applications. The onset of drop rebound is an important

**Fig. 13** Drop residence time on the hot substrate depending on the substrate superheat  
 $\Delta T_{w0} = T_{w0} - T_{\text{sat}}$ . The residence time remains constant for temperatures above  $T^*$



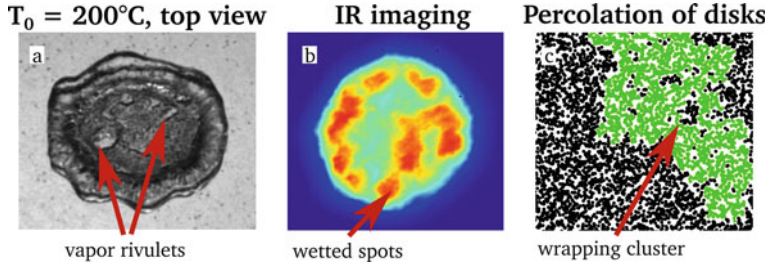
transition, since it indicates that a vapour layer between the drop liquid and the hot substrate has been established, lowering the removable heat flux.

Figure 13 shows the residence time of single drops impacting onto a hot stainless steel target. At low surface temperatures, the impacting drops are in the drop deposition regime. The residence time  $t_{\text{deposit}}$  in the drop deposition regime is described in [5]. The experimental data exhibit good agreement with the model of the residence time. With increasing substrate temperature, more liquid is ejected by secondary droplets or rebound. The residence time decreases faster than described by the model. Above a certain transition temperature  $\Delta T^* = T^* - T_{\text{sat}}$ , the residence time remains constant, since most of the drop liquid rebounds. The residence time is comparable with the natural oscillation time of drops [11]

$$t_\sigma \approx \sqrt{\frac{\rho D_0^3}{\sigma}} = \frac{D_0 W e^{1/2}}{V_0}. \quad (19)$$

The same behaviour can be observed for drop impacts on all substrate materials within this study. Vapour rivulets or clusters are visible from top view observations of drop impacts onto hot aluminium above  $\Delta T^*$ , as shown in Fig. 14a. A similar behaviour can be observed from IR measurements, in which large clusters with a low heat flux can be observed, during drop impact onto a hot sapphire window, as shown in Fig. 14b. The occurrence of large vapour clusters can be described by the percolation of single bubbles within the lamella, as shown in Fig. 14c and described in [25]. The remaining wetted area, which is not covered by vapour, is described by  $\epsilon_c \approx 0.32$ . The heat removed from the surface goes into the evaporation of the liquid. This leads to

$$\rho h_{\text{res}} L^* \epsilon'(t) = -\dot{q}, \quad (20)$$



**Fig. 14** **a** Vapour rivulets from top view observations during drop impacts onto a 200 °C hot aluminium substrate. **b** Similar clusters of low and high heat flux areas can be observed from IR measurements of drop impacts onto a hot sapphire window in the drop rebound regime. **c** Exemplary cluster of discs as described by percolation theory. (Adapted from [25])

where  $\rho$  is the liquid density,  $h_{\text{res}}$  is the height of the liquid lamella  $L^*$  is the sensible heat  $c_p(T_{\text{sat}} - T_{l0})$  and latent heat of liquid evaporation,  $c_p$  is the specific heat capacity and  $\epsilon$  is the wetted area. The height of the liquid lamella is described by  $h_{\text{res}} \approx 0.79 D_0 Re^{-2/5}$ . Solving the differential Eq. (20) and assuming  $t = t_\sigma$  leads to a temperature superheat of

$$\Delta T = b \frac{D_0^{1/4} L^* \rho^{3/4} \sigma^{1/4}}{e_w Re^{2/5}}, \quad (21)$$

with  $b = 0.48$ . This assumption is only valid as long as the drop impact is surface tension dominated or  $We < 2.5 Re^{2/5}$ .

In the case of fast and small droplets the relevant time for the drop rebound is defined by the time in which the viscous boundary layer reaches the top of the lamella, which is  $t_v = \frac{D_0 Re^{1/5}}{V_0}$ . Solving the differential Eq. (20) and assuming  $t = t_v$  leads to

$$\Delta T_v = \frac{\rho \sqrt{v} L^*}{e_w}. \quad (22)$$

In Fig. 15 the experimental data of spray cooling experiments and single drop experiments are compared to the scales shown in Eqs. (21) and (22). Figure 15a shows how the experimental data of single drop impacting with different drop impact velocities onto different substrate materials scale well with the model of Eq. (21). Figure 15b shows experimental data from literature and in-house data and how they correlate with Eq. (22).

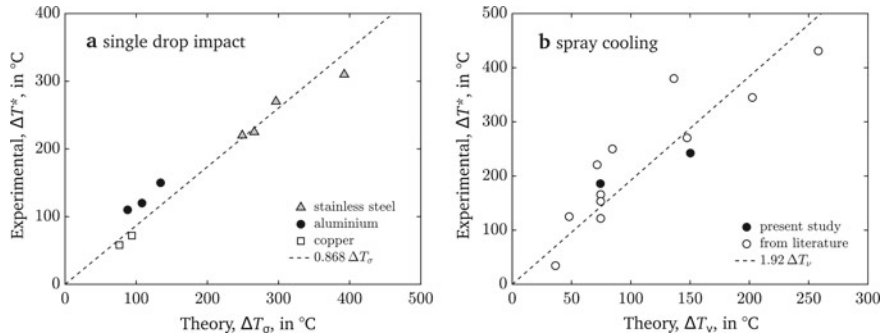


**Fig. 15** Comparison of the thermosuperrepellency threshold temperature  $\Delta T^* = T^* - T_{\text{sat}}$  with the models given in **a** Eq. (21) and **b** Eq. (22). (Reprinted from [25])

### 3.4 Drop Chain Impact

The single drop experiments on a hot substrate are generic experiments and a major simplification of spray-wall interactions. To transfer the knowledge from single drop experiments to spray-wall interaction it is necessary to increase the complexity towards drop/drop interactions, like in drop chains. Monodisperse drop chain impacts onto a hot substrate are used in the following as a generic one-dimensional spray. The drop chain experiments allow to study single drop impacts onto the substrate in greater detail, while measuring the overall heat flux during the cooling of the substrate. This combination will allow to transfer knowledge of single drop experiments to spray cooling.

In Fig. 16a an exemplary drop chain experiment is shown. The substrate is heated up to 550 °C, the heater is switched off and a drop chain with a frequency of  $f_c = 0.8$  Hz is applied. Each drop impact causes a strong temperature drop, as shown in the detailed view (insert). After the drop rebounds or evaporates the substrate is dry and the surface temperature increases again. Even for higher drop chain frequencies of  $f_c = 5.19$  Hz the drops do not interact or accumulate in the drop rebound regime. The wetting increases for lower surface temperatures, leading to a higher amplitude of the temperature drop. At even lower surface temperatures the substrate is continuously wetted, leading to weaker temperature oscillations. In Fig. 16b the corresponding heat flux is shown. The black shaded area corresponds to the oscillations of the heat flux caused by the temperature drop of each drop impact. In the detailed view (insert) the heat flux of three single drop impacts is shown. After a strong temperature drop and high heat flux, the surface is dry and reheats. The red dashed line indicates the average heat flux, while the green dashed line shows one standard deviation of heat flux fluctuations, valid as an indicator of the oscillation amplitude. At early times the heat flux oscillations are low, since a vapor layer insulates the drop from the substrate. The heat flux oscillations increase significantly as soon as the surface is wetted, since the contact temperature is significantly lower. The oscillations as

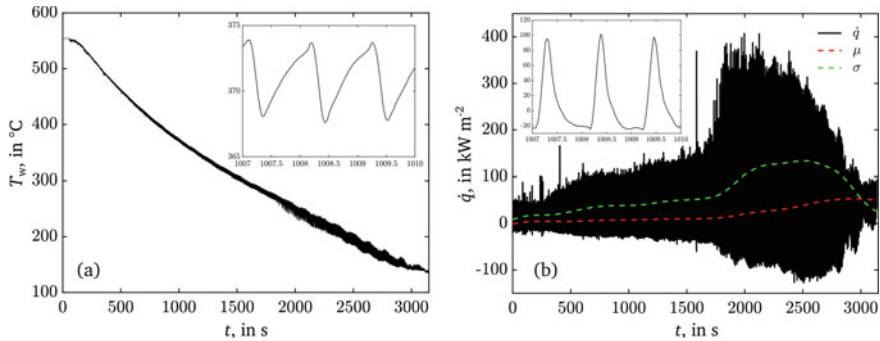
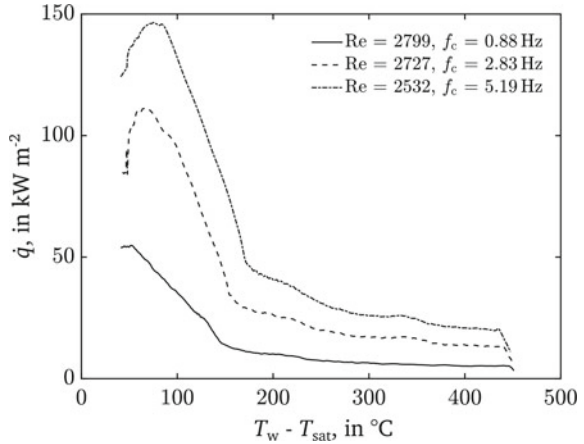


**Fig. 16** **a** The surface temperature during transient cooling by a monodisperse drop chain. The insert view shows three single drop impacts at a high surface temperature. **b** The corresponding heat flux. The red dashed line shows the moving average, while the green dashed line indicates one standard deviation of the fluctuations. In the insert the heat flux caused by three single drop impacts is shown. (Adapted from [24])

**Fig. 17** Heat flux as a function of the wall superheat for different drop chain frequencies  $f_c$ , but similar impact parameters (Reynolds number)



well as the standard deviation increases. In addition, the average heat flux increases slightly. For even lower surface temperatures the residence time of the drops increase and the drops start to interact until they accumulate and the substrate is uniformly wetted with a continuous liquid film. Due to the liquid film, the contact temperature and heat flux oscillates less, while the average heat flux continues to rise.

Several parameters of sprays can be varied, which potentially influence the heat flux during spray cooling. One of the parameters is the mass flux in a spray or in the case of an one-dimensional drop chain the frequency of drops. Figure 17 compares the average heat flux for different drop chain frequencies  $f_c$ . At high surface temperatures the heat flux scales linearly with  $f_c$ , since no interaction of drops can be observed. With lower surface temperature the heat flux does not scale linearly anymore with  $f_c$ . The heat flux removed per drop decreases with increasing  $f_c$ .

### 3.5 Conclusion

The focus of this experimental and theoretical study is the impact of single drops and sprays onto hot substrates over a wide range of ambient conditions as well as substrate materials. It is motivated by many technical applications, mainly related to spray cooling. The topic is highly interdisciplinary. It includes hydrodynamics of drop impact and spreading, thermodynamics of boiling and evaporation, diagnostic techniques of sprays and drops, and mathematical modeling of the basic phenomena.

The research strategy is built on the accurate investigation and theoretical modeling of a single drop impact and its further application to the chain of drops impact and spray cooling.

During the first period, the outcome of single drop impacts onto hot surfaces has been characterized regarding the ambient conditions. The main drop impact regimes, drop deposition, drop dancing, thermal atomization and drop rebound have been identified and described. The heat flux as the key interest of cooling technologies has been modeled on a physical base, for single phase cooling, as well as nucleate boiling in the drop deposition regime, thermal atomization and drop rebound based on film boiling. Additionally, the model of the heat flux in the film boiling regime is transferred from single drop to spray impact at a hot surface, which allows prediction of the heat transfer during spray cooling in film boiling. All models are validated with the performed experiments and showed a good agreement within the single regimes.

The main focus of the last project period is the accurate study of the temperature distribution in the substrate during the impact. The wall temperature and local heat flux is measured with a high temporal and spatial resolution. A model of the local heat flux distribution is shown for the thermal atomization regime with good agreement between the model and experimental data. The thermosuperrepellency phenomena has been identified as a thermodynamic regime which is accompanied by nucleate boiling and leading vapor percolation and partial drop rebound at temperatures much smaller than the real Leidenfrost point.

Finally the cooling effects of a chain of liquid drops are characterized to better understand the transient cooling of a substrate by multiple droplets.

**Acknowledgements** The authors kindly acknowledge the financial support by the Deutsche Forschungsgemeinschaft (DFG) within the SFB-TRR 75, project number 84292822.

## References

1. Abu-Zaid M (2004) An experimental study of the evaporation characteristics of emulsified liquid droplets. *Heat Mass Transf* 40(9):737–741
2. Auman PM, Griffiths DK, Hill DR (1967) Hot strip mill runout table temperature control. *Iron Steel Eng* 9:174–179
3. Batzdorf S, Breitenbach J, Schlawitschek C, Roisman IV, Tropea C, Stephan P, Gambaryan-Roisman T (2017) Heat transfer during simultaneous impact of two drops onto a hot solid substrate. *Int J Heat Mass Transf* 898–907
4. Breitenbach J, Kissing J, Roisman IV, Tropea C (2018) Characterization of secondary droplets during thermal atomization regime. *Exp Therm Fluid Sci* 98:516–522

5. Breitenbach J, Roisman IV, Tropea C (2017) Drop collision with a hot, dry solid substrate: heat transfer during nucleate boiling. *Phys Rev Fluids* 2(7):074301
6. Breitenbach J, Roisman IV, Tropea C (2017) Heat transfer in the film boiling regime: single drop impact and spray cooling. *Int J Heat Mass Transf* 110:34–42
7. Breitenbach J, Roisman IV, Tropea C (2018) From drop impact physics to spray cooling models: a critical review. *Exp Fluids* 59(3):418
8. Buchmüller I (2014) Influence of pressure on leidenfrost effect. PhD thesis, Technische Universität Darmstadt, Darmstadt
9. Buchmüller I, Roisman IV, Tropea C (2012) Influence of elevated pressure on impingement of a droplet upon a hot surface. In: ICLASS 2012, 12th international conference on liquid atomization and spray systems. Heidelberg, DE
10. Carey VP (1992) Liquid-vapor phase-change phenomena: an introduction to the thermophysics of vaporization and condensation processes in heat transfer equipment. Series in chemical and mechanical engineering. Taylor & Francis, Bristol
11. Castanet G, Caballina O, Lemoine F (2015) Drop spreading at the impact in the leidenfrost boiling. *Phys Fluids* 27(6):063302
12. Eugene A, Mizikar A (1970) Spray-cooling investigation for continuous casting of billets and blooms. *Iron Steel Eng* 47(6):53–60
13. Fischer S, Gambaryan-Roisman T, Stephan P (2015) On the development of a thin evaporating liquid film at a receding liquid/vapour-interface. *Int J Heat Mass Transf* 88:346–356
14. Hatakenaka R, Breitenbach J, Roisman IV, Tropea C, Tagawa Y (2019) Magic carpet breakup of a drop impacting onto a heated surface in a depressurized environment. *Int J Heat Mass Transf* 145:118729
15. Itaru M, Kunihide M (1978) Heat transfer characteristics of evaporation of a liquid droplet on heated surfaces. *Int J Heat Mass Transf* 21(5):605–613
16. Müller HR, Jeschar R (1983) Wärmeübergang bei der Spritzwasserkühlung von Nichteisenmetallen. VDI-Verlag
17. Piskunov M, Breitenbach J, Schmidt JB, Strizhak P, Tropea C, Roisman IV (2021) Secondary atomization of water-in-oil emulsion drops impinging on a heated surface in the film boiling regime. *Int J Heat Mass Transf* 165:120672
18. Puschmann F (2003) Experimentelle Untersuchung der Spraykühlung zur Qualitätsverbesserung durch definierte Einstellung des Wärmeübergangs. PhD thesis, Otto-von-Guericke-Universität Magdeburg, Universitätsbibliothek
19. Reiners U (1987) Wärmeübertragung durch Spritzwasserkühlung heißer Oberflächen im Bereich der stabilen Filmverdampfung. PhD thesis, Technische Universität Clausthal
20. Roisman IV (2009) Inertia dominated drop collisions. II. An analytical solution of the Navier–Stokes equations for a spreading viscous film. *Phys Fluids* 21(5):052104
21. Roisman IV (2010) Fast forced liquid film spreading on a substrate: flow, heat transfer and phase transition. *J Fluid Mech* 656:189
22. Roisman IV, Breitenbach J, Tropea C (2018) Thermal atomisation of a liquid drop after impact onto a hot substrate. *J Fluid Mech* 842:87
23. Schmidt JB, Breitenbach J, Roisman IV, Tropea C (2020) Measurement of the heat flux during a drop impact onto a hot dry solid surface using infrared thermal imaging. In: Dillmann A, Heller G, Krämer E, Wagner C, Tropea C, Jakirlić S (eds) New results in numerical and experimental fluid mechanics XII. Springer International Publishing, Cham, pp 553–562
24. Schmidt JB, Breitenbach J, Roisman IV, Tropea C, Hussong J (2021) Transition from drop deposition to drop rebound during drop chainimpact onto a hot target. In: ICLASS 2021, 15th Triennial international conference on liquid atomization and spray systems. Edinburgh, UK
25. Schmidt JB, Hofmann J, Tenzer FM, Breitenbach J, Tropea C, Roisman IV (2021) Thermosuperrepellency of a hot substrate caused by vapour percolation. *Commun Phys* 4(1):181
26. Tartarini P, Lorenzini G, Randi MR (1999) Experimental study of water droplet boiling on hot, non-porous surfaces. *Heat Mass Transf* 34(6):437–447
27. Tenzer FM, Roisman IV, Tropea C (2019) Fast transient spray cooling of a hot thick target. *J Fluid Mech* 881:84–103

28. Tran T, Staat HJJ, Prosperetti A, Sun C, Lohse D (2012) Drop impact on superheated surfaces. *Phys Rev Lett* 108(3):036101
29. Wendelstorf J, Spitzer KH, Wendelstorf R (2008) Spray water cooling heat transfer at high temperatures and liquid mass fluxes. *Int J Heat Mass Transf* 51(19):4902–4910
30. Woodfield PL, Monde M, Mitsutake Y (2006) Improved analytical solution for inverse heat conduction problems on thermally thick and semi-infinite solids. *Int J Heat Mass Transf* 49(17–18):2864–2876

**Open Access** This chapter is licensed under the terms of the Creative Commons Attribution 4.0 International License (<http://creativecommons.org/licenses/by/4.0/>), which permits use, sharing, adaptation, distribution and reproduction in any medium or format, as long as you give appropriate credit to the original author(s) and the source, provide a link to the Creative Commons license and indicate if changes were made.

The images or other third party material in this chapter are included in the chapter's Creative Commons license, unless indicated otherwise in a credit line to the material. If material is not included in the chapter's Creative Commons license and your intended use is not permitted by statutory regulation or exceeds the permitted use, you will need to obtain permission directly from the copyright holder.



# Mechanical and Electrical Phenomena of Droplets Under the Influence of High Electric Fields



Jens-Michael Löwe, Michael Kempf, and Volker Hinrichsen

**Abstract** High-voltage composite insulators are specially designed to withstand different environmental conditions to ensure a reliable and efficient electric power distribution and transmission. Especially, outdoor insulators are exposed to rain, snow or ice, which might significantly affect the performance of the insulators. The interaction of sessile water droplets and electric fields is investigated under various boundary conditions. Besides the general behavior of sessile droplets, namely the deformation and oscillation, the inception field strength for partial discharges is examined depending on the droplet volume, strength and frequency of the electric field and the electric charge. Particularly, the electric charge is identified to significantly affect the droplet behavior as well as the partial discharge inception field strength. In addition to ambient conditions, the impact of electric fields on ice nucleation is investigated under well-defined conditions with respect to the temperature and electric field strength. High electric field strengths are identified to significantly promote ice nucleation, especially in case of alternating and transient electric fields. Different influencing factors like the strengths, frequencies and time constants of the electric fields are investigated. Consequently, the performed experiments enhance the knowledge of the behavior of water droplets under the impact of electric fields under various conditions.

## 1 Introduction

The transmission and distribution of electric power relies on its components, which are specifically designed to withstand various different environmental stresses like rain, snow, UV-light and extreme temperatures for many years [13, 15]. The efficiency and reliability of the system mainly depends on the performance of the individual components within the system. High-voltage insulators are used to insulate the high-voltage potential present on the line conductor from the ground potential

---

J.-M. Löwe · M. Kempf · V. Hinrichsen (✉)  
High-Voltage Laboratories, Technical University Darmstadt, Darmstadt, Germany  
e-mail: [volker.hinrichsen@tu-darmstadt.de](mailto:volker.hinrichsen@tu-darmstadt.de)

of the pylons. Nowadays, more and more composite insulators are used due to their advantages compared to glass or ceramic insulators [39]. Composite insulators are typically made out of a fibre-glass rod covered by weather sheds consisting of silicone rubber. The most important advantages are the high robustness, the lowered weight and the hydrophobic surface properties, which prevents the formation of a liquid layer on the surface [39]. Any contamination of the insulators surface might increase the surface conductivity and, thus, lead to undesired creeping currents on the surface, which significantly affect the efficiency of the system. The hydrophobic surface properties of composite insulators prevent the formation of conductive liquid layers on the surface and cause the formation of single sessile droplets instead. Even though the hydrophobicity of the silicone rubber is an advantage with respect to creeping currents, the formation of sessile droplets causes electrically critical points directly at the three-phase contact line. Due to the different electric and dielectric properties of the involved materials, namely air, water and silicone rubber, the electric field is suppressed or completely vanishes inside the water droplet. Furthermore, the electric field strength in the material with the lowest relative permittivity (air) is significantly enhanced. Hence, the breakdown strength of air might be locally exceeded resulting in the formation of partial discharges [51]. The presence of partial discharges is associated with locally increased temperatures and the generation of UV-light, which contribute to an accelerated aging of the silicone rubber [2, 12]. To ensure a reliable and efficient power transmission and distribution the aging behavior of composite insulators caused by sessile droplets has to be investigated in detail. This behavior comprising the general behavior of water droplets under the impact of an electric field and various conditions as well as the corresponding partial discharge inception is experimentally investigated in this work. During the last twelve years various different influencing factors such as surface properties, droplet volume, droplet-droplet interaction, electric field strength, type of electric field, frequency of electric field, electric charge and orientation of the substrate were investigated. In collaboration with the Institute for Accelerator Science and Electromagnetic Fields (TEMF) of the Technical University of Darmstadt the experimental results are extended by numerical simulations.

Based on the knowledge of the general behavior of water droplets under the impact of electric fields, which highly affects the shape and motion of the droplets, the impact of high electric fields on ice nucleation is investigated. High-voltage insulators operated in cold regions might be affected by accreted ice [9]. The ice accretion causes an altered shape of the insulators and might also lead to a conductive impurity layer on the surface [10]. In addition, a large amount of ice can lead to bridging of the weather sheds causing a decreased insulation distance eventually resulting in flashovers [11]. Besides the impact on the electrical properties the ice accretion leads to additional static and dynamic loads on the pylons, which might cause a collapse of the pylons in the worst case [9]. While the general behavior of water droplets under cold conditions or under the influence of electric fields was already intensively investigated [1, 3, 7, 14, 36, 43, 49, 50, 55, 57], the impact of electric fields on ice nucleation is controversially discussed in literature [5, 6, 8, 16, 29–31, 37, 40, 41, 44, 47, 48, 52–54, 56]. However, the strong interaction of the

droplets and the electric fields under ambient conditions leads to the suggestion that also ice nucleation is significantly affected by strong electric fields. To determine the impact of electric fields on ice nucleation an experimental setup has been developed, and several experiments under different conditions with respect to the type, strength and frequency of the electric field are performed.

The aim of this work is to enhance the knowledge about droplets under the impact of strong electric fields under well-defined conditions. The main focus is to determine the underlying physical mechanisms to be able to predict and control the behavior of the droplets. Hence, the presented work aids the development of theoretical models for the forecast of the aging of high-voltage insulators or the prediction of ice nucleation of water droplets under the impact of electric fields.

The following sections briefly summarize the results of the progress of the project but mainly focus on the most recent results. The chapter is divided into two main sections, which present the results of the experiments of droplets at ambient temperature and the nucleation behavior of droplets under low temperature conditions affected by different types of electric fields.

## 2 Sessile Droplets in Electric Fields Under Normal Ambient Conditions

The general behavior of sessile droplets under the impact of strong electric fields is investigated using a generic insulator model. The specimen is made out of a typical high-voltage insulation material, such as silicone rubber or epoxy, containing two embedded brass electrodes. The electric field strength is evaluated at the droplets position in absence of the droplet. In case of alternating or transient electric fields the amplitude or the maximum field strength is used to characterize the electric field strength. The generated electric field is tangentially aligned to the substrate surface because tangentially aligned electric fields are known to have the largest impact on the droplet [45]. In addition, tangentially aligned electric fields reproduce the electrical situation at the surface of a high-voltage insulator very accurately. Different types of electric fields, namely constant, alternating and transient electric fields are generated by different high-voltage sources connected to one of the electrodes, while the other electrode is grounded. The general behavior of the droplets is investigated using shadowgraphy and a high-speed camera. Prior to each experiment the substrate surface is cleaned using anti-static wipes soaked with isopropanol to remove surface contamination such as dust and to minimize surface charges [28]. The droplets are generated either with a conventional pipette or using an automated high precision syringe to ensure a well-defined droplet volume. The electric charge of the droplets can be actively controlled by using a grounded needle to produce uncharged droplets or a droplet charger, similar to [4], to generate charged droplets. A single droplet is placed on the center of the specimen without touching the surface to prevent the generation of surface charges.

## 2.1 General Droplet Behavior

The behavior of sessile droplets mainly depends on the type of the applied electric field. To determine the influence of each type of electric field, three-different types are used, namely constant, alternating and transient electric fields. For each type different influencing factors such as strength and frequency of the electric field are investigated. The following sections shortly summarize the outcome of the different experiments. A more detailed description of the experiments and the results can be found in the corresponding publications.

### 2.1.1 Constant (Time-Invariant) Electric Fields

Constant (time-invariant) electric fields are identified to affect the behavior of a sessile droplet [32]. The forces generated by the electric field causes an elongation of the droplet. The droplet always moves towards the negative electrode. The contact line facing the positive electrode is pinned during this motion. However, after reaching a certain deformation a jumping motion towards the positive electrode is observed. The position of the droplet on the insulator is changed, and the droplet adapts to a new equilibrium shape. The principal behavior of a droplet under the influence of a constant electric field is shown in Fig. 1. The volume of the droplets is identified to influence the motion of the droplets. The smaller the volume of the droplets, the shorter is the elongation process compared to larger droplets.

### 2.1.2 Alternating Electric Fields

While constant electric fields lead to deformations of the droplets, alternating electric fields cause an oscillation of the droplets. The behavior of the droplets mainly depends on the electric field strength but is also influenced by the e.g. the droplet volume, electric charge or wetting properties of the substrate. For low electric field strengths the droplet only oscillates, and the three-phase contact line is static and does not

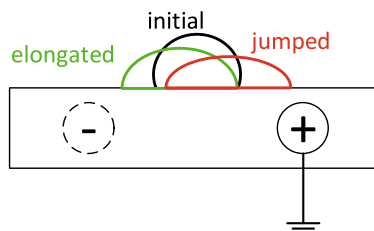


**Fig. 1** Principal motion of a sessile droplet under the impact of a constant electric field. Reprinted (adapted) figure with permission from [32] under the Creative Common License (CC-BY-NC-ND 3.0 International)

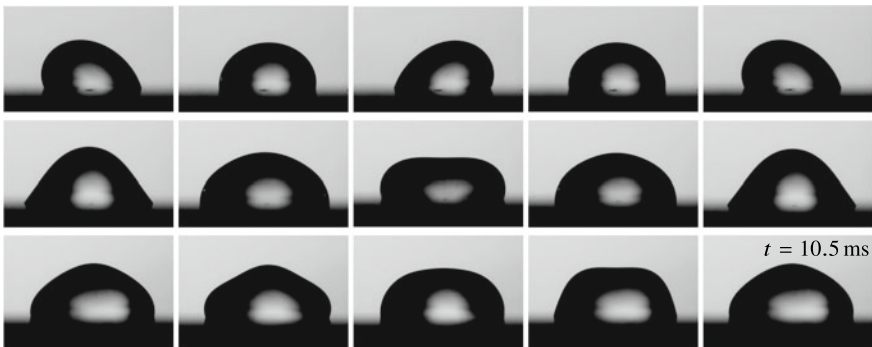


**Fig. 2** One cycle of the first three modes for  $n = 2, 3, 4$  of uncharged drops. **a** Example of Mode 1 ( $n = 2$ ) of a  $20 \mu\text{l}$  droplet at  $27 \text{ Hz}$  and  $\hat{E} = 3.81 \text{ kV/cm}$ , **b** example of Mode 2 ( $n = 3$ ) of a  $30 \mu\text{l}$  droplet at  $23 \text{ Hz}$  and  $\hat{E} = 4.67 \text{ kV/cm}$  and **c** example of Mode 3 ( $n = 4$ ) of a  $60 \mu\text{l}$  droplet at  $48 \text{ Hz}$  and  $\hat{E} = 7.37 \text{ kV/cm}$ . Reprinted (adapted) figure with permission from [20], Copyright 2020 by the American Physical Society

move. Increasing the electric field strength leads to larger oscillation amplitudes finally resulting in a movement of the three-phase contact line if the contact angles exceed the advancing contact angle. In the following the main focus lies on the droplet oscillation, which depends on the droplet volume, strength of the electric field as well as the frequency of the electric field. The principal motion of a droplet under the impact of an alternating electric field oscillating in the first three resonance modes is shown in Fig. 2. The motion of the droplets is affected by the frequency of the electric field and is different for each resonance mode. While droplets in first resonance mode are periodically leaning sideways, which results in a principal motion tangentially aligned to the substrate, higher resonance modes cause a stretching and compression cycle of the droplet perpendicular to the substrate. For hydrophobic substrates the resonance frequency of the droplet is well described by the resonance frequencies of a free droplet [46]. The characteristic frequencies of the droplet depend on the droplet volume. The larger the droplet volume, the lower is the frequency of the corresponding resonance mode.

Besides the frequency of the electric field and the droplet volume, the electric charge of the droplet is identified to have a significant influence on the droplet motion [19, 20]. Generally, uncharged droplets are assumed to oscillate with twice the frequency of the applied voltage because the electric field causes a force proportional to the square of the electric field. Thus, a sinusoidal voltage leads to  $f_d \propto \hat{E}^2 \propto 1 - \cos(2\omega t)$ , where  $f_d$  is the oscillation frequency of the droplet,  $\hat{E}$  the amplitude of the electric field strength,  $t$  the time and  $\omega$  the pulsatance of the applied voltage. In contrast, a charged droplet should oscillate with the same frequency as that of the applied voltage because of the Coulomb force ( $f_d \propto \hat{E} \propto \sin(\omega t)$ ) acting on the droplet. Whether the droplet oscillates with the same or twice the frequency of the applied voltage depends on the droplet volume, the amount of charge present on the droplet and the applied electric field strength, which define the predominant

force. The droplet oscillates with the same frequency if the amount of charge present on the droplet is high enough to cause a sufficiently large Coulomb force. However, the charge on a droplet is limited by the Rayleigh charge [42], so that sufficiently high electric field strengths will always force the droplet to oscillate with twice the frequency of the electric field. Note that the transition between the different oscillation frequencies is continuous, because of the different forces simultaneously act on the droplet. The performed experiments revealed the amount of charge necessary to cause a change of the behavior depending on the droplet volume, electric charge, electric field strength and resonance mode. While this behavior is observed for droplets oscillating in resonance mode two or higher, a different behavior is observed for droplets oscillating in first resonance mode. Independently of the amount of charge present on the droplet, the droplet always behaves like a charged droplet and oscillates with the same frequency of the applied voltage. Hence, the behavior of a droplet oscillating in first resonance mode is not changed by the presence of charges. In contrast, the oscillation behavior in higher resonance modes can be actively controlled by the electric field strength, the droplet volume, the frequency of the electric field and the electric charge on the droplet. Especially, small droplets are highly affected by the presence of electric charges. Consequently, the electric charge has a significant impact on the motion of the droplets and has to be taken into account whenever an electric field is present. Corresponding numerical simulations of the droplet motion for specific conditions can be found in [38].

## 2.2 Transient Electric Fields

In addition to constant and alternating electric fields, the behavior of single and multiple droplets under the impact of transient electric fields are investigated [25]. Standard lightning and switching impulse voltages ( $1.2/50\ \mu\text{s}$  and  $250/2500\ \mu\text{s}$ ) as defined by IEC 60060 are used to generate well-defined transient electric fields. The general behavior of a droplet under the impact of a standard switching impulse voltage is shown in Fig. 3. The force generated by the electric field is mainly concentrated at the three-phase contact line, and causes an outward motion of the contact line. The footprint of the droplet is increased and small disturbances are initiated, which propagate as surface waves on the droplet. The disturbances generated at both sides of the droplet interact as soon as they reach the top of the droplet and

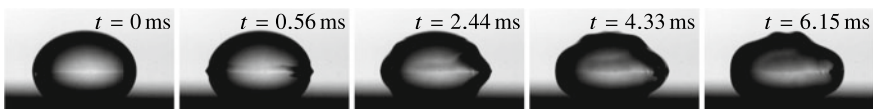


**Fig. 3** Side view time series of a sessile water droplet ( $V = 50\ \mu\text{l}$ ) surrounded by air and exposed to a switching impulse voltage ( $\hat{E} = 18.43\ \text{kV}/\text{cm}$ ) under ambient conditions [23] (Creative Common License (CC-BY-NC-ND 4.0 International)

result in large droplet oscillations. In case of standard lightning impulse the general behavior is similar, but the impact of the electric field is much smaller. The movement of the contact line and the amplitude of the oscillations are barely visible on the high-speed videos. Hence, the standard switching impulse voltages have a larger impact on droplets compared to standard lightning impulse voltages. While the initial impact of the electric field, namely the increase of the footprint, usually does not lead to coalescence of neighbouring droplets, the droplet oscillation might cause droplet coalescence depending on droplet volume and droplet-droplet distance. However, for small droplet-droplet distances ( $h_{d-d} < 1 \text{ mm}$ ) the initial increase of the footprint can lead to coalescence of the neighboring droplets. The interaction of nearby droplets is investigated in more detail, and a region map is generated to determine the behavior of the droplets depending on the droplet-droplet distance, the droplet volume, electric field strength and impulse type [25]. While sufficiently high electric field strengths and small droplet-droplet distances always lead to droplet coalescence in case of standard switching impulse voltages, droplet coalescence under the impact of standard lightning impulse voltage also depends on the droplet volume. Small droplets (droplet volume  $V_d < 40 \mu\text{l}$ ) do not interact even for small droplet-droplet distances of  $h_{d-d} \approx 1 \text{ mm}$ . However, large droplets might coalesce depending on the electric field strength and the droplet-droplet distance.

Consequently, the behavior of the droplets clearly depends on the type and characteristic time constants of the electric field. The characteristic time scales of the standard switching impulse are much larger compared to those of standard lightning impulse voltages, as defined by IEC 60060. Thus, the electric field is present for a longer time, which leads to a larger macroscopic motion, potentially resulting in coalescence.

## 2.3 Partial Discharge Inception Field Strength

As already mentioned the electric field is significantly enhanced near the three-phase contact line. The local field enhancement can lead to a field strength locally exceeding the breakdown strength of air resulting in the generation of partial discharges. The associated generation of UV-light and locally high temperatures contribute to the accelerated aging of composite insulators [2, 17, 18]. To determine the various influencing factors and the impact of different boundary conditions, the partial discharge inception field strength is investigated under various different conditions. The partial discharge inception field strength is determined for different types of electric fields [32, 35], droplet volumes [32–34], surface orientations [32, 34] and wetting properties of the substrate [32, 34]. In addition, the impact of the conductivity of the droplet [34], the electric charges and the oscillation of the droplet are investigated [27].

Generally, partial discharges are identified to occur directly at the three-phase contact line as shown in Fig. 4. The UV-light generated by the partial discharges is used to visualize the location of the partial discharges with high resolution. The UV-light is

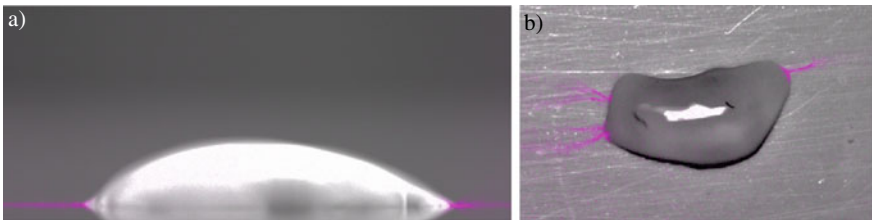


**Fig. 4** Exemplary images of a water droplets with superimposed image of UV-camera to visualize the partial discharges (colored in magenta). **a** Water droplet with  $V_d = 20 \mu\text{l}$  in side view for  $\tilde{E} = 9.02 \text{ kV/cm}$  and **b** in top view for  $\tilde{E} = 9.63 \text{ kV/cm}$ . Reprinted (adapted) figure with permission from [21], Copyright 2021 by the American Physical Society

colored in magenta and is superimposed to the daylight image of the droplet. Due to the forces generated by the electric field, the shape of the droplet is altered and takes a complex form. The occurrence of partial discharges mainly depends on the shape of the droplet, so that the partial discharges are only observed at specific locations at the contact line. The partial discharges are mainly located at conical tips of the droplet as shown in Fig. 4b. Especially, at this location the curvature of the interface is low and, thus these locations are more prone to generate partial discharges because of a significantly increased electric field strength. The partial discharge inception field strength depends on the type of electric field. For constant electric fields the critical partial discharge inception is determined for different droplet volumes [35]. Generally, the generation of partial discharges is observed to be independent of the polarity of the applied potential. The higher the electric field strength, the higher is the measured partial discharge impulse.

In addition to constant electric fields, the inception field strength is investigated under the impact of alternating electric fields. The inception field strength is identified to depend on various influencing factors. An increasing droplet volume generally leads to a decreasing inception field strength for partial discharges [34]. Due to the fact that the water droplets used for the experiments can be assumed as perfect conductors for low frequencies ( $f < 1000 \text{ Hz}$  for the given liquid), a change of the conductivity revealed a negligible effect on the inception field strength [32]. This assumption is valid as long as the charge relaxation time of the liquid  $\tau_{\text{el}}$  is much lower than the characteristic time of the electric field  $\tau_E$ . In contrast, the frequency of the electric field and the wettability of the substrate have a significant influence on the inception of partial discharges. The lower the contact angle of the single sessile droplets (the better the wettability of the substrate), the lower is the inception field strength for partial discharges. Hence, the inception field strength of sessile water droplets on silicone rubber is higher compared to epoxy resin. The presence of electrical charges also influences the inception field strength [27]. The higher the amount of charges present on the droplet, the lower is the inception field strength of partial discharges. Besides the already mentioned influencing factors, the inception field strength is determined for the first three resonance modes [27]. The higher the frequency of the electric field i.e. the higher the resonance mode, the higher is the

inception field strength of partial discharges. Additionally, the surface inclination and the presence of further droplets affect the generation of partial discharges. Especially, nearby droplets can significantly reduce the partial discharge inception field strength [27].

The combination of constant and alternating electric fields revealed that the inception field strength of partial discharges can be further lowered by the presence of a superimposed constant electric field compared to an alternating electric field [35].

Simulation results of the partial discharge inception field strength are performed by [38]. Based on the performed experiments the inception field strength is estimated and compared to measured values. The generation of partial discharges is affected by various influencing factors and very sensitive to changes of the boundary conditions.

### 3 Ice Nucleation Under the Impact of Electric Fields

The presence of an electric field impacts the behavior of a sessile water droplet under normal ambient conditions. Due to the fact that the electric field significantly affects the mechanical and electrical behavior of a droplet under ambient conditions, it is assumed that the electric field might also affect additional physical mechanisms like ice nucleation. There is an ongoing discussion in literature as shown in Sect. 1 whether ice nucleation can be affected by electric fields or not. In the scope of this work an experimental setup called SAPPHIRE is developed to investigate the impact of electric fields on ice nucleation in more detail [27]. The temperature as well as the electric field are precisely controlled to determine even small influences of the electric field on ice nucleation. Different types of electric fields, namely constant, alternating and transient electric fields, are used to determine the impact of various influencing factors such as the electric field strength, frequency of the electric field and type of the electric field. The electric field strength is evaluated at the droplets position in absence of the droplets. In case of alternating or transient electric fields, the amplitude of the electric field is used to characterize the electric field strength. Furthermore, the variety of experimental conditions is assumed to improve the understanding of the underlying physical mechanisms.

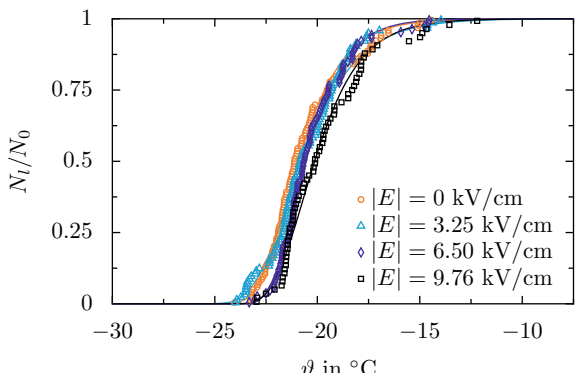
A droplet ensemble consisting of 40 droplets with well-controlled volumes are cooled with a constant cooling rate or hold at a constant temperature. Ice nucleation inside the individual droplets is observed with a video camera and identified by the vanishing glare point during the freezing of the droplets. To generate a sufficient number of nucleation events the same droplet ensemble is used several times to ensure well-defined boundary conditions and to rule out any influence of changed contamination inside the droplets. Hence, for the investigation of each parameter like the electric field strength a fixed droplet ensemble is used. The droplets are exposed to several freezing and thawing cycles resulting in a large number of nucleation events. The impact of the electric field is determined by a comparison of the different

experiments with and without an electric field present. Subsequently, the results for the different types of electric fields are shortly summarized and exemplary results are shown.

### 3.1 Constant (Time-Invariant) Electric Fields

The impact of constant (time-invariant) electric fields on ice nucleation is extensively studied in [22, 26]. The same set of droplets is exposed to various freezing and thawing cycles while the electric field strength is continuously increased up to a value of  $E = 9.76 \text{ kV/cm}$ . Using the same set of droplets ensures that the contamination and the position of the droplets do not affect ice nucleation because any influence present is constant for all cycles. The droplets are cooled at a constant rate of  $\dot{T} = 5 \text{ K/min}$ . The nucleation events and the associated temperatures are used to analyze the impact of a constant electric field on ice nucleation. Based on the freezing events droplet survival curves are generated, which correlate the liquid fraction  $N_l/N_0$ , where  $N_l$  is the number of liquid droplets at a certain temperature  $\vartheta$  and  $N_0$  is the number of initially liquid droplets, and the droplet temperature  $\vartheta$ . The comparison of the survival curves generated under different conditions reveals the impact of the electric field on ice nucleation. Exemplary results are shown in Fig. 5. Survival curves depending on the electric field strength are presented. Low electric field strengths  $E < 6.50 \text{ kV/cm}$  do not influence ice nucleation as shown by the almost perfect accordance of the different survival curves [26]. However, increasing the electric field strength ( $E \geq 9.76 \text{ kV/cm}$ ) leads to a survival curve shifted to higher temperatures [26]. The individual droplets freeze at a higher temperature so that ice nucleation is promoted by the electric field. Nevertheless, the impact is rather small. To quantify the increase of the nucleation temperature, the mean nucleation temperature  $\vartheta_{0.5}$  can be used. The mean nucleation temperature is the temperature associated to  $N_l/N_0 = 0.5$  and, thus characterizes the temperature necessary to cause half of the ensemble to

**Fig. 5** Liquid fraction  $N_l/N_0$ , where  $N_l$  is the number of liquid droplets at a certain temperature  $\vartheta$  and  $N_0$  is the number of initially liquid droplets, depending on the droplet temperature  $\vartheta$  for different electric field strengths  $|E|$ . Republished with permission of/from [26]; permission conveyed through Copyright Clearance Center, Inc



be frozen. The increase of the temperature is always correlated to the run without an electric field. In case of a constant electric field the largest increase of the nucleation temperature is observed at  $E = 9.76 \text{ kV/cm}$  and yields approximately  $\Delta\vartheta \approx 1 \text{ K}$  [26]. Consequently, ice nucleation can be influenced by the constant electric fields, but the influence is rather small and might be masked by other influencing factors such as the measurement uncertainty of the temperature or the stochastic nature of ice nucleation.

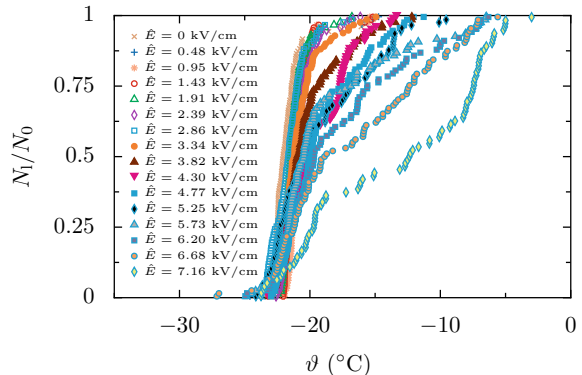
Even though ice nucleation is a stochastic process, the performed experiments revealed a singular nucleation behavior of the droplets in absence of an electric field. Due to the fact that the same droplet ensemble is used for the different freezing and thawing cycles the nucleation temperature of each droplet can be compared to the previous and subsequent runs. In absence of an electric field, the nucleation temperature of the individual droplets is almost constant and suggests that ice nucleation is mainly influenced by the ice nucleation particles inside the droplets and their characteristic temperature [26]. Therefore, the experimental data is described very well by the singular nucleation model.

In summary, the experiments revealed a rather small influence of constant electric fields on nucleation. However, the used procedure is capable to reveal even small influences with good accuracy.

### 3.2 Alternating Electric Fields

In addition to constant electric fields, the impact of alternating electric fields is investigated with respect to the electric field strength and the frequency [24]. Similar to the investigation of the impact of constant electric fields, a fixed droplet ensemble is used to investigate the impact of each influencing parameter such as the electric field strength or frequency. The droplet ensemble containing up to 40 droplets is cooled at a constant cooling rate of  $\dot{T} = 5 \text{ K/min}$ . To generate a large number of nucleation events the same ensemble is used to perform several freezing and thawing cycles. Overall a minimum of 55 droplets is used for analyzing the behavior of the droplets. The occurring nucleation events are correlated to the actual nucleation temperature and analyzed using droplet survival curves. Exemplary results are given by the droplet survival curves shown in Fig. 6. The liquid fraction  $N_1/N_0$  depending on the droplet temperature  $\vartheta$  for various electric field strengths  $\hat{E}$  is presented. While small electric field strengths ( $\hat{E} < 3.34 \text{ kV/cm}$ ) have an almost negligible influence on ice nucleation, larger electric field strengths ( $\hat{E} \geq 3.34 \text{ kV/cm}$ ) significantly influence ice nucleation. The impact of the electric field on ice nucleation is twofold. First, the general shape of the droplet survival curves is altered from the typical ‘S’-like shape. Second, individual droplets are forced to freeze at higher temperatures, so that the temperature of the first freezing event is significantly increased. Hence, the temperature range of ice nucleation is increased. Generally, the impact of the electric field increases with increasing electric field strength. The impact of an alternating electric field can be quantified by the mean nucleation temperature  $\vartheta_{0.5}$ . The max-

**Fig. 6** Liquid fraction  $N_1/N_0$ , where  $N_1$  is the number of liquid droplets at a certain temperature  $\vartheta$  and  $N_0$  is the number of initially liquid droplets, depending on the droplet temperature  $\vartheta$  for different electric field strengths  $\hat{E}$  ( $f = 50$  Hz). Reprinted (adapted) figure with permission from [24], Copyright 2021 by the American Physical Society



imum change of the mean nucleation temperature is observed for  $\hat{E} = 7.16$  kV/cm and yields  $\Delta\vartheta_{0.5} \approx 10$  K. However, for  $N_1/N_0 < 0.5$  the change of the characteristic nucleation temperature is even higher. Even though the temperature of individual droplets is increased, the lowest freezing temperature is almost constant independent of the applied electric field. Hence, the electric field does not influence all droplets in the same manner. A more detailed analysis of the individual nucleation events revealed that not all droplets are affected by the electric field. Consequently, the impact of an alternating electric field is of singular rather than stochastic nature. Due to the fact that the number of droplets affected by the electric field increases with increasing electric field strength, it seems that each droplet is associated with a characteristic electric field strength necessary to influence ice nucleation. To reveal if additional influencing factors (besides the electric field strength) also have a singular impact on ice nucleation, the singular and stochastic behavior of the nucleation events is analyzed in more detail with respect to the temperature and time. The analysis revealed that the individual droplet can be characterized by a specific nucleation temperature according to the singular nucleation model. However, stochastic processes still play a role, which is shown by the scatter of the experimental data. Even though ice nucleation is a time dependent process, the electric history of the droplets does not influence the outcome of the experiments. Hence, a previously applied electric field does not influence the actual nucleation behavior at a different electric field strength. Ice nucleation is only affected on a small time scale and the boundary conditions present at the time instant of nucleation.

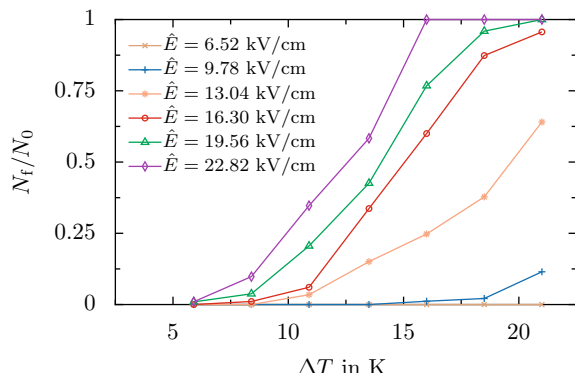
Besides the magnitude of the electric field strength, its frequency has large influence on the nucleation behavior. Specific frequencies to promote ice nucleation are identified ( $f = 100$  Hz or  $f = 110$  Hz for the given setup). Thus, the macroscopic motion, namely the oscillation of the droplets seems to have a large impact on the nucleation behavior. However, the influence of the electric field on ice nucleation is not completely understood yet.

Compared to constant electric fields, the impact of alternating electric field is significantly increased. Individual droplets are highly affected by the electric field, so that ice nucleation is promoted by the presence of the electric field.

### 3.3 Transient Electric Fields

In contrast to the investigation of constant and alternating electric fields, the impact of transient electric fields is determined at constant temperature. The droplet ensemble is cooled to a constant temperature. Afterwards the electric field is applied and the number of frozen droplets is analyzed. To determine the impact of different types of transient electric fields standard lightning and standard switching impulse voltages are used to investigate the nucleation behavior. A more detailed overview is given by [23]. Exemplary results for an ensemble exposed to standard lightning impulse voltage are shown in Fig. 7. The frozen fraction  $N_f/N_0$ , where  $N_f$  is the number of frozen droplets at the temperature  $\vartheta$  and  $N_0$  is the number of initially liquid droplets, depending on the degree of supercooling  $\Delta T$  and the electric field strength  $\hat{E}$  is shown. The electric field strength corresponds to the highest electric field strength present while the electric field is applied. While low electric field strength ( $\hat{E} < 9.78 \text{ kV/cm}$ ) does not affect ice nucleation, i.e. does not cause any droplet to freeze, higher electric field strength have an impact on ice nucleation. The higher the electric field strengths, the higher is the frozen fraction depending on the degree of supercooling. Note that the frozen fraction is always analyzed at  $t = 1.5 \text{ s}$  after the electric field is applied for comparison reasons and to ensure that the nucleation event is caused by the electric field rather than by the stochastic nature of ice nucleation. Electric field strengths higher than  $\hat{E} = 19.56 \text{ kV/cm}$  lead to a completely frozen ensemble at least for a supercooling of  $\Delta T = 20 \text{ K}$ . Comparing the impact of standard lightning and standard switching impulse voltage reveals that the impact of standard switching impulse voltage is higher, i.e. the number of frozen

**Fig. 7** Frozen fraction  $N_f/N_0$  depending on the degree of supercooling  $\Delta T$  under the impact of standard lightning impulse voltages generating an electric field strength of  $E$  [23] (Creative Common License (CC-BY-NC-ND 4.0 International)



droplets is increased for the same degree of supercooling and applied electric field strength. However, the influence of an electric field strength of  $E = 6.52 \text{ kV/cm}$  is also almost negligible for standard switching impulse voltages. In contrast, the mean freezing temperature  $\vartheta_{0.5}$  can be significantly increased for both impulse types. The highest change of the mean freezing temperature can be observed at high electric field strength and yields  $\Delta \approx 6 \text{ K}$ .

Not only the impact of standard switching impulse voltage on ice nucleation is higher compared to standard lightning impulse voltage but also the macroscopic behavior of the droplets. While standard switching impulse voltages lead to significant droplet oscillations, the standard lightning impulse voltages have an almost negligible impact for the investigated electric field strength. As a conclusion the impact of the electric field might be associated with the motion of the droplets. Nevertheless, even in case of small droplet oscillations, the electric field does influence the nucleation behavior. However, the physical mechanism affecting ice nucleation is not completely understood yet, because no general model is available to describe the influence of electric field on ice nucleation.

The freezing of the individual droplets is not always observed during the highest electric field strength but also after the electric field has already completely decayed. The moment of nucleation of the individual droplets with respect to the application of the electric field covers several orders of magnitude (from milliseconds to seconds). Hence, ice nucleation is clearly a time dependent process. However, the stochastic nature of the process can only be observed on a small time scale. A larger time scale might mask the stochastic nature of ice nucleation and causes a singular behavior.

Generally, transient electric fields can be used to actively affect ice nucleation. The presence of sufficiently high electric fields significantly promotes ice nucleation and increases the nucleation temperature of the individual droplets.

## 4 Conclusions

The behavior of sessile droplets is highly affected by the presence of electric fields. The impact of the electric field mainly depends on the type of the electric field but is also influenced by other factors such as droplet volume or electric field strength. Generally, the electric field causes oscillations or deformations of the droplet and might even lead to an enhanced surface wetting. In addition to the mechanical phenomena, the interaction of a sessile water droplet and the electric field causes a field enhancement at the three-phase contact line of the droplet. The locally enhanced electric field causes the formation of partial discharges, which contribute to an accelerated aging of the insulators. In the scope of this work the main influencing factors of the electrical and mechanical phenomena are investigated in detail. Especially, the electric charge is identified to have a large impact on the mechanical and electrical behavior of the droplet and might have been underestimated in many other investigations performed in the past and reported in literature. In addition, droplet volume, strength, frequency and type of the electric field as well as the electrical

and geometrical properties of the experimental setup clearly affect the motion of the droplets and the formation of partial discharges.

The electric field does not only impact the mechanical and electrical behavior of a droplet under normal ambient conditions but also additional physical mechanisms like ice nucleation. The developed experimental setup called SAPPHIRE allows the investigation of ice nucleation of sessile and emulsified droplets under well-defined conditions with respect to temperature and electric field strength. While constant electric fields are identified to have a rather small impact on ice nucleation, alternating and transient electric fields significantly promote ice nucleation. The nucleation temperature of individual droplets can be notably increased by the presence of an electric field. The nucleation temperature of each droplet is not only associated with a characteristic temperature, as defined by the singular nucleation model, but also by a characteristic electric field strength necessary to cause an impact on ice nucleation. Hence, the impact of an electric field can also be of singular rather than stochastic nature. Generally, the presence of an electric field can clearly promote ice nucleation and can be actively used to force ice nucleation.

The experimental work performed in this work is expanded by numerical simulations performed by Institute for Accelerator Science and Electromagnetic Fields of the Technical University of Darmstadt. The results enhance the knowledge of the behavior of water droplets under the impact of electric fields, which might be the origin for the development of more advanced prediction models for the inception of partial discharges of sessile water droplet or the icing of high-voltage insulators.

**Acknowledgements** The authors kindly acknowledge the financial support by the Deutsche Forschungsgemeinschaft (DFG) within the SFB-TRR 75, project number 84292822.

## References

1. Acharya PV, Bahadur V (2018) Fundamental interfacial mechanisms underlying electrofreezing. *Adv Coll Interface Sci* 251:26–43. <https://doi.org/10.1016/j.cis.2017.12.003>
2. Akbar M, Ullah R, Alam S (2019) Aging of silicone rubber-based composite insulators under multi-stressed conditions: an overview. *Mater Res Express* 6(10):102003. <https://doi.org/10.1088/2053-1591/ab3f0d>
3. Borzsák I, Cummings PT (1997) Electrofreezing of water in molecular dynamics simulation accelerated by oscillatory shear. *Phys Rev E* 56(6):R6279–R6282. <https://doi.org/10.1103/PhysRevE.56.R6279>
4. Brandenbourger M, Dorbolo S (2014) Electrically charged droplet: case study of a simple generator. *Can J Phys* 92(10):1203–1207. <https://doi.org/10.1139/cjp-2013-0479>
5. Braslavsky I, Lipson SG (1998) Electrofreezing effect and nucleation of ice crystals in free growth experiments. *Appl Phys Lett* 72(2):264. <https://doi.org/10.1063/1.120705>
6. Carpenter K, Bahadur V (2015) Electrofreezing of water droplets under electrowetting fields. *Langmuir: ACS J Surf Colloids* 31(7):2243–2248. <https://doi.org/10.1021/la504792n>
7. Dalvi-Isfahan M, Hamdami N, Xanthakis E, Le-Bail A (2017) Review on the control of ice nucleation by ultrasound waves, electric and magnetic fields. *J Food Eng* 195:222–234. <https://doi.org/10.1016/j.jfoodeng.2016.10.001>

8. Doolittle JB, Vali G (1975) Heterogeneous Freezing Nucleation in Electric Fields. *J Atmos Sci* 32(2):375–379. [https://doi.org/10.1175/1520-0469\(1975\)032<0375:HFNIEF>2.0.CO;2](https://doi.org/10.1175/1520-0469(1975)032<0375:HFNIEF>2.0.CO;2)
9. Farzaneh M (2008) Atmospheric icing of power networks, 1. aufl. edn. Springer Netherlands, s.l. <http://site.ebrary.com/lib/alltitles/docDetail.action?docID=10239530>
10. Farzaneh M, Chisholm WA (2009) Insulators for icing and polluted environments. IEEE press series on power engineering. Wiley-Blackwell, Oxford (2009). <https://doi.org/10.1002/9780470496251>
11. Farzaneh M, Kiernicki J (1995) Flashover problems caused by ice build up on insulators. *IEEE Electr Insul Mag* 11(2):5–17. <https://doi.org/10.1109/57.372510>
12. Goudie JL, Owen MJ, Orbeck T (1998) A review of possible degradation mechanisms of silicone elastomers in high voltage insulation applications. In: 1998 annual report conference on electrical insulation and dielectric phenomena (Cat. No.98CH36257). IEEE, pp 120–127. <https://doi.org/10.1109/CEIDP.1998.733878>
13. Hackam R (1998) Outdoor high voltage polymeric insulators. In: Proceedings of 1998 international symposium on electrical insulating materials. Institute of Electrical Engineers of Japan, Tokyo and Piscataway, NJ, pp 1–16. <https://doi.org/10.1109/ISEIM.1998.741674>
14. Kashchiev D (1972) Nucleation in external electric field. *J Cryst Growth* 13–14:128–130. [https://doi.org/10.1016/0022-0248\(72\)90074-7](https://doi.org/10.1016/0022-0248(72)90074-7)
15. Khan H, Amin M, Ahmad A (2018) Characteristics of silicone composites for high voltage insulations. *Rev Adv Mater Sci* 56(1):91–123. <https://doi.org/10.1515/rams-2018-0040>
16. Koizumi H, Fujiwara K, Uda S (2010) Role of the electric double layer in controlling the nucleation rate for Tetragonal Hen Egg White Lysozyme crystals by application of an external electric field. *Cryst Growth & Des* 10(6):2591–2595. <https://doi.org/10.1021/cg901621x>
17. König D, Rao YN (1993) Teilentladungen in Betriebsmitteln der Energietechnik. VDE-Verl, Berlin
18. Küchler A (2018) High voltage engineering: fundamentals - technology - applications. VDI-Buch. Springer Vieweg, Berlin. <http://www.springer.com/de/book/978-3-642-11992-7>
19. Löwe JM, Hinrichsen V (2019) Experimental investigation of the influence of electric charge on the behavior of water droplets in electric fields. In: 2019 IEEE 20th international conference on dielectric liquids (ICDL). IEEE, pp 1–6. <https://doi.org/10.1109/ICDL.2019.8796707>
20. Löwe JM, Hinrichsen V, Roisman IV, Tropea C (2020) Behavior of charged and uncharged drops in high alternating tangential electric fields. *Phys Rev E* 101(2):023102. <https://doi.org/10.1103/PhysRevE.101.023102>
21. Löwe JM, Hinrichsen V, Roisman IV, Tropea C (2020) Impact of electric charge and motion of water drops on the inception field strength of partial discharges. *Phys Rev E* 102(6):063101. <https://doi.org/10.1103/PhysRevE.102.063101>
22. Löwe JM, Hinrichsen V, Schremp M, Dorau T, Tropea C (2017) Experimental investigation of electro-freezing of supercooled droplets. In: 9th world conference on experimental heat transfer, fluid mechanics and thermodynamics. Foz do Iguacu, Brasilien. <http://tubiblio.ulb.tu-darmstadt.de/88192/>
23. Löwe JM, Hinrichsen V, Schremp M, Tropea C (2021) Ice nucleation forced by transient electric fields. *Phys Rev E* 104:064801. <https://doi.org/10.1103/PhysRevE.104.064801>
24. Löwe JM, Hinrichsen V, Schremp M, Tropea C (2021) Ice nucleation in high alternating electric fields: effect of electric field strength and frequency. *Phys Rev E* 103(1):012801. <https://doi.org/10.1103/PhysRevE.103.012801>
25. Löwe JM, Hinrichsen V, Tropea C (2018) Droplet behavior under the impact of lightning and switching impulse voltage. In: 2018 IEEE electrical insulation conference (EIC). IEEE, pp 443–447. <https://doi.org/10.1109/EIC.2018.8480884>
26. Löwe JM, Schremp M, Hinrichsen V, Tropea C (2019) Ice nucleation in the presence of electric fields: an experimental study. In: SAE International (ed.) International conference on icing of aircraft, engines, and structures, SAE technical paper series. SAE International400 Commonwealth Drive, Warrendale, PA, United States. <https://doi.org/10.4271/2019-01-2020>
27. Löwe JM, Schremp M, Hinrichsen V, Tropea C (2021) Experimental methodology and procedure for SAPPHIRE: a semi-automatic APParatus for High-voltage Ice nucleation REsearch. *Atmos Meas Techn* 14(1):223–238. <https://doi.org/10.5194/amt-14-223-2021>

28. Löwe JM, Secklehner M, Hinrichsen V (2017) Investigation of surface charges on polymeric insulators and the influence of sessile water droplets. In: 2017 INSUCON - 13th international electrical insulation conference (INSUCON). IEEE, pp 1–7. <https://doi.org/10.23919/INSUCON.2017.8097170>
29. Ma, Y., Zhong, L., Gao, J., Liu, L., Hu, H., Yu, Q.: Manipulating ice crystallization of 0.9 wt. % NaCl aqueous solution by alternating current electric field. *Applied Physics Letters* **102**(18), 183701 (2013). DOI <https://doi.org/10.1063/1.4804287>
30. Mandal G, Pradeep Kumar P (2002) A laboratory study of ice nucleation due to electrical discharge. *Atmos Res* 61(2):115–123. [https://doi.org/10.1016/S0169-8095\(01\)00129-6](https://doi.org/10.1016/S0169-8095(01)00129-6)
31. Nardone M, Karpov VG (2012) Nucleation of metals by strong electric fields. *Appl Phys Lett* 100(15):151912. <https://doi.org/10.1063/1.3703611>
32. Nazemi MH (2016) Experimental investigations on water droplets on polymeric insulating surfaces under the impact of high electric fields. PhD thesis, Technische Universität Darmstadt, Darmstadt. <http://tuprints.ulb.tu-darmstadt.de/5363/>
33. Nazemi MH, Hinrichsen V (2013) Experimental investigations on water droplet oscillation and partial discharge inception voltage on polymeric insulating surfaces under the influence of AC electric field stress. *IEEE Trans Dielectr Electr Insul* 20(2):443–453. <https://doi.org/10.1109/TDEI.2013.6508746>
34. Nazemi MH, Hinrichsen V (2013) Partial discharge investigation and electric field analysis of different oscillation modes of water droplets on the surface of polymeric insulator under tangential AC electric field stress. In: 2013 IEEE international conference on solid dielectrics (ICSD), pp. 194–197. <https://doi.org/10.1109/ICSD.2013.6619788>
35. Nazemi MH, Hinrichsen V (2015) Experimental investigations on partial discharge characteristics of water droplets on polymeric insulating surfaces at AC, DC and combined AC-DC voltages. *IEEE Trans Dielectr Electr Insul* 22(4):2261–2270. <https://doi.org/10.1109/TDEI.2015.005007>
36. Nie GX, Wang Y, Huang JP (2015) Role of confinement in water solidification under electric fields. *Fron Phys* 10(5). <https://doi.org/10.1007/s11467-015-0504-y>
37. Orlowska M, Havet M, Le-Bail A (2009) Controlled ice nucleation under high voltage DC electrostatic field conditions. *Food Res Int* 42(7):879–884. <https://doi.org/10.1016/j.foodres.2009.03.015>
38. Ouedraogo Y (2020) Modelling of electrohydrodynamic droplet motion under the influence of strong electric fields. PhD thesis, Technische Universität Darmstadt, Darmstadt. <https://doi.org/10.25534/tuprints-00014008>
39. Papailiou KO, Schmuck F (2012) Silikon-Verbundisolatoren: Werkstoffe, Dimensionierung, Anwendungen. Springer, Heidelberg
40. Petersen A, Schneider H, Rau G, Glasmacher B (2006) A new approach for freezing of aqueous solutions under active control of the nucleation temperature. *Cryobiology* 53(2):248–257. <https://doi.org/10.1016/j.cryobiol.2006.06.005>
41. Pruppacher HR (1973) Electrofreezing of supercooled water. *Pure Appl Geophys PAGEOPH* 104(1):623–634. <https://doi.org/10.1007/BF00875907>
42. Rayleigh (1882) On the equilibrium of liquid conducting masses charged with electricity. *Philosoph Mag Ser 5* 14(87):184–186. <https://doi.org/10.1080/14786448208628425>
43. Saban KV, Thomas J, Varughese PA, Varghese G (2002) Thermodynamics of Crystal Nucleation in an External Electric Field. *Cryst Res Technol* 37(11):1188–1199. [https://doi.org/10.1002/1521-4079\(200211\)37:11<1188::AID-CRAT1188>3.0.CO;2-5](https://doi.org/10.1002/1521-4079(200211)37:11<1188::AID-CRAT1188>3.0.CO;2-5)
44. Salt RW (1961) Effect of electrostatic field on freezing of supercooled water and insects. *Science (New York, N.Y.)* 133(3451):458–459. <https://doi.org/10.1126/science.133.3451.458>
45. Sarang B, Basappa P, Lakdawala V, Shivaraj G (2011) Electric field computation of water droplets on a model insulator. In: 2011 electrical insulation conference (EIC) (Formerly EIC/EME), pp 377–381. <https://doi.org/10.1109/EIC.2011.5996182>
46. Schütte, T., Hornfeldt, S.: Dynamics of electrically stressed water drops on insulating surfaces. In: IEEE International Symposium on Electrical Insulation, pp. 202–207 (3–6 June 1990). DOI <https://doi.org/10.1109/ELINSL.1990.109741>

47. Stan CA, Tang SKY, Bishop KJM, Whitesides GM (2011) Externally applied electric fields up to  $1.6 \times 10(5)$  V/m do not affect the homogeneous nucleation of ice in supercooled water. *J Phys Chem B* 115(5):1089–1097. <https://doi.org/10.1021/jp110437x>
48. Sun W, Xu X, Sun W, Ying L, Xu C (2006) Effect of alternated electric field on the ice formation during freezing process of 0.9%K<sub>2</sub>MnO<sub>4</sub> water. In: 2006 IEEE 8th international conference on properties and applications of dielectric materials. IEEE, pp 774–777. <https://doi.org/10.1109/ICPADM.2006.284293>
49. Svishchev Kusalik (1994) Crystallization of liquid water in a molecular dynamics simulation. *Phys Rev Lett* 73(7):975–978. <https://doi.org/10.1103/PhysRevLett.73.975>
50. Svishchev IM, Kusalik PG (1996) Electrofreezing of liquid water: a microscopic perspective. *J Amer Chem Soc* 118(3):649–654. <https://doi.org/10.1021/ja951624l>
51. Vallet M, Vallade M, Berge B (1999) Limiting phenomena for the spreading of water on polymer films by electrowetting. *Eur Phys J B* 11(4):583–591. <https://doi.org/10.1007/s100510051186>
52. Wilson PW, Osterday K, Haymet ADJ (2009) The effects of electric field on ice nucleation may be masked by the inherent stochastic nature of nucleation. *Cryo Lett* 30(2):96–99
53. Xanthakis E, Havet M, Chevallier S, Abadie J, Le-Bail A (2013) Effect of static electric field on ice crystal size reduction during freezing of pork meat. *Innov Food Sci & Emer Technol: IFSET: Off Sci J Eur Feder Food Sci Technol* 20:115–120. <https://doi.org/10.1016/j.ifset.2013.06.011>
54. Yahong M, Lisheng Z, Huiyu H, Qinxue Y, Yewen Z (2012) A micro electro-freezing chip used in the crystallization of aqueous solutions under AC electric field. In: ICPADM 2012, pp 1–4. IEEE, [Piscataway, N.J.] (2012). <https://doi.org/10.1109/ICPADM.2012.6319024>
55. Yan JY, Patey GN (2011) Heterogeneous Ice Nucleation Induced by Electric Fields. *J Phys Chem Lett* 2(20):2555–2559. <https://doi.org/10.1021/jz201113m>
56. Yang F, Shaw RA, Gurganus CW, Chong SK, Yap YK (2015) Ice nucleation at the contact line triggered by transient electrowetting fields. *Appl Phys Lett* 107(26):264101. <https://doi.org/10.1063/1.4938749>
57. Zangi R, Mark AE (2004) Electrofreezing of confined water. *J Chem Phys* 120(15):7123–7130. <https://doi.org/10.1063/1.1687315>

**Open Access** This chapter is licensed under the terms of the Creative Commons Attribution 4.0 International License (<http://creativecommons.org/licenses/by/4.0/>), which permits use, sharing, adaptation, distribution and reproduction in any medium or format, as long as you give appropriate credit to the original author(s) and the source, provide a link to the Creative Commons license and indicate if changes were made.

The images or other third party material in this chapter are included in the chapter's Creative Commons license, unless indicated otherwise in a credit line to the material. If material is not included in the chapter's Creative Commons license and your intended use is not permitted by statutory regulation or exceeds the permitted use, you will need to obtain permission directly from the copyright holder.

